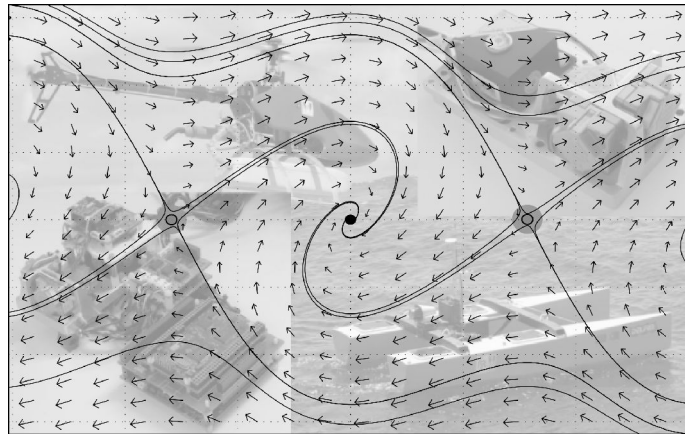




INSTITUTO  
SUPERIOR  
TÉCNICO

UNIVERSIDADE TÉCNICA DE LISBOA  
INSTITUTO SUPERIOR TÉCNICO



# Nonlinear Navigation System Design with Application to Autonomous Vehicles

**José Maria Fernandes Vasconcelos**  
(Licenciado)

Dissertação para a obtenção do Grau de Doutor em  
Engenharia Electrotécnica e de Computadores

**Orientador:** Doutor Carlos Jorge Ferreira Silvestre  
**Co-orientador:** Doutor Paulo Jorge Coelho Ramalho Oliveira

## Júri

**Presidente:** Presidente do Conselho Científico do IST

**Vogais:** Doutor Anders Rantzer  
Doutor Carlos Alberto Varelas da Rocha  
Doutora Maria Isabel Lobato de Faria Ribeiro  
Doutor Jorge Manuel Miranda Dias  
Doutor Carlos Jorge Ferreira Silvestre  
Doutor Paulo Jorge Coelho Ramalho Oliveira

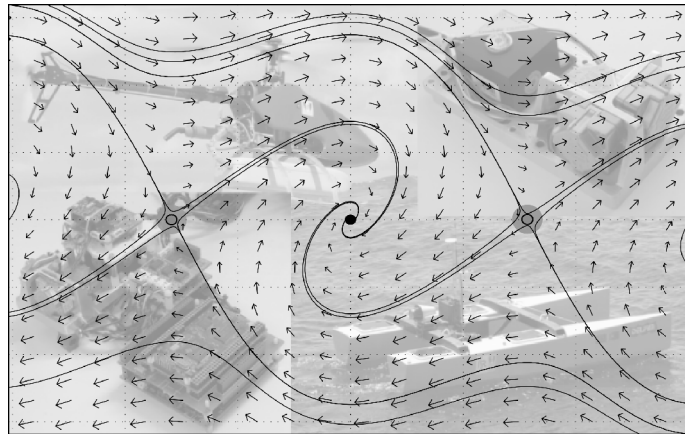
**Janeiro de 2010**





INSTITUTO  
SUPERIOR  
TÉCNICO

UNIVERSIDADE TÉCNICA DE LISBOA  
INSTITUTO SUPERIOR TÉCNICO



**Nonlinear Navigation System Design  
with Application to Autonomous Vehicles**

**José Maria Fernandes Vasconcelos**  
(Licenciado)

Dissertação para a obtenção do Grau de Doutor em  
Engenharia Electrotécnica e de Computadores

**Orientador:** Doutor Carlos Jorge Ferreira Silvestre  
**Co-orientador:** Doutor Paulo Jorge Coelho Ramalho Oliveira

**Júri**

**Presidente:** Presidente do Conselho Científico do IST

**Vogais:** Doutor Anders Rantzer  
Doutor Carlos Alberto Varelas da Rocha  
Doutora Maria Isabel Lobato de Faria Ribeiro  
Doutor Jorge Manuel Miranda Dias  
Doutor Carlos Jorge Ferreira Silvestre  
Doutor Paulo Jorge Coelho Ramalho Oliveira

**Janeiro de 2010**





“We observe a fraction of the process, like hearing a single string in an orchestra of supergiants. We know, but cannot grasp, that above and below, beyond the limits of perception or imagination, thousands and millions of simultaneous transformations are at work, interlinked like a musical score by mathematical counterpoint.”

- Stanislaw Lem, *Solaris*



# Abstract

This thesis addresses the design of nonlinear navigation systems for autonomous vehicles, following two main approaches: Kalman filter based estimators, and Lyapunov theory based nonlinear observers.

The proposed Kalman filter architectures are designed for accurate position and attitude estimation using low-cost sensor suites. An extended Kalman filter is adopted to merge a high accuracy inertial navigation system with advanced aiding information, namely *i)* frequency contents of vector measurements, *ii)* vehicle model dynamics, and *iii)* LASER range measurements. In alternative, simple yet effective multirate complementary Kalman filters are proposed, endowed with stability and performance properties. The navigation systems are validated using realistic vehicle simulators, and experimental data collected onboard the DELFIMx autonomous surface craft.

The second approach addresses the design of nonlinear observers in non-Euclidean spaces. The observers are derived resorting to Lyapunov theory, bearing stability and robustness properties in the presence of inertial sensor non-idealities. The considered sensor readings are provided by an inertial measurement unit and *i)* landmark measurements, *ii)* vector observations, and *iii)* GPS receivers. The regions of attraction are explicitly characterized, and an output feedback configuration is proposed, allowing for the practical implementation of the algorithms.

**Keywords:** Nonlinear observers, Lyapunov stability theory, Navigation systems, Kalman filters, Complementary filters, Autonomous vehicles.



# Resumo

Esta tese aborda o projecto de sistemas de navegação não-lineares para veículos autónomos, com recurso a duas metodologias: estimadores baseados em filtros de *Kalman*, e observadores não-lineares baseados em teoria de *Lyapunov*.

As arquitecturas de filtragem de *Kalman* são desenhadas para estimação precisa de posição e orientação, com recurso a sensores de baixo custo. As estimativas de um sistema de navegação inercial de alta precisão são processadas por um filtro de *Kalman* estendido, utilizando informação auxiliar como *i)* conteúdos na frequência de leituras vectoriais *ii)* modelo dinâmico de veículos, e *iii)* leituras de distância *LASER*. São também propostos filtros complementares de *Kalman*, com estrutura simples, dotados de garantias de estabilidade e de desempenho. Os sistemas de navegação são validados utilizando simuladores realistas de veículos e dados experimentais obtidos com o catamarã autónomo DELFIMx.

A segunda metodologia proposta assenta em observadores não-lineares formulados em variedades. Recorrendo à teoria de *Lyapunov*, os observadores derivados são estáveis e robustos a não-idealidades presentes na unidade de medida inercial. Os dispositivos sensoriais auxiliares considerados são *i)* leitura de marcas, *ii)* observações vectoriais, e *iii)* receptores de GPS. A determinação de regiões de atracção explícitas, e a possibilidade de utilização directa do dados dos sensores auxiliares permitem a implementação prática dos algoritmos.

**Palavras-chave:** Observadores não-lineares, Teoria de estabilidade de *Lyapunov*, Sistemas de navegação, Filtros de *Kalman*, Filtros complementares, Veículos autónomos.



# Acknowledgments

First and foremost, I would like to express my gratitude to my thesis supervisor, Professor Carlos Silvestre. Under his stimulating guidance, I was introduced to the exciting world of scientific research, exposed to challenging problems, and taught valuable research methods. I also owe much to his unusual ability of overcoming difficulties and boosting achievements. The thesis supervision was strengthened by the enthusiastic support of my co-advisor, Professor Paulo Oliveira, that provided timely comments, suggestions, and criticisms, and was always open to passionate discussions and good laughs.

Among the decisive moments in the making of this thesis, I'm grateful to Professor João Sentieiro for encouraging me to pursue a PhD, and for keeping in touch throughout these years. Professor Michael Athans was a cornerstone in my personal development, whose supportive and provocative discussions helped me grow more confident and broadened my researcher skills. Besides his enlightening insights over many matters, Professor Athans is a living encyclopedia of control theory and a wonderful storyteller, and I hope that someday he will present the scientific community with his memoirs.

I would also like to acknowledge the follow-up thesis committee, Professor Maria Isabel Ribeiro and Professor José Leitão, for the interesting comments and for supporting the thesis proposal. I also wish to thank Professor António Pascoal, Professor João Miranda Lemos, Professor João Xavier, and Professor Pedro Aguiar for enlightening discussions.

During the course of this PhD thesis, I was given the exciting opportunity to study abroad, and had the joy of learning and working with Professor Gabriel Elkaim at University of California Santa Cruz, and with Professor Anders Rantzer at Lund University. I felt very welcome, and the exposure to new working environments enriched my research practices. I am grateful to Professor Elkaim for his friendship and enthusiastic approach to engineering problems, and to Professor Rantzer for his interest in the nonlinear attitude observer and for daring me to derive new theoretical results using his mathematical tools.

The creative ideas and work of Bruno Guerreiro, Pedro Batista, Rita Cunha, and Sérgio Brás were instrumental for the success of our joint papers. A special word goes to the co-authors Bruno Carneira, Marco Morgado, and Sajjad Fekri for building a strong friendship that will surely stand the test of time and distance.

The DSOR laboratory was a fun and stimulating place to work in thanks to Alex Alcocer Peñas, André Oliveira, David Cabecinhas, Duarte Antunes, Francisco Curado, João Alves, João Almeida, Luís Sebastião, Manuel Rufino, Nuno Paulino, Paulo Rosa, Pedro

Gomes, Pedro Serra, Reza Ghabcheloo, and Tiago Gaspar. Lunch and coffee time were more diverse whenever Alberto Vale, Andreas Häusler, Francesco Vanni, Manuel Marques, Mohammadreza Bayat, Nelson Martins, Pramod Maurya, Ricardo Ferreira, Vahid Hassani, or Victor Silva were around.

Outside the academic domain, my friends Adélia, Filipe, João Neto, João Pequeno, and Sérgio gave me all the optimism and motivation a friend can give, and I'm indebted for their moral support and tolerance to non-returned phone calls. The last thanks go to my family. To my mother and my father, for raising me with their love and providing wise advice. To my brothers, for showing other worlds when research was becoming the absolute reference. And to my wife Ana for her uniqueness.

### **Financial support**

This work was financially supported by Fundação para a Ciência e a Tecnologia and by the European Social Fund under the Community Support Framework III.



# Contents

<b>Abstract</b>	<b>i</b>
<b>Resumo</b>	<b>iii</b>
<b>Acknowledgments</b>	<b>v</b>
<b>Notation</b>	<b>xix</b>
<b>1 Introduction</b>	<b>1</b>
1.1 Kalman filtering based navigation systems . . . . .	2
1.1.1 Advanced aiding techniques for EKF/INS architectures . . . . .	4
1.1.2 Nonlinear complementary Kalman filter . . . . .	9
1.2 Lyapunov based navigation system design . . . . .	10
1.2.1 Nonlinear observers for attitude and position estimation . . . . .	12
1.2.2 New results for stability analysis of nonlinear systems . . . . .	15
1.3 Thesis outline . . . . .	17
<b>2 INS/GPS aided by frequency contents of vector observations</b>	<b>19</b>
2.1 Inertial navigation system algorithm . . . . .	21
2.2 Inertial error dynamics . . . . .	23
2.3 Vector aiding techniques . . . . .	24
2.3.1 Vector measurement residual model . . . . .	25
2.3.2 Magnetic and pendular measurements integration . . . . .	26
2.4 Implementation . . . . .	29
2.5 Simulation results . . . . .	31
2.5.1 Initial calibration error . . . . .	32
2.5.2 Linear accelerated motion . . . . .	33
2.5.3 Trimming trajectory . . . . .	33
2.6 Experimental results . . . . .	34
2.6.1 Experimental results analysis . . . . .	34
2.7 Conclusion . . . . .	43

<b>3</b>	<b>Embedded UAV Model and LASER aiding techniques for high accuracy inertial navigation systems</b>	<b>45</b>
3.1	Navigation system structure . . . . .	47
3.1.1	Inertial navigation system . . . . .	47
3.1.2	Extended Kalman Filter . . . . .	48
3.2	Vehicle model aiding . . . . .	50
3.2.1	Rigid body dynamics . . . . .	50
3.2.2	External vehicle model aiding . . . . .	51
3.2.3	Embedded vehicle model aiding . . . . .	53
3.3	LASER aiding . . . . .	56
3.4	Implementation . . . . .	58
3.4.1	EKF/INS state model . . . . .	58
3.4.2	Vehicle model aiding . . . . .	59
3.4.3	LASER aiding . . . . .	62
3.4.4	State model discretization . . . . .	63
3.4.5	State estimation and error compensation . . . . .	63
3.5	Simulation results . . . . .	64
3.5.1	Vehicle model aiding . . . . .	65
3.5.2	Vario X-Treme helicopter . . . . .	70
3.5.3	LASER aiding . . . . .	76
3.6	Conclusions . . . . .	77
<b>4</b>	<b>Complementary Kalman filter based navigation system</b>	<b>79</b>
4.1	Attitude and position complementary filters . . . . .	80
4.1.1	Attitude filter . . . . .	80
4.1.2	Position filter . . . . .	85
4.2	Navigation system implementation . . . . .	89
4.2.1	Magneto-pendular sensor . . . . .	90
4.2.2	Complementary filter coupling . . . . .	91
4.2.3	Multirate filtering . . . . .	92
4.3	Experimental results . . . . .	93
4.3.1	Filter parameter design . . . . .	94
4.3.2	Experimental results analysis . . . . .	95
4.4	Conclusions . . . . .	101
<b>5</b>	<b>Landmark based nonlinear navigation system</b>	<b>105</b>
5.1	Problem formulation . . . . .	106
5.2	Observer synthesis with ideal velocity measurements . . . . .	108
5.2.1	Synthesis Lyapunov function properties . . . . .	108
5.2.2	Attitude feedback law . . . . .	111
5.2.3	Position feedback law . . . . .	114

5.2.4	Output feedback configuration . . . . .	116
5.2.5	Directionality of the observer estimates . . . . .	117
5.3	Observer synthesis with biased velocity readings . . . . .	119
5.3.1	Biased linear velocity readings . . . . .	119
5.3.2	Biased linear and angular velocity readings . . . . .	121
5.3.3	Output feedback configuration . . . . .	126
5.4	Simulations . . . . .	127
5.4.1	Ideal velocity readings . . . . .	127
5.4.2	Biased velocity readings . . . . .	130
5.5	Conclusions . . . . .	133
<b>6</b>	<b>Nonlinear attitude observer using vector observations</b>	<b>135</b>
6.1	Synthesis Lyapunov function . . . . .	136
6.1.1	Vector measurements model . . . . .	136
6.1.2	Lyapunov function . . . . .	137
6.2	Observer synthesis . . . . .	138
6.2.1	Unbiased angular velocity measurements . . . . .	138
6.2.2	Biased angular velocity measurements . . . . .	140
6.2.3	Output feedback configuration . . . . .	144
6.3	Simulations . . . . .	145
6.4	Conclusions . . . . .	147
<b>7</b>	<b>Combination of Lyapunov and density functions for stability analysis with application to a nonlinear attitude observer</b>	<b>149</b>
7.1	Attitude observer . . . . .	149
7.2	Stability in the presence of unmodeled inputs . . . . .	151
7.2.1	Almost ISS using Lyapunov and density functions . . . . .	151
7.2.2	Stability of the nonlinear observer in the presence of inertial sensor noise . . . . .	154
7.3	Local stability analysis using density functions . . . . .	159
7.3.1	Stability using density functions and LaSalle’s invariance principle . . . . .	159
7.3.2	Stability of the nonlinear observer in the presence of biased inertial readings . . . . .	161
7.4	Conclusions . . . . .	163
<b>8</b>	<b>GPS/IMU based nonlinear navigation system</b>	<b>165</b>
8.1	Sensor description . . . . .	166
8.2	Observer architecture . . . . .	166
8.2.1	Attitude observer . . . . .	168
8.2.2	Position observer . . . . .	172
8.2.3	Stability in the presence of inertial sensor noise . . . . .	175
8.3	Simulations . . . . .	176

8.4	Conclusions . . . . .	180
<b>9</b>	<b>Concluding remarks</b>	<b>181</b>
9.1	Directions for future work . . . . .	184
<b>A</b>	<b>Matrix results</b>	<b>187</b>
A.1	Linear algebra . . . . .	187
A.2	Special orthogonal group . . . . .	187
<b>B</b>	<b>DELFIMx characteristics</b>	<b>189</b>
<b>C</b>	<b>Vario X-Treme helicopter model</b>	<b>193</b>
<b>D</b>	<b>Performance of the complementary attitude filter</b>	<b>197</b>
<b>E</b>	<b>Extensions of the landmark based nonlinear observer</b>	<b>199</b>
E.1	Position estimation in Earth coordinate frame . . . . .	199
E.2	Landmark coordinate transformation with minimal set of landmarks . . . . .	203
<b>F</b>	<b>Uniform exponential stability of parameterized time-varying systems</b>	<b>205</b>
<b>G</b>	<b>Directionality of the vector based nonlinear attitude observer</b>	<b>207</b>
<b>H</b>	<b>Supporting results for density function methods</b>	<b>213</b>
H.1	Stability of nonlinear systems . . . . .	213
H.2	Set measure results . . . . .	214
H.3	Divergence of vector fields defined on $SO(3)$ . . . . .	215
<b>I</b>	<b>Closed-form solution to the pseudorange equations</b>	<b>217</b>
<b>J</b>	<b>Exponential stability of a cascade system</b>	<b>219</b>
<b>K</b>	<b>Magnetometer calibration in sensor frame</b>	<b>223</b>
K.1	Introduction to magnetometer calibration . . . . .	223
K.2	Magnetometer calibration and alignment . . . . .	225
K.2.1	Magnetometer errors characterization . . . . .	226
K.2.2	Magnetometer error parameterization . . . . .	227
K.2.3	Magnetometer calibration . . . . .	229
K.2.4	Magnetometer alignment . . . . .	232
K.3	Algorithm implementation and results . . . . .	233
K.3.1	Simulation results . . . . .	233
K.3.2	Experimental results . . . . .	236
K.4	Auxiliary results . . . . .	238
K.4.1	External magnetic noise . . . . .	238
K.4.2	Likelihood function derivatives . . . . .	238

<b>Bibliography</b>	<b>241</b>
<b>Publications</b>	<b>253</b>



# List of Figures

1.1	Thesis outline, organized according to the proposed navigation systems. The chapters numbers associated with each topic are identified in brackets.	3
1.2	Feedback configuration of an EKF/INS architecture. . . . .	4
1.3	Classical architecture of an EKF/INS aided by vehicle dynamics. . . . .	5
1.4	Navigation system using advanced vector observation integration. . . . .	6
1.5	Proposed EKF/INS architecture aided by embedded vehicle dynamics. . . .	7
1.6	Complementary filter block diagram. . . . .	9
1.7	Representation of an unwinding phenomenon described in [13]. . . . .	11
1.8	Illustration of topological limitation to global stabilization on manifolds. . .	12
1.9	Adopted sensors and estimated quantities of the nonlinear observers based on landmark measurements and vector observations. . . . .	13
1.10	Structure of the GPS/IMU based nonlinear navigation system. . . . .	15
2.1	Navigation system block diagram. . . . .	20
2.2	Inertial navigation system with estimation error compensation. . . . .	22
2.3	Vector measurement residual computation (magnetometer and pendular readings). . . . .	27
2.4	Linear acceleration modeling. . . . .	28
2.5	Initial estimation error compensation. . . . .	32
2.6	Linear accelerated motion compensation results. . . . .	33
2.7	Trimming trajectory results. . . . .	35
2.8	Position results for sparse GPS signal, sampled at 0.2 Hz. . . . .	35
2.9	Measured and estimated DELFIMx trajectory. . . . .	36
2.10	Attitude estimation results (DELFIMx trajectory). . . . .	37
2.11	Velocity estimation results (DELFIMx trajectory). . . . .	37
2.12	Bias estimation results (DELFIMx trajectory). . . . .	38
2.13	Frequency contents of the pendular reading and estimated linear acceleration.	39
2.14	Frequency contents of the pendular reading and estimated linear accelera- tion (low frequency region). . . . .	39
2.15	Measured and estimated DELFIMx trajectory with GPS outage. . . . .	40
2.16	Estimated and measured position at the time intervals of the GPS outage. .	41

2.17	Difference between the estimated and the measured positions, with GPS outage (DELFINx trajectory). . . . .	42
3.1	Navigation system block diagram. . . . .	46
3.2	External vehicle model aiding for the 6-DOF rigid body polyhedron. . . . .	53
3.3	Embedded vehicle model aiding for the 6-DOF rigid body polyhedron. . . . .	55
3.4	LASER range finder reading ( ${}^B_M \mathbf{R} = \mathbf{I}$ ). . . . .	56
3.5	Rigid body trimming trajectory. . . . .	65
3.6	Bias estimation errors of the GPS and the VD aided navigation systems (rigid body, magnetometer on). . . . .	66
3.7	Rate gyro bias estimation error of the GPS and the VD aided navigation systems (Rigid body, Magnetometer off). . . . .	67
3.8	Velocity estimation errors of the GPS and the VD aided navigation systems (rigid body, magnetometer on). . . . .	68
3.9	Vario X-Treme model-scale helicopter. . . . .	71
3.10	Vario X-Treme simulated trajectory. . . . .	72
3.11	Vario X-Treme VD vs GPS aiding estimation errors (solid line) and estimated error standard deviation (dashed line). . . . .	73
3.12	Vario X-Treme VD vs GPS aiding estimation errors (solid line) and estimated error standard deviation (dashed line). . . . .	74
3.13	Trajectory estimation for the Vario X-Treme. . . . .	75
3.14	LASER aiding estimation errors (solid line) and estimated error standard deviation (dashed line). . . . .	77
3.15	LASER aiding estimation errors (solid line) and estimated error standard deviation (dashed line). . . . .	78
4.1	Complementary filter block diagram. . . . .	79
4.2	Attitude complementary filter. . . . .	81
4.3	Position complementary filter. . . . .	87
4.4	Navigation system architecture. . . . .	89
4.5	Complementary filter transfer functions. . . . .	94
4.6	Attitude filter performance ( $T = \frac{1}{56}$ s). . . . .	95
4.7	DELFINx trajectory estimation results. . . . .	96
4.8	Attitude estimation results. . . . .	96
4.9	Linear and angular velocity estimation results. . . . .	97
4.10	Slalom maneuver at [760 880] s. . . . .	98
4.11	Rate gyro bias estimation. . . . .	99
4.12	DELFINx trajectory estimation results (GPS signal jamming). . . . .	99
4.13	Details of the estimated trajectory with GPS outage. . . . .	100
4.14	Spectrograms of the yaw measurements and filter estimate. . . . .	102
4.15	Spectrograms of the pitch measurements and filter estimate. . . . .	103
4.16	Spectrograms of the $\mathbf{p}_x$ measurements and filter estimate. . . . .	104



5.1	Landmark based navigation. . . . .	106
5.2	Landmark placement. . . . .	128
5.3	Attitude estimation error and exponential convergence bounds for diverse landmark coordinate transformations (ideal velocity readings, $\phi(t_0) = \frac{1}{\sqrt{3}}\mathbf{1}'$ ). . . . .	129
5.4	Euler axis trajectories on $S(2)$ . . . . .	129
5.5	Error of the position estimate with respect to local and to Earth frames (ideal velocity readings, $\varphi(t_0) = \frac{1}{3}\pi$ rad, $\phi(t_0) = \frac{1}{\sqrt{3}}\mathbf{1}_3$ ). . . . .	130
5.6	Estimation errors ( $\tilde{\mathbf{b}}_v \neq 0, \tilde{\mathbf{b}}_\omega = 0$ ). . . . .	131
5.7	Estimation errors ( $\tilde{\mathbf{b}}_v \neq 0, \tilde{\mathbf{b}}_\omega \neq 0$ ). . . . .	132
5.8	Exponential convergence of $V_b$ (biased linear and angular velocity measurements). . . . .	133
6.1	Attitude and bias estimation errors. . . . .	146
6.2	Exponential convergence of $V_b$ ( $\varphi(t_0) = \frac{3\pi}{4}$ , $\tilde{\mathbf{b}}_\omega \neq 0$ ). . . . .	147
7.1	Combination of Lyapunov and density functions for almost ISS of the origin. . . . .	153
7.2	Region of convergence as a function of the noise to gain ratio $\frac{\ \mathbf{d}_\omega\ _\infty}{k_\omega}$ . . . . .	155
7.3	Simulation results of the attitude observer, illustrating almost ISS. Convergence for $\ \mathbf{I} - \tilde{\mathcal{R}}(t_0)\ ^2 \leq r(d_{\max})$ is guaranteed by Lyapunov methods; convergence for $\ \mathbf{I} - \tilde{\mathcal{R}}(t_0)\ ^2 > r(d_{\max})$ is guaranteed by combining Lyapunov and density functions. . . . .	159
7.4	Phase portrait of the reduced order attitude observer. Using the density function property $\text{div}(\rho f) > 0$ in a neighborhood of the equilibrium points $(\varphi, b) = (\pi + 2\pi k, 0)$ , $k \in \mathbb{Z}$ , shows that these are unstable. . . . .	162
8.1	Navigation system configuration. . . . .	167
8.2	Cascaded position and attitude observer. . . . .	168
8.3	Body fixed vectors, defined by the position of the GPS receivers. . . . .	169
8.4	Attitude and bias estimation (biased angular velocity readings). . . . .	177
8.5	Position and velocity estimation (biased angular velocity readings). . . . .	178
8.6	Attitude, position and velocity estimation (inertial sensor noise). . . . .	179
B.1	The DELFIMx autonomous surface craft (length: 4.5 m; width: 2.45 m; mass: 300 Kg). . . . .	190
B.2	Hardware and sensors installed onboard the DELFIMx ASC. . . . .	190
E.1	Landmark configurations described by Assumption E.1 and Corollary E.2. . . . .	202
K.1	Affine transformation of a two dimensional sphere. . . . .	228
K.2	Alignment estimation ambiguity with two vector readings. . . . .	233
K.3	Ellipsoid fitting (simulation data). . . . .	234
K.4	Convergence of the log-likelihood function (arch shaped data). . . . .	235
K.5	Convergence of the log-likelihood gradient (arch shaped data). . . . .	235

K.6	Estimation error vs. signal-to-noise ratio (100 MC, ring shaped data). . . .	236
K.7	Ellipsoid fitting (real data). . . . .	237
K.8	Magnetometer data fitting. . . . .	237

# List of Tables

2.1	Sensor non-idealities. . . . .	31
2.2	Filter results, straight path trajectory. . . . .	33
2.3	Filter results, trimming trajectory. . . . .	35
2.4	Position drift due to GPS outage. . . . .	40
3.1	Comparison of the vehicle model aiding techniques with a standard GPS aided IMU. . . . .	61
3.2	Sensor non-idealities. . . . .	64
3.3	Rigid body characteristics. . . . .	65
3.4	Velocity estimation error (rigid body). . . . .	69
3.5	Position estimation error (rigid body). . . . .	69
3.6	Attitude estimation error (rigid body). . . . .	69
3.7	Estimation error for the embedded VD aiding, $B\mathbf{v}$ observation only (rigid body). . . . .	70
3.8	Execution time of the navigation systems for 200s of simulation time. . . . .	70
3.9	Velocity estimation error (Vario X-Treme helicopter). . . . .	71
3.10	Position estimation error (Vario X-Treme helicopter). . . . .	71
3.11	Attitude estimation error (Vario X-Treme helicopter). . . . .	74
3.12	Estimation error for the embedded VD aiding, $B\mathbf{v}$ observation only (Vario X-Treme helicopter). . . . .	75
4.1	Complementary filter parameters. . . . .	94
4.2	GPS outage results. . . . .	101
K.1	Calibration results (gradient method). . . . .	234
K.2	Calibration results (Newton method). . . . .	234



# Notation

The notation used in this work is fairly standard. A list of conventions, definitions, symbols, and quantities frequently adopted is listed in the ensuing.

## Notational Conventions

- Column vectors are denoted by lowercase boldface type, e.g.  $\mathbf{s}$ .
- Matrices are denoted by uppercase boldface type, e.g.  $\mathbf{S}$ .
- Matrix dimensionality subscripts are omitted whenever clear from the context.

## Cartesian Coordinate Frames

$\{B\}$	body frame.
$\{E\}$	Earth frame.
$\{L\}$	local frame.

## Sets

$B(n)$	$n$ -dimensional ball, $\{\mathbf{x} \in \mathbb{R}^n : \mathbf{x}'\mathbf{x} \leq 1\}$ .
$D(n)$	set of diagonal matrices, $\{\mathbf{S} \in M(n) : \mathbf{S} = \text{diag}(\mathbf{s}), \mathbf{s} \in \mathbb{R}^n\}$ .
$D^+(n)$	set of diagonal, positive definite matrices, $\{\mathbf{S} \in D(n) : \mathbf{S} > 0\}$ .
$K(n)$	set of skew-symmetric matrices, $\{\mathbf{K} \in M(n) : \mathbf{K} = -\mathbf{K}'\}$ .
$L(n)$	set of symmetric matrices, $\{\mathbf{S} \in L(n) : \mathbf{S} = \mathbf{S}'\}$ .
$M(n, m)$	set of $n \times m$ matrices with real entries.
$M(n)$	set of $n \times n$ matrices with real entries, $\{\mathbf{M} \in M(n, n)\}$ .
$O(n)$	set of orthogonal matrices, $\{\mathbf{U} \in M(n) : \mathbf{U}'\mathbf{U} = \mathbf{I}_n\}$ .
$S(n)$	$n$ -dimensional sphere, $\{\mathbf{x} \in \mathbb{R}^{n+1} : \mathbf{x}'\mathbf{x} = 1\}$ .
$SO(n)$	set of special orthogonal matrices, $\{\mathbf{R} \in O(n) : \det(\mathbf{R}) = 1\}$ .
$SE(n)$	set of special Euclidean matrices, i.e. the product space of $SO(n)$ with $\mathbb{R}^n$ .
$\mathbb{R}$	set of real numbers.
$\mathbb{R}^n$	set of $n$ -dimensional column vectors with real entries.

$\mathbb{Z}$  set of integers.

## Symbols

$\mathbf{a}$	acceleration expressed in $\{E\}$ .
$\mathbf{a}_{\text{SF}}$	accelerometer measurement (specific force), expressed in $\{B\}$ .
$\alpha_i(\mathbf{S})$	$i$ th largest eigenvalue of $\mathbf{S}$ having real eigenvalues.
$\mathbf{b}_s$	bias of the sensor measuring $\mathbf{s}$ , expressed in $\{B\}$ .
$b_\rho$	pseudorange measurement bias.
$\mathbf{e}_i$	unit norm vector with element $e_i = 1$ .
$\mathbf{g}$	Earth's gravitic field expressed in $\{E\}$ .
$h$	height.
$\mathbf{I}_n$	$n \times n$ identity matrix.
$\boldsymbol{\lambda}$	vector of the Z-Y-X Euler angles, i.e. $\boldsymbol{\lambda} = [\psi \theta \phi]$ .
$\mathbf{m}$	Earth's magnetic field expressed in $\{E\}$ .
$\mathbf{n}_s$	measurement or process noise associated with $\mathbf{s}$ .
$\mathcal{N}(\boldsymbol{\mu}, \boldsymbol{\Xi})$	Gaussian distribution with mean $\boldsymbol{\mu}$ and covariance $\boldsymbol{\Xi}$ .
$\mathcal{N}(\mathbf{S})$	null space of $\mathbf{S}$ .
$\boldsymbol{\omega}$	angular velocity of $\{B\}$ with respect to $\{E\}$ , expressed in $\{B\}$ .
$\mathbf{1}_{m \times n}$	$m \times n$ matrix with all entries equal to 1.
$\mathbf{1}_m$	shorthand notation for $\mathbf{1}_{m \times 1}$ .
$\mathbf{p}$	position expressed in $\{E\}$ .
$\phi$	roll angle.
$\boldsymbol{\phi}$	unit vector of the Euler angle-axis attitude parameterization.
$\varphi$	angle of the Euler angle-axis attitude parameterization.
$\psi$	yaw angle.
$\mathbf{q}$	landmark coordinates expressed in $\{B\}$ .
$\mathbf{Q}(\boldsymbol{\lambda})$	transformation from angular rate to Euler angle rate.
${}_{A_1}^{A_2}\mathbf{R}$	rotation matrix from coordinate frame $\{A_1\}$ to coordinate frame $\{A_2\}$ .
$\rho_{ij}$	pseudorange measurement of receiver $j$ with respect to satellite $i$ .
$\mathcal{R}$	shorthand notation for ${}^E_B\mathbf{R}$ .
$\sigma_i(\mathbf{S})$	$i$ th largest singular value of $\mathbf{S}$ .
$t$	time.
$\theta$	pitch angle.
$\mathbf{v}$	velocity expressed in $\{E\}$ .
$\mathbf{0}_{m \times n}$	$m \times n$ matrix with all entries equal to 0.
$\mathbf{0}_m$	shorthand notation for $\mathbf{0}_{m \times 1}$ .
$0_M$	origin of manifold $M$ .
$\mathbf{z}_s$	Kalman filter measurement residual of $\mathbf{s}$ .
$\hat{\mathbf{s}}$	estimate of vector $\mathbf{s}$ .
$\delta\mathbf{s}$	perturbation of vector $\mathbf{s}$ , defined as $\delta\mathbf{s} = \hat{\mathbf{s}} - \mathbf{s}$ unless otherwise noted.

$\tilde{\mathbf{s}}$  estimation error of vector  $\mathbf{s}$ .

## Subscripts and Superscripts

$f(x)|_{x_0}$  function  $f(x)$  evaluated at point  $x_0$ .  
 $[s_{ij}]$  matrix with element  $s_{ij}$  in row  $i$  and column  $j$ .  
 $s_{ij}$  element in row  $i$  and column  $j$  of matrix  $\mathbf{S}$ .  
 $s_i$   $i$ th element of vector  $\mathbf{s}$ .  
 $\mathbf{s}_k$  vector  $\mathbf{s}$  at the discrete-time instant  $t_k$ ,  $k \in \mathbb{Z}$ .  
 $\mathbf{s}_r$  measurement of vector  $\mathbf{s}$ .  
 $s_x, s_y, s_z$  x-, y- and z-axis components of the  $3 \times 1$  vector  $\mathbf{s}$ .  
 ${}^A\mathbf{s}$  vector represented in coordinate frame  $\{A\}$ .  
 ${}^B\dot{\mathbf{s}}$  derivative of  ${}^B\mathbf{s}$ , i.e.  $\frac{d{}^B\mathbf{s}}{dt}$ .  
 ${}^B(\dot{\mathbf{s}})$  derivative of  $\mathbf{s}$  expressed in  $\{B\}$ , i.e.  ${}^B(\frac{d\mathbf{s}}{dt})$ .  
 $\hat{\mathbf{s}}_k^-$  predicted estimate of vector  $\mathbf{s}$ .  
 $\hat{\mathbf{s}}_k^+$  updated estimate of vector  $\mathbf{s}$ .

## Functions

$\mathbf{S}^{-1}$  inverse of  $\mathbf{S}$ .

$\mathbf{S}'$  transpose of  $\mathbf{S}$ .

$(\mathbf{s})_\times$  cross-product matrix of the  $3 \times 1$  vector  $\mathbf{s}$ , defined as 
$$\begin{bmatrix} 0 & -s_z & s_y \\ s_z & 0 & -s_x \\ -s_y & s_x & 0 \end{bmatrix}.$$

$E(\cdot)$  expected value.

$\text{blkdiag}(\cdot)$  block diagonal concatenation of matrices.

$\text{diag}(\mathbf{s})$  diagonal matrix with  $i$ th diagonal element given by  $s_i$ .

$\text{div}(\cdot)$  divergence operator [85, 121].

$\text{eigvec}(\cdot)$  set of eigenvectors.

$\|\cdot\|$  Frobenius norm.

$|\cdot|$  absolute value.

$\text{rank}(\cdot)$  rank.

$\text{rot}(\varphi, \phi)$  rotation matrix parameterized by Euler angle-axis coordinates  $\varphi$  and  $\phi$ .

$\text{sign}(s)$  sign of  $s$ , i.e.  $\frac{s}{|s|}$  if  $s \neq 0$ , 0 if  $s = 0$ .

$\text{span}(\cdot)$  span.

$\text{tr}(\cdot)$  trace.

$(\cdot)_\otimes$  unskew operator such that  $((\mathbf{s})_\times)_\otimes = \mathbf{s}$ ,  $\mathbf{s} \in \mathbb{R}^3$ .

$\text{vec}(\cdot)$  vector obtained by stacking the columns of a matrix from left to right.

## Acronyms

a.a.	almost all.
aGAS	almost Globally Asymptotically Stable.
aISS	almost Input-to-State Stable.
ASC	Autonomous Surface Craft.
CKF	Complementary Kalman Filter.
DCM	Direction Cosine Matrix.
DSP	Digital Signal Processing.
EKF	Extended Kalman Filter.
ES	Exponentially Stable.
GAS	Globally Asymptotically Stable.
GES	Globally Exponentially Stable.
GPS	Global Positioning System.
IMU	Inertial Measurement Unit.
INS	Inertial Navigation System.
ISS	Input-to-State Stable.
KF	Kalman Filter.
LASER	Light Amplification by Stimulated Emission of Radiation.
LTI	Linear Time-Invariant.
LTV	Linear Time-Varying.
MEKF	Multiplicative Extended Kalman Filter.
MLE	Maximum Likelihood Estimator.
PSD	Power Spectral Density.
RMS	Root Mean Square.
SVD	Singular Value Decomposition.
UAV	Uninhabited Air Vehicle.
UAS	Uniformly Asymptotically Stable.
UES	Uniformly Exponentially Stable.
VD	Vehicle Dynamics.
VTOL	Vertical Take-Off and Landing.



# Chapter 1

## Introduction

The latest technological developments bring about autonomous vehicles as versatile platforms, capable of performing a wide and valuable range of operational tasks in challenging scenarios. Autonomous surface crafts (ASCs) are increasingly being adopted for inspection of coastal areas and the maintenance of large critical semi-submerged infrastructures, like bridges and breakwaters. Likewise, unmanned air vehicles (UAVs) are being considered for coastal surveillance, power line monitoring, traffic watch, to domestic security, and search and rescue missions in extreme environments. Most of these operations are complex and expensive, and great emphasis is being placed on the use of autonomous vehicles as a cost-effective, high-quality solution.

These practical applications often demand for high performance, robust navigation systems to provide high resolution position and attitude localization. To satisfy the accuracy requirements, most autonomous vehicles are usually equipped with ultra light weight, low-cost, low-power strapdown systems, that integrate the information from the available sensors. The low-cost sensors found in these systems are strongly affected by non-idealities, such as bias and noise, that degrade the accuracy of the estimates in the short term. The severe limitations to open-loop estimation motivate the autonomous vehicles community to continuously develop new navigation algorithms, that take full advantage of the available data, compensate for sensor non-idealities, and satisfy stability and performance criteria.

This thesis studies the design of nonlinear navigation systems, for position and attitude determination of autonomous vehicles, using inertial sensors and advanced aiding information sources. The main contributions are:

- advanced aiding techniques for inertial navigation system/extended Kalman filtering (INS/EKF) architectures, that exploit the available models of the robotic platform. The characterization of the vehicle dynamics, provided by a state model or a frequency domain description, are integrated in the navigation system to produce high accuracy results. The integration techniques are computationally efficient and designed for implementation on low-cost hardware.
- nonlinear complementary Kalman filters for attitude and position estimation, en-

dowed with stability and performance properties. The frequency domain approach of complementary filters is combined with the stability and performance properties of Kalman filters, to yield a nonlinear attitude and position filter for autonomous surface crafts. A steady-state like architecture is formulated, bearing straightforward gain design, and filter implementation.

- nonlinear observers for the problem of attitude and position determination, using velocity and landmark readings. The rigorous formulation in non-Euclidean spaces where attitude is represented, namely  $SO(3)$ , allows for almost global stabilization of the estimation errors, and for stability and convergence properties with non-ideal velocity sensors. A technique for the derivation of the observers is proposed, based on a synthesis Lyapunov function conveniently defined by the measurement error of the aiding sensors.
- new stability results for nonlinear systems, based on the combination of density and Lyapunov functions. The dual characterizations of the state space trajectories, provided by Lyapunov and density functions, are combined to produce new analysis tools for almost global stability, and input-to-state stability of nonlinear systems. The proposed techniques are illustrated for nonlinear observers with disturbances in the velocity sensors.
- a nonlinear navigation system using an inertial measurement unit (IMU) aided by GPS receivers. The solution illustrates the results for nonlinear systems proposed in the thesis, for a classical navigation problem that is commonly addressed using Kalman filtering techniques.

As shown in the diagram of Fig. 1.1, the contributions of the thesis can be grouped in two approaches: Kalman filter based estimators, and nonlinear observers designed using Lyapunov methods. The following sections present a brief overview of these fields of research, and relate the contributions of the thesis with the latest development in those areas.

## 1.1 Kalman filtering based navigation systems

The first part of this work studies the design of high-performance, low-cost navigation systems based on Kalman filtering techniques. Kalman filtering is a classical estimation theory [4, 56, 69], widely adopted in attitude and position estimation [10, 22, 46, 62], and still subject to new advances in the present [35, 37, 54, 71]. Recent navigation systems for oceanic vehicles resorting to Kalman filtering are found in [2, 47, 48, 64, 86, 105, 132], and further references can be found in the valuable survey on ocean vehicle navigation [79]. The choice of Kalman filtering architectures ranges from classical methodologies, to recently proposed approaches [37]. As depicted in Fig. 1.1(a), the Kalman filtering techniques

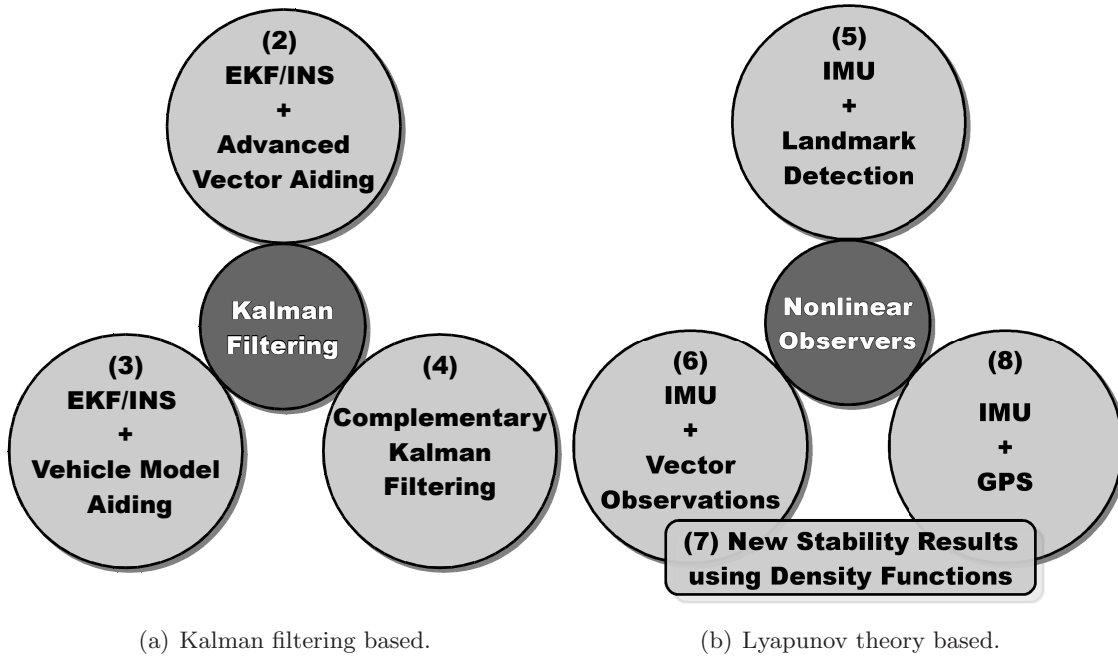


Figure 1.1: Thesis outline, organized according to the proposed navigation systems. The chapters numbers associated with each topic are identified in brackets.

considered in this thesis are the extended Kalman filter (EKF) and the complementary Kalman filter (CKF).

The EKF is one of the most well known and widely adopted filtering algorithms [37], based on the linearization of the system dynamics [56], and that keeps track of the global quantities by processing incremental estimates. The EKF algorithms adopted in this thesis merge aiding information with a low-cost inertial navigation system (INS), to produce high accuracy estimation results. While global positioning system (GPS) measurements are a common aiding source [22, 46, 62], this work studies the integration of diverse and advanced aiding information in the EKF/INS architecture. Namely, the efficient integration of vector observations, LASER measurements, vehicle dynamics model and frequency domain information is studied, allowing for accuracy enhancements of classical GPS aided EKF/INS architectures.

The proposed CKF architecture is focused on stability and performance, as well as ease of implementation. Although the EKF is one of the most widely adopted filtering algorithms, filter divergence due to the use of a linearized models can occur. The proposed CKF solution is derived for position and attitude estimation, endowed with stability and performance properties for operating conditions usually found in ASCs. Interestingly enough, the CKF is also a motivational approach to the nonlinear observers presented in the second part of the thesis.

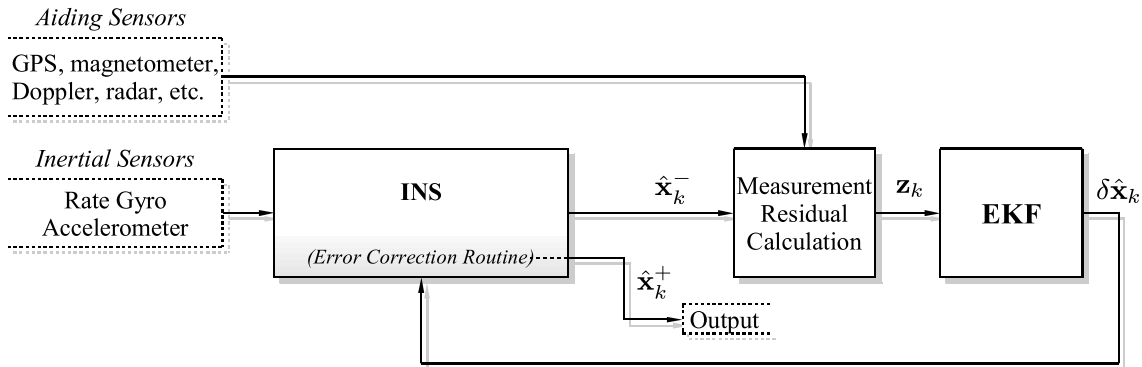


Figure 1.2: Feedback configuration of an EKF/INS architecture.

### 1.1.1 Advanced aiding techniques for EKF/INS architectures

The proposed EKF/INS system is based on the classical feedback configuration architecture [22], depicted in Fig. 1.2. The INS is a dead-reckoning algorithm that computes attitude, velocity and position by integrating rate gyro and accelerometer triads data [17, 20, 67, 68, 119, 120, 126, 127], rigidly mounted on the vehicle structure (strapdown configuration). For highly maneuverable vehicles, the INS numerical integration must properly address the fast dynamics of inertial sensors output, to avoid estimation errors buildup. High precision, multirate INS algorithms that accounts for high frequency attitude, velocity and position motions (denoted as coning, sculling and scrolling respectively), have been developed in [68, 126, 127], and a technique to convert the high accuracy attitude algorithms into its velocity/position counterpart was later proposed in [120].

Since the INS is based on open-loop integration of the inertial sensors, the resulting position and attitude estimates are corrupted by sensor bias and noise, among other error sources. A unified error analysis for INS can be found in the literature [20, 119]. Filtering techniques such as the EKF are adopted to dynamically compensate for non-ideal sensor characteristics, that otherwise would yield unbounded INS errors. The EKF compares the aiding sensor and vehicle model information with the INS output, under the form of a measurement residual. The inertial unit errors are compensated using a direct feedback configuration [22] illustrated in Fig. 1.2, where the error estimates are corrected internally in the INS, as opposed to correcting only the INS output. This method prevents the estimation error buildup, and hence preserves the validity of the linearized state model used in the EKF.

Navigation strategies based on GPS and INS fusion are commonly integrated using the EKF algorithm, see [10, 22, 46, 62, 119] and references therein. Classical GPS/INS architectures comprising inertial sensor biases estimation are found to hold only partial observability for a time-invariant configuration, as discussed in [59, 60]. The observability of position, attitude, and sensor non-idealities can be enhanced by using advanced filtering techniques to fully exploit aiding sensors, as well as information about the vehicle

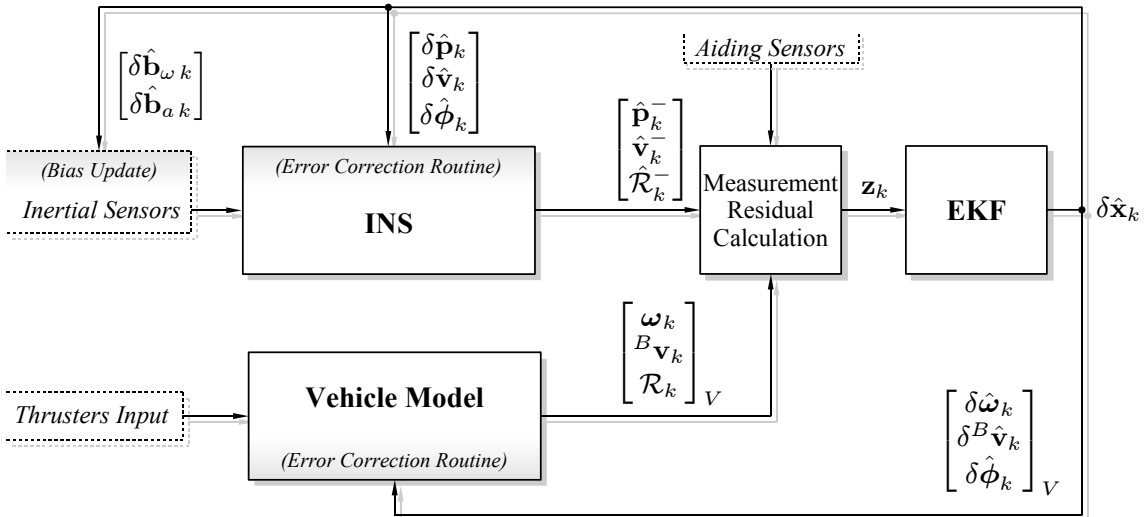


Figure 1.3: Classical architecture of an EKF/INS aided by vehicle dynamics.

dynamics.

Vehicle dynamics aiding is a software based solution that provides information about the vehicle motion, and is combined with the inertial navigation estimates using filtering techniques, allowing for the compensation of inertial estimation errors. This aiding technique can be adopted in nearly any application where the vehicle dynamics are known, bearing performance improvements on state variables that are critical for precise maneuvering. It is of paramount importance in indoor applications, urban scenarios, or hostile environments, where other aiding sensor can be inoperative or subject to jamming or distortion.

Simple motion constraints have been successfully implemented in the past for land vehicle applications, by introducing the concept of virtual observations, see [23, 42, 95]. Non-holonomic constraints of wheeled vehicles, namely the inability to takeoff or perform lateral translation, are exploited in the navigation system by inputting zero valued virtual measurements of the body frame  $y$  and  $z$  axes velocity. Full state, complex aircraft dynamics have been adopted to enhance the observability of the navigation system in recent work presented in [23, 82], and experimental results for a model-aided inertial navigation system for underwater vehicles can be found in [64].

The classical technique to integrate the vehicle in the EKF/INS architecture, described in [23, 64, 82] and illustrated in Fig. 1.3, is composed by a vehicle dynamics (VD) block that plays the role of an extra INS unit. In this configuration, the vehicle dynamics are computed by a vehicle model simulator, and the output is compared with the INS state estimates, producing a measurement residual that is processed by the EKF. The EKF state model is augmented to dynamically estimate both the INS and the VD errors, and error compensation routines are implemented in the VD and INS algorithms. The distinct nature of the error sources and system dynamics allows the EKF to separate the INS errors from the VD errors and to perform their mutual updating in the compensation routines.

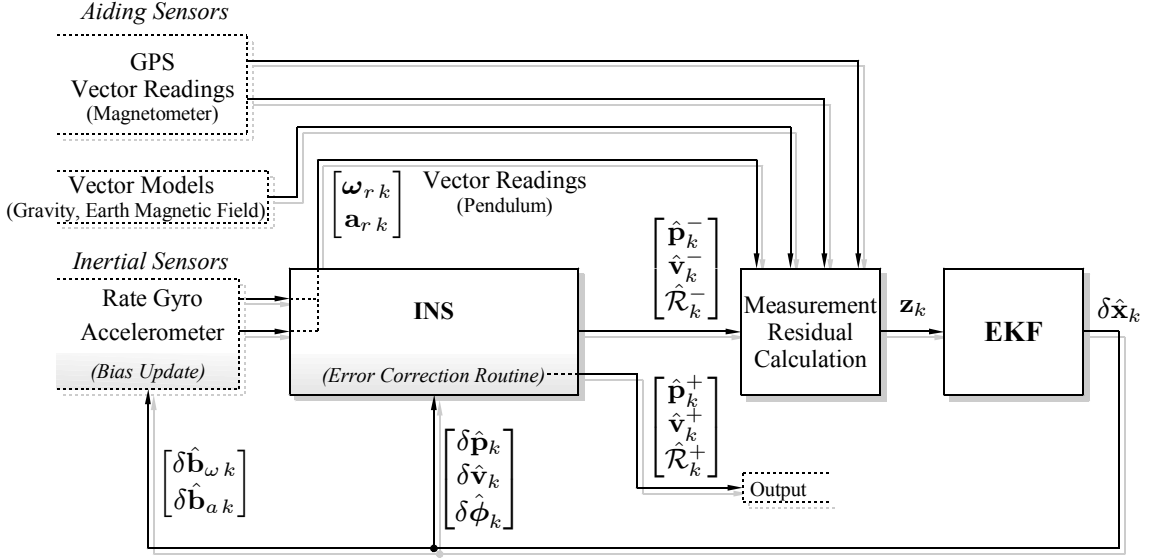


Figure 1.4: Navigation system using advanced vector observation integration.

Recalling the fundamentals of filtering and sensor fusion, the VD and INS ensemble is expected to yield better performance than any of the systems independently [82].

A limitation in complex vehicle dynamics lies in the modeling errors, over-parameterization of the model, and poor observability of the vehicle states, which degrades the filter performance, and that must be accounted for as state model uncertainty and/or using weak constraints. A discussion about the impact of process model complexity on the improvement of the navigation system performance is presented in [70]. In this reference, vehicle model aiding is shown to tackle state uncertainty, and it is evidenced that small improvements in the VD model are more relevant to the performance enhancement than the choice of aiding sensor suites.

The development of advanced aiding techniques for EKF/INS architectures is presented in Chapters 2 and 3. The aiding techniques studied in Chapter 2 exploit vector observations and frequency domain characterization of the autonomous vehicle. As illustrated in Fig. 1.4, aiding magnetic and pendular observations are integrated in the EKF, to compensate for inertial sensor non-idealities. Information about the vehicle is provided to the EKF, by modeling the pendular reading as the result of a gravitic measurement, and of disturbances due to the vehicle motion, that are characterized in the frequency domain. The proposed aiding techniques enhance the observability of the system errors, and hence allow the EKF to compensate the inertial sensor non-idealities, such as bias and noise, improving the attitude and position estimates.

The aiding techniques presented in Chapter 2 resort to a simple vehicle characterization in the frequency domain, that is straightforward to implement. In Chapter 3, a new methodology is derived to exploit the explicit, nonlinear dynamic model of the vehicle. Whereas the classical vehicle model integration method, illustrated in Fig. 1.3, considers a full state VD simulator and requires the estimation and compensation of the vehicle model

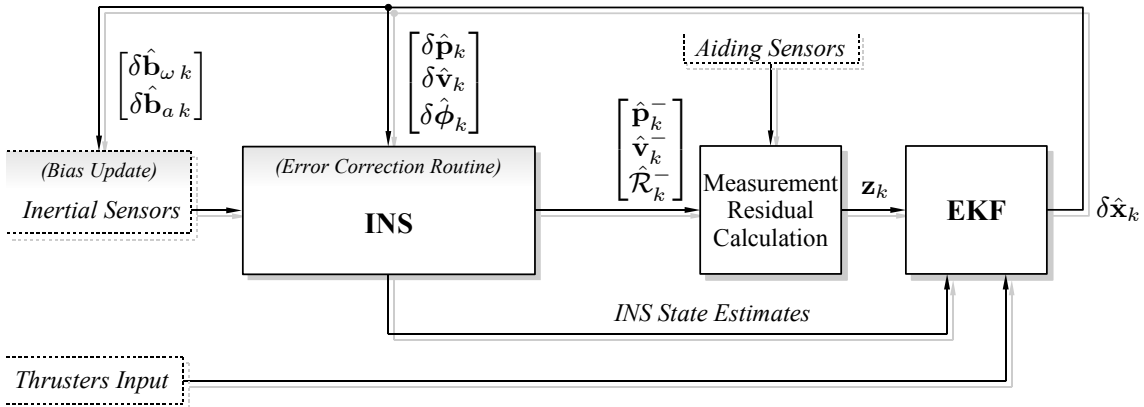


Figure 1.5: Proposed EKF/INS architecture aided by embedded vehicle dynamics.

errors, the new method integrates the VD directly in the EKF to estimate exclusively the INS errors, as shown in Fig. 1.5. The proposed technique is based on using the vehicle dynamics to propagate the INS state estimates, exploiting the redundancy of the information provided by the VD and by the INS integration algorithm.

The proposed technique reduces the computational load associated with the classical VD aiding, and introduces flexibility in the implementation of the vehicle model, while preserving the accuracy enhancements. Vehicle model differential equations are decoupled using the INS states in the VD computations, and it is possible to select only those dynamics that are more accurately modeled, or that yield relevant information. For example, the classical VD aiding technique computes the attitude kinematics in the INS and in the vehicle simulator [82], whereas the proposed VD aiding technique computes the attitude kinematics only in the INS. Also, in the proposed aiding technique, some of the vehicle differential equations are integrated numerically, while others are formulated directly as a filter measurement, which reduces the number of computations associated with the vehicle model aiding. The correction routines adopted in the classical vehicle model aiding, illustrated in Fig. 1.3, are not necessary in the proposed technique due to the embedding of the vehicle dynamics in the filter state model.

The integration of other aiding sources is also studied. A solution to integrate vector observations directly in the EKF is discussed. Although a snapshot attitude reconstruction can be obtained from the vector measurements using numerically efficient algorithms such as QUEST or TRIAD [8, 37, 129], the vector readings are fed directly to the Kalman filter. The measurement residual is obtained by comparing the estimated and measured vector observations, and it is modeled in the filter as a function of the attitude estimation error. Consequently, the EKF acts as an attitude determination algorithm, by computing the perturbational attitude term based on vector observations. Vector measurement characteristics, such as sensor noise covariance, are described directly in the filter state model, providing physical interpretation to the filter design parameters that are used in the computation of optimal gains. Also, a LASER range finder sensor implementation is

detailed, to estimate the coordinates of a target, necessary in structure surveillance, or to enhance the distance-to-ground estimation, critical for takeoff and landing maneuvers of aerial vehicles.

Interestingly enough, the navigation system architecture adopted in Chapters 2 and 3 comprises state-of-the-art EKF and INS algorithms. The adopted INS solution is a discrete-time, high accuracy integration algorithm, based on the work presented in [126, 127]. The inertial integration algorithm resorts to a multirate approach to properly account for high-order dynamic angular and acceleration effects, namely coning, sculling and scrolling. The high-frequency dynamics are accounted for in a high-speed computation that performs simple incremental updates, while the moderate-speed computations estimate the attitude and position using analytically exact formulations, that sum up the contribution of the high-speed and moderate-speed integrations.

The EKF developed in this work is based on the Multiplicative EKF (MEKF) [22, 99]. One of the caveats in Kalman filtering for attitude estimation lies in the use global attitude representations in the filter: linear Kalman filter operates in Euclidean spaces, and hence the update step violates the constraints of global attitude representations, such as the rotation matrix or the unit quaternion. Although projection methods can be used in the update process to force the normalization of the attitude representation [32, 33], the optimality of the measurement fusion process and the physical interpretation of the covariance matrix become arguable [37]. The problem of attitude representation is dealt with in the MEKF by adopting a perturbational representation of the attitude error, that is locally linear and non-singular. The linear differential equations of the filter are derived using a perturbational analysis of a rigid body kinematics, a detailed derivation of this classical methodology can be found in [20]. Consequently, the local attitude parameterization can be estimated by the Kalman filter, while a global attitude parameterization, such as the rotation matrix, is stored in the INS. As shown in Fig. 1.2, the estimated attitude error is transferred from the EKF to the INS to update the nonlinear global attitude estimate, and reset in the filter. This incremental procedure can be regarded as a storage technique that prevents the filter's attitude error estimates to fall outside the linearization region. As evidenced in [99], the uncertainty of the estimate, i.e. the estimation error covariance, is unaffected by the reset step.

The proposed EKF/INS architectures are designed for application to autonomous aerial and oceanic vehicles. The aiding techniques and the performance of the EKF/INS system proposed in Chapter 2 are assessed using experimental data, obtained at sea trials with a low-cost hardware architecture installed on-board the DELFIMx platform, an autonomous surface craft developed at Instituto for Systems and Robotics/Instituto Superior Técnico (ISR/IST) for automatic marine data acquisition. A description of the DELFIMx characteristics and of the implemented hardware architecture is found in Appendix B. The vehicle and LASER aiding techniques presented in Chapter 3 are motivated by considering a generic fully actuated rigid body, and extended to a model-scale Vario X-Treme helicopter, to demonstrate the application of the navigation system to realistic robotic



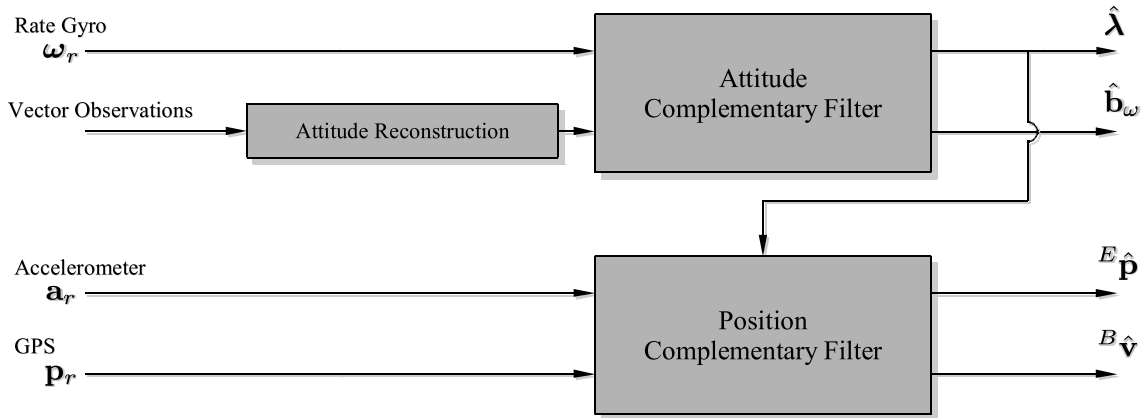


Figure 1.6: Complementary filter block diagram.

platforms. A summary of the Vario X-Treme helicopter model, derived from first principles in [39], is presented in Appendix C.

### 1.1.2 Nonlinear complementary Kalman filter

The complementary filtering theory is deeply rooted in the work of Wiener [142]: an unknown signal can be estimated using corrupted measurements from one or more sensors, whose information naturally stands in distinct and complementary frequency bands [10, 21, 22, 65]. The minimum mean-square estimation (MMSE criteria) problem was first solved by Wiener [142], assuming that the unknown signal had noise-like characteristics, which usually does not fit the signal description. Complementary filtering estimates a generic signal by exploiting the sensor redundancy and rejecting measurement disturbances in complementary frequency regions, without distorting the signal. The slight loss of performance in complementary filters, due to disregarding noise stochastic description, is beneficial in the presence of irregular measures that occur out of the expected variance, as convincingly argued in [21].

Complementary filters have been widely used in the past in sensor fusion problems. The frequency domain formulation, and the simple filter structure, allow for straightforward implementation without requiring high performance signal processing hardware, see [76, 102] and references therein. These algorithms are highly appealing in face of expensive computational resources, and are adopted in navigation systems for autonomous vehicles such as oceanic crafts [113, 141, 143], model-scale helicopters [118], and autonomous aircrafts [72, 112] due to the algorithm simplicity and reliability in practical implementations.

In Chapter 4, a navigation system based on complementary filtering, for position and attitude estimation, is derived. The problem of accurate position and attitude estimation is addressed by exploiting information over distinct but complementary frequency regions, that is provided by the inertial and aiding sensors. Namely, inertial measurements from accelerometers and rate gyros are merged with the linear position computed by a low-cost GPS receiver, and with Earth's magnetic field observations, respectively.

The derivation of the proposed complementary filters is focused on *i)* stability and performance of the algorithms, and *ii)* obtaining a simple navigation system architecture that can be easily implemented on low-cost, low-power signal processing hardware. The navigation system is formulated in discrete-time and, as shown in Fig. 1.6, comprises an attitude filter and a position filter.

The attitude filter inputs are the rate gyro readings, corrupted by bias, and a snapshot attitude reconstruction based on vector observations, such as Earth's magnetic field and pendular readings. The rigid body attitude is parameterized using Euler angles, that is a simple representation and bears physical intuition about the attitude of the vehicle. The position filter resorts to accelerometers readings and to GPS measurements, and estimates velocity in body frame and position in Earth frame.

Stability and performance properties of the proposed attitude and position filters, under operating conditions usually found in oceanic and terrestrial applications, are derived. Moreover, steady state feedback gains are adopted, that can be tuned given either the frequency domain or the stochastic characterization of the sensors, yielding filtering algorithms that are easy to implement in practice.

The navigation system is also endowed with a multirate synthesis methodology, based on optimality results for periodic systems [15], that can integrate aiding sensors sampled at diverse rates. Experimental results are presented, obtained in tests at sea with an implementation of the proposed navigation system, running on-board the DELFIMx catamaran.

The attitude observations, used in the complementary attitude filter as shown in Fig. 1.6, are obtained by deriving an attitude reconstruction algorithm, based on magnetic and pendular measurements. Denoted as the Magneto-Pendular Sensor (MPS), the algorithm computes pitch and roll from the pendular measurements, and yaw using the magnetic field observations.

The magnetometer readings adopted in the MPS are often distorted by the influence of the vehicle structure, sensor bias and scaling. Consequently, the sensor non-idealities and magnetic disturbances must be compensated prior to integrating the magnetometer readings in the navigation system. Appendix K derives a magnetometer calibration algorithm, that is formulated in the sensor frame and allows for online calibration of the magnetometer without external references. Also, insight on the magnetometer errors and on the corresponding mathematical model is obtained in the derivation of the algorithm.

## 1.2 Lyapunov based navigation system design

The second part of this work addresses the design of nonlinear navigation systems, formulated rigorously in non-Euclidean spaces where attitude is represented, such as the groups of rotation matrices  $SO(3)$  and unit quaternions  $S(3)$  [107]. Using global parameterizations of the rigid body orientation, exciting properties can be derived, such as almost global stabilization of the estimation error [28, 97, 123], and explicit characterization of

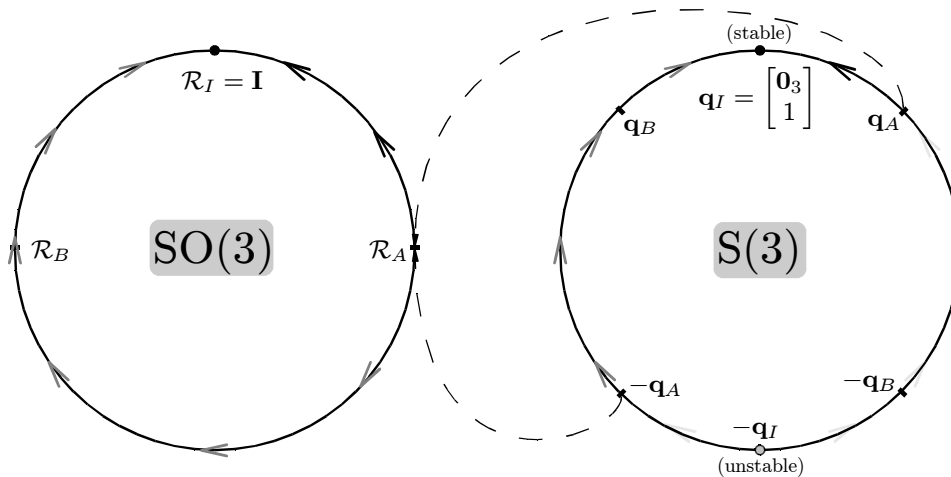


Figure 1.7: Representation of an unwinding phenomenon described in [13]. The rotation matrix  $\mathbf{R}_I = \mathbf{I}$  is lifted to the quaternions  $\mathbf{q}_I = [\mathbf{0}_3 \ 1]'$  and  $-\mathbf{q}_I$ , and the controller/estimator is derived on  $S(3)$  such that  $\mathbf{q}_I$  is a GAS and  $-\mathbf{q}_I$  is an unstable equilibrium point. The rotation matrix  $\mathcal{R}_A$  is lifted to the quaternions  $\mathbf{q}_A$  and  $-\mathbf{q}_A$  and, conversely,  $\mathbf{q}_A$  and  $-\mathbf{q}_A$  project to  $\mathcal{R}_A$ . Consequently, two distinct trajectories emanate from  $\mathcal{R}_A$  on  $SO(3)$ : the trajectory with initial condition  $\mathbf{q}_A$  (dark arrows), that converges monotonically to the origin on  $SO(3)$ , and the trajectory with initial condition  $-\mathbf{q}_A$  (gray arrows), that exhibits unwinding on  $SO(3)$ .

the regions of attraction [96, 117, 124, 137].

This approach brings about insight on the topological issues for achieving global stabilization on manifolds. Guidelines for observer design on manifolds such as  $SO(3)$  and  $S(3)$  are presented in [13, 28, 49, 81, 97]. For example, [13] discusses the “unwinding” phenomenon, verified in the stabilization of rotation motion on coverings of  $SO(3)$  such as the quaternion group  $S(3)$ . As demonstrated in [13], stabilization in the covering manifold, combined with the one to many correspondence of coverings, may lead to an unwinding phenomenon in the covered manifold. A representation of the unwinding phenomenon on  $SO(3)$  is suggested in Fig. 1.7, where it is shown that an asymptotically stable trajectory on  $S(3)$  projects to a trajectory on  $SO(3)$  that circulates away from, before converging to, the origin.

Moreover, an important topological obstacle to continuous global stabilization arises from the fact that, for any continuous state feedback law, the region of attraction of a stable equilibrium point is homeomorphic to some Euclidean vector space [28, 81, 97]. Since  $SO(3)$  and  $SE(3)$  are not diffeomorphic to an Euclidean vector space, there is no continuous state feedback law that yields global asymptotic stability of an equilibrium point. An illustration of this limitation for  $S(1)$  is shown in Fig. 1.8. This result motivates the relaxation from global to almost global stability [81], and from input-to-state to almost input-to-state stability [5], providing a suitable framework for stabilization of rotational motion, where stability of the equilibrium point is guaranteed for any initial condition outside a set of zero measure.

The second part of the thesis proposes new nonlinear observers for attitude and posi-

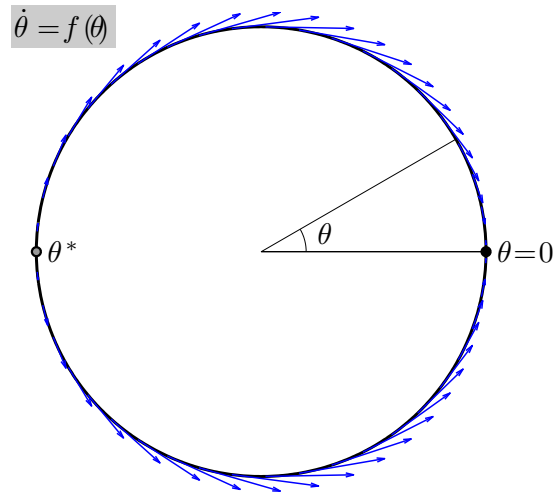


Figure 1.8: Illustration of topological limitation to global stabilization on manifolds, for the case of a system  $\dot{\theta} = f(\theta)$  defined on  $S(1)$ , where  $f(\theta)$  is continuous on  $\theta$ . The arrows depict the “direction” and magnitude of  $f(\theta)$ , and show that if the origin is stable, there is another  $\theta^*$  such that  $f(\theta^*) = 0$ .

tion estimation of autonomous vehicles, using sensor suites adopted in classical navigation systems. In general, the design of nonlinear observers is sensor-dependent, and incorporating new aiding sensors or accounting for other sensor non-idealities requires guessing a new stabilizing feedback law. An observer design technique is proposed, which derives the feedback law using a Lyapunov function defined by the observation error of the aiding sensors.

As depicted in Fig. 1.1(b), the Lyapunov based design technique is adopted in the synthesis of three nonlinear observers: an attitude and position observer based on landmark and velocity measurements; an attitude observer based on vector measurements; and an attitude and position observer using an IMU aided by GPS readings. The systems are formulated on  $SO(3)$  and  $SE(3)$  manifolds, and the derivation is focused on the stability of the systems, using the sensor readings directly, and considering sensor non-idealities such as bias and noise.

The stability of the observers is studied using advanced tools for nonlinear systems, such as analysis techniques based on density functions [115], and recently derived results for parameterized LTV systems [92]. Motivated by the presence of non-modeled disturbances in the inertial measurements, new stability results for nonlinear systems are derived in this work. These results yield new techniques for the study of input-state and almost global stability of nonlinear systems.

### 1.2.1 Nonlinear observers for attitude and position estimation

Nonlinear attitude and position observers, with application to aerospace, terrestrial and oceanic vehicles, have been proposed in recent literature. A seminal nonlinear attitude

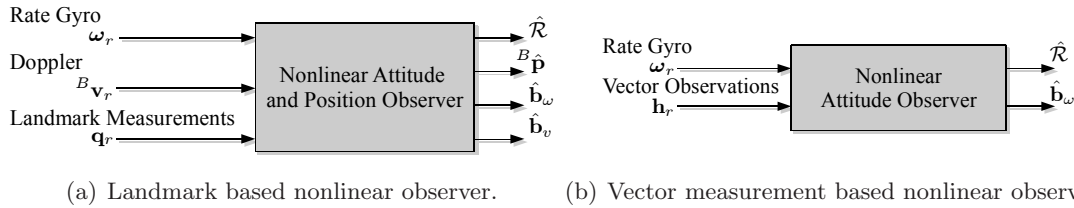


Figure 1.9: Adopted sensors and estimated quantities of the nonlinear observers based on landmark measurements and vector observations.

observer is found in [123], which derives an eventually globally exponentially convergent observer, expressed in the unit quaternion representation, and that resorts to attitude and torque measurements. In many applications it is of interest to construct an attitude observer based only on the rotation kinematics, that can be implemented on any robotic platform, irrespective of its dynamics. Research work devoted to the development of nonlinear observers based on the attitude and position kinematics, is found in [80, 96, 117, 135, 138].

Kinematic observers endowed with almost global stability can be found in [96, 135, 138], and methodologies for the design of this class of observers have been put forth in recent publications [16, 28, 83]. These recent advances motivate the growing interest in extending the design of nonlinear observers, namely to exploit information sources adopted in classical navigation problems. Also, it is desirable to integrate the sensor readings directly in the observer, without using intermediate state reconstruction algorithms. This approach enables the analysis of how the observer estimates are influenced by the characteristics of the sensor measurements.

Landmark based navigation is recognized as a promising strategy for providing aerial vehicles with critical position and attitude information for operations in delimited scenarios. Chapter 5 presents a nonlinear observer for position and attitude estimation on  $SE(3)$  using landmark observations and velocity measurements, as shown in Fig. 1.9(a). A design technique for nonlinear observers is proposed, based on a Lyapunov function conveniently defined by the observation error of the landmarks. Almost global asymptotic stabilization (aGAS) of the position and attitude errors is obtained, which is the most embracing stability property that can be obtained for systems defined on manifolds. Moreover, the region of attraction of the origin is characterized explicitly, and the trajectories are shown to converge exponentially fast to the origin.

The observer structure exploits directly the sensor readings, without intermediate attitude/position reconstruction, which brings about the characterization of the observer given the sensor properties. Namely, the proposed attitude feedback laws are explicit functions of the landmark measurements and velocity readings, exploiting the sensor information directly in the observer. Also, it is shown that the landmark geometry defines the directionality of the observer trajectories, as well as the shape and coordinates of the anti-stable manifold. This characterization of the observer trajectories allows for the

modeling of the convergence properties of the observer, using the available feedback design parameters.

The problem of non-ideal velocity readings is also addressed, and the observer is augmented to compensate for bias in the angular and linear velocity readings. In this case, the stability analysis is more complex due to the stronger coupling of the attitude and position observer, and to the non-autonomous formulation of the error dynamics. Recent results for parameterized linear time-varying systems [93] are adopted in the stability analysis of the system. The resulting position, attitude, and bias estimation errors are shown to converge exponentially fast to the desired equilibrium points, for bounded initial estimation errors.

The stability and convergence properties of the observer are verified in simulation, for trajectories described by time-varying linear and angular velocities. Simulation results illustrate the directionality and convergence properties of the observer given the landmark geometry. Also, the convergence rate and the transient response for distinct initial conditions on  $SE(3)$  are analyzed.

An attitude observer using vector observations is proposed in Chapter 6. The sensors adopted and the quantities estimated by the observer are presented in Fig. 1.9(b). The derivation of the attitude observer evidences how the design technique of Chapter 5 can be used to address the classical problem of attitude estimation using inertial measurements and attitude aiding sensors, such as magnetometers, star trackers and pendulums [37]. Resorting to the proposed technique, the attitude feedback law is obtained constructively, using a Lyapunov function conveniently defined by the measurement error of the vector observations.

Consequently, the stability properties of the attitude observer are similar to those of the landmark based observer. Namely, almost global asymptotic stabilization of the attitude errors is obtained, with exponential convergence, for ideal angular velocity measurements; the region of attraction is characterized explicitly; exponential stability of the origin is obtained in the presence of biased velocity readings, given worst-case initial estimation errors; and the proposed attitude feedback law is an explicit function of the vector measurements and observer estimates. The properties of the observer are illustrated in simulation for time-varying angular velocities, and diverse initial estimation errors.

In Chapter 7, the stability analysis of the nonlinear attitude observer is extended for the case of velocity measurements corrupted by bounded disturbances. The properties of the system are analyzed using new stability results, which are one of the main contributions of this thesis. Input-to-state stability of the attitude estimation error, with known ultimate bounds, is guaranteed for almost all disturbances. Also, new seminal results are presented for the derivation of aGAS with biased angular velocity measurements. The novelty of the results, and the concepts underlying their derivation are described later in this introductory chapter.

The design of a nonlinear navigation system, comprising an IMU aided by GPS measurements, is studied in Chapter 8. The derivation of a nonlinear navigation system for the

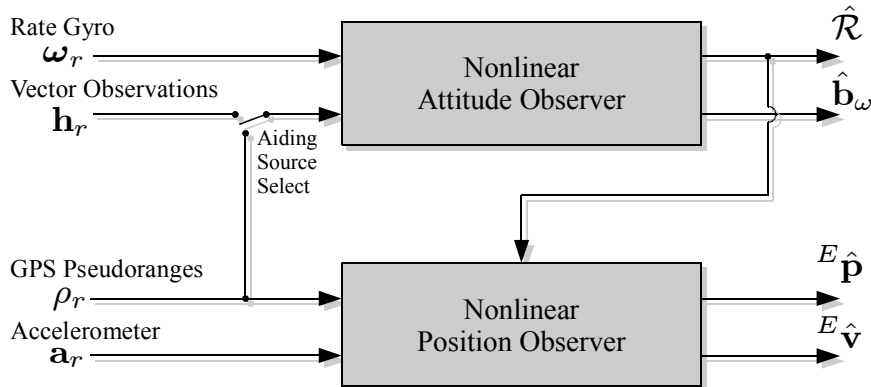


Figure 1.10: Structure of the GPS/IMU based nonlinear navigation system.

GPS/IMU configuration demonstrates how the results for nonlinear observers, proposed in the second part of the thesis, can be adopted for a classical estimation problem, that is studied in the first part of the thesis using the Kalman filtering approach.

The GPS/IMU based nonlinear navigation system is formulated on  $SE(3)$  and, as illustrated in Fig. 1.10, is characterized by a cascade composition of attitude and position observers. The GPS receiver, installed onboard the vehicle, provides the position observer with pseudorange measurements with respect to satellites in view. The GPS pseudorange measurements are used directly in the position observer, without resorting to the position computation from the GPS units. The observations of the attitude observer are also obtained directly from GPS pseudorange measurements from multiple GPS units, without using an intermediate attitude reconstruction. The integration of vector observations in the attitude observer is also discussed.

The stability results are obtained for non-ideal sensor measurements. The navigation system compensates dynamically for the bias in the angular velocity sensor and the clock offset in GPS pseudorange measurements. The resulting navigation solution yields exponential convergence of the position and attitude estimation errors, for worst-case initial estimation errors. It is also shown that the origin is stable in the presence of bounded measurement disturbances in the accelerometer and in the rate gyro. The properties of the GPS/IMU based observer are illustrated in simulation, for sensor disturbances found in very low quality IMUs and for a rigid body describing a challenging trajectory.

### 1.2.2 New results for stability analysis of nonlinear systems

Global stability is usually a highly desirable property in control and estimation algorithms. However, topological obstacles to continuous global stabilization arise in many dynamic systems, due to the fact that no smooth vector field can have a global attractor, unless the state space on which it is defined is homeomorphic to  $\mathbb{R}^n$  [81]. As a consequence, controllers and observers designed using continuous state feedback on smooth manifolds, will always produce some trajectories that do not converge to the origin [13, 97]. Due to



the presence of unstable manifolds, stability analysis using Lyapunov's second theorem is more complex.

New analysis tools have been introduced recently for the study of the milder notion of almost global stability [5, 115]. In this framework, an equilibrium is "almost globally stable" in the sense that for all initial states outside of a set of zero measure, the dynamics converge to the equilibrium. A dual to the Lyapunov second method for analysis of almost global stability is developed in [115, 116], based on density functions, that represent the stationary density of a substance that flows along the system trajectories [101, 103, 115]. Almost global stability is obtained by verifying that, for a time-invariant density function, particles are generated almost everywhere and hence must flow to a sink, located at the origin.

A similar approach has been adopted for the analysis of input-to-state stability (ISS). The ISS paradigm has been extensively developed in recent years, as presented in the comprehensive survey of ISS notions and results found in [131], and in the list of references contained therein. The limitations to global stability on non-Euclidean spaces, and the fact that global stability is a necessary condition for ISS, motivate the relaxation to almost ISS, proposed in [5]. The notions of robust and weakly almost ISS are proposed, and results for these properties using density functions are investigated. More important, it is suggested that a combination of Lyapunov methods with density function results may be the right technique for proving almost ISS in general. Surprisingly enough, this enriching insight seems to have gone unnoticed in the subsequent literature.

The work presented in Chapter 7 develops the idea of combining Lyapunov and density functions, for the stability analysis of nonlinear systems. Results are formulated for the analysis of almost global asymptotic stability, and of almost input-to-state stability of the origin. In the proposed analysis techniques, the Lyapunov function is adopted to characterize the system trajectories, however the Lyapunov stability analysis is limited by the existence of unstable manifolds. On the regions where the Lyapunov method is inconclusive, the convergence is studied using density functions. Using a suitable density function, sufficient conditions for instability of undesirable equilibrium points are derived, yielding convergence of almost all solutions to the region where stability is guaranteed by the Lyapunov function. Consequently, the proposed combination of Lyapunov and density functions bears stabilization of almost all trajectories.

As depicted in Fig. 1.1(b), the proposed techniques are adopted for the stability analysis of the nonlinear observers proposed in Chapters 6 and 8. Using the derived techniques, the stability of the attitude observer in the presence of bounded angular velocity disturbances is demonstrated, and seminal results for aGAS of the origin with biased velocity readings are presented. The stability of the GPS/IMU observer in the presence of disturbances in the inertial sensors is also obtained.



### 1.3 Thesis outline

As shown in Fig. 1.1, the contents of this thesis are organized according to navigation solutions, in chapters that are mostly self-contained, while minimizing repetition. In general, the concepts and formulations that are common to more than one chapter will be detailed in the first occurrence, or presented in appendix, and briefly reviewed or referenced to in subsequent chapters.

In the first part, the design of high-performance, low-cost navigation systems based on Kalman filtering techniques is studied. In Chapters 2 and 3, the adopted architecture is based on a high accuracy, multirate INS, combined with an EKF and a GPS unit, for precise inertial estimation error compensation. The key problem of integrating diverse aiding sources with the low cost INS is studied.

Advanced aiding techniques are presented in Chapter 2, for precise position and attitude estimation of autonomous vehicles. Aiding magnetic and gravitic observations are integrated using the EKF, enabling the compensation of inertial sensor non-idealities such as bias and noise. The magnetometer measurements and the information embodied in pendular measurements, modeled using a characterization of the vehicle dynamics in the frequency domain, are exploited to properly trace attitude errors and reject measurement disturbances. The techniques are demonstrated in experimental tests, performed by the DELFIMx autonomous surface craft described in Appendix B.

Chapter 3 proposes a methodology to embed dynamic models of autonomous vehicles in the EKF/INS architecture. The proposed methodology integrates the vehicle model information directly in the EKF state model, bearing a computationally efficient vehicle model aiding. A LASER range finder sensor is also integrated in the navigation system, to provide high precision distance-to-ground readings for critical takeoff and landing maneuvers. The aiding techniques are implemented and simulated for the nonlinear dynamics of a Vario X-Treme model-scale helicopter, detailed in Appendix C.

Chapter 4 derives a navigation system architecture based on the theory of complementary filtering. The proposed complementary filters provide attitude estimates in Euler angles representation and position estimates in inertial frame coordinates, using strapdown inertial measurements, vector observations, and GPS aiding. Filter stability and performance properties are presented, under operating conditions usually found in oceanic and terrestrial applications. The filter is designed for simplicity and to be easily implemented on low-cost, low-power signal processing hardware, and experimental results with an implementation of the proposed algorithm running on-board the DELFIMx catamaran are presented.

Interestingly enough, the practical implementation of the algorithms in the DELFIMx catamaran motivated the derivation of a calibration algorithm for magnetometers, presented in Appendix K. The proposed calibration method is independent of external attitude aiding, and compensates for non-idealities such as soft iron, hard iron, sensor non-orthogonality and bias. Experimental results with low-cost magnetometers are presented

and discussed.

The second part of the thesis addresses the design of nonlinear observers, formulated rigorously in non-Euclidean spaces where attitude is represented. Design and analysis techniques based on Lyapunov and density functions are derived, and illustrated in the synthesis of nonlinear observers that resort to diverse aiding sensors.

Chapter 5 presents a nonlinear observer for position and attitude estimation on  $SE(3)$ , using velocity measurements and landmark observations. An observer synthesis technique is proposed, that resorts to a Lyapunov function based on the observation error of the aiding sensors. Exponential stabilization of the estimation error is derived, and the directionality of the observer is discussed. The topological obstacles to stabilization in manifolds are also illustrated using the proposed observer. The derived synthesis technique and the stability analysis results will be central to the development of the nonlinear observers presented in the following chapters.

Chapter 6 derives an attitude observer based on angular velocity and vector measurements. The observer is obtained using the synthesis techniques proposed in Chapter 5. By appealing to the stability results found therein, it is shown that the attitude and angular velocity bias estimation errors converge exponentially fast to the origin. The attitude observer is obtained under a uniform design transformation for the sake of presentation, and a similar attitude observer endowed with directionality is presented in Appendix G.

Chapter 7 proposes new stability results, based on the combination of Lyapunov and density functions. Stability tools are discussed for almost global stability and input-to-state stability of nonlinear systems. The results are motivated by, and applied to the nonlinear attitude observer presented in Chapter 6.

Chapter 8 describes a nonlinear observer for attitude and position estimation, using the GPS and inertial sensor ensemble studied in the first part of the thesis. The design of the nonlinear GPS/IMU observer illustrates the proposed observer derivation techniques, and the new stability analysis results for nonlinear systems, applied to a classical sensor configuration. Exponential convergence of the attitude and position estimates is obtained, with stability in the presence of bounded noise in the inertial sensors.

A review of the main results of this work, and a discussion of directions for future work are presented at the end of the thesis.

## Chapter 2

# INS/GPS aided by frequency contents of vector observations

This chapter presents a high accuracy, multirate Inertial Navigation System (INS) integrating Global Position System (GPS) measurements and advanced vector aiding techniques for precise position and attitude estimation of Autonomous Surface Crafts (ASCs). A multirate, high accuracy INS is proposed to compute attitude, velocity and position, and is combined with an Extended Kalman Filter (EKF) to integrate GPS position measurements, vector observations and frequency domain characterization of the vehicle. Magnetic and gravitic observations are integrated optimally in the EKF, by modeling the sensor readings directly in the filter and by taking into account the vehicle's dynamics bandwidth information.

The direct-feedback configuration of the proposed architecture is illustrated in Fig. 2.1. The INS computations adopted in this work account for high frequency attitude, velocity and position motions (denoted as coning, sculling and scrolling respectively), and are based on the algorithm developed in [126, 127]. The magnetometer and pendular readings are fed directly to the system, and the measurement residual is obtained by comparing the estimated and measured vector observations. The proposed vector aiding technique decomposes and optimally integrates gravitic observations in the EKF, however gravity readings are distorted in the presence of linear and angular accelerations. In this work, angular acceleration is compensated using the INS information, while linear acceleration of the vehicle is compensated by characterizing the dynamics of the vehicle in the frequency domain. The resulting measurement model allows the EKF to exploit the frequency contents of the gravity readings, compensating for inertial sensor errors and enhancing the attitude estimates.

The proposed aiding techniques and the performance of the navigation system are assessed using experimental data obtained at sea trials with a low-cost hardware architecture installed on-board the DELFIMx platform. It is shown that inertial sensor non-idealities such as bias and noise are effectively compensated for, using the magnetometer measurements and the low frequency information embodied in pendular measurements. Also, the

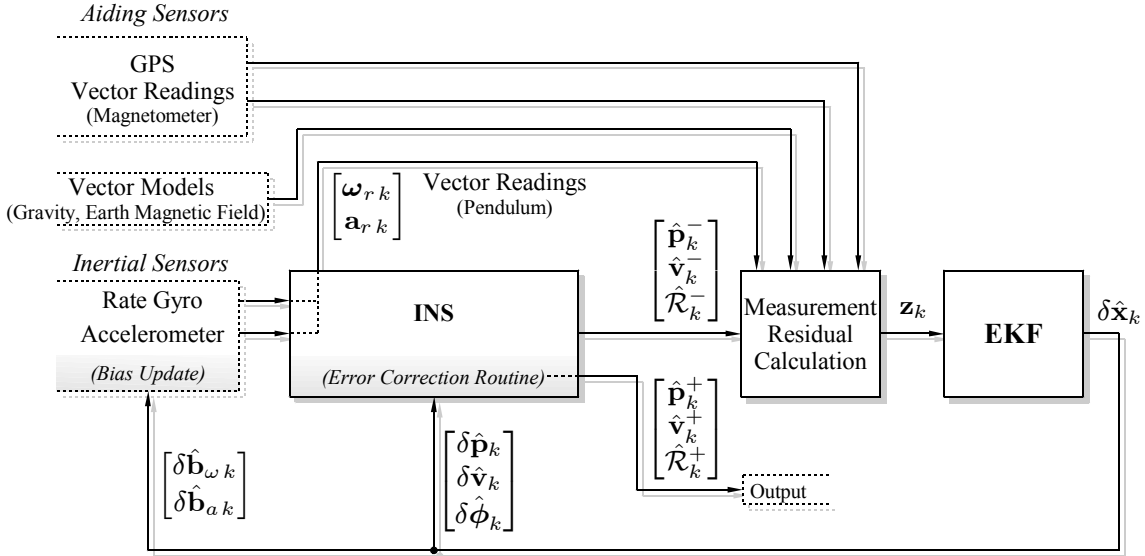


Figure 2.1: Navigation system block diagram.

problem of poor GPS signal detection when the vehicle operates in the vicinity of structures, such as bridges and breakwaters, demands for a navigation system able to operate under medium term position aiding shortage. The overall improvements obtained with the vector aiding observations are illustrated for the case of GPS signal outage, emphasizing the extended autonomy of the navigation system with respect to position aiding.

The chapter is organized as follows. Section 2.1 briefly discusses the INS algorithm adopted in this work. In Section 2.2, the linear differential equations describing the inertial sensor errors are derived and introduced in the EKF state space model. In Section 2.3, the integration of vector measurements directly in the EKF is derived using perturbational techniques and illustrated for magnetometer measurements. The method is extended for gravity measurements obtained from the accelerometer triad, which require modeling vehicle dynamics bandwidth information in the EKF, compensating in the frequency domain for accelerated motion. The EKF state space model is summarized in Section 2.4, the discrete-time equivalent filter is obtained, and the correction and reset procedures to update the INS states using the EKF estimates are detailed. Simulation results to validate the proposed navigation system prior to experimental testing are shown in Section 2.5. The contribution of vector measurements and gravity selective frequency contents to the accuracy of the estimation results is analyzed. Experimental results obtained during the DELFIMx sea trials are presented in Section 2.6, to assess the navigation system performance in practice. Concluding remarks are found in Section 2.7.

## 2.1 Inertial navigation system algorithm

In this section, an INS algorithm is briefly introduced, based upon the tutorial work presented in [126, 127] for attitude, velocity, and position computation, where complex angular, velocity and position high-frequency motions, referred to as coning, sculling, and scrolling respectively, are properly accounted for using a multirate integration approach.

In this framework, a high-speed, low order algorithm computes dynamic angular rate/acceleration effects at a small sampling interval, and its output is periodically fed to a moderate-speed algorithm that computes attitude/velocity resorting to exact, closed-form equations. Given the limited operational time and confined mission scenarios for the application at hand, an invariant gravity model is adopted without loss of precision, while equations were derived to the highest accuracy. Also, the intermediate coordinate frames, such as local and navigation frames, are identified with Earth frame, denoted as  $\{E\}$ . As depicted in Fig. 2.2, the inputs provided to the inertial algorithms are the integrated inertial sensor output increments

$$\mathbf{v}(\tau) = \int_{t_{k-1}}^{\tau} \mathbf{a}_r dt, \quad \boldsymbol{\alpha}(\tau) = \int_{t_{k-1}}^{\tau} \boldsymbol{\omega}_r dt,$$

which correspond to the integral of the inertial sensor readings, obtained using strapdown accelerometer and rate gyro triads, corrupted by white noise and bias errors and modeled as follows

$$\mathbf{a}_r = {}^B \mathbf{a} - {}^B \mathbf{g} + \mathbf{b}_a + \mathbf{n}_a - \hat{\mathbf{b}}_a, \quad (2.1a)$$

$$\boldsymbol{\omega}_r = \boldsymbol{\omega} + \mathbf{b}_\omega + \mathbf{n}_\omega - \hat{\mathbf{b}}_\omega, \quad (2.1b)$$

where  $\mathbf{g}$  represents Earth's gravitic field, the sensor biases are denoted by  $\mathbf{b}_a$  and  $\mathbf{b}_\omega$ , and  $\mathbf{n}_a \sim \mathcal{N}(\mathbf{0}, \Xi_a)$ ,  $\mathbf{n}_\omega \sim \mathcal{N}(\mathbf{0}, \Xi_\omega)$  are Gaussian white noises.

The attitude moderate-speed integration algorithm detailed in [126] computes body attitude in DCM form

$${}^{B_{k-1}}_{B_k} \mathbf{R}(\boldsymbol{\phi}_k) = \mathbf{I}_3 + \frac{\sin(\|\boldsymbol{\phi}_k\|)}{\|\boldsymbol{\phi}_k\|} (\boldsymbol{\phi}_k)_\times + \frac{1 - \cos(\|\boldsymbol{\phi}_k\|)}{\|\boldsymbol{\phi}_k\|^2} (\boldsymbol{\phi}_k)_\times^2, \quad (2.2)$$

where  $\{B\}$  denotes the body frame,  $\{B_k\}$  is the body frame at time  $k$ , and  $(\mathbf{s})_\times$  represents the skew symmetric matrix defined by the vector  $\mathbf{s} \in \mathbb{R}^3$  such that  $(\mathbf{s})_\times \mathbf{r} = \mathbf{s} \times \mathbf{r}$ ,  $\mathbf{r} \in \mathbb{R}^3$ . Rotation vector dynamics, based on Bortz equation [17], are formulated in order to denote angular integration and coning attitude terms  $\boldsymbol{\alpha}_k$  and  $\boldsymbol{\beta}_k$ , respectively

$$\boldsymbol{\phi}_k = \boldsymbol{\alpha}_k + \boldsymbol{\beta}_k, \quad (2.3)$$

where  $\boldsymbol{\alpha}_k = \boldsymbol{\alpha}(t)|_{t=t_k}$  and the coning attitude term measures the attitude changes due to the effects of angular rate vector rotation. A high-speed attitude algorithm is required to compute  $\boldsymbol{\beta}_k$  as a summation of the high-frequency angular rate vector changes using simple, recursive computations [126]. Equations (2.2) and (2.3) summarize both the moderate

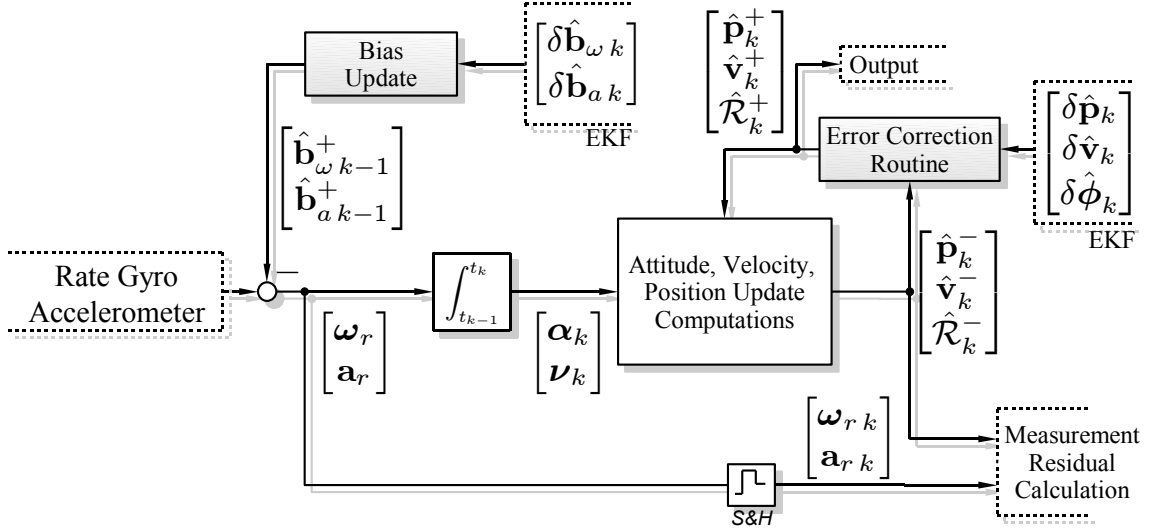


Figure 2.2: Inertial navigation system with estimation error compensation.

and high-speed attitude dynamics in the DCM format using exact, error-free equations, enabling high accuracy results.

Exact linear velocity updates can be computed at moderate-speed rate using the equivalence between strapdown attitude and velocity/position algorithms [120], that yields

$$\mathbf{v}_k = \mathbf{v}_{k-1} + \frac{E}{B_{k-1}} \mathbf{R} \Delta^{B_{k-1}} \mathbf{v}_{\text{SF}k} + \Delta \mathbf{v}_{\text{G/Cor}k},$$

where  $\Delta^{B_{k-1}} \mathbf{v}_{\text{SF}k}$  is the velocity increment related to the specific force, and  $\Delta \mathbf{v}_{\text{G/Cor}k}$  represents the velocity increment due to gravity and Coriolis effects, see [127] for further details. High-speed velocity rotation and high-frequency dynamic variations due to angular rate vector rotation, are likewise accounted for in the high-frequency algorithm and included in the moderate-speed calculations as

$$\Delta^{B_{k-1}} \mathbf{v}_{\text{SF}k} = \mathbf{v}_k + \Delta \mathbf{v}_{\text{rot}k} + \Delta \mathbf{v}_{\text{scul}k},$$

where  $\mathbf{v}_k = \mathbf{v}(t)|_{t=t_k}$  and  $\Delta \mathbf{v}_{\text{rot}k}$  and  $\Delta \mathbf{v}_{\text{scul}k}$  represent velocity increments due to rotation and sculling, respectively.

The INS algorithm execution rates are set as a trade-off between the available hardware and the performance requirements [68, 126, 127]. Simulation environments and trajectory profiles to tune the algorithm's repetition rate according to the accuracy requirements are thoroughly described in [128] and algorithm evaluation procedures are presented in [126, 127]. Interestingly enough, high repetition rates can be implemented in a standard low-power consumption Digital Signal Processing (DSP) based hardware architecture. This allows for accurate integration results, that are only diminished by inertial sensor non-idealities such as noise and bias.

## 2.2 Inertial error dynamics

In a stand-alone INS, bias and inertial sensor errors compensation is usually performed offline. The usage of filtering techniques in navigation systems, such as the EKF, allows for the dynamic estimation of inertial sensor non-idealities, bounding the INS errors. The EKF error equations adopted in this work are based on perturbational rigid body kinematics, and were brought to full detail in [20]. The nominal rigid body kinematics are given by

$$\dot{\mathbf{p}} = \mathbf{v}, \quad \dot{\mathbf{v}} = \mathcal{R}^B \mathbf{a}, \quad \dot{\mathcal{R}} = \mathcal{R}(\boldsymbol{\omega})_{\times}, \quad \dot{\mathbf{b}}_a = \mathbf{n}_{b_a}, \quad \dot{\mathbf{b}}_{\omega} = \mathbf{n}_{b_{\omega}}, \quad (2.4)$$

where  $\mathcal{R}$  is the shorthand notation for  ${}^E_B \mathbf{R}$ , the inertial sensor biases are modeled as random walk processes, and  $\mathbf{n}_{b_a} \sim \mathcal{N}(\mathbf{0}, \Xi_{b_a})$ ,  $\mathbf{n}_{b_{\omega}} \sim \mathcal{N}(\mathbf{0}, \Xi_{b_{\omega}})$  are Gaussian white noises. The position, velocity and bias estimation errors are defined by the difference of the estimated and nominal quantities,

$$\delta \mathbf{p} := \hat{\mathbf{p}} - \mathbf{p}, \quad \delta \mathbf{v} := \hat{\mathbf{v}} - \mathbf{v}, \quad \delta \mathbf{b}_a := \hat{\mathbf{b}}_a - \mathbf{b}_a, \quad \delta \mathbf{b}_{\omega} := \hat{\mathbf{b}}_{\omega} - \mathbf{b}_{\omega},$$

and the attitude error, denoted as  $\delta \boldsymbol{\phi}$ , is parameterized by an unconstrained rotation vector representation in Earth coordinates, which can be assumed locally linear and non-singular, for details and equivalent attitude parameterizations, see [99, 114]. Define the rotation error matrix as  $\mathbf{R}(\delta \boldsymbol{\phi}) := \hat{\mathcal{R}} \mathcal{R}'$ , the attitude error rotation vector  $\delta \boldsymbol{\phi}$  is described by the first order approximation

$$\mathbf{R}(\delta \boldsymbol{\phi}) \simeq \mathbf{I}_3 + (\delta \boldsymbol{\phi})_{\times} \Rightarrow (\delta \boldsymbol{\phi})_{\times} \simeq \hat{\mathcal{R}} \mathcal{R}' - \mathbf{I}_3, \quad (2.5)$$

that is valid for “small-angle” attitude errors [20]. The rigid body coordinates are estimated using the available inertial sensor information

$$\dot{\hat{\mathbf{p}}} = \hat{\mathbf{v}}, \quad \dot{\hat{\mathbf{v}}} = \hat{\mathcal{R}} \mathbf{a}_r + {}^E \mathbf{g}, \quad \dot{\hat{\mathcal{R}}} = \hat{\mathcal{R}}(\boldsymbol{\omega}_r)_{\times}, \quad \dot{\hat{\mathbf{b}}}_a = \mathbf{0}, \quad \dot{\hat{\mathbf{b}}}_{\omega} = \mathbf{0}, \quad (2.6)$$

Combining (2.4-2.6), the attitude, velocity, and position error kinematics are obtained by retaining the first-order terms of Taylor’s series expansions or by using perturbation algebraic techniques [20], producing

$$\delta \dot{\mathbf{p}} = \delta \mathbf{v}, \quad \delta \dot{\mathbf{v}} = \hat{\mathcal{R}}(\mathbf{a}_r - \mathbf{a}_{SF}) - \left( \hat{\mathcal{R}} \mathbf{a}_r \right)_{\times} \delta \boldsymbol{\phi}, \quad \delta \dot{\boldsymbol{\phi}} = \mathcal{R}(\boldsymbol{\omega}_r - \boldsymbol{\omega}), \quad (2.7a)$$

$$\delta \dot{\mathbf{b}}_a = -\mathbf{n}_{b_a}, \quad \delta \dot{\mathbf{b}}_{\omega} = -\mathbf{n}_{b_{\omega}}, \quad (2.7b)$$

where  $\mathbf{a}_{SF} = {}^B \mathbf{a} - {}^B \mathbf{g}$  is the specific force, defined as the nominal reading of an accelerometer. The terms  $(\mathbf{a}_r - \mathbf{a}_{SF})$  and  $(\boldsymbol{\omega}_r - \boldsymbol{\omega})$  represent the non-idealities of the accelerometer and rate gyro readings, (2.1a) and (2.1b) respectively, and are described by

$$(\mathbf{a}_r - \mathbf{a}_{SF}) = -\delta \mathbf{b}_a + \mathbf{n}_a, \quad (\boldsymbol{\omega}_r - \boldsymbol{\omega}) = -\delta \mathbf{b}_{\omega} + \mathbf{n}_{\omega}. \quad (2.8)$$

Combining (2.7) and (2.8), the error state space model is

$$\delta \dot{\mathbf{p}} = \delta \mathbf{v}, \quad \delta \dot{\mathbf{v}} = -\hat{\mathcal{R}} \delta \mathbf{b}_a - \left( \hat{\mathcal{R}} \mathbf{a}_r \right)_{\times} \delta \boldsymbol{\phi} + \hat{\mathcal{R}} \mathbf{n}_a, \quad \delta \dot{\boldsymbol{\phi}} = -\hat{\mathcal{R}} \delta \mathbf{b}_{\omega} + \hat{\mathcal{R}} \mathbf{n}_{\omega}, \quad (2.9a)$$

$$\delta \dot{\mathbf{b}}_a = -\mathbf{n}_{b_a}, \quad \delta \dot{\mathbf{b}}_{\omega} = -\mathbf{n}_{b_{\omega}} \quad (2.9b)$$

The continuous-time error state space model  $\delta\dot{\mathbf{x}} = \mathbf{F}(\hat{\mathbf{x}}, \mathbf{u})\delta\mathbf{x} + \mathbf{G}(\hat{\mathbf{x}})\mathbf{n}_x$  is described by

$$\delta\mathbf{x} = \begin{bmatrix} \delta\mathbf{p}' & \delta\mathbf{v}' & \delta\phi' & \delta\mathbf{b}'_a & \delta\mathbf{b}'_\omega \end{bmatrix}', \quad \mathbf{n}_x = \begin{bmatrix} \mathbf{n}'_p & \mathbf{n}'_v & \mathbf{n}'_\omega & \mathbf{n}'_{b_a} & \mathbf{n}'_{b_\omega} \end{bmatrix}', \quad (2.10a)$$

$$\mathbf{F}(\hat{\mathbf{x}}, \mathbf{u}) = \begin{bmatrix} \mathbf{0} & \mathbf{I} & \mathbf{0} & \mathbf{0} & \mathbf{0} \\ \mathbf{0} & \mathbf{0} & -\left(\hat{\mathcal{R}}\mathbf{a}_r\right)_\times & -\hat{\mathcal{R}} & \mathbf{0} \\ \mathbf{0} & \mathbf{0} & \mathbf{0} & \mathbf{0} & -\hat{\mathcal{R}} \\ \mathbf{0} & \mathbf{0} & \mathbf{0} & \mathbf{0} & \mathbf{0} \\ \mathbf{0} & \mathbf{0} & \mathbf{0} & \mathbf{0} & \mathbf{0} \end{bmatrix}, \quad \mathbf{G}(\hat{\mathbf{x}}) = \text{blkdiag}(\mathbf{I}_3, \hat{\mathcal{R}}, \hat{\mathcal{R}}, -\mathbf{I}_3, -\mathbf{I}_3), \quad (2.10b)$$

where  $\mathbf{x} = (\mathbf{p}, \mathbf{v}, \mathcal{R})$  are the quantities computed by the INS algorithm,  $\mathbf{u} = (\mathbf{a}_r, \boldsymbol{\omega}_r)$  are the inertial measurements,  $\text{blkdiag}(\cdot)$  denotes a block diagonal matrix obtained by the concatenation of its matrix arguments,  $\mathbf{n}_v = \mathbf{n}_a$ , and  $\mathbf{n}_p \sim \mathcal{N}(\mathbf{0}, \Xi_p)$  is a Gaussian white noise that accounts for linearization and modeling errors and is used in the practical tuning of the filter.

In the adopted architecture, the INS calculates the body attitude using the high-precision algorithms described in Section 2.1, and the EKF estimates the attitude, velocity, position errors using the aiding sensor measurements. After each filter update step, the EKF estimated inertial errors are transferred to the INS, as illustrated in Figs. 2.1 and 2.2, and reset in the filter. As evidenced in [99], this procedure preserves the small error assumption underlying the linearized model (2.10) used in the EKF. Note that normalization procedures usually found in linear attitude filtering are avoided in this architecture, that resorts to a locally linear parameterization for attitude estimation in the EKF, while a global attitude representation is propagated and stored in the INS [99].

### 2.3 Vector aiding techniques

The EKF relies on aiding sensor readings to successfully estimate the INS errors. The physical coupling between attitude and velocity errors (2.7) enables the use of GPS position readings to partially estimate attitude errors. As convincingly argued in [60], for observability analysis purposes a GPS based navigation system with bias estimation can be approximated by a concatenation of piece-wise time-invariant systems and, under that assumption, full observability is met by performing specific maneuvers along the desired trajectory. Recent work has been directed towards replacing the necessity for alignment maneuvers by equipping the filter with additional information sources, namely aiding sensors or vehicle dynamic model information, see [64, 82, 95, 136].

The vector observation technique enhances the system accuracy by providing attitude observations and vehicle dynamics bandwidth information to the EKF. For example, batch attitude determination algorithms can be used to compute an attitude matrix observation  $\mathcal{R}_{VO}$ , using the measurements of the Earth's magnetic and gravitic field in  $\{B\}$ , provided by the magnetometer and the accelerometer triads. Several batch attitude determination



algorithms can be found in the literature [8, 37, 61, 129] and an intuitive, easy to implement, TRIAD-like algorithm is also proposed in Section 4.2.1. A straightforward but naive method to introduce the attitude measurement  $\mathcal{R}_{VO}$  in the filter is obtained by defining the attitude measurement residual  $\mathbf{z}_{VO}$  after the attitude error (2.5), yielding

$$(\mathbf{z}_{VO})_{\times} = \hat{\mathcal{R}}\mathcal{R}'_{VO} - \mathbf{I}_3,$$

and modeling it in the filter as

$$\mathbf{z}_{VO} = \delta\phi + \mathbf{n}_{VO},$$

using a noise term  $\mathbf{n}_{VO}$  to compensate for the effect of magnetometer, accelerometer, rate gyro and INS disturbances on the attitude computation  $\mathcal{R}_{VO}$ . Nonetheless, characterizing  $\mathbf{n}_{VO}$  as white noise can degrade the filter performance because it does not properly model the non-linear influence of pendular/magnetic sensors errors in  $\mathcal{R}_{VO}$  computations. Also, the aiding attitude matrix  $\mathcal{R}_{VO}$  is computed using the vector measurements available at each time instant (snapshot algorithm), and hence dynamic disturbances in the vector observation readings are not accounted for.

In this work, vector observations are embedded in the EKF, as depicted in Fig. 2.1. The magnetometer reading and gravity selective frequency contents provided by the accelerometer triad are modeled directly in the filter, bearing a more clear and accurate stochastic description of the measurement errors and disturbances.

The EKF computes the attitude based on the vector observations, without external attitude determination algorithms and using optimality criteria, yielding an alternate solution to Wahba's problem [37, 139]. Sensor error characteristics other than just white noise are properly modeled in the filter, using the EKF covariance matrices and the structure of the error state space model. The algorithm presented herein can be generalized to any number of vector observations, devising a straightforward procedure to enhance the accuracy of the navigation system results, which also reinforces the EKF linearization assumption.

### 2.3.1 Vector measurement residual model

The attitude measurement residual is obtained by comparing the estimated and the measured vectors. The considered vector measurement model is

$$\mathbf{s}_r = \mathcal{R}'^E \mathbf{s} + \mathbf{n}_s, \quad (2.11)$$

where  $\mathbf{n}_s \sim \mathcal{N}(\mathbf{0}, \Xi_s)$  is a Gaussian white noise. The attitude measurement residual in Earth frame coordinates is described by

$${}^E \mathbf{z}_s = {}^E \mathbf{s} - \hat{\mathcal{R}} \mathbf{s}_r.$$

Using the sensor model (2.11) and replacing the INS attitude estimate  $\hat{\mathcal{R}}$  by the attitude error approximation (2.5) yields

$${}^E \mathbf{z}_s = {}^E \mathbf{s} - \hat{\mathcal{R}}\mathcal{R}'^E \mathbf{s} - \hat{\mathcal{R}}\mathbf{n}_s \approx {}^E \mathbf{s} - (\mathbf{I} + (\delta\phi)_{\times})^E \mathbf{s} - \hat{\mathcal{R}}\mathbf{n}_s = -(\delta\phi)_{\times} {}^E \mathbf{s} - \hat{\mathcal{R}}\mathbf{n}_s,$$

which relates the EKF measurement residual  ${}^E\mathbf{z}_s$  with the attitude error  $\delta\boldsymbol{\phi}$ , producing the linearized model

$${}^E\mathbf{z}_s \approx ({}^E\mathbf{s})_{\times} \delta\boldsymbol{\phi} - \hat{\mathcal{R}}\mathbf{n}_s. \quad (2.12)$$

The measurement residual can be represented in Earth or in body frame coordinates, which are related by a rotation transformation and hence contains the same information. Repeating the same algebraic manipulations, the linearized model of the measurement residual in body coordinates is given by

$${}^B\mathbf{z}_s := \hat{\mathcal{R}}'{}^E\mathbf{s} - \mathbf{s}_r \approx \hat{\mathcal{R}}'({}^E\mathbf{s})_{\times} \delta\boldsymbol{\phi} - \mathbf{n}_s. \quad (2.13)$$

Although the measurement residuals (2.12) and (2.13) describe the same attitude information, the linearized measurement matrix for (2.12) is constant and the components of  $\delta\boldsymbol{\phi}$  can be related directly with those of  ${}^E\mathbf{z}_s$ . For example, the measurement model (2.12) for the vector  ${}^E\mathbf{s} = [0 \ 0 \ 1]'$  is given by  ${}^E\mathbf{z}_s = [-\delta\phi_y \ \delta\phi_x \ 0]'$  -  $\hat{\mathcal{R}}\mathbf{n}_s$ , that contains information solely about the rotation error along the x-axis and y-axis, and illustrates the fact that the yaw angle error, i.e.  $\delta\phi_z$ , cannot be determined by gravity readings.

In general, the vector reading  $\mathbf{s}_r$  can be corrupted by other additive sensor disturbances, namely biases  $\mathbf{b}_s$ , and dynamic disturbances  $\mathbf{d}_s$ , as follows

$$\mathbf{s}_r = \mathcal{R}'{}^E\mathbf{s} + \mathbf{n}_s - \delta\mathbf{b}_s + \mathbf{d}_s, \quad (2.14)$$

where  $\delta\mathbf{b}_s$  is the bias compensation error term, and  $\mathbf{d}_s$  is the output of a process modeled in the state space form. The linearized measurement residual representations for the sensor reading (2.14), in Earth and in body coordinates, are respectively described by

$${}^E\mathbf{z}_s = ({}^E\mathbf{s})_{\times} \delta\boldsymbol{\phi} + \hat{\mathcal{R}}\delta\mathbf{b}_s - \hat{\mathcal{R}}\mathbf{d}_s - \hat{\mathcal{R}}\mathbf{n}_s, \quad {}^B\mathbf{z}_s = \hat{\mathcal{R}}'({}^E\mathbf{s})_{\times} \delta\boldsymbol{\phi} + \delta\mathbf{b}_s - \mathbf{d}_s - \mathbf{n}_s. \quad (2.15)$$

Using the measurement model (2.15), vector observations obtained by sensors such as pendulums and magnetometers can be introduced directly in the EKF. The sensor non-idealities are modeled in the filter, as opposed to using intermediate attitude reconstruction, which allows for the integration of any number of vector measurements, at different sampling rates, and compensating for dynamic disturbances. The observation noise covariance matrix, used in the computation of the optimal feedback gains, is directly given by the sensor noise variance  $\Xi_s$ .

### 2.3.2 Magnetic and pendular measurements integration

The magnetometer model considered in this work is given by

$$\mathbf{m}_r = \mathcal{R}'{}^E\mathbf{m} + \mathbf{n}_m, \quad (2.16)$$

where  $\mathbf{m}$  denotes Earth's magnetic field,  $\mathbf{n}_m \sim \mathcal{N}(\mathbf{0}, \Xi_m)$  is a Gaussian white noise, and magnetic distortions such as soft iron and hard iron are compensated offline using the

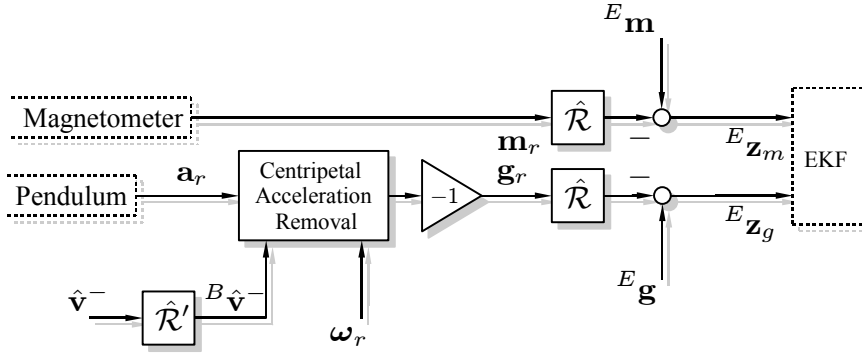


Figure 2.3: Vector measurement residual computation (magnetometer and pendular readings).

calibration algorithm proposed in Appendix K. The sensor description (2.16) is identical to the vector reading model (2.11). As illustrated in Fig. 2.3, the measurement residual (2.12) is adopted to integrate the magnetometer information in the EKF, yielding

$$\mathbf{z}_m := {}^E \mathbf{m} - \hat{\mathcal{R}} \mathbf{m}_r = ({}^E \mathbf{m})_{\times} \delta \phi - \hat{\mathcal{R}} \mathbf{n}_m.$$

A gravity vector measurement is obtained from the accelerometer reading (2.1a), which can be decomposed in Coriolis and linear acceleration components

$$\mathbf{a}_r = \frac{d {}^B \mathbf{v}}{dt} + \boldsymbol{\omega} \times {}^B \mathbf{v} - {}^B \mathbf{g} - \delta \mathbf{b}_a + \mathbf{n}_a. \quad (2.17)$$

To obtain a gravity measurement reading  $\mathbf{g}_r$ , adequate modeling is adopted to remove the acceleration terms in (2.17). Typical maneuvers of autonomous oceanic vehicles involve mostly short term linear accelerations, and hence the  $\frac{d {}^B \mathbf{v}}{dt}$  term is modeled in the filter state model as a high-frequency process. The Coriolis term  $\boldsymbol{\omega} \times {}^B \mathbf{v}$  occurs in transient but also in trimming maneuvers such as helicoidal paths, and is compensated for using the linear and angular velocities information provided by the INS. The gravity vector measurement  $\mathbf{g}_r$  is given by

$$\mathbf{g}_r \triangleq -(\mathbf{a}_r - \hat{\boldsymbol{\omega}} \times {}^B \hat{\mathbf{v}}) = {}^B \mathbf{g} - \frac{d {}^B \mathbf{v}}{dt} + \delta(\boldsymbol{\omega} \times {}^B \mathbf{v}) + \delta \mathbf{b}_a - \mathbf{n}_a. \quad (2.18)$$

where the  $\delta(\boldsymbol{\omega} \times {}^B \mathbf{v}) = \hat{\boldsymbol{\omega}} \times {}^B \hat{\mathbf{v}} - \boldsymbol{\omega} \times {}^B \mathbf{v}$  is the error of the centripetal acceleration removal, and  ${}^B \hat{\mathbf{v}} = \hat{\mathcal{R}}' {}^E \mathbf{v}$  is the estimated velocity in body coordinates. The gravity reading (2.18) is modeled as

$$\mathbf{g}_r = {}^B \mathbf{g} - \mathbf{a}_{\text{LA}} + \delta(\boldsymbol{\omega} \times {}^B \mathbf{v}) + \delta \mathbf{b}_a - \mathbf{n}_a, \quad (2.19)$$

where  $\mathbf{a}_{\text{LA}} = [a_{\text{LA}x} \ a_{\text{LA}y} \ a_{\text{LA}z}]'$  represents the linear acceleration estimate. Each of the  $\mathbf{a}_{\text{LA}}$  components is modeled as a band-pass signal whose bandwidth is shaped according to the vehicle characteristics, often to filter out high-frequency INS acceleration jitter and to simultaneously avoid the influence of erroneous low-frequency accelerometer bias. The

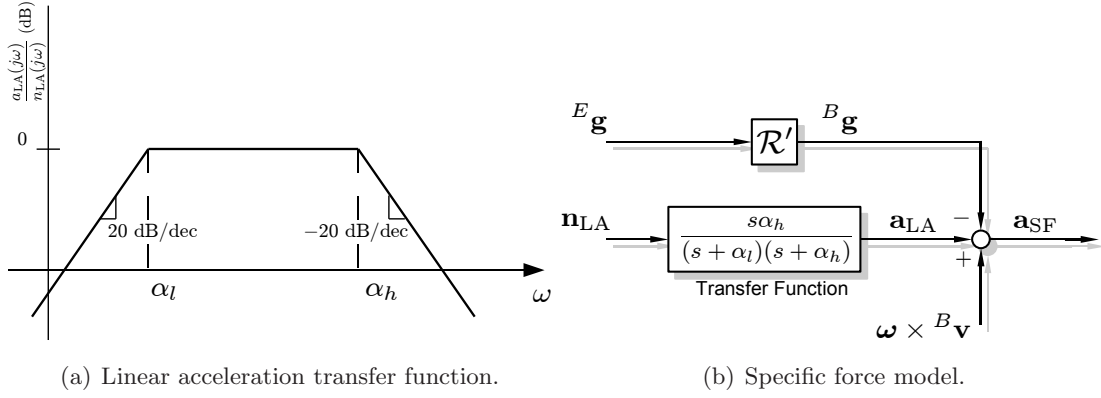


Figure 2.4: Linear acceleration modeling.

state model dynamics for the x-axis component is generically represented in Fig. 2.4, and can be written as

$$\dot{\mathbf{x}}_{LAx} = \begin{bmatrix} 0 & 1 \\ -\alpha_h\alpha_l & -(\alpha_h + \alpha_l) \end{bmatrix} \mathbf{x}_{LAx} + \begin{bmatrix} 0 \\ \alpha_h \end{bmatrix} n_{LAx}, \quad (2.20a)$$

$$a_{LAx} = \begin{bmatrix} 0 & 1 \end{bmatrix} \mathbf{x}_{LAx}. \quad (2.20b)$$

where  $\alpha_h$  and  $\alpha_l$  are the high-frequency and low-frequency cutoff frequencies, respectively, and  $n_{LAx}$  is modeled as a zero-mean, Gaussian white noise process with variance  $\sigma_{LA}^2$ .

Using the results for the vector reading model (2.14), the measurement residual for the gravity reading (2.18) is defined as  ${}^E\mathbf{z}_g = {}^E\mathbf{g} - \hat{\mathcal{R}}\mathbf{g}_r$  and the first-order formulation is given by

$${}^E\mathbf{z}_g \approx ({}^E\mathbf{g})_{\times} \delta\phi - \hat{\mathcal{R}}\delta\mathbf{b}_a - \hat{\mathcal{R}}\delta(\boldsymbol{\omega} \times {}^B\mathbf{v}) + \hat{\mathcal{R}}\mathbf{a}_{LA} + \hat{\mathcal{R}}\mathbf{n}_a.$$

Using (2.1b) and (2.5), the centripetal acceleration compensation term is given by

$$\delta(\boldsymbol{\omega} \times {}^B\mathbf{v}) \approx (\hat{\boldsymbol{\omega}})_{\times} \hat{\mathcal{R}}'\delta\mathbf{v} + (\hat{\boldsymbol{\omega}})_{\times} ({}^B\hat{\mathbf{v}})_{\times} \hat{\mathcal{R}}'\delta\phi + ({}^B\hat{\mathbf{v}})_{\times} (\delta\mathbf{b}_{\omega} - \mathbf{n}_{\omega}),$$

and the observation equation of the gravity measurement residual equation is

$$\begin{aligned} {}^E\mathbf{z}_g = & -(\hat{\mathcal{R}}\hat{\boldsymbol{\omega}})_{\times} \delta\mathbf{v} + \left( ({}^E\mathbf{g})_{\times} - (\hat{\mathcal{R}}\hat{\boldsymbol{\omega}})_{\times} ({}^E\hat{\mathbf{v}})_{\times} \right) \delta\phi - \hat{\mathcal{R}}\delta\mathbf{b}_a \\ & - ({}^E\hat{\mathbf{v}})_{\times} \hat{\mathcal{R}}\delta\mathbf{b}_{\omega} + \hat{\mathcal{R}}\mathbf{a}_{LA} + \hat{\mathcal{R}}\mathbf{n}_a + ({}^E\hat{\mathbf{v}})_{\times} \hat{\mathcal{R}}\mathbf{n}_{\omega}, \end{aligned} \quad (2.21)$$

where  $\mathbf{a}_{LA}$  is the output of triaxial generalization of the state model dynamics (2.20), integrated in the EKF, and tuned according to the maneuverability characteristics of the vehicles. Fig. 2.3 illustrates the computation of the gravity measurement residual  ${}^E\mathbf{z}_g$ , which is fed to the filter using the observation model (2.21).

## 2.4 Implementation

The continuous-time state space model  $\dot{\mathbf{x}}_C = \mathbf{F}_C(\hat{\mathbf{x}}, \mathbf{u})\mathbf{x}_C + \mathbf{G}_C(\hat{\mathbf{x}})\mathbf{n}_{xC}$  adopted in the filter is described by

$$\begin{aligned} \mathbf{x}_C &= \begin{bmatrix} \delta\mathbf{x}' & \mathbf{x}'_{LAx} & \mathbf{x}'_{LAy} & \mathbf{x}'_{LAz} \end{bmatrix}', & \mathbf{n}_{xC} &= \begin{bmatrix} \mathbf{n}'_x & n_{LAx} & n_{LAy} & n_{LAz} \end{bmatrix}', \\ \mathbf{F}_C(\mathbf{x}, \mathbf{u}) &= \text{blkdiag}(\mathbf{F}(\mathbf{x}, \mathbf{u}), \mathbf{F}_{LA}, \mathbf{F}_{LA}, \mathbf{F}_{LA}), & \mathbf{G}_C(\mathbf{x}) &= \text{blkdiag}(\mathbf{G}(\mathbf{x}), \mathbf{G}_{LA}, \mathbf{G}_{LA}, \mathbf{G}_{LA}), \\ \mathbf{F}_{LA} &= \begin{bmatrix} 0 & 1 \\ -\alpha_l\alpha_h & -(\alpha_l + \alpha_h) \end{bmatrix}, & \mathbf{G}_{LA} &= \begin{bmatrix} 0 \\ \alpha_h \end{bmatrix}, \end{aligned}$$

where  $\delta\mathbf{x}$ ,  $\mathbf{n}_x$ ,  $\mathbf{F}(\mathbf{x}, \mathbf{u})$  and  $\mathbf{G}(\mathbf{x})$  are defined in (2.10). The measurement model  $\mathbf{z} = \mathbf{H}(\hat{\mathbf{x}}, \mathbf{u})\mathbf{x}_C + \mathbf{n}_z$  can be written as

$$\begin{aligned} \mathbf{z} &= \begin{bmatrix} \mathbf{z}'_{\text{GPS}} & {}^E\mathbf{z}'_m & {}^E\mathbf{z}'_g \end{bmatrix}', & \mathbf{n}_z &= \begin{bmatrix} -\mathbf{n}'_{\text{GPS}} & -\hat{\mathcal{R}}\mathbf{n}'_m & \left(-\hat{\mathcal{R}}\mathbf{n}_a + ({}^E\hat{\mathbf{v}})_\times \hat{\mathcal{R}}\mathbf{n}_\omega + \hat{\mathcal{R}}\mathbf{n}_g\right)' \end{bmatrix}', \\ \mathbf{H}(\hat{\mathbf{x}}, \mathbf{u}) &= \begin{bmatrix} \mathbf{I}_3 & \mathbf{0} & \mathbf{0} & \mathbf{0} & \mathbf{0} & \mathbf{0} \\ \mathbf{0} & \mathbf{0} & ({}^E\mathbf{m})_\times & \mathbf{0} & \mathbf{0} & \mathbf{0} \\ \mathbf{0} & (\hat{\mathcal{R}}\boldsymbol{\omega})_\times & ({}^E\mathbf{g})_\times + (\hat{\mathcal{R}}\boldsymbol{\omega})_\times & ({}^E\hat{\mathbf{v}})_\times & -\hat{\mathcal{R}} & -({}^E\hat{\mathbf{v}})_\times \hat{\mathcal{R}} & \hat{\mathcal{R}}\mathbf{H}_{LA} \end{bmatrix}, \\ \mathbf{H}_{LA} &= \text{blkdiag} \left( \begin{bmatrix} 0 & -1 \end{bmatrix}, \begin{bmatrix} 0 & -1 \end{bmatrix}, \begin{bmatrix} 0 & -1 \end{bmatrix} \right), \end{aligned} \quad (2.22)$$

where  $\mathbf{n}_g$  is a fictitious white noise associated with  $\mathbf{z}_g$  observation, and  $\mathbf{z}_{\text{GPS}}$  is the GPS measurement residual, classically defined by the difference between the position estimated by the INS and that measured by the GPS [22], that is

$$\mathbf{z}_{\text{GPS}} := \hat{\mathbf{p}} - \mathbf{p}_{\text{GPS}} = \delta\mathbf{p} - \mathbf{n}_{\text{GPS}},$$

where  $\mathbf{n}_{\text{GPS}} \mathcal{N}(\mathbf{0}, \Xi_{\text{GPS}})$  is a Gaussian white noise that models the GPS measurement noise.

The state and observation noise covariance matrices are

$$\begin{aligned} \mathbf{Q}_C &= \text{blkdiag}(\Xi_p, \Xi_a, \Xi_\omega, \Xi_{b_a}, \Xi_{b_\omega}, \Xi_{LA}), \\ \mathbf{R}_C(\hat{\mathbf{x}}) &= \text{blkdiag}(\Xi_{\text{GPS}}, \Xi_m, \hat{\mathcal{R}}\Xi_a\hat{\mathcal{R}}' - ({}^E\hat{\mathbf{v}})_\times \hat{\mathcal{R}}\Xi_\omega\hat{\mathcal{R}}' ({}^E\hat{\mathbf{v}})_\times + \hat{\mathcal{R}}\Xi_g\hat{\mathcal{R}}'), \end{aligned}$$

where  $\Xi_{LA} = \sigma_{LA}^2 \mathbf{I}_3$ . The discrete-time state space model

$$\mathbf{x}_{k+1} = \Phi_k \mathbf{x}_k + \mathbf{w}_k, \quad \mathbf{z}_k = \mathbf{H}_k \mathbf{x}_k + \mathbf{v}_k,$$

is obtained by sample-and-hold of the inputs [22] and is given by

$$\Phi_k = e^{\mathbf{F}_k T}, \quad \mathbf{H}_k = \mathbf{H}(\mathbf{x}, \mathbf{u})|_{t=t_k},$$

and the discrete-time noise covariance matrices are [56]

$$\mathbf{Q}_k \simeq \mathbf{G}_k \mathbf{Q}_C \mathbf{G}_k' T, \quad \mathbf{R}_k \simeq \frac{\mathbf{R}_{Ck}}{T},$$

where  $T$  is the sampling period,  $\mathbf{F}_k = \mathbf{F}_C(\mathbf{x}, \mathbf{u})|_{t=t_k}$ ,  $\mathbf{G}_k = \mathbf{G}_C(\mathbf{x})|_{t=t_k}$ ,  $\mathbf{R}_{Ck} = \mathbf{R}_C(\mathbf{x})|_{t=t_k}$  and  $\Phi_k = \Phi(t_{k+1}, t_k)$  denotes the state transition matrix.

The gravity measurement residual  ${}^E\mathbf{z}_g$  introduces state and measurement noise correlation matrix [22]

$$\mathbf{C}_C(\hat{\mathbf{x}}) = \begin{bmatrix} \mathbf{0} & \mathbf{0} & \mathbf{0} & \mathbf{0} & \mathbf{0} & \mathbf{0} \\ \mathbf{0} & \mathbf{0} & \mathbf{0} & \mathbf{0} & \mathbf{0} & \mathbf{0} \\ \mathbf{0} & -\hat{\mathcal{R}}\Xi_a & -({}^E\hat{\mathbf{v}})'_{\times} \hat{\mathcal{R}}\Xi_{\omega} & \mathbf{0} & \mathbf{0} & \mathbf{0} \end{bmatrix}',$$

$$\mathbf{C}_k = \frac{1}{T} \int_{t_{k-1}}^{t_k} \Phi(t_k, \tau) \mathbf{G}(\tau) \mathbf{C}_C(\tau) d\tau \simeq (\mathbf{I}_3 + \frac{\mathbf{F}_k T}{2}) \mathbf{G}_k \mathbf{C}_{Ck},$$

where  $\mathbf{C}_C(\mathbf{x})$  is the continuous state and measurement noises correlation matrix,  $\mathbf{C}_{Ck} = \mathbf{C}_C(\mathbf{x})|_{t=t_k}$ , and the discrete-time equivalent matrix  $\mathbf{C}_k$  is computed using a first order approximation similar to those discussed in [22] for  $\mathbf{Q}_k$  and  $\mathbf{R}_k$ . The following Kalman gains and error covariance matrix equations are modified to include the state and measurement noises correlation matrix

$$\mathbf{K}_k = (\mathbf{P}_k^- \mathbf{H}_k' + \mathbf{C}_k) [\mathbf{H}_k \mathbf{P}_k^- \mathbf{H}_k' + \mathbf{R}_k + \mathbf{H}_k \mathbf{C}_k + \mathbf{C}_k' \mathbf{H}_k']^{-1},$$

$$\mathbf{P}_k^+ = (\mathbf{I}_n - \mathbf{K}_k \mathbf{H}_k) \mathbf{P}_k^- - \mathbf{K}_k \mathbf{C}_k',$$

and the filter covariance matrix is updated using  $\mathbf{P}_{k+1}^- = \Phi_k \mathbf{P}_k^+ \Phi_k' + \mathbf{Q}_k$ .

After each EKF update, error estimates are fed into the INS error correction routines as depicted in Figs. 2.1 and 2.2, where the quantities predicted by the INS are denoted by the superscript  $-$  and the updated quantities are identified with the superscript  $+$ . It is important to stress that linearization assumptions are kept valid during the algorithm execution since the EKF error estimates are reset after being used to compensate the corresponding variables [99]. The error correction procedures are specific to the INS algorithms and error state space representations. For the INS adopted in this work, error routines are detailed next.

The attitude estimate is compensated using the rotation error matrix  $\mathbf{R}(\delta\phi)$  definition, which yields

$$\hat{\mathcal{R}}_k^+ = \mathbf{R}'(\delta\hat{\phi}_k) \hat{\mathcal{R}}_k^-, \quad (2.23)$$

where matrix  $\mathbf{R}'(\delta\hat{\phi}_k)$  is described exactly as

$$\mathbf{R}'(\delta\hat{\phi}_k) = \mathbf{I}_3 - \frac{\sin(\|\delta\hat{\phi}_k\|)}{\|\delta\hat{\phi}_k\|} (\delta\hat{\phi}_k)_{\times} + \frac{1 - \cos(\|\delta\hat{\phi}_k\|)}{\|\delta\hat{\phi}_k\|^2} (\delta\hat{\phi}_k)_{\times}^2,$$

and is computationally implemented using power series expansion of the scalar trigonometric terms up to an arbitrary accuracy [128]. In the case where few computational resources are available,  $\mathcal{R}'(\delta\hat{\phi}_k)$  can be approximated to first order by  $\mathcal{R}'(\delta\hat{\phi}_k) \simeq \mathbf{I}_3 - (\delta\hat{\phi}_k)_{\times}$  that, nonetheless, introduces DCM orthogonalization problems in  $\hat{\mathcal{R}}_k^+$  whose compensation usually requires considerable computational effort [9]. The remaining state variables are simply compensated using

$$\hat{\mathbf{p}}_k^+ = \hat{\mathbf{p}}_k^- - \delta\hat{\mathbf{p}}_k, \quad \hat{\mathbf{v}}_k^+ = \hat{\mathbf{v}}_k^- - \delta\hat{\mathbf{v}}_k, \quad \hat{\mathbf{b}}_{ak}^+ = \hat{\mathbf{b}}_{ak}^- - \delta\hat{\mathbf{b}}_{ak}, \quad \hat{\mathbf{b}}_{\omega k}^+ = \hat{\mathbf{b}}_{\omega k}^- - \delta\hat{\mathbf{b}}_{\omega k}. \quad (2.24)$$

Table 2.1: Sensor non-idealities.

Sensor	Bias	Noise Variance
Rate Gyro	5 °/s	(0.02 °/s) <sup>2</sup>
Accelerometer	12 mg	(0.6 mg) <sup>2</sup>
Magnetometer	(calibrated)	(60 μG) <sup>2</sup>
GPS	-	10 m <sup>2</sup>

The INS block structure with EKF corrections is depicted in Fig. 2.2, where the error compensation and bias update routines, (2.23) and (2.24) respectively, are executed after the INS outputs have been fed to the EKF and errors estimates are available. Note that the EKF sampling rate is synchronized with the moderate-speed INS output rate and that no corrections are involved in the high-speed computation algorithms. After the error correction procedure is completed, the EKF error estimates are reset  $\delta\hat{\mathbf{x}}_k = 0$ . The INS error correction and EKF estimate reset do not influence the uncertainty of the estimated quantities, and hence the estimation error covariance is unaffected by this procedure [99]. At the start of the next computation cycle ( $t = t_{k+1}$ ), the INS attitude and velocity/position updates presented in Section 2.1 are performed on the corrected estimates  $(\hat{\mathcal{R}}_k^+, \hat{\mathbf{v}}_k^+, \hat{\mathbf{p}}_k^+)$  to provide new inputs  $(\hat{\mathcal{R}}_{k+1}^-, \hat{\mathbf{v}}_{k+1}^-, \hat{\mathbf{p}}_{k+1}^-)$  to the EKF.

## 2.5 Simulation results

This section presents a simulation study of the proposed navigation system, prior to the practical implementation of the algorithm in the autonomous surface craft. The impact of the vector observation in the estimation results is analyzed, by considering three case study simulations. In the first case, the navigation system is initialized with large estimation errors to evidence how the estimation results can be enhanced by the use of vector measurements. A standard rigid body trimming trajectory with constant centripetal acceleration is generated to demonstrate the necessity of centripetal acceleration removal in the pendular measurements. In the second case study, the linear acceleration model (2.19) is validated, by presenting the response of the navigation system when the vehicle is subject to a step acceleration with damping. In the third case study, poor GPS signal detection is simulated to illustrate how the position estimates remain within acceptable bounds by means of the pendular measurements.

The INS high-speed algorithm is executed at 100 Hz and the normal-speed algorithm is synchronized with the EKF discrete-time frequency of 50 Hz. The GPS position measurements are obtained at the nominal frequency of 1 Hz. The characteristics of the simulated inertial and aiding sensors are presented in Table 2.1.

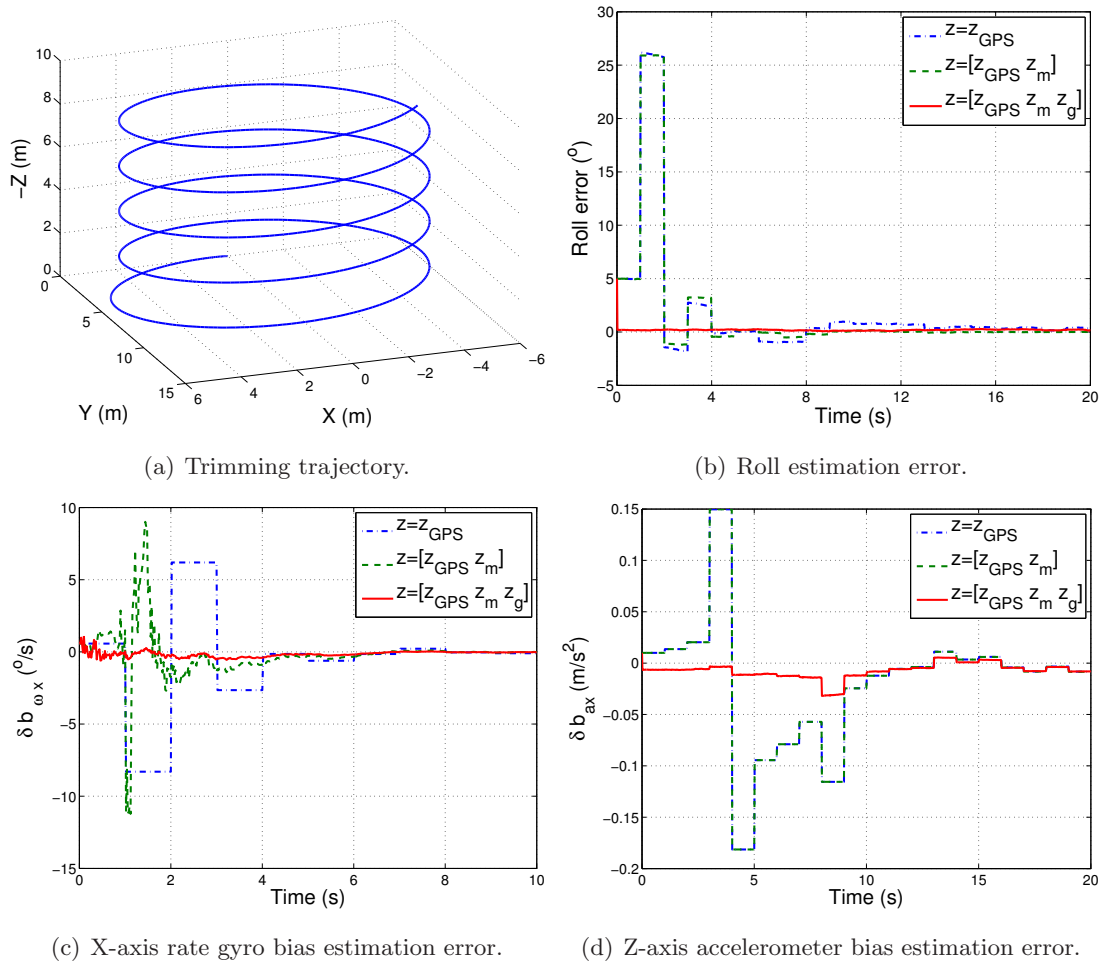


Figure 2.5: Initial estimation error compensation.

### 2.5.1 Initial calibration error

The contribution of the magnetic and pendular measurements to the accuracy of the estimates is studied for the initial estimation error of  $5^\circ$  in the roll angle, and calibration errors in the rate gyro and accelerometer bias given by  $\delta b_{\omega_x} = 0.57^\circ/\text{s}$  and  $\delta b_{a_z} = 1 \text{ mg}$ , respectively. The rigid body describes the ascending helix depicted in Fig. 2.5(a), which is a standard trimming trajectory subject to constant centripetal acceleration. The convergence of the estimation errors shown in Figs. 2.5(b), 2.5(c) and 2.5(d) evidences that the pendular readings improve on the GPS and magnetometer aiding, by enhancing the observability of errors such as the gyro bias, roll angle and vertical accelerometer bias, as expected from physical intuition and analysis of the observability matrix for trimming trajectories. Interestingly enough, the obtained estimation results were stable and accurate although the small error assumption underlying the EKF derivation was not verified by the initial estimation errors.



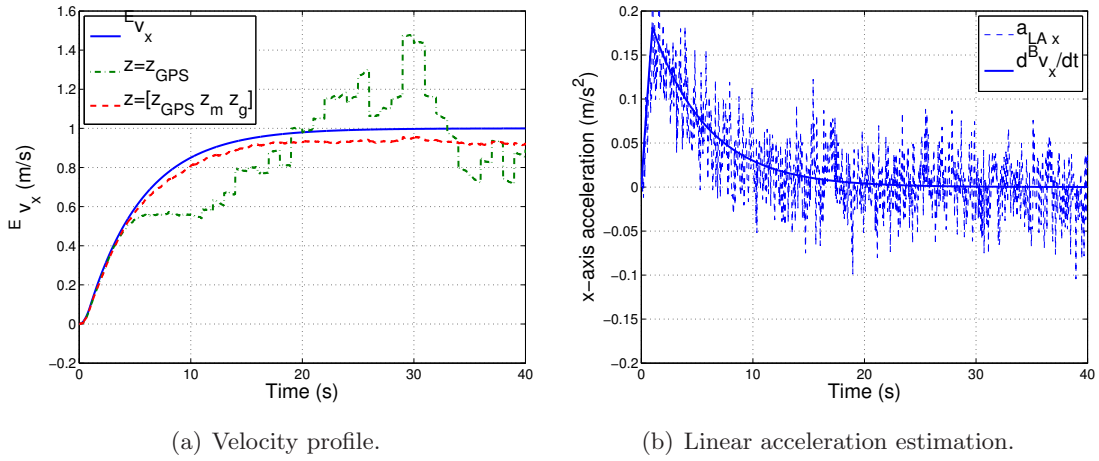


Figure 2.6: Linear accelerated motion compensation results.

Table 2.2: Filter results, straight path trajectory.

	RMS Error					
	$p_x$ (m)	$p_y$ (m)	$p_z$ (m)	Yaw ( $^\circ$ )	Pitch ( $^\circ$ )	Roll ( $^\circ$ )
$\mathbf{z} = \mathbf{z}_{\text{GPS}}$	1.35	1.77	0.91	12.97	0.26	0.17
$\mathbf{z} = [\mathbf{z}'_{\text{GPS}} \quad \mathbf{z}'_m \quad \mathbf{z}'_g]'$	0.65	1.51	0.91	$3.16 \times 10^{-3}$	0.18	0.14

### 2.5.2 Linear accelerated motion

The impact of the vector aiding in the navigation system results is analyzed for the case of a straight line trajectory. The vehicle is subject to a constant acceleration input that is progressively compensated by the linear drag effects, as depicted in Fig. 2.6(a), and linear uniform motion is attained. Fig. 2.6(b) validates the assumption that vehicle's linear acceleration component in  $\mathbf{z}_g$  can be modeled as a band-pass signal (2.20), and hence the low frequency contents of  $\mathbf{z}_g$  are used to estimated the inertial system errors. Numerical results obtained with the proposed technique are presented in Table 2.2, where improvements due to the inclusion of aiding vector observations are evidenced.

### 2.5.3 Trimming trajectory

The medium term navigation system behavior is assessed for the trimming trajectory with standard initial estimation errors. Fig. 2.7 demonstrates the performance enhancements introduced by the magnetometer readings and the selective frequency contents of the accelerometers measurements. As presented in Table 2.3, the magnetometer readings smooth out yaw errors, and pendular observations enhance the estimation of roll and pitch. Due to the position and attitude errors correlation expressed in (2.9), x-axis and y-axis position errors are improved by the magnetic and pendular observations, respectively. Also, the constant centripetal acceleration of the trimming trajectory is successfully compensated

for.

Simulation results for a GPS signal with output frequency of 0.2 Hz are depicted in Fig. 2.8, with and without pendular measurement aiding. The figure shows that x- and y-axes position estimates are enhanced by the selective frequency contents of the accelerometers measurements. The filter exploits the pendular measurements, limiting the position estimate divergence when the GPS signal is sparse, and extending the navigation system autonomy with respect to the GPS aiding source.

## 2.6 Experimental results

The proposed navigation system is validated using a low-power hardware architecture enclosing low-cost sensors and mounted on-board the DELFIMx catamaran. Experimental results obtained at sea illustrate the performance of the navigation system in practice for standard ASC trajectories, emphasizing its robustness characteristics. Namely, the compensation of the pendular measurements disturbances in the frequency domain is validated, and the autonomy of the navigation system with respect to GPS measurements is demonstrated. A detailed description of the DELFIMx craft and the adopted hardware is found in Appendix B.

### 2.6.1 Experimental results analysis

This section evaluates the navigation system for a set of experimental data. The results were obtained for a DELFIMx sea-trial conducted on October 2007 on the coast of Sesimbra, Portugal, located at  $38^\circ 26'N$ ,  $9^\circ 6'W$ . The trajectory described by the catamaran was obtained using the path-following preview controller proposed in [57], and was designed to demonstrate the maneuverability of the vehicle in challenging applications by comprising straight lines, curves and oscillatory trajectories generated by coning motion, as shown in Fig. 2.9.

The parameters of the EKF were tuned as follows. The covariances of the inertial and aiding sensors were computed by processing sensor data obtained with the DELFIMx at rest on the harbor facilities. The pendular model (2.20) was characterized by the covariance  $\sigma_{LA}^2 = 10^{-5}$  and the poles  $\alpha_l = 3.64$  Hz and  $\alpha_h = 27$  Hz, which describe a high frequency process given that the sampling frequency of the navigation system is 56 Hz. The classical technique of system robustification by inflating the noise covariances was adopted [4], namely the covariance of the pendular observation noise  $\mathbf{n}_g$  was defined as  $\Xi_g = 10^{-5}\mathbf{I}_3$  to account for second order terms in the observation model (2.21), and the velocity error state covariance was set as  $\Xi_v = \Xi_a + 7 \times 10^{-4}\mathbf{I}_3$ , to balance the influence of the GPS aiding and the IMU computations in the estimated position and velocity. To validate the adopted covariances, it will be shown that the navigation system successfully merges the available information and, to better illustrate the qualities of the proposed solution, navigation system results with GPS signal blockage are also considered.

Table 2.3: Filter results, trimming trajectory.

	RMS Error					
	$p_x$ (m)	$p_y$ (m)	$p_z$ (m)	Yaw ( $^\circ$ )	Pitch ( $^\circ$ )	Roll ( $^\circ$ )
$\mathbf{z} = \mathbf{z}_{\text{GPS}}$	1.35	1.77	0.91	12.96	0.26	0.17
$\mathbf{z} = [\mathbf{z}'_{\text{GPS}} \quad \mathbf{z}'_m]'$	0.66	1.79	0.91	$3.17 \times 10^{-3}$	0.20	0.17
$\mathbf{z} = [\mathbf{z}'_{\text{GPS}} \quad \mathbf{z}'_m \quad \mathbf{z}'_g]'$	0.65	1.51	0.91	$3.16 \times 10^{-3}$	0.18	0.14

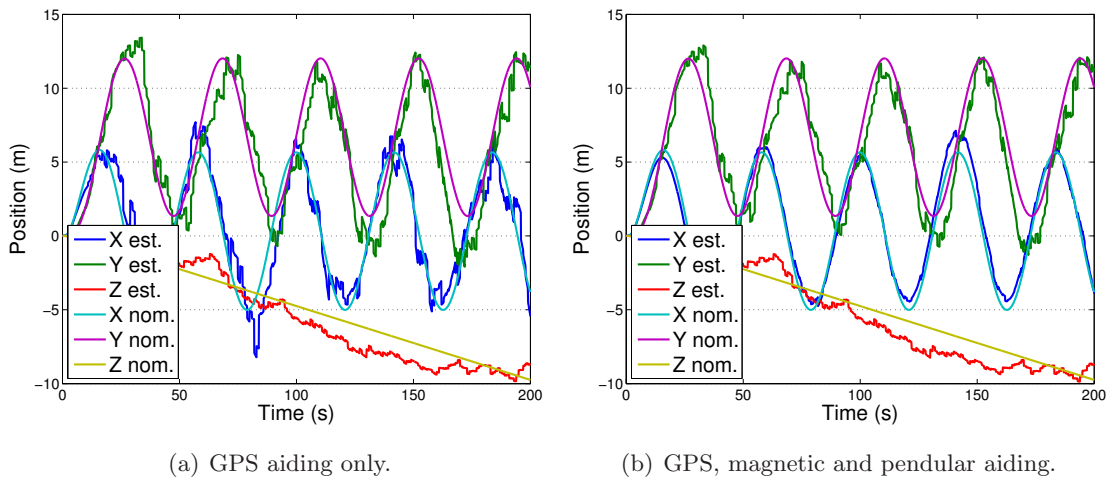


Figure 2.7: Trimming trajectory results.

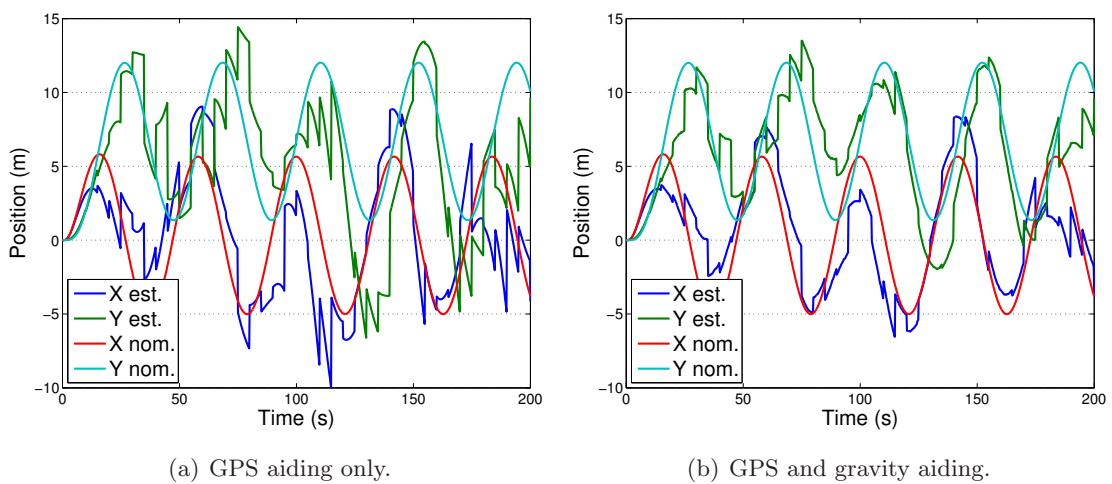


Figure 2.8: Position results for sparse GPS signal, sampled at 0.2Hz.

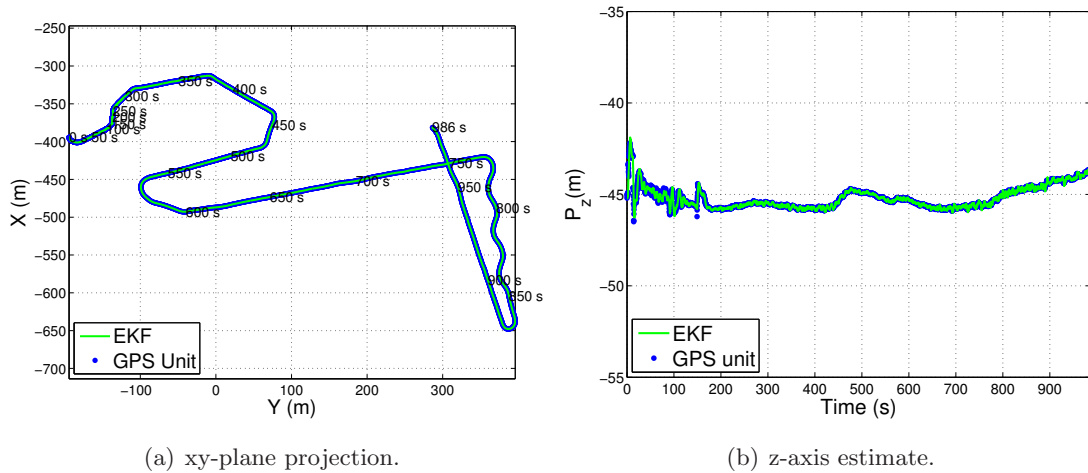


Figure 2.9: Measured and estimated DELFIMx trajectory.

The navigation system was initialized using attitude and position estimates provided by the aiding sensors. The diverse frequency rates of the aiding sensors, i.e. GPS, magnetometer, and pendular measurement, are easily handled in the filter by selecting the rows of the measurement matrix (2.22) according to the available measurement at each time instant. The initial attitude guess was obtained using the QUEST attitude reconstruction algorithm [129] to process the first magnetometer and accelerometer measurements, and the position estimate was acquired directly from the first good quality GPS measurement available.

The position and attitude estimation results are presented in Figs. 2.9 and 2.10, and are consistent with the trajectory outlined by the GPS measurements. The estimated position smoothly tracks the trajectory described by the DELFIMx catamaran. The estimated yaw is according to the described trajectory, and to the heading measurement provided by the GPS, which is depicted only for comparison purposes. The average estimated pitch and roll angles are according to the installation angles of the IMU architecture in the DELFIMx platform.

The estimated angular and linear velocities of the catamaran are shown in Fig. 2.11. The angular velocity is consistent with the vehicle maneuvers. The linear velocity is represented in body fixed coordinates because the velocity variations occur naturally in the body axis. As expected,  ${}^B v_x$  is positive and characterized roughly by concatenation of forward velocities, while the lateral and vertical velocities fluctuate around zero.

Although the navigation system was stable in extensive simulation studies where large initial bias estimation error was considered, offline calibration was adopted in practice to guarantee that the small error assumption of the EKF perturbational model was kept valid from the start. An initial guess of the accelerometer and rate gyro biases was obtained offline and after warming up the IMU. The initial covariance of the filter was set to compensate for small errors of the offline calibration, and to account for the bias fluctuations between the time instants of the calibration procedure and the navigation system initial-

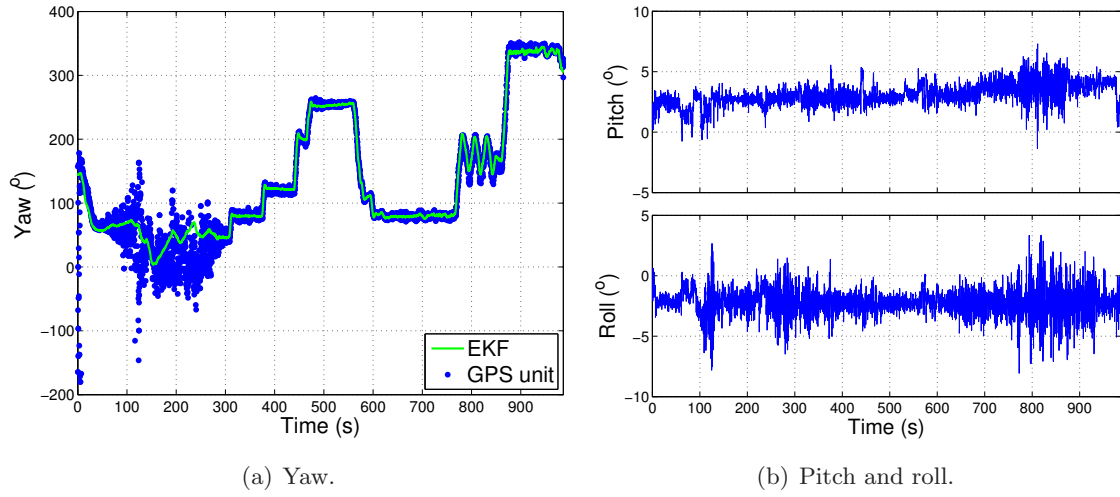


Figure 2.10: Attitude estimation results (DELFINx trajectory).

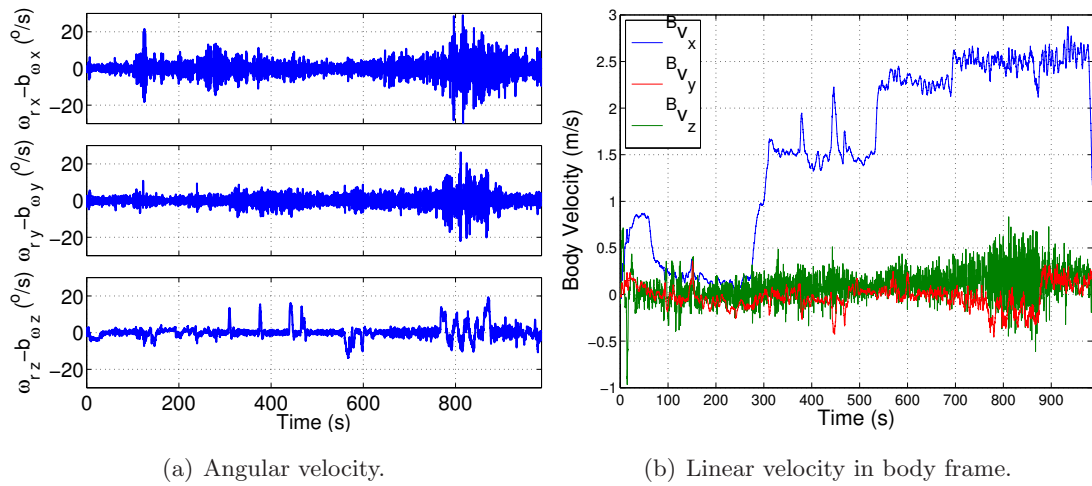


Figure 2.11: Velocity estimation results (DELFINx trajectory).

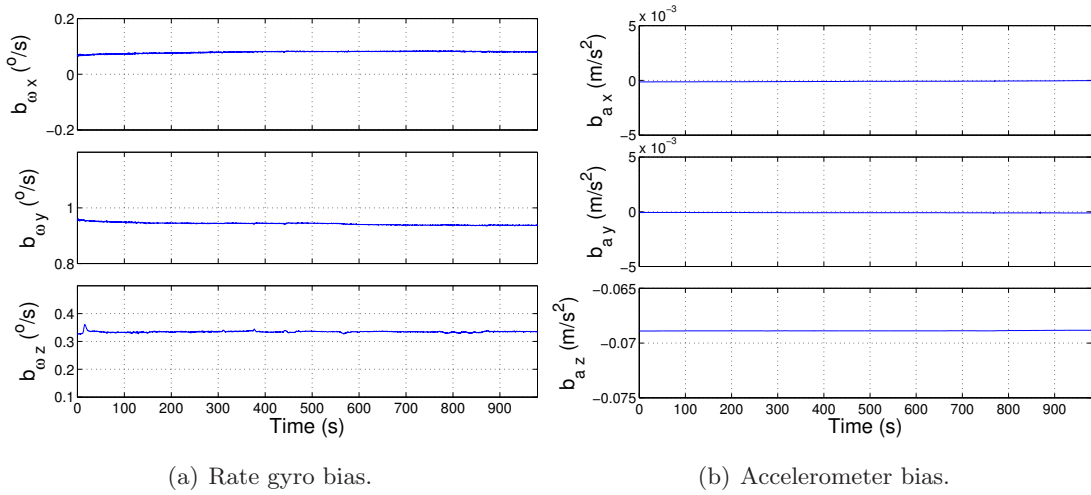


Figure 2.12: Bias estimation results (DELFINx trajectory).

ization. The filter covariances  $\Xi_{b_a}$ ,  $\Xi_{b_\omega}$  were designed small enough to compensate for the slow variations of the bias in the course of the mission,  $\Xi_{b_a} = \Xi_{b_\omega} = 10^{-12} \mathbf{I}_3$ . As shown in Fig. 2.12, the bias estimate is approximately constant, which supports the slowly varying bias model.

The vector aiding technique described in Section 2.3 was adapted to the application at hand. Analyzing the measurement model (2.21) for  ${}^E \mathbf{g} = [0 \ 0 \ g]'$ , it is straightforward to verify that the z-axis measurement residual  ${}^E z_z$  does not relate to the attitude error  $\delta\phi$ , i.e. it is uninformative for the purpose of attitude determination. Also, the collected magnetometer data were roughly planar and hence enough to calibrate only the soft iron and hard iron distortions in the  $xy$  plane of the magnetometer. Consequently, the vertical components of the measurement residuals  ${}^E z_z$  and  ${}^E z_m$  were neglected in the filtering algorithm, by omitting the corresponding rows of the measurement matrix  $\mathbf{H}$ . The aiding measurements components can be easily selected, which shows the flexibility of the present navigation solution.

The modeling of the pendular vector measurements described in Section 2.3.2 is validated using frequency domain analysis of the measured and estimated signals. The power spectral density (PSD) of the desired signals was obtained using Matlab's `pwelch` function, i.e. Welch's averaged modified periodogram method of spectral approximation. Fig. 2.13 presents the frequency contents of the pendular reading  $\mathbf{g}_r$ , defined in (2.18), and of the linear acceleration estimate  $\mathbf{a}_{LA}$ , defined in (2.20). The PSDs of  $\mathbf{g}_r$  and  $\mathbf{a}_{LA}$  are very similar in the medium and high frequency regions, and diverge in the low frequency domain where the PSD of  $\mathbf{a}_{LA}$  is smaller than the PSD of  $\mathbf{g}_r$ . This shows that the filter exploits in fact the low frequency contents of  $\mathbf{g}_r$  for attitude estimation, while the medium and high frequency linear acceleration disturbances are associated with the signal  $\mathbf{a}_{LA}$ , as desired. The PSD of the signals in the low frequency region is shown in detail in Fig. 2.14.

The dependency of the navigation system with respect to the aiding measurements is

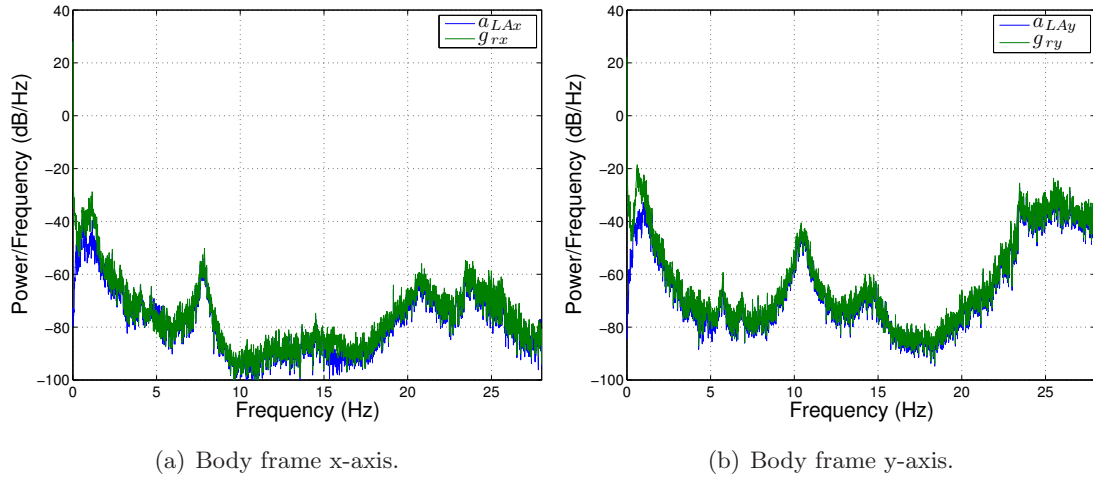


Figure 2.13: Frequency contents of the pendular reading and estimated linear acceleration.

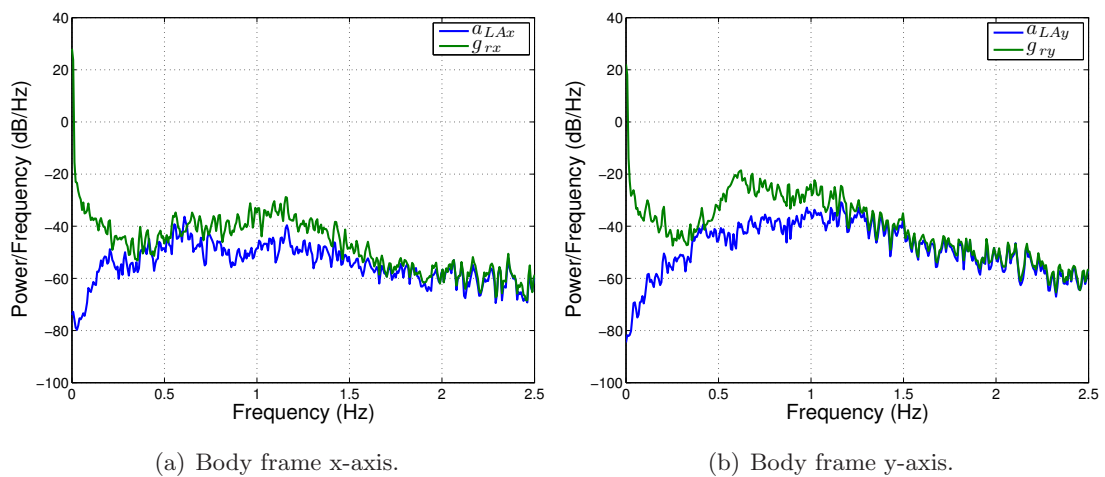


Figure 2.14: Frequency contents of the pendular reading and estimated linear acceleration (low frequency region).

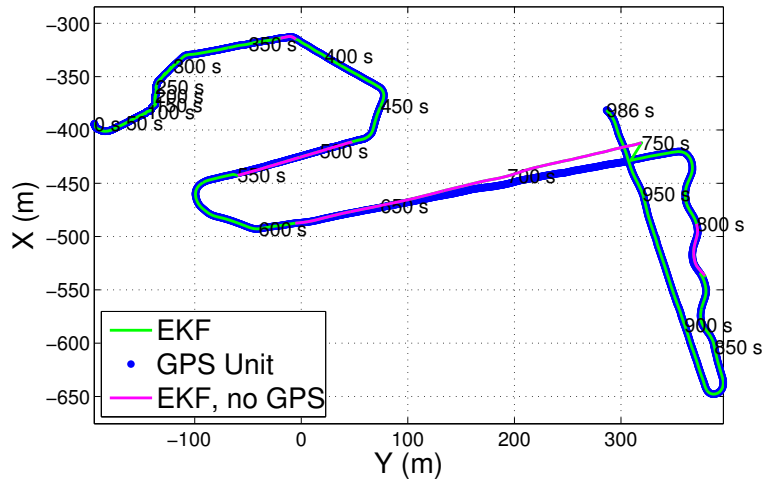


Figure 2.15: Measured and estimated DELFIMx trajectory with GPS outage.

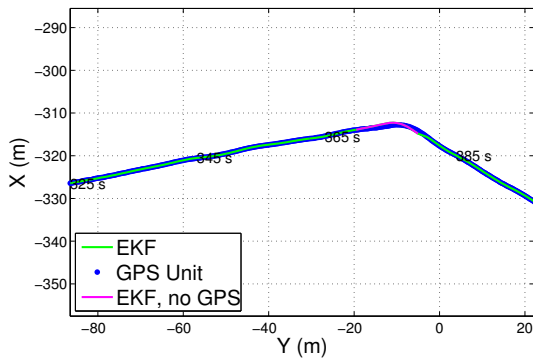
Table 2.4: Position drift due to GPS outage.

Time Interval (s)	With Pendular Aiding		Without Pendular Aiding	
	Final (m)	Average (m/s)	Final (m)	Average (m/s)
[370 380]	1.76	0.176	5.65	0.565
[480 550]	4.24	0.061	28.51	0.407
[615 750]	20.3	0.150	720.5	5.337
[800 820]	5.60	0.280	11.96	0.598

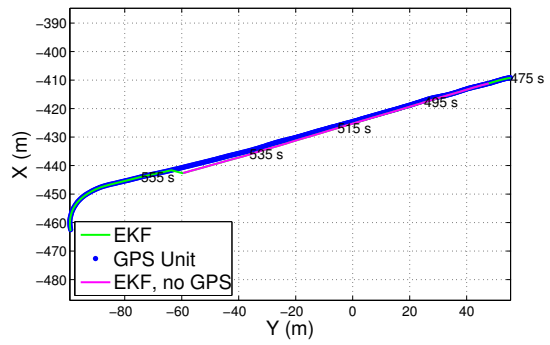
studied by disabling the GPS measurements at selected time intervals when the vehicle turns or enters in long straight paths. The nominal and estimated trajectories are shown in Fig. 2.15, a zoom of the trajectories at the GPS outage time intervals is presented in Fig. 2.16, and an estimate of the position estimation error is presented in Fig. 2.17. The position and attitude estimates track the curve and straight line paths in the short term, which shows that the performance of the system without GPS aiding is adequate for practical applications. It also evidences that the navigation system acts according to the concept of filtering, by merging the IMU and aiding measurements without relying solely on the GPS data.

The tests in the presence of GPS outage also illustrate the necessity of pendular measurements, as shown in Table 2.4, where the position drift is approximated by the first measurement residual  $\mathbf{z}_{\text{GPS}}$  when the GPS is successfully reacquired. The performance of the navigation system is clearly enhanced by the pendular measurements, which extend the autonomy of the unit with respect to GPS measurements.

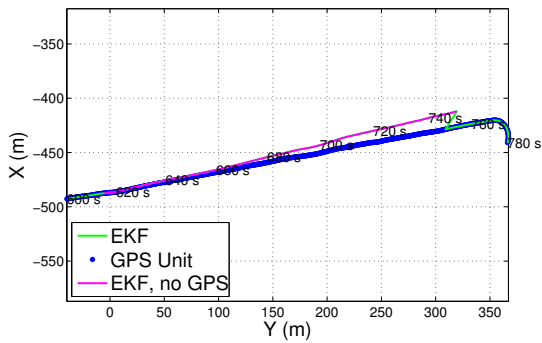




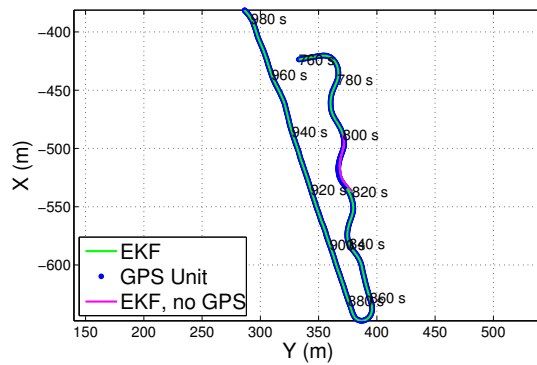
(a) GPS outage at [370 380] s.



(b) GPS outage at [480 550] s.



(c) GPS outage at [615 750] s.



(d) GPS outage at [800 820] s.

Figure 2.16: Estimated and measured position at the time intervals of the GPS outage.

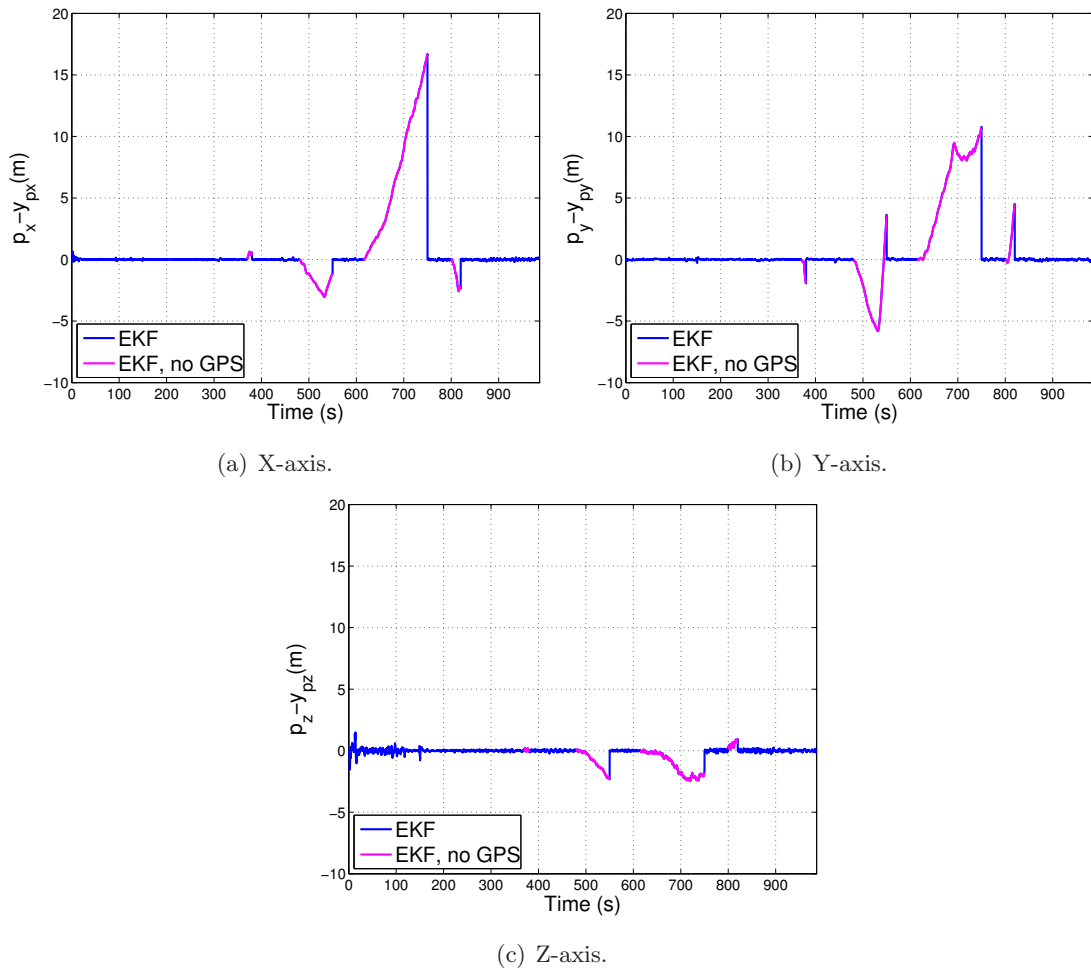


Figure 2.17: Difference between the estimated and the measured positions, with GPS outage (DELFI<sub>M</sub>x trajectory).

## 2.7 Conclusion

An advanced GPS/INS architecture combined with an EKF algorithm and integrating vector observations was described. The navigation system comprised an high accuracy, multirate INS algorithm, combined with an EKF in a direct-feedback configuration to compensate for inertial sensors non-idealities. An aiding technique that directly integrates vector measurements in the filter was detailed, allowing for the use of a frequency domain model of the vehicle motion in the filter. The experimental results obtained at sea with the DELFIMx ASC showed that the proposed navigation system can accurately estimate position and attitude. The compensation of sensor non-idealities such as bias and noise effects, and the autonomy with respect to GPS aiding by exploiting the vector measurement directly in the filter, were evidenced in practice.



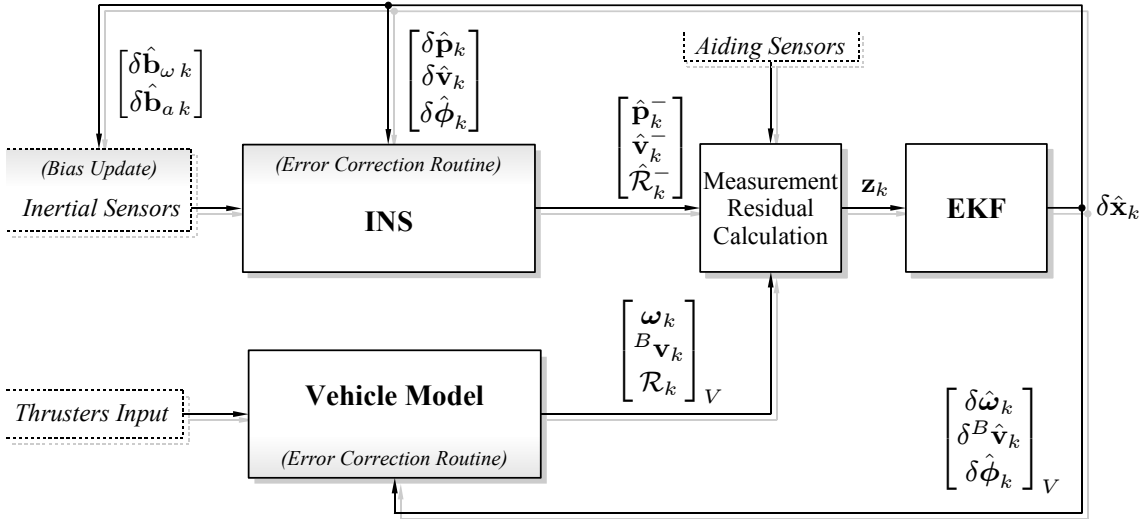
## Chapter 3

# Embedded UAV Model and LASER aiding techniques for high accuracy inertial navigation systems

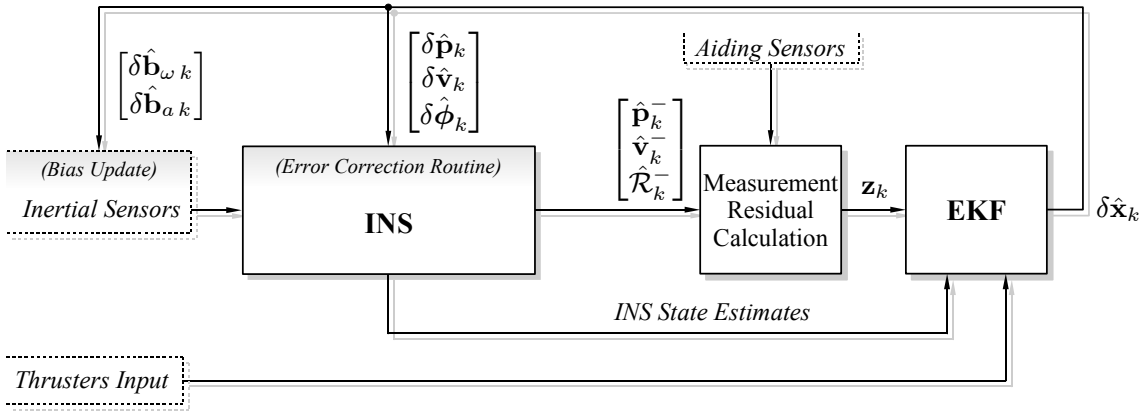
This chapter proposes advanced aiding techniques for precise position and attitude estimation of autonomous vehicles, using low-cost sensors. The navigation system architecture considered in this chapter is obtained by merging a high accuracy inertial navigation system (INS) with the information obtained from the vehicle dynamics (VD), using an Extended Kalman Filter (EKF). A new method to integrate the vehicle dynamics in the navigation system is proposed, based on using the vehicle dynamics to propagate the INS state estimates, exploiting the redundancy of the information provided by the VD and by the high quality INS integration algorithms.

The backbone structure of the navigation system is based on a classical EKF/INS architecture, depicted in Fig. 3.1, and previously detailed in Sections 2.1 and 2.2. In classical architectures using vehicle dynamics aiding, the VD block plays the role of an extra INS unit [23, 64, 82], as shown in Fig. 3.1(a). That is, the vehicle dynamics are computed by a vehicle model simulator and the output is compared to the INS estimates. The EKF state model is augmented to dynamically estimate both the INS and the VD errors, improving the overall navigation system accuracy. This classical VD aiding configuration enhances the accuracy of the INS at the cost of integrating the VD model, augmenting the EKF states to compensate for the VD errors, and using error compensation routines in the external vehicle model.

The proposed technique to integrate the VD dynamics, depicted in Fig. 3.1(b), merges the VD information directly in the EKF. In this technique, the INS estimates are propagated simultaneously using the vehicle dynamics and the INS algorithm. The distinct VD and INS differential equations applied to the same inertial quantity enables the EKF to



(a) External vehicle dynamics.



(b) Embedded vehicle dynamics.

Figure 3.1: Navigation system block diagram.

estimate and compensate for the inertial errors. The computational cost associated with VD aiding is reduced due to *i*) the embedding of the vehicle model, that allows for the exclusive estimation of the INS errors, and *ii*) the use of inertial estimates in the computation of the vehicle dynamics, that enables formulating some of the VD equations directly as a filter measurement. Also, the VD equations are decoupled, and it is possible to select only those that characterize the vehicle more accurately.

The advanced aiding techniques proposed in this chapter are motivated by model-scale helicopters, that are highly maneuverable platforms with the ability to perform Vertical Takeoff and Landing (VTOL). The derived vehicle aiding techniques are introduced and validated using a generic fully actuated rigid body simulator example, and extended to a model-scale Vario X-Treme helicopter model simulator to demonstrate its application to realistic setups. Since takeoff and landing maneuvers of VTOL crafts require precise estimates of the distance-to-ground, a LASER range finder sensor implementation is also detailed, enhancing the vertical channel position and velocity estimates.

This chapter is organized as follows. Section 3.1 describes the inertial navigation system and the Kalman filtering algorithm adopted in this work. Section 3.2 presents the vehicle model aiding architectures, and the two methods to integrate the vehicle information in the navigation system are detailed. The dynamics of a fully actuated rigid body are described, and adopted to illustrate the VD aiding techniques. Section 3.3 characterizes the LASER sensor and describes the integration of the sensor information in the navigation system structure. Section 3.4 provides the implementation details. Namely, the state model of the EKF for each aiding technique, the discretization process and the error correction routines are detailed. Simulation results for the VD model and LASER range finder sensor are presented in Section 3.5. The classical VD is validated using a standard UAV trajectory, and tested with the Vario X-Treme helicopter model. The LASER aiding is studied by simulating a landing maneuver where the distance-to-ground is unknown. Concluding remarks are presented in Section 3.6.

## 3.1 Navigation system structure

This section describes the adopted navigation system architecture, that comprises a high accuracy, multirate INS integration algorithm, combined with advanced error compensation techniques based on Kalman filtering, as illustrated in Fig. 3.1. The INS algorithm integrates the rigid body kinematics differential equations from the output of inertial sensors, which allows for its use in any robotic platform regardless of the available position and attitude references, and irrespective of the vehicle dynamics. However, the INS position and attitude estimation errors will drift with time under the influence of accelerometer and rate gyro non-idealities such as noise, scaling factors, sensor misalignment and bias calibration errors, among others.

The EKF dynamically estimates the INS errors, by merging available aiding information such as GPS position measurements, attitude information contained in vector observations, and vehicle model dynamics, as illustrated in Fig. 3.1. The INS errors are then compensated by modeling their first order description in state space form, comparing the aiding information with the INS estimates, and feeding back the errors estimate to the INS (direct-feedback configuration).

This section presents the main characteristics of the INS and EKF algorithms adopted in this work. The concept of multirate high accuracy inertial integration algorithm, the EKF state space formulation and the error compensation routines are introduced. The navigation system is presented concisely and for the sake of completeness, providing the necessary background for the LASER and the vehicle dynamics aiding techniques, for further details on the present architecture see Sections 2.1 and 2.2.

### 3.1.1 Inertial navigation system

The INS performs attitude, velocity and position numerical integration from rate gyro and accelerometer triads data, rigidly mounted on the vehicle structure (strapdown configu-

ration). For highly maneuverable vehicles, the INS numerical integration algorithm must properly address the fast dynamics of inertial sensors output, to avoid estimation errors buildup. The adopted INS algorithm is proposed on the tutorial work found in [126, 127] and is described in Section 2.1. The INS multirate approach accounts for angular position, linear velocity, and linear position high frequency motions, referred to as coning, sculling, and scrolling, respectively. In this framework, a high speed, low order algorithm computes dynamic angular rate/acceleration effects at a small sampling interval, and its output is periodically fed to a moderate-speed algorithm that computes attitude/velocity resorting to exact, closed-form equations.

The moderate-speed inertial algorithms represent attitude in rotation matrix form, and velocity and position are expressed in Earth frame coordinates. Simulation environments and case study trajectories to tune the algorithm's execution rates according to performance specifications are described in [126, 127]. A standard low-power consumption DSP based hardware architecture is found sufficient to run the algorithm at the highest accuracy repetition rates. Therefore, for a low cost architecture, high computational precision is obtained and the discrete-time integration errors are very small with respect to the other INS error sources such as inertial sensor bias and noise.

### 3.1.2 Extended Kalman Filter

The inertial estimation errors are compensated for by merging the INS estimates with aiding information in the EKF algorithm [22]. The EKF error equations, based on perturbational rigid body kinematics, were brought to full detail in [20], and yield a first-order model of the INS estimation errors and sensor non-idealities. The nominal rigid body kinematics are given by

$$\dot{\mathbf{p}} = \mathbf{v}, \quad \dot{\mathbf{v}} = \mathcal{R}^B \mathbf{a}, \quad \dot{\mathcal{R}} = \mathcal{R}(\boldsymbol{\omega})_{\times}, \quad (3.1)$$

where the Earth and body frames are respectively denoted by  $\{E\}$  and  $\{B\}$ ,  $\mathcal{R}$  is the shorthand notation for the rotation matrix  ${}^E_B \mathbf{R}$ , and  $(\mathbf{s})_{\times}$  represents the skew symmetric matrix defined by the vector  $\mathbf{s} \in \mathbb{R}^3$  such that  $(\mathbf{s})_{\times} \mathbf{r} = \mathbf{s} \times \mathbf{r}$ ,  $\mathbf{r} \in \mathbb{R}^3$ . The angular velocity and the acceleration of the body are measured respectively by the rate gyro and accelerometer triads, corrupted by noise and bias as follows

$$\boldsymbol{\omega}_r = \boldsymbol{\omega} + \mathbf{b}_{\omega} + \mathbf{n}_{\omega} - \hat{\mathbf{b}}_{\omega}, \quad (3.2a)$$

$$\mathbf{a}_r = {}^B \mathbf{a} - {}^B \mathbf{g} + \mathbf{b}_a + \mathbf{n}_a - \hat{\mathbf{b}}_a, \quad (3.2b)$$

where  $\mathbf{g}$  represents Earth's gravitic field, the sensor biases are denoted by  $\mathbf{b}_a$  and  $\mathbf{b}_{\omega}$ , and  $\mathbf{n}_a \sim \mathcal{N}(\mathbf{0}, \Xi_a)$ ,  $\mathbf{n}_{\omega} \sim \mathcal{N}(\mathbf{0}, \Xi_{\omega})$  are Gaussian white noise processes. The inertial sensor biases are modeled as random walk processes,

$$\dot{\mathbf{b}}_{\omega} = \mathbf{n}_{b_{\omega}}, \quad \dot{\mathbf{b}}_a = \mathbf{n}_{b_a},$$

where  $\mathbf{n}_{b_{\omega}} \sim \mathcal{N}(\mathbf{0}, \Xi_{b_{\omega}})$  and  $\mathbf{n}_{b_a} \sim \mathcal{N}(\mathbf{0}, \Xi_{b_a})$  are Gaussian white noise processes.



The rigid body coordinates are estimated using the available inertial sensor information

$$\dot{\hat{\mathbf{p}}} = \hat{\mathbf{v}}, \quad \dot{\hat{\mathbf{v}}} = \hat{\mathcal{R}}\mathbf{a}_r + {}^E\mathbf{g}, \quad \dot{\hat{\mathcal{R}}} = \hat{\mathcal{R}}(\boldsymbol{\omega}_r)_\times, \quad \dot{\hat{\mathbf{b}}}_a = \mathbf{0}, \quad \dot{\hat{\mathbf{b}}}_\omega = \mathbf{0}. \quad (3.3)$$

The position, velocity and bias estimation errors are defined by the difference between the estimated and nominal quantities,

$$\delta\mathbf{p} := \hat{\mathbf{p}} - \mathbf{p}, \quad \delta\mathbf{v} := \hat{\mathbf{v}} - \mathbf{v}, \quad \delta\mathbf{b}_a := \hat{\mathbf{b}}_a - \mathbf{b}_a, \quad \delta\mathbf{b}_\omega := \hat{\mathbf{b}}_\omega - \mathbf{b}_\omega,$$

and the attitude error, denoted as  $\delta\boldsymbol{\phi}$ , is parameterized by an unconstrained rotation vector representation in Earth coordinates, which can be assumed locally linear and non-singular, for details and equivalent attitude parameterizations, see [99, 114]. Define the rotation error matrix as  $\mathbf{R}(\delta\boldsymbol{\phi}) := \hat{\mathcal{R}}\mathcal{R}'$ , the attitude error rotation vector  $\delta\boldsymbol{\phi}$  is described by the first order approximation

$$\mathbf{R}(\delta\boldsymbol{\phi}) \simeq \mathbf{I}_3 + (\delta\boldsymbol{\phi})_\times \Rightarrow (\delta\boldsymbol{\phi})_\times \simeq \hat{\mathcal{R}}\mathcal{R}' - \mathbf{I}_3, \quad (3.4)$$

that is valid for ‘‘small-angle’’ attitude errors [20].

Combining (3.1-3.3), the attitude, velocity, and position error kinematics are obtained by retaining the first-order terms of Taylor’s series expansions or by using perturbation algebraic techniques [20], producing

$$\delta\dot{\mathbf{p}} = \delta\mathbf{v}, \quad \delta\dot{\mathbf{v}} = \hat{\mathcal{R}}(\mathbf{a}_r - \mathbf{a}_{\text{SF}}) - \left(\hat{\mathcal{R}}\mathbf{a}_r\right)_\times \delta\boldsymbol{\phi}, \quad \delta\dot{\boldsymbol{\phi}} = \mathcal{R}(\boldsymbol{\omega}_r - \boldsymbol{\omega}), \quad (3.5a)$$

$$\delta\dot{\mathbf{b}}_a = -\mathbf{n}_{b_a}, \quad \delta\dot{\mathbf{b}}_\omega = -\mathbf{n}_{b_\omega}, \quad (3.5b)$$

where  $\mathbf{a}_{\text{SF}} = {}^B\mathbf{a} - {}^B\mathbf{g}$  is the specific force, defined as the nominal reading of an accelerometer. The terms  $(\boldsymbol{\omega}_r - \boldsymbol{\omega})$  and  $(\mathbf{a}_r - \mathbf{a}_{\text{SF}})$  represent the non-idealities of the accelerometer and rate gyro readings (3.2a) and (3.2b) respectively, and are described by

$$(\boldsymbol{\omega}_r - \boldsymbol{\omega}) = -\delta\mathbf{b}_\omega + \mathbf{n}_\omega, \quad (\mathbf{a}_r - \mathbf{a}_{\text{SF}}) = -\delta\mathbf{b}_a + \mathbf{n}_a. \quad (3.6)$$

Combining (3.5) and (3.6), the error state space model is

$$\delta\dot{\mathbf{p}} = \delta\mathbf{v}, \quad \delta\dot{\mathbf{v}} = -\hat{\mathcal{R}}\delta\mathbf{b}_a - \left(\hat{\mathcal{R}}\mathbf{a}_r\right)_\times \delta\boldsymbol{\phi} + \hat{\mathcal{R}}\mathbf{n}_a, \quad \delta\dot{\boldsymbol{\phi}} = -\hat{\mathcal{R}}\delta\mathbf{b}_\omega + \hat{\mathcal{R}}\mathbf{n}_\omega, \quad (3.7a)$$

$$\delta\dot{\mathbf{b}}_a = -\mathbf{n}_{b_a}, \quad \delta\dot{\mathbf{b}}_\omega = -\mathbf{n}_{b_\omega}. \quad (3.7b)$$

The Kalman filter adopted in this work is based on the concept of Multiplicative EKF [90, 99]. In this architecture, global position and attitude parameterizations are adopted in INS algorithm, while local representations of the estimation errors are modeled in the EKF. In particular, the adopted attitude error parameterization is locally linear and hence can be integrated in the EKF algorithm without violating the constraints found in global attitude parameterizations, such as rotation matrices and quaternions. As illustrated in Fig. 3.1, the EKF estimates the INS error vector  $\delta\mathbf{x} = \left[\delta\mathbf{p}' \ \delta\mathbf{v}' \ \delta\boldsymbol{\phi}' \ \delta\mathbf{b}'_a \ \delta\mathbf{b}'_\omega\right]'$ , that is then fed back and stored in the global quantity  $\mathbf{x}_{\text{INS}} = (\mathbf{p}, \mathbf{v}, \mathcal{R}, \mathbf{b}_a, \mathbf{b}_\omega)$ , and reset in the filter. This process preserves the small error assumption underlying the linearized model (3.7), and its validity is demonstrated in [99], where it is also evidenced that the estimation error covariance is unaffected when  $\delta\mathbf{x}$  is incorporated in  $\mathbf{x}_{\text{INS}}$ .

## 3.2 Vehicle model aiding

In this section, the vehicle model aiding techniques are detailed. The classical technique to exploit the vehicle dynamics in the navigation system is presented, and a new methodology to directly embed the VD information in the EKF is proposed.

The external VD structure, depicted in Fig. 3.1(a), follows from previous work found in [23, 82], where the integration of the VD in the system is analogous to that adopted for the INS. Vehicle state estimates are computed by a vehicle simulator block, using the thrusters input information. The full state vehicle model algorithm computes attitude and velocity estimates that are compared to the INS output, under the form of measurement residuals. Whereas the vehicle aiding information is expected to help the INS, computational and modeling errors of the vehicle dynamics itself must be addressed by the filter. Therefore, the EKF state model is also augmented to compensate for the vehicle modeling errors.

This work presents an alternative method to exploit the VD model by including the vehicle simulator equations directly in the EKF state model. Vehicle dynamics are integrated in the filter state space, linearized about the inertial state estimates. The vehicle dynamics propagate the inertial estimates, so the VD integration is a function of the INS errors. Therefore, the EKF algorithm internally solves the VD equations and only outputs the INS error estimates, as shown in Fig. 3.1(b).

Without any loss of generality, the VD aiding technique proposed in this work is illustrated using the dynamics of a 6-DOF rigid body polyhedron with uniform mass density and fully actuated. Afterwards, the proposed technique is applied to a Vario X-Treme helicopter dynamic model, to demonstrate that the VD aiding technique is valid for realistic robotic platforms. Note that the Vario X-Treme helicopter is a challenging platform due to the complex dynamics of the vehicle, detailed in Appendix C, that are highly nonlinear and coupled.

### 3.2.1 Rigid body dynamics

The body coordinate frame origin, denoted  $\mathbf{p}_{Borg}$ , is located at the body's center of mass and geometric center. The axes of the body frame define a plane of symmetry for the mass distribution of the body, so the resulting body inertia tensor, denoted  $\mathbf{I}_B$ , is described by the principal moments of inertia [34], yielding

$$\mathbf{I}_B = \frac{m}{12} \begin{bmatrix} h^2 + l^2 & 0 & 0 \\ 0 & w^2 + h^2 & 0 \\ 0 & 0 & l^2 + w^2 \end{bmatrix},$$

where  $m$  is the body mass and  $(l, w, h)$  represent the polyhedron length, width and height, respectively. The rigid body is subject to the thrusters force and momentum, denoted by  $\mathbf{f}_{th}$  and  $\mathbf{n}_{th}$  respectively, and to viscous linear and angular damping, denoted by  $\mathbf{f}_d$  and  $\mathbf{n}_d$

respectively, yielding

$${}^B \mathbf{f}_{\text{th}} = \sum_i {}^B \mathbf{f}_i, \quad {}^B \mathbf{n}_{\text{th}} = \sum_i {}^B \mathbf{p}_{\text{th}i} \times {}^B \mathbf{f}_i, \quad {}^B \mathbf{f}_d = -K_{\text{lin}} {}^B \mathbf{v}, \quad {}^B \mathbf{n}_d = -K_{\text{ang}} \boldsymbol{\omega},$$

where  $i = 1, \dots, 6$  is the index of the thruster applying force  $\mathbf{f}_i$  to the body,  ${}^B \mathbf{p}_{\text{th}i}$  are the thrusters' coordinates in body frame, and  $K_{\text{lin}}$  and  $K_{\text{ang}}$  are respectively the linear and the angular damping coefficients.

Applying the Newton and Euler equations to determine body's translation and rotation with respect to the inertial frame, the body dynamics are expressed by the nonlinear state space model

$$\dot{\boldsymbol{\omega}}_V := f_{\omega}(\boldsymbol{\omega}_V, \mathbf{n}_{\text{th}}) = -\mathbf{I}_B^{-1} ((\boldsymbol{\omega}_V)_{\times} \mathbf{I}_B \boldsymbol{\omega}_V + K_{\text{ang}} \boldsymbol{\omega}_V) + \mathbf{I}_B^{-1} \mathbf{n}_{\text{th}}, \quad (3.8a)$$

$$\begin{aligned} {}^B \dot{\mathbf{v}}_V &:= f_v(\boldsymbol{\omega}_V, {}^B \mathbf{v}_V, \mathbf{f}_{\text{th}}) \\ &= -\mathbf{M}_T^{-1} ((\boldsymbol{\omega}_V)_{\times} \mathbf{M}_T {}^B \mathbf{v}_V + K_{\text{lin}} {}^B \mathbf{v}_V) + \mathbf{M}_T^{-1} \mathbf{f}_{\text{th}} + \mathcal{R}'_V {}^E \mathbf{g}, \end{aligned} \quad (3.8b)$$

$$\dot{\mathcal{R}}_V := f_{\mathcal{R}}(\boldsymbol{\omega}_V, \mathcal{R}_V) = \mathcal{R}_V (\boldsymbol{\omega}_V)_{\times}, \quad (3.8c)$$

where the body and center of mass coordinate frames are defined with the same orientation and position, so that the body frame attitude dynamics (3.8a) do not depend on the linear velocity. To avoid ambiguity in the adopted notation,  ${}^B \dot{\mathbf{v}}$  denotes  $\frac{d{}^B \mathbf{v}}{dt}$ , whereas  ${}^B (\frac{d\mathbf{v}}{dt})$  is denoted by  ${}^B (\dot{\mathbf{v}})$ .

The simple rigid body dynamics (3.8) allow for physical intuition on the contribution of the vehicle model to the inertial states errors compensation. The  $V$  subscript for the angular velocity and body linear velocity (3.8) is adopted to emphasize that these quantities are computed using the vehicle dynamics, given that some are also computed by the INS, using distinct integration algorithms and inputs.

The position is not computed in the vehicle model aiding technique because the position is decoupled from the other vehicle states in (3.8), and the vehicle position kinematics are identical to those of the INS. Although the vehicle attitude kinematics are also identical to those of the INS, the attitude is coupled with the other states of the vehicle and hence is explicitly modeled in (3.8). Interestingly enough, (3.8c) is computed in the external vehicle model aiding technique, replicating the INS computations, while the embedded vehicle model aiding technique exploits the INS attitude computations directly, as shown in the ensuing.

### 3.2.2 External vehicle model aiding

In the classical VD aiding, presented in Fig. 3.1(a), the vehicle dynamics are computed using a standalone vehicle simulator, included in the navigation system but external to the EKF/INS system. The EKF state model is augmented to estimate and compensate for the VD block errors, using model specific error compensation routines.

The VD block error dynamics are formulated using the technique adopted to describe the INS error dynamics in Section 3.1.2. These are obtained by applying a perturbational

analysis to the nominal dynamics (3.8). Let  $\hat{\mathbf{x}}_V = (\hat{\boldsymbol{\omega}}_V, {}^B\hat{\mathbf{v}}_V, \hat{\mathcal{R}}_V)$  denote the states estimated by the vehicle model simulator, the vehicle model error dynamics are described by the first order terms of the Taylor series expansion

$$\dot{\hat{\boldsymbol{\omega}}}_V = f_\omega(\hat{\boldsymbol{\omega}}_V, \hat{\mathbf{n}}_{\text{th}}) \Rightarrow \delta\dot{\boldsymbol{\omega}}_V \approx \left. \frac{\partial f_\omega}{\partial \boldsymbol{\omega}} \right|_{\mathbf{x}_V} \delta\boldsymbol{\omega}_V + \left. \frac{\partial f_\omega}{\partial \mathbf{n}_{\text{th}}} \right|_{\mathbf{x}_V} \delta\mathbf{n}_{\text{th}}, \quad (3.9a)$$

$$\begin{aligned} {}^B\dot{\hat{\mathbf{v}}}_V &= f_v(\hat{\boldsymbol{\omega}}_V, {}^B\hat{\mathbf{v}}_V, \hat{\mathcal{R}}_V, \hat{\mathbf{f}}_{\text{th}}) \Rightarrow \\ \delta {}^B\dot{\mathbf{v}}_V &\approx \left. \frac{\partial f_v}{\partial \boldsymbol{\omega}} \right|_{\mathbf{x}_V} \delta\boldsymbol{\omega}_V + \left. \frac{\partial f_v}{\partial {}^B\mathbf{v}_V} \right|_{\mathbf{x}_V} \delta {}^B\mathbf{v}_V + \left. \frac{\partial f_v}{\partial \delta\boldsymbol{\phi}} \right|_{\mathbf{x}_V} \delta\boldsymbol{\phi}_V + \left. \frac{\partial f_v}{\partial \mathbf{f}_{\text{th}}} \right|_{\mathbf{x}_V} \delta\mathbf{f}_{\text{th}}, \end{aligned} \quad (3.9b)$$

$$\dot{\hat{\mathcal{R}}}_V = f_{\mathcal{R}}(\hat{\boldsymbol{\omega}}_V, \hat{\mathcal{R}}_V) \Rightarrow \delta\dot{\boldsymbol{\phi}}_V = \mathcal{R}_V \delta\boldsymbol{\omega}_V, \quad (3.9c)$$

where  $\delta\boldsymbol{\omega}_V = \hat{\boldsymbol{\omega}}_V - \boldsymbol{\omega}$ ,  $\delta {}^B\mathbf{v}_V = {}^B\hat{\mathbf{v}}_V - {}^B\mathbf{v}$ ,  $\delta\mathbf{n}_{\text{th}} = \hat{\mathbf{n}}_{\text{th}} - \mathbf{n}_{\text{th}}$ ,  $\delta\mathbf{f}_{\text{th}} = \hat{\mathbf{f}}_{\text{th}} - \mathbf{f}_{\text{th}}$ , and the Jacobians are given by

$$\left. \frac{\partial f_\omega}{\partial \boldsymbol{\omega}} \right|_{\mathbf{x}_V} = \mathbf{I}_B^{-1} ((\mathbf{I}_B \boldsymbol{\omega}_V)_\times - (\boldsymbol{\omega}_V)_\times \mathbf{I}_B - \mathbf{I}_3 K_{\text{ang}}), \quad \left. \frac{\partial f_\omega}{\partial \mathbf{n}_{\text{th}}} \right|_{\mathbf{x}_V} = \mathbf{I}_B^{-1}, \quad (3.10a)$$

$$\left. \frac{\partial f_v}{\partial \boldsymbol{\omega}} \right|_{\mathbf{x}_V} = \mathbf{M}_T^{-1} (\mathbf{M}_T {}^B\mathbf{v}_V)_\times, \quad \left. \frac{\partial f_v}{\partial \mathbf{f}_{\text{th}}} \right|_{\mathbf{x}_V} = \mathbf{M}_T^{-1}, \quad (3.10b)$$

$$\left. \frac{\partial f_v}{\partial {}^B\mathbf{v}_V} \right|_{\mathbf{x}_V} = \mathbf{M}_T^{-1} (-(\boldsymbol{\omega}_V)_\times \mathbf{M}_T - \mathbf{I}_3 K_{\text{lin}}), \quad \left. \frac{\partial f_v}{\partial \delta\boldsymbol{\phi}} \right|_{\mathbf{x}_V} = \mathcal{R}'_V ({}^E\mathbf{g})_\times, \quad (3.10c)$$

The first order model (3.9) can also be obtained by perturbational analysis of the dynamics (3.8). The rotation matrix kinematics (3.8c) are identical to the inertial rigid body kinematics expressed in (3.1), and consequently do not yield new information to the system. However, the computation of  $\mathcal{R}_V$  is necessary for the vehicle dynamics simulator (3.8), and the associated error dynamics (3.9c), which are identical to the INS attitude error (3.5), must be compensated for.

The INS and VD state estimates are compared under the form of measurement residuals, obtained by the perturbational method adopted in [20], and described by

$$\mathbf{z}_\omega := \hat{\boldsymbol{\omega}} - \hat{\boldsymbol{\omega}}_V = \boldsymbol{\omega} + \delta\boldsymbol{\omega} - (\boldsymbol{\omega} + \delta\boldsymbol{\omega}_V) = \delta\boldsymbol{\omega} - \delta\boldsymbol{\omega}_V = -\delta\mathbf{b}_\omega - \delta\boldsymbol{\omega}_V + \mathbf{n}_\omega, \quad (3.11a)$$

$$\begin{aligned} \mathbf{z}_u &:= \hat{\mathcal{R}}' \hat{\mathbf{v}} - {}^B\hat{\mathbf{v}}_V = \hat{\mathcal{R}}' \mathbf{v} - ({}^B\mathbf{v} + \delta {}^B\mathbf{v}_V) = (\hat{\mathcal{R}}' - \mathcal{R}') \mathbf{v} + \mathcal{R}' \delta\mathbf{v} - \delta {}^B\mathbf{v}_V \\ &= -\hat{\mathcal{R}}' (\boldsymbol{\phi})_\times \mathbf{v} + \mathcal{R}' \delta\mathbf{v} - \delta {}^B\mathbf{v}_V \approx \mathcal{R}' \delta\mathbf{v} + \mathcal{R}' (\mathbf{v})_\times \delta\boldsymbol{\phi} - \delta {}^B\mathbf{v}_V, \end{aligned} \quad (3.11b)$$

$$\mathbf{z}_{\mathcal{R}} := \hat{\mathcal{R}} \hat{\mathcal{R}}'_V - \mathbf{I} \approx [\mathbf{I} + (\delta\boldsymbol{\phi})_\times] \mathcal{R} \mathcal{R}' [\mathbf{I} - (\delta\boldsymbol{\phi}_V)_\times] - \mathbf{I} \approx \delta\boldsymbol{\phi} - \delta\boldsymbol{\phi}_V. \quad (3.11c)$$

where  $\hat{\boldsymbol{\omega}}$  is the angular velocity estimate given by the INS, i.e.  $\hat{\boldsymbol{\omega}} = \boldsymbol{\omega}_r$ .

The external VD aiding technique is detailed in Fig. 3.2. The vehicle model equations (3.8) are computed by a variable-step Runge-Kutta differential equation solver, using the thrusters force  $\mathbf{f}_{\text{th}}$  and momentum  $\mathbf{n}_{\text{th}}$  information. The vehicle state errors and covariances are propagated by the EKF using the first order model (3.9) and assuming that the thrusters input is known from the control system,  $\delta\mathbf{n}_{\text{th}} = \delta\mathbf{f}_{\text{th}} = \mathbf{0}$ . In experimental applications the inputs of the vehicle model may not be accurately known, and  $\delta\mathbf{n}_{\text{th}}$ ,  $\delta\mathbf{f}_{\text{th}}$  may be modeled as small stochastic uncertainties to increase the navigation system robustness.

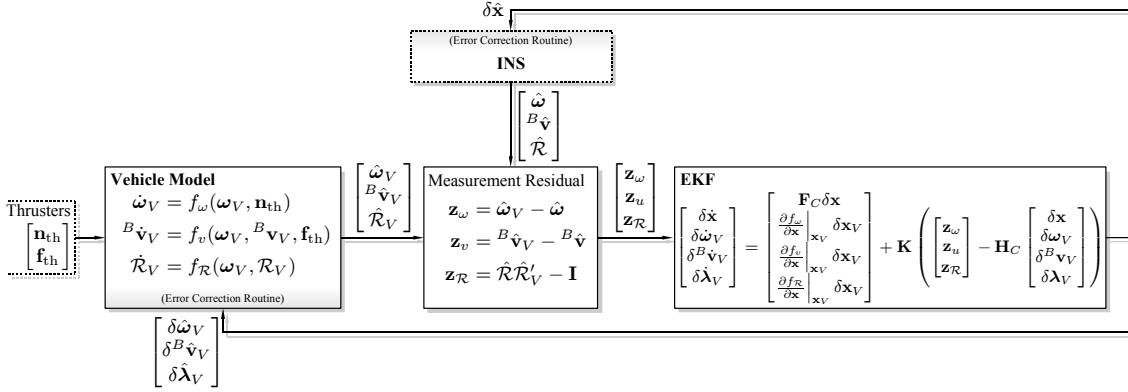


Figure 3.2: External vehicle model aiding for the 6-DOF rigid body polyhedron.

The INS and VD errors are estimated by processing the measurement residuals (3.11) in the EKF algorithm. Similar to the storage technique used for the INS error compensation, described in Section 3.1.2, the estimated VD errors  $\delta \mathbf{x}_V = \left[ \delta \omega'_V \quad \delta {}^B \mathbf{v}'_V \quad \delta \phi'_V \right]'$  are transferred to the external VD block and used to update the state  $\mathbf{x}_V = (\omega_V, {}^B \mathbf{v}_V, \mathcal{R}_V)$ . This method preserves the small error conditions of the first order model (3.8), however it requires the implementation of error compensation routines in the vehicle model.

### 3.2.3 Embedded vehicle model aiding

The vehicle model aiding enhances the accuracy of the navigation system by providing specific information about the robotic platform, e.g. its linear and angular velocity dynamics, (3.8a) and (3.8b) respectively. In the classical technique described in the last section, the attitude kinematics (3.8c) are computed simultaneously in the INS and in the self-contained vehicle simulator, and vehicle model errors compensation routines must be implemented, as illustrated in Fig. 3.1. The necessity of these auxiliary computational routines, and of distinct vehicle states that partially replicate those found in the INS, motivates an alternative vehicle model integration method.

The embedded VD aiding concept is based on using the vehicle dynamics to propagate the INS estimates. Due to the presence of inertial estimation errors, the results obtained by solving the vehicle dynamics using the inertial estimates is different from the INS state estimate derivatives, that is  $\dot{\hat{\omega}} \neq f_\omega(\hat{\omega}, \hat{\mathbf{n}}_{th})$ ,  ${}^B \dot{\hat{\mathbf{v}}} \neq f_v(\hat{\omega}, {}^B \hat{\mathbf{v}}, \hat{\mathcal{R}}, \hat{\mathbf{f}}_{th})$ . To exploit the distinct, but compatible models enclosed in the VD and INS computations, the VD results are described as a function of the INS errors, enabling the EKF to estimate and compensate for the inertial errors. Interestingly enough, the proposed embedded VD aiding reduces the computational cost associated with vehicle aiding, while bearing the same estimation error accuracy.

With a slight abuse of notation, let  $\hat{\mathbf{x}} = (\hat{\omega}, \hat{\mathbf{v}}, \hat{\mathcal{R}}, \hat{\mathbf{b}}_a, \hat{\mathbf{b}}_\omega)$  denote the INS state estimates. In the embedded VD methodology, nominal vehicle dynamics (3.8) are linearized about the INS state estimates, using the first order terms of the Taylor series expansion,

yielding

$$\begin{aligned}\dot{\boldsymbol{\omega}} &= f_{\boldsymbol{\omega}}(\boldsymbol{\omega}, \mathbf{n}_{\text{th}}) \approx f_{\boldsymbol{\omega}}(\hat{\boldsymbol{\omega}}, \hat{\mathbf{n}}_{\text{th}}) + \left. \frac{\partial f_{\boldsymbol{\omega}}}{\partial \boldsymbol{\omega}} \right|_{\hat{\mathbf{x}}} (\boldsymbol{\omega} - \hat{\boldsymbol{\omega}}) + \left. \frac{\partial f_{\boldsymbol{\omega}}}{\partial \mathbf{n}_{\text{th}}} \right|_{\hat{\mathbf{x}}} (\mathbf{n}_{\text{th}} - \hat{\mathbf{n}}_{\text{th}}), \\ {}^B \dot{\mathbf{v}} &= f_v(\boldsymbol{\omega}, {}^B \mathbf{v}, \mathcal{R}, \mathbf{f}_{\text{th}}) \approx f_v(\hat{\boldsymbol{\omega}}, {}^B \hat{\mathbf{v}}, \hat{\mathcal{R}}, \hat{\mathbf{f}}_{\text{th}}) + \left. \frac{\partial f_v}{\partial \boldsymbol{\omega}} \right|_{\hat{\mathbf{x}}} (\boldsymbol{\omega} - \hat{\boldsymbol{\omega}}) \\ &\quad + \left. \frac{\partial f_v}{\partial {}^B \mathbf{v}} \right|_{\hat{\mathbf{x}}} ({}^B \mathbf{v} - {}^B \hat{\mathbf{v}}) + \left. \frac{\partial f_v}{\partial \delta \phi} \right|_{\hat{\mathbf{x}}} \delta \phi + \left. \frac{\partial f_v}{\partial \mathbf{f}_{\text{th}}} \right|_{\hat{\mathbf{x}}} (\mathbf{f}_{\text{th}} - \hat{\mathbf{f}}_{\text{th}}).\end{aligned}$$

Given the definition of the INS estimation error, the nominal angular and linear velocities are expressed as a function of the INS states and estimation errors by

$$\begin{aligned}\dot{\boldsymbol{\omega}} &\approx f_{\boldsymbol{\omega}}(\hat{\boldsymbol{\omega}}, \hat{\mathbf{n}}_{\text{th}}) - \left. \frac{\partial f_{\boldsymbol{\omega}}}{\partial \boldsymbol{\omega}} \right|_{\hat{\mathbf{x}}} \delta \boldsymbol{\omega} - \left. \frac{\partial f_{\boldsymbol{\omega}}}{\partial \mathbf{n}_{\text{th}}} \right|_{\hat{\mathbf{x}}} \delta \mathbf{n}_{\text{th}} \\ &= f_{\boldsymbol{\omega}}(\hat{\boldsymbol{\omega}}, \hat{\mathbf{n}}_{\text{th}}) + \left. \frac{\partial f_{\boldsymbol{\omega}}}{\partial \boldsymbol{\omega}} \right|_{\hat{\mathbf{x}}} \delta \mathbf{b}_{\boldsymbol{\omega}} - \left. \frac{\partial f_{\boldsymbol{\omega}}}{\partial \boldsymbol{\omega}} \right|_{\hat{\mathbf{x}}} \mathbf{n}_{\boldsymbol{\omega}} - \left. \frac{\partial f_{\boldsymbol{\omega}}}{\partial \mathbf{n}_{\text{th}}} \right|_{\hat{\mathbf{x}}} \delta \mathbf{n}_{\text{th}},\end{aligned}\tag{3.12a}$$

$$\begin{aligned}{}^B \dot{\mathbf{v}} &\approx f_v(\hat{\boldsymbol{\omega}}, {}^B \hat{\mathbf{v}}, \hat{\mathcal{R}}, \hat{\mathbf{f}}_{\text{th}}) - \left. \frac{\partial f_v}{\partial \boldsymbol{\omega}} \right|_{\hat{\mathbf{x}}} \delta \boldsymbol{\omega} - \left. \frac{\partial f_v}{\partial {}^B \mathbf{v}} \right|_{\hat{\mathbf{x}}} \delta {}^B \mathbf{v} - \left. \frac{\partial f_v}{\partial \delta \phi} \right|_{\hat{\mathbf{x}}} \delta \phi \\ &\quad - \left. \frac{\partial f_v}{\partial \mathbf{n}_{\text{th}}} \right|_{\hat{\mathbf{x}}} \delta \mathbf{n}_{\text{th}} - \left. \frac{\partial f_v}{\partial \mathbf{f}_{\text{th}}} \right|_{\hat{\mathbf{x}}} \delta \mathbf{f}_{\text{th}} \\ &= f_v(\hat{\boldsymbol{\omega}}, {}^B \hat{\mathbf{v}}, \hat{\mathcal{R}}, \hat{\mathbf{f}}_{\text{th}}) - \left. \frac{\partial f_v}{\partial {}^B \mathbf{v}} \right|_{\hat{\mathbf{x}}} \mathcal{R}' \delta \mathbf{v} - \left( \left. \frac{\partial f_v}{\partial \delta \phi} \right|_{\hat{\mathbf{x}}} + \left. \frac{\partial f_v}{\partial \mathbf{v}} \right|_{\hat{\mathbf{x}}} \mathcal{R}'(\mathbf{v})_{\times} \right) \delta \phi \\ &\quad + \left. \frac{\partial f_v}{\partial \boldsymbol{\omega}} \right|_{\hat{\mathbf{x}}} \delta \mathbf{b}_{\boldsymbol{\omega}} - \left. \frac{\partial f_v}{\partial \boldsymbol{\omega}} \right|_{\hat{\mathbf{x}}} \mathbf{n}_{\boldsymbol{\omega}} - \left. \frac{\partial f_v}{\partial \mathbf{n}_{\text{th}}} \right|_{\hat{\mathbf{x}}} \delta \mathbf{n}_{\text{th}} - \left. \frac{\partial f_v}{\partial \mathbf{f}_{\text{th}}} \right|_{\hat{\mathbf{x}}} \delta \mathbf{f}_{\text{th}},\end{aligned}\tag{3.12b}$$

where body linear velocity error  $\delta {}^B \mathbf{v}$  is rewritten as a function of the INS state errors  $\delta {}^B \mathbf{v} := \hat{\mathcal{R}}' \hat{\mathbf{v}} - \mathcal{R}' \mathbf{v} \approx \mathcal{R}'(\mathbf{v})_{\times} \delta \phi + \mathcal{R}' \delta \mathbf{v}$ .

The angular velocity information expressed in (3.8a) is exploited by modeling the error dynamics (3.12a) in the EKF, and feeding the angular velocity measurement to the filter

$$\mathbf{z}_{\boldsymbol{\omega}} := \hat{\boldsymbol{\omega}} = \boldsymbol{\omega} - \delta \mathbf{b}_{\boldsymbol{\omega}} + \mathbf{n}_{\boldsymbol{\omega}}.\tag{3.13}$$

The dynamics of  ${}^B \mathbf{v}$  expressed in (3.8b) are exploited by feeding the filter with the measurement residual

$$\mathbf{z}_v := f_v(\hat{\boldsymbol{\omega}}, {}^B \hat{\mathbf{v}}, \hat{\mathcal{R}}, \hat{\mathbf{f}}_{\text{th}}) - {}^B \dot{\hat{\mathbf{v}}},\tag{3.14}$$

where  $f_v(\hat{\boldsymbol{\omega}}, {}^B \hat{\mathbf{v}}, \hat{\mathcal{R}}, \hat{\mathbf{f}}_{\text{th}})$  is given by computing (3.8b) with the inertial estimates. The estimate  ${}^B \dot{\hat{\mathbf{v}}}$  is obtained from the INS measurements and estimates by rewriting the accelerometer measurement (3.2b) as the sum of the linear acceleration and Coriolis terms

$$\mathbf{a}_r = \frac{d {}^B \mathbf{v}}{dt} + \boldsymbol{\omega} \times {}^B \mathbf{v} - \mathcal{R}'^E \mathbf{g} - \delta \mathbf{b}_a + \mathbf{n}_a,$$

yielding

$$\frac{d {}^B \hat{\mathbf{v}}}{dt} = \mathbf{a}_r - \hat{\boldsymbol{\omega}} \times {}^B \hat{\mathbf{v}} + \hat{\mathcal{R}}'^E \mathbf{g}.$$

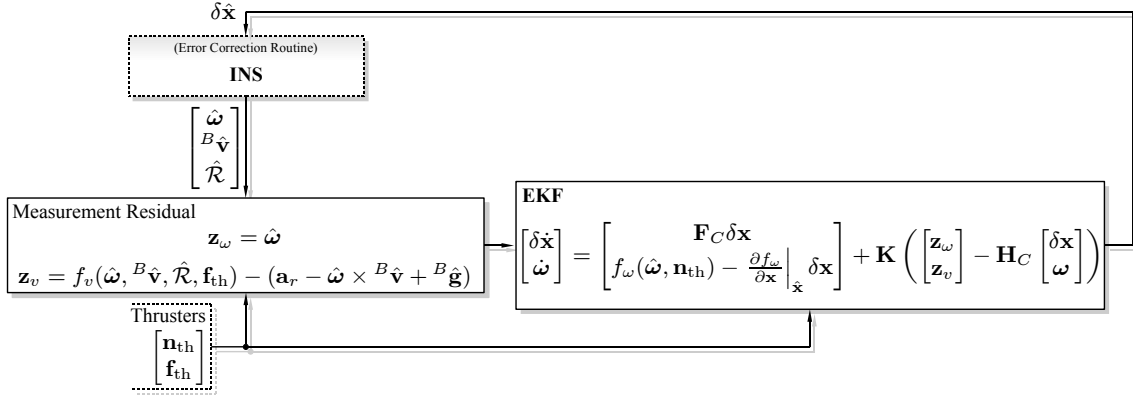


Figure 3.3: Embedded vehicle model aiding for the 6-DOF rigid body polyhedron.

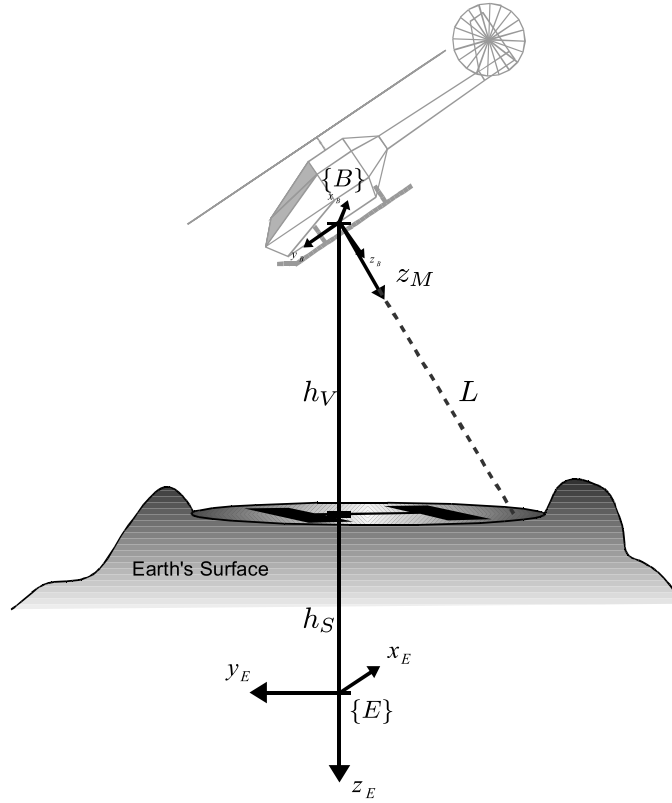
The measurement residual  $\mathbf{z}_v$  is formulated in the EKF using a linearized model, that is obtained by expanding (3.14) as follows

$$\begin{aligned} \mathbf{z}_v &= f_v(\hat{\boldsymbol{\omega}}, {}^B \hat{\mathbf{v}}, \hat{\mathcal{R}}, \hat{\mathbf{f}}_{\text{th}}) - \left( \mathbf{a}_r - \hat{\boldsymbol{\omega}} \times {}^B \hat{\mathbf{v}} + \hat{\mathcal{R}}^E \mathbf{g} \right) \\ &\approx f_v(\hat{\boldsymbol{\omega}}, {}^B \hat{\mathbf{v}}, \hat{\mathcal{R}}, \hat{\mathbf{f}}_{\text{th}}) - \left( f_v(\boldsymbol{\omega}, {}^B \mathbf{v}, \mathcal{R}, \mathbf{f}_{\text{th}}) - \delta(\boldsymbol{\omega} \times {}^B \mathbf{v}) + \delta^B \mathbf{g} - \delta \mathbf{b}_a + \mathbf{n}_a \right). \end{aligned}$$

Using the first order expansion (3.12b) and applying the perturbational method described in [20], produces

$$\begin{aligned} \mathbf{z}_v &= \left( (\boldsymbol{\omega})_{\times} + \frac{\partial f_v}{\partial {}^B \mathbf{v}} \right) \mathcal{R}' \delta \mathbf{v} + \left( (\boldsymbol{\omega})_{\times} ({}^B \mathbf{v})_{\times} - ({}^B \mathbf{g})_{\times} + \frac{\partial f_v}{\partial {}^B \mathbf{v}} ({}^B \mathbf{v})_{\times} + \frac{\partial f_v}{\partial \delta \phi} \mathcal{R} \right) \mathcal{R}' \delta \phi \\ &\quad + \delta \mathbf{b}_a + \left( ({}^B \mathbf{v})_{\times} - \frac{\partial f_v}{\partial \boldsymbol{\omega}} \right) \delta \mathbf{b}_{\boldsymbol{\omega}} - \mathbf{n}_a + \left( \frac{\partial f_{\boldsymbol{\omega}}}{\partial \boldsymbol{\omega}} - ({}^B \mathbf{v})_{\times} \right) \mathbf{n}_{\boldsymbol{\omega}}. \end{aligned}$$

A block diagram of the embedded vehicle model aiding technique is presented in Fig. 3.3. The propagation of the vehicle dynamics using INS estimates allows for valuable computational savings and flexibility. Namely, in the embedded VD aiding *i*) the number of filter states is smaller than that of the external VD aiding, since the linear velocity information is used in the form of measurement residual (3.14), and the attitude kinematics are computed using the INS algorithm, *ii*) numerical integration methods are necessary only for the computation of (3.9a), while the linear velocity information is used without integrating the differential equation (3.9b), and the attitude kinematics (3.9c) are computed by the INS, *iii*) the angular and linear velocity aiding can be implemented separately, i.e. (3.9a) and (3.9b) can be exploited independently, whereas the external VD aiding requires the computation of the full vehicle dynamics (3.9) *iv*) error compensation routines are only performed in the INS, as opposed to implementing error compensation routines associated with the external vehicle model aiding. From the viewpoint of algebraic derivation, the Jacobians computed for the embedded VD aiding are also computed in the classical method, see (3.10), and hence the first order analytical results needed to integrate the vehicle model in the EKF are the same for both architectures. The computational advantages of the embedded vehicle model are illustrated in the simulation results presented later in this work.

Figure 3.4: LASER range finder reading ( ${}^B_M\mathbf{R} = \mathbf{I}$ ).

### 3.3 LASER aiding

In this section, the LASER range finder aiding sensor is described and the corresponding filter observation equation is introduced. By definition, and without loss of generality, the sensor is mounted along the  $z$  axis of the frame  $\{M\}$ , whose relative orientation to the body frame is described by the known installation rotation matrix  ${}^B_M\mathbf{R}$ , for calibration methods see [63] and references therein. The LASER reads the distance  $L$  from the vehicle to the ground, along the  $z$  axis of the  $\{M\}$  coordinate frame, as depicted in Fig. 3.4. By processing this information in the filter architecture, an estimate of the vehicle's distance to the ground can be obtained with high accuracy, as required for landing and takeoff operations of an air vehicle.

In the current work, the landing area is assumed to be locally planar. The ground height  $h_S$ , given by the distance from the Earth frame origin to the helicopter landing zone, is modeled as being approximately constant

$$\dot{h}_S = n_{h_S}, \quad (3.15)$$

where  $n_{h_S} \sim \mathcal{N}(0, \Xi_{h_S})$  is a Gaussian white noise process whose variance reflects small variations on the ground's flatness. As depicted in Fig. 3.4, the  $z$  axis Earth coordinate of



the vehicle is given by

$$p_z = -(h_S + h_V), \quad (3.16)$$

where  $h_V \geq 0$  is the vehicle's height, that is, the distance from Body frame origin to the ground.

Using elementary trigonometric relations yields

$$\frac{h_V}{L} = \frac{|{}^M\mathbf{h}'_V\mathbf{e}_3|}{|{}^E\mathbf{h}'_V\mathbf{e}_3|},$$

where  ${}^E\mathbf{h}_V = [0 \ 0 \ -h_V]'$  is the vehicle's height in Earth coordinates,  $\mathbf{e}_3 = [0 \ 0 \ 1]'$  is the unit z axis vector and  ${}^M\mathbf{h}'_V\mathbf{e}_3$  corresponds to the projection of  $\mathbf{h}_V$  on the z axis of the  $\{M\}$  frame. Applying the coordinate transform  ${}^M\mathbf{h}_V = {}^B_M\mathbf{R}'\mathcal{R}'{}^E\mathbf{h}_V$  and developing the terms in the previous equation, the LASER range is described by

$$L = \begin{cases} \frac{h_V}{\mathbf{e}'_3\mathcal{R}_M^B\mathbf{R}\mathbf{e}_3}, & \text{if } \mathbf{e}'_3\mathcal{R}_M^B\mathbf{R}\mathbf{e}_3 > 0 \\ \text{not defined,} & \text{if } \mathbf{e}'_3\mathcal{R}_M^B\mathbf{R}\mathbf{e}_3 \leq 0 \end{cases}, \quad (3.17)$$

that is not defined for the cases where the LASER is pointing upwards. The LASER range finder sensor measures the actual range  $L$  corrupted by the sensor noise

$$L_r = L + \delta L, \quad (3.18)$$

where  $\delta L = n_L \sim \mathcal{N}(0, \Xi_L)$  is modeled as a Gaussian white noise process. The measurement residual is computed by

$$\mathbf{z}_L := \hat{p}_z - (-\hat{h}_V), \quad (3.19)$$

where the height estimate from the LASER reading is given by rearranging the terms in (3.17) and using the INS estimates in the unknown terms, producing

$$\hat{h}_V = \mathbf{e}'_3\hat{\mathcal{R}}_M^B\mathbf{R}\mathbf{e}_3L_r. \quad (3.20)$$

The vehicle and ground heights,  $h_S$  and  $h_V$  respectively, are filtered apart by modeling the  $h_S$  dynamics (3.15) in the EKF, measuring  $h_V$  from the LASER reading as in (3.20), and feeding the measurement residual (3.19) to the EKF.

To model the measurement residual (3.19) in the EKF, the INS position estimate is expressed as a function of the vehicle and ground heights, given by

$$\hat{p}_z = p_z + \delta p_z = -h_S - h_V + \mathbf{e}'_3\delta\mathbf{p}.$$

Expanding the INS attitude estimate  $\hat{\mathcal{R}}$  with the attitude error approximation (3.4) and neglecting second order terms yields the  $\hat{h}_V$  description

$$\begin{aligned} \hat{h}_V &= \mathbf{e}'_3\hat{\mathcal{R}}_M^B\mathbf{R}\mathbf{e}_3L_r \approx \mathbf{e}'_3[\mathbf{I}_{3\times 3} + (\delta\phi)_\times]\mathcal{R}_M^B\mathbf{R}\mathbf{e}_3L_r \\ &\approx \mathbf{e}'_3\mathcal{R}_M^B\mathbf{R}\mathbf{e}_3(L + \delta L) - L_r\mathbf{e}'_3(\mathcal{R}_M^B\mathbf{R}\mathbf{e}_3)_\times\delta\phi \\ &= h_V + \mathbf{e}'_3\mathcal{R}_M^B\mathbf{R}\mathbf{e}_3\delta L - L_r\mathbf{e}'_3(\mathcal{R}_M^B\mathbf{R}\mathbf{e}_3)_\times\delta\phi, \end{aligned} \quad (3.21)$$

Combining (3.18-3.21), the measurement residual is described as a function of the EKF state variables as

$$\mathbf{z}_L = \mathbf{e}'_3 \delta \mathbf{p} - L_r \mathbf{e}'_3 (\mathcal{R}_M^B \mathbf{R} \mathbf{e}_3)_\times \delta \phi - h_S + \mathbf{e}'_3 \mathcal{R}_M^B \mathbf{R} \mathbf{e}_3 \mathbf{n}_L. \quad (3.22)$$

In practical applications, the terrain height  $h_S$  is unknown along the flight path. After the takeoff and during flight operations, the LASER sensor is switched off to prevent erroneous readings due to the terrain height fluctuations, and to the interference of obstacles located between the vehicle and the ground. When the landing maneuver starts, the LASER is switched on to estimate the new  $h_S$  and the distance-to-ground.

### 3.4 Implementation

This section details the state model of the EKF, that integrates the INS with the vehicle model and LASER aiding techniques. The state dynamics and measurement residuals of the EKF are determined by the choice of aiding techniques, and obtained by the concatenation of the INS error model presented in Section 3.1 with the state and measurement models of the aiding sources described in Sections 3.2 and 3.3. The state models for the external and the embedded vehicle model aiding techniques evidence the differences between the two approaches, and clarify the computational savings and flexibility of the proposed technique. The discretization of the continuous state space model and the Kalman filter algorithm are presented for the purpose of implementation.

The standard continuous-time state space model can be described by

$$\dot{\mathbf{x}}_C = \mathbf{F}_C(\mathbf{x}_C) \mathbf{x}_C + \mathbf{G}_C(\mathbf{x}_C) \mathbf{n}_{x_C} + \mathbf{u}_C, \quad \mathbf{z}_C = \mathbf{H}_C(\mathbf{x}_C) \mathbf{x}_C + \mathbf{n}_{z_C}, \quad (3.23)$$

where  $\mathbf{x}_C$  is the state vector,  $\mathbf{F}_C$  is the state dynamics matrix,  $\mathbf{n}_{x_C}$  is the state noise transformed by matrix  $\mathbf{G}_C$ ,  $\mathbf{u}_C$  is the system input vector, and  $\mathbf{z}$  is the state measurement, corrupted by the noise vector  $\mathbf{n}_{z_C}$ . The state and measurement noises are modeled as zero-mean, Gaussian white noise processes with covariance matrices denoted by  $\mathbf{Q}_C$  and  $\mathbf{R}_C$ , respectively.

#### 3.4.1 EKF/INS state model

The state model dynamics for the INS errors are obtained directly from (3.5). Let  $\mathbf{x}_{\text{INS}} = (\mathbf{p}, \mathbf{v}, \mathcal{R}, \mathbf{b}_a, \mathbf{b}_\omega)$  denote the INS quantities, the state model dynamics of the EKF describing the INS errors are given by

$$\dot{\delta \mathbf{x}} = \mathbf{F}_I(\mathbf{x}_{\text{INS}}) \delta \mathbf{x} + \mathbf{G}_I(\mathbf{x}_{\text{INS}}) \mathbf{n}_{\text{INS}}, \quad (3.24)$$

where

$$\delta \mathbf{x} = \begin{bmatrix} \delta \mathbf{p}' & \delta \mathbf{v}' & \delta \phi' & \delta \mathbf{b}'_a & \delta \mathbf{b}'_\omega \end{bmatrix}', \quad \mathbf{n}_{\text{INS}} = \begin{bmatrix} \mathbf{n}'_p & \mathbf{n}'_a & \mathbf{n}'_\omega & \mathbf{n}'_{b_a} & \mathbf{n}'_{b_\omega} \end{bmatrix}',$$

$$\mathbf{F}_I(\mathbf{x}_{\text{INS}}) = \begin{bmatrix} \mathbf{0} & \mathbf{I}_3 & \mathbf{0} & \mathbf{0} & \mathbf{0} \\ \mathbf{0} & \mathbf{0} & -(\mathcal{R}\mathbf{a}_r)_\times & -\mathcal{R} & \mathbf{0} \\ \mathbf{0} & \mathbf{0} & \mathbf{0} & \mathbf{0} & -\mathcal{R} \\ \mathbf{0} & \mathbf{0} & \mathbf{0} & \mathbf{0} & \mathbf{0} \\ \mathbf{0} & \mathbf{0} & \mathbf{0} & \mathbf{0} & \mathbf{0} \end{bmatrix}, \quad \mathbf{G}_I(\mathbf{x}_{\text{INS}}) = \text{blkdiag}(\mathbf{I}_3, \mathcal{R}, \mathcal{R}, -\mathbf{I}_3, -\mathbf{I}_3),$$

where  $\text{blkdiag}(\dots)$  represents a block diagonal matrix,  $\mathbf{n}_p \sim \mathcal{N}(\mathbf{0}, \Xi_p)$  is a Gaussian white noise process associated with the position error estimate and the state noise covariance matrix is given by

$$\mathbf{Q}_{\text{INS}} = \text{blkdiag}(\Xi_p, \Xi_a, \Xi_\omega, \Xi_{b_a}, \Xi_{b_\omega}).$$

The measurement model for the proposed VD and LASER aiding techniques are described in the ensuing, however additional information sources are considered. A GPS receiver and a magnetometer are integrated in the system using the measurement residuals

$$\mathbf{z}_{\text{GPS}} := \hat{\mathbf{p}} - \mathbf{p}_{\text{GPS}} \approx \delta \mathbf{p} - \mathbf{n}_{\text{GPS}}, \quad (3.25a)$$

$$\mathbf{z}_m := {}^E \mathbf{m} - \hat{\mathcal{R}} \mathbf{m}_r \approx ({}^E \mathbf{m})_\times \delta \phi - \mathcal{R} \mathbf{n}_m, \quad (3.25b)$$

where  $\mathbf{p}_{\text{GPS}}$  is the position measured by the GPS unit,  $\mathbf{m}_r$  is the magnetometer reading,  ${}^E \mathbf{m}$  represents the Earth's magnetic field in Earth coordinates, and  $\mathbf{n}_{\text{GPS}} \sim \mathcal{N}(\mathbf{0}, \Xi_{\text{GPS}})$ ,  $\mathbf{n}_m \sim \mathcal{N}(\mathbf{0}, \Xi_m)$  are Gaussian white noise processes. For further details on the derivation of the measurement residuals (3.25), the reader is referred to Sections 2.3 and 2.4.

### 3.4.2 Vehicle model aiding

The EKF state space model, formulated using (3.23), is obtained by concatenating the state space model (3.24) that describes the INS estimation errors, with the state model and measurements of the vehicle model aiding techniques described in Sections 3.2.2 and 3.2.3. With a slight abuse of notation, the state model (3.23) is defined for the external and embedded vehicle model dynamics using the same state  $\mathbf{x}_C$  and measurement  $\mathbf{z}_C$  variables.

#### External vehicle model aiding

In the external vehicle model aiding technique, the vehicle dynamics are computed by a self-contained VD simulator as shown in Fig. 3.2, and consequently the INS and the VD states are distinct. As a mean to estimate and compensate for the INS errors, the EKF state model is augmented with the VD error dynamics (3.9), and the measurement residuals (3.11) are a linear combination of the INS and the VD errors. The classical VD aiding methodology requires specific computational routines to compensate for the estimation errors in the VD simulator.

The continuous-time error state space model for the navigation system with external VD aiding is obtained directly from the EKF/INS state model (3.24) augmented with the VD error dynamics (3.9), yielding

$$\begin{aligned} \mathbf{x}_C &:= \begin{bmatrix} \delta \mathbf{x}' & \delta \mathbf{x}'_V \end{bmatrix}', & \mathbf{n}_{x_C} &:= \begin{bmatrix} \mathbf{n}'_{\text{INS}} & \mathbf{n}'_{x_V} \end{bmatrix}', & \mathbf{u}_C &= \mathbf{0}, \\ \mathbf{F}_C(\mathbf{x}_{\text{INS}}, \mathbf{x}_V) &= \begin{bmatrix} \mathbf{F}_I(\mathbf{x}_{\text{INS}}) & \mathbf{0}_{15 \times 9} \\ \mathbf{0}_{9 \times 15} & \mathbf{F}_V(\mathbf{x}_V) \end{bmatrix}, & \mathbf{G}_C(\mathbf{x}_{\text{INS}}) &= \begin{bmatrix} \mathbf{G}_I(\mathbf{x}_{\text{INS}}) & \mathbf{0}_{15 \times 9} \\ \mathbf{0}_{9 \times 15} & \mathbf{G}_V \end{bmatrix}, \end{aligned}$$

with the vehicle states, noises and model submatrices given by

$$\begin{aligned} \delta \mathbf{x}_V &:= \begin{bmatrix} \delta \boldsymbol{\omega}'_V & \delta {}^B \mathbf{v}'_V & \delta \phi'_V \end{bmatrix}', & \mathbf{n}_{x_V} &:= \begin{bmatrix} \mathbf{n}'_{\boldsymbol{\omega}_V} & \mathbf{n}'_{\mathbf{v}_V} & \mathbf{n}'_{\phi_V} \end{bmatrix}', \\ \mathbf{F}_V(\mathbf{x}_V) &= \left. \begin{bmatrix} \frac{\partial f_\omega}{\partial \boldsymbol{\omega}} & \mathbf{0} & \mathbf{0} \\ \frac{\partial f_v}{\partial \boldsymbol{\omega}} & \frac{\partial f_v}{\partial {}^B \mathbf{v}} & \frac{\partial f_v}{\partial \phi} \\ \mathcal{R}_V & \mathbf{0} & \mathbf{0} \end{bmatrix} \right|_{\mathbf{x}_V}, & \mathbf{G}_V &= \begin{bmatrix} \mathbf{I} & \mathbf{0} & \mathbf{0} \\ \mathbf{0} & \mathbf{I} & \mathbf{0} \\ \mathbf{0} & \mathbf{0} & \mathbf{I} \end{bmatrix}, \end{aligned}$$

where  $\mathbf{n}_{\boldsymbol{\omega}_V}$ ,  $\mathbf{n}_{\mathbf{v}_V}$ , and  $\mathbf{n}_{\phi_V}$  are zero-mean, Gaussian white noise processes with covariances  $\boldsymbol{\Xi}_{\boldsymbol{\omega}_V}$ ,  $\boldsymbol{\Xi}_{\mathbf{v}_V}$ , and  $\boldsymbol{\Xi}_{\phi_V}$  respectively, that characterize the vehicle modeling errors.

The measurement residuals (3.11) are a function of the INS and VD errors, given in the state space form by

$$\begin{aligned} \mathbf{z}_C &:= \begin{bmatrix} \mathbf{z}'_\omega & \mathbf{z}'_u & \mathbf{z}'_{\mathcal{R}} \end{bmatrix}', & \mathbf{n}_{z_V} &:= \begin{bmatrix} \mathbf{n}'_\omega + \mathbf{n}'_{z_\omega} & \mathbf{n}'_{z_u} & \mathbf{n}'_{z_{\mathcal{R}}} \end{bmatrix}', \\ \mathbf{H}_C(\mathbf{x}_{\text{INS}}) &= \begin{bmatrix} \mathbf{0} & \mathbf{0} & \mathbf{0} & \mathbf{0} & -\mathbf{I} & -\mathbf{I} & \mathbf{0} & \mathbf{0} \\ \mathbf{0} & \mathcal{R}' & \mathcal{R}'(\mathbf{v})_\times & \mathbf{0} & \mathbf{0} & \mathbf{0} & -\mathbf{I} & \mathbf{0} \\ \mathbf{0} & \mathbf{0} & \mathbf{I} & \mathbf{0} & \mathbf{0} & \mathbf{0} & \mathbf{0} & -\mathbf{I} \end{bmatrix}, \end{aligned}$$

where  $\mathbf{n}_{z_\omega}$ ,  $\mathbf{n}_{z_u}$ , and  $\mathbf{n}_{z_{\mathcal{R}}}$  are zero-mean Gaussian white noise processes associated with the  $\mathbf{z}_\omega$ ,  $\mathbf{z}_u$ , and  $\mathbf{z}_{\mathcal{R}}$  observations, with covariances  $\boldsymbol{\Xi}_{z_\omega}$ ,  $\boldsymbol{\Xi}_{z_u}$ , and  $\boldsymbol{\Xi}_{z_{\mathcal{R}}}$ , respectively. The vehicle states and measurements noise covariance matrices are

$$\mathbf{Q}_C = \text{blkdiag}(\mathbf{Q}_{\text{INS}}, \boldsymbol{\Xi}_{\boldsymbol{\omega}_V}, \boldsymbol{\Xi}_{u_V}, \boldsymbol{\Xi}_{\mathcal{R}_V}), \quad \mathbf{R}_C = \text{blkdiag}(\boldsymbol{\Xi}_{z_\omega} + \boldsymbol{\Xi}_\omega, \boldsymbol{\Xi}_{z_u}, \boldsymbol{\Xi}_{z_{\mathcal{R}}}),$$

where the white noise variances account for the effects of neglecting high order terms and unmodeled uncertainties in the measurement residual derivation.

The observation  $\mathbf{z}_\omega$  is disturbed by rate gyro noise, so a state and measurement noise correlation matrix is introduced in the Kalman filter equations

$$\mathbf{C}_C = \begin{bmatrix} \mathbf{0} & \mathbf{0} & \boldsymbol{\Xi}_\omega & \mathbf{0} & \mathbf{0} & \mathbf{0}_{3 \times 9} \\ & \mathbf{0}_{6 \times 15} & & \mathbf{0}_{6 \times 9} & & \end{bmatrix}',$$

for details on the definition and derivation see [22] and references therein.

As presented in Table 3.1, the external vehicle model aiding increases the EKF dimensionality by 9 states, and propagate  $f_\omega(\boldsymbol{\omega}, \mathbf{n}_{\text{th}})$ ,  $f_v(\boldsymbol{\omega}_V, {}^B \mathbf{v}_V, \mathbf{f}_{\text{th}})$ , and  $f_{\mathcal{R}}(\boldsymbol{\omega}_V, \mathcal{R}_V)$  although the latter is also computed by the inertial integration algorithm. As discussed in Section 3.2.3, the proposed embedded VD aiding technique reduces the computational cost of vehicle model integration, by requiring a smaller state space augmentation and by propagating only the necessary vehicle model differential equations.

Table 3.1: Comparison of the vehicle model aiding techniques with a standard GPS aided IMU.

	Aiding Technique		
	GPS	External VD	Embedded VD
EKF State Space Dimension	15	24	18
Propagated VD equations	-	$f_\omega(\boldsymbol{\omega}, \mathbf{n}_{th})$ $f_v(\boldsymbol{\omega}_V, {}^B\mathbf{v}_V, \mathbf{f}_{th})$ $f_{\mathcal{R}}(\boldsymbol{\omega}_V, \mathcal{R}_V)$	$f_\omega(\boldsymbol{\omega}, \mathbf{n}_{th})$

### Embedded vehicle model aiding

The implementation of the embedded vehicle model aiding technique for the 6 DOF rigid body is illustrated in Fig. 3.3. In this technique, the VD angular velocity is integrated in the navigation system by augmenting the EKF state model with (3.12a), propagating  $f_\omega(\boldsymbol{\omega}, \mathbf{n}_{th})$  using the INS estimates, and using the measurement residual (3.13). The VD linear velocity information is integrated in the filter using the measurement residual (3.14), where  $\mathbf{f}_v(\boldsymbol{\omega}, {}^B\mathbf{v}, \mathcal{R}, \mathbf{f}_{th})$  is computed using the INS estimates. The continuous-time state space model is given by

$$\mathbf{x}_C := [\delta\mathbf{x}' \quad \mathbf{x}'_V]', \quad \mathbf{n}_{x_C} := [\mathbf{n}'_{INS} \quad \mathbf{n}'_{x_V}]', \quad \mathbf{u}_C = f_\omega(\boldsymbol{\omega}, \mathbf{n}_{th}),$$

$$\mathbf{F}_C(\mathbf{x}_{INS}) = \begin{bmatrix} \mathbf{F}_I(\mathbf{x}_{INS}) & \mathbf{0}_{15 \times 3} \\ \mathbf{F}_V(\mathbf{x}_{INS}) & \mathbf{0}_{3 \times 3} \end{bmatrix}, \quad \mathbf{G}_C(\mathbf{x}_{INS}) = \begin{bmatrix} \mathbf{G}_I(\mathbf{x}_{INS}) & \mathbf{0}_{9 \times 3} \\ \mathbf{G}_V(\mathbf{x}_{INS}) & \mathbf{I}_3 \end{bmatrix},$$

where

$$\mathbf{x}_V = \boldsymbol{\omega}, \quad \mathbf{n}_{x_V} = \mathbf{n}_{\boldsymbol{\omega}_V},$$

$$\mathbf{F}_V(\mathbf{x}_{INS}) = \begin{bmatrix} \mathbf{0} & \mathbf{0} & \mathbf{0} & \mathbf{0} & \left. \frac{\partial f_\omega}{\partial \boldsymbol{\omega}} \right|_{\hat{\mathbf{x}}} \end{bmatrix}, \quad \mathbf{G}_V(\mathbf{x}_{INS}) = \begin{bmatrix} \mathbf{0} & \mathbf{0} & - \left. \frac{\partial f_\omega}{\partial \boldsymbol{\omega}} \right|_{\hat{\mathbf{x}}} & \mathbf{0} & \mathbf{0} \end{bmatrix},$$

where  $\mathbf{n}_{\boldsymbol{\omega}_V}$  is a zero-mean, Gaussian white noise with covariance  $\boldsymbol{\Xi}_{\boldsymbol{\omega}_V}$ , that characterizes the vehicle modeling errors. The  $\mathbf{x}_V$  state variable is propagated using the INS estimates as expressed in (3.12a), and the EKF state matrices depend only on the INS quantities  $\mathbf{x}_{INS}$ , as expected from the derivation of the technique presented in Section 3.2.3.

The measurement state model (3.13, 3.14) is described in the state space form by

$$\mathbf{z} := [\mathbf{z}'_\omega \quad \mathbf{z}'_v]', \quad \mathbf{n}_{z_V} := \left[ \mathbf{n}'_\omega + \mathbf{n}'_{z_\omega} \quad -\mathbf{n}'_a + \left( \left( \frac{\partial f_\omega}{\partial \boldsymbol{\omega}} - ({}^B\mathbf{v})_\times \right) \mathbf{n}_\omega \right)' + \mathbf{n}'_{z_v} \right]',$$

$$\mathbf{H}_C(\mathbf{x}_{INS}) = \begin{bmatrix} \mathbf{0} & \mathbf{0} & \mathbf{0} & \mathbf{0} & -\mathbf{I} & \mathbf{I} \\ \mathbf{0} & \left( (\boldsymbol{\omega})_\times + \frac{\partial f_v}{\partial {}^B\mathbf{v}} \right) \mathcal{R}' & \mathbf{H}_{v\mathcal{R}}(\mathbf{x}_{INS}) & \mathbf{I} & ({}^B\mathbf{v})_\times - \frac{\partial f_v}{\partial \boldsymbol{\omega}} & \mathbf{0} \end{bmatrix} \Bigg|_{\hat{\mathbf{x}}},$$

where  $\mathbf{H}_{v\mathcal{R}}(\mathbf{x}_{INS}) := \left( (\boldsymbol{\omega})_\times ({}^B\mathbf{v})_\times - ({}^B\mathbf{g})_\times + \frac{\partial f_v}{\partial {}^B\mathbf{v}} ({}^B\mathbf{v})_\times + \frac{\partial f_v}{\partial \delta\phi} \mathcal{R} \right) \mathcal{R}'$ , and  $\mathbf{n}_{z_\omega} \sim \mathcal{N}(\mathbf{0}, \boldsymbol{\Xi}_{z_\omega})$  and  $\mathbf{n}_{z_v} \sim \mathcal{N}(\mathbf{0}, \boldsymbol{\Xi}_{z_v})$  are zero-mean Gaussian white noise processes associated with the

measurement. The vehicle states and measurements noise covariance and covariance correlation matrices are given by

$$\begin{aligned}\mathbf{Q}_C &= \text{blkdiag}(\mathbf{Q}_{\text{INS}}, \Xi_{\omega_v}), \\ \mathbf{R}_C &= \text{blkdiag}\left(\Xi_{\omega} + \Xi_{z_{\omega}}, \Xi_a + \left(\frac{\partial f_{\omega}}{\partial \omega} - ({}^B \mathbf{v})_{\times}\right) \Xi_{\omega} \left(\frac{\partial f_{\omega}}{\partial \omega} - ({}^B \mathbf{v})_{\times}\right)' + \Xi_{z_v}\right), \\ \mathbf{C}_C &= \begin{bmatrix} \mathbf{0} & \mathbf{0} & \Xi_{\omega} & \mathbf{0} & \mathbf{0} & \mathbf{0}_{3 \times 3} \\ \mathbf{0} & -\Xi_a & \left(\frac{\partial f_{\omega}}{\partial \omega} - ({}^B \mathbf{v})_{\times}\right) \Xi_{\omega} & \mathbf{0} & \mathbf{0} & \mathbf{0}_{3 \times 3} \end{bmatrix}'.\end{aligned}$$

The number of EKF states for the embedded VD aiding is smaller than that of the external VD aiding, as evidenced in Table 3.1, due to the use of  $f_v(\hat{\omega}, {}^B \hat{\mathbf{v}}, \hat{\mathcal{R}}, \hat{\mathbf{f}}_{\text{th}})$  directly in the measurement (3.14) and to the propagation of the attitude kinematics using the INS. The computational cost of using VD model is also smaller because numerical integration methods are only adopted to solve for  $f_{\omega}(\hat{\omega}, \hat{\mathbf{n}}_{\text{th}})$ . Moreover, the angular velocity and linear velocity aiding can be independently enabled or disabled, contrary to the external VD aiding, by including or omitting  $\mathbf{z}_{\omega}$  and  $\mathbf{z}_v$  respectively.

### 3.4.3 LASER aiding

The LASER sensor is integrated with the INS by defining the variables and matrices of the EKF state model (3.23) as

$$\begin{aligned}\mathbf{x}_C &:= [\delta \mathbf{x}' \quad h_S]', \quad \mathbf{n}_{x_C} := [\mathbf{n}'_{\text{INS}} \quad n_{h_S}]', \quad \mathbf{u}_C = \mathbf{0}, \\ \mathbf{F}_C(\mathbf{x}_{\text{INS}}) &= \begin{bmatrix} \mathbf{F}_I(\mathbf{x}_{\text{INS}}) & \mathbf{0}_{15 \times 1} \\ \mathbf{0}_{1 \times 15} & 0 \end{bmatrix}, \quad \mathbf{G}_C(\mathbf{x}_{\text{INS}}) = \begin{bmatrix} \mathbf{G}_I(\mathbf{x}_{\text{INS}}) & \mathbf{0}_{9 \times 1} \\ \mathbf{0}_{1 \times 9} & 1 \end{bmatrix}.\end{aligned}$$

The measurement model is obtained from (3.22) and given by

$$\begin{aligned}\mathbf{z}_C &:= \mathbf{z}_L, \quad \mathbf{n}_{z_C} := \mathbf{n}_{z_L}, \\ \mathbf{H}_C(\mathbf{x}_{\text{INS}}) &= \begin{bmatrix} \mathbf{e}'_3 & \mathbf{0}_{1 \times 3} & -\mathbf{e}'_3 (\mathcal{R}_M^B \mathbf{R} \mathbf{e}_3)_{\times} & \mathbf{0}_{1 \times 3} & \mathbf{0}_{1 \times 3} & -1 \end{bmatrix},\end{aligned}$$

where

$$\mathbf{Q}_C = \text{blkdiag}(\mathbf{Q}_{\text{INS}}, \Xi_{h_S}), \quad \mathbf{R}_C = (\mathbf{e}'_3 \mathcal{R}_M^B \mathbf{R} \mathbf{e}_3)^2 \Xi_L, \quad \mathbf{C}_C = \mathbf{0}.$$

The LASER sensor is adopted for takeoff and landing maneuvers. Previous to the LASER's activation, the estimation covariance of  $h_S$  is defined large enough to account for the uncertainty in the terrain height. When the LASER sensor is activated, the EKF recursively estimates the terrain height  $h_S$  based on the sensor measurements, and the uncertainty on the terrain's height converges asymptotically to a steady state value, that depends on the sensor's accuracy.

When the LASER is switched off, the uncertainty on the terrain height  $h_S$  will grow at a rate defined by the noise covariance  $\Xi_{h_S}$ . Techniques to avoid numerical problems in the EKF covariance matrices should be adopted, namely square root filtering [22] or by setting  $\Xi_{h_S} = 0$  if the uncertainty reaches a specific upper bound.

### 3.4.4 State model discretization

The discrete-time state space model

$$\mathbf{x}_{k+1} = \Phi_k \mathbf{x}_k + \mathbf{w}_k, \quad \mathbf{z}_k = \mathbf{H}_k \mathbf{x}_k + \mathbf{v}_k,$$

is obtained using the zero-order hold discretization technique [22], and is given by

$$\Phi_k = e^{\mathbf{F}_k T}, \quad \mathbf{H}_k = \mathbf{H}_C|_{t=t_k},$$

and the discrete-time noise covariance matrices are described by

$$\begin{aligned} \mathbf{Q}_k &\simeq [\mathbf{G}_k \mathbf{Q}_C \mathbf{G}'_k] T, \quad \mathbf{R}_k \simeq \frac{\mathbf{R}_{Ck}}{T}, \\ \mathbf{C}_k &= \frac{1}{T} \int_{t_{k-1}}^{t_k} \Phi(t_{k+1}, \varphi) \mathbf{G}_C(\tau) \mathbf{C}_C(\tau) d\tau \approx \left( \mathbf{I} + \frac{\mathbf{F}_k T}{2} + \frac{\mathbf{F}_k^2 T^2}{6} \right) \mathbf{G}_k \mathbf{C}_{Ck}, \end{aligned}$$

where  $T$  is the sampling period,  $\mathbf{x}_k = \mathbf{x}_C|_{t=t_k}$ ,  $\mathbf{z}_k = \mathbf{z}_C|_{t=t_k}$ ,  $\mathbf{w}_k$  and  $\mathbf{v}_k$  are discrete-time zero-mean Gaussian white noise processes,  $\mathbf{F}_k = \mathbf{F}_C|_{t=t_k}$ ,  $\mathbf{G}_k = \mathbf{G}_C|_{t=t_k}$ ,  $\mathbf{R}_{Ck} = \mathbf{R}_C|_{t=t_k}$ ,  $\mathbf{C}_{Ck} = \mathbf{C}_C|_{t=t_k}$  and  $\Phi_k = \Phi(t_{k+1}, t_k)$  denotes the state transition matrix.

### 3.4.5 State estimation and error compensation

The Kalman filter state estimation is described by the following linear, recursive form

$$\hat{\mathbf{x}}_k^+ = \hat{\mathbf{x}}_k^- + \mathbf{K}_k (\mathbf{z}_k - \mathbf{H}_k \hat{\mathbf{x}}_k^-)$$

where the  $-$  and  $+$  superscripts denote respectively the quantities before and after the update using the measurement  $\mathbf{z}_k$ , more details can be found in the classical Kalman filtering reference [56] and in [22]. The Kalman filter gain  $\mathbf{K}_k$  and updated error covariance matrix are given by

$$\begin{aligned} \mathbf{K}_k &= (\mathbf{P}_k^- \mathbf{H}'_k + \mathbf{C}_k) [\mathbf{H}_k \mathbf{P}_k^- \mathbf{H}'_k + \mathbf{R}_k + \mathbf{H}_k \mathbf{C}_k + \mathbf{C}'_k \mathbf{H}'_k]^{-1}, \\ \mathbf{P}_k^+ &= (\mathbf{I}_n - \mathbf{K}_k \mathbf{H}_k) \mathbf{P}_k^- - \mathbf{K}_k \mathbf{C}'_k. \end{aligned}$$

In the current direct feedback configuration, the position and attitude estimates stored in the INS are updated using the EKF error estimates as follows

$$\begin{aligned} \hat{\mathbf{p}}_k^+ &= \hat{\mathbf{p}}_k^- - \delta \hat{\mathbf{p}}_k^+, \quad \hat{\mathbf{v}}_k^+ = \hat{\mathbf{v}}_k^- - \delta \hat{\mathbf{v}}_k^+, \quad \hat{\mathcal{R}}_k^+ = \mathcal{R}'(\delta \hat{\phi}_k^+) \hat{\mathcal{R}}_k^-, \\ \hat{\mathbf{b}}_{ak}^+ &= \hat{\mathbf{b}}_{ak}^- - \delta \hat{\mathbf{b}}_{ak}^+, \quad \hat{\mathbf{b}}_{\omega k}^+ = \hat{\mathbf{b}}_{\omega k}^- - \delta \hat{\mathbf{b}}_{\omega k}^+, \end{aligned} \quad (3.26)$$

where matrix  $\mathcal{R}'(\delta \hat{\phi}_k^+)$  is implemented using power series expansion of trigonometric terms up to an arbitrary accuracy [126]. This procedure updates the linearization point and keeps filter perturbational dynamics valid under the first order assumptions. The EKF error estimates are reset after being applied to compensate the INS states, i.e. the error estimates are set as  $\delta \hat{\mathbf{p}}_k^+ = \delta \hat{\mathbf{v}}_k^+ = \delta \hat{\phi}_k^+ = \delta \hat{\mathbf{b}}_{ak}^+ = \delta \hat{\mathbf{b}}_{\omega k}^+ = \mathbf{0}$  after computing (3.26). The state estimate and the estimation error covariance matrix are propagated using

$$\hat{\mathbf{x}}_{k+1}^- = \Phi_k \hat{\mathbf{x}}_k^+, \quad \mathbf{P}_{k+1}^- = \Phi_k \mathbf{P}_k^+ \Phi'_k + \mathbf{Q}_k.$$

Table 3.2: Sensor non-idealities.

Sensor	Bias	Noise Variance
Rate Gyro	0.05 °/s	(0.02 °/s) <sup>2</sup>
Accelerometer	10 mg	(0.6 mg) <sup>2</sup>
LASER	-	(10 <sup>-2</sup> m) <sup>2</sup>
Magnetometer	-	(1 mG) <sup>2</sup>
GPS	-	10 m <sup>2</sup>

Note that the derivation of the external vehicle model aiding technique is similar to that adopted for the INS, and hence it is necessary to feed back the estimated VD errors as shown in Figs. 3.1(a) and 3.2. The VD error compensation routines are described by

$$\hat{\omega}_{V_k}^+ = \hat{\omega}_{V_k}^- - \delta \hat{\omega}_{V_k}, \quad {}^B \hat{\mathbf{v}}_{V_k}^+ = {}^B \hat{\mathbf{v}}_{V_k}^- - \delta {}^B \hat{\mathbf{v}}_{V_k}, \quad \hat{\mathcal{R}}_{V_k}^+ = \hat{\mathcal{R}}_{V_k}' (\delta \hat{\phi}_V) \hat{\mathcal{R}}_{V_k}^-.$$

By construction, the embedded VD technique propagates some vehicle dynamics using the EKF state space. Vehicle model error compensation routines are not necessary in this technique, since the estimation error compensation is automatically performed by the EKF in the state update step.

### 3.5 Simulation results

This section presents the simulations results that validate and illustrate the properties of the proposed aiding techniques. The integration of the VD and LASER range finder information in the navigation system is studied using three simulation setups. The first simulation compares the estimation results of the VD aided navigation system with those obtained using a classical GPS/INS architecture, for a 6-DOF rigid body describing a trimming trajectory, and the embedded VD aiding technique is validated with respect to the classical VD aided navigation system.

In the second simulation, the proposed VD aiding is applied for the case of a model-scale Vario X-Treme helicopter, to demonstrate the implementation of the technique for highly nonlinear, realistic vehicle models. Simulation results are presented for a takeoff and turning trajectory, and the estimation results of a GPS based and the VD aided navigation architectures are analyzed.

The third simulation emphasizes the role of the LASER range finder sensor for critical maneuvers. The vehicle describes a hovering maneuver, and has to acquire the distance-to-ground for automatic landing. Accuracy improvements obtained with the LASER range finder sensor integrated on a GPS/INS configuration are evidenced. Dynamic estimation of distance-to-ground is performed, and position and velocity vertical channel accuracy enhancements are shown.

The INS high speed algorithm is set to run at 100 Hz and the normal speed algorithm is synchronized with the EKF, both executed at 50Hz. The LASER sensor operates at



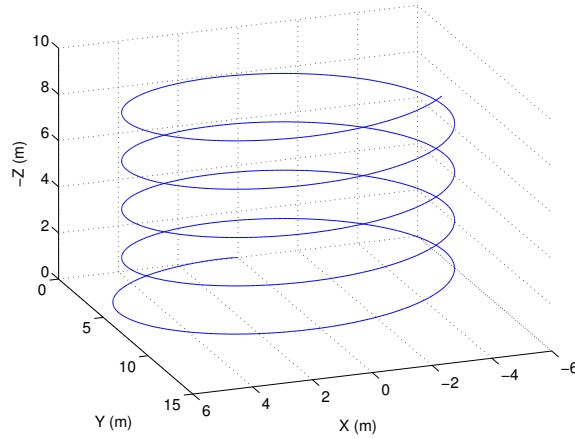


Figure 3.5: Rigid body trimming trajectory.

Table 3.3: Rigid body characteristics.

Property	Nominal Value
Mass	$m = 10$ Kg
Length, Width, Height	$(l, w, h) = (1.00, 0.75, 0.25)$ m
Rear Thrusters Position	${}^B \mathbf{p}_{th 1,2} = \begin{bmatrix} -0.50 & \pm 0.30 & 0 \end{bmatrix}$ m
Side Thrusters Position	${}^B \mathbf{p}_{th 3,4} = \begin{bmatrix} 0 & -0.375 & \pm 0.10 \end{bmatrix}$ m
Bottom Thrusters Position	${}^B \mathbf{p}_{th 5,6} = \begin{bmatrix} \pm 0.40 & 0 & -0.125 \end{bmatrix}$ m
Damping Coefficients	$K_{ang} = 4, K_{lin} = 2$

10Hz and the GPS provides position measurements at the nominal frequency of 1Hz. The characteristics of the sensors non-idealities are presented in Table 3.2.

### 3.5.1 Vehicle model aiding

The VD aiding technique is validated using the 6-DOF rigid body model described in Section 3.2.1, with the parameters detailed in Table 3.3. The external VD, embedded VD and a classical GPS/INS architectures are studied for the rigid body model subject to constant linear and centripetal acceleration, describing the upwards trimming trajectory shown in Fig. 3.5. The bias estimation and compensation is analyzed by considering a 30% bias calibration error in each channel of the accelerometer and rate gyro sensors. A magnetometer is also integrated in the system, using the measurement residual model (3.25).

The linear and angular velocity information provided by the vehicle model clearly endows the filter to compensate for the inertial sensor biases, as shown in Fig. 3.6. Bias calibration errors are reduced almost instantly by the VD aided navigation system, yielding smaller bias steady-state estimation error, and allowing for smaller estimations errors of the other state variables. While accelerometer bias compensation using a GPS/INS

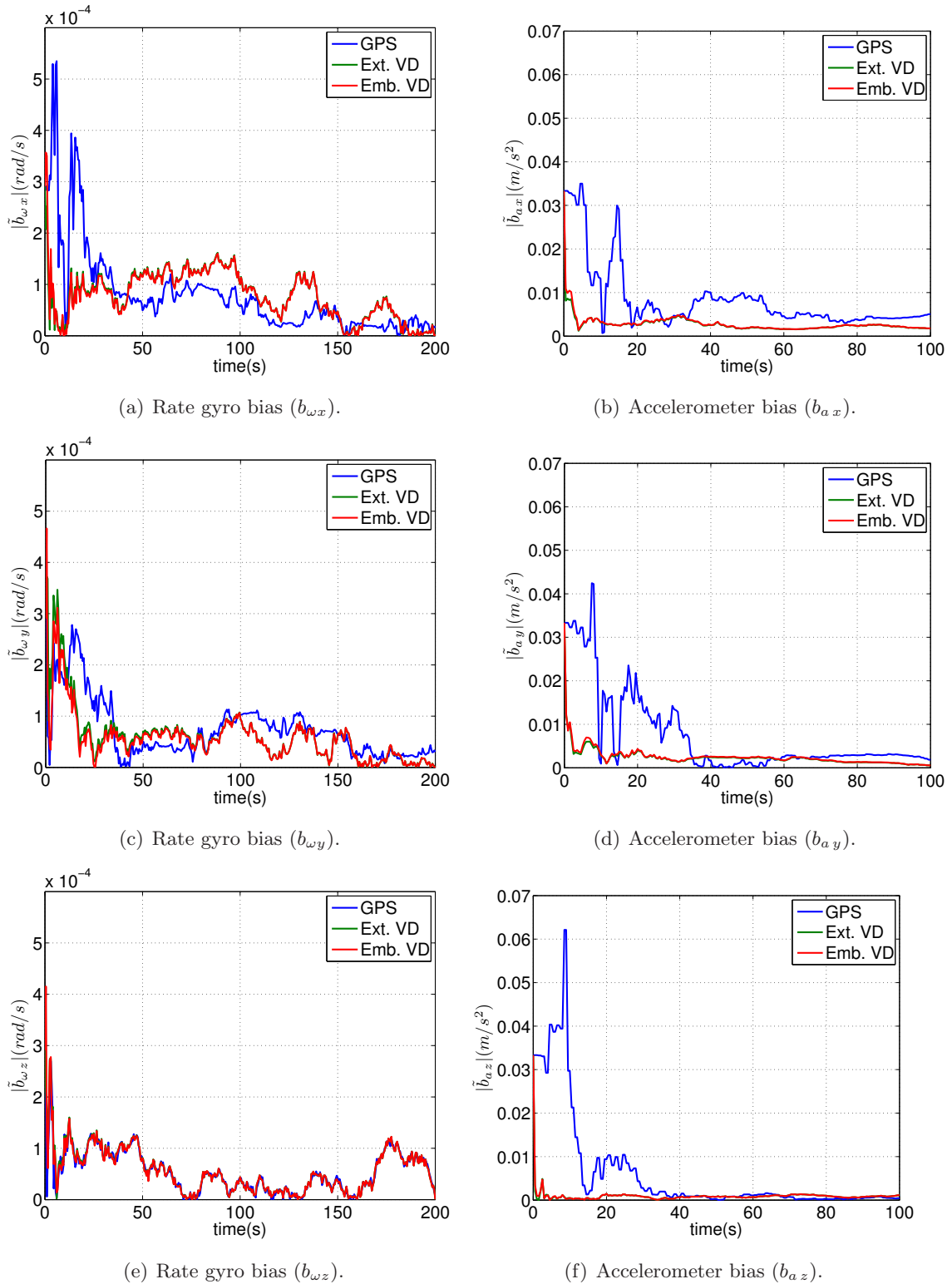


Figure 3.6: Bias estimation errors of the GPS and the VD aided navigation systems (rigid body, magnetometer on).

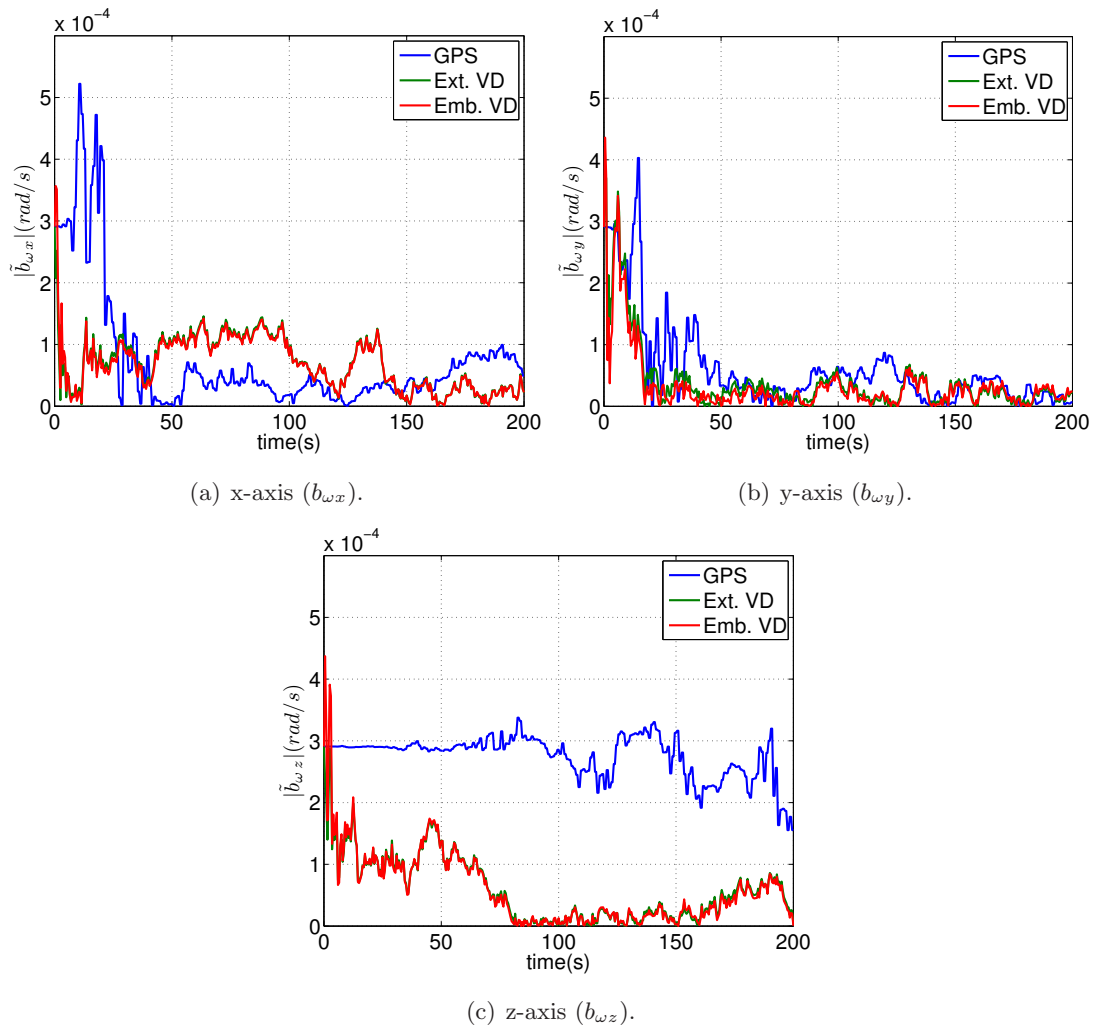


Figure 3.7: Rate gyro bias estimation error of the GPS and the VD aided navigation systems (Rigid body, Magnetometer off).

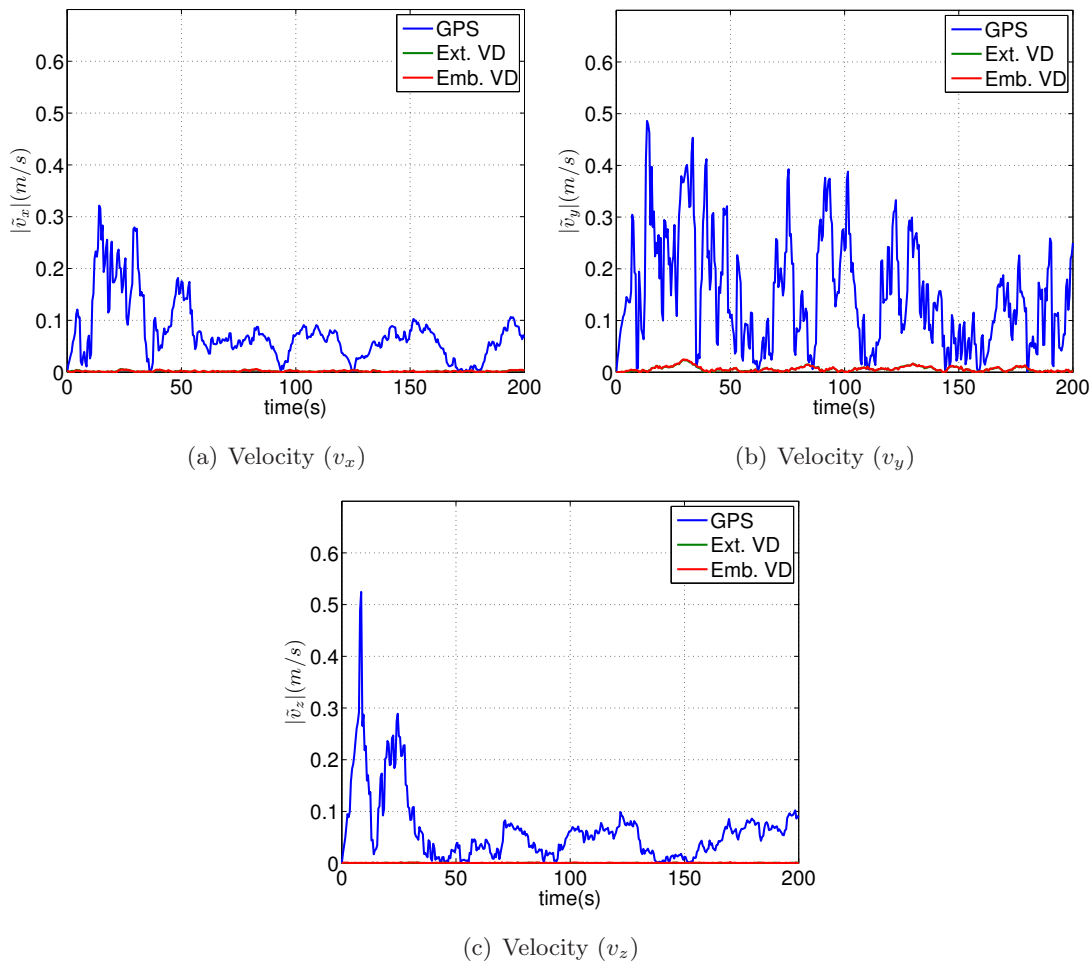


Figure 3.8: Velocity estimation errors of the GPS and the VD aided navigation systems (rigid body, magnetometer on).

architecture requires specific maneuvers that excite the unobservable directions, the VD aiding can effectively estimate the sensor bias in a standard trimming trajectory, as shown in the simulation results. Given that the contribution of the VD aiding to the rate gyro bias compensation is occluded by the use of a magnetometer, Fig. 3.7 presents the bias estimation results for a VD aided navigation system without magnetometer observations, showing that VD aiding is critical for the bias estimation, in particular in the z-axis.

The velocity results are dramatically enhanced by the VD aiding, as shown in Fig. 3.8 and detailed in Table 3.4. Although position and attitude information are not directly provided for by the vehicle model, position and attitude estimates are more accurate with VD aiding, as shown in Tables 3.5 and 3.6, due to the smaller velocity and bias estimation errors.

The accuracy of the embedded and the external VD architectures are similar, which validates the proposed aiding technique. Both architectures use the same vehicle model, and hence the aiding information introduced in the filter is the same, and the estimation results are thus similar. However, the embedded VD aiding brings about computational

Table 3.4: Velocity estimation error (rigid body).

<b>Aiding information</b>	<b>RMS Error</b>		
	$v_x$ (m/s)	$v_y$ (m/s)	$v_z$ (m/s)
GPS	$9.55 \times 10^{-2}$	0.19	$9.09 \times 10^{-2}$
Ext. VD	$2.07 \times 10^{-3}$	$7.68 \times 10^{-3}$	$4.35 \times 10^{-4}$
Emb. VD	$2.15 \times 10^{-3}$	$7.94 \times 10^{-3}$	$5.94 \times 10^{-4}$

Table 3.5: Position estimation error (rigid body).

<b>Aiding information</b>	<b>RMS Error</b>		
	$p_x$ (m)	$p_y$ (m)	$p_z$ (m)
GPS	0.93	1.16	1.07
Ext. VD	$3.92 \times 10^{-2}$	0.11	$1.90 \times 10^{-2}$
Emb. VD	$4.71 \times 10^{-2}$	0.12	$8.13 \times 10^{-3}$

Table 3.6: Attitude estimation error (rigid body).

<b>Aiding information</b>	<b>RMS Error</b>		
	Yaw ( $^\circ$ )	Pitch ( $^\circ$ )	Roll ( $^\circ$ )
GPS	$1.35 \times 10^{-2}$	$7.60 \times 10^{-2}$	$7.58 \times 10^{-2}$
Ext. VD	$1.22 \times 10^{-2}$	$1.70 \times 10^{-2}$	$1.74 \times 10^{-2}$
Emb. VD	$1.21 \times 10^{-2}$	$1.70 \times 10^{-2}$	$1.70 \times 10^{-2}$

Table 3.7: Estimation error for the embedded VD aiding,  ${}^B\mathbf{v}$  observation only (rigid body).

	RMS Error		
Yaw, Pitch, Roll ( $^\circ$ )	$1.35 \times 10^{-2}$	$1.70 \times 10^{-2}$	$1.63 \times 10^{-2}$
$v_x, v_y, v_z$ (m/s)	$2.26 \times 10^{-2}$	$7.50 \times 10^{-3}$	$5.93 \times 10^{-4}$
$p_x, p_y, p_z$ (m)	$4.88 \times 10^{-2}$	0.12	$7.60 \times 10^{-3}$

Table 3.8: Execution time of the navigation systems for 200 s of simulation time.

	GPS Aided	External VD Aided	Embedded VD Aided	
			$(\boldsymbol{\omega}, {}^B\mathbf{v})$ aiding	${}^B\mathbf{v}$ aiding
Execution Time (s)	293	543	400	310

savings, as demonstrated in the simulation execution times presented in Table 3.8. As discussed in Section 3.2.3, the smaller number of states associated with the embedded VD aiding, and the propagation of solely the angular velocity, reduce the computational cost of using the vehicle model information in the system.

The embedded VD aiding allows for the independent use of the angular and linear velocity aiding, as opposed to using the full dynamics computed by the external vehicle simulator. Interestingly enough, simulation runs for the embedded VD aiding using only the velocity observation, i.e.  $\mathbf{z}_C = \mathbf{z}_v$ , show that the execution time is close to that of the GPS aided architecture, while the estimation results, shown in Table 3.7, are very similar to those of the linear and angular velocity aiding case. Although the angular velocity component is a valuable contribution in general, the accuracy improvements obtained by using solely the linear velocity aiding suggest that, for some operating scenarios, merging the velocity information of the vehicle model brings about good accuracy results, at a very small computational cost.

Note that the execution times presented in Table 3.8 were obtained in a Matlab 7.3 implementation, running on a Pentium 4 CPU 3 Ghz with a Linux operating system, and were presented for the purpose of comparing the diverse navigation systems. The computational efficiency of the implemented EKF algorithm, that is common to all of the analyzed architectures, is beyond the scope of the present work. The filter implementation can be further improved by adopting numerically efficient and/or suboptimal formulations described in [22, 56] and references therein.

### 3.5.2 Vario X-Treme helicopter

The simple dynamic model of the fully actuated 6-DOF rigid body was adopted to illustrate and validate the proposed aiding technique. In this section, simulation results are presented for the Vario X-Treme helicopter, depicted in Fig. 3.9. This autonomous helicopter features a six degrees of freedom rigid body dynamic model driven by external



Figure 3.9: Vario X-Treme model-scale helicopter.

Table 3.9: Velocity estimation error (Vario X-Treme helicopter).

<b>Aiding information</b>	<b>RMS error</b>		
	$v_x$ (m/s)	$v_y$ (m/s)	$v_z$ (m/s)
GPS	0.13	0.26	0.20
Vario X-Treme Model	$2.65 \times 10^{-2}$	$9.62 \times 10^{-3}$	$3.75 \times 10^{-3}$

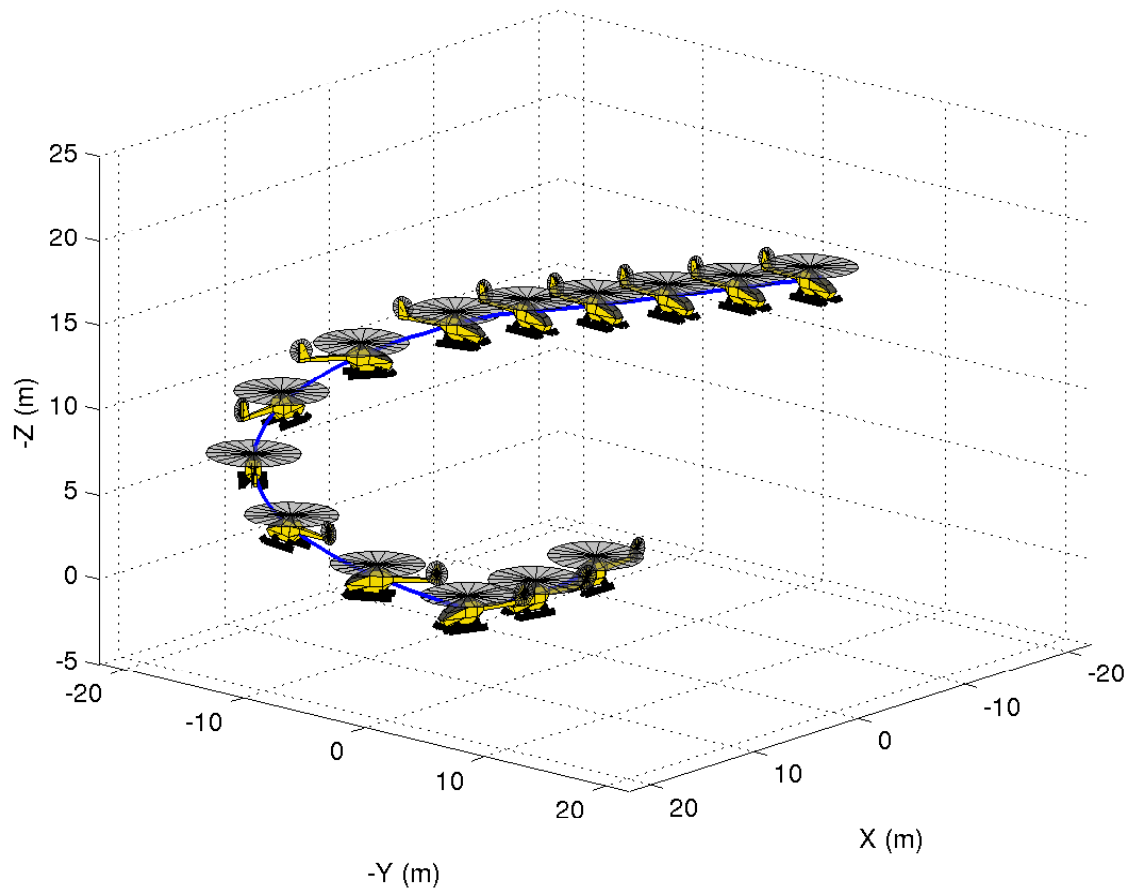
forces and moments that encompass the main rotor and tail rotor effects, including the first order blade pitching dynamics with Bell-Hiller mechanism and the steady-state blade flapping dynamics. The model dynamics, derived from first-principles in [39, 40], are summarized in Appendix C. The considered model, although simplified, is highly nonlinear and coupled, and is adopted to take a step towards the implementation of the embedded VD aiding technique in field applications.

The simulated takeoff trajectory, depicted in Fig. 3.10, consists of an ascending turn, followed by a straight upwards path. A 30% bias calibration error is assumed and a magnetometer is also incorporated in the navigation system.

Although the Vario X-Treme model is highly nonlinear, the combination of the embedded VD aiding with the linear extended Kalman filtering yields accurate velocity, position, and attitude estimates, as presented in Tables 3.9, 3.10, and 3.11 respectively. The helicopter model aiding enhances the INS estimates, as shown in the bias and velocity errors illustrated in Figs. 3.11 and 3.12, and in the position results of Fig. 3.13. Bias compensation errors are effectively reduced and velocity estimation is enhanced. The position results presented in Table 3.10 and depicted in Fig. 3.13 show that the VD aiding tech-

Table 3.10: Position estimation error (Vario X-Treme helicopter).

<b>Aiding information</b>	<b>RMS error</b>		
	$p_x$ (m)	$p_y$ (m)	$p_z$ (m)
GPS	1.15	1.46	1.55
Vario X-Treme Model	0.23	$5.71 \times 10^{-2}$	0.20



(a) 3D view

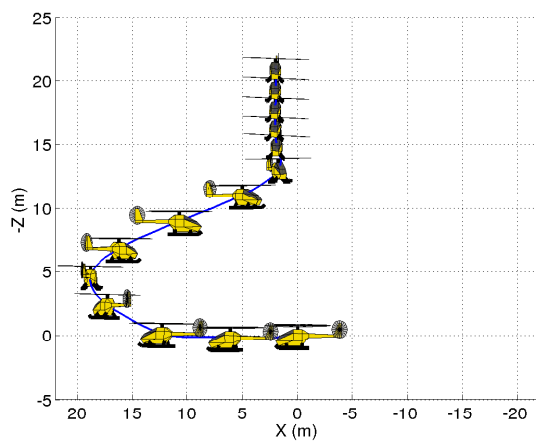
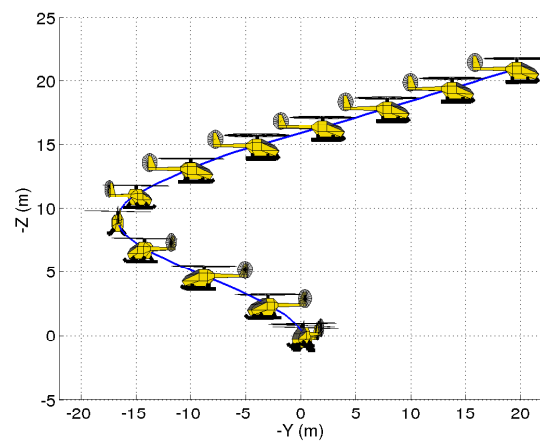
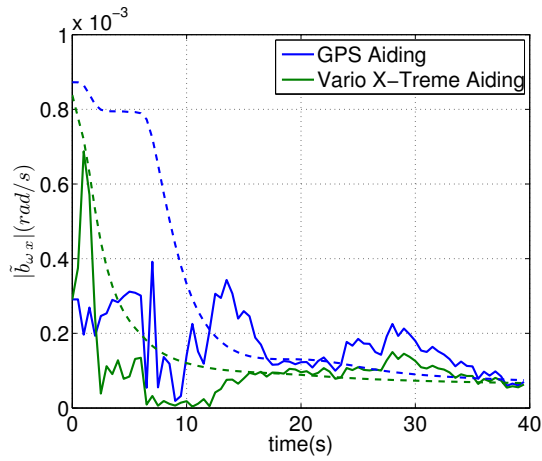
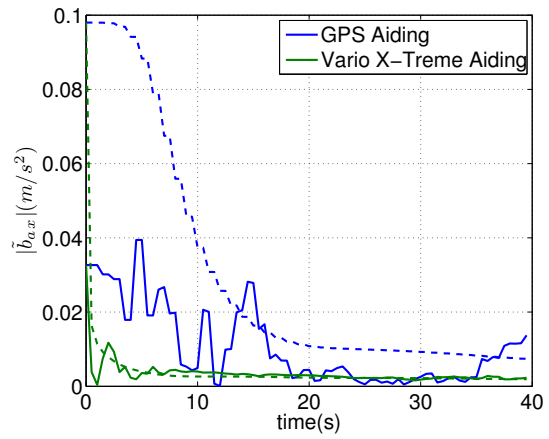
(b)  $xz$ -plane projection(c)  $yz$ -plane projection

Figure 3.10: Vario X-Treme simulated trajectory.

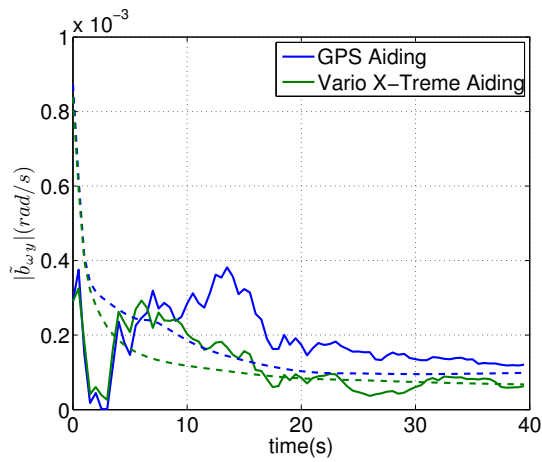




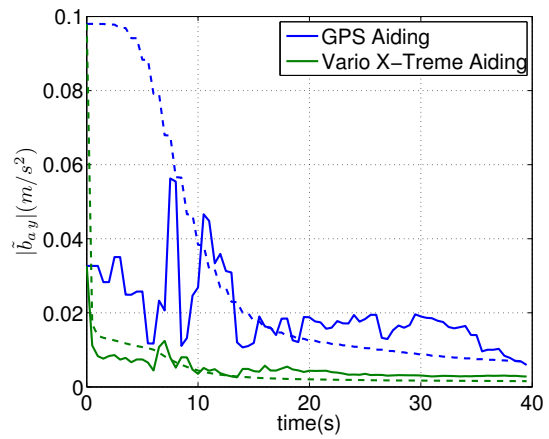
(a) Rate gyro bias ( $b_{\omega_x}$ ).



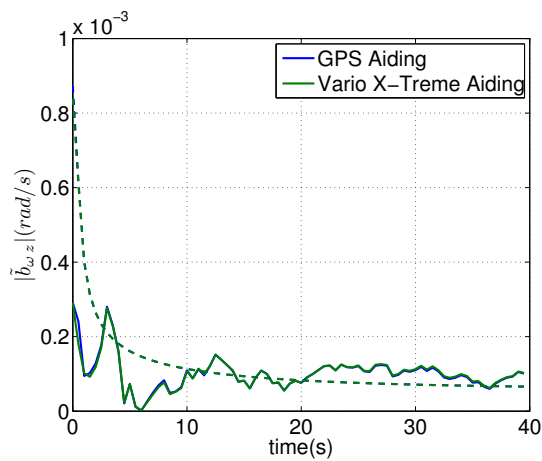
(b) Accelerometer bias ( $b_{a_x}$ ).



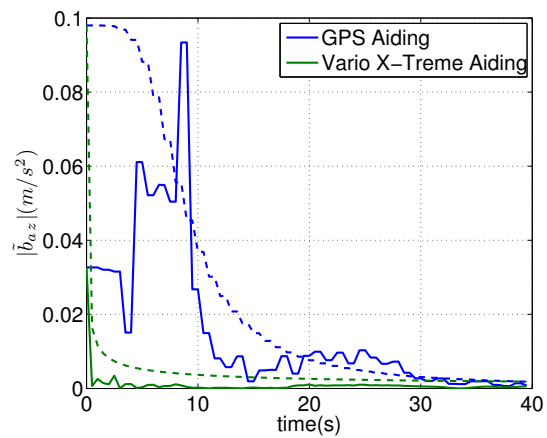
(c) Rate gyro bias ( $b_{\omega_y}$ ).



(d) Accelerometer bias ( $b_{a_y}$ ).



(e) Rate gyro bias ( $b_{\omega_z}$ ).



(f) Accelerometer bias ( $b_{a_z}$ ).

Figure 3.11: Vario X-Treme VD vs GPS aiding estimation errors (solid line) and estimated error standard deviation (dashed line).

Table 3.11: Attitude estimation error (Vario X-Treme helicopter).

Aiding information	RMS error		
	Yaw ( $^{\circ}$ )	Pitch ( $^{\circ}$ )	Roll ( $^{\circ}$ )
GPS	$1.26 \times 10^{-2}$	$9.15 \times 10^{-2}$	$7.95 \times 10^{-2}$
Vario X-Treme Model	$1.27 \times 10^{-2}$	$2.10 \times 10^{-2}$	$1.31 \times 10^{-2}$

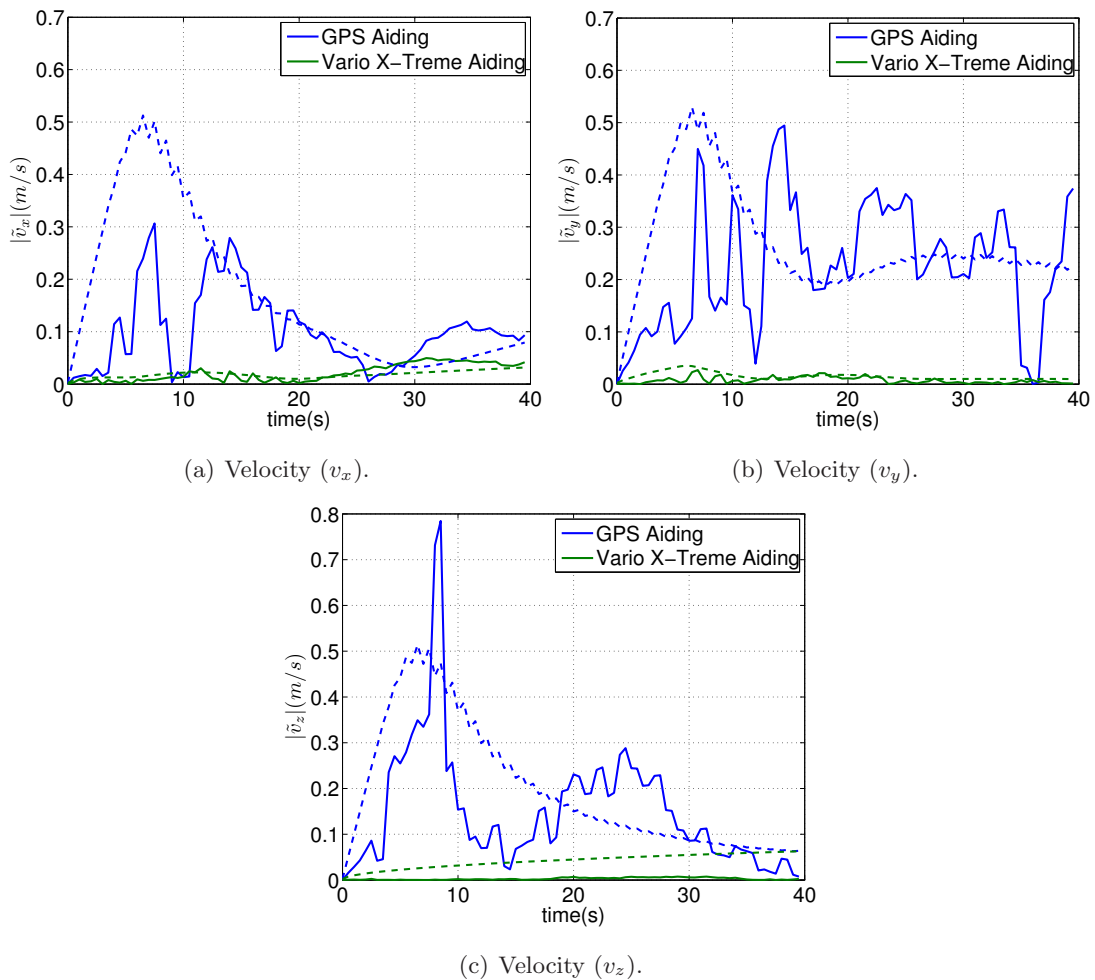


Figure 3.12: Vario X-Treme VD vs GPS aiding estimation errors (solid line) and estimated error standard deviation (dashed line).

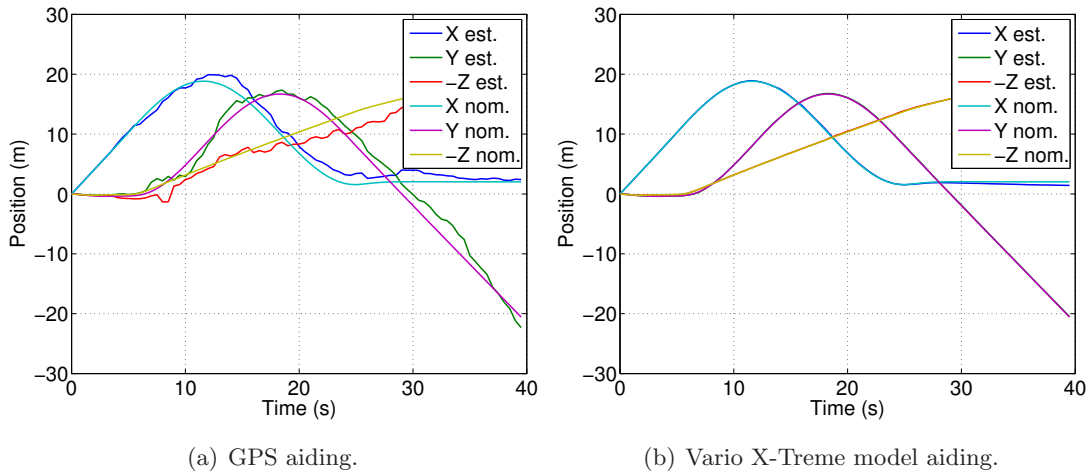


Figure 3.13: Trajectory estimation for the Vario X-Treme.

Table 3.12: Estimation error for the embedded VD aiding,  ${}^B\mathbf{v}$  observation only (Vario X-Treme helicopter).

	<b>RMS Error</b>		
Yaw, Pitch, Roll ( $^\circ$ )	$1.26 \times 10^{-2}$	$2.17 \times 10^{-2}$	$1.40 \times 10^{-2}$
$v_x, v_y, v_z$ (m/s)	$2.81 \times 10^{-2}$	$1.47 \times 10^{-2}$	$3.76 \times 10^{-3}$
$p_x, p_y, p_z$ (m)	0.50	0.25	0.19

nique effectively enhances the trajectory estimation to a submetric accuracy. The filter estimated error covariance is, in general, consistent with the estimation errors.

Interestingly enough, the estimation errors using only the linear velocity information of the helicopter model, shown in Table 3.12, are close to the results using the full information of the helicopter dynamics. This suggests that the linear velocity information of the vehicle model can be exploited in aerial applications, requiring only the computational resources necessary to process a state observation.

As discussed in [70, 82], the VD aiding results must be addressed with care. Vehicle modeling errors, model simplification assumptions or unmodeled time-varying parameters and disturbances, such as vehicle load and wind gusts, may severely affect the navigation system performance if not correctly accounted for in the filter. The tuning of the noise covariance matrices, the estimation of additional states and parameters and the use of more accurate vehicle model dynamics, among other techniques [70], are adopted to allow for the use of VD in real navigation systems. Nonetheless, side effects such as the poor observability of the augmented states, the over-parameterization of the vehicle model or even the inability to obtain a vehicle model which yields information on the real vehicle dynamics may occur.

Encouraging experimental results with the HUGIN 4500 underwater vehicle have been recently reported in [64]. Also, exploiting simple vehicle motion constraints yields no-

ticeable accuracy improvements in the experimental results presented in [42] for a land vehicle. Vehicle model aiding is also suitable for indoor missions where the vehicle model are known, and aiding information may be limited. The practical results evidence that either full, or simplified, vehicle models can effectively enhance the estimation results of GPS/INS architectures. The integration of the vehicle dynamics in the navigation system is a valuable aiding technique, for applications where other external sensors are not available or provide poor observability of the vehicle states.

### 3.5.3 LASER aiding

The LASER range sensor implementation is analyzed for a landing operation of an air vehicle equipped with a standard GPS/INS unit. The vehicle hovers the landing zone, as illustrated in Fig. 3.4, and activates the LASER at  $t = 20$  s to acquire an accurate distance-to-ground estimate. The terrain height is  $h_S = 4$  m, the LASER is oriented along the  $z$  axis of the body frame, that is  ${}^B_M \mathbf{R} = \mathbf{I}$ , and the sensor noise is characterized in Table 3.2.

The estimation results depicted in Fig. 3.14 show that the LASER sensor brings about accurate position and velocity estimates on the  $z$ -axis, whereas using solely the GPS sensor yields high uncertainty on the position estimate, which may render landing unfeasible. The velocity and distance-to-ground estimation errors, illustrated in Figs. 3.14(b) and 3.14(d) respectively, are reduced almost instantly when the LASER is activated. Assuming that the initial terrain height  $h_S$  uncertainty is 0.1 m, as depicted in Fig. 3.14(c), the position estimate is also enhanced, as shown in 3.14(a). If the uncertainty about the terrain height is larger, then the position estimate error will converge slower to smaller values, as illustrated in Fig. 3.15 for an initial  $h_S$  uncertainty of 1 m.

This behavior is justified by noting that  $p_z$  is related to  $h_S$  and  $h_V$  by (3.16), and that accurate LASER range measurements bring about precise  $h_V$  estimates. If little is known about  $h_S$ , then (3.16) implies that the uncertainty of  $h_S$  and of  $p_z$  are identical, and the filter can reduce the uncertainty on  $p_z$  only by using the model (3.15), that is a low frequency process, and hence  $\hat{h}_S$  and  $\hat{p}_z$  will converge slowly in time. This behavior is illustrated in Figs. 3.15(a) and 3.15(c). Conversely, if  $h_S$  is known accurately, then (3.16) implies that  $p_z$  can be inferred accurately, as shown in Figs. 3.14(a) and 3.14(c).

As expected, the velocity and distance-to-ground estimate enhancements are independent of the available terrain height information, as seen by comparing Figs. 3.14(b) and 3.14(d) with Figs. 3.15(b) and 3.15(d), respectively. These results show that the LASER range finder is critical for landing the robotic platform without risking the robotic platform, by allowing for accurate distance-to-ground and vehicle velocity estimates. Position and ground height estimation is also enhanced in the medium term, by combining LASER and GPS measurements.

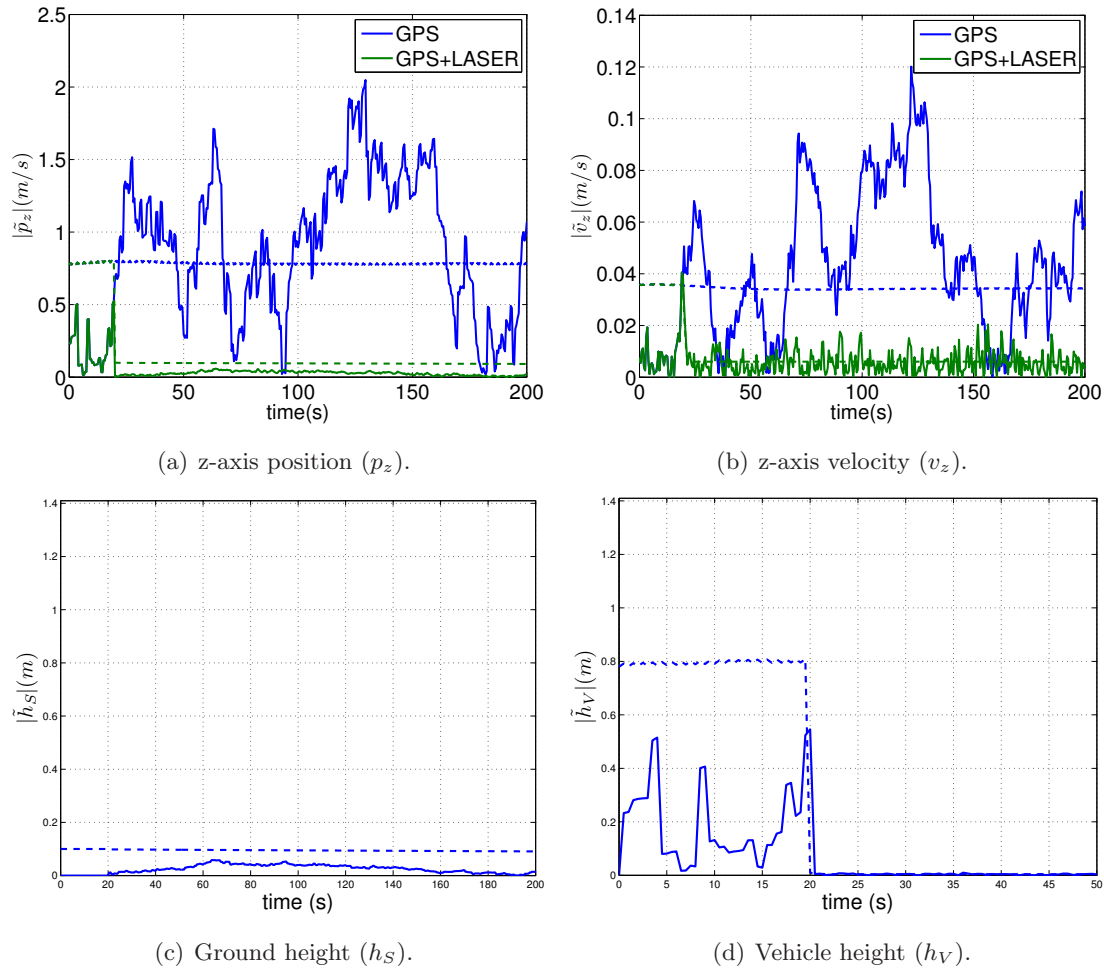


Figure 3.14: LASER aiding estimation errors (solid line) and estimated error standard deviation (dashed line).

### 3.6 Conclusions

A new embedded methodology to integrate the vehicle dynamics in the navigation system was proposed. The embedded VD system accuracy was shown to be equivalent to that of the classical external vehicle model architecture, but with smaller computational cost and with a flexible choice of vehicle model differential equations. The application of the proposed technique to a highly nonlinear Vario X-Treme helicopter model validated the approach for realistic Uninhabited Air Vehicles.

Trimming trajectory simulation results showed that the bias calibration errors were quickly compensated and that long-term bias estimates were enhanced. The linear and angular velocity were improved with respect to the classical GPS/INS configuration. Position and attitude errors, although not directly observable by the VD model, were improved due to the enhancements in velocity estimation.

The proposed methodology allows for the decoupling of the vehicle model differential equations. In particular, the linear velocity information of the VD model was exploited

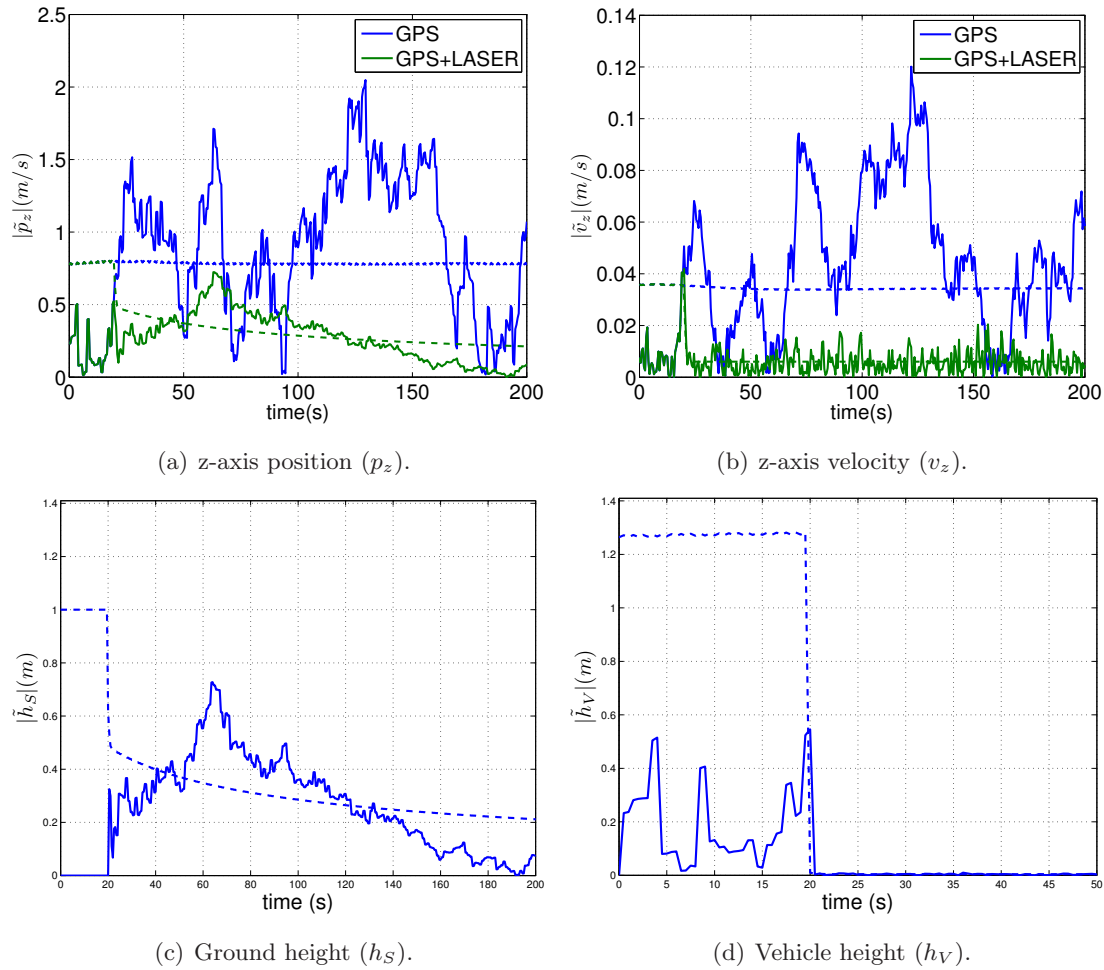


Figure 3.15: LASER aiding estimation errors (solid line) and estimated error standard deviation (dashed line).

directly in the filter in the form of a measurement residual, and the associated computational cost was only that of computing the measurement matrix and the Kalman gain. Given the exciting accuracy enhancements obtained using solely the linear velocity model, and the small computational cost of the implementation, this aiding information steps forward as an exciting, software based technique, suitable for most practical applications even with computational constraints.

Finally, the LASER range finder sensor provided high precision distance-to-ground estimates for takeoff and landing maneuvers. It was shown that integrating the sensor produced accurate vehicle height and the vertical velocity estimates, suitable for safe maneuvering of the autonomous vehicle. It was shown that the estimate of the vehicle position with respect to Earth frame is also improved, according to the uncertainty on the terrain height.

## Chapter 4

# Complementary Kalman filter based navigation system

This chapter develops a navigation system based on complementary filtering for position and attitude estimation, with application to autonomous surface crafts. The problem of accurate position and attitude estimation is addressed by exploiting sensor measurement information over distinct, yet complementary frequency regions. Using strapdown inertial measurements, vector observations, and GPS aiding, the derivation of the proposed complementary filters is focused on the stability, performance, and practical implementation of the filtering algorithms.

The complementary filter structure, shown in Fig. 4.1, consists of an attitude filter and a position filter. Formulated in discrete-time, the attitude filter entries are the rate gyro readings, and a snapshot attitude reconstruction based on vector observations, such as magnetic-field and pendular readings. The attitude of the vehicle is parameterized by Euler angles, due to its simplicity, and steady-state feedback gains are adopted in the filter design. The position filter resorts to accelerometers readings and to GPS, and estimates velocity in body frame and position in Earth frame.

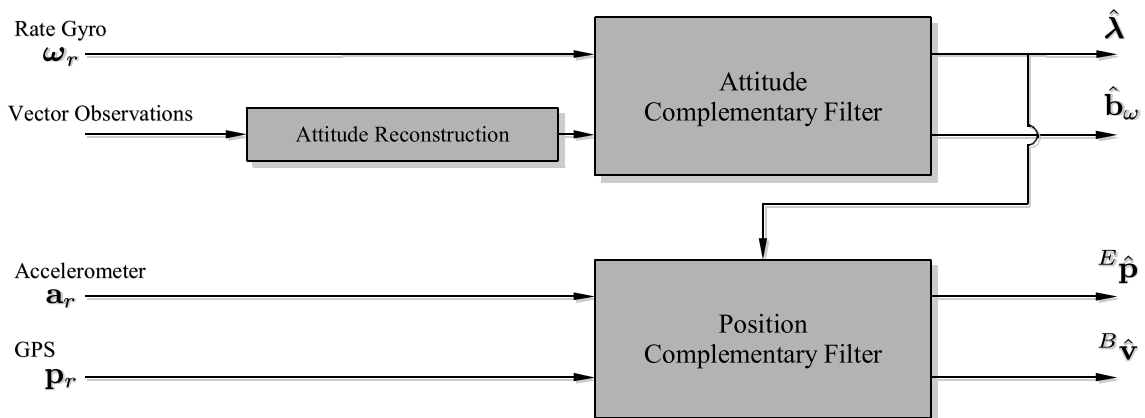


Figure 4.1: Complementary filter block diagram.

Stability and performance properties of the proposed filters are derived, and the region of attraction is explicitly characterized. The problem of diverse sensor sampling rates is accounted for using a multirate synthesis methodology, based on optimality results for periodic systems. An attitude determination algorithm that computes pitch and roll from the pendular measurements and yaw using the magnetic field observations, referred to as Magneto-Pendular Sensor (MPS), is also presented.

The small computational requirements of the proposed navigation system make it suitable for implementation on low-power hardware and using low-cost sensors, providing a simple yet effective multirate architecture. The implementation of the proposed architecture is straightforward and the performance results of the navigation system are demonstrated using experimental data obtained in tests at sea with the DELFIMx catamaran.

This chapter is organized as follows. Section 4.1 presents the complementary filters for attitude and position estimation. Stability properties are derived and the conditions that guarantee performance are discussed. Section 4.2 focuses on the implementation of the attitude and position filters, that are combined to produce a navigation system with the multirate architecture, and details the MPS algorithm. The navigation system performance is shown in the experimental results of Section 4.3, for the DELFIMx catamaran sea trials. Concluding remarks are pointed out in Section 4.4.

## 4.1 Attitude and position complementary filters

In this section, complementary filters for attitude and position estimation are proposed, and their stability and performance properties are derived. The design of the filters in the frequency domain is motivated by discussing the complementary characteristics of the inertial and aiding sensors in the frequency domain.

### 4.1.1 Attitude filter

Let  $\boldsymbol{\lambda} = [\psi \ \theta \ \phi]'$  denote the vector containing the yaw, pitch and roll angles, respectively, of the Z-Y-X Euler angles convention [34], also known in the literature as Cardan, Bryant or Tait-Bryant angles [104]. Without loss of generality, the considered Euler angles sequence rotates from Earth frame  $\{E\}$  to body frame  $\{B\}$  coordinates. The Euler angle kinematics are described by

$$\dot{\boldsymbol{\lambda}} = \mathbf{Q}(\boldsymbol{\lambda})\boldsymbol{\omega}, \quad \mathbf{Q}(\boldsymbol{\lambda}) = \begin{bmatrix} 0 & \sin \phi \sec \theta & \cos \phi \sec \theta \\ 0 & \cos \phi & -\sin \phi \\ 1 & \sin \phi \tan \theta & \cos \phi \tan \theta \end{bmatrix}. \quad (4.1)$$

The discrete-time equivalent of the system (4.1) considered in this work, is obtained by the Euler method [50] with the right-hand side subject to sample-and-hold, yielding

$$\boldsymbol{\lambda}_{k+1} = \boldsymbol{\lambda}_k + T\mathbf{Q}(\boldsymbol{\lambda}_k)\boldsymbol{\omega}_k. \quad (4.2)$$



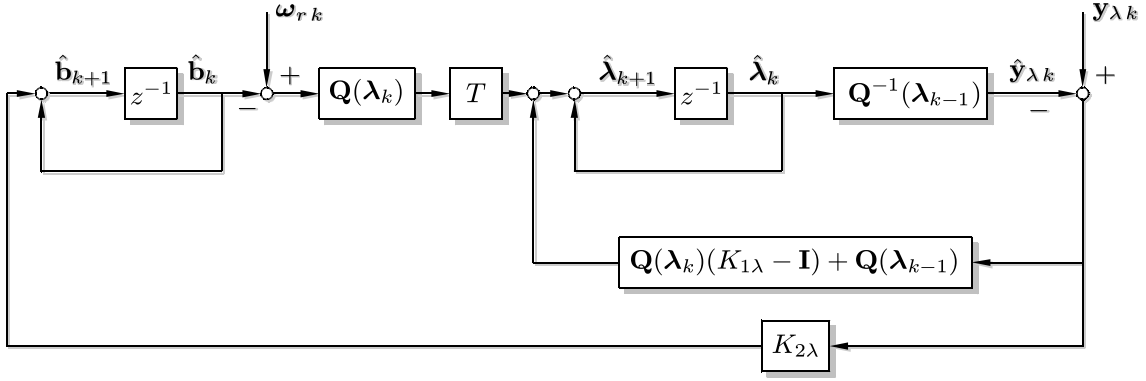


Figure 4.2: Attitude complementary filter.

where  $T$  is the sampling interval and the index  $k$  abbreviates the time instant  $t = kT$ . In this work, the attitude is estimated by exploiting the angular velocity and attitude measurements provided by strapdown sensors. The angular velocity is measured by a rate gyro affected by noise and random-walk bias [22],

$$\boldsymbol{\omega}_{rk} = \boldsymbol{\omega}_k + \mathbf{b}_{\omega k} + \mathbf{w}_{\omega rk}, \quad \mathbf{b}_{\omega k+1} = \mathbf{b}_{\omega k} + \mathbf{w}_{bk}, \quad (4.3)$$

where  $\mathbf{w}_{\omega r} \sim \mathcal{N}(\mathbf{0}, \Xi_{\omega})$  is zero-mean, Gaussian white noise and  $\mathbf{b}_{\omega}$  is the sensor bias driven by the Gaussian white noise  $\mathbf{w}_b \sim \mathcal{N}(\mathbf{0}, \Xi_b)$ .

The proposed attitude filter estimates the attitude of the vehicle expressed in Euler angles and compensates for the rate gyro bias. Rewriting the Euler angle kinematics (4.2-4.3) in state space form gives

$$\begin{bmatrix} \boldsymbol{\lambda}_{k+1} \\ \mathbf{b}_{k+1} \end{bmatrix} = \begin{bmatrix} \mathbf{I} & -T\mathbf{Q}(\boldsymbol{\lambda}_k) \\ \mathbf{0} & \mathbf{I} \end{bmatrix} \begin{bmatrix} \boldsymbol{\lambda}_k \\ \mathbf{b}_k \end{bmatrix} + \begin{bmatrix} T\mathbf{Q}(\boldsymbol{\lambda}_k) \\ \mathbf{0} \end{bmatrix} \boldsymbol{\omega}_{rk} + \begin{bmatrix} -T\mathbf{Q}(\boldsymbol{\lambda}_k) & \mathbf{0} \\ \mathbf{0} & \mathbf{I} \end{bmatrix} \begin{bmatrix} \mathbf{w}_{\omega rk} \\ \mathbf{w}_{bk} \end{bmatrix}. \quad (4.4)$$

Consider the following nonlinear feedback system as the proposed attitude filter

$$\begin{aligned} \begin{bmatrix} \hat{\boldsymbol{\lambda}}_{k+1} \\ \hat{\mathbf{b}}_{k+1} \end{bmatrix} &= \begin{bmatrix} \mathbf{I} & -T\mathbf{Q}(\boldsymbol{\lambda}_k) \\ \mathbf{0} & \mathbf{I} \end{bmatrix} \begin{bmatrix} \hat{\boldsymbol{\lambda}}_k \\ \hat{\mathbf{b}}_k \end{bmatrix} + \begin{bmatrix} T\mathbf{Q}(\boldsymbol{\lambda}_k) \\ \mathbf{0} \end{bmatrix} \boldsymbol{\omega}_{rk} \\ &+ \begin{bmatrix} \mathbf{Q}(\boldsymbol{\lambda}_k)(K_{1\lambda} - \mathbf{I}) + \mathbf{Q}(\boldsymbol{\lambda}_{k-1}) \\ K_{2\lambda} \end{bmatrix} (\mathbf{y}_{\lambda k} - \hat{\mathbf{y}}_{\lambda k}), \end{aligned} \quad (4.5a)$$

$$\hat{\mathbf{y}}_{\lambda k} = \mathbf{Q}^{-1}(\boldsymbol{\lambda}_{k-1})\hat{\boldsymbol{\lambda}}_k, \quad \mathbf{y}_{\lambda k} = \mathbf{Q}^{-1}(\boldsymbol{\lambda}_{k-1})\boldsymbol{\lambda}_k + \mathbf{v}_{\lambda k}, \quad (4.5b)$$

where  $\mathbf{y}_{\lambda k}$  is the vector of observed Euler angles transformed to the space of angular rate and corrupted by the Gaussian white observation noise  $\mathbf{v}_{\lambda} \sim \mathcal{N}(\mathbf{0}, \Theta_{\lambda})$ , and  $K_{1\lambda}, K_{2\lambda} \in \mathbf{M}(3, 3)$  are feedback gain matrices. The block diagram of the proposed attitude filter is depicted in Fig. 4.2.

The attitude observation  $\mathbf{y}_{\lambda}$  can be obtained from two vectors measured in body frame, such as the Earth's gravitic and magnetic fields, or from observations provided by other devices like cameras or star trackers. As an example, pitch and roll angles can be determined

from Earth's gravitational field, available from two on-board inclinometers (pendula), and the yaw angle can be computed from the Earth's magnetic field measurements provided by a magnetometer triad. The choice of attitude observation depends on the available sensors and computational resources, and hence the attitude observation adopted in this work is detailed later in the navigation system implementation section.

Consider the following auxiliary linear time invariant system

$$\begin{bmatrix} \mathbf{x}_{\lambda k+1} \\ \mathbf{x}_{b k+1} \end{bmatrix} = \begin{bmatrix} \mathbf{I} & -T\mathbf{I} \\ \mathbf{0} & \mathbf{I} \end{bmatrix} \begin{bmatrix} \mathbf{x}_{\lambda k} \\ \mathbf{x}_{b k} \end{bmatrix} + \begin{bmatrix} -T\mathbf{I} & \mathbf{0} \\ \mathbf{0} & \mathbf{I} \end{bmatrix} \begin{bmatrix} \mathbf{w}_{\omega_r k} \\ \mathbf{w}_{b k} \end{bmatrix}, \quad (4.6a)$$

$$\mathbf{y}_{x k} = \begin{bmatrix} \mathbf{I} & \mathbf{0} \end{bmatrix} \begin{bmatrix} \mathbf{x}_{\lambda k} \\ \mathbf{x}_{b k} \end{bmatrix} + \mathbf{v}_{\lambda k}, \quad (4.6b)$$

which will be used in the sequel as the frequency domain design setup for the time varying attitude filter (4.5). In the proposed design technique, the feedback gains  $K_{1\lambda}$  and  $K_{2\lambda}$  in (4.5) are identified with the steady-state Kalman gains for the system (4.6), where the covariance matrices  $\Xi_{\omega}$ ,  $\Xi_b$  and  $\Theta_{\lambda}$  act as "tuning knobs" to shape the desired frequency response of the attitude filter.

The time-invariant system (4.6) adopted for the determination of the feedback gains and associated frequency response is similar to the attitude kinematics (4.4) for  $\mathbf{Q}(\boldsymbol{\lambda}) = \mathbf{Q}(\mathbf{0})$ . Although this suggests at first glance that the properties of the proposed filter could be limited to the specific case of  $\boldsymbol{\lambda}_k = \mathbf{0}$ , the filter is in fact asymptotically stable for any attitude trajectory parameterized by nonsingular Euler angle configurations. The stability properties are derived in the following theorem for the specific case of Z-Y-X Euler angles, however the extension of the results to other Euler angle set conventions [34] is immediate.

**Theorem 4.1.** *Consider the discrete-time attitude kinematics (4.4). Let  $K_{1\lambda}$  and  $K_{2\lambda}$  be the steady-state Kalman gains for the system (4.6) and assume that the pitch described by the platform is bounded,  $|\theta| \leq \theta_{max} < \frac{\pi}{2}$ . Then the attitude complementary filter (4.5) is uniformly asymptotically stable (UAS).*

*Proof.* Let  $\tilde{\boldsymbol{\lambda}}_k = \boldsymbol{\lambda}_k - \hat{\boldsymbol{\lambda}}_k$ ,  $\tilde{\mathbf{b}}_{\omega k} = \mathbf{b}_{\omega k} - \hat{\mathbf{b}}_{\omega k}$  denote the estimation errors. The associated estimation error dynamics are given by

$$\begin{bmatrix} \tilde{\boldsymbol{\lambda}}_{k+1} \\ \tilde{\mathbf{b}}_{k+1} \end{bmatrix} = \begin{bmatrix} \mathbf{Q}(\boldsymbol{\lambda}_k)(\mathbf{I} - K_{1\lambda})\mathbf{Q}^{-1}(\boldsymbol{\lambda}_{k-1}) & -T\mathbf{Q}(\boldsymbol{\lambda}_k) \\ -K_{2\lambda}\mathbf{Q}^{-1}(\boldsymbol{\lambda}_{k-1}) & \mathbf{I} \end{bmatrix} \begin{bmatrix} \tilde{\boldsymbol{\lambda}}_k \\ \tilde{\mathbf{b}}_k \end{bmatrix} + \begin{bmatrix} -T\mathbf{Q}(\boldsymbol{\lambda}_k) & \mathbf{0} \\ \mathbf{0} & \mathbf{I} \end{bmatrix} \begin{bmatrix} \mathbf{w}_{\omega_r k} \\ \mathbf{w}_{b k} \end{bmatrix} + \begin{bmatrix} \mathbf{Q}(\boldsymbol{\lambda}_k)(\mathbf{I} - K_{1\lambda}) - \mathbf{Q}(\boldsymbol{\lambda}_{k-1}) \\ -K_{2\lambda} \end{bmatrix} \mathbf{v}_{\lambda k}. \quad (4.7)$$

By definition, the filter is said to be UAS if the origin of the system (4.7) is UAS in the absence of state and measurement noises [69]. However, the state and measurement noises are denoted in the proof for the sake of convenience. The system (4.6) can be written in the compact state space formulation

$$\mathbf{x}_{k+1} = \mathbf{F}\mathbf{x}_k + \mathbf{G}\mathbf{w}_k, \quad \mathbf{y}_k = \mathbf{H}\mathbf{x}_k + \mathbf{v}_k,$$

where  $\mathbf{x}_k = [\mathbf{x}'_{\lambda k} \ \mathbf{x}'_{b k}]'$ ,  $\mathbf{w}_k = [\mathbf{w}'_{\omega_r k} \ \mathbf{w}'_{b k}]'$ ,  $\mathbf{y}_k = \mathbf{y}_{x k}$ ,  $\mathbf{v}_k = \mathbf{v}_{\lambda k}$ ,  $\mathbf{F} = \begin{bmatrix} \mathbf{I} & -T\mathbf{I} \\ \mathbf{0} & \mathbf{I} \end{bmatrix}$ ,  $\mathbf{G} = \begin{bmatrix} -T\mathbf{I} & \mathbf{0} \\ \mathbf{0} & \mathbf{I} \end{bmatrix}$ , and  $\mathbf{H} = \begin{bmatrix} \mathbf{I} & \mathbf{0} \end{bmatrix}$ . It is straightforward to show that  $[\mathbf{F}, \mathbf{H}']$  is detectable and  $[\mathbf{F}, \mathbf{G}]$  is completely stabilizable, hence the closed-loop system

$$\tilde{\mathbf{x}}_{k+1} = (\mathbf{F} - \mathbf{K}\mathbf{H})\tilde{\mathbf{x}}_k + \mathbf{G}\mathbf{w}_k - \mathbf{K}\mathbf{v}_k, \quad (4.8)$$

where  $\mathbf{K} = [K'_{1\lambda} \ K'_{2\lambda}]'$ , is UAS [4]. Define the Lyapunov transformation of variables

$$\begin{bmatrix} \tilde{\lambda}_{x k} \\ \tilde{\mathbf{b}}_{x k} \end{bmatrix} = \mathbf{T}_k \begin{bmatrix} \tilde{\mathbf{x}}_{\lambda k} \\ \tilde{\mathbf{x}}_{b k} \end{bmatrix}, \quad \mathbf{T}_k = \begin{bmatrix} \mathbf{Q}(\lambda_{k-1}) & \mathbf{0} \\ \mathbf{0} & \mathbf{I} \end{bmatrix}, \quad (4.9)$$

that is well defined [122] because  $\theta$  is bounded by assumption. Applying the transformation of variables  $\mathbf{T}_k$  to (4.8) yields

$$\begin{aligned} \begin{bmatrix} \tilde{\lambda}_{x k+1} \\ \tilde{\mathbf{b}}_{x k+1} \end{bmatrix} &= \mathbf{T}_{k+1}(\mathbf{F} - \mathbf{K}\mathbf{H})\mathbf{T}_k^{-1} \begin{bmatrix} \tilde{\lambda}_{x k} \\ \tilde{\mathbf{b}}_{x k} \end{bmatrix} + \mathbf{T}_{k+1}\mathbf{G}\mathbf{w}_k - \mathbf{T}_{k+1}\mathbf{K}\mathbf{v}_k \\ &= \begin{bmatrix} \mathbf{Q}(\lambda_k)(\mathbf{I} - K_{1\lambda})\mathbf{Q}^{-1}(\lambda_{k-1}) & -T\mathbf{Q}(\lambda_k) \\ -K_{2\lambda}\mathbf{Q}^{-1}(\lambda_{k-1}) & \mathbf{I} \end{bmatrix} \begin{bmatrix} \tilde{\lambda}_{x k} \\ \tilde{\mathbf{b}}_{x k} \end{bmatrix} \\ &\quad + \begin{bmatrix} -T\mathbf{Q}(\lambda_k)\mathbf{w}_{\omega_r k} \\ \mathbf{w}_{b k} \end{bmatrix} - \begin{bmatrix} \mathbf{Q}(\lambda_k)K_{1\lambda} \\ K_{2\lambda} \end{bmatrix} \mathbf{v}_{\lambda k}. \end{aligned} \quad (4.10)$$

The origin of (4.8) is UAS and, by the properties of Lyapunov transformations, the origin of (4.10) is UAS. Hence, the origin of (4.7) is uniform asymptotic stability, as desired.  $\square$

The stability properties derived in Theorem 4.1 are valid for nonsingular configurations, where the pitch satisfies  $\theta < \frac{\pi}{2}$ . This is a weak condition for most terrestrial and oceanic applications, namely those based on autonomous surface crafts, that are studied in this chapter to illustrate the proposed navigation system.

The stability results can be extended for time-varying Kalman gains, however the proposed complementary filter is designed in the frequency domain by means of the time-invariant formulation (4.6), to obtain a desired transfer function that merges the low-frequency contents of the attitude observations with the high-frequency information from the angular rate readings. Steady-state Kalman filter gains are adopted to yield an asymptotically stable filter that can be easily implemented and tested in low-cost hardware.

Interestingly enough, under operating conditions found in some terrestrial and oceanic applications, the gains adopted in the proposed filter (4.5) are identified with the steady-state gains of the Kalman filter for the system (4.4). This implies that, for ASC trimming maneuvers found in surveillance operations, the performance of the proposed attitude filter is identical to that of a Kalman filter designed for the time-varying system (4.4).

**Theorem 4.2.** *Let the state and observation disturbances in the attitude kinematics (4.4) be characterized by the Gaussian white noises  $\mathbf{w}_{\omega_r} \sim \mathcal{N}(\mathbf{0}, \Xi_{\omega})$ ,  $\mathbf{w}_b \sim \mathcal{N}(\mathbf{0}, \Xi_b)$  and  $\mathbf{v}_{\lambda} \sim \mathcal{N}(\mathbf{0}, \Theta_{\lambda})$ , respectively, and assume that the pitch and roll angles are constant. Then the*

complementary attitude filter (4.5) is the “steady-state” Kalman filter for the system (4.4) in the sense that the Kalman feedback gain  $K_{optk}$  converges asymptotically as follows

$$\lim_{k \rightarrow \infty} \left\| K_{optk} - \begin{bmatrix} \mathbf{Q}(\boldsymbol{\lambda}_k)(K_{1\lambda} - \mathbf{I}) + \mathbf{Q}(\boldsymbol{\lambda}_{k-1}) \\ K_{2\lambda} \end{bmatrix} \right\| = 0. \quad (4.11)$$

*Proof.* The estimation error covariance matrix of the Kalman filter for the system (4.6) satisfies

$$\mathbf{P}_{x\lambda k+1|k} = \mathbf{F}\mathbf{P}_{x\lambda k|k-1}\mathbf{F}' + \mathbf{G}\boldsymbol{\Xi}\mathbf{G}' - \mathbf{F}\mathbf{P}_{x\lambda k|k-1}\mathbf{H}'\mathbf{S}_{P\lambda k}^{-1}\mathbf{H}\mathbf{P}_{x\lambda k|k-1}\mathbf{F}', \quad (4.12)$$

where  $\mathbf{S}_{P\lambda k} = \mathbf{H}\mathbf{P}_{x\lambda k|k-1}\mathbf{H}' + \Theta_\lambda$ ,  $\boldsymbol{\Xi} = \begin{bmatrix} \boldsymbol{\Xi}_\omega & \mathbf{0} \\ \mathbf{0} & \boldsymbol{\Xi}_b \end{bmatrix}$ , see references [4, 69] for a derivation of (4.12). Given the transformation of variables (4.9), the covariance matrix  $\boldsymbol{\Sigma}_{x\lambda k+1|k} = E\left(\begin{bmatrix} \tilde{\boldsymbol{\lambda}}_{x k+1} \\ \tilde{\mathbf{b}}_{x k+1} \end{bmatrix} \begin{bmatrix} \tilde{\boldsymbol{\lambda}}'_{x k+1} & \tilde{\mathbf{b}}'_{x k+1} \end{bmatrix}\right)$  is given by  $\boldsymbol{\Sigma}_{x\lambda k+1|k} = \mathbf{T}_{k+1}\mathbf{P}_{x\lambda k+1|k}\mathbf{T}'_{k+1}$  and, using (4.12), satisfies

$$\begin{aligned} \mathbf{T}_{k+1}^{-1}\boldsymbol{\Sigma}_{x\lambda k+1|k}\mathbf{T}'_{k+1} &= \mathbf{F}\mathbf{T}_k^{-1}\boldsymbol{\Sigma}_{x\lambda k|k-1}\mathbf{T}'_k\mathbf{F}' + \mathbf{G}\boldsymbol{\Xi}\mathbf{G}' \\ &\quad - \mathbf{F}\mathbf{T}_k^{-1}\boldsymbol{\Sigma}_{x\lambda k|k-1}\mathbf{T}'_k\mathbf{H}'\mathbf{S}_{P\lambda k}^{-1}\mathbf{H}\mathbf{T}_k^{-1}\boldsymbol{\Sigma}_{x\lambda k|k-1}\mathbf{T}'_k\mathbf{F}' \\ &\quad \Downarrow \\ \boldsymbol{\Sigma}_{x\lambda k+1|k} &= \mathbf{T}_{k+1}\mathbf{F}\mathbf{T}_k^{-1}\boldsymbol{\Sigma}_{x\lambda k|k-1}\mathbf{T}'_k\mathbf{F}'\mathbf{T}'_{k+1} + \mathbf{T}_{k+1}\mathbf{G}\boldsymbol{\Xi}\mathbf{G}'\mathbf{T}'_{k+1} \\ &\quad - \mathbf{T}_{k+1}\mathbf{F}\mathbf{T}_k^{-1}\boldsymbol{\Sigma}_{x\lambda k|k-1}\mathbf{T}'_k\mathbf{H}'\mathbf{S}_{\Sigma\lambda k}^{-1}\mathbf{H}\mathbf{T}_k^{-1}\boldsymbol{\Sigma}_{x\lambda k|k-1}\mathbf{T}'_k\mathbf{F}'\mathbf{T}'_{k+1}, \end{aligned}$$

where  $\mathbf{S}_{\Sigma\lambda k} = \mathbf{H}\mathbf{T}_k^{-1}\boldsymbol{\Sigma}_{x\lambda k|k-1}\mathbf{T}'_k\mathbf{H}' + \Theta_\lambda$ .

With a slight abuse of notation, let  $K_{1\lambda k}$  and  $K_{2\lambda k}$  denote the time-varying Kalman gains for the system (4.6) and formulate the attitude filter (4.5) with time-varying gains

$$\begin{aligned} \begin{bmatrix} \hat{\boldsymbol{\lambda}}_{k+1} \\ \hat{\mathbf{b}}_{k+1} \end{bmatrix} &= \begin{bmatrix} \mathbf{I} & -T\mathbf{Q}(\boldsymbol{\lambda}_k) \\ \mathbf{0} & \mathbf{I} \end{bmatrix} \begin{bmatrix} \hat{\boldsymbol{\lambda}}_k \\ \hat{\mathbf{b}}_k \end{bmatrix} + \begin{bmatrix} T\mathbf{Q}(\boldsymbol{\lambda}_k) \\ \mathbf{0} \end{bmatrix} \boldsymbol{\omega}_{rk} \\ &\quad + \begin{bmatrix} \mathbf{Q}(\boldsymbol{\lambda}_k)(K_{1\lambda k} - \mathbf{I}) + \mathbf{Q}(\boldsymbol{\lambda}_{k-1}) \\ K_{2\lambda k} \end{bmatrix} (\mathbf{y}_{\lambda k} - \hat{\mathbf{y}}_{\lambda k}). \end{aligned} \quad (4.13)$$

To identify the attitude filter (4.5) as the steady-state Kalman filter for the system (4.4), it is shown that the attitude filter (4.13) is the Kalman filter for the system (4.4). This condition is satisfied if i)  $\boldsymbol{\Sigma}_{x\lambda k+1|k}$  is the error covariance of the attitude filter (4.13) and that ii)  $\boldsymbol{\Sigma}_{x\lambda k+1|k}$  is the error covariance of the optimal (i.e. Kalman) filter for the attitude kinematics (4.4), for a discussion on the optimality of the Kalman filter and uniqueness of the optimal gains, the reader is referred to [4, 69].

The condition of constant pitch and roll implies that  $\mathbf{Q}(\boldsymbol{\lambda}_{k+1}) = \mathbf{Q}(\boldsymbol{\lambda}_k)$ , hence the kinematics (4.7) and (4.10) are identical,  $[\tilde{\boldsymbol{\lambda}}'_{x k} \quad \tilde{\mathbf{b}}'_{x k}]' = [\tilde{\boldsymbol{\lambda}}'_k \quad \tilde{\mathbf{b}}'_k]'$  and  $\boldsymbol{\Sigma}_{x\lambda k+1|k}$  is the error covariance matrix of the attitude filter (4.13).

The matrix  $\boldsymbol{\Sigma}_{x\lambda k+1|k}$  is the covariance error of the Kalman filter for the system

$$\mathbf{z}_{k+1} = \mathbf{T}_{k+1}\mathbf{F}\mathbf{T}_k^{-1}\mathbf{z}_k + \mathbf{T}_{k+1}\mathbf{G}\mathbf{w}_{zk}, \quad (4.14a)$$

$$\mathbf{y}_{zk} = \mathbf{H}\mathbf{T}_k^{-1}\mathbf{z}_k + \mathbf{v}_{zk}, \quad (4.14b)$$

where  $\mathbf{z}_k \in \mathbb{R}^6$ ,  $\mathbf{w}_z \sim \mathcal{N}(\mathbf{0}, \Xi)$ ,  $\mathbf{v}_z \sim \mathcal{N}(\mathbf{0}, \Theta_\lambda)$ . Using  $\mathbf{Q}(\lambda_{k+1}) = \mathbf{Q}(\lambda_k)$ , the matrices of the system (4.14) are given by

$$\begin{aligned} \mathbf{T}_{k+1} \mathbf{F} \mathbf{T}_k^{-1} &= \begin{bmatrix} \mathbf{I} & -T\mathbf{Q}(\lambda_k) \\ \mathbf{0} & \mathbf{I} \end{bmatrix}, \quad \mathbf{T}_{k+1} \mathbf{G} = \begin{bmatrix} -T\mathbf{Q}(\lambda_k) & \mathbf{0} \\ \mathbf{0} & \mathbf{I} \end{bmatrix}, \\ \mathbf{H} \mathbf{T}_k^{-1} &= \begin{bmatrix} \mathbf{Q}^{-1}(\lambda_{k-1}) & \mathbf{0} \end{bmatrix}, \end{aligned}$$

which are identical to the state matrices of the attitude kinematics (4.4) with attitude observation given by (4.5b). Consequently, the attitude filter (4.13) produces the optimal estimation error covariance matrix  $\Sigma_{x\lambda_{k+1}|k}$  for the system (4.4) and, by uniqueness, the attitude filter (4.13) is a Kalman filter. Using  $K_{1\lambda k} \rightarrow K_{1\lambda}$  and  $K_{2\lambda k} \rightarrow K_{2\lambda}$  as  $k \rightarrow \infty$  yields (4.11), that completes the proof.  $\square$

The performance results presented in Theorem 4.2 hold for applications where the pitch and roll angles are constant or can be considered approximately constant. It should be emphasized that it is of interest for terrestrial and oceanic platforms considered in this work, subject to repetitive monitoring trajectories. For the case of time-varying pitch and roll angles, and for aggressive maneuvers, the performance of the complementary and of the Kalman filters can be compared offline by computing the estimation error covariances of the filters, as detailed in Appendix D. Later in this work, the performance of the complementary filter is analyzed for the experimental data obtained on-board the DELFIMx catamaran.

Although performance results for the complementary filter are presented in Theorem 4.2, the design of the feedback gains is performed in the frequency domain due to the characteristics of the attitude aiding sensor at hand, and to unmodeled sensor disturbances often found in experimental setups. This approach exploits the low-frequency region where the attitude observations are typically more accurate, and the high-frequency region where the integration of the rate gyro yields better attitude measurements.

#### 4.1.2 Position filter

The continuous-time position kinematics are given by

$$\dot{\mathbf{p}} = \mathbf{v}, \quad \dot{\mathbf{v}} = \mathcal{R}^B \mathbf{a},$$

where  $\mathbf{p}$  and  $\mathbf{v}$  are the position and velocity in Earth frame coordinates,  $\mathcal{R}$  is the shorthand notation for the rotation matrix from body frame  $\{B\}$  to Earth frame  $\{E\}$  coordinates, and  ${}^B \mathbf{a}$  is the acceleration in body frame coordinates. The discrete-time equivalent is obtained by sample-and-hold of the inputs [50] and is given by

$$\mathbf{p}_{k+1} = \mathbf{p}_k + T\mathbf{v}_k + \frac{T^2}{2} \mathcal{R}_k \mathbf{a}_k, \quad \mathbf{v}_{k+1} = \mathbf{v}_k + T\mathcal{R}_k^B \mathbf{a}_k. \quad (4.15)$$

The accelerometer measures the specific force, which is the difference between the inertial and the gravitic accelerations of the rigid body [20],  ${}^B \mathbf{a}_k$  and  ${}^B \mathbf{g}_k$  respectively, expressed

in body frame coordinates,

$$\mathbf{a}_{r k} = {}^B \mathbf{a}_k - {}^B \mathbf{g}_k + \mathbf{w}_{a_r},$$

where  $\mathbf{w}_{a_r} \sim \mathcal{N}(\mathbf{0}, \Xi_a)$  is zero-mean, Gaussian white noise. The position kinematics (4.15) using the accelerometer measurements are described by

$$\begin{aligned} \begin{bmatrix} \mathbf{p}_{k+1} \\ {}^B \mathbf{v}_{k+1} \end{bmatrix} &= \begin{bmatrix} \mathbf{I} & T\mathcal{R}_k \\ \mathbf{0} & \mathcal{R}'_{k+1}\mathcal{R}_k \end{bmatrix} \begin{bmatrix} \mathbf{p}_k \\ {}^B \mathbf{v}_k \end{bmatrix} + \begin{bmatrix} \frac{T^2}{2}\mathcal{R}_k \\ T\mathcal{R}'_{k+1}\mathcal{R}_k \end{bmatrix} (\mathbf{a}_r + \mathcal{R}'_k {}^E \mathbf{g}) \\ &+ \begin{bmatrix} \mathbf{I} & -\frac{T^2}{2}\mathcal{R}_k \\ \mathbf{0} & -T\mathcal{R}'_{k+1}\mathcal{R}_k \end{bmatrix} \begin{bmatrix} \mathbf{w}_{p k} \\ \mathbf{w}_{a_r k} \end{bmatrix}, \end{aligned} \quad (4.16)$$

where  ${}^B \mathbf{v}_k = \mathcal{R}'_k \mathbf{v}_{k+1}$  is the velocity expressed in body coordinates,  ${}^E \mathbf{g}$  is the gravitic acceleration expressed in Earth coordinates, and  $\mathbf{w}_p \sim \mathcal{N}(\mathbf{0}, \Xi_p)$  is zero-mean, Gaussian white noise that accounts for small disturbances in the position. The position observer kinematics, depicted in Fig. 4.3, are given by

$$\begin{aligned} \begin{bmatrix} \hat{\mathbf{p}}_{k+1} \\ {}^B \hat{\mathbf{v}}_{k+1} \end{bmatrix} &= \begin{bmatrix} \mathbf{I} & T\mathcal{R}_k \\ \mathbf{0} & \mathcal{R}'_{k+1}\mathcal{R}_k \end{bmatrix} \begin{bmatrix} \hat{\mathbf{p}}_k \\ {}^B \hat{\mathbf{v}}_k \end{bmatrix} + \begin{bmatrix} \frac{T^2}{2}\mathcal{R}_k \\ T\mathcal{R}'_{k+1}\mathcal{R}_k \end{bmatrix} (\mathbf{a}_r + \mathcal{R}'_k {}^E \mathbf{g}) \\ &+ \begin{bmatrix} K_{1p} \\ \mathcal{R}'_{k+1}K_{2p} \end{bmatrix} (\mathbf{y}_{p k} - \hat{\mathbf{y}}_{p k}), \end{aligned} \quad (4.17a)$$

$$\hat{\mathbf{y}}_{p k} = \hat{\mathbf{p}}_k, \quad \mathbf{y}_{p k} = \mathbf{p}_k + \mathbf{v}_{p k}, \quad (4.17b)$$

where  $\mathbf{y}_{p k}$  is the position computed using the readings of the GPS receiver, and  $\mathbf{v}_p \sim \mathcal{N}(\mathbf{0}, \Theta_p)$  is zero-mean, Gaussian observation noise. The propulsion force of a vehicle is, in general, physically oriented along a body fixed axis, producing a predominant body fixed direction of motion, e.g. when thrusters are mounted and act along the x-axis of the body, the main velocity variations are naturally expressed along that axis. Also, high angular rates due to aggressive maneuvering introduce high-frequency shifts in Earth frame velocity, while the velocity in the body frame remains aligned with the vehicle's predominant direction of motion, e.g. the body velocity of a ship remains constant while describing uniform circular motion but the components of the velocity vector in Earth coordinates are sinusoidal. Consequently, the velocity estimate of the position filter is expressed in body frame coordinates, as opposed to being expressed in Earth frame, to reduce bandwidth requirements under attitude changes and vehicle actuation.

The feedback terms  $K_{1p}$  and  $K_{2p}$  are identified with the Kalman filter gains for the system

$$\begin{bmatrix} \mathbf{x}_{p k+1} \\ \mathbf{x}_{v k+1} \end{bmatrix} = \begin{bmatrix} \mathbf{I} & T\mathbf{I} \\ \mathbf{0} & \mathbf{I} \end{bmatrix} \begin{bmatrix} \mathbf{x}_{p k} \\ \mathbf{x}_{v k} \end{bmatrix} + \begin{bmatrix} \mathbf{I} & -\frac{T^2}{2} \\ \mathbf{0} & -T \end{bmatrix} \begin{bmatrix} \mathbf{w}_{p k} \\ \mathbf{w}_{v k} \end{bmatrix}, \quad (4.18a)$$

$$\mathbf{y}_{x k} = \begin{bmatrix} \mathbf{I} & \mathbf{0} \end{bmatrix} \begin{bmatrix} \mathbf{x}_{p k} \\ \mathbf{x}_{v k} \end{bmatrix} + \mathbf{v}_{p k}, \quad (4.18b)$$

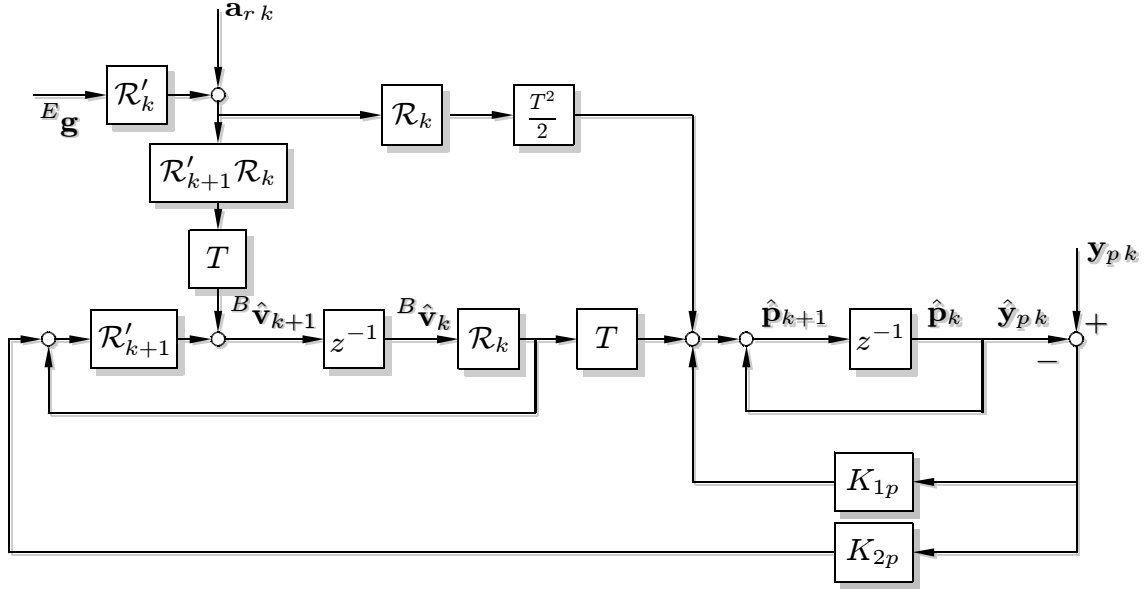


Figure 4.3: Position complementary filter.

where  $\mathbf{w}_v \sim \mathcal{N}(\mathbf{0}, \Xi_a)$  is zero-mean, Gaussian white noise with the covariance of the accelerometer noise  $\mathbf{w}_{a_r}$ . In the design of the position filter, the covariance matrices  $\Xi_p$ ,  $\Xi_a$ , and  $\Theta_p$  are used as tuning knobs to shape the frequency response of the filter. The stability and performance of the position complementary filter (4.17) are addressed in the following propositions.

**Theorem 4.3.** *Consider the discrete-time position kinematics (4.16), and let  $K_{1p}$  and  $K_{2p}$  be the steady-state Kalman filter gains for the system (4.18). Then the position complementary filter (4.17) is UAS.*

*Proof.* The structure of the proof is similar to that of Theorem 4.1. Define the estimation errors  $\tilde{\mathbf{p}}_k = \mathbf{p}_k - \hat{\mathbf{p}}_k$  and  ${}^B\tilde{\mathbf{v}}_k = {}^B\mathbf{v}_k - {}^B\hat{\mathbf{v}}_k$ . The associated kinematics are described by

$$\begin{aligned} \begin{bmatrix} \tilde{\mathbf{p}}_{k+1} \\ {}^B\tilde{\mathbf{v}}_{k+1} \end{bmatrix} &= \begin{bmatrix} \mathbf{I} - K_{1p} & T\mathcal{R}_k \\ -K_{2p} & \mathcal{R}'_{k+1}\mathcal{R}_k \end{bmatrix} \begin{bmatrix} \tilde{\mathbf{p}}_k \\ {}^B\tilde{\mathbf{v}}_k \end{bmatrix} \\ &+ \begin{bmatrix} \mathbf{I} & -\frac{T^2}{2}\mathcal{R}_k \\ \mathbf{0} & -T\mathcal{R}'_{k+1}\mathcal{R}_k \end{bmatrix} \begin{bmatrix} \mathbf{w}_{pk} \\ \mathbf{w}_{a_r k} \end{bmatrix} - \begin{bmatrix} K_{1p} \\ \mathcal{R}'_{k+1}K_{2p} \end{bmatrix} \mathbf{v}_{pk}. \end{aligned} \quad (4.19)$$

The compact state space formulation for the system (4.18) is given by

$$\mathbf{x}_{k+1} = \mathbf{F}\mathbf{x}_k + \mathbf{G}\mathbf{w}_k, \quad \mathbf{y}_k = \mathbf{H}\mathbf{x}_k + \mathbf{v}_k, \quad (4.20)$$

where  $\mathbf{x}_k = [\mathbf{x}'_{pk} \quad \mathbf{x}'_{vk}]'$ ,  $\mathbf{w}_k = [\mathbf{w}'_{pk} \quad \mathbf{w}'_{vk}]'$ ,  $\mathbf{y}_k = \mathbf{y}_{pk}$ ,  $\mathbf{v}_k = \mathbf{v}_{pk}$ ,  $\mathbf{F} = [\mathbf{I} \quad T\mathbf{I}]$ ,  $\mathbf{G} = [\mathbf{I} \quad -\frac{T^2}{2}]$ , and  $\mathbf{H} = [\mathbf{I} \quad \mathbf{0}]$ . The pairs  $[\mathbf{F}, \mathbf{H}]$  and  $[\mathbf{F}, \mathbf{G}]$  are detectable and completely stabilizable, respectively and the closed-loop system

$$\tilde{\mathbf{x}}_{k+1} = (\mathbf{F} - \mathbf{K}\mathbf{H})\tilde{\mathbf{x}}_k + \mathbf{G}\mathbf{w}_k - \mathbf{K}\mathbf{v}_k, \quad (4.21)$$

where  $\mathbf{K} = \begin{bmatrix} K'_{1p} & K'_{2p} \end{bmatrix}'$ , is UAS [4]. Define the Lyapunov transformation of variables, adopted in previous work by the authors [11], given by

$$\begin{bmatrix} \tilde{\mathbf{p}}_k \\ \tilde{\mathbf{v}}_k \end{bmatrix} = \mathbf{T}_k \begin{bmatrix} \tilde{\mathbf{x}}_{pk} \\ \tilde{\mathbf{x}}_{vk} \end{bmatrix}, \quad \mathbf{T}_k = \begin{bmatrix} \mathbf{I} & \mathbf{0} \\ \mathbf{0} & \mathcal{R}_k \end{bmatrix}, \quad (4.22)$$

and consider  $\mathbf{w}_{vk} = \mathcal{R}_k \mathbf{w}_{ar k}$ . Applying the Lyapunov transformation to (4.21) yields (4.19), and hence the origin of (4.19) is uniformly asymptotically stable by the properties of Lyapunov transformations [122].  $\square$

In the following theorem it is shown that the proposed position filter is identified with the steady-state Kalman filter for the position kinematics (4.17), under the mild assumption that the Gaussian white noises of the accelerometer triad are stochastically independent and characterized by the same variance. The stochastic independence is verified in realistic setups where the acceleration measurements are provided by three sensors from the same model, mounted orthogonally.

**Theorem 4.4.** *Let the state and observation disturbances in the position kinematics (4.16) be characterized by Gaussian white noises  $\mathbf{w}_p \sim \mathcal{N}(\mathbf{0}, \Xi_p)$ ,  $\mathbf{w}_{ar} \sim \mathcal{N}(\mathbf{0}, \xi_a \mathbf{I})$ , and  $\mathbf{v}_p \sim \mathcal{N}(\mathbf{0}, \Theta_p)$ . Then the position complementary filter (4.17) is the “steady-state” Kalman filter for the system (4.16) in the sense that the Kalman feedback gain  $K_{optk}$  converges asymptotically as follows*

$$\lim_{k \rightarrow \infty} \left\| K_{optk} - \begin{bmatrix} K_{1p} \\ \mathcal{R}'_{k+1} K_{2p} \end{bmatrix} \right\| = 0. \quad (4.23)$$

*Proof.* The estimation error covariance matrix of the Kalman filter for the system (4.20) satisfies

$$\mathbf{P}_{xp k+1|k} = \mathbf{F} \mathbf{P}_{xp k|k-1} \mathbf{F}' + \mathbf{G} \Xi \mathbf{G}' - \mathbf{F} \mathbf{P}_{xp k|k-1} \mathbf{H}' \mathbf{S}_{Pp}^{-1} \mathbf{H} \mathbf{P}_{xp k|k-1} \mathbf{F}',$$

where  $\mathbf{S}_{Pp} = \mathbf{H} \mathbf{P}_{xp k|k-1} \mathbf{H}' + \Theta$ ,  $\Xi = \begin{bmatrix} \Xi_p & \mathbf{0} \\ \mathbf{0} & \Xi_a \end{bmatrix}$ . With a slight abuse of notation, let  $K_{1pk}$  and  $K_{2pk}$  denote the time-varying Kalman gains for the system (4.18) and formulate the attitude filter (4.17) with time-varying gains

$$\begin{bmatrix} \hat{\mathbf{p}}_{k+1} \\ {}^B \hat{\mathbf{v}}_{k+1} \end{bmatrix} = \begin{bmatrix} \mathbf{I} & T \mathcal{R}_k \\ \mathbf{0} & \mathcal{R}'_{k+1} \mathcal{R}_k \end{bmatrix} \begin{bmatrix} \hat{\mathbf{p}}_k \\ {}^B \hat{\mathbf{v}}_k \end{bmatrix} + \begin{bmatrix} \frac{T^2}{2} \mathcal{R}_k \\ T \mathcal{R}'_{k+1} \mathcal{R}_k \end{bmatrix} (\mathbf{a}_r + \mathcal{R}'_k \mathbf{g}) \\ + \begin{bmatrix} K_{1pk} \\ \mathcal{R}'_{k+1} K_{2pk} \end{bmatrix} (\mathbf{y}_{pk} - \hat{\mathbf{y}}_{pk}).$$

Applying the Lyapunov transformation (4.22), the covariance matrix  $\Sigma_{pk+1|k} = E \left( \begin{bmatrix} \tilde{\mathbf{p}}_{k+1} \\ \tilde{\mathbf{v}}_{k+1} \end{bmatrix} \begin{bmatrix} \tilde{\mathbf{p}}'_{k+1} & \tilde{\mathbf{v}}'_{k+1} \end{bmatrix} \right)$  is given by  $\Sigma_{pk+1|k} = \mathbf{T}_{k+1} \mathbf{P}_{xk+1|k} \mathbf{T}'_{k+1}$  and satisfies

$$\begin{aligned} \Sigma_{pk+1|k} &= \mathbf{T}_{k+1} \mathbf{F} \mathbf{T}_k^{-1} \Sigma_{pk|k-1} \mathbf{T}_k^{-1} \mathbf{F}' \mathbf{T}'_{k+1} + \mathbf{T}_{k+1} \mathbf{G} \Xi \mathbf{G}' \mathbf{T}'_{k+1} \\ &\quad - \mathbf{T}_{k+1} \mathbf{F} \mathbf{T}_k^{-1} \Sigma_{pk|k-1} \mathbf{T}_k^{-1} \mathbf{H}' \mathbf{S}_{\Sigma pk}^{-1} \mathbf{H} \mathbf{T}_k^{-1} \Sigma_{pk|k-1} \mathbf{T}_k^{-1} \mathbf{F}' \mathbf{T}'_{k+1}, \end{aligned} \quad (4.24)$$



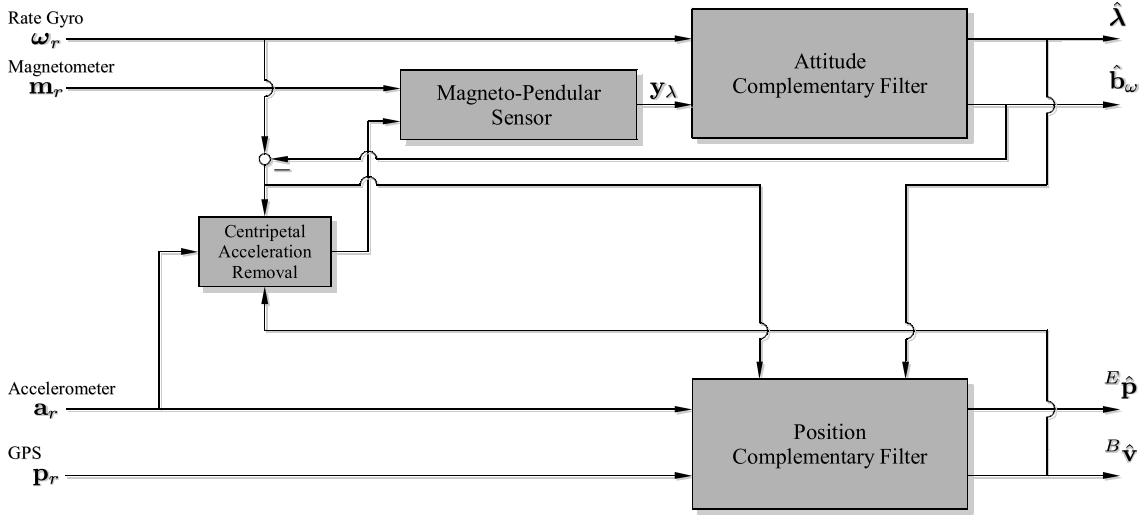


Figure 4.4: Navigation system architecture.

where  $\mathbf{S}_{\Sigma p k} = \mathbf{H}\mathbf{T}_k^{-1}\Sigma_{pk|k-1}\mathbf{T}'_k^{-1}\mathbf{H}' + \Theta$ . Assuming that the accelerometer noise covariance matrix is diagonal,  $\Xi_a = \xi_a\mathbf{I}$ , the matrices in (4.24) are given by

$$\begin{aligned} \mathbf{T}_{k+1}\mathbf{F}\mathbf{T}_k^{-1} &= \begin{bmatrix} \mathbf{I} & T\mathcal{R}_k \\ \mathbf{0} & \mathcal{R}'_{k+1}\mathcal{R}_k \end{bmatrix}, \quad \mathbf{H}\mathbf{T}_k^{-1} = \begin{bmatrix} \mathbf{I} & \mathbf{0} \end{bmatrix}, \\ \mathbf{T}_{k+1}\mathbf{G}\Xi\mathbf{G}'\mathbf{T}'_{k+1} &= \mathbf{T}_{k+1}\mathbf{G} \begin{bmatrix} \Xi_p & \mathbf{0} \\ \mathbf{0} & \Xi_a \end{bmatrix} \mathbf{G}'\mathbf{T}'_{k+1} = \mathbf{T}_{k+1}\mathbf{G} \begin{bmatrix} \Xi_p & \mathbf{0} \\ \mathbf{0} & \mathcal{R}_k\Xi_a\mathcal{R}'_k \end{bmatrix} \mathbf{G}'\mathbf{T}'_{k+1} \\ &= \begin{bmatrix} \mathbf{I} & -\frac{T^2}{2}\mathcal{R}_k \\ \mathbf{0} & -T\mathcal{R}'_{k+1}\mathcal{R}_k \end{bmatrix} \begin{bmatrix} \Xi_p & \mathbf{0} \\ \mathbf{0} & \Xi_a \end{bmatrix} \begin{bmatrix} \mathbf{I} & -\frac{T^2}{2}\mathcal{R}_k \\ \mathbf{0} & -T\mathcal{R}'_{k+1}\mathcal{R}_k \end{bmatrix}', \end{aligned}$$

which shows that  $\Sigma_{pk+1|k}$  is the optimal error covariance matrix for the position kinematics (4.16). Using  $K_{1pk} \rightarrow K_{1p}$  and  $K_{2pk} \rightarrow K_{2p}$  as  $k \rightarrow \infty$  produces (4.23) and completes the proof.  $\square$

Although some performance results are presented for the position filter, the closed-loop system is obtained by design in the frequency domain, and the feedback gains  $K_{1p}$  and  $K_{2p}$  are the steady-state Kalman gains for the design system (4.18). In this framework, the high-frequency contents of the accelerometer measurements are exploited, filtering out gravity and bias compensation errors, and merged with the low-frequency information available from the GPS position observations.

## 4.2 Navigation system implementation

This section presents the overall navigation system architecture that builds on the attitude and position complementary filters derived separately in the previous section, and discusses the problem of implementing the filter with different sampling rates.

### 4.2.1 Magneto-pendular sensor

The attitude observation  $\mathbf{y}_{\lambda k}$  in Euler angles coordinates is determined using the body and Earth frame representations of two vectors, namely the Earth's magnetic and gravitic fields. The problem of determining attitude using vector measurements is known in the literature as the orthogonal Procrustes problem [61] or as Wahba's problem [139] and several solutions have been proposed along time-spread articles [37]. The solution proposed in this work computes the Euler angles observation using a deterministic approach, similar to that of a TRIAD algorithm [8, 25]. Note that  $\mathbf{y}_{\lambda k}$  can be obtained using other attitude reconstruction algorithms and sensors, for more details see [37] and references therein.

The magnetic field vector is measured in the body frame by the magnetometer

$$\mathbf{m}_r = \mathbf{R}'_X(\phi)\mathbf{R}'_Y(\theta)\mathbf{R}'_Z(\psi)^E\mathbf{m} + \mathbf{n}_m, \quad (4.25)$$

where the magnetic field in Earth frame coordinates, denoted by  $^E\mathbf{m}$ , is known,  $\mathbf{n}_m$  is the magnetometer measurement noise and  $\mathbf{R}_X(\phi)$ ,  $\mathbf{R}_Y(\theta)$  and  $\mathbf{R}_Z(\psi)$  represent the roll, pitch, and yaw elementary rotation matrices, respectively. Denoting the projection of the magnetometer reading on the x-y plane by  $^P\mathbf{m} = \mathbf{R}_Y(\theta)\mathbf{R}_X(\phi)\mathbf{m}_r$ , the yaw angle is obtained by algebraic manipulation of (4.25), producing

$$\psi = \arctan 2 \left( ^E m_y ^P m_x - ^E m_x ^P m_y, ^E m_x ^P m_x + ^E m_y ^P m_y \right), \quad (4.26)$$

where the four quadrant arctan, denoted as  $\arctan 2$ , was adopted. The pitch and roll angles are obtained from the accelerometer, which is regarded as a pendular sensor

$$\mathbf{a}_p \approx -^B\mathbf{g} = -\mathbf{R}'_X(\phi)\mathbf{R}'_Y(\theta)^E\mathbf{g} = \begin{bmatrix} g \sin \theta \\ -g \cos \theta \sin \phi \\ -g \cos \theta \cos \phi \end{bmatrix}, \quad (4.27)$$

where  $\mathbf{a}_p$  denotes the accelerometer reading assuming that external accelerations are negligible,  $^E\mathbf{g} = [0 \ 0 \ g]'$  is the gravity vector in Earth frame coordinates, and  $g$  is the local gravitic acceleration. The pitch and roll angles are given by algebraic manipulation of (4.27), producing

$$\phi = \arctan 2(-a_y, -a_z), \quad (4.28a)$$

$$\theta = \begin{cases} \arctan \left( -\frac{a_x \sin \phi}{a_y} \right), & \sin \phi \neq 0 \\ \arctan \left( -\frac{a_x \cos \phi}{a_z} \right), & \cos \phi \neq 0 \end{cases}. \quad (4.28b)$$

The computation of pitch and roll angles using directly the accelerometer reading in (4.28) is distorted in the presence of external linear and angular accelerations. The accelerometer measurement model is given by [20]

$$\mathbf{a}_r = \frac{d^B\mathbf{v}}{dt} + \boldsymbol{\omega} \times ^B\mathbf{v} - ^B\mathbf{g},$$

where  $\frac{d^B \mathbf{v}}{dt}$  is the linear acceleration and  $\boldsymbol{\omega} \times^B \mathbf{v}$  is the centripetal acceleration. Typical maneuvers of autonomous vehicles involve mostly short term linear accelerations, which hence are high-frequency and the resulting distortion in pitch and roll can be smoothed out by the complementary lowpass filter. On the other hand, centripetal accelerations occur even in trimming maneuvers, e.g. a helicoidal path, and must be compensated for. As depicted in Fig. 4.4, the pendular reading estimate  $\hat{\mathbf{a}}_p$  used in (4.28) is obtained by compensating the centripetal acceleration

$$\hat{\mathbf{a}}_p = \mathbf{a}_r - \hat{\boldsymbol{\omega}} \times^B \hat{\mathbf{v}}, \quad (4.29)$$

where  $\hat{\boldsymbol{\omega}} = \boldsymbol{\omega}_r - \hat{\mathbf{b}}_\omega$  is the angular rate drawn from the rate gyro measurement with bias compensation and  ${}^B \hat{\mathbf{v}}$  is the velocity estimate provided by the complementary position filter or by a Doppler sensor if available. The effect of linear acceleration in  $\hat{\mathbf{a}}_p$  is compensated in the frequency domain by appropriate design of the complementary filter.

The yaw, pitch, and roll observations (4.26, 4.28, 4.29) define a virtual attitude sensor measurement that is referred to as Magneto-Pendular Sensor (MPS). The MPS observation noise  $\mathbf{v}_\lambda$  is a nonlinear function of the magnetometer and accelerometer noises, the attitude of the vehicle and the (linear and angular) acceleration compensation errors, and is mostly high-frequency due to the influence of linear accelerations. If modeled stochastically, the noise covariance  $\Theta_\lambda$  can be inflated to account for the time-varying covariance of  $\mathbf{v}_\lambda$ , however this technique leads to undesirable performance degradation, for a discussion on the subject see [4] and references therein. In the frequency domain design approach, adopted in this work, the observation noise weight matrix is tuned to yield good steady-state high-frequency rejection of the MPS noise.

### 4.2.2 Complementary filter coupling

The proposed navigation system integrates the attitude and position complementary filters to produce an estimate of the vehicle attitude and position. The blocks of the diagram depicted in Fig. 4.4 have been introduced previously in this work: the attitude and position complementary filters are detailed in Section 4.1 and illustrated in Fig. 4.2 and Fig. 4.3, respectively, and the Magneto-Pendular Sensor and the Centripetal Acceleration Removal blocks are detailed in Section 4.2.1. The attitude terms in the position filter kinematics and the use of pendular readings to obtain the MPS measurement produce a coupling between the attitude and the position filters, illustrated by the block connections of Fig. 4.4, which are described as follows.

The attitude rotation matrix  $\mathcal{R}_k$  and the attitude update term  $\mathcal{R}'_{k+1} \mathcal{R}_k$  are adopted in the kinematics of the position filter (4.17), as illustrated in the block diagram of Fig. 4.3. The attitude term  $\mathcal{R}_k$  is obtained from the attitude filter, which is the best attitude estimate available in the practical implementation of the navigation system, and the update term described by  $\mathcal{R}'_{k+1} \mathcal{R}_k \approx e^{-T(\boldsymbol{\omega}_r - \hat{\mathbf{b}}_\omega)_\times}$  is obtained using the rate gyro measurement and the bias estimate, where  $(\mathbf{a})_\times$  is the skew symmetric matrix defined by the vector

$\mathbf{a} \in \mathbb{R}^3$  such that  $(\mathbf{a})_{\times} \mathbf{b} = \mathbf{a} \times \mathbf{b}$ ,  $\mathbf{b} \in \mathbb{R}^3$ . Likewise, the transformation matrix  $\mathbf{Q}(\boldsymbol{\lambda}_k)$  is constructed using the best attitude estimate at each time  $k$ , which is given by the attitude filter.

The gravitic measurements used in the computation of the attitude measurement  $\mathbf{y}_{\lambda}$  are distorted by linear and angular accelerations. As a way to robustify the attitude measurement  $\mathbf{y}_{\lambda}$ , the angular accelerations are compensated for by using the angular rate and linear velocity estimates as shown in (4.27), allowing for valid MPS measurements in the presence of centripetal accelerations, that occur even in trimming conditions such as helicoidal trajectories.

The theoretical stability and performance properties of the attitude and position filters derived in Section 4.1 cannot be directly inferred for the overall navigation system due to the filter coupling and to the use of pendular measurements in the attitude aiding observation. This limitation is a consequence of the adopted attitude aiding sensors, and stability and performance can be guaranteed in other experimental setups, e.g. by using non-pendular, vision-based attitude aiding sensors and by decoupling the attitude and position filters using external attitude reference units. For the proposed navigation system implementation, extensive Monte Carlo simulations showed that the architecture is stable in practice.

### 4.2.3 Multirate filtering

In general, the GPS output rate is slower than the sampling rate of the inertial sensors. In this case, the position feedback gains are obtained by considering the multirate position filter as a periodic estimator, and adopting the optimality results for periodic systems derived in [15], which are briefly described in the ensuing for the position filter for the sake of clarity. Let the GPS and inertial sensors' sampling periods be denoted by  $T_{\text{GPS}}$  and  $T_{\text{INS}}$ , respectively, and define the ratio  $n_T = \frac{T_{\text{GPS}}}{T_{\text{INS}}}$ ,  $n_T \in \mathbb{N}$ . The design system (4.6) is periodic with period  $n_T$  and is written in the compact form

$$\mathbf{x}_{k+1} = \mathbf{F}\mathbf{x}_k + \mathbf{G}\mathbf{w}_k, \quad \mathbf{y}_k = \mathbf{H}_k\mathbf{x}_k + \mathbf{v}_k, \quad (4.30)$$

where  $\mathbf{x}_k = [\mathbf{x}'_{\lambda k} \quad \mathbf{x}'_{b k}]'$ ,  $\mathbf{w}_k = [\mathbf{w}'_{\omega k} \quad \mathbf{w}'_{b k}]'$ ,  $\mathbf{y}_k = \mathbf{y}_{x k}$ ,  $\mathbf{v}_k = \mathbf{v}_{\lambda k}$ ,  $\mathbf{F} = \begin{bmatrix} \mathbf{I} & -T\mathbf{I} \\ \mathbf{0} & \mathbf{I} \end{bmatrix}$ ,  $\mathbf{G} = \begin{bmatrix} -T\mathbf{I} & \mathbf{0} \\ \mathbf{0} & \mathbf{I} \end{bmatrix}$ , and the observation matrix of the system is given by

$$\mathbf{H}_k = \begin{cases} [\mathbf{I} & \mathbf{0}] & \text{if } \frac{k}{n_T} \in \mathbb{N}_0, \\ [\mathbf{0} & \mathbf{0}] & \text{otherwise.} \end{cases} \quad (4.31)$$

The system (4.30) can be associated with the time-invariant system that models the dynamics of the state at time  $k = in_T$ ,  $i \in \mathbb{N}_0$ , described by

$$\underline{\mathbf{x}}_{k+1} = \underline{\mathbf{F}}\underline{\mathbf{x}}_k + \underline{\mathbf{G}}\underline{\mathbf{w}}_k, \quad \underline{\mathbf{y}}_k = \underline{\mathbf{H}}\underline{\mathbf{x}}_k + \underline{\mathbf{D}}\underline{\mathbf{w}}_k + \underline{\mathbf{v}}_k, \quad (4.32)$$

where  $\underline{\mathbf{x}}_k = \mathbf{x}_{kn_T}$ ,  $\underline{\mathbf{x}}_k \in \mathbb{R}^6$ ,

$$\begin{aligned}\underline{\mathbf{w}}_k &= \left[ \mathbf{w}'_{kn_T} \quad \mathbf{w}'_{kn_T+1} \quad \cdots \quad \mathbf{w}'_{(k+1)n_T-1} \right]', & \underline{\mathbf{w}}_k &\in \mathbb{R}^{6n_T}, \\ \underline{\mathbf{v}}_k &= \left[ \mathbf{v}'_{kn_T} \quad \mathbf{v}'_{kn_T+1} \quad \cdots \quad \mathbf{v}'_{(k+1)n_T-1} \right]', & \underline{\mathbf{v}}_k &\in \mathbb{R}^{3n_T}, \\ \underline{\mathbf{y}}_k &= \left[ \mathbf{y}'_{kn_T} \quad \mathbf{y}'_{kn_T+1} \quad \cdots \quad \mathbf{y}'_{(k+1)n_T-1} \right]', & \underline{\mathbf{y}}_k &\in \mathbb{R}^{3n_T},\end{aligned}$$

are the augmented noise and measurement vectors, respectively, and

$$\begin{aligned}\underline{\mathbf{F}} &= \mathbf{F}^{n_T}, \underline{\mathbf{F}} \in \text{M}(6, 6), \\ \underline{\mathbf{G}} &= \left[ \mathbf{F}^{n_T-1} \mathbf{G} \quad \mathbf{F}^{n_T-2} \mathbf{G} \quad \cdots \quad \mathbf{G} \right], \underline{\mathbf{G}} \in \text{M}(6, 6n_T), \\ \underline{\mathbf{H}} &= \left[ \mathbf{H}'_0 \quad \mathbf{F}' \mathbf{H}'_1 \quad \cdots \quad \mathbf{F}^{n_T-1'} \mathbf{H}'_{n_T-1} \right]', \underline{\mathbf{H}} \in \text{M}(3n_T, 6), \\ \underline{\mathbf{D}} &= \begin{bmatrix} \mathbf{0} & \mathbf{0} & \cdots & \cdots & \mathbf{0} \\ \mathbf{H}_1 \mathbf{G} & \mathbf{0} & & & \vdots \\ \mathbf{H}_2 \mathbf{F} \mathbf{G} & \mathbf{H}_2 \mathbf{G} & \mathbf{0} & & \vdots \\ \vdots & & \ddots & \ddots & \vdots \\ \mathbf{H}_{n_T-1} \mathbf{F}^{n_T-1} \mathbf{G} & \cdots & \cdots & \mathbf{H}_{n_T-1} \mathbf{G} & \mathbf{0} \end{bmatrix}, \underline{\mathbf{D}} \in \text{M}(3n_T, 6n_T),\end{aligned}$$

which defines a time-invariant system, with correlated measurement and the state noises [15]. The optimal feedback gain for the time-invariant system (4.32) is given by

$$\underline{\mathbf{K}} = \left[ \underline{\mathbf{F}} \underline{\mathbf{P}} \underline{\mathbf{H}}' + \underline{\mathbf{G}} \underline{\Xi} \underline{\mathbf{D}}' \right] \left[ \underline{\Theta} + \underline{\mathbf{D}} \underline{\Xi} \underline{\mathbf{D}}' + \underline{\mathbf{H}} \underline{\mathbf{P}} \underline{\mathbf{H}}' \right]^{-1}, \quad (4.33)$$

where  $\underline{\mathbf{K}} \in \text{M}(6, 3n_T)$ ,  $\underline{\Xi} = E(\underline{\mathbf{w}}_k \underline{\mathbf{w}}_k')$ ,  $\underline{\Theta} = E(\underline{\mathbf{v}}_k \underline{\mathbf{v}}_k')$ , and  $\underline{\mathbf{P}}$  is the steady-state optimal estimation error covariance matrix, given by the solution of the Riccati equation

$$\underline{\mathbf{P}} = \underline{\mathbf{F}}_* \underline{\mathbf{P}} \underline{\mathbf{F}}_*' + \underline{\mathbf{G}}_* \underline{\mathbf{G}}_*' - \underline{\mathbf{F}}_* \underline{\mathbf{P}} \underline{\mathbf{H}}' \underline{\mathbf{S}}^{-1} \underline{\mathbf{H}} \underline{\mathbf{P}} \underline{\mathbf{F}}_*',$$

where  $\underline{\mathbf{S}} = \underline{\Theta} + \underline{\mathbf{D}} \underline{\Xi} \underline{\mathbf{D}}' + \underline{\mathbf{H}} \underline{\mathbf{P}} \underline{\mathbf{H}}'$ ,  $\underline{\mathbf{G}}_* \underline{\mathbf{G}}_*' = \underline{\mathbf{G}} \underline{\Xi} \underline{\mathbf{G}}' - \underline{\mathbf{G}} \underline{\Xi} \underline{\mathbf{D}}' \left[ \underline{\Theta} + \underline{\mathbf{D}} \underline{\Xi} \underline{\mathbf{D}}' \right]^{-1} \underline{\mathbf{D}} \underline{\Xi} \underline{\mathbf{G}}'$  and  $\underline{\mathbf{F}}_* = \underline{\mathbf{F}} - \underline{\mathbf{G}} \underline{\Xi} \underline{\mathbf{D}}' \left[ \underline{\Theta} + \underline{\mathbf{D}} \underline{\Xi} \underline{\mathbf{D}}' \right]^{-1} \underline{\mathbf{H}}$ . Considering the partition of the feedback gain (4.33) given by  $\underline{\mathbf{K}} = \left[ K_0 \quad K_1 \quad \cdots \quad K_{n_T-1} \right]$ ,  $\mathbf{K}_i \in \text{M}(6, 3)$ ,  $i \in \mathbb{N}_0$ , for the system (4.30-4.31), it can be easily shown that  $\underline{\mathbf{D}} = \mathbf{0}$ ,  $K_i = \mathbf{0}$ ,  $i \neq 0$ , and hence that the feedback gain  $K_p = \left[ K'_{1p} \quad K'_{2p} \right]'$  is simply given by selecting the gain sub-matrix  $K_0$  and propagating back to the time instant of the GPS measurement, i.e.  $K_p = \mathbf{F}^{1-n_T} K_0$ .

For further details on the synthesis of optimal estimator for discrete-time linear periodic systems, the reader is referred to [15] and references therein. A multirate filter channel to channel frequency analysis methodology can be found in [113] and references therein.

### 4.3 Experimental results

The proposed navigation system is validated in this section using a low-power hardware architecture enclosing low-cost sensors and mounted on-board the DELFIMx catamaran. The properties of the complementary filters in the frequency domain are discussed and the resulting performance of the filters is analyzed. The attitude and position estimation

Table 4.1: Complementary filter parameters.

	State Weights	Observation Weight	Filter Gain
Attitude	$\Xi_\omega = 3\mathbf{I}$	$\Theta_\lambda = 0.8 \times 10^{-2}\mathbf{I}$	$K_{1\lambda} = 2.97 \times 10^{-1}\mathbf{I}$
Filter	$\Xi_b = 10^{-10}\mathbf{I}$		$K_{2\lambda} = 9.41 \times 10^{-5}\mathbf{I}$
Position	$\Xi_p = 5 \times 10^{-2}\mathbf{I}$	$\Theta_p = \mathbf{I}$	$K_{1p} = 0.59\mathbf{I}$
Filter	$\Xi_a = 10\mathbf{I}$		$K_{2p} = 0.14\mathbf{I}$

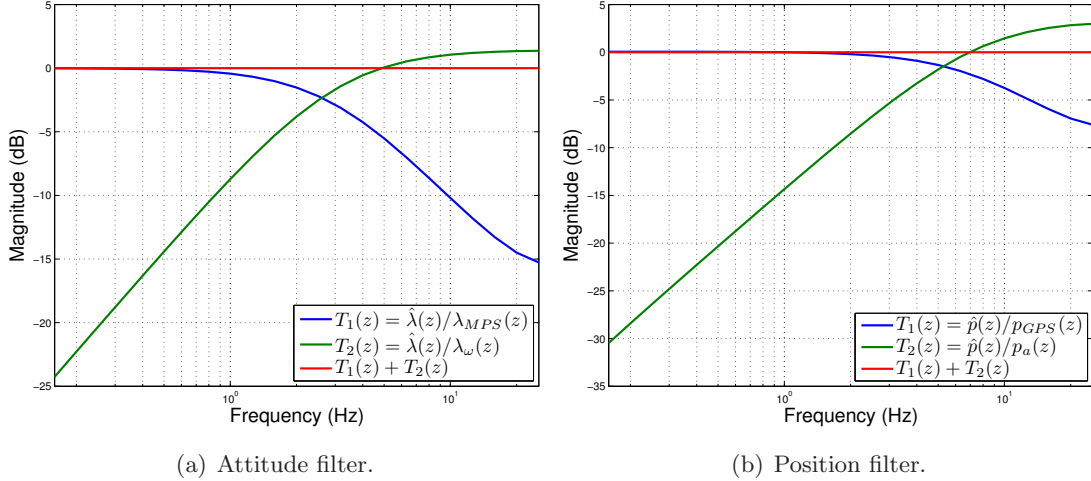


Figure 4.5: Complementary filter transfer functions.

results using the experimental data collected in the catamaran sea tests are presented, and the usual cases of GPS signal outage and of initial calibration error of the rate gyro bias are addressed. A detailed description of the DELFIMx craft and the adopted hardware is found in Appendix B. Due to the distinct sampling rates of the magnetometer and inertial sensors, a multirate formulation similar to that described in Section 4.2.3 is adopted for the yaw estimation.

### 4.3.1 Filter parameter design

The attitude and position filters derived in Section 4.1 are designed to produce a closed-loop frequency response which blends the complementary frequency contents of the inertial and the aiding sensor measurements. In this frequency domain framework, the state and measurement weight matrices are used as tuning parameters and the filter gains are identified with the steady-state Kalman filter gains. The adopted weights and corresponding gains are detailed in Table 4.1.

The complementary frequency response of the closed-loop filters is depicted in Fig. 4.5 and was obtained by considering  $\mathbf{Q}(\boldsymbol{\lambda}) = \mathbf{Q}(0)$  and  $\mathcal{R}_k = \mathbf{I}$ , i.e. the frequency response of the time invariant systems (4.6) and (4.18) used in the filter design. As shown in Fig. 4.5, the low-frequency region of the MPS and GPS are blended with the high-frequency

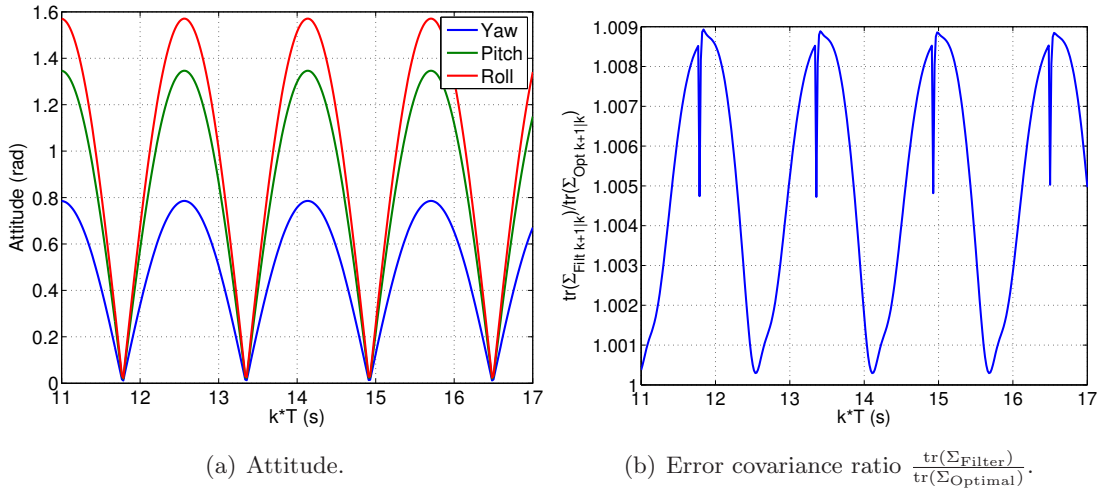


Figure 4.6: Attitude filter performance ( $T = \frac{1}{56}$  s).

contents of the open-loop integration of the inertial measurements, which is given by

$$\begin{aligned} \boldsymbol{\lambda}_{\omega k+1} &= \boldsymbol{\lambda}_{\omega k} + T\mathbf{Q}(0)\boldsymbol{\omega}_{rk}, \\ \mathbf{p}_{\mathbf{a}k+1} &= \mathbf{p}_{\mathbf{a}k} + T\mathbf{v}_{\mathbf{a}k} + \frac{T^2}{2}\mathbf{a}_{rk}, \quad \mathbf{v}_{\mathbf{a}k+1} = \mathbf{v}_{\mathbf{a}k} + T\mathbf{a}_{rk}. \end{aligned}$$

The sum of the transfer functions of the filters, depicted in Fig. 4.5, is unitary, which shows that the adopted steady-state Kalman gains bear complementary filters, as expected. The obtained complementary transfer functions are validated in practice with the experimental data obtained on-board the DELFIMx catamaran.

As discussed in Section 4.1.1, the proposed attitude filter is identified with the steady-state Kalman filter for constant pitch and roll angles and, in case of time-varying pitch and roll angles, the performance degradation can be analyzed using the covariance propagation equations detailed in Appendix D. A numerical comparison of the Kalman and the obtained estimation error covariances is shown in Fig. 4.6, considering the design weights presented in Table 4.1. As shown in Fig. 4.6(b), the estimation error covariance of the proposed attitude complementary filter is less than 1% above the optimal estimation error covariance for the aggressive pitch and roll trajectory depicted in Fig. 4.6(a).

### 4.3.2 Experimental results analysis

This section presents the navigation system estimation results obtained with the experimental data collected on-board the DELFIMx catamaran during tests at sea using the hardware architecture detailed previously. The trajectory described by the DELFIMx vehicle is mainly characterized by straight line and circular paths, as depicted in Fig. 4.7(a), to assess the performance of the navigation system in realistic operational scenarios.

The attitude estimation results presented in Fig. 4.8, are according to the maneuvers described by the robotic platform, whose forward velocity is mainly along the body frame x-axis, and hence describes mostly yaw turns. The yaw estimate depicted in Fig. 4.8(a)

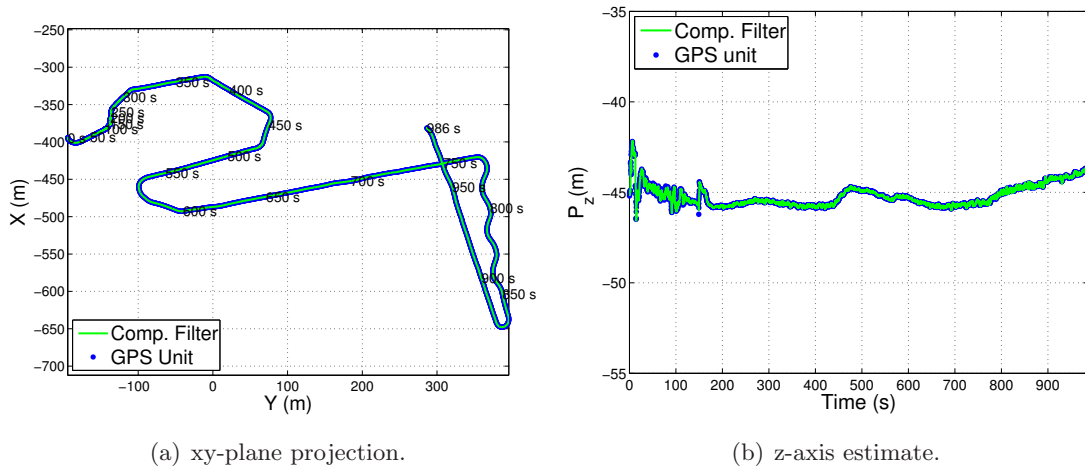


Figure 4.7: DELFIMx trajectory estimation results.

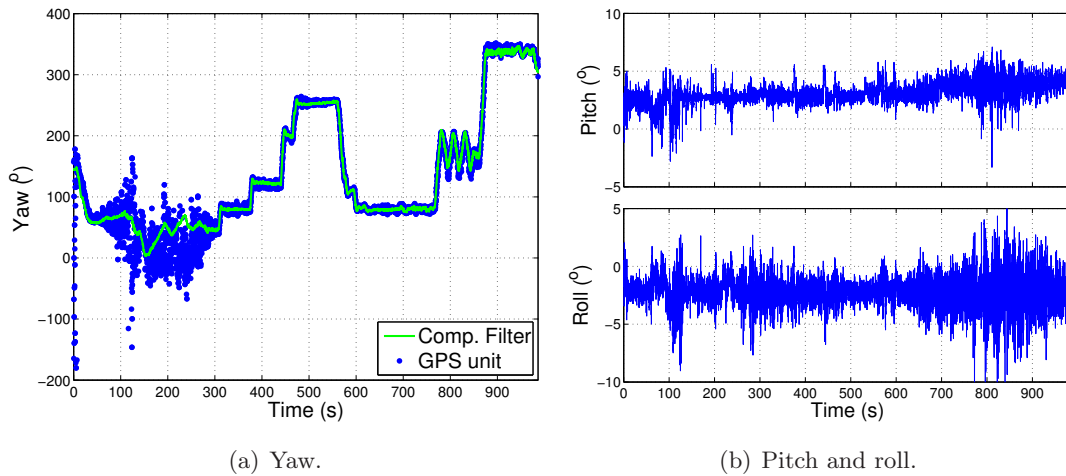


Figure 4.8: Attitude estimation results.

is consistent with the turning maneuvers and the heading directions of the straight paths performed by the platform, illustrated in Fig. 4.7(a), and with the yaw measurement given by the GPS unit. Clearly, the filter estimate is more accurate than the GPS yaw measurement, that is used only for the sake of validation of the estimation results and is not fed to the filter. The yaw measurement of the GPS unit is degraded for small velocities, as shown in Fig. 4.8(a) for the time interval  $t \in [50 \ 300]$  s where the platform maneuver is characterized by small forward velocity, as presented in Fig. 4.9(b).

The pitch and roll angles, presented in Fig. 4.8(b), oscillate around the mean values of  $3.08^\circ$  and  $-2.20^\circ$  respectively, that correspond approximately to the installation angles of the hardware architecture. Pitch and roll fluctuations occur due to platform turning, interference of waves, and vibration of the hull due to the propellers. Larger oscillations are verified when the vehicle turns, for example the slalom trajectory at  $[760 \ 880]$  s, detailed in Fig. 4.10, bears larger peak to peak values of the pitch and roll angles, depicted in



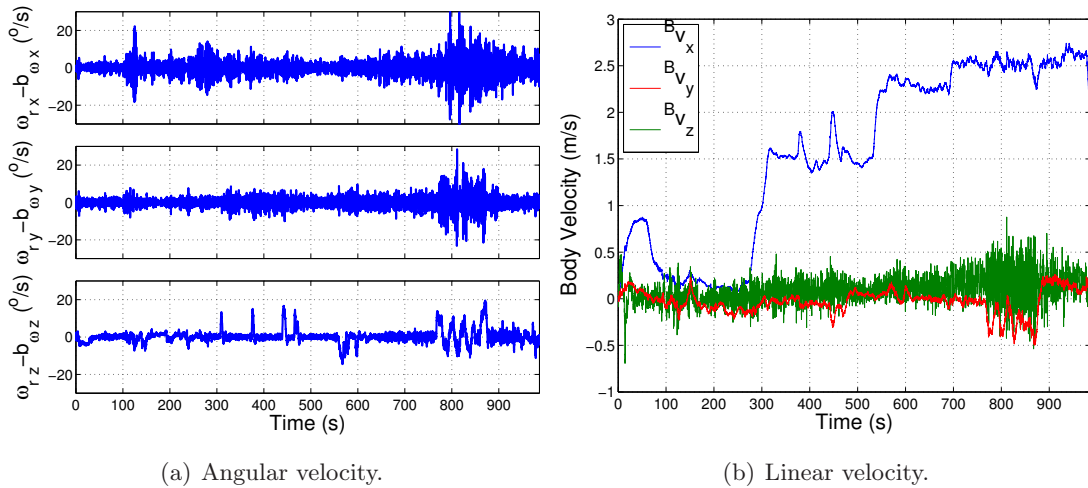


Figure 4.9: Linear and angular velocity estimation results.

Fig. 4.10(a), due to the oscillation of the catamaran while performing the maneuver, and to the vibration induced by the propellers. The pitch values satisfy the conditions under which the stability propositions derived in Sections 4.1 hold. Interestingly enough, the standard deviations of the pitch and roll estimates are  $0.95^\circ$  and  $1.42^\circ$  respectively, which suggests that the performance degradation of the attitude filter due to time-varying pitch and roll is small for the present application.

The velocity estimation results are shown in Fig. 4.9. The proposed filter is based on the attitude kinematics and hence does not estimate explicitly the angular velocity, in spite of compensating for the rate gyro noise and bias to estimate attitude. The angular velocity estimate, presented in Fig. 4.9(a), is given by the rate gyro measurements, compensated with the bias estimate, and is presented to verify the consistency of the attitude estimates. The z-axis angular velocity is synchronous with the yaw changes in Fig. 4.8(a), namely in the initial turn, and in turning maneuvers at the time intervals where a variations in the angular velocity are verified, such as [305 315] s, [370 380] s, [435 450] s, [465 470] s, [560 600] s, and [760 880] s. These turning maneuvers can be easily identified in Fig. 4.7(a) by analyzing the time tags. The x- and y-axes angular velocities are consistent with the pitch and roll estimates, i.e. are approximately zero mean and the most noticeable fluctuation occurs at the slalom maneuver at [760 880] s, see Fig. 4.10(b).

The estimate of the linear velocity, expressed in body coordinates, is shown in Fig. 4.9(b). The x-axis body velocity is positive and approximately stepwise constant at the straight paths trajectories at the time intervals [320 365] s, [385 430] s, [480 550] s, [615 750] s and [880 980] s. The y-axis body velocity is approximately zero-mean during straight path trajectories, and centrifugal during turning maneuvers due to sideslip of the catamaran, as evidenced for the slalom maneuver results, see Fig. 4.9(b) and detail in Fig. 4.10(c). Also, the mean of the y-axis body velocity is nonzero when the vehicle is subject to external, Earth fixed forces such as waves induced by nearby vessels and oceanic currents, such as

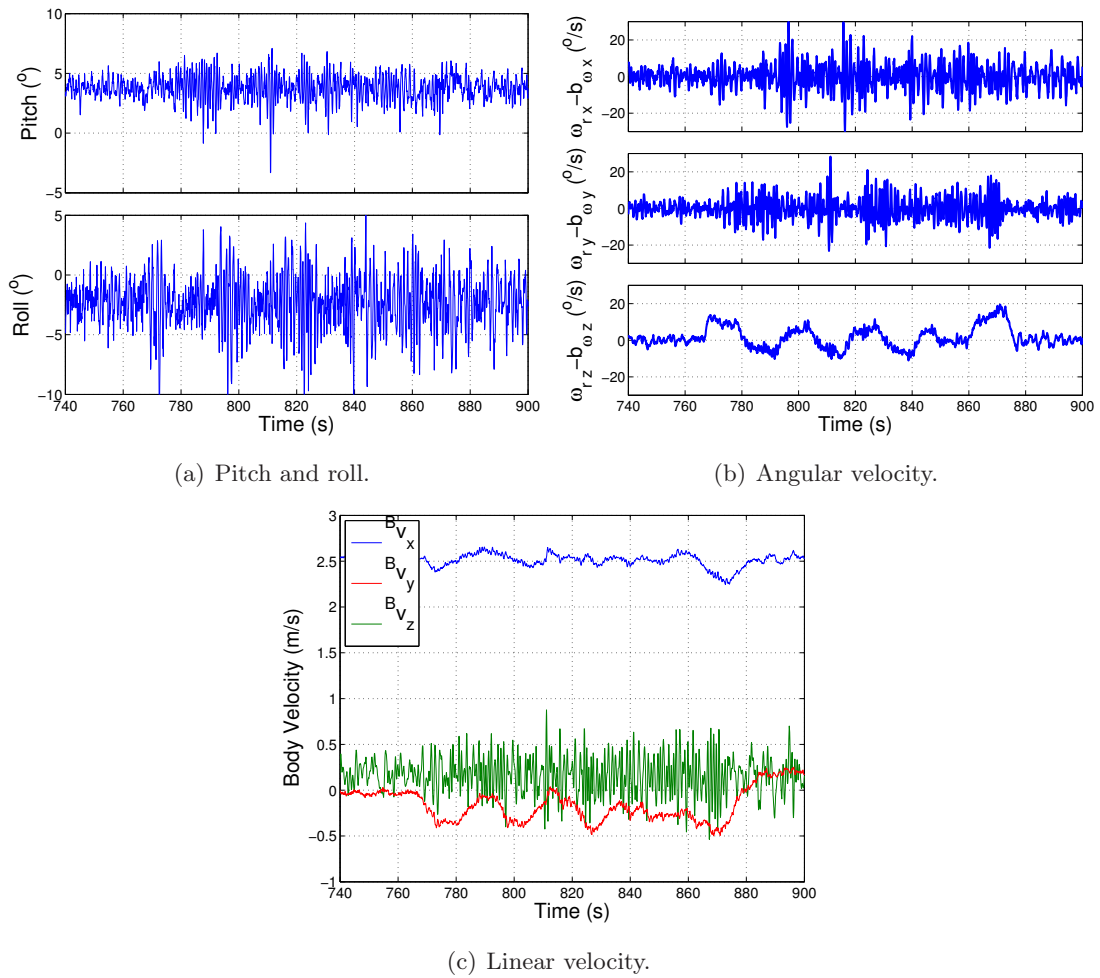
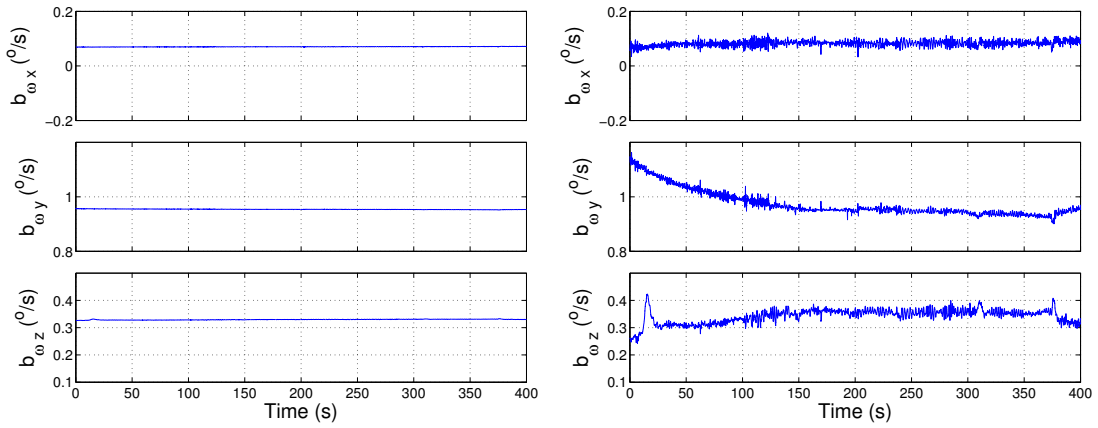


Figure 4.10: Slalom maneuver at [760 880] s.

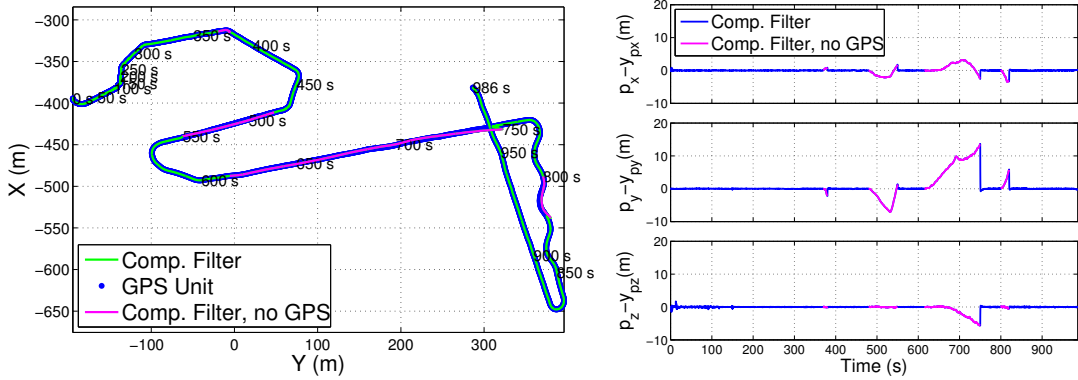
in the time interval [760 980] s illustrated in Fig. 4.9(b) and Fig. 4.10(c). The z-axis body velocity is approximately zero-mean, as expected for an oceanic platform, and oscillates due to the influence of waves.

The rate gyro bias estimation results are presented in Fig. 4.11(a). The results show that the attitude complementary filter compensates for slowly time-varying bias, by means of the small design weight  $\Xi_b$  in the computation of the feedback gain, see Table 4.1 for details. However, the Kalman gains are stationary and the initial bias uncertainty should be close to the steady-state bias covariance, i.e. the bias calibration error should be small. As shown in Fig. 4.11(b), using a larger design weight  $\Xi_b$  enables the filter to compensate for the bias calibration error at the cost of larger steady state covariance. The trade-off between compensating for calibration errors and the long-term accuracy of the bias estimate should be accounted for in the design process, and a simple gain switching technique, using a large design weight  $\Xi_b$  for initialization of the filter and a smaller design weight  $\Xi_b$  in the long term, should be considered for the case where online calibration is required.



(a) Compensation of slowly time-varying bias,  $\Xi_b = 10^{-7}$ . Calibration error compensation,  $\Xi_b = 10^{-7}$ .

Figure 4.11: Rate gyro bias estimation.



(a) xy-plane projection.

(b) Difference between the estimated and the measured positions.

Figure 4.12: DELFIMx trajectory estimation results (GPS signal jamming).

The position estimation results are coherent with the GPS measurements, as evidenced in Figs. 4.7(a) and 4.7(b). To analyze the weight of GPS aiding in the filter estimation results, the case of GPS outage is considered by canceling the GPS measurement feedback at selected time intervals when the vehicle turns or enters long straight paths. The GPS outage time instants are detailed in Table 4.2, and the corresponding trajectories are illustrated in Fig. 4.12(a). The position estimation results for the trajectory paths subject to GPS outage are shown in detail in Fig. 4.13. The navigation system results presented in Table 4.2 show that the position drift rate is small during GPS signal outage. Consequently, the position filter operates without relying too much on the GPS position observations, by exploiting the inertial measurements information. The navigation system follows closely the straight path trajectories, as depicted in Figs. 4.13(b) and 4.13(c), and successfully exploits the angular information during the turning maneuvers detailed in Figs. 4.13(a) and 4.13(d). The position estimates are bounded for the GPS outage time

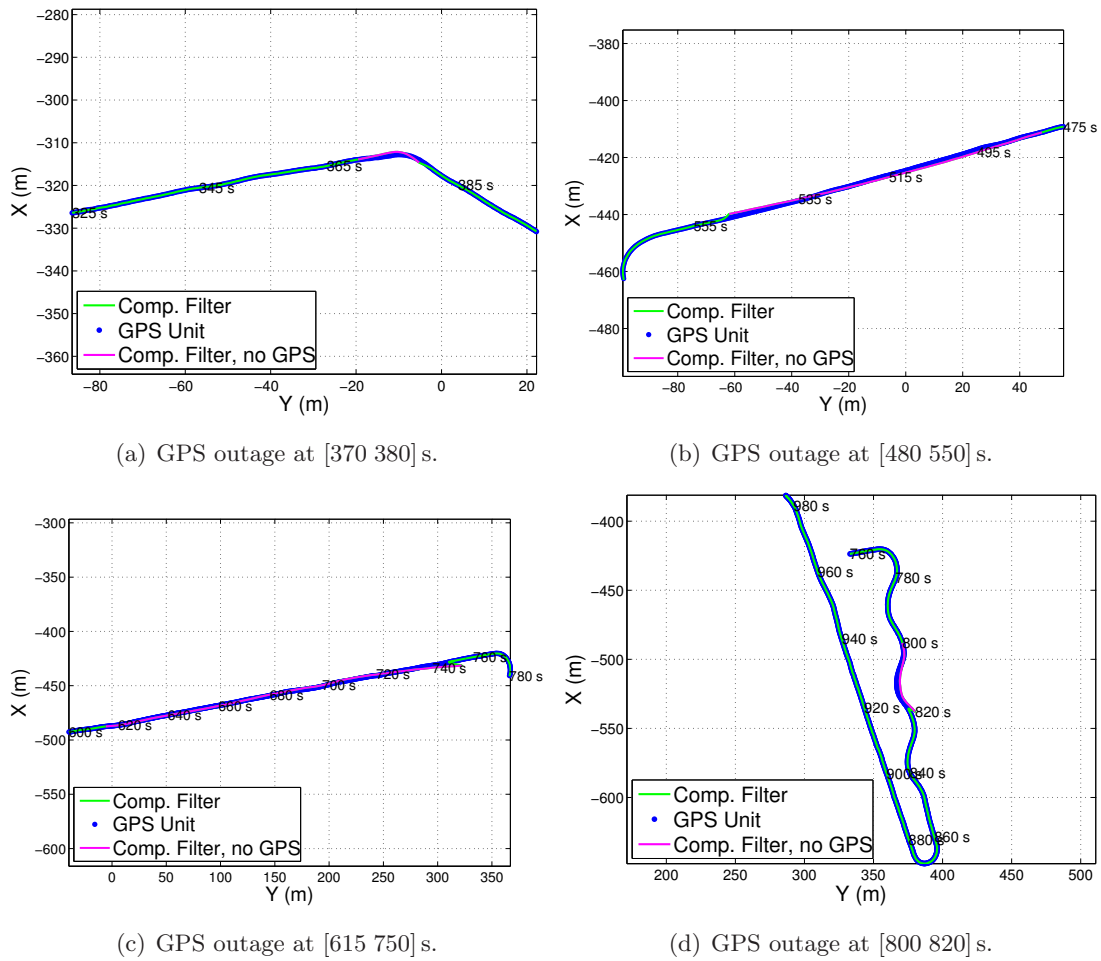


Figure 4.13: Details of the estimated trajectory with GPS outage.

intervals, as shown in Fig. 4.12(b), however position error buildup occurs due to the open-loop integration of the accelerometers, combined with pitch and roll estimation errors that induce position estimate drift, as expected.

The frequency domain validation of the complementary transfer functions is performed using the Matlab `spectrogram` function to compute the short-time Fourier transform of the position and attitude estimates, aiding sensor measurements, and inertial sensor measurements integration. The short-time Fourier transform computes a time-dependent Fourier transform of the signal multiplied by a sliding window function, and allows for a characterization of the time-varying frequency contents of a signal at each time instant [109]. The choice of the window function size is a trade-off between good resolution in the time domain (short window), and good resolution in the frequency domain (large window).

Using a Hamming window of length 512 and 500 overlapping segments, the frequency contents of the attitude and position signals are analyzed, and the blending of the low frequency contents of the aiding sensors with the high frequency contents of the inertial sensor integration is studied. Namely, Figs. 4.14 and 4.15 illustrate the fusion in the frequency domain of the pendular measurements with the inertial readings, i.e. the yaw

Table 4.2: GPS outage results.

Time Interval	Final Position Drift (m)	Average Position Drift (m/s)
[370 380] s	2.38	0.238
[480 550] s	1.91	0.027
[615 750] s	15.37	0.114
[800 820] s	7.14	0.357

and pitch angles given by the MPS attitude computation and by the rate gyro integration, and the resulting attitude filter estimate. Also, the position filtering in the frequency domain is demonstrated in Fig. 4.16, where the frequency contents of the x-axis position  $\mathbf{p}_x$  given by the GPS observation and by the accelerometer integration are presented, and the position filter estimate is depicted. Although a rigorous analysis in the frequency domain using the spectrogram is precluded by the multirate formulation of the navigation system, it is possible to verify qualitatively that the sensor measurements are blended using complementary transfer functions. The low-frequency contents of the aiding observations presented in Figs. 4.14(a), 4.15(a) and 4.16(a) are blended with the high-frequency contents of the open-loop integration of the inertial measurements, shown in Figs. 4.14(b), 4.15(b), and 4.16(b), producing the attitude and position estimates with the frequency contents depicted in Figs. 4.14(c), 4.15(c) and 4.16(c), respectively. Qualitatively, it is verified that the filter estimates are similar to the aiding sensor measurements, smoothed by the inertial measurement integration. This blending in the frequency domain of the aiding and inertial sensors data is according to the complementary transfer functions depicted in Fig. 4.5 and derived in Section 4.3.1.

The experimental results obtained on-board the DELFIMx catamaran validate the proposed navigation system architecture. The adopted design parameters yield the desired sensor fusion in the frequency domain, and produce good attitude and position estimation and rate gyro bias compensation results in the time domain. The attitude and position estimates were consistent with the trajectory profile, and the navigation system endured GPS outage, which shows that the proposed complementary filter based architecture is suitable for the oceanic application under study.

## 4.4 Conclusions

Complementary filters for attitude and position estimation were proposed, and their stability and performance properties were derived theoretically. Using the Euler angles parameterization, the attitude filter compensates for rate gyro bias and is stable for trajectories described by nonsingular configurations. The position filter estimates velocity in body coordinates and position in Earth frame, and is asymptotically stable. The attitude and position complementary filters were integrated to produce a complete navigation system, whose structure can be represented in a simple block diagram and, using steady-state feed-

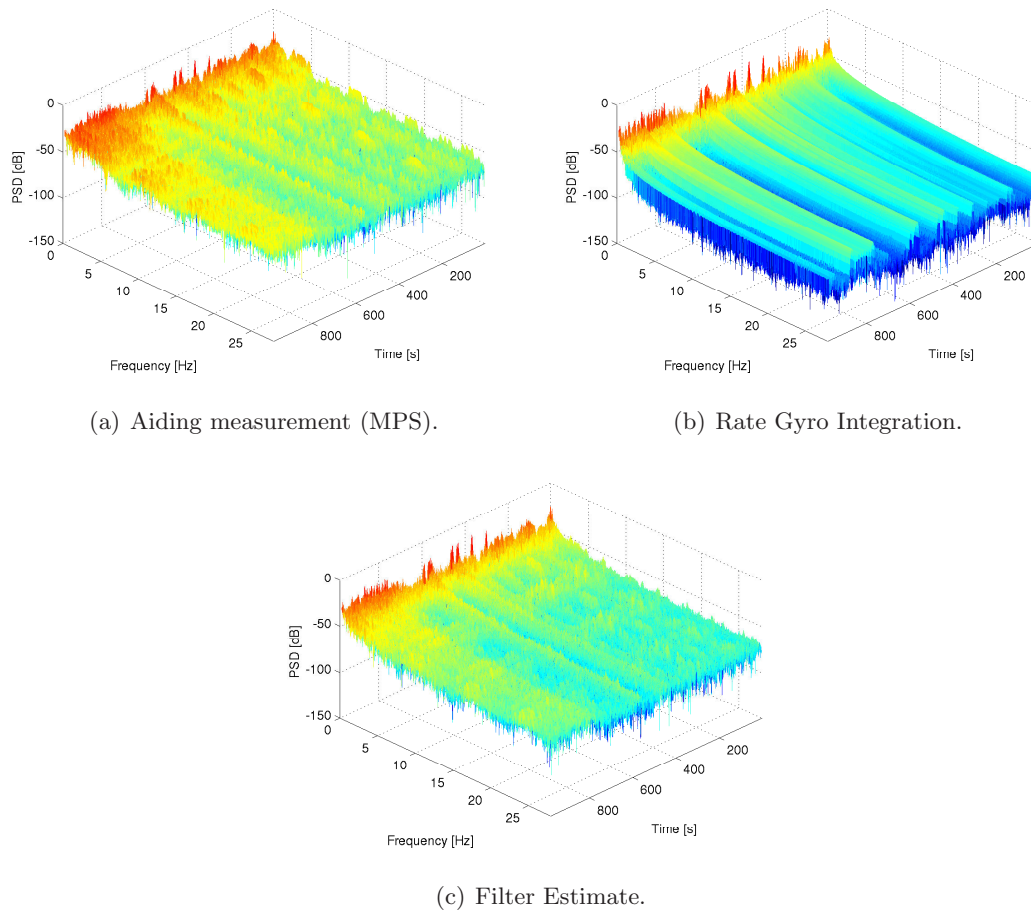


Figure 4.14: Spectrograms of the yaw measurements and filter estimate.

back gains, was easily implemented on a low-cost, low-power consumption hardware. The filter gains are computed using frequency domain design to shape a frequency response that exploits the low-frequency contents of the aiding sensors and the high-frequency contents of the inertial sensors. Implementation aspects were detailed, namely an attitude aiding observation based on magnetic and pendular measurements was derived, and the problem of multiple sampling rates was tackled using optimal results for periodic systems. The navigation system was validated using experimental data, in tests at sea with the DELFIMx catamaran. Rate gyro bias was compensated for, and the complementary frequency contents of the aiding and the inertial sensors produced good attitude and position estimates. Also, the navigation system was shown to yield accurate results and small drift in the case of GPS outage.

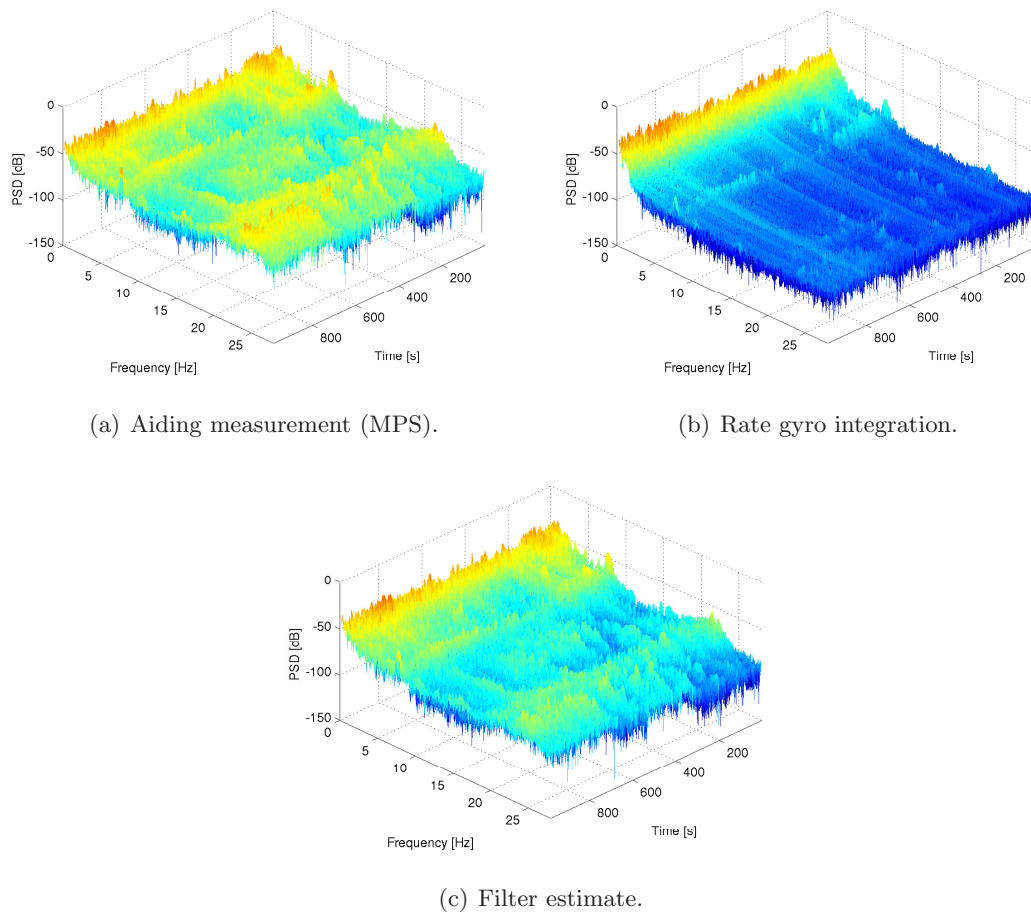
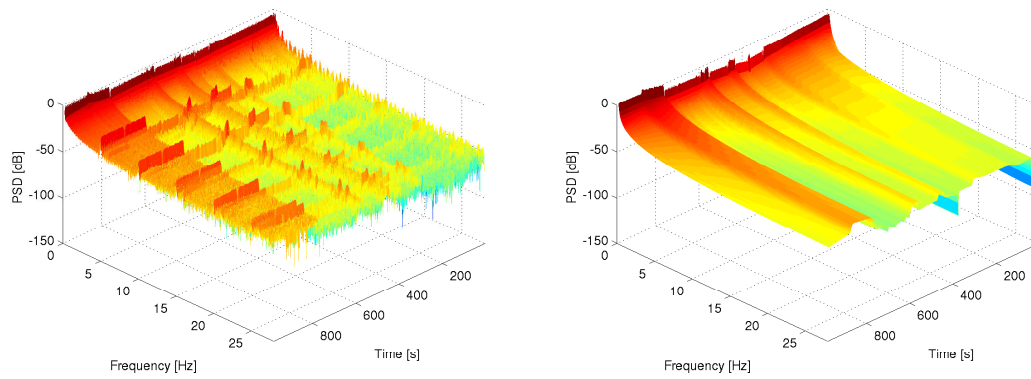
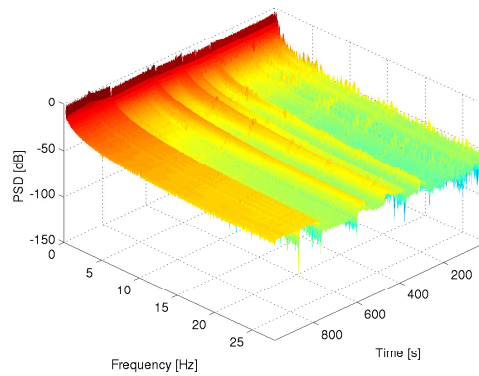


Figure 4.15: Spectrograms of the pitch measurements and filter estimate.



(a) Aiding Observation (GPS).

(b) Accelerometer Integration.



(c) Filter Estimate.

Figure 4.16: Spectrograms of the  $\mathbf{p}_x$  measurements and filter estimate.



## Chapter 5

# Landmark based nonlinear navigation system

This chapter addresses the problem of nonlinear observer design, for position and attitude estimation based on landmark readings and velocity measurements. A nonlinear observer formulated on  $SE(3)$  is derived constructively, using a Lyapunov function conveniently defined by the landmark measurement error. The derived observer yields almost global asymptotic stability (GAS) of the desired equilibrium point on  $SE(3)$ , and exponential convergence of the attitude and position estimates.

The proposed feedback laws are explicit functions of the landmark measurements and velocity readings, exploiting the sensor information directly in the observer, and providing for a geometric insight on the properties of the observer. Namely, the necessary and sufficient landmark configuration for attitude and position determination is discussed, and the asymptotic convergence of the observer estimates is characterized given the landmark geometry and the observer design parameters, that can be thus modified to shape the directionality of the system.

The problem of non-ideal velocity readings is also addressed, and the observer is augmented to compensate for bias in the angular and linear velocity readings. The resulting position, attitude, and bias estimation errors are shown to converge exponentially fast to the desired equilibrium points, for bounded initial estimation errors. Simulation results for trajectories described by time-varying linear and angular velocities, and for distinct initial conditions on  $SE(3)$ , are presented to illustrate the stability and convergence properties of the observer.

The chapter is organized as follows. In Section 5.1, the position and attitude estimation problem is introduced and the available sensor information is detailed. The attitude and position observer is derived in Section 5.2. A convenient landmark-based coordinate transformation and Lyapunov function are defined, and the necessary and sufficient landmark configuration for attitude determination is discussed. The proposed Lyapunov function is decoupled into independent position and attitude components that are addressed separately, and almost global stabilizing feedback laws are obtained for attitude

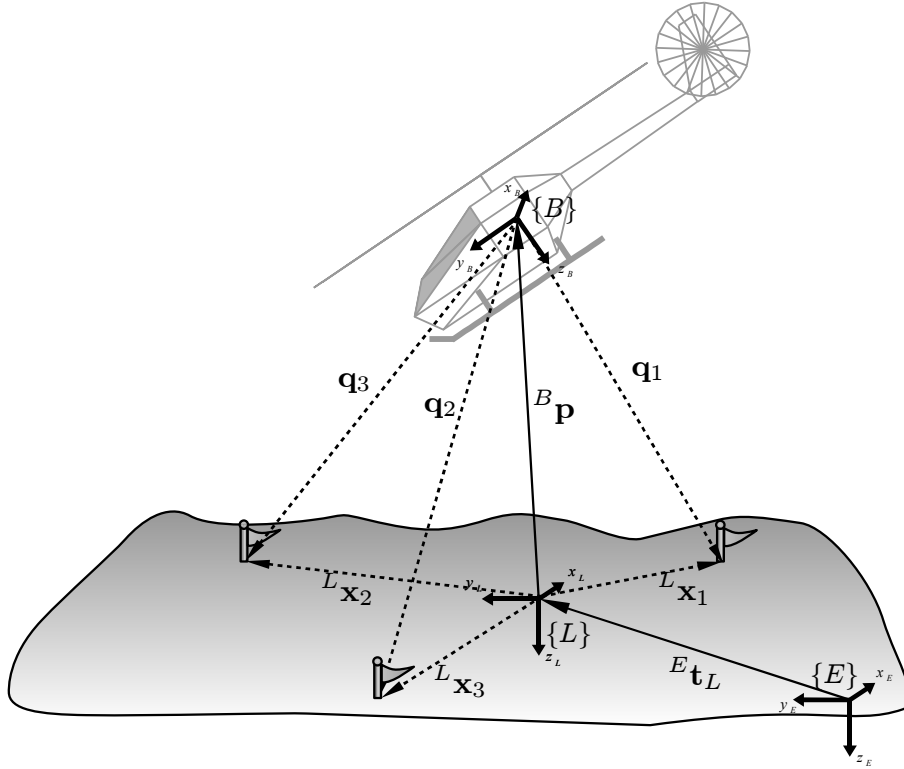


Figure 5.1: Landmark based navigation.

and position estimation. The resulting observer dynamics are expressed as a function of the sensor readings, and it is shown that the asymptotic convergence of the system trajectories is determined by the landmark geometry, and by the design parameters. The problem of unknown velocity sensor bias is studied in Section 5.3. The observer dynamics are extended to dynamically compensate for the bias in the linear and angular velocity measurements, and stability results are derived. In Section 5.4, simulation results illustrate the observer properties for time-varying linear and angular velocities. Concluding remarks are presented in Section 5.5.

## 5.1 Problem formulation

Landmark based navigation, illustrated in Fig. 5.1, can be summarized as the problem of determining attitude and position of a rigid body using landmark observations and velocity measurements, given by sensors installed onboard the autonomous platform. The rigid body kinematics are described by

$$\dot{\mathcal{R}} = \mathcal{R}(\boldsymbol{\omega})_{\times}, \quad {}^B \dot{\mathbf{p}} = {}^B \mathbf{v} - (\boldsymbol{\omega})_{\times} {}^B \mathbf{p}, \quad (5.1)$$

where  $\mathcal{R}$  is the shorthand notation for the rotation matrix  ${}^L_B \mathbf{R}$  from body frame  $\{B\}$  to local frame  $\{L\}$  coordinates,  $\boldsymbol{\omega}$  and  ${}^B \mathbf{v}$  are the body angular and linear velocities, respectively, expressed in  $\{B\}$ ,  ${}^B \mathbf{p}$  is the position of the rigid body with respect to  $\{L\}$

expressed in  $\{B\}$ , and  ${}^B\dot{\mathbf{p}}$  denotes the time derivative of  ${}^B\mathbf{p}$ , that is  $\frac{d{}^B\mathbf{p}}{dt}$ .

The body angular and linear velocities are measured by a rate gyro sensor triad and a Doppler sensor, respectively

$$\boldsymbol{\omega}_r = \boldsymbol{\omega}, \quad \mathbf{v}_r = {}^B\mathbf{v}. \quad (5.2)$$

The landmark measurements, denoted as  $\mathbf{q}_i$  and illustrated in Fig. 5.1, are obtained by on-board sensors that are able to track terrain characteristics, such as CCD cameras or ladars,

$$\mathbf{q}_i = \mathcal{R}'L\mathbf{x}_i - {}^B\mathbf{p}, \quad (5.3)$$

where  ${}^L\mathbf{x}_i$  represent the coordinates of landmark  $i$  in the local frame  $\{L\}$ . The concatenation of (5.3) is expressed in matrix form as

$$\mathbf{Q} = \mathcal{R}'\mathbf{X} - {}^B\mathbf{p}\mathbf{1}'_n,$$

where  $\mathbf{Q} = [\mathbf{q}_1 \ \dots \ \mathbf{q}_n]$ ,  $\mathbf{X} = [{}^L\mathbf{x}_1 \ \dots \ {}^L\mathbf{x}_n]$ ,  $\mathbf{Q}, \mathbf{X} \in \mathbb{M}(3, n)$ . Without loss of generality, the origin of the local frame is defined at the landmarks centroid, as depicted in Fig. 5.1, bearing

$$\sum_{i=1}^n {}^L\mathbf{x}_i = \mathbf{X}\mathbf{1}_n = \mathbf{0}. \quad (5.4)$$

The proposed observer reproduces the rigid body kinematics (5.1), taking the form

$$\dot{\hat{\mathcal{R}}} = \hat{\mathcal{R}}(\hat{\boldsymbol{\omega}})_\times, \quad {}^B\dot{\hat{\mathbf{p}}} = {}^B\hat{\mathbf{v}} - (\hat{\boldsymbol{\omega}})_\times {}^B\hat{\mathbf{p}}, \quad (5.5)$$

where  $\hat{\boldsymbol{\omega}}$  and  ${}^B\hat{\mathbf{v}}$  are the feedback terms constructed to compensate for the attitude and position estimation errors.

The position and attitude errors are defined as  ${}^B\tilde{\mathbf{p}} := {}^B\hat{\mathbf{p}} - {}^B\mathbf{p}$  and  $\tilde{\mathcal{R}} := \hat{\mathcal{R}}\mathcal{R}'$ , respectively. The Euler angle-axis parameterization of the rotation error matrix  $\tilde{\mathcal{R}}$  is described by the rotation vector  $\boldsymbol{\phi} \in \mathbb{S}(2)$  and by the rotation angle  $\varphi \in [0 \ \pi]$ , yielding the DCM formulation [107]

$$\tilde{\mathcal{R}} = \text{rot}(\varphi, \boldsymbol{\phi}) := \cos(\varphi)\mathbf{I} + \sin(\varphi)(\boldsymbol{\phi})_\times + (1 - \cos(\varphi))\boldsymbol{\phi}\boldsymbol{\phi}'. \quad (5.6)$$

While the observer results are formulated directly in the SE(3) manifold, the rotation angle  $\varphi$  is adopted to characterize some of the convergence properties of the observer.

The attitude and position error dynamics are a function of the linear and angular velocity estimates and given by

$$\dot{\tilde{\mathcal{R}}} = \tilde{\mathcal{R}}(\mathcal{R}(\hat{\boldsymbol{\omega}} - \boldsymbol{\omega}))_\times, \quad (5.7a)$$

$${}^B\dot{\tilde{\mathbf{p}}} = ({}^B\hat{\mathbf{v}} - {}^B\mathbf{v}) - (\boldsymbol{\omega})_\times {}^B\tilde{\mathbf{p}} + ({}^B\hat{\mathbf{p}})_\times (\hat{\boldsymbol{\omega}} - \boldsymbol{\omega}). \quad (5.7b)$$

The attitude and position feedback laws are obtained by defining  $\hat{\boldsymbol{\omega}}$  and  ${}^B\hat{\mathbf{v}}$  as a function of the velocity readings (5.2) and landmark observations (5.3), so that the closed loop position

and attitude estimation errors converge asymptotically to the origin, i.e.  $\tilde{\mathcal{R}} \rightarrow \mathbf{I}$ ,  ${}^B\tilde{\mathbf{p}} \rightarrow 0$  as  $t \rightarrow \infty$ .

The observer for the case of unbiased velocity measurements is presented first to motivate the derivation of the attitude and position feedback laws, and expose topological limitations to global stabilization. The cases of biased linear and angular velocity measurements are considered in the ensuing.

## 5.2 Observer synthesis with ideal velocity measurements

In this section, the attitude and position feedback laws are derived for the case of ideal angular and linear velocity measurements, expressed in (5.2). It is shown that the proposed Lyapunov function is a linear combination of two independent position and attitude Lyapunov functions, which allows for the separate derivation of the position and attitude feedback laws. The closed loop system is demonstrated to have an almost GAS equilibrium point at  $\tilde{\mathcal{R}} = \mathbf{I}$ ,  ${}^B\tilde{\mathbf{p}} = 0$ , and the trajectories are shown to converge exponentially fast to the origin.

Some relevant characteristics of the observer are pointed out. It is shown that the position and attitude feedback laws can be expressed as an explicit function of the sensor readings, allowing for the observer implementation in practice. Also, the asymptotic behavior of the attitude observer trajectories are studied in the Euler angle-axis representation, characterizing the directionality of the observer estimates given the directionality of the design feedback law.

### 5.2.1 Synthesis Lyapunov function properties

The observer is derived resorting to Lyapunov's stability theory. To exploit the landmark readings information, vector and position measurements are constructed from a linear combination of (5.3), producing respectively

$${}^B\mathbf{u}_j = \sum_{i=1}^{n-1} a_{ij}(\mathbf{q}_{i+1} - \mathbf{q}_i), \quad {}^B\mathbf{u}_n = -\frac{1}{n} \sum_{i=1}^n \mathbf{q}_i, \quad (5.8)$$

where  $j = 1, \dots, n-1$ . The transformation (5.8) can be expressed in matrix form as

$${}^B\mathbf{U}_X = \mathbf{Q}\mathbf{D}_X\mathbf{A}_X = \mathcal{R}'\mathbf{U}_X, \quad {}^B\mathbf{u}_n = \mathbf{Q}\mathbf{d}_p = {}^B\mathbf{p}, \quad (5.9)$$

where the matrices  $\mathbf{A}_X \in \mathbb{M}(n-1)$ ,  ${}^B\mathbf{U}_X, \mathbf{U}_X \in \mathbb{M}(3, n-1)$ ,  $\mathbf{D}_X \in \mathbb{M}(n, n-1)$  are given by

$${}^B\mathbf{U}_X = \begin{bmatrix} {}^B\mathbf{u}_1 & \dots & {}^B\mathbf{u}_{n-1} \end{bmatrix}, \quad \mathbf{D}_X = \begin{bmatrix} \mathbf{0}_{1 \times n-1} \\ \mathbf{I}_{n-1} \end{bmatrix} - \begin{bmatrix} \mathbf{I}_{n-1} \\ \mathbf{0}_{1 \times n-1} \end{bmatrix},$$

$$\mathbf{A}_X = [a_{ij}], \quad \mathbf{U}_X = \mathbf{X}\mathbf{D}_X\mathbf{A}_X, \quad \mathbf{d}_p = -\frac{1}{n}\mathbf{1}_n,$$

and the fact that  $\mathbf{p}\mathbf{1}'_n\mathbf{D}_X = \mathbf{0} \Rightarrow \mathbf{Q}\mathbf{D}_X = \mathcal{R}'\mathbf{X}\mathbf{D}_X$  and that (5.4) implies that  $\mathbf{X}\mathbf{d}_p = \mathbf{0} \Rightarrow \mathbf{Q}\mathbf{d}_p = {}^B\mathbf{p}$ , were used. The linear transformation  $\mathbf{A}_X$  is considered invertible by construction.

An estimate of the landmarks coordinates in body frame can be obtained using the observer estimates  $\hat{\mathcal{R}}$  and  ${}^B\hat{\mathbf{p}}$ , yielding

$$\hat{\mathbf{q}}_i = \hat{\mathcal{R}}'L\mathbf{x}_i - {}^B\hat{\mathbf{p}},$$

where  $\hat{\mathbf{q}}_i$  denotes the coordinate estimate of landmark  $i$ , and the coordinates of the landmarks in the local frame  $L\mathbf{x}_i$  are known. The estimates of the transformed landmarks (5.9) are described by

$${}^B\hat{\mathbf{U}}_X = \hat{\mathcal{R}}'\mathbf{U}_X, \quad {}^B\hat{\mathbf{u}}_n = {}^B\hat{\mathbf{p}}, \quad (5.10)$$

where the columns of  ${}^B\hat{\mathbf{U}}_X$  and  $\mathbf{U}_X$  are denoted as  ${}^B\hat{\mathbf{u}}_i$  and  $L\mathbf{u}_i$ , respectively, i.e.  ${}^B\hat{\mathbf{U}}_X = \begin{bmatrix} {}^B\hat{\mathbf{u}}_1 & \dots & {}^B\hat{\mathbf{u}}_{n-1} \end{bmatrix}$ , and  $\mathbf{U}_X = \begin{bmatrix} L\mathbf{u}_1 & \dots & L\mathbf{u}_{n-1} \end{bmatrix}$ .

The candidate Lyapunov function is defined by the estimation error of the transformed vectors

$$V = \frac{1}{2} \sum_{i=1}^n \|{}^B\hat{\mathbf{u}}_i - {}^B\mathbf{u}_i\|^2, \quad (5.11)$$

that can be described as a linear combination of distinct position and attitude components, as presented next.

**Proposition 5.1.** *The Lyapunov function (5.11) is characterized by distinct attitude and position components  $V = V_{\mathcal{R}} + V_p$ . The attitude component is given by*

$$\begin{aligned} V_{\mathcal{R}} &= \frac{1}{2} \sum_{i=1}^{n-1} \|{}^B\hat{\mathbf{u}}_i - {}^B\mathbf{u}_i\|^2 = \text{tr} \left[ (\mathbf{I} - \tilde{\mathcal{R}})\mathbf{U}_X\mathbf{U}_X' \right] \\ &= \frac{1}{4} \|\mathbf{I} - \tilde{\mathcal{R}}\|^2 \boldsymbol{\phi}'\mathbf{P}\boldsymbol{\phi} = (1 - \cos(\varphi)) \boldsymbol{\phi}'\mathbf{P}\boldsymbol{\phi}, \end{aligned} \quad (5.12)$$

where

$$\mathbf{P} = \text{tr}(\mathbf{U}_X\mathbf{U}_X')\mathbf{I} - \mathbf{U}_X\mathbf{U}_X', \quad (5.13)$$

and the position component is given by

$$V_p = \frac{1}{2} \|{}^B\hat{\mathbf{u}}_n - {}^B\mathbf{u}_n\|^2 = \frac{1}{2} {}^B\tilde{\mathbf{p}}'{}^B\tilde{\mathbf{p}}. \quad (5.14)$$

*Proof.* The decoupling is obtained by straightforward algebraic manipulation of (5.11),

$$V = \frac{1}{2} \sum_{i=1}^{n-1} \|{}^B\hat{\mathbf{u}}_i - {}^B\mathbf{u}_i\|^2 + \frac{1}{2} \|{}^B\hat{\mathbf{u}}_n - {}^B\mathbf{u}_n\|^2 = V_{\mathcal{R}} + V_p.$$

The alternative formulations for the attitude component of the Lyapunov function, expressed in (5.12), are obtained using the properties of the trace, presented Appendix A, producing

$$\begin{aligned} V_{\mathcal{R}} &= \frac{1}{2} \sum_{i=1}^{n-1} \|{}^B\hat{\mathbf{u}}_i - {}^B\mathbf{u}_i\|^2 = \frac{1}{2} \sum_{i=1}^{n-1} \|(\hat{\mathcal{R}}' - \mathcal{R}')L\mathbf{u}_i\|^2 \\ &= \frac{1}{2} \sum_{i=1}^{n-1} \|(\mathbf{I} - \tilde{\mathcal{R}})L\mathbf{u}_i\|^2 = \frac{1}{2} \text{tr} \left[ (\mathbf{I} - \tilde{\mathcal{R}})(\mathbf{I} - \tilde{\mathcal{R}})'\mathbf{U}_X\mathbf{U}_X' \right]. \end{aligned}$$

Applying the properties of the rotation matrix and the DCM expansion (5.6) yields

$$\begin{aligned} V_{\mathcal{R}} &= \text{tr} \left[ (\mathbf{I} - \tilde{\mathcal{R}}) \mathbf{U}_X \mathbf{U}'_X \right] = \text{tr} \left[ (1 - \cos(\varphi)) (\mathbf{I} - \phi \phi') \mathbf{U}_X \mathbf{U}'_X \right] \\ &= (1 - \cos(\varphi)) \phi' (\text{tr}(\mathbf{U}_X \mathbf{U}'_X) \mathbf{I} - \mathbf{U}_X \mathbf{U}'_X) \phi = (1 - \cos(\varphi)) \phi' \mathbf{P} \phi. \end{aligned}$$

□

The derivation of the Lyapunov function along the system trajectories is characterized in the following statement.

**Lemma 5.2.** *The time derivatives of proposed Lyapunov functions (5.12) and (5.14) are respectively given by*

$$\dot{V}_{\mathcal{R}} = \left( \mathbf{U}_X \mathbf{U}'_X \tilde{\mathcal{R}} - \tilde{\mathcal{R}}' \mathbf{U}_X \mathbf{U}'_X \right)'_{\otimes} \mathcal{R}(\hat{\boldsymbol{\omega}} - \boldsymbol{\omega}) = \phi' \mathbf{P} \mathbf{Q}(\varphi, \phi) \mathcal{R}(\hat{\boldsymbol{\omega}} - \boldsymbol{\omega}), \quad (5.15a)$$

$$\dot{V}_p = {}^B \tilde{\mathbf{p}}' \left( ({}^B \hat{\mathbf{p}} \right)_{\times} (\hat{\boldsymbol{\omega}} - \boldsymbol{\omega}) + ({}^B \hat{\mathbf{v}} - {}^B \mathbf{v}) \right), \quad (5.15b)$$

where  $\mathbf{Q}(\varphi, \phi) = \sin(\varphi) \mathbf{I} + (1 - \cos(\varphi)) (\phi)_{\times}$ .

*Proof.* Deriving the Lyapunov function (5.14) with respect to time and using (5.7b) yields

$$\begin{aligned} \dot{V}_p &= {}^B \tilde{\mathbf{p}}' \dot{{}^B \mathbf{p}} = {}^B \tilde{\mathbf{p}}' ({}^B \hat{\mathbf{v}} - {}^B \mathbf{v}) - {}^B \tilde{\mathbf{p}}' (\boldsymbol{\omega})_{\times} {}^B \tilde{\mathbf{p}} + {}^B \tilde{\mathbf{p}}' ({}^B \hat{\mathbf{p}})_{\times} (\hat{\boldsymbol{\omega}} - \boldsymbol{\omega}) \\ &= {}^B \tilde{\mathbf{p}}' \left( ({}^B \hat{\mathbf{p}} \right)_{\times} (\hat{\boldsymbol{\omega}} - \boldsymbol{\omega}) + ({}^B \hat{\mathbf{v}} - {}^B \mathbf{v}) \right). \end{aligned}$$

Deriving the Lyapunov function (5.12) with respect to time and using (5.7a) yields

$$\dot{V}_{\mathcal{R}} = -\text{tr}(\dot{\tilde{\mathcal{R}}} \mathbf{U}_X \mathbf{U}'_X) = -\text{tr}((\mathcal{R}(\hat{\boldsymbol{\omega}} - \boldsymbol{\omega}))_{\times} \mathbf{U}_X \mathbf{U}'_X \tilde{\mathcal{R}}). \quad (5.16)$$

Using the properties of the trace, presented in Appendix A, produces

$$\begin{aligned} \dot{V}_{\mathcal{R}} &= -\frac{1}{2} \text{tr}((\mathcal{R}(\hat{\boldsymbol{\omega}} - \boldsymbol{\omega}))_{\times} (\mathbf{U}_X \mathbf{U}'_X \tilde{\mathcal{R}} - \tilde{\mathcal{R}}' \mathbf{U}_X \mathbf{U}'_X)) \\ &= \left( \mathbf{U}_X \mathbf{U}'_X \tilde{\mathcal{R}} - \tilde{\mathcal{R}}' \mathbf{U}_X \mathbf{U}'_X \right)'_{\otimes} \mathcal{R}(\hat{\boldsymbol{\omega}} - \boldsymbol{\omega}), \end{aligned}$$

which yields the first formulation expressed in (5.15a). Define the auxiliary quantities  $\mathbf{a} = \mathcal{R}(\hat{\boldsymbol{\omega}} - \boldsymbol{\omega})$  and  $\mathbf{W} = \mathbf{U}_X \mathbf{U}'_X$ . Using  $\tilde{\mathcal{R}} = \mathbf{I} + \mathbf{Q}(\varphi, \phi) (\phi)_{\times}$ ,  $\mathbf{Q}(\varphi, \phi) \phi = \phi \sin(\varphi)$  and the properties of the trace in (5.16), bears

$$\begin{aligned} \dot{V}_{\mathcal{R}} &= -\text{tr}((\mathbf{a})_{\times} \mathbf{W} (\mathbf{I} + \mathbf{Q}(\varphi, \phi) (\phi)_{\times})) = -\text{tr}((\phi)_{\times} (\mathbf{a})_{\times} \mathbf{W} \mathbf{Q}(\varphi, \phi)) \\ &= -\text{tr}((\mathbf{a} \phi' - \mathbf{a}' \phi \mathbf{I}) \mathbf{W} \mathbf{Q}(\varphi, \phi)) = -\phi' \mathbf{W} \mathbf{Q}(\varphi, \phi) \mathbf{a} + \text{tr}(\mathbf{W}) \mathbf{a}' \phi \sin(\varphi) \\ &= -\phi' \mathbf{W} \mathbf{Q}(\varphi, \phi) \mathbf{a} + \text{tr}(\mathbf{W}) \mathbf{a}' \mathbf{Q}(\varphi, \phi) \phi = \phi' (\text{tr}(\mathbf{W}) - \mathbf{W}) \mathbf{Q}(\varphi, \phi) \mathbf{a} \\ &= \phi' \mathbf{P} \mathbf{Q}(\varphi, \phi) \mathbf{a} = \phi' \mathbf{P} \mathbf{Q}(\varphi, \phi) \mathcal{R}(\hat{\boldsymbol{\omega}} - \boldsymbol{\omega}), \end{aligned}$$

which concludes the proof. □

The Lyapunov function (5.11), based on the estimation error of the transformed landmark measurements, is adopted to derive a feedback law  $\hat{\boldsymbol{\omega}}$  and  ${}^B \hat{\mathbf{v}}$  that stabilizes the attitude and position errors. The decoupling property of the Lyapunov function allows for the attitude and position estimation problems to be addressed separately. The feedback law for the attitude kinematics (5.7a) is derived using the Lyapunov function  $V_{\mathcal{R}}$ , while the feedback law for the position kinematics (5.7b) relies on  $V_p$ .

### 5.2.2 Attitude feedback law

The attitude feedback law, derived in this section, exploits angular velocity sensors and landmark measurements. While velocity sensors allow for the propagation of attitude in time, attitude with respect to a reference frame is observed only by means of the landmark measurements. The geometric placement of the landmarks is required to satisfy the following assumption.

**Assumption 5.1** (Landmark Configuration). *The landmarks are not all collinear, that is,  $\text{rank}(\mathbf{X}) \geq 2$ .*

Assumption 5.1 formulates the necessary and sufficient landmark configuration under which zero observation error is equivalent to correct attitude estimation, i.e.  $\forall_{i=1..n-1} \|{}^B\hat{\mathbf{u}}_i - {}^B\mathbf{u}_i\| = 0 \Leftrightarrow \tilde{\mathcal{R}} = \mathbf{I}$ . This is shown in the following proposition, using the fact that the Lyapunov function  $V_{\mathcal{R}}$  expresses the landmark measurement error.

**Lemma 5.3.** *The Lyapunov function  $V_{\mathcal{R}}$ , expressed in (5.12), has a unique global minimum (at  $\tilde{\mathcal{R}} = \mathbf{I}$ ) if and only if Assumption 5.1 is verified.*

*Proof.* From (5.12), the zeros of  $V_{\mathcal{R}}$  are  $\varphi = 0$  or  $\phi \in \mathcal{N}(\mathbf{P})$ . To show that  $\mathbf{P} > 0$  if and only if  $\text{rank}(\mathbf{X}) \geq 2$ , denote the singular value decomposition of  $\mathbf{U}_X$  as  $\mathbf{U}_X = \mathbf{U}\mathbf{S}\mathbf{V}'$ , where  $\mathbf{U} \in \text{O}(3)$ ,  $\mathbf{V} \in \text{O}(n)$ , the off-diagonal elements of  $\mathbf{S} \in \text{M}(3, n)$  are zero ( $\forall_{i \neq j} s_{ij} = 0$ ) and the diagonal elements are the singular values of  $\mathbf{U}_X$ , i.e.  $s_{ii} = \sigma_i(\mathbf{U}_X)$ ,  $i \in \{1, 2, 3\}$ . Then

$$\begin{aligned} \mathbf{P} &= \text{tr}(\mathbf{U}_X \mathbf{U}'_X) \mathbf{I} - \mathbf{U}_X \mathbf{U}'_X = \text{tr}(\mathbf{S}^2) \mathbf{I} - \mathbf{U} \mathbf{S}^2 \mathbf{U}' \\ &= \mathbf{U} \text{diag}(s_{22}^2 + s_{33}^2, s_{11}^2 + s_{33}^2, s_{11}^2 + s_{22}^2) \mathbf{U}' \end{aligned}$$

and hence  $\mathbf{P} > 0$  if and only if  $s_{22}, s_{33} \neq 0$ , i.e.  $\text{rank}(\mathbf{U}_X) \geq 2$ . Given that  $\mathbf{A}_X$  and  $\begin{bmatrix} \mathbf{D}_X & \mathbf{1}_n \end{bmatrix}$  are nonsingular, the equality

$$\text{rank}(\mathbf{U}_X) = \text{rank} \left( \begin{bmatrix} \mathbf{U}_X & \mathbf{0}_3 \end{bmatrix} \right) = \text{rank} \left( \mathbf{X} \begin{bmatrix} \mathbf{D}_X & \mathbf{1}_n \end{bmatrix} \begin{bmatrix} \mathbf{A}_X & \mathbf{0}_{n-1} \\ \mathbf{0}'_{n-1} & 1 \end{bmatrix} \right) = \text{rank}(\mathbf{X}),$$

completes the proof.  $\square$

It is instructive to analyze why a landmark configuration given by  $\text{rank}(\mathbf{X}) = 1$  is not sufficient to determine the attitude of the rigid body. If all  ${}^L\mathbf{x}_i$  are collinear, then all  ${}^L\mathbf{u}_i$  are collinear and any  $\tilde{\mathcal{R}} = \text{rot}(\varphi, {}^L\mathbf{u}_i / \|{}^L\mathbf{u}_i\|)$  satisfies  ${}^B\hat{\mathbf{u}}_i = {}^B\mathbf{u}_i$ , i.e. the estimated and observed landmarks are identical for some  $\tilde{\mathcal{R}} \neq \mathcal{R}$ . This is related to the well known fact that a single vector observation (such as the Earth's magnetic field) yields attitude information except for the rotation about the vector itself [88, 140].

Given the Lyapunov function derivatives along the system trajectories (5.15a), consider the following feedback law,

$$\hat{\omega} = \omega_r - k_\omega \mathbf{s}_\omega, \quad (5.17)$$

where the feedback term is given by

$$\mathbf{s}_\omega = \mathcal{R}' \left( \mathbf{U}_X \mathbf{U}'_X \tilde{\mathcal{R}} - \tilde{\mathcal{R}}' \mathbf{U}_X \mathbf{U}'_X \right)_{\otimes} = \mathcal{R}' \mathbf{Q}'(\varphi, \boldsymbol{\phi}) \mathbf{P} \boldsymbol{\phi}, \quad (5.18)$$

and  $k_\omega$  is a positive scalar. The attitude feedback yields the autonomous attitude error dynamics

$$\dot{\tilde{\mathcal{R}}} = -k_\omega \tilde{\mathcal{R}} (\mathbf{U}_X \mathbf{U}'_X \tilde{\mathcal{R}} - \tilde{\mathcal{R}}' \mathbf{U}_X \mathbf{U}'_X), \quad (5.19)$$

and a negative semidefinite derivative for  $V_{\mathcal{R}}$  given by

$$\dot{V}_{\mathcal{R}} = -k_\omega \mathbf{s}'_\omega \mathbf{s}_\omega \leq 0.$$

It is immediate that the attitude feedback law produces a Lyapunov function that decreases along the system trajectories and, by LaSalle's invariance principle, guarantees global convergence to the largest invariant set contained in the set defined by  $\dot{V}_{\mathcal{R}} = 0$ .

**Lemma 5.4.** *Under Assumption 5.1, the set of points where  $\dot{V}_{\mathcal{R}} = 0$  is given by*

$$\begin{aligned} \mathcal{C}_{V_{\mathcal{R}}} &= \{ \tilde{\mathcal{R}} \in \text{SO}(3) : \tilde{\mathcal{R}} = \mathbf{I} \vee \tilde{\mathcal{R}} = \text{rot}(\pi, \boldsymbol{\phi} \in \text{eigvec}(\mathbf{P})) \} \\ &= \{ (\varphi, \boldsymbol{\phi}) \in \mathcal{D}_\phi : \varphi = 0 \vee (\varphi = \pi, \boldsymbol{\phi} \in \text{eigvec}(\mathbf{P})) \}, \end{aligned}$$

where  $\mathcal{D}_\phi = \begin{bmatrix} 0 & \pi \end{bmatrix} \times \text{S}(2)$ .

*Proof.* The points where  $\dot{V}_{\mathcal{R}} = 0$  are given by  $\mathbf{s}_\omega = 0 \Leftrightarrow \mathbf{Q}'(\varphi, \boldsymbol{\phi}) \mathbf{P} \boldsymbol{\phi} = 0$  and, therefore, satisfy  $\mathbf{P} \boldsymbol{\phi} \in \mathcal{N}(\mathbf{Q}'(\varphi, \boldsymbol{\phi}))$ , which is equivalent to

$$\mathbf{Q}'(\varphi, \boldsymbol{\phi}) \mathbf{P} \boldsymbol{\phi} = 0 \Leftrightarrow \sin(\varphi) \mathbf{P} \boldsymbol{\phi} - (1 - \cos(\varphi)) (\boldsymbol{\phi})_{\times} \mathbf{P} \boldsymbol{\phi} = 0.$$

Since, for any  $\mathbf{x} \in \mathbb{R}^3$ ,  $\mathbf{x}$  and  $(\boldsymbol{\phi})_{\times} \mathbf{x}$  are noncollinear,  $\mathbf{Q}'(\varphi, \boldsymbol{\phi}) \mathbf{P} \boldsymbol{\phi} = 0$  if and only if  $\varphi = 0$  or  $\varphi = \pi$ . For the  $\varphi = \pi$  case, the cross product of two vectors is null if and only if they are collinear,  $(\boldsymbol{\phi})_{\times} \mathbf{P} \boldsymbol{\phi} = 0 \Leftrightarrow \exists \alpha \mathbf{P} \boldsymbol{\phi} = \alpha \boldsymbol{\phi}$ , so  $\dot{V}_{\mathcal{R}} = 0$  if and only if  $\varphi = 0 \vee (\varphi = \pi \wedge \boldsymbol{\phi} \in \text{eigvec}(\mathbf{P}))$ .  $\square$

The open loop dynamics of the Euler angle-axis representation [17] are given by

$$\dot{\varphi} = \boldsymbol{\phi}' \mathcal{R} (\hat{\boldsymbol{\omega}} - \boldsymbol{\omega}), \quad \dot{\boldsymbol{\phi}} = \frac{1}{2} \left( \mathbf{I} - \frac{\sin(\varphi)}{1 - \cos(\varphi)} (\boldsymbol{\phi})_{\times} \right) (\boldsymbol{\phi})_{\times} \mathcal{R} (\hat{\boldsymbol{\omega}} - \boldsymbol{\omega}).$$

The closed loop dynamics are straightforward from (5.17)

$$\dot{\varphi} = -k_\omega \sin(\varphi) \boldsymbol{\phi}' \mathbf{P} \boldsymbol{\phi}, \quad (5.20a)$$

$$\dot{\boldsymbol{\phi}} = k_\omega (\boldsymbol{\phi})_{\times} (\boldsymbol{\phi})_{\times} \mathbf{P} \boldsymbol{\phi}, \quad (5.20b)$$

where the dynamics of  $\boldsymbol{\phi}$  are autonomous.

The closed loop dynamics (5.20) show that  $\mathcal{C}_{V_{\mathcal{R}}}$  is invariant and, from LaSalle's invariance principle, the attitude error converges to the set  $\mathcal{C}_{V_{\mathcal{R}}}$ . The equilibrium points  $\varphi = \pi$  illustrate the topological obstacles to global stabilization of the system (5.7a), arising from



the limitations of continuous state feedback on manifolds. As discussed in [13, 81, 97], the region of attraction of a stable equilibrium point is homeomorphic to some Euclidean vector space, which precludes global stabilization in  $\text{SO}(3)$  given that it is not diffeomorphic to an Euclidean vector space.

However, convergence for almost all initial conditions can be obtained, bearing that any trajectory emanating from outside a set of zero measure is attracted to the origin. In the present case, the set  $\varphi = \pi$  has zero measure, and the convergence of the trajectories emanating outside this set, i.e.  $\varphi(t_0) < \pi$  can be studied. To show that the trajectories of the closed loop converge to the origin  $\tilde{\mathcal{R}} = \mathbf{I}$  for any initial condition outside a zero measure set, the notion of global stability is relaxed by introducing the definitions of region of attraction and almost global stability [5, 78, 125].

**Definition 5.1** (Region of Attraction [78]). Consider the autonomous system  $\dot{\mathbf{x}} = f(\mathbf{x})$  evolving on a smooth manifold  $\mathcal{M}$ , where  $\mathbf{x} \in \mathcal{M}$  and  $f : \mathcal{M} \rightarrow T\mathcal{M}$  is a locally Lipschitz manifold map. Suppose that  $\mathbf{x} = \mathbf{x}^*$  is an asymptotically stable equilibrium point of the system. The region of attraction of  $\mathbf{x}^*$  is defined as

$$R_A = \{\mathbf{x}_0 \in \mathcal{M} : \phi(t, \mathbf{x}_0) \rightarrow \mathbf{x}^* \text{ as } t \rightarrow \infty\},$$

where  $\phi(t, \mathbf{x}_0)$  denotes the solution of the system with initial condition  $\mathbf{x} = \mathbf{x}_0$ .

**Definition 5.2** (Almost GAS [5, 78]). Consider the autonomous system  $\dot{\mathbf{x}} = f(\mathbf{x})$  evolving on a smooth manifold  $\mathcal{M}$ , where  $\mathbf{x} \in \mathcal{M}$  and  $f : \mathcal{M} \rightarrow T\mathcal{M}$  is a locally Lipschitz manifold map. The equilibrium point  $\mathbf{x} = \mathbf{x}^*$  is said to be almost globally asymptotically stable if it is stable and  $\mathcal{M} \setminus R_A$  is a set of zero measure.

Defining the distance on  $\text{SO}(3)$  as that inherited by the Euclidean norm [104],  $d(\mathcal{R}_1, \mathcal{R}_2) = \|\mathcal{R}_1 - \mathcal{R}_2\|$ , the following theorem shows that the origin is almost globally asymptotically stable and that the trajectories converge exponentially fast to the desired equilibrium point.

**Theorem 5.5.** *The attitude error  $\tilde{\mathcal{R}} = \mathbf{I}$  of the closed-loop system (5.19) is an exponentially stable and almost globally asymptotically stable equilibrium point, with the region of attraction given by*

$$\begin{aligned} R_A &= \text{SO}(3) \setminus \{\tilde{\mathcal{R}} \in \text{SO}(3) : \|\mathbf{I} - \tilde{\mathcal{R}}\|^2 = 8\} \\ &= \{(\varphi, \phi) \in \text{D}_\phi : \varphi < \pi\}. \end{aligned}$$

For any  $\tilde{\mathcal{R}}(t_0) \in R_A$ , the solution of the system (5.19) satisfies

$$\|\tilde{\mathcal{R}}(t) - \mathbf{I}\| \leq \|\tilde{\mathcal{R}}(t_0) - \mathbf{I}\| e^{-\frac{1}{2}\gamma_{\mathcal{R}}(t-t_0)}, \quad (5.21)$$

where  $\gamma_{\mathcal{R}} = \frac{k_\omega}{4}(8 - \|\tilde{\mathcal{R}}(t_0) - \mathbf{I}\|^2)\sigma_3(\mathbf{P}) = k_\omega(1 + \cos(\varphi(t_0)))\sigma_3(\mathbf{P})$ .

*Proof.* Define the Lyapunov function

$$W_{\mathcal{R}} = \frac{\|\mathbf{I} - \tilde{\mathcal{R}}\|^2}{8} = \frac{1 - \cos(\varphi)}{2}, \quad \dot{W}_{\mathcal{R}} = -\frac{k_{\omega}}{2} \sin^2(\varphi) \phi' \mathbf{P} \phi. \quad (5.22)$$

The set of points where  $\dot{W}_{\mathcal{R}} = 0$  is given by

$$C_W = \{\tilde{\mathcal{R}} \in \text{SO}(3) : \tilde{\mathcal{R}} = \mathbf{I} \vee \tilde{\mathcal{R}} = \text{rot}(\pi, \phi)\}.$$

Since  $\dot{W}_{\mathcal{R}} \leq 0$ , the set contained in a Lyapunov function surface

$$\Omega_{\rho} = \{\tilde{\mathcal{R}} \in \text{SO}(3) : W_{\mathcal{R}} \leq \rho\}$$

is positively invariant [78], that is any trajectory starting at  $t_0$  in  $\Omega_{\rho}$  satisfies  $\tilde{\mathcal{R}}(t) \in \Omega_{\rho}$  for all  $t > t_0$ , where the dependence on time  $t$  is explicitly denoted for the sake of clarity.

Given that  $W_{\mathcal{R}} < 1 \Rightarrow \varphi < \pi$ , the Lyapunov function is strictly decreasing in  $\Omega_{\rho}$  for any  $\rho < 1$ , which implies that  $-[1 + \cos(\varphi(t))] < -[1 + \cos(\varphi(t_0))] < 0$ . Rewriting the Lyapunov function time derivative yields

$$\begin{aligned} \dot{W}(\tilde{\mathcal{R}}(t)) &= -k_{\omega}(1 + \cos(\varphi)) \phi' \mathbf{P} \phi W(\tilde{\mathcal{R}}(t)) \Rightarrow \\ \dot{W}(\tilde{\mathcal{R}}(t)) &\leq -k_{\omega}[1 + \cos(\varphi(t_0))] \sigma_3(\mathbf{P}) W(\tilde{\mathcal{R}}(t)) = -\gamma_{\mathcal{R}} W(\tilde{\mathcal{R}}(t)) \end{aligned}$$

Applying the comparison lemma [78] and  $W_{\mathcal{R}} = \frac{1}{8} \|\tilde{\mathcal{R}} - \mathbf{I}\|^2$  produces (5.21), which characterizes the trajectories for  $\varphi(t_0) < \pi$ .

Given the closed loop dynamics (5.20b), it is straightforward to show that  $\varphi(t_0) = \pi \Rightarrow \dot{\varphi} = 0$  so the set  $C_W \setminus \{\mathbf{I}\}$ , which corresponds to the boundary of  $R_A$ , is positively invariant, and hence  $R_A$  is the region of attraction of  $\tilde{\mathcal{R}} = \mathbf{I}$ .  $\square$

### 5.2.3 Position feedback law

The position feedback law is obtained using the methodology adopted for the attitude feedback law derivation. It is immediate that  $V_p$ , expressed in (5.14), is positive definite, and that  $V_p = 0$  if and only if  ${}^B \tilde{\mathbf{p}} = 0$ . Given the time derivative of the Lyapunov function (5.15b), the position feedback law for the system (5.7b) is defined as

$${}^B \hat{\mathbf{v}} = \mathbf{v}_r + ((\boldsymbol{\omega}_r)_{\times} - k_v \mathbf{I}) {}^B \tilde{\mathbf{p}} - ({}^B \hat{\mathbf{p}})_{\times} (\hat{\boldsymbol{\omega}} - \boldsymbol{\omega}_r) \quad (5.23a)$$

$$= {}^B \mathbf{v} + ((\boldsymbol{\omega})_{\times} - k_v \mathbf{I}) \mathbf{s}_v + k_{\omega} ({}^B \hat{\mathbf{p}})_{\times} \mathbf{s}_{\omega}, \quad (5.23b)$$

where the feedback term is

$$\mathbf{s}_v = {}^B \tilde{\mathbf{p}}, \quad (5.24)$$

and  $k_v$  is a positive scalar. The position feedback law produces a closed loop linear time-invariant system

$${}^B \dot{\tilde{\mathbf{p}}} = -k_v {}^B \tilde{\mathbf{p}}, \quad (5.25)$$

where the origin is clearly stable.

**Theorem 5.6.** *The equilibrium point  ${}^B\tilde{\mathbf{p}} = 0$  of the position error dynamics (5.25) is globally exponentially stable in  $\mathbb{R}^3$ .*

*Proof.* Exponential convergence to the origin is immediate from the solution of the linear time invariant system (5.25), given by  ${}^B\tilde{\mathbf{p}}(t) = e^{-k_v(t-t_0)}{}^B\tilde{\mathbf{p}}(t_0)$ .  $\square$

In some applications, it is necessary to estimate the position with respect to the origin of a specific coordinate frame  $\{E\}$ , described by

$${}^B\hat{\mathbf{p}}_E = {}^B\hat{\mathbf{p}} + {}^E\hat{\mathbf{R}}'{}^E\mathbf{t}_L, \quad (5.26)$$

where  ${}^E\mathbf{t}_L$  represents the coordinates of the origin of  $\{L\}$  with respect to  $\{E\}$ , expressed in  $\{E\}$ , as illustrated in Fig. 5.1. In other applications, it is of interest to estimate  ${}^B\hat{\mathbf{p}}_E$  expressed in Earth frame coordinates

$${}^E\hat{\mathbf{p}}_E = {}^E\hat{\mathbf{R}}{}^B\hat{\mathbf{p}} + {}^E\mathbf{t}_L.$$

The position estimation error of  ${}^B\hat{\mathbf{p}}_E$  and  ${}^E\hat{\mathbf{p}}_E$  are respectively given by

$${}^B\tilde{\mathbf{p}}_E = {}^B\tilde{\mathbf{p}} + {}^E\hat{\mathbf{R}}'(\mathbf{I} - \tilde{\mathcal{R}}'){}^E\mathbf{t}_L, \quad {}^E\tilde{\mathbf{p}}_E = (\tilde{\mathcal{R}} - \mathbf{I}){}^E\hat{\mathbf{R}}{}^B\tilde{\mathbf{p}} + {}^E\hat{\mathbf{R}}{}^B\tilde{\mathbf{p}}. \quad (5.27)$$

As presented in the following propositions, the estimation errors  ${}^B\tilde{\mathbf{p}}_E$  and  ${}^E\tilde{\mathbf{p}}_E$  converge exponentially fast to the origin. Without loss of generality, it is considered that the orientations of  $\{E\}$  and  $\{L\}$  are identical ( $\mathcal{R} = {}^E\hat{\mathbf{R}} = {}^L\hat{\mathbf{R}}$ ).

**Proposition 5.7.** *The position estimation error  ${}^B\tilde{\mathbf{p}}_E$  converges exponentially fast to the origin, with the bound*

$$\|{}^B\tilde{\mathbf{p}}_E(t)\| \leq e^{-\frac{1}{2}\gamma_{BE}(t-t_0)}c_{BE}, \quad (5.28)$$

where  $\gamma_{BE} = \min\{2k_v, \gamma_{\mathcal{R}}\}$  and  $c_{BE} = \|{}^B\tilde{\mathbf{p}}(t_0)\| + \|\tilde{\mathcal{R}}(t_0) - \mathbf{I}\| \|{}^E\mathbf{t}_L\|$ .

*Proof.* Using elementary properties of the Euclidean norm yields

$$\begin{aligned} \|{}^B\tilde{\mathbf{p}}_E\| &= \|{}^B\tilde{\mathbf{p}} + {}^E\hat{\mathbf{R}}'(\mathbf{I} - \tilde{\mathcal{R}}'){}^E\mathbf{t}_L\| \leq \|{}^B\tilde{\mathbf{p}}\| + \|\tilde{\mathcal{R}} - \mathbf{I}\| \|{}^E\mathbf{t}_L\| \\ &\leq e^{-k_v(t-t_0)}\|{}^B\tilde{\mathbf{p}}(t_0)\| + e^{-\frac{1}{2}\gamma_{\mathcal{R}}(t-t_0)}\|\tilde{\mathcal{R}}(t_0) - \mathbf{I}\| \|{}^E\mathbf{t}_L\| \\ &\leq e^{-\frac{1}{2}\gamma_{BE}(t-t_0)}(\|{}^B\tilde{\mathbf{p}}(t_0)\| + \|\tilde{\mathcal{R}}(t_0) - \mathbf{I}\| \|{}^E\mathbf{t}_L\|). \end{aligned}$$

$\square$

**Proposition 5.8.** *Assume that there exist positive scalars  $p_0$  and  $\gamma_v$  such that the position of the body satisfies*

$$\|{}^B\mathbf{p}(t)\| \leq e^{\frac{1}{2}\gamma_B(t-t_0)}p_0, \quad (5.29)$$

for some  $\gamma_B < \gamma_{\mathcal{R}}$ . Then, the position estimation error  ${}^E\tilde{\mathbf{p}}_E$  converges exponentially fast to the origin, with the bound

$$\|{}^E\tilde{\mathbf{p}}_E(t)\| \leq e^{-\frac{1}{2}\gamma_{EE}(t-t_0)}c_{EE},$$

where  $\gamma_{EE} = \min\{\gamma_{\mathcal{R}} - \gamma_B, 2k_v\}$  and  $c_{EE} = \|\tilde{\mathcal{R}}(t_0) - \mathbf{I}\|p_0 + \|{}^B\tilde{\mathbf{p}}(t_0)\|$ .

*Proof.* If  $\|{}^B\mathbf{p}\|$  satisfies (5.29), using (5.27) and the properties of the Euclidean norm produces

$$\begin{aligned}\|{}^E\tilde{\mathbf{p}}_E\| &= \|(\tilde{\mathcal{R}} - \mathbf{I})_B^E \mathbf{R}^B \mathbf{p} + {}_B^E \hat{\mathbf{R}}^B \tilde{\mathbf{p}}\| \leq \|\tilde{\mathcal{R}} - \mathbf{I}\| \|{}^B\mathbf{p}\| + \|{}^B\tilde{\mathbf{p}}\| \\ &\leq e^{-\frac{1}{2}(\gamma_{\mathcal{R}} - \gamma_B)(t-t_0)} \|\tilde{\mathcal{R}}(t_0) - \mathbf{I}\| p_0 + e^{-k_v(t-t_0)} \|{}^B\tilde{\mathbf{p}}(t_0)\| \\ &\leq e^{-\gamma_{EE}(t-t_0)} (\|\tilde{\mathcal{R}}(t_0) - \mathbf{I}\| p_0 + \|{}^B\tilde{\mathbf{p}}(t_0)\|).\end{aligned}$$

□

In many applications, the condition (5.29) is easily satisfied by choosing a sufficiently large  $p_0$  and a sufficiently small  $\gamma_B$ . In particular, if  $\|{}^B\mathbf{p}(t)\|$  is bounded, define  $p_0 = \max_{t \geq 0} \|{}^B\mathbf{p}(t)\|$  and small  $\gamma_B \approx 0$ . Although  ${}^E\tilde{\mathbf{p}}_E = 0$  and  ${}^B\tilde{\mathbf{p}}_E = 0$  are not exponentially stable according to the classical definition [78, 125], these quantities are bounded by an exponential decaying function. Interestingly enough, the observer formulation can be modified to produce exponential convergence of  ${}^B\tilde{\mathbf{p}}_E$ . The alternative derivation of the observer is presented in Appendix E.1, and, at the cost of a slightly more complex formulation, yields exponential stability results for the position estimate with respect to the Earth frame.

#### 5.2.4 Output feedback configuration

The feedback terms formulated in (5.18) and (5.24) are functions of the nominal attitude  $\mathcal{R}$  and position  $\mathbf{p}$ , which are not available directly from the landmark readings. In this section, it is shown that the position and attitude feedback laws, (5.17) and (5.23b) respectively, can be expressed as an explicit function of the velocity measurements (5.2), landmark readings (5.3), and observer estimates.

**Theorem 5.9.** *The dynamics of the attitude and position observer are explicit functions of the sensor readings and state estimates. The position and attitude dynamics are given by*

$$\dot{\tilde{\mathcal{R}}} = \tilde{\mathcal{R}}(\hat{\boldsymbol{\omega}})_{\times}, \quad {}^B\dot{\tilde{\mathbf{p}}} = {}^B\hat{\mathbf{v}} - (\hat{\boldsymbol{\omega}})_{\times} {}^B\hat{\mathbf{p}},$$

where the feedback terms are given by

$$\hat{\boldsymbol{\omega}} = \boldsymbol{\omega}_r - k_{\omega} \mathbf{s}_{\omega}, \quad {}^B\hat{\mathbf{v}} = \mathbf{v}_r + ((\boldsymbol{\omega}_r)_{\times} - k_v \mathbf{I}) \mathbf{s}_v + k_{\omega} ({}^B\hat{\mathbf{p}})_{\times} \mathbf{s}_{\omega},$$

and

$$\mathbf{s}_{\omega} = \sum_{i=1}^n (\hat{\mathcal{R}}' \mathbf{X} \mathbf{D}_X \mathbf{A}_X \mathbf{e}_i) \times (\mathbf{Q} \mathbf{D}_X \mathbf{A}_X \mathbf{e}_i), \quad \mathbf{s}_v = {}^B\hat{\mathbf{p}} + \frac{1}{n} \sum_{i=1}^n \mathbf{q}_i. \quad (5.30)$$

*Proof.* The formulation for the observer and the feedback terms  $\hat{\boldsymbol{\omega}}$  and  $\hat{\mathbf{v}}$  are presented in (5.5), (5.17) and (5.23a) respectively. Using the landmark measurement formulation (5.3) produces

$$\mathbf{s}_v = {}^B\hat{\mathbf{p}} + \frac{1}{n} \sum_{i=1}^n \mathbf{q}_i = {}^B\hat{\mathbf{p}} + \frac{1}{n} \sum_{i=1}^n L \mathbf{x}_i - \frac{1}{n} \sum_{i=1}^n {}^B\mathbf{p} = {}^B\hat{\mathbf{p}} - {}^B\mathbf{p} - \frac{1}{n} \sum_{i=1}^n L \mathbf{x}_i.$$

Using the property (5.4) bears  $\mathbf{s}_v = {}^B\tilde{\mathbf{p}}$ , as desired.

Using the properties of the skew and unskew operator, presented in Appendix A, and the rotation error definition in the formulation of  $\mathbf{s}_\omega$  expressed in (5.18), yields

$$\begin{aligned}\mathbf{s}_\omega &= \mathcal{R}' \left( \mathbf{U}_X \mathbf{U}'_X \tilde{\mathcal{R}} - \tilde{\mathcal{R}}' \mathbf{U}_X \mathbf{U}'_X \right)_{\otimes} = \left( \mathcal{R}' \mathbf{U}_X \mathbf{U}'_X \hat{\mathcal{R}} - \hat{\mathcal{R}}' \mathbf{U}_X \mathbf{U}'_X \mathcal{R} \right)_{\otimes} \\ &= \left( {}^B\mathbf{U}_X {}^B\hat{\mathbf{U}}'_X - {}^B\hat{\mathbf{U}}_X {}^B\mathbf{U}'_X \right)_{\otimes} = \left( \sum_{i=1}^n ({}^B\mathbf{u}_i {}^B\hat{\mathbf{u}}'_i - {}^B\hat{\mathbf{u}}_i {}^B\mathbf{u}'_i) \right)_{\otimes} \\ &= \left( \sum_{i=1}^n ({}^B\hat{\mathbf{u}}_i \times {}^B\mathbf{u}_i)_{\times} \right)_{\otimes} = \sum_{i=1}^n ({}^B\hat{\mathbf{u}}_i \times {}^B\mathbf{u}_i).\end{aligned}$$

Expanding  ${}^B\mathbf{u}_i$  and  ${}^B\hat{\mathbf{u}}_i$  using (5.9) and (5.10), respectively, produces

$${}^B\mathbf{u}_i = {}^B\mathbf{U}_X \mathbf{e}_i = \mathbf{Q} \mathbf{D}_X \mathbf{A}_X \mathbf{e}_i, \quad {}^B\hat{\mathbf{u}}_i = {}^B\hat{\mathbf{U}}_X \mathbf{e}_i = \hat{\mathcal{R}}' \mathbf{U}_X \mathbf{e}_i = \hat{\mathcal{R}}' \mathbf{X} \mathbf{D}_X \mathbf{A}_X \mathbf{e}_i,$$

which concludes the proof.  $\square$

### 5.2.5 Directionality of the observer estimates

The closed loop trajectories of the observer are analyzed in the Euler angle-axis parameterization, allowing for the characterization of asymptotic behavior of the solutions of the system (5.19) given the adopted landmark transformation and the associated matrix  $\mathbf{P}$ .

**Theorem 5.10.** *The origin of the system (5.20) is asymptotically stable, with region of attraction described by*

$$R_A = \{(\varphi, \phi) \in D_\lambda : \varphi < \pi\}.$$

*The attitude error angle  $\varphi$  decreases monotonically.*

*Let the singular values of  $\mathbf{P}$  satisfy  $\sigma_1(\mathbf{P}) > \sigma_2(\mathbf{P}) > \sigma_3(\mathbf{P})$ , the asymptotic convergence of the Euler axis is described by*

$$\begin{cases} \lim_{t \rightarrow \infty} \phi(t) = \text{sign}(\mathbf{n}'_3 \phi(t_0)) \mathbf{n}_3, & \text{if } \mathbf{n}'_3 \phi(t_0) \neq 0 \\ \lim_{t \rightarrow \infty} \phi(t) \in \{\mathbf{n}_1, \mathbf{n}_2\}, & \text{if } \mathbf{n}'_3 \phi(t_0) = 0 \end{cases},$$

where  $\mathbf{n}_i$  is the unit eigenvector of  $\mathbf{P}$  associated with  $\sigma_i(\mathbf{P})$ .

*Proof.* The region of attraction of  $\varphi = 0$  is immediate from Theorem 5.5. The Lyapunov function (5.22) is strictly decreasing in  $R_A$ , and

$$\forall_{t_2, t_1} W(\tilde{\mathcal{R}}(t_2)) < W(\tilde{\mathcal{R}}(t_1)) \Rightarrow \varphi(t_2) < \varphi(t_1),$$

so  $\varphi(t)$  converges monotonically to the origin.

The rotation vector dynamics (5.20b) are autonomous. Define the Lyapunov functions

$$V_s = 1 + s \mathbf{n}'_3 \phi, \quad \dot{V}_s = s \mathbf{n}'_3 \dot{\phi} (\phi' \mathbf{P} \phi - \sigma_3(\mathbf{P})), \quad (5.31)$$

in the domain  $S(2)$ , where  $s \in \{-1, +1\}$ . From the Schwartz inequality, the Lyapunov function is positive definite and  $V_s = 0 \Leftrightarrow \phi = -s\mathbf{n}_3$ . Assuming that the eigenvalue has multiplicity 1, the set of point where  $\dot{V}_s = 0$  is given by

$$C_{V_s} = \{\phi \in S(2) : \phi = \pm\mathbf{n}_3 \vee \mathbf{n}'_3\phi = 0\}.$$

The Lyapunov time derivatives  $\dot{V}_s$  are indefinite in the domain  $S(2)$ . For each initial condition  $\phi(t_0)$  choose  $s$  and  $0 < \beta < 1$  such that  $s\mathbf{n}'_3\phi(t_0) \leq \beta - 1 < 0$ , i.e.  $V_s(\phi(t_0)) \leq \beta$ . The level sets

$$\Omega_\beta^s = \{\phi \in S(2) : V_s(\phi) \leq \beta\},$$

are positively invariant. The unique points where  $\dot{V}_s = 0$  in  $\Omega_\beta^s$ , given by  $\phi = -s\mathbf{n}_3$ , are asymptotically stable.

To analyze the case  $\mathbf{n}'_3\phi(t_0) = 0$ , the property  $\mathbf{n}'_3\phi = 0 \Rightarrow \mathbf{n}'_3\dot{\phi} = 0$  shows that the set defined by  $\mathbf{n}'_3\phi = 0$  is positively invariant, and hence  $\phi(t) \in \text{span}(\mathbf{n}_1, \mathbf{n}_2)$  for all  $t$ . Using Lemma 5.4 implies that  $\phi(t) \rightarrow \{\mathbf{n}_1, \mathbf{n}_2\}$  as  $t \rightarrow \infty$ .  $\square$

The asymptotic convergence for the specific case  $\exists_{i \neq j} \sigma_i(\mathbf{P}) = \sigma_j(\mathbf{P})$  can be obtained by following the same steps of the proof of Theorem 5.10. In particular, if  $\exists_\sigma \mathbf{P} = \sigma \mathbf{I}$ , then the solution of (5.20b) is given by  $\phi(t) = \phi(t_0)$ , i.e. every point  $\phi(t) \in S(2)$  is stable.

**Proposition 5.11.** *If  $\exists_{i \neq j} \sigma_i(\mathbf{P}) = \sigma_j(\mathbf{P})$ , the solution to the attitude error vector dynamics satisfies*

$$\begin{cases} \sigma_1(\mathbf{P}) = \sigma_2(\mathbf{P}) \\ \sigma_2(\mathbf{P}) > \sigma_3(\mathbf{P}) \end{cases} \Rightarrow \begin{cases} \lim_{t \rightarrow \infty} \phi(t) = \text{sign}(\mathbf{n}'_3\phi(t_0))\mathbf{n}_3, & \text{if } \mathbf{n}'_3\phi(t_0) \neq 0 \\ \phi(t) = \phi(t_0) & \text{if } \mathbf{n}'_3\phi(t_0) = 0 \end{cases}, \quad (5.32a)$$

$$\begin{cases} \sigma_1(\mathbf{P}) > \sigma_2(\mathbf{P}) \\ \sigma_2(\mathbf{P}) = \sigma_3(\mathbf{P}) \end{cases} \Rightarrow \begin{cases} \lim_{t \rightarrow \infty} \phi(t) = \text{span}(\mathbf{n}_2, \mathbf{n}_3), & \text{if } \phi(t_0) \neq \pm\mathbf{n}_1 \\ \phi(t) = \phi(t_0), & \text{if } \phi(t_0) = \pm\mathbf{n}_1 \end{cases}, \quad (5.32b)$$

$$\sigma_3(\mathbf{P}) = \sigma_2(\mathbf{P}) = \sigma_1(\mathbf{P}) \Rightarrow \phi(t) = \phi(t_0). \quad (5.32c)$$

*Proof.* The asymptotic convergence (5.32a) is obtained by using the same steps of proof of Theorem 5.10 and, from the system dynamics (5.20b),

$$\mathbf{n}'_3\phi(t_0) = 0 \Rightarrow \phi(t_0) \in \text{span}(\mathbf{n}_1, \mathbf{n}_2) \Rightarrow \phi(t_0) \in \text{eigvec}(\mathbf{P}) \Rightarrow \dot{\phi}(t_0) = 0.$$

The asymptotic convergence (5.32b) is obtained by defining the same Lyapunov functions (5.31). The set of points where  $\dot{V}_s = 0$  is given by

$$C_{V_s} = \{\phi \in S(2) : \phi \in \text{span}(\mathbf{n}_2, \mathbf{n}_3) \vee \mathbf{n}'_3\phi = 0\},$$

and, defining the positively invariant sets  $\Omega_\beta^s$  and using LaSalle's principle, yields  $\phi \rightarrow \text{span}(\mathbf{n}_2, \mathbf{n}_3)$  as  $t \rightarrow \infty$  if  $s\mathbf{n}'_3\phi(t_0) < 0$ , i.e.  $\mathbf{n}'_3\phi(t_0) \neq 0$ . Using a similar Lyapunov functions based on  $\mathbf{n}_2$ ,

$$V_s(\phi) = 1 + s\mathbf{n}'_2\phi,$$

and the using the positively invariant sets  $\Omega_\beta^s$  and LaSalle's principle, shows that  $\phi \rightarrow \text{span}(\mathbf{n}_2, \mathbf{n}_3)$  as  $t \rightarrow \infty$  if  $\mathbf{n}'_2\phi(t_0) \neq 0$ . Using the kinematics (5.20b), if  $\phi \in \text{span}(\mathbf{n}_2, \mathbf{n}_3)$  then  $\dot{\phi} = 0$  so  $\text{span}(\mathbf{n}_2, \mathbf{n}_3)$  is a positively invariant set. Finally, the initial condition  $\mathbf{n}'_2\phi(t_0) = \mathbf{n}'_3\phi(t_0) = 0$  is equivalent to  $\phi(t_0) = \pm\mathbf{n}_1$ , which satisfies  $\dot{\phi} = 0$  and hence  $\phi(t_0) = \pm\mathbf{n}_1 \Rightarrow \phi(t) = \phi(t_0)$ .  $\square$

The results of Theorem 5.10 and Proposition 5.11 show that, for almost all initial conditions,  $\phi$  converges to the direction of the smallest singular value of  $\mathbf{P}$ . This characterization of the attitude error is of interest in navigation system design, allowing the system designer to shape the fastest and slowest directions of estimation using the landmark coordinate transformation (5.8).

### 5.3 Observer synthesis with biased velocity readings

In this section, the attitude and position observer is derived for velocity readings corrupted by unknown sensor bias. The observer architecture is obtained by extending the feedback laws and the observer kinematics to compensate for the bias in the linear and angular velocity readings, tackling the effect of sensor bias in the propagation of attitude and position, and thus allowing for the estimation errors to converge to the origin.

The case of bias in the linear velocity measurements is addressed first, to illustrate how the position feedback law proposed in Section 5.2 is extended to compensate for the bias non-ideality. The problem of bias in the linear and angular velocity measurements is addressed in the ensuing. In this case, the derived attitude and position feedback laws bear coupled, non-autonomous position and attitude error kinematics. Consequently, the stability of the resulting attitude and position observer is analyzed using an unique Lyapunov function, and exponential stability of the origin is obtained using advanced techniques, based on stability results for parameterized LTVs.

#### 5.3.1 Biased linear velocity readings

In this section, the observer presented in Section 5.2 is extended for the case where the linear velocity sensor measurement is corrupted by a bias term, that is

$$\mathbf{v}_r = {}^B\mathbf{v} + \mathbf{b}_v,$$

where the nominal bias is considered constant,  $\dot{\mathbf{b}}_v = \mathbf{0}$ . The proposed Lyapunov function (5.11) is augmented to account for the effect of the velocity bias

$$V_{b_v} = \frac{1}{2} \sum_{i=1}^n \| {}^B\hat{\mathbf{u}}_i - {}^B\mathbf{u}_i \|^2 + \frac{1}{2} \tilde{\mathbf{b}}'_v \mathbf{W}_{b_v} \tilde{\mathbf{b}}_v,$$

where  $\tilde{\mathbf{b}}_v = \hat{\mathbf{b}}_v - \mathbf{b}_v$  is the bias compensation error,  $\hat{\mathbf{b}}_v$  is the estimated bias and  $\mathbf{W}_{b_v}$  is a positive definite matrix. The Lyapunov function  $V_{b_v}$  can be decoupled as  $V_{b_v} = V_{\mathcal{R}} + V_p$ ,

where  $V_{\mathcal{R}}$  and  $\dot{V}_{\mathcal{R}}$  are described as before in (5.12) and (5.15a), and

$$V_p = \frac{n}{2} {}^B \tilde{\mathbf{p}}' {}^B \tilde{\mathbf{p}} + \frac{1}{2} \tilde{\mathbf{b}}_v' \mathbf{W}_{b_v} \tilde{\mathbf{b}}_v, \quad \dot{V}_p = {}^B \tilde{\mathbf{p}}' (({}^B \hat{\mathbf{p}})_{\times} (\hat{\boldsymbol{\omega}} - \boldsymbol{\omega}) + ({}^B \hat{\mathbf{v}} - {}^B \mathbf{v})) + \tilde{\mathbf{b}}_v' \mathbf{W}_{b_v} \dot{\tilde{\mathbf{b}}}_v.$$

Clearly,  $V_p$  has an unique global minimum at  $({}^B \tilde{\mathbf{p}}, \tilde{\mathbf{b}}_v) = (0, 0)$ .

The feedback law for the linear velocity is given by compensating the bias of the velocity reading in (5.23a) and using the feedback term  $\hat{\boldsymbol{\omega}}$  defined in (5.17), producing

$$\begin{aligned} {}^B \hat{\mathbf{v}} &= \mathbf{v}_r - \hat{\mathbf{b}}_v + ((\boldsymbol{\omega}_r)_{\times} - k_v \mathbf{I}) {}^B \tilde{\mathbf{p}} - ({}^B \hat{\mathbf{p}})_{\times} (\hat{\boldsymbol{\omega}} - \boldsymbol{\omega}_r) \\ &= {}^B \mathbf{v} - \tilde{\mathbf{b}}_v + ((\boldsymbol{\omega})_{\times} - k_v \mathbf{I}) \mathbf{s}_v + k_{\omega} ({}^B \hat{\mathbf{p}})_{\times} \mathbf{s}_{\omega}. \end{aligned} \quad (5.33)$$

Using the linear and angular velocity feedback laws (5.33) and (5.17) respectively, the augmented Lyapunov function dynamics are

$$\dot{V}_p = -k_v {}^B \tilde{\mathbf{p}}' {}^B \tilde{\mathbf{p}} + (\dot{\tilde{\mathbf{b}}}_v' \mathbf{W}_{b_v} - {}^B \tilde{\mathbf{p}}') \tilde{\mathbf{b}}_v.$$

Noting that  $\dot{\tilde{\mathbf{b}}}_v = \dot{\hat{\mathbf{b}}}_v$ , the bias feedback law is defined as

$$\dot{\hat{\mathbf{b}}}_v = k_{b_v} {}^B \tilde{\mathbf{p}} = k_{b_v} \mathbf{s}_v,$$

and  $\mathbf{W}_{b_v} = \frac{1}{k_{b_v}} \mathbf{I}$  where  $k_{b_v}$  is a positive scalar. The resulting closed loop dynamics are autonomous and given by

$${}^B \dot{\tilde{\mathbf{p}}} = -\tilde{\mathbf{b}}_v - k_v {}^B \tilde{\mathbf{p}}, \quad \dot{\hat{\mathbf{b}}}_v = k_{b_v} {}^B \tilde{\mathbf{p}}, \quad (5.34)$$

and the Lyapunov function dynamics are described by  $\dot{V}_p = -k_v {}^B \tilde{\mathbf{p}}' {}^B \tilde{\mathbf{p}} < 0$ .

**Theorem 5.12.** *The equilibrium point  $({}^B \tilde{\mathbf{p}}, \tilde{\mathbf{b}}_v) = (0, 0)$  of the system (5.34) is globally exponentially stable.*

*Proof.* The set of points where  $\dot{V}_p = 0$  is given by

$$\mathcal{C}_{V_p} = \{({}^B \tilde{\mathbf{p}}, \tilde{\mathbf{b}}_v) \in \mathbb{R}^3 \times \mathbb{R}^3 : {}^B \tilde{\mathbf{p}} = 0\}.$$

To show asymptotic stability, we apply LaSalle's invariance principle [78]. The closed loop system (5.34) satisfies  ${}^B \tilde{\mathbf{p}} \in \mathcal{C}_{V_p} \Rightarrow {}^B \dot{\tilde{\mathbf{p}}} = 0 \Rightarrow \tilde{\mathbf{b}}_v = 0$ , so the largest invariant set in  $\mathcal{C}_{V_p}$  is  $\{(0, 0)\}$ . Exponential stability of the origin is a direct consequence of the solution of stable linear time-invariant systems [122].  $\square$

The decoupling property of  $V_{b_v}$  holds in the presence of  $\mathbf{b}_v$ . Consequently, the attitude observer is identical to that derived in Section 5.2, producing the convergence properties of Theorem 5.5.



### 5.3.2 Biased linear and angular velocity readings

This section presents the derivation of an exponentially stabilizing observer for attitude and position estimation in the presence of bias in the angular and linear velocity readings, given by

$$\boldsymbol{\omega}_r = \boldsymbol{\omega} + \mathbf{b}_\omega, \quad \mathbf{v}_r = {}^B\mathbf{v} + \mathbf{b}_v, \quad (5.35)$$

where the nominal biases are considered constant, i.e.  $\dot{\mathbf{b}}_\omega = \mathbf{0}$ ,  $\dot{\mathbf{b}}_v = \mathbf{0}$ .

The proposed Lyapunov function (5.11) is augmented to account for the effect of the angular and linear velocity bias

$$\begin{aligned} V_b &= \frac{\gamma_\varphi}{2} \sum_{i=1}^{n-1} \| {}^B\hat{\mathbf{u}}_i - {}^B\mathbf{u}_i \|^2 + \frac{\gamma_p}{2} \| {}^B\hat{\mathbf{u}}_n - {}^B\mathbf{u}_n \|^2 + \frac{\gamma_{b_\omega}}{2} \tilde{\mathbf{b}}_\omega' \tilde{\mathbf{b}}_\omega + \frac{\gamma_{b_v}}{2} \tilde{\mathbf{b}}_v' \tilde{\mathbf{b}}_v \\ &= \frac{\gamma_\varphi}{4} \| \mathbf{I} - \tilde{\mathcal{R}} \|^2 \boldsymbol{\phi}' \mathbf{P} \boldsymbol{\phi} + \frac{\gamma_p}{2} \| {}^B\tilde{\mathbf{p}} \|^2 + \frac{\gamma_{b_\omega}}{2} \| \tilde{\mathbf{b}}_\omega \|^2 + \frac{\gamma_{b_v}}{2} \| \tilde{\mathbf{b}}_v \|^2, \end{aligned} \quad (5.36)$$

where  $\tilde{\mathbf{b}}_\omega = \hat{\mathbf{b}}_\omega - \mathbf{b}_\omega$ ,  $\tilde{\mathbf{b}}_v = \hat{\mathbf{b}}_v - \mathbf{b}_v$  are the bias compensation errors,  $\hat{\mathbf{b}}_\omega$ ,  $\hat{\mathbf{b}}_v$  are the estimated biases, and  $\gamma_\varphi$ ,  $\gamma_p$ ,  $\gamma_{b_\omega}$  and  $\gamma_{b_v}$  are positive scalars.

Under Assumption 5.1 and given the result of Lemma 5.3, the Lyapunov function  $V_b$  has an unique global minimum at  $({}^B\tilde{\mathbf{p}}, \tilde{\mathcal{R}}, \tilde{\mathbf{b}}_\omega, \tilde{\mathbf{b}}_v) = (\mathbf{0}, \mathbf{I}, \mathbf{0}, \mathbf{0})$ . The stability analysis of the closed-loop system is based on studying the level sets described by  $V_b \leq \beta$ , which are positively invariant. For  $\beta$  large enough, the level sets of  $V_b$  contain multiple critical points due to the directionality of  $\mathbf{P}$ , as evidenced in the results of Lemma 5.4. In this section, the observer using biased velocity readings is designed by shaping  $\mathbf{P}$  with uniform directionality, using the transformation  $\mathbf{A}_X$ .

**Proposition 5.13.** *Let  $\mathbf{H} := \mathbf{X}\mathbf{D}_X$  be full rank, there is a nonsingular  $\mathbf{A}_X \in \mathbb{M}(n)$  such that  $\mathbf{U}_X \mathbf{U}'_X = \mathbf{I}$ .*

*Proof.* Take the singular value decomposition of  $\mathbf{H} = \mathbf{U}\mathbf{S}\mathbf{V}'$  where  $\mathbf{U} \in \mathbb{O}(3)$ ,  $\mathbf{V} \in \mathbb{O}(n)$ ,  $\mathbf{S} = \begin{bmatrix} \text{diag}(s_1, s_2, s_3) & \mathbf{0}_{3 \times (n-3)} \end{bmatrix} \in \mathbb{M}(3, n)$ , and  $s_1 > s_2 > s_3 > 0$  are the singular values of  $\mathbf{H}$ . Any  $\mathbf{A}_X$  given by

$$\mathbf{A}_X = \mathbf{V} \begin{bmatrix} \text{diag}(s_1^{-1}, s_2^{-1}, s_3^{-1}) & \mathbf{0}_{3 \times (n-3)} \\ \mathbf{0}_{(n-3) \times 3} & \mathbf{B} \end{bmatrix} \mathbf{V}'_A,$$

where  $\mathbf{B} \in \mathbb{M}(n-3)$  is nonsingular and  $\mathbf{V}_A \in \mathbb{O}(n)$ , produces  $\mathbf{U}_X \mathbf{U}'_X = \mathbf{H}\mathbf{A}_X \mathbf{A}'_X \mathbf{H} = \mathbf{U}\mathbf{V}'_A \mathbf{V}_A \mathbf{U}' = \mathbf{I}$ .  $\square$

**Remark 5.1.** Given that  $\text{rank}(\mathbf{H}) = \text{rank}(\mathbf{X})$ , the condition  $\text{rank}(\mathbf{X}) = 2$  of Assumption 5.1 does not satisfy directly the conditions of Proposition 5.13. In that case, the observer equations can be rewritten, by taking two linearly independent columns of  $\mathbf{H}$ ,  ${}^L\mathbf{h}_i$  and  ${}^L\mathbf{h}_j$ , and constructing a full rank matrix,  $\mathbf{H}_a = \begin{bmatrix} \mathbf{H} & {}^L\mathbf{h}_i \times {}^L\mathbf{h}_j \end{bmatrix}$ . The cross product is commutable with rotation transformations,  $(\mathcal{R}' {}^L\mathbf{h}_i) \times (\mathcal{R}' {}^L\mathbf{h}_j) = \mathcal{R}' ({}^L\mathbf{h}_i \times {}^L\mathbf{h}_j)$ , hence a modified observer can be derived, without loss of generality, by replacing  $\mathbf{H}$  with  $\mathbf{H}_a$ . This procedure is discussed in detail in Appendix E.2.

Using the transformation  $\mathbf{A}_X$  defined in Proposition 5.13, the Lyapunov function expressed in (5.36) is given by

$$V_b = \frac{\gamma_\varphi}{2} \|\mathbf{I} - \tilde{\mathcal{R}}\|^2 + \frac{\gamma_p}{2} \|{}^B \tilde{\mathbf{p}}\|^2 + \frac{\gamma_{b_\omega}}{2} \|\tilde{\mathbf{b}}_\omega\|^2 + \frac{\gamma_{b_v}}{2} \|\tilde{\mathbf{b}}_v\|^2. \quad (5.37)$$

The Lyapunov time derivative is given by

$$\begin{aligned} \dot{V}_b = & \gamma_p \mathbf{s}'_v \left( ({}^B \hat{\mathbf{p}})_\times (\hat{\boldsymbol{\omega}} - \boldsymbol{\omega}) + ({}^B \hat{\mathbf{v}} - {}^B \mathbf{v}) - (\boldsymbol{\omega})_\times {}^B \tilde{\mathbf{p}} \right) \\ & + \gamma_\varphi \mathbf{s}'_\omega (\hat{\boldsymbol{\omega}} - \boldsymbol{\omega}) + \gamma_{b_\omega} \tilde{\mathbf{b}}'_\omega \tilde{\mathbf{b}}_\omega + \gamma_{b_v} \tilde{\mathbf{b}}'_v \tilde{\mathbf{b}}_v, \end{aligned} \quad (5.38)$$

where  $\mathbf{s}_\omega$  and  $\mathbf{s}_v$  are given by (5.18) and (5.24), and by considering the transformation  $\mathbf{A}_X$  formulated in Proposition 5.13, that is

$$\mathbf{s}_\omega = \mathcal{R}' \left( \tilde{\mathcal{R}} - \tilde{\mathcal{R}}' \right)_\otimes, \quad \mathbf{s}_v = {}^B \tilde{\mathbf{p}}. \quad (5.39)$$

The feedback laws for the angular and linear velocities are given by rewriting (5.17) and (5.23a) respectively, with compensation of the velocity sensors bias, producing

$$\hat{\boldsymbol{\omega}} = (\boldsymbol{\omega}_r - \hat{\mathbf{b}}_\omega) - k_\omega \mathbf{s}_\omega = (\boldsymbol{\omega} - \tilde{\mathbf{b}}_\omega) - k_\omega \mathbf{s}_\omega, \quad (5.40a)$$

$${}^B \hat{\mathbf{v}} = \mathbf{v}_r - \hat{\mathbf{b}}_v + \left( (\boldsymbol{\omega}_r - \hat{\mathbf{b}}_\omega)_\times - k_v \mathbf{I} \right) \mathbf{s}_v - ({}^B \hat{\mathbf{p}})_\times (\hat{\boldsymbol{\omega}} - (\boldsymbol{\omega}_r - \hat{\mathbf{b}}_\omega)) \quad (5.40b)$$

$$= {}^B \mathbf{v} - \tilde{\mathbf{b}}_v + \left( (\boldsymbol{\omega} - \tilde{\mathbf{b}}_\omega)_\times - k_v \mathbf{I} \right) \mathbf{s}_v + k_\omega ({}^B \hat{\mathbf{p}})_\times \mathbf{s}_\omega. \quad (5.40c)$$

Using the feedback terms  $\hat{\boldsymbol{\omega}}$  and  $\hat{\mathbf{v}}$  in (5.38) yields

$$\begin{aligned} \dot{V}_b = & -\gamma_p k_v \|\mathbf{s}_v\|^2 - \gamma_\varphi k_\omega \|\mathbf{s}_\omega\|^2 \\ & + (\gamma_p ({}^B \hat{\mathbf{p}})_\times {}^B \tilde{\mathbf{p}} - \gamma_\varphi \mathbf{s}_\omega + \gamma_{b_\omega} \dot{\tilde{\mathbf{b}}}_\omega)' \tilde{\mathbf{b}}_\omega + (\gamma_{b_v} \dot{\tilde{\mathbf{b}}}_v - \gamma_p \mathbf{s}_v)' \tilde{\mathbf{b}}_v. \end{aligned}$$

The bias estimates satisfy  $\dot{\hat{\mathbf{b}}}_\omega = \dot{\tilde{\mathbf{b}}}_\omega$ ,  $\dot{\hat{\mathbf{b}}}_v = \dot{\tilde{\mathbf{b}}}_v$ , and the bias feedback laws are defined as

$$\dot{\hat{\mathbf{b}}}_\omega = \frac{1}{\gamma_{b_\omega}} \left( \gamma_\varphi \mathbf{s}_\omega - \gamma_p ({}^B \hat{\mathbf{p}})_\times {}^B \tilde{\mathbf{p}} \right), \quad \dot{\hat{\mathbf{b}}}_v = \frac{\gamma_p}{\gamma_{b_v}} \mathbf{s}_v, \quad (5.41)$$

producing the Lyapunov function time derivative

$$\dot{V}_b = -\gamma_p k_v \mathbf{s}'_v \mathbf{s}_v - \gamma_\varphi k_\omega \mathbf{s}'_\omega \mathbf{s}_\omega,$$

that is negative semi-definite.

The dynamics of the closed-loop estimation errors are described by

$${}^B \dot{\tilde{\mathbf{p}}} = - ({}^B \mathbf{p})_\times \tilde{\mathbf{b}}_\omega - k_v {}^B \tilde{\mathbf{p}} - \tilde{\mathbf{b}}_v, \quad (5.42a)$$

$$\dot{\tilde{\mathcal{R}}} = -k_\omega \tilde{\mathcal{R}} (\tilde{\mathcal{R}} - \tilde{\mathcal{R}}') - \tilde{\mathcal{R}} \left( \mathcal{R} \tilde{\mathbf{b}}_\omega \right)_\times, \quad (5.42b)$$

$$\dot{\tilde{\mathbf{b}}}_\omega = \frac{\gamma_\varphi}{\gamma_{b_\omega}} \mathcal{R} \left( \tilde{\mathcal{R}} - \tilde{\mathcal{R}}' \right)_\otimes - \frac{\gamma_p}{\gamma_{b_\omega}} ({}^B \mathbf{p})_\times {}^B \tilde{\mathbf{p}}, \quad (5.42c)$$

$$\dot{\tilde{\mathbf{b}}}_v = \frac{\gamma_p}{\gamma_{b_v}} {}^B \tilde{\mathbf{p}}. \quad (5.42d)$$

If  $\tilde{\mathbf{b}}_\omega = 0$ , the system (5.42) reduces to the error dynamics (5.34) with  $k_{b_v} = \frac{\gamma_p}{\gamma_{b_v}}$ , as expected. For the general case  $\tilde{\mathbf{b}}_\omega \neq 0$ , the system (5.42) becomes nonautonomous, and the compensation of rate gyro bias couples the attitude and position dynamics.

To analyze the stability of (5.42), define the state  $\mathbf{x}_b = ({}^B\tilde{\mathbf{p}}, \tilde{\mathcal{R}}, \tilde{\mathbf{b}}_\omega, \tilde{\mathbf{b}}_p)$  and the domain  $D_b = \mathbb{R}^3 \times \text{SO}(3) \times \mathbb{R}^3 \times \mathbb{R}^3$ , the set of points where  $\dot{V}_b = 0$  is given by

$$\begin{aligned} C_{V_b} &= \{\mathbf{x}_b \in D_b : ({}^B\tilde{\mathbf{p}}, \tilde{\mathbf{b}}_\omega, \tilde{\mathbf{b}}_p) = (\mathbf{0}, \mathbf{0}, \mathbf{0}), \tilde{\mathcal{R}} \in C_{\mathcal{R}}\}, \\ C_{\mathcal{R}} &= \{\tilde{\mathcal{R}} \in \text{SO}(3) : \tilde{\mathcal{R}} = \mathbf{I} \vee \tilde{\mathcal{R}} = \text{rot}(\pi, \phi \in \text{S}(2))\}. \end{aligned}$$

As discussed in Section 5.2, global asymptotic stability of the origin is precluded by topological limitations associated with the estimation error  $\tilde{\mathcal{R}} = \text{rot}(\pi, \phi)$ . In the next proposition, the boundedness of the estimation errors is shown and used to provide sufficient conditions for excluding convergence to the equilibrium points satisfying  $\tilde{\mathcal{R}} = \text{rot}(\pi, \phi)$ .

**Lemma 5.14.** *The estimation errors  $({}^B\tilde{\mathbf{p}}, \tilde{\mathcal{R}}, \tilde{\mathbf{b}}_\omega, \tilde{\mathbf{b}}_p)$  are bounded. For any initial condition such that*

$$\frac{\gamma_{b_v} \|\tilde{\mathbf{b}}_v(t_0)\|^2 + \gamma_p \|{}^B\tilde{\mathbf{p}}(t_0)\|^2 + \gamma_{b_\omega} \|\tilde{\mathbf{b}}_\omega(t_0)\|^2}{\gamma_\varphi (8 - \|\mathbf{I} - \tilde{\mathcal{R}}(t_0)\|^2)} < 1, \quad (5.43)$$

the attitude error is bounded by  $\|\mathbf{I} - \tilde{\mathcal{R}}(t)\|^2 \leq c_{\max} < 8$  for all  $t \geq t_0$ .

*Proof.* Define the set  $\Omega_\rho = \{\mathbf{x}_b \in D_b : V_b \leq \rho\}$ . The Lyapunov function (5.37) is the weighted distance of the state to the origin, so  $\exists \alpha \|\mathbf{x}_b\|^2 \leq \alpha V_b$  and the set  $\Omega_\rho$  is compact. The Lyapunov function decreases along the system trajectories,  $\dot{V}_b \leq 0$ , so any trajectory starting in  $\Omega_\rho$  will remain in  $\Omega_\rho$  and satisfy  $V_b(\mathbf{x}_b(t)) \leq V_b(\mathbf{x}_b(t_0))$ . Consequently,  $\forall t \geq t_0 \|\mathbf{x}_b(t)\|^2 \leq \alpha V_b(\mathbf{x}_b(t_0))$  and the state is bounded.

The gain condition (5.43) is equivalent to  $V_b(\mathbf{x}_b(t_0)) \leq \gamma_\varphi (4 - \varepsilon)$  for some  $\varepsilon$  sufficiently small. Using  $V_b(\mathbf{x}_b(t)) \leq V_b(\mathbf{x}_b(t_0))$  implies that  $\gamma_\varphi \|\mathbf{I} - \tilde{\mathcal{R}}(t)\|^2 \leq 2V_b(\mathbf{x}_b(t_0))$  for all  $t \geq t_0$ , hence choosing  $c_{\max} = 8 - 2\varepsilon$  concludes the proof.  $\square$

**Remark 5.2.** The formulation of Lemma 5.14 can be expressed as a function of the rotation error  $\varphi$ , which is a scalar quantity and hence provide for a more intuitive representation of the bounds. The inequality (5.43) can be rewritten as

$$\frac{\gamma_{b_v} \|\tilde{\mathbf{b}}_v(t_0)\|^2 + \gamma_p \|{}^B\tilde{\mathbf{p}}(t_0)\|^2 + \gamma_{b_\omega} \|\tilde{\mathbf{b}}_\omega(t_0)\|^2}{4\gamma_\varphi (1 + \cos(\varphi(t_0)))} < 1,$$

and the bound  $\|\mathbf{I} - \tilde{\mathcal{R}}(t)\|^2 \leq c_{\max} < 8$  is equivalent to  $\varphi(t) \leq \varphi_{\max} < \pi$ , where  $\varphi_{\max} = \arccos(1 - \frac{c_{\max}}{4})$ .

Adopting the analysis tools for parameterized LTV systems [93], the system (5.42), in the form  $\dot{\mathbf{x}}_b = f(t, \mathbf{x}_b)\mathbf{x}_b$ , is rewritten as  $\dot{\mathbf{x}}_\star = \mathbf{A}(\lambda, t)\mathbf{x}_\star$ . In this formulation, the parameter  $\lambda \in D_b \times \mathbb{R}$  is associated with the initial conditions of the nonlinear system and the solutions of both systems are identical whenever the initial conditions of both systems coincide,  $\mathbf{x}_\star(t_0) = \mathbf{x}(t_0)$ , and the parameter satisfies  $\lambda = (t_0, \mathbf{x}(t_0))$ .

The results derived in [93] establish sufficient conditions for exponential stability of the parameterized LTV system, uniformly in the parameter  $\lambda$  ( $\lambda$ -UGES). As discussed in [93],  $\lambda$ -UGES of the parameterized LTV system implies that the origin of the associated nonlinear system is exponentially stable, see Appendix F for more details. Using these results, exponential convergence of the estimation errors in the presence of biased velocity measurements is shown.

**Theorem 5.15.** *Let  $\gamma_{b_v} = \gamma_{b_\omega}$  and assume that  ${}^B\mathbf{p}$ ,  ${}^B\mathbf{v}$  and  $\boldsymbol{\omega}$  are bounded. For any initial condition that satisfies (5.43), the position, attitude and bias estimation errors converge exponentially fast to the stable equilibrium point  $({}^B\tilde{\mathbf{p}}, \tilde{\mathcal{R}}, \tilde{\mathbf{b}}_\omega, \tilde{\mathbf{b}}_v) = (0, \mathbf{I}, 0, 0)$ .*

*Proof.* The stability of (5.42) is obtained by a change of coordinates, using an attitude representation similar to that proposed in [135]. Let the attitude error vector be given by  $\tilde{\mathbf{q}}_q = \frac{(\tilde{\mathcal{R}} - \mathcal{R})_\otimes}{\|(\tilde{\mathcal{R}} - \mathcal{R})_\otimes\|} \frac{\|\mathbf{I} - \tilde{\mathcal{R}}\|}{2\sqrt{2}}$ , the closed loop kinematics are described by

$${}^B\dot{\tilde{\mathbf{p}}} = -({}^B\mathbf{p})_\times \tilde{\mathbf{b}}_\omega - k_v {}^B\tilde{\mathbf{p}} - \tilde{\mathbf{b}}_v, \quad (5.44a)$$

$$\dot{\tilde{\mathbf{q}}}_q = \frac{1}{2} \mathbf{Q}(\tilde{\mathbf{q}})(-\tilde{\mathcal{R}}\tilde{\mathbf{b}}_\omega - 4k_\omega \tilde{\mathbf{q}}_q \tilde{q}_s), \quad (5.44b)$$

$$\dot{\tilde{\mathbf{b}}}_\omega = 4 \frac{\gamma_\varphi}{\gamma_{b_\omega}} \mathcal{R}' \mathbf{Q}'(\tilde{\mathbf{q}}) \tilde{\mathbf{q}}_q - \frac{\gamma_p}{\gamma_{b_\omega}} ({}^B\mathbf{p})_\times {}^B\tilde{\mathbf{p}}, \quad (5.44c)$$

$$\dot{\tilde{\mathbf{b}}}_v = \frac{\gamma_p}{\gamma_{b_v}} {}^B\tilde{\mathbf{p}}, \quad (5.44d)$$

where  $\mathbf{Q}(\tilde{\mathbf{q}}) := \tilde{q}_s \mathbf{I} + (\tilde{\mathbf{q}}_q)_\times$ ,  $\tilde{\mathbf{q}} = [\tilde{\mathbf{q}}_q' \quad \tilde{q}_s]'$ ,  $\tilde{q}_s = \frac{1}{2} \sqrt{1 + \text{tr}(\tilde{\mathcal{R}})}$  and  $\dot{\tilde{q}}_s = 2k_\omega \tilde{\mathbf{q}}_q' \tilde{\mathbf{q}}_q \tilde{q}_s - \frac{1}{2} \tilde{\mathbf{q}}_q' \tilde{\mathbf{b}}_\omega$ . The vector  $\tilde{\mathbf{q}}$  is the well known Euler quaternion representation [107]. Using  $\|\tilde{\mathbf{q}}_q\|^2 = \frac{1}{8} \|\tilde{\mathcal{R}} - \mathbf{I}\|^2$ , the Lyapunov function in quaternion coordinates is described by  $V_b = 4\gamma_\varphi \|\tilde{\mathbf{q}}_q\|^2 + \frac{\gamma_p}{2} \|{}^B\tilde{\mathbf{p}}\|^2 + \frac{\gamma_{b_\omega}}{2} \|\tilde{\mathbf{b}}_\omega\|^2 + \frac{\gamma_{b_v}}{2} \|\tilde{\mathbf{b}}_v\|^2$ .

Let  $\mathbf{x}_q := ({}^B\tilde{\mathbf{p}}, \tilde{\mathbf{q}}_q, \tilde{\mathbf{b}}_\omega, \tilde{\mathbf{b}}_v)$ ,  $\mathbf{x}_q \in D_q$ , and  $D_q := \mathbb{R}^3 \times \mathbf{B}(3) \times \mathbb{R}^3 \times \mathbb{R}^3$ , define the system (5.44) in the domain  $D_q = \{\mathbf{x} \in D_q : V_b \leq \gamma_\varphi(4 - \varepsilon_q)\}$ ,  $0 < \varepsilon_q < 4$ . The set  $D_q$  is given by the interior of the Lyapunov surface, so it is positively invariant and well defined. The condition (5.43) implies that the initial condition is contained in the set  $D_q$  for  $\varepsilon_q$  small enough and, by Lemma 5.14, the components of the attitude error quaternion are bounded by  $\|\tilde{\mathbf{q}}_q\|^2 \leq \frac{c_{\max}}{8}$  and  $\|\tilde{q}_s\|^2 \geq 1 - \frac{c_{\max}}{8}$ , with  $c_{\max} = 8 - 2\varepsilon_q$ .

Let  $\mathbf{x}_\star := ({}^B\tilde{\mathbf{p}}_\star, \tilde{\mathbf{q}}_{q\star}, \tilde{\mathbf{b}}_{\omega\star}, \tilde{\mathbf{b}}_{v\star})$ ,  $D_q := \mathbb{R}^3 \times \mathbb{R}^3 \times \mathbb{R}^3 \times \mathbb{R}^3$ ,  $\gamma_b := \gamma_{b_\omega} = \gamma_{b_v}$ , and define the parameterized LTV system

$$\dot{\mathbf{x}}_\star = \begin{bmatrix} \mathcal{A}(t, \lambda) & \mathcal{B}'(t, \lambda) \\ -\mathcal{C}(t, \lambda) & \mathbf{0}_{3 \times 3} \end{bmatrix} \mathbf{x}_\star, \quad (5.45)$$

where  $\lambda \in \mathbb{R}_{\geq 0} \times D_q$ , the submatrices are described by

$$\mathcal{A}(t, \lambda) = \begin{bmatrix} -k_v \mathbf{I} & \mathbf{0}_{3 \times 3} \\ \mathbf{0}_{3 \times 3} & -2k_\omega \tilde{q}_s(t, \lambda) \mathbf{Q}(\tilde{\mathbf{q}}(t, \lambda)) \end{bmatrix},$$

$$\mathcal{B}(t, \lambda) = \begin{bmatrix} ({}^B\mathbf{p})_\times & -\frac{\mathcal{R}' \mathbf{Q}'(\tilde{\mathbf{q}}(t, \lambda))}{2} \\ -\mathbf{I} & \mathbf{0}_{3 \times 3} \end{bmatrix}, \mathcal{C}(t, \lambda) = \frac{\mathcal{B}(t, \lambda)}{\gamma_b} \begin{bmatrix} \gamma_p \mathbf{I} & 0 \\ 0 & 8\gamma_\varphi \mathbf{I} \end{bmatrix},$$

and the quaternion  $\tilde{\mathbf{q}}(t, \lambda)$  represents the solution of (5.44) with initial condition  $\lambda = (t_0, {}^B\tilde{\mathbf{p}}(t_0), \tilde{\mathbf{q}}_q(t_0), \tilde{\mathbf{b}}_\omega(t_0), \tilde{\mathbf{b}}_v(t_0))$ . By the boundedness of  ${}^B\mathbf{p}$ , the matrices  $\mathcal{A}(t, \lambda)$ ,  $\mathcal{B}(t, \lambda)$  and  $\mathcal{C}(t, \lambda)$  are bounded, and the system is well defined [77, p. 626]. If the parameterized LTV (5.45) is  $\lambda$ -UGES, then the nonlinear system (5.44) is uniformly exponentially stable in the domain  $\mathcal{D}_q$ , see Appendix F for details. The parameterized LTV system verifies the assumptions of [93, Theorem 1]:

1) Given the boundedness of  ${}^B\mathbf{p}$ ,  ${}^B\mathbf{v}$  and  $\boldsymbol{\omega}$ ,  ${}^B\dot{\mathbf{p}}$  is bounded, and the elements of  $\mathcal{B}(t, \lambda)$  and

$$\frac{\partial \mathcal{B}(t, \lambda)}{\partial t} = \begin{bmatrix} ({}^B\dot{\mathbf{p}})_\times & -\frac{1}{2}\dot{\mathcal{R}}'\mathbf{Q}'(\tilde{\mathbf{q}}(t, \lambda)) + \mathcal{R}'\mathbf{Q}'(\dot{\tilde{\mathbf{q}}}(t, \lambda)) \\ \mathbf{0}_{3 \times 3} & \mathbf{0}_{3 \times 3} \end{bmatrix},$$

as well as the corresponding induced Euclidean norm, are bounded for all  $\lambda \in \mathbb{R}_{\geq 0} \times \mathcal{D}_q$ ,  $t \geq t_0$ .

2) The positive definite matrices

$$\mathbf{P}(t, \lambda) = \frac{1}{\gamma_b} \begin{bmatrix} \gamma_p \mathbf{I} & \mathbf{0} \\ \mathbf{0} & 8\gamma_\varphi \mathbf{I} \end{bmatrix}, \quad \mathbf{Q}(t, \lambda) = \frac{1}{\gamma_b} \begin{bmatrix} 2k_v \gamma_p \mathbf{I} & \mathbf{0} \\ \mathbf{0} & 32\tilde{q}_s^2(t, \lambda) k_\omega \gamma_\varphi \mathbf{I} \end{bmatrix},$$

satisfy

$$\begin{aligned} \mathbf{P}(t, \lambda) \mathcal{B}'(t, \lambda) &= \mathcal{C}'(t, \lambda), \quad -\mathbf{Q}(t, \lambda) = \mathcal{A}'(t, \lambda) \mathbf{P}(t, \lambda) + \mathbf{P}(t, \lambda) \mathcal{A}(t, \lambda) + \dot{\mathbf{P}}(t, \lambda), \\ \min(C_P) \mathbf{I} &\leq \mathbf{P}(t, \lambda) \leq \max(C_P) \mathbf{I}, \quad \min(C_Q) \mathbf{I} \leq \mathbf{Q}(t, \lambda) \leq \max(C_Q) \mathbf{I}, \end{aligned}$$

with  $C_P = \frac{1}{\gamma_b} \{\gamma_p, 8\gamma_\varphi\}$  and  $C_Q = \frac{1}{\gamma_b} \{32k_\omega \gamma_\varphi, 32k_\omega \gamma_\varphi (1 - \frac{c_{\max}}{8}), 2k_v \gamma_p\}$ .

The system (5.45) is  $\lambda$ -UGES if and only if  $\mathcal{B}(t, \lambda)$  is  $\lambda$ -uniformly persistently exciting [93]. Algebraic manipulation produces

$$\mathcal{B}(\tau, \lambda) \mathcal{B}'(\tau, \lambda) = \begin{bmatrix} \frac{1}{4} \mathcal{R}' \mathbf{Q}'(\tilde{\mathbf{q}}) \mathbf{Q}(\tilde{\mathbf{q}}) \mathcal{R} - ({}^B\mathbf{p})_\times^2 & -({}^B\mathbf{p})_\times \\ ({}^B\mathbf{p})_\times & \mathbf{I} \end{bmatrix},$$

and for any  $\mathbf{y} \in \mathbb{R}^3$ ,

$$\frac{1}{4} \mathbf{y}' \mathcal{R}' \mathbf{Q}'(\tilde{\mathbf{q}}) \mathbf{Q}(\tilde{\mathbf{q}}) \mathcal{R} \mathbf{y} = \frac{1}{4} (\|\mathbf{y}\|^2 - (\mathbf{y}' \mathcal{R}' \tilde{\mathbf{q}}_q)^2) \geq \frac{\|\mathbf{y}\|^2}{4} (1 - \|\tilde{\mathbf{q}}_q\|^2) \geq \|\mathbf{y}\|^2 c_B,$$

where  $c_B := \frac{1}{4} (1 - \frac{c_{\max}}{8})$ . Therefore

$$\mathcal{B}(\tau, \lambda) \mathcal{B}'(\tau, \lambda) \geq \mathbf{B}(\tau), \quad \text{where } \mathbf{B}(\tau) := \begin{bmatrix} c_B \mathbf{I} - ({}^B\mathbf{p})_\times^2 & -({}^B\mathbf{p})_\times \\ ({}^B\mathbf{p})_\times & \mathbf{I} \end{bmatrix},$$

Simple but long algebraic manipulations show that the eigenvalues of  $\mathbf{B}(\tau)$  are given by  $\alpha(\mathbf{B}(\tau)) \in \{\frac{1}{2}(1 + c_B + \|\mathbf{p}\|^B \pm \sqrt{(1 + c_B + \|\mathbf{p}\|^B)^2 - 4c_B}), 1, c_B\}$ , which are positive and lower bounded by a positive constant  $c_B$ , independent of  $\tau$ , if  ${}^B\mathbf{p}$  is bounded, i.e.  $\forall \tau \alpha_{\min}(\mathbf{B}(\tau)) \geq c_B$  where  $\alpha_{\min}(\mathbf{B}(\tau))$  denotes the smallest eigenvalue of  $\mathbf{B}(\tau)$ . Using the property  $\mathbf{B}(\tau) \geq \alpha_{\min}(\mathbf{B}(\tau)) \mathbf{I}$  produces  $\mathcal{B}(\tau, \lambda) \mathcal{B}'(\tau, \lambda) \geq \alpha_{\min}(\mathbf{B}(\tau)) \mathbf{I} \geq c_B \mathbf{I}$  and persistency of excitation condition is satisfied. Consequently, the parameterized LTV (5.45) is  $\lambda$ -UGES, and the nonlinear system (5.44) is exponentially stable in the domain  $\mathcal{D}_q$ .  $\square$

Given  $\gamma_p, \gamma_\varphi, \gamma_{b_\omega}$ , and  $\gamma_{b_v}$ , any initial estimation error  $\mathbf{x}_b(t_0)$  satisfying (5.43) converges exponentially fast to the origin. The following corollary establishes that the origin is uniform exponential stable, i.e. the convergence rate bounds are independent of  $\mathbf{x}_b(t_0)$ , for a bounded initial estimation error, which is a reasonable assumption for most applications.

**Corollary 5.16.** *Assume that the initial estimation errors are bounded*

$$\|{}^B\tilde{\mathbf{p}}(t_0)\| \leq \tilde{p}_0, \quad \|\mathbf{I} - \tilde{\mathcal{R}}(t_0)\|^2 \leq c_0 < 8, \quad (5.46a)$$

$$\|\tilde{\mathbf{b}}_\omega(t_0)\| \leq \tilde{b}_{\omega 0}, \quad \|\tilde{\mathbf{b}}_v(t_0)\| \leq \tilde{b}_{v0}, \quad (5.46b)$$

for some  $\tilde{p}_0, c_0, \tilde{b}_{\omega 0}, \tilde{b}_{v0}$ , and let  $(\gamma_p, \gamma_\varphi, \gamma_{b_\omega}, \gamma_{b_v})$  be such that

$$\gamma_{b_v} \tilde{b}_{v0}^2 + \gamma_p {}^B\tilde{p}_0^2 + \gamma_{b_\omega} \tilde{b}_{\omega 0}^2 < \gamma_\varphi(8 - c_0), \quad (5.47)$$

and  $\gamma_{b_\omega} = \gamma_{b_v}$  are satisfied. Then the equilibrium point  $\mathbf{x}_b = (0, \mathbf{I}, 0, 0)$  is exponentially stable, uniformly in the set defined by (5.46).

**Remark 5.3.** The formulation of Corollary 5.16 can be expressed as a function of the rotation error  $\varphi$ , yielding an intuitive representation of the bounds. The attitude inequality in (5.46a) can be rewritten as  $\varphi(t_0) \leq \varphi_0 < \pi$  and the condition (5.47) is given by  $\gamma_{b_v} \tilde{b}_{v0}^2 + \gamma_p {}^B\tilde{p}_0^2 + \gamma_{b_\omega} \tilde{b}_{\omega 0}^2 < 4\gamma_\varphi(1 + \cos(\varphi_0))$ . The formulation in  $\varphi$  evidences that the exponential stability property derived in Corollary 5.16 is independent of the rotation error axis  $\phi$ . This enables the observer to operate on conditions where an upper bound  $\varphi_0 < \pi$  for the initial estimation error is known, irrespective of the directionality of the attitude error.

Convergence rate bounds can be obtained by applying [92, Theorem 1 and Remark 2], however the obtained values were conservative. The conservativeness of the obtained bounds can be justified by the sufficiency of the adopted stability analysis tools based on parameterized LTVs, and, most important, by the fact that the computation of bounds for the matrix exponential is non-trivial in general [73].

### 5.3.3 Output feedback configuration

This section shows that the feedback laws can be expressed in terms of the landmark and velocity readings, (5.3) and (5.35) respectively.

**Theorem 5.17.** *The dynamics of the attitude and position observer are explicit functions of the sensor readings and state estimates, described by*

$$\dot{\hat{\mathcal{R}}} = \hat{\mathcal{R}}(\hat{\boldsymbol{\omega}})_\times, \quad (5.48a)$$

$${}^B\dot{\hat{\mathbf{p}}} = {}^B\hat{\mathbf{v}} - (\hat{\boldsymbol{\omega}})_\times {}^B\hat{\mathbf{p}}, \quad (5.48b)$$

$$\dot{\hat{\mathbf{b}}}_\omega = \frac{1}{\gamma_b}(\gamma_\varphi \mathbf{s}_\omega - \gamma_p ({}^B\hat{\mathbf{p}})_\times \mathbf{s}_v), \quad (5.48c)$$

$$\dot{\hat{\mathbf{b}}}_v = \frac{\gamma_p}{\gamma_b} \mathbf{s}_v, \quad (5.48d)$$

where  $\gamma_b = \gamma_{b_\omega} = \gamma_{b_v}$ , the feedback terms are given by

$$\hat{\boldsymbol{\omega}} = \boldsymbol{\omega}_r - \hat{\mathbf{b}}_\omega - k_\omega \mathbf{s}_\omega, \quad (5.49a)$$

$${}^B \hat{\mathbf{v}} = \mathbf{v}_r - \hat{\mathbf{b}}_v + \left( \left( \boldsymbol{\omega}_r - \hat{\mathbf{b}}_\omega \right)_\times - k_v \mathbf{I} \right) \mathbf{s}_v + k_\omega ({}^B \hat{\mathbf{p}})_\times \mathbf{s}_\omega, \quad (5.49b)$$

and

$$\mathbf{s}_\omega = \sum_{i=1}^n (\hat{\mathcal{R}}' \mathbf{X} \mathbf{D}_X \mathbf{A}_X \mathbf{e}_i) \times (\mathbf{Q} \mathbf{D}_X \mathbf{A}_X \mathbf{e}_i), \quad \mathbf{s}_v = {}^B \hat{\mathbf{p}} + \frac{1}{n} \sum_{i=1}^n \mathbf{q}_i.$$

*Proof.* The expressions (5.48c), (5.48d) and (5.49) are directly obtained from (5.40) and (5.41). The feedback term  $\mathbf{s}_\omega$  expressed in (5.39) is produced by taking (5.18) with the transformation  $\mathbf{A}_X$  defined in Proposition 5.13. Consequently,  $\mathbf{s}_\omega$  can be written in the form  $\mathbf{s}_\omega = \mathcal{R}' \left( \mathbf{U}_X \mathbf{U}'_X \tilde{\mathcal{R}} - \tilde{\mathcal{R}}' \mathbf{U}_X \mathbf{U}'_X \right)_\otimes$ , and following the proof of Theorem 5.9 produces  $\mathbf{s}_\omega = \sum_{i=1}^n (\hat{\mathcal{R}}' \mathbf{X} \mathbf{D}_X \mathbf{A}_X \mathbf{e}_i) \times (\mathbf{Q} \mathbf{D}_X \mathbf{A}_X \mathbf{e}_i)$ , where  $\mathbf{A}_X$  is defined such that  $\mathbf{U}_X \mathbf{U}'_X = \mathbf{I}$ . The feedback term  $\mathbf{s}_v$  is obtained by Theorem 5.9.  $\square$

## 5.4 Simulations

In this section, the proposed attitude and position observer properties are illustrated in simulation. A rigid body oscillating trajectory is considered, to analyze the almost global stabilization of the position and attitude errors, the exponential convergence of the estimates, and the directionality brought about by the landmark configuration. The simulation results are presented for the cases of ideal and of biased velocity readings, studied in Sections 5.2 and 5.3, respectively.

### 5.4.1 Ideal velocity readings

As illustrated in Fig. 5.2, the landmarks are placed on the  $xy$  plane

$$L_{\mathbf{x}_1} = \frac{1}{5} \begin{bmatrix} -4 \\ -3 \\ 0 \end{bmatrix} \text{ m}, \quad L_{\mathbf{x}_2} = \frac{1}{5} \begin{bmatrix} 2 \\ -3 \\ 0 \end{bmatrix} \text{ m}, \quad L_{\mathbf{x}_3} = \frac{1}{5} \begin{bmatrix} 2 \\ 6 \\ 0 \end{bmatrix} \text{ m}, \quad (5.50)$$

which satisfies the non-collinearity condition expressed in Assumption 5.1. The landmark coordinate transformation (5.9) is defined by  $\mathbf{A}_X = \mathbf{I}$ , and the matrix  $\mathbf{P}$  defined in (5.13) and its singular values and eigenvectors are given by

$$\mathbf{P} = \begin{bmatrix} 3.24 & 0 & 0 \\ 0 & 1.44 & 0 \\ 0 & 0 & 4.68 \end{bmatrix}, \quad \begin{aligned} \sigma_1(\mathbf{P}) &= 4.68, & \mathbf{n}_1 &= \begin{bmatrix} 0 & 0 & 1 \end{bmatrix}, \\ \sigma_2(\mathbf{P}) &= 3.24, & \mathbf{n}_2 &= \begin{bmatrix} 1 & 0 & 0 \end{bmatrix}, \\ \sigma_3(\mathbf{P}) &= 1.44, & \mathbf{n}_3 &= \begin{bmatrix} 0 & 1 & 0 \end{bmatrix}. \end{aligned}$$

The feedback gains are given by  $k_v = k_\omega = 1$ , and the rigid body trajectory is computed using oscillatory angular and linear rates of 1 Hz, and ideal velocity measurements.

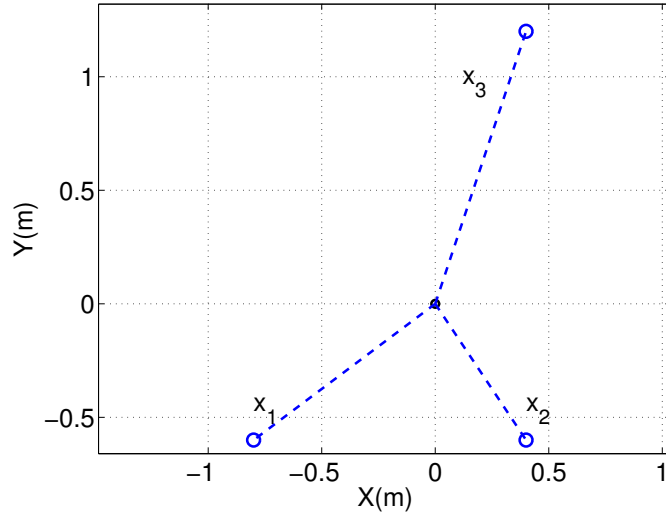


Figure 5.2: Landmark placement.

The attitude error, shown in Fig. 5.3 for two different initial conditions, converges exponentially fast to the equilibrium point  $\tilde{\mathcal{R}} = \mathbf{I}$ , and is below the exponential bound (5.21). The convergence rate of the exponential bound is defined by the smallest singular value of  $\mathbf{P}$ , and provides for a worst-case convergence bound that is more conservative when  $\sigma_1(\mathbf{P}) \gg \sigma_3(\mathbf{P})$ , and tighter when the directionality of  $\mathbf{P}$  is more uniform. This is evidenced in Fig. 5.3(b), where the convergence of the attitude error for a landmark transformation such that  $\mathbf{P} = \mathbf{I}$  is shown. The actual convergence rate to the origin is slower for larger initial estimation error  $\varphi(t_0)$ , due to the stickiness effect [5] in the proximity of the anti-stable manifold defined by  $\varphi = \pi$ . A convincing discussion and illustration of the influence of anti-stable manifolds in the trajectories of the nonlinear system can be found in [89].

The Euler axis trajectories in the hemisphere  $\mathbf{n}'_3\phi \geq 0$ , depicted in Fig. 5.4, illustrate the directionality of the attitude error discussed in Section 5.2.5. As derived in Theorem 5.10, the trajectories of the Euler axis converge to the direction of the smallest singular value of  $\mathbf{P}$ , that is  $\phi(t) \rightarrow \mathbf{n}_3$  as  $t \rightarrow \infty$  for  $\mathbf{n}'_3\phi > 0$ . Fig. 5.4 also shows that the boundary  $\mathbf{n}'_3\phi = 0$  is an invariant, zero-measure set, and that the trajectories near  $\mathbf{n}'_3\phi = 0$  converge slower to  $\mathbf{n}_1$ , due to the stickiness effect of the set defined by  $\mathbf{n}'_3\phi = 0$ .

The position estimation error  ${}^B\tilde{\mathbf{p}}$  decreases exponentially, as illustrated in Fig. 5.5. Using  ${}^B\hat{\mathbf{p}}$  and  $\hat{\mathcal{R}}$  to compute the position with respect to Earth frame  ${}^B\mathbf{p}_E$ , with  ${}^E\mathbf{t}_L = \mathbf{1}_3$ , produces the estimation error  ${}^B\tilde{\mathbf{p}}_E$  shown in Fig. 5.5, that is bounded by an exponentially decaying term, as expected. Nonetheless, the bound can be inflated by large attitude errors, as evidenced in (5.28). In that case, the observer can be modified to estimate directly  ${}^B\mathbf{p}_E$ , as discussed in Appendix E.1, producing a tight converge bound.



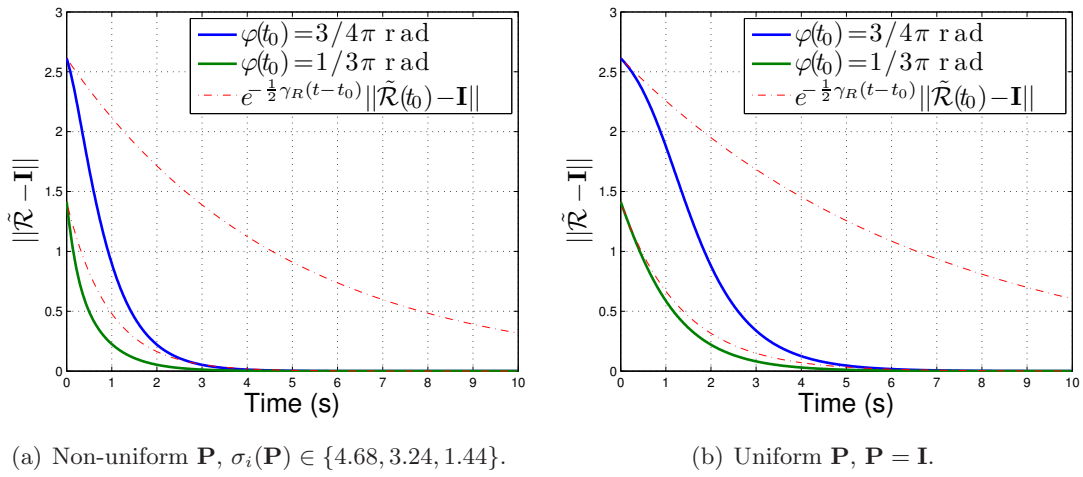


Figure 5.3: Attitude estimation error and exponential convergence bounds for diverse landmark coordinate transformations (ideal velocity readings,  $\phi(t_0) = \frac{1}{\sqrt{3}}\mathbf{1}'$ ).

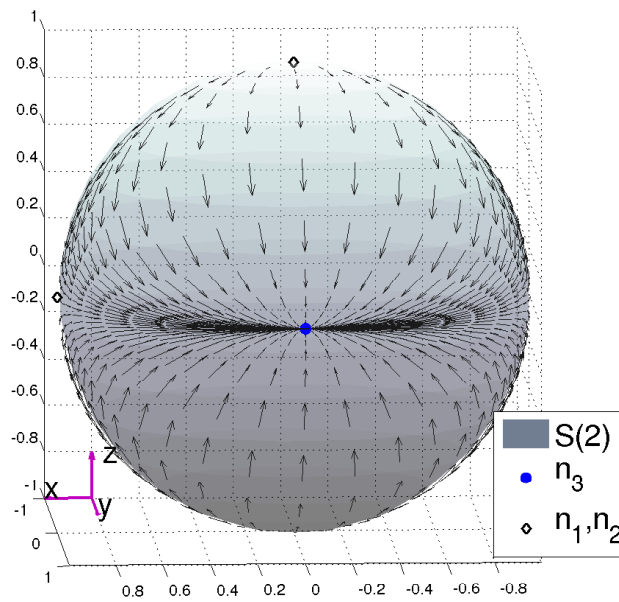


Figure 5.4: Euler axis trajectories on  $S(2)$ .

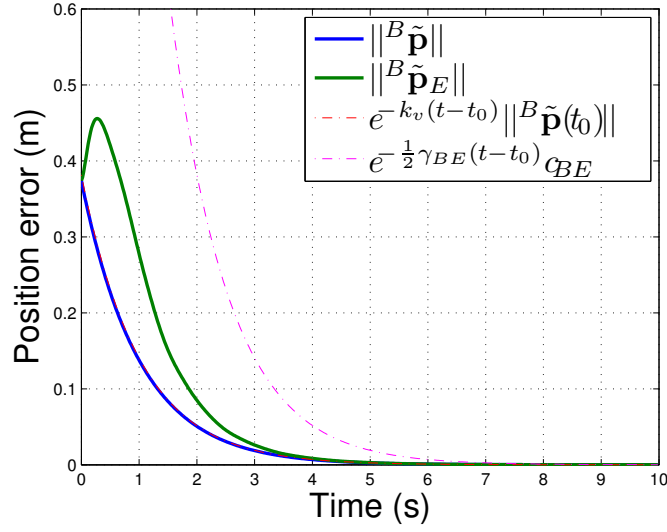


Figure 5.5: Error of the position estimate with respect to local and to Earth frames (ideal velocity readings,  $\varphi(t_0) = \frac{1}{3}\pi$  rad,  $\phi(t_0) = \frac{1}{\sqrt{3}}\mathbf{1}_3$ ).

#### 5.4.2 Biased velocity readings

The attitude and position observer with biased velocity readings is analyzed using the landmark configuration (5.50), that satisfies the non-collinearity conditions expressed in Assumption 5.1 and corresponds to the case of planar landmarks discussed in Remark 5.1 and Appendix E.2. The landmark coordinate transformation  $\mathbf{A}_X$  is designed so that  $\mathbf{U}_X \mathbf{U}'_X = \mathbf{I}$ , using the constructive method presented in the proof of Proposition 5.13.

The feedback gains are given by  $k_\omega = k_v = 1$ , and the values of  $\gamma_p$ ,  $\gamma_\varphi$  and  $\gamma_b$  are computed to satisfy the condition of Corollary 5.16 for large bounds on the initial estimation errors, given by

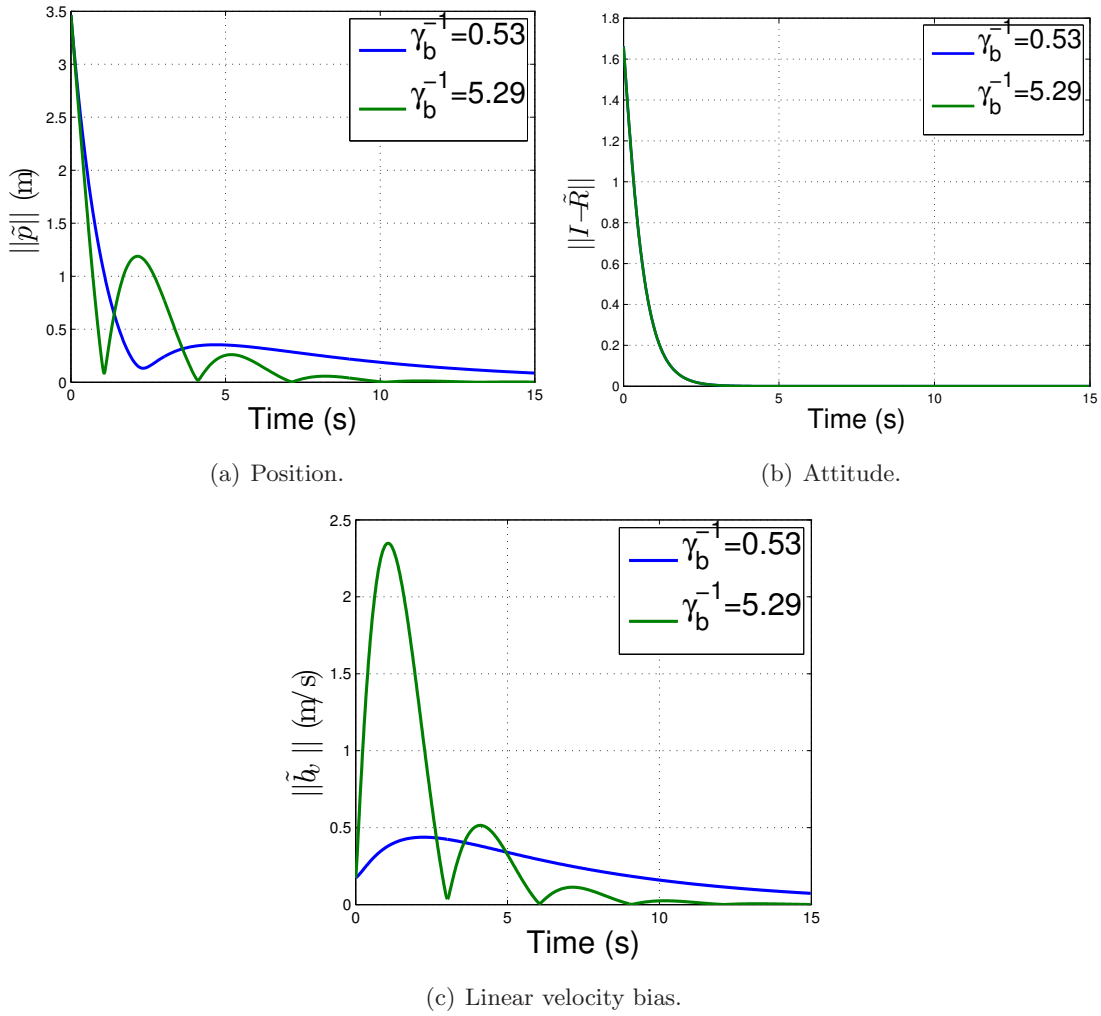
$$\tilde{p}_0 = 2\sqrt{3} \text{ m}, \quad \varphi_0 = \frac{\pi}{2} \text{ rad}, \quad \tilde{\omega}_0 = 5 \frac{\sqrt{3}\pi}{180} \text{ rad/s}, \quad \tilde{v}_0 = \sqrt{3} \times 10^{-1} \text{ m/s}. \quad (5.51)$$

The adopted values are given by  $\gamma_\varphi = 1$ ,  $\gamma_p = \frac{1}{4}$ , and multiple values of  $\gamma_b$  are used to study the convergence of the observer, namely  $\gamma_b \in \{0.19, 1.89\}$  that bear  $(\frac{\gamma_\varphi}{\gamma_b}, \frac{\gamma_p}{\gamma_b}) \in \{(0.53, 0.13), (5.29, 1.32)\}$ .

The initial attitude and position of the rigid body are  $\mathcal{R} = \mathbf{I}$ ,  ${}^B \mathbf{p} = \begin{bmatrix} 1 & 1 & 1 \end{bmatrix}'$  m, and the initial estimation errors are given by

$${}^B \tilde{\mathbf{p}}(t_0) = \begin{bmatrix} -2 \\ 2 \\ 2 \end{bmatrix} \text{ m}, \quad \varphi(t_0) = \frac{72\pi}{180} \text{ rad}, \quad \phi(t_0) = \frac{1}{\sqrt{3}} \begin{bmatrix} 1 \\ 1 \\ 1 \end{bmatrix},$$

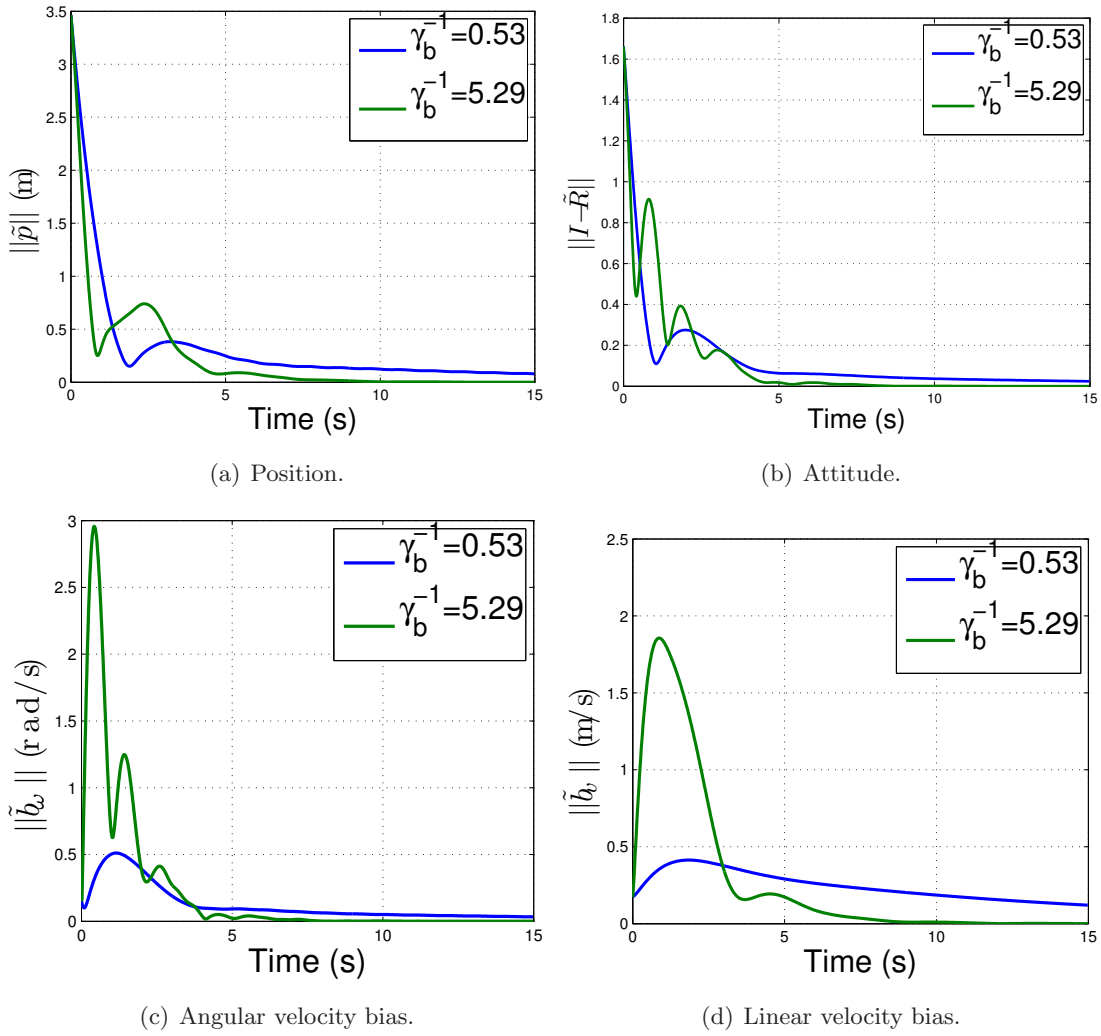
$$\tilde{\boldsymbol{\omega}}(t_0) = \frac{5\pi}{180} \begin{bmatrix} 1 \\ -1 \\ 1 \end{bmatrix} \text{ rad/s}, \quad \tilde{\mathbf{v}}(t_0) = 10^{-1} \begin{bmatrix} 1 \\ 1 \\ -1 \end{bmatrix} \text{ m/s},$$

Figure 5.6: Estimation errors ( $\tilde{\mathbf{b}}_v \neq 0, \tilde{\mathbf{b}}_\omega = 0$ ).

that are within the bounds (5.51). The rigid body trajectory is computed using oscillatory angular and linear velocities of 1 Hz.

The estimation error trajectories are depicted in Fig 5.6 for the case where only the linear velocity measurements are corrupted by bias ( $\tilde{\mathbf{b}}_v \neq 0, \tilde{\mathbf{b}}_\omega = 0$ ), studied in Section 5.3.1. The position and bias estimates converge faster for larger feedback gain  $k_v = \frac{\gamma_p}{\gamma_b}$ , as shown in Figs. 5.6(a) and 5.6(c). The convergence of the attitude error is independent of the position and bias errors, as shown in Fig. 5.6(b), due to the decoupling of the position and attitude error dynamics, that is verified for the case of biased linear velocity readings, as described in Section 5.3.1.

The results for the case where both angular and linear velocity readings are biased, are presented in Fig. 5.7. The convergence of the estimation error to the origin is faster for larger feedback gains. The estimation of  $\mathbf{b}_\omega$  influences the convergence of the attitude and position estimates, which is slower than that with  $\tilde{\mathbf{b}}_\omega = 0$ , as evidenced by comparing Fig. 5.6 and Fig. 5.7. In other words, the stability of the observer in the presence of biased

Figure 5.7: Estimation errors ( $\tilde{\mathbf{b}}_v \neq 0, \tilde{\mathbf{b}}_\omega \neq 0$ ).

velocity readings is obtained at the cost of convergence rate, as expected.

Larger gains introduce faster convergence, yet higher peaks in the bias estimates are also obtained. These can be justified by analyzing the level sets of the Lyapunov function  $V_b \leq c$ , that are positively invariant and contain points with small attitude and position error  $\|\mathbf{I} - \tilde{\mathcal{R}}\| \approx 0$ ,  $\|\tilde{\mathbf{p}}\| \approx 0$ , but with large bias error  $\|\tilde{\mathbf{b}}_\omega\|^2 + \|\tilde{\mathbf{b}}_v\|^2 \approx \frac{2c}{\gamma_b}$ .

The Lyapunov function convergence is shown in Fig. 5.8, where the logarithmic scale is adopted to demonstrate exponentially fast convergence to the origin. Given that  $V_b$  provides for an upper bound for the estimation error ( ${}^B\tilde{\mathbf{p}}, \tilde{\mathcal{R}}, \tilde{\mathbf{b}}_\omega, \tilde{\mathbf{b}}_v$ ), Fig. 5.8 shows that, in spite of the peak values attained for ( $\tilde{\mathbf{b}}_\omega, \tilde{\mathbf{b}}_v$ ), the norm of the estimation error converges exponentially fast to  $(\mathbf{0}, \mathbf{I}, \mathbf{0}, \mathbf{0})$ .

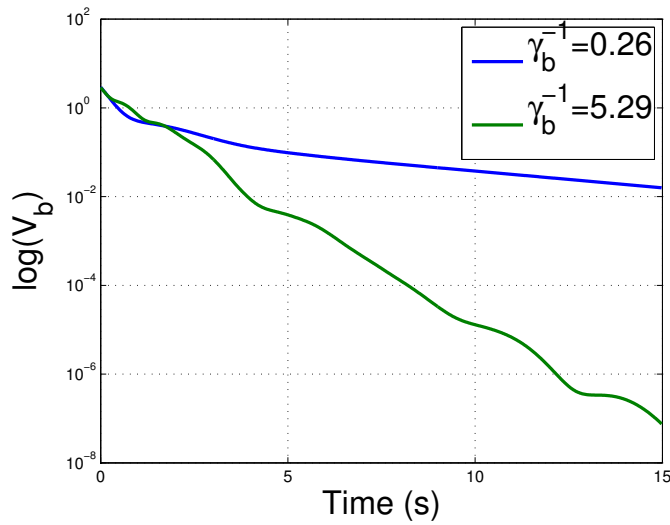


Figure 5.8: Exponential convergence of  $V_b$  (biased linear and angular velocity measurements).

## 5.5 Conclusions

A nonlinear observer for position and attitude estimation on  $SE(3)$  was proposed, using landmark measurements and non-ideal velocity readings. A Lyapunov function, conveniently defined by the landmark measurement error, was adopted to derive the position and attitude feedback laws. This approach provided for an insight on the necessary and sufficient landmark configuration for position and attitude estimation, and produced an output feedback architecture, expressed as a function of the sensor readings and state estimates.

The case of ideal velocity readings allowed for the decoupling of the position and attitude systems, and almost global stability of the origin, with exponential convergence of the trajectories, was obtained. The asymptotic behavior of the trajectories was also characterized, showing that the attitude error converges to the axis of the smallest eigenvalue of a matrix defined by the landmark geometry. The stability results were extended for the case of biased linear velocity readings, where the position and attitude systems were coupled by the presence of rate gyro bias. Using recently results for parameterized LTVs, exponential stabilization of the origin for bounded initial estimation errors was shown.

Simulation results illustrated the convergence properties of the observer for diverse feedback gains and initial conditions. The theoretical exponential convergence bounds were shown to be close to the real estimation error. Trajectories emanating from initial conditions near the anti-stable manifolds showed smaller convergence rate, as expected from the continuity of the solutions of dynamical systems. In the case of biased linear and angular velocity readings, exponential convergence to the origin was evidenced. The effects of time-varying velocities in the solutions of the nonautonomous error dynamics was negligible. The trade-off between convergence rate and the peak values of the estimates was justified using the level sets of the Lyapunov function.



## Chapter 6

# Nonlinear attitude observer using vector observations

This chapter presents a nonlinear observer for attitude estimation on  $SO(3)$ , based on vector observations and biased angular rate measurements. The observer is obtained using the technique proposed in Chapter 5, that derives the feedback law constructively, using a Lyapunov function conveniently defined by the measurement error of the aiding sensor. The resulting attitude feedback law is an explicit function of the vector measurements and observer estimates, and the stability properties of the attitude observer are similar to those of the landmark based observer presented in Chapter 5. Namely, almost global stability with exponential convergence is obtained for ideal velocity measurements, and exponential stability is shown for biased velocity readings, and initial estimation errors within a desired region.

The derivation of the attitude observer evidences how the design technique of Chapter 5 can be used to address the classical problem of attitude estimation using inertial measurements and attitude aiding sensors, such as magnetometers, star trackers and pendulums [37]. Also, the attitude observer is used to motivate and illustrate the stability analysis tools presented in Chapter 7, that yield input-to-state stability with respect to noise in the angular velocity reading, and almost global stability of a reduced order observer in the presence of bias.

The chapter is organized as follows. Section 6.1 introduces the vector measurements, proposes the synthesis Lyapunov function, and the necessary sensor setup for attitude determination is discussed. In Section 6.2, the attitude observer is derived for the cases of unbiased and biased angular velocity readings. The feedback law is written as an explicit function of the sensor readings, exponential convergence of the attitude and bias estimation errors to the origin is demonstrated, and exponential convergence bounds are obtained using the recent results for parameterized LTVs. The stability results are obtained by considering convenient design parameters, however a formulation of the attitude observer with generic design parameters is presented in Appendix G. In Section 6.3, the convergence of the estimation errors is illustrated in simulation for distinct initial conditions and feedback

gain values. Section 6.4 presents concluding remarks.

## 6.1 Synthesis Lyapunov function

The attitude feedback law is derived resorting to the Lyapunov's stability theory and to a conveniently defined transformation of the vector observations. This section proposes a Lyapunov function based on the measurement error of the vector observations, and derives the necessary and sufficient sensor setup for attitude estimation.

### 6.1.1 Vector measurements model

The vector observations are a function of the rigid body's orientation. While vector observations yield a snapshot attitude estimate for each time instant, inertial sensors allow for the propagation of the attitude in time. The attitude estimator combines the inertial measurements with the vector observations, hence exploiting both information sources. On-board sensors such as magnetometers, star trackers and pendulums, among others, provide vector observations expressed in body frame coordinates

$$\mathbf{h}_{r_i} = {}^B\mathbf{h}_i := \mathcal{R}'^L\mathbf{h}_i, \quad (6.1)$$

where  $i = 1..n$  is the vector index,  $n$  is the number of vector measuring sensors and the vector representation in the local coordinate frame  $\{L\}$ , denoted by  ${}^L\mathbf{h}_i$ , is known.

Define the linear combination of the sensed vector  ${}^L\mathbf{h}_i$  expressed in the local coordinate frame, given by

$${}^L\mathbf{u}_j := \sum_{i=1}^n a_{ij} {}^L\mathbf{h}_i, \quad j = 1..n. \quad (6.2)$$

The vector transformation (6.2) is represented in matrix form by

$$\mathbf{U}_H = \mathbf{H}\mathbf{A}_H,$$

where  $\mathbf{U}_H := [{}^L\mathbf{u}_1 \ \dots \ {}^L\mathbf{u}_n]$ ,  $\mathbf{H} := [{}^L\mathbf{h}_1 \ \dots \ {}^L\mathbf{h}_n]$ ,  $\mathbf{U}_H, \mathbf{H} \in \mathbb{M}(3, n)$  and  $\mathbf{A}_H := [a_{ij}] \in \mathbb{M}(n)$  is invertible.

The estimated and the nominal representation of  ${}^L\mathbf{u}_j$  in Body frame coordinates, are respectively denoted by

$${}^B\mathbf{u}_i := \mathcal{R}'^L\mathbf{u}_i, \quad {}^B\hat{\mathbf{u}}_i := \hat{\mathcal{R}}'^L\mathbf{u}_i,$$

which are represented in matrix form as

$${}^B\mathbf{U}_H = \mathcal{R}'\mathbf{U}_H, \quad {}^B\hat{\mathbf{U}}_H = \hat{\mathcal{R}}'\mathbf{U}_H,$$

where  ${}^B\hat{\mathbf{U}}_H := [{}^B\hat{\mathbf{u}}_1 \ \dots \ {}^B\hat{\mathbf{u}}_n]$  and  ${}^B\mathbf{U}_H := [{}^B\mathbf{u}_1 \ \dots \ {}^B\mathbf{u}_n]$ ,  ${}^B\hat{\mathbf{U}}_H, {}^B\mathbf{U}_H \in \mathbb{M}(3, n)$ .



### 6.1.2 Lyapunov function

The proposed observer estimates the orientation of the rigid body by computing the kinematics

$$\dot{\hat{\mathcal{R}}} = \hat{\mathcal{R}}(\hat{\omega})_{\times},$$

where  $\hat{\mathcal{R}}$  is the estimated attitude and  $\hat{\omega}$  is the feedback term constructed to compensate for the attitude estimation error.

In this chapter, the attitude error is defined as  $\tilde{\mathcal{R}} := \hat{\mathcal{R}}'\mathcal{R}$ , which is an alternate error definition to that proposed in Chapter 5. An interesting insight on the error functions for invariant systems on Lie-groups can be found in [84]. The attitude error kinematics are a function of the angular velocity estimates and given by

$$\dot{\tilde{\mathcal{R}}} = -\tilde{\mathcal{R}}\left(\tilde{\mathcal{R}}'\hat{\omega} - \omega\right)_{\times}.$$

The attitude feedback law  $\hat{\omega}$  is defined as function of the angular velocity readings and vector observations (6.1), so that the closed loop attitude estimation errors converge to the origin, i.e.,  $\tilde{\mathcal{R}} \rightarrow \mathbf{I}$ , as  $t \rightarrow \infty$ .

The candidate Lyapunov function is defined by the estimation error of the transformed vectors

$$V = \frac{1}{2} \sum_{i=1}^n \|{}^B\hat{\mathbf{u}}_i - {}^B\mathbf{u}_i\|^2 = \frac{1}{2} \|{}^B\hat{\mathbf{U}}_H - {}^B\mathbf{U}_H\|^2. \quad (6.3)$$

Algebraic manipulation produces the equivalent Lyapunov formulation and time derivative

$$V = \text{tr} \left[ (\mathbf{I} - \tilde{\mathcal{R}}) \mathbf{U}_H \mathbf{U}_H' \right], \quad (6.4a)$$

$$\dot{V} = \left( \tilde{\mathcal{R}}' \mathbf{U}_H \mathbf{U}_H' - \mathbf{U}_H \mathbf{U}_H' \tilde{\mathcal{R}} \right)'_{\otimes} (\tilde{\mathcal{R}}' \hat{\omega} - \omega). \quad (6.4b)$$

where  $\mathbf{P} = \text{tr}(\mathbf{U}_H \mathbf{U}_H') \mathbf{I} - \mathbf{U}_H \mathbf{U}_H'$ ,  $\mathbf{P} \in \text{M}(3)$ .

The proposed Lyapunov function measures the error of the vector observations. To guarantee that  $V = 0$  if and only if the attitude is correctly estimated, i.e.  $\tilde{\mathcal{R}} = \mathbf{I}$ , the geometric configuration of the measured vectors is required to satisfy the following assumption.

**Assumption 6.1.** *There are at least two noncollinear vectors  ${}^L\mathbf{h}_i$ , that is,  $\text{rank}(\mathbf{H}) \geq 2$ .*

**Lemma 6.1.** *The Lyapunov function  $V$  has a unique global minimum at  $\tilde{\mathcal{R}} = \mathbf{I}$  if and only if Assumption 6.1 is verified*

$$\forall_{\tilde{\mathcal{R}} \neq \mathbf{I}} V > 0 \quad \text{if and only if} \quad \exists_{i \neq j} \forall_{\alpha \in \mathbb{R}} : {}^L\mathbf{h}_i \neq \alpha {}^L\mathbf{h}_j.$$

*Proof.* The result can be obtained by following the proof of Lemma 5.3, where the properties of a similar Lyapunov function are derived.  $\square$

To illustrate the necessity of Assumption 6.1, assume that  $\text{rank}(\mathbf{H}) = 1$ , i.e. all  ${}^L\mathbf{h}_i$  (and  ${}^L\mathbf{u}_i$ ) are collinear. Any attitude error  $\tilde{\mathcal{R}}$  represented by an arbitrary rotation  $\varphi$  about the vector  $\phi = {}^L\mathbf{u}_i / \|{}^L\mathbf{u}_i\|$  satisfies  $V = 0$ . A detailed insight on the limitations of attitude estimation using single direction measurements can be found in [88] and references therein.

In the present chapter, the transformation  $\mathbf{A}_H$  is designed to shape uniformly the directionality of the transformed vector observations, and is similar to that adopted for the landmark observer with biased velocity readings, described in Section 5.3.

**Proposition 6.2.** *Assume that  $\mathbf{H}$  is full rank, then there is a nonsingular  $\mathbf{A}_H \in \mathbb{M}(n)$  such that  $\mathbf{U}_H \mathbf{U}'_H = \mathbf{I}$ .*

*Proof.* See proof of Proposition 5.13. □

Using the transformation  $\mathbf{A}_H$  defined in Proposition 6.2, the Lyapunov function (6.4a) is expressed by

$$V = \frac{1}{2} \|\mathbf{I} - \tilde{\mathcal{R}}\|^2, \quad \dot{V} = \left( \tilde{\mathcal{R}}' - \tilde{\mathcal{R}} \right)'_{\otimes} (\tilde{\mathcal{R}}' \hat{\omega} - \omega). \quad (6.5)$$

Note that the conditions of Proposition 6.2 are not satisfied directly by Assumption 6.1. As discussed in Appendix E.2 for the landmark based observer, in case  $\text{rank}(\mathbf{H}) = 2$ , the direction orthogonal to the columns of  $\mathbf{H}$  can be generated from the columns of  $\mathbf{H}$ , producing a full rank matrix  $\mathbf{H}_a$  that is used in the observer equations. Taking two linearly independent columns of  $\mathbf{H}$ ,  ${}^L\mathbf{h}_i$  and  ${}^L\mathbf{h}_j$ , the augmented matrices are given by  $\mathbf{H}_a := \begin{bmatrix} \mathbf{H} & {}^L\mathbf{h}_i \times {}^L\mathbf{h}_j \end{bmatrix}$ ,  $\mathbf{U}_{H_a} = \mathbf{H}_a \mathbf{A}_{H_a}$ , where  $\mathbf{H}_a, \mathbf{U}_{H_a} \in \mathbb{M}(3, n+1)$ ,  $\mathbf{A}_{H_a} \in \mathbb{M}(n+1)$  is a nonsingular matrix such that  $\mathbf{U}_{H_a} \mathbf{U}'_{H_a} = \mathbf{I}$ . Using the fact that the cross product is commutable with coordinate transformations,  $(\mathcal{R}' {}^L\mathbf{h}_i) \times (\mathcal{R}' {}^L\mathbf{h}_j) = \mathcal{R}' ({}^L\mathbf{h}_i \times {}^L\mathbf{h}_j)$ , the representation of the vector measurements in body coordinates is given by  ${}^B\mathbf{U}_{H_a} = \mathcal{R}' \mathbf{U}_{H_a}$  and  ${}^B\hat{\mathbf{U}}_{H_a} = \hat{\mathcal{R}}' \mathbf{U}_{H_a}$ . The modified observer is obtained by replacing the matrices  $\mathbf{U}_H$  and  $\mathbf{H}$  by  $\mathbf{U}_{H_a}$  and  $\mathbf{H}_a$ , respectively.

## 6.2 Observer synthesis

In this section, the feedback law for attitude estimation in the presence of rate gyro bias is derived using the proposed Lyapunov function.

### 6.2.1 Unbiased angular velocity measurements

The case of ideal body angular velocity measurements is considered first. The body angular velocity is measured by a rate gyro sensor triad

$$\omega_r = \omega.$$

Under Assumption 6.1 and given the Lyapunov function time derivative (6.5), a feedback law is proposed to drive the attitude error to zero,

$$\hat{\omega} = \tilde{\mathcal{R}}\omega - k_\omega \mathbf{s}_\omega, \quad (6.6)$$

where the feedback term is given by

$$\mathbf{s}_\omega = \left( \tilde{\mathcal{R}}' - \tilde{\mathcal{R}} \right)_\otimes, \quad (6.7)$$

and  $k_\omega > 0$  is a positive scalar. The feedback law  $\hat{\boldsymbol{\omega}}$  is slightly diverse from that defined in (5.17), due to reasons that will be more clear in the case of biased velocity readings. The attitude feedback yields the autonomous closed loop attitude kinematics

$$\dot{\tilde{\mathcal{R}}} = -k_\omega \tilde{\mathcal{R}}(\tilde{\mathcal{R}} - \tilde{\mathcal{R}}'), \quad (6.8)$$

and the closed loop Lyapunov function time derivative is given by

$$\dot{V} = -k_\omega \mathbf{s}'_\omega \mathbf{s}_\omega = -\frac{k_\omega}{2} \|\tilde{\mathcal{R}} - \tilde{\mathcal{R}}'\|^2 \leq 0,$$

so it is immediate that the attitude feedback law produces a Lyapunov function that decreases along the system trajectories.

The system (6.8) is identical to the error dynamics of the landmark based observer, presented in (5.19), and hence the stability properties can be derived directly using the results of Section 5.2. Using  $\|\tilde{\mathcal{R}} - \tilde{\mathcal{R}}'\|^2 = \frac{1}{2}(8 - \|\mathbf{I} - \tilde{\mathcal{R}}\|^2)\|\mathbf{I} - \tilde{\mathcal{R}}\|^2$ , the set of points where  $\dot{V} = 0$  is characterized by

$$C_{\mathcal{R}} = \{\tilde{\mathcal{R}} \in \text{SO}(3) : \tilde{\mathcal{R}} = \mathbf{I} \vee \|\mathbf{I} - \tilde{\mathcal{R}}\|^2 = 8\}.$$

By direct substitution in the closed loop system (6.8), it is easy to see that  $\tilde{\mathcal{R}} = \tilde{\mathcal{R}}' \Rightarrow \dot{\tilde{\mathcal{R}}} = 0$ , i.e.  $C_{\mathcal{R}}$  is invariant, and hence convergence to the origin by LaSalle's invariance principle is inconclusive. However, the set  $\tilde{\mathcal{R}} = \tilde{\mathcal{R}}'$  is described by the rotations such that the angle is  $\varphi = \pi$ , i.e.  $\|\tilde{\mathcal{R}} - \mathbf{I}\|^2 = 8$ , and has zero measure. The observer stability results, obtained by adaptation of the results presented in Section 5.2, establish that the trajectories emanating from almost everywhere in  $\text{SO}(3)$  converge exponentially fast to the origin.

**Theorem 6.3.** *The closed-loop system (6.8) has an exponentially stable point at  $\tilde{\mathcal{R}} = \mathbf{I}$ . For any initial condition in the region of attraction*

$$\tilde{\mathcal{R}}(t_0) \in \{\tilde{\mathcal{R}} \in \text{SO}(3) : \|\mathbf{I} - \tilde{\mathcal{R}}\|^2 < 8\}$$

*the trajectory satisfies*

$$\|\tilde{\mathcal{R}}(t) - \mathbf{I}\| \leq k_{\mathcal{R}} \|\tilde{\mathcal{R}}(t_0) - \mathbf{I}\| e^{-\frac{1}{2}\gamma_{\mathcal{R}}(t-t_0)}, \quad (6.9)$$

where  $\gamma_{\mathcal{R}} = \frac{k_\omega}{2}(8 - \|\tilde{\mathcal{R}}(t_0) - \mathbf{I}\|^2)$ .

*Proof.* The proof can be obtained from that of Theorem 5.5. In alternative, algebraic manipulation of the time derivative of the Lyapunov function produces

$$\dot{V} = -\frac{k_\omega}{2} \|\tilde{\mathcal{R}} - \tilde{\mathcal{R}}'\|^2 = -\frac{k_\omega}{4} (8 - \|\mathbf{I} - \tilde{\mathcal{R}}\|^2) \|\mathbf{I} - \tilde{\mathcal{R}}\|^2 = -\frac{k_\omega}{2} (8 - \|\mathbf{I} - \tilde{\mathcal{R}}\|^2) V.$$

The Lyapunov function is decreasing with time, and hence  $\|\mathbf{I} - \tilde{\mathcal{R}}(t)\|^2 \leq \|\mathbf{I} - \tilde{\mathcal{R}}(t_0)\|^2$ , yielding  $\dot{V} \leq -\frac{k_\omega}{2} (8 - \|\mathbf{I} - \tilde{\mathcal{R}}(t_0)\|^2) V$ . Applying (6.5) and the comparison lemma produces the desired result.  $\square$

The results of Theorem 6.3 are valid for ideal velocity measurements. In the next section, the observer is extended to compensate for bias in the velocity measurements. Also, stability of the observer with unmodeled disturbances in the velocity readings is shown in Chapter 7, which illustrates the combination of Lyapunov and density functions proposed later in this thesis.

The directionality introduced by the landmarks is made uniform by the adopted transformation  $\mathbf{A}_H$ . To see that, denote the Euler angle-axis parameterization of the attitude error as  $\tilde{\mathcal{R}} = \text{rot}(\varphi, \phi)$ . The kinematics of the parameterization are given by

$$\dot{\varphi} = -2k_\omega \sin(\varphi), \quad \dot{\phi} = 0,$$

which shows that the directionality of the attitude error is invariant, i.e.  $\phi(t) = \phi(t_0)$ . As discussed in Appendix G, a generic  $\mathbf{A}_H$  can be considered to endow the observer with faster and slower directions of estimation.

### 6.2.2 Biased angular velocity measurements

In this section, asymptotic stabilization of the attitude error in the presence of angular velocity bias is derived and exponential convergence to the origin is obtained. The rate gyro readings are corrupted by a bias term

$$\boldsymbol{\omega}_r = \boldsymbol{\omega} + \mathbf{b}_\omega,$$

where the nominal bias is considered constant,  $\dot{\mathbf{b}}_\omega = \mathbf{0}$ . The proposed Lyapunov function (6.5) is augmented to account for the effect of the rate gyro bias

$$V_b = \frac{1}{2} \|\tilde{\mathcal{R}} - \mathbf{I}\|^2 + \frac{1}{2k_{b_\omega}} \|\tilde{\mathbf{b}}_\omega\|^2,$$

where  $\tilde{\mathbf{b}}_\omega = \hat{\mathbf{b}}_\omega - \mathbf{b}_\omega$  is the bias compensation error,  $\hat{\mathbf{b}}_\omega$  is the estimated bias and  $k_{b_\omega}$  is a positive scalar. Under Assumption 6.1 and by Lemma 6.1, the Lyapunov function  $V_b$  has an unique global minimum at  $(\tilde{\mathcal{R}}, \tilde{\mathbf{b}}_\omega) = (\mathbf{I}, \mathbf{0})$ .

The feedback law for the angular velocity is obtained by compensating the bias of the angular velocity reading in (6.6), producing

$$\hat{\boldsymbol{\omega}} = \tilde{\mathcal{R}}(\boldsymbol{\omega} + \mathbf{b}_\omega - \hat{\mathbf{b}}_\omega) - k_\omega \mathbf{s}_\omega = \tilde{\mathcal{R}}(\boldsymbol{\omega} - \tilde{\mathbf{b}}_\omega) - k_\omega \mathbf{s}_\omega.$$

The time derivative of the augmented Lyapunov function is described by

$$\dot{V}_b = -k_\omega \mathbf{s}'_\omega \mathbf{s}_\omega + \tilde{\mathbf{b}}'_\omega \left( \frac{1}{k_{b_\omega}} \dot{\tilde{\mathbf{b}}}_\omega - \mathbf{s}_\omega \right),$$

that motivates the bias feedback law defined by

$$\dot{\hat{\mathbf{b}}}_\omega = k_{b_\omega} \mathbf{s}_\omega.$$

Using  $\dot{\tilde{\mathbf{b}}}_\omega = \dot{\hat{\mathbf{b}}}_\omega$ , the time derivative of the Lyapunov function is described by

$$\dot{V}_b = -k_\omega \mathbf{s}'_\omega \mathbf{s}_\omega = -\frac{k_\omega}{2} \|\tilde{\mathcal{R}} - \tilde{\mathcal{R}}'\|^2 \leq 0,$$

and the closed loop kinematics are given by

$$\dot{\tilde{\mathcal{R}}} = -k_\omega \tilde{\mathcal{R}}(\tilde{\mathcal{R}} - \tilde{\mathcal{R}}') + \tilde{\mathcal{R}} \left( \tilde{\mathbf{b}}_\omega \right)_\times, \quad \dot{\tilde{\mathbf{b}}}_\omega = k_{b_\omega} \left( \tilde{\mathcal{R}}' - \tilde{\mathcal{R}} \right)_\otimes. \quad (6.10)$$

The set of points where  $\dot{V}_b = 0$  is characterized by

$$C_b = \{(\tilde{\mathcal{R}}, \tilde{\mathbf{b}}_\omega) \in \text{SO}(3) \times \mathbb{R}^3 : \tilde{\mathcal{R}} = \mathbf{I} \vee \|\mathbf{I} - \tilde{\mathcal{R}}\|^2 = 8\}.$$

The positively invariant subsets of  $C_b$  where  $\|\mathbf{I} - \tilde{\mathcal{R}}\|^2 = 8$  are a consequence of the topological limitation to global stabilization on  $\text{SO}(3)$  discussed in Chapter 5. By analyzing the level sets of  $V_b$ , the next lemma shows that the attitude and bias estimation errors are bounded, providing sufficient conditions that exclude convergence to the attitude error  $\|\mathbf{I} - \tilde{\mathcal{R}}\|^2 = 8$ .

**Lemma 6.4.** *The attitude and bias estimation errors,  $\tilde{\mathcal{R}}$  and  $\tilde{\mathbf{b}}_\omega$  respectively, are bounded. For any initial condition such that*

$$k_{b_\omega} > \frac{\|\tilde{\mathbf{b}}_\omega(t_0)\|^2}{8 - \|\mathbf{I} - \tilde{\mathcal{R}}(t_0)\|^2}, \quad (6.11)$$

*the attitude error is bounded by  $\|\mathbf{I} - \tilde{\mathcal{R}}(t)\|^2 \leq c_{\max} < 8$  for all  $t \geq t_0$ .*

*Proof.* The proof is obtained by reproducing the steps adopted in the demonstration of Lemma 5.14. Let  $\mathbf{x} := (\tilde{\mathcal{R}}, \tilde{\mathbf{b}}_\omega)$ , the Lyapunov function  $V_b$  is given by the weighted distance of the state to the origin, and  $\dot{V}_b \leq 0$ , so  $\forall_{t \geq t_0} \frac{1}{2}(\|\mathbf{I} - \tilde{\mathcal{R}}(t)\|^2 + \frac{1}{k_{b_\omega}} \|\tilde{\mathbf{b}}_\omega(t)\|^2) \leq V_b(\mathbf{x}(t_0))$ , and hence the state is bounded. The gain condition (6.11) is equivalent to  $V_b(\mathbf{x}(t_0)) < 4$ . Given that  $V_b(\mathbf{x}(t)) \leq V_b(\mathbf{x}(t_0))$ , then  $\frac{1}{2}\|\mathbf{I} - \tilde{\mathcal{R}}(t)\|^2 \leq V_b(\mathbf{x}(t_0)) < 4$  which concludes the proof.  $\square$

The feedback law  $\hat{\omega}$  is diverse from that adopted in the landmark based observer, and produces autonomous error kinematics (6.10). The time-invariance of the dynamics yields trajectories that are uniform with respect to time, and can be analyzed using stronger stability results, such as LaSalle's invariance principle [78, 125], to attain asymptotic stability of the origin. Analysis tools based on density functions can be also adopted, to address almost global stability, and stabilization in the presence of inertial sensor noise, as shown in Chapter 7.

The time-invariance of the attitude observer error kinematics is obtained at the cost of an output feedback formulation of  $\hat{\omega}$  that is slightly more complex than that of the landmark observer, presented in Theorem 5.17. Consequently, the feedback laws  $\hat{\omega}$  of the landmark and vector based observers are both of interest, since the stability of the observers may be diverse in the practical implementation of the algorithms, while further theoretical developments may lead to distinct and enriching results.

The stability of the observer is presented in the following result. Asymptotic stability of the origin is obtained by LaSalle's invariance principle and Lemma 6.4, and asymptotic stability with exponential convergence is shown by using the stability results for parameterized LTV systems adopted in Section 5.3.

**Theorem 6.5.** *For any initial condition that satisfies (6.11), the attitude and bias estimation errors converge exponentially fast to the stable equilibrium point  $(\tilde{\mathcal{R}}, \tilde{\mathbf{b}}_\omega) = (\mathbf{I}, 0)$ .*

*Proof.* The proof is identical to that of Theorem 5.15, and presented for the sake of clarity. Using the quaternion form to describe the attitude error, the closed loop attitude and bias compensation errors kinematics are described by

$$\dot{\tilde{\mathbf{q}}}_q = \frac{1}{2}\mathbf{Q}(\tilde{\mathbf{q}})(\tilde{\mathbf{b}}_\omega - 4k_\omega\tilde{\mathbf{q}}_q\tilde{q}_s), \quad \dot{\tilde{\mathbf{b}}}_\omega = -4k_{b_\omega}\mathbf{Q}'(\tilde{\mathbf{q}})\tilde{\mathbf{q}}_q, \quad (6.12)$$

where  $\mathbf{Q}(\tilde{\mathbf{q}}) := \tilde{q}_s\mathbf{I} + (\tilde{\mathbf{q}}_q)_\times$ ,  $\dot{\tilde{q}}_s = 2k_\omega\tilde{\mathbf{q}}_q'\tilde{\mathbf{q}}_q\tilde{q}_s - \frac{1}{2}\tilde{\mathbf{q}}_q'\tilde{\mathbf{b}}_\omega$ , and  $\tilde{\mathbf{q}} = \begin{bmatrix} \tilde{\mathbf{q}}_q' & \tilde{q}_s \end{bmatrix}'$  is the Euler quaternion representation of matrix  $\tilde{\mathcal{R}}$ . Using  $\|\tilde{\mathbf{q}}_q\|^2 = \frac{1}{8}\|\tilde{\mathcal{R}} - \mathbf{I}\|^2$ , the Lyapunov function in quaternion coordinates is described by  $V_b = 4\|\tilde{\mathbf{q}}_q\|^2 + \frac{1}{2k_{b_\omega}}\|\tilde{\mathbf{b}}_\omega\|^2$ .

Define the system (6.12) in the domain  $\mathcal{D}_q = \{(\tilde{\mathbf{q}}_q, \tilde{\mathbf{b}}_\omega) \in \text{B}(3) \times \mathbb{R}^3 : V_b \leq 4 - \varepsilon_q\}$ ,  $0 < \varepsilon_q < 4$ . The set  $\mathcal{D}_q$  is given by the interior of the Lyapunov surface, so it is positively invariant and well defined. The condition (6.11) implies that the initial condition is in the set  $\mathcal{D}_q$  for  $\varepsilon_q$  small enough, and by Lemma 6.4, the components of the attitude error quaternion are bounded by  $\|\tilde{\mathbf{q}}_q\|^2 \leq \frac{c_{\max}}{8}$  and  $\|\tilde{q}_s\|^2 \geq 1 - \frac{c_{\max}}{8}$ , with  $c_{\max} = 8 - 2\varepsilon_q$ .

Define the parameterized LTV system

$$\begin{bmatrix} \dot{\tilde{\mathbf{q}}}_{q\star} \\ \dot{\tilde{\mathbf{b}}}_{\omega\star} \end{bmatrix} = \begin{bmatrix} \mathcal{A}(t, \lambda) & \mathcal{B}'(t, \lambda) \\ -\mathcal{C}(t, \lambda) & \mathbf{0}_{3 \times 3} \end{bmatrix} \begin{bmatrix} \tilde{\mathbf{q}}_{q\star} \\ \tilde{\mathbf{b}}_{\omega\star} \end{bmatrix}, \quad (6.13)$$

where  $(\tilde{\mathbf{q}}_{q\star}, \tilde{\mathbf{b}}_{\omega\star}) \in \mathbb{R}^3 \times \mathbb{R}^3$ ,  $\lambda \in \mathbb{R}_{\geq 0} \times \mathcal{D}_q$ , and the matrices

$$\mathcal{A}(t, \lambda) = -2k_\omega\tilde{q}_s(t, \lambda)\mathbf{Q}(\tilde{\mathbf{q}}(t, \lambda)), \quad \mathcal{B}(t, \lambda) = \frac{1}{2}\mathbf{Q}'(\tilde{\mathbf{q}}(t, \lambda)), \quad \mathcal{C}(t, \lambda) = 8k_{b_\omega}\mathcal{B}(t, \lambda),$$

are bounded, so the system is well defined. The quaternion  $\tilde{\mathbf{q}}(t, \lambda)$  represents the solution of (6.12) with initial condition  $\lambda = (t_0, \tilde{\mathbf{q}}_q(t_0), \tilde{\mathbf{b}}_\omega(t_0))$ . If the parameterized LTV system (6.13) is  $\lambda$ -UGES, then the nonlinear system (6.12) is uniformly exponentially stable in the domain  $\mathcal{D}_q$ . The parameterized LTV system verifies the assumptions of [93, Theorem 1]:

1) The elements of  $\mathcal{B}(t, \lambda)$  and  $\frac{\partial \mathcal{B}(t, \lambda)}{\partial t} = \frac{1}{2}\mathbf{Q}'(\dot{\tilde{\mathbf{q}}}(t, \lambda))$  are bounded, so there exists  $b_M$  such that

$$\max_{\lambda \in \mathbb{R}_{\geq 0} \times \mathcal{D}_q, t \geq 0} \left\{ \|\mathcal{B}(t, \lambda)\|, \left\| \frac{\partial \mathcal{B}(t, \lambda)}{\partial t} \right\| \right\} \leq b_M.$$

2) The positive definite matrices

$$\mathbf{P}(t, \lambda) = 8k_{b_\omega}\mathbf{I}, \quad \mathbf{Q}(t, \lambda) = 32k_{b_\omega}k_\omega\tilde{q}_s^2(t, \lambda),$$

satisfy

$$\begin{aligned} \mathbf{P}(t, \lambda)\mathcal{B}'(t, \lambda) &= \mathcal{C}'(t, \lambda), \quad -\mathbf{Q}(t, \lambda) = \mathcal{A}'(t, \lambda)\mathbf{P}(t, \lambda) + \mathbf{P}(t, \lambda)\mathcal{A}(t, \lambda) + \dot{\mathbf{P}}(t, \lambda), \\ p_m\mathbf{I} &\leq \mathbf{P}(t, \lambda) \leq p_M\mathbf{I}, \quad q_m\mathbf{I} \leq \mathbf{Q}(t, \lambda) \leq q_M\mathbf{I}, \end{aligned}$$

with  $p_m = p_M = 8k_{b_\omega}$ ,  $q_m = q_M(1 - \frac{c_{\max}}{8})$  and  $q_M = 32k_\omega k_{b_\omega}$ .

The system (6.13) is  $\lambda$ -UGES if and only if  $\mathcal{B}(t, \lambda)$  is  $\lambda$ -uniformly persistently exciting ( $\lambda$ -uPE) [93]. For any unit norm vector  $\mathbf{y}$

$$\|\mathcal{B}'(\tau, \lambda)\mathbf{y}\|^2 = \frac{1 - (\mathbf{y}'\tilde{\mathbf{q}}_q)^2}{4} \geq \frac{1 - \|\tilde{\mathbf{q}}_q\|^2}{4} \geq c_{\mathcal{B}},$$

where  $c_{\mathcal{B}} = \frac{1}{4}(1 - \frac{c_{\max}}{8})$ . The persistency of excitation condition is satisfied,  $\mathbf{y}' \int_t^{t+T} \mathcal{B}(\tau, \lambda)\mathcal{B}'(\tau, \lambda)d\tau\mathbf{y} \geq Tc_{\mathcal{B}}$ , the parameterized LTV (6.13) is  $\lambda$ -UGES, and the nonlinear system (6.12) is exponentially stable in the domain  $\mathcal{D}_q$ .  $\square$

Theorem 5.15 guarantees that the trajectories emanating from the initial conditions in the set  $\{(\tilde{\mathcal{R}}, \tilde{\mathbf{b}}_\omega) \in \text{SO}(3) \times \mathbb{R}^3 : \frac{1}{2}\|\mathbf{I} - \tilde{\mathcal{R}}\|^2 + \frac{1}{2k_{b_\omega}}\|\tilde{\mathbf{b}}_\omega\|^2 < 4\}$  converge exponentially fast to the origin if  $k_{b_\omega}$  satisfies (6.11). The following corollary establishes sufficient conditions in  $k_{b_\omega}$  for uniform exponential stability, i.e. the exponential convergence rate bounds are independent of the initial condition  $\mathbf{x}(t_0)$ .

**Corollary 6.6.** *Assume that the initial estimation errors are bounded*

$$\|\mathbf{I} - \tilde{\mathcal{R}}(t_0)\|^2 \leq c_0 < 8, \quad \|\tilde{\mathbf{b}}_\omega(t_0)\| \leq \tilde{b}_0, \quad (6.14)$$

for some  $c_0$  and  $\tilde{b}_0$ , and let  $k_{b_\omega}$  be such that  $\frac{\tilde{b}_0^2}{8-c_0} < k_{b_\omega}$ . Then the origin  $(\tilde{\mathcal{R}}, \tilde{\mathbf{b}}_\omega) = (\mathbf{I}, 0)$  is exponentially stable, uniformly in the set defined by (6.14).

The tools for stability analysis of parameterized LTVs provide for convergence rate bounds. The computation of bounds for exponential convergence is a non-trivial problem [73], and the bounds obtained for the attitude observer, presented in the following, were found conservative in practice, but are presented for completeness.

**Corollary 6.7.** *Under the conditions described in Corollary 6.6, the trajectories of the system (6.10) satisfy*

$$\|\mathbf{x}(t)\| \leq k_{b_\omega}\|\mathbf{x}(t_0)\|e^{-\frac{1}{2}\gamma_{b_\omega}(t-t_0)}, \forall t \geq t_0,$$

where

$$\mathbf{x}(t) := \left( \frac{\tilde{\mathcal{R}}(t) - \mathbf{I}}{\sqrt{8}}, \tilde{\mathbf{b}}_\omega(t) \right), \quad k_{b_\omega} = t_M t_M^{inv} e^{\frac{1}{2}\gamma_{b_\omega}^{-\frac{1}{2}}}, \quad \gamma_{b_\omega} = \frac{\rho}{\pi_c},$$

$$t_M = \left( \frac{5}{4} + \frac{2}{1 + \sqrt{17}} \right)^{\frac{1}{2}}, \quad t_M^{inv} = \left( \frac{5}{4} + \frac{2}{1 - \sqrt{17}} \right)^{-\frac{1}{2}},$$

and

$$\begin{aligned}
a_M &= 2k_\omega, \quad b_M = \max \left\{ \frac{1}{2}, \frac{1}{2} \left( 16K_\omega^2 + \tilde{b}_{\max}^2 \right)^{\frac{1}{2}} \right\}, \quad p_m = p_M = 8k_{b_\omega}, \\
q_m &= q_M \left( 1 - \frac{c_{\max}}{8} \right), \quad q_M = 32k_\omega k_{b_\omega}, \quad k_M := b_M(1 + p_M + a_M + b_M^2(1 + 2p_M)), \\
c_* &:= \sqrt{\frac{p_M + 1}{q_m}}, \quad 0 < \rho \leq \min \left\{ p_m, \frac{1}{2b_M^2} \right\}, \quad \gamma_x = \frac{8 - c_{\max}}{32(1 + b_M^2 T)}, T > 0, \\
c_{32} &:= \max \left\{ p_M, \frac{1}{2\gamma_x} \right\}, \quad \pi_c := c_{32} + (c_* t_M^{inv})^2 \left[ \frac{(c_{32} k_M)^2}{4(1 - \rho)} \right], \quad k_{b_\omega} = \rho_\omega \frac{\tilde{b}_0^2}{8 - c_0}, \\
\rho_\omega &> 1, \quad \tilde{b}_{\max} = \tilde{b}_0 \left( \rho_\omega \frac{c_0}{1 - c_0} + 1 \right)^{\frac{1}{2}}, \quad c_{\max} = \frac{1}{\rho_\omega} (8 + (\rho_\omega - 1)c_0).
\end{aligned}$$

*Proof.* The convergence rate bounds are given by [92, Theorem 1 and Remark 2], and the analytical derivation of the constants for the case of the attitude observer is lengthy, but straightforward.  $\square$

### 6.2.3 Output feedback configuration

In Chapter 5, the landmark based observer was expressed as a function of the sensor readings and landmark estimates. The attitude observer proposed in this chapter was derived using the same methodology, and thus it can also be formulated explicitly as a function of the vector measurements, the non-ideal angular velocity readings, and the attitude and bias estimates.

**Theorem 6.8.** *The dynamics of the attitude observer are explicit functions of the sensor readings and state estimates, described by*

$$\begin{aligned}
\dot{\hat{\mathcal{R}}} &= \hat{\mathcal{R}}(\hat{\omega})_\times, \\
\dot{\hat{\mathbf{b}}}_\omega &= k_{b_\omega} \mathbf{s}_\omega,
\end{aligned}$$

where the feedback terms are given by

$$\begin{aligned}
\hat{\omega} &= \hat{\mathcal{R}}' \mathbf{H} \mathbf{A}_H \mathbf{A}'_H \mathbf{H}'_r (\omega_r - \hat{\mathbf{b}}_\omega) - k_\omega \mathbf{s}_\omega, \\
\mathbf{s}_\omega &= \sum_{i=1}^n (\hat{\mathcal{R}}' \mathbf{H} \mathbf{A}_H \mathbf{e}_i) \times (\mathbf{H}_r \mathbf{A}_H \mathbf{e}_i),
\end{aligned} \tag{6.15}$$

where  $\mathbf{H}_r := [\mathbf{h}_{r1} \ \cdots \ \mathbf{h}_{rn}]$  is the concatenation of the vector readings.

*Proof.* Using  ${}^B \hat{\mathbf{U}}_H {}^B \mathbf{U}'_H = \hat{\mathcal{R}}' \mathbf{U}_H \mathbf{U}'_H \mathcal{R} = \tilde{\mathcal{R}}$  in (6.7) yields  $\mathbf{s}_\omega = \left( {}^B \mathbf{U}_H {}^B \hat{\mathbf{U}}'_H - {}^B \hat{\mathbf{U}}_H {}^B \mathbf{U}'_H \right)_\otimes$ . Using  ${}^B \mathbf{U}_H {}^B \hat{\mathbf{U}}'_H = \sum_{i=1}^n {}^B \mathbf{u}_i {}^B \hat{\mathbf{u}}'_i$  and  ${}^B \mathbf{u}_i {}^B \hat{\mathbf{u}}'_i - {}^B \hat{\mathbf{u}}_i {}^B \mathbf{u}'_i = \left( ({}^B \hat{\mathbf{u}}_i \times {}^B \mathbf{u}_i) \right)_\times$ , bears  $\mathbf{s}_\omega = \sum_{i=1}^n ({}^B \hat{\mathbf{u}}_i \times {}^B \mathbf{u}_i) = \sum_{i=1}^n ({}^B \hat{\mathbf{U}}_H \mathbf{e}_i) \times ({}^B \mathbf{U}_H \mathbf{e}_i)$ . Applying  ${}^B \mathbf{U}_H = \hat{\mathcal{R}}' \mathbf{H} \mathbf{A}_H$  and  $\mathbf{H}_r = \mathcal{R}' \mathbf{H}$  produces the desired results.  $\square$



The formulation of  $\hat{\omega}$  expressed in (6.15) is diverse from that adopted in Theorem 5.17, for the landmark observer. The error dynamics of the attitude observer are autonomous and can be analyzed using stronger stability results, such as LaSalle's invariance principle and density functions, however the formulated landmark based observer is simpler and may exhibit nice practical properties, such as good sensitivity to noise in the discrete-time implementation of the algorithm. This illustrates that the same observer can be designed using distinct feedback laws, and that the choice of a canonical formulation is still an open question. Recent work in methods to design controllers in Riemannian manifolds can be found in [28], and the design of observers for invariant systems on Lie-groups is addressed in [16, 84], yet much is to be studied with respect to stability and performance of observers in manifolds, as evidenced in [87].

### 6.3 Simulations

In this section, simulation results for the proposed attitude observer are presented. The directions of the sensed vectors are given by

$${}^L\mathbf{h}_1 = \begin{bmatrix} 1 \\ 0 \\ 0 \end{bmatrix}, \quad {}^L\mathbf{h}_2 = \begin{bmatrix} 0 \\ 0 \\ 1 \end{bmatrix},$$

which are a simple representation of the vectors that are measured in the body coordinates by a magnetic compass and a pendulum, respectively. Under strong accelerations or magnetic distortions, other vector measurements such as star trackers or image based feature detection can be adopted. The matrix  $\mathbf{H}$  satisfies the non-collinearity condition of Assumption 6.1, and corresponds to the case discussed in Appendix E.2. The attitude feedback gain is given by  $k_\omega = 2$  and the rigid body trajectory is computed using oscillatory angular rates of 1 Hz.

For the case of biased velocity readings, the feedback gain is  $k_{b_\omega} = 1$ . The bounds of Proposition 6.6 are defined by

$$c_0 = 4 \left( 1 - \cos \left( \frac{3}{4}\pi \right) \right), \quad \tilde{b}_0 = \frac{5\sqrt{3}\pi}{180} \text{ rad/s},$$

that correspond to the maximum rotation error of  $\varphi(t_0) = \frac{3}{4}\pi$  rad, and to the minimum gain  $k_{b_\omega \min} = 1.95 \times 10^{-2}$ . The initial estimation errors are

$$\tilde{\mathbf{b}}_\omega(t_0) = \frac{5\pi}{180} \begin{bmatrix} 1 \\ -1 \\ 1 \end{bmatrix} \text{ rad/s}, \quad \phi(t_0) = \frac{1}{\sqrt{3}} \begin{bmatrix} 1 \\ 1 \\ 1 \end{bmatrix}.$$

The attitude estimation error, depicted in Fig. 6.1(a) for the case of unbiased angular rate readings, converges exponentially fast to the origin. As expected, the convergence bound (6.9) is more conservative as  $\varphi(t_0)$  is closer to the anti-stable manifold defined by  $\varphi = \pi$ , for a discussion of the behavior of trajectories near saddle points see [89].

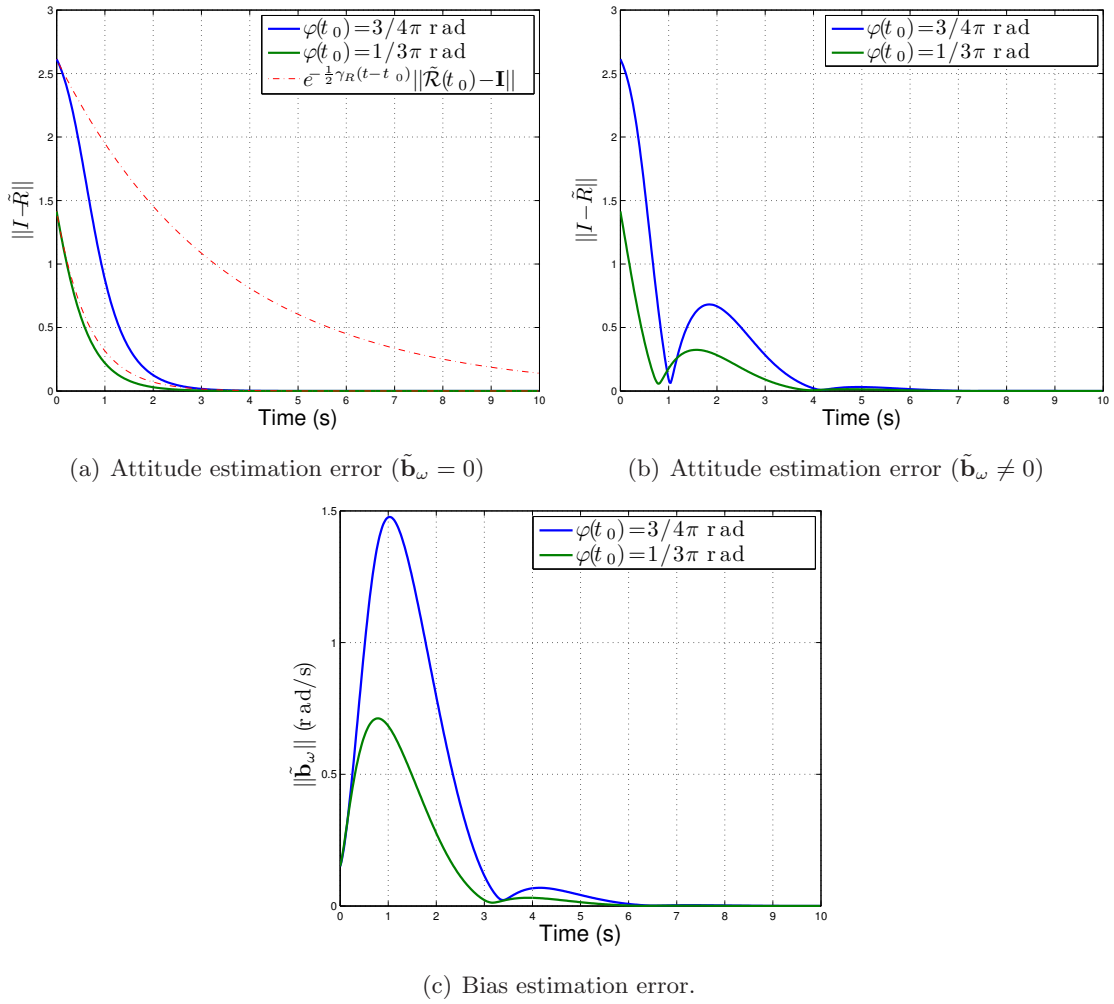


Figure 6.1: Attitude and bias estimation errors.

The attitude and bias errors converge to the origin, as shown in Figs. 6.1(b) and 6.1(c). The convergence of the attitude error is slower than the convergence obtained for  $\tilde{\mathbf{b}} = 0$ , because the observer has to compensate dynamically the large bias errors before estimating attitude accurately. Interestingly enough, the attitude error dynamics (6.10) are autonomous and, consequently, the estimation results are independent of the trajectory described by the rigid body.

The peak of the bias estimation error is justified by the level set  $V_b \leq c$  containing points with small attitude error  $\frac{1}{2}\|\mathbf{I} - \tilde{\mathcal{R}}\|^2 \approx 0$ , but with large bias error  $\|\tilde{\mathbf{b}}_\omega\|^2 \approx 2k_{b_\omega}c$ . This can be verified by noting that the peak of the bias estimation error in Fig. 6.1(b) occurs for a minimum of the attitude estimation error in Fig. 6.1(c). The convergence bounds of Corollary 6.7 are very conservative,  $\gamma_{b_\omega} = 6.50 \times 10^{-18}$  and  $k_{b_\omega} = 7.50 \times 10^8$  with optimized  $\rho$ , and should be subject to further study. However, the estimation error convergence rate obtained in simulation are encouraging, and suggest that the algorithm can be implemented in practice.

In Fig. 6.2, the exponential convergence of the Lyapunov function (and of the estima-

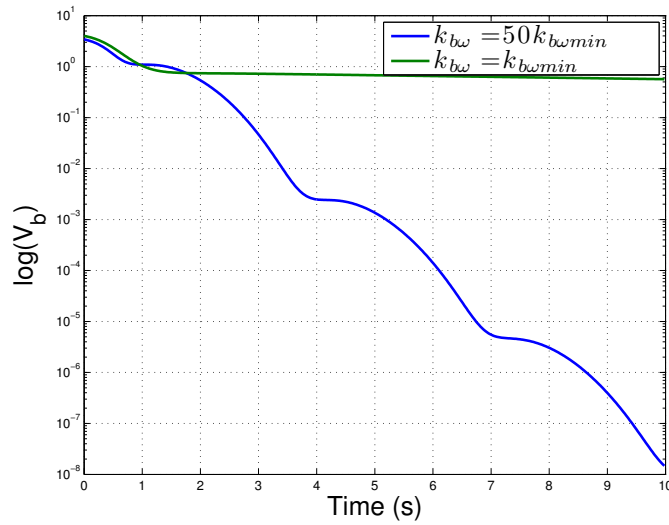


Figure 6.2: Exponential convergence of  $V_b$  ( $\varphi(t_0) = \frac{3\pi}{4}$ ,  $\tilde{\mathbf{b}}_\omega \neq 0$ ).

tion error) is illustrated using a logarithmic scale. Large feedback gains  $k_{b\omega}$  are beneficial for tackling the estimation errors, and the peak values of  $\tilde{\mathbf{b}}_\omega$  do not degrade the exponential convergence of the state  $(\tilde{\mathcal{R}}, \tilde{\mathbf{b}}_\omega)$ .

## 6.4 Conclusions

A nonlinear observer for attitude estimation on  $SO(3)$  exploiting vector measurements and biased angular velocity readings was derived. The observer was obtained by the technique proposed in Chapter 5, that derives the feedback law based on a Lyapunov function, defined by the measurement error of the aiding sensor. The properties derived for the landmark based observer were inherited by the vector based observer, namely exponential convergence of the attitude and bias estimation errors, an output feedback formulation, and insight on the necessary and sufficient conditions for state estimation.

Interestingly enough, the feedback law is diverse from that obtained with the landmark observer, which shows that distinct observers can be derived from the same technique. The criteria for deciding which is the “best” nonlinear observer is still an open question, and caveats for performance of estimators in manifolds have been identified in the literature [87].

Simulation results depicted the exponential convergence of the estimation errors, and the effect of the anti-stable manifold in the rate of convergence of the trajectories. The theoretical convergence rate bounds were tight for the case of ideal velocity measurements, but conservative for the case of biased velocity sensors. The trajectories of the estimation error were independent of the rigid body trajectory due to the autonomous estimation error dynamics.

For the purpose of implementation of the algorithms, it is of interest to study the stability observer when the sensor measurements are corrupted by noise. In the next

chapter, the stability of the observer in the presence of inertial sensor noise is studied, using stability analysis based on the combination of Lyapunov and density functions.

## Chapter 7

# Combination of Lyapunov and density functions for stability analysis with application to a nonlinear attitude observer

Lyapunov methods and density functions provide dual characterizations of the solutions of a nonlinear dynamic system. This work exploits the idea of combining both techniques, to yield stability results that are valid for almost all the solutions of the system. Based on the combination of Lyapunov and density functions, analysis methods are proposed for the derivation of almost input-to-state stability, and of almost global stability in nonlinear systems. The techniques are illustrated for the attitude observer based on vector measurements proposed in the previous chapter, with angular velocity readings corrupted by non-idealities.

This work is organized as follows. Section 7.1 summarizes the attitude observer, based on that derived in Chapter 6, and adopted to illustrate the combination of Lyapunov and density function methods. The derivation of almost ISS for nonlinear systems, using the combination of Lyapunov and density functions, is discussed in Section 7.2. The approach is applied to demonstrate the stability of the attitude observer in the presence of inertial sensor noise. A new result for almost global stability of nonlinear systems is presented in Section 7.3, and is illustrated for a nonlinear system, that is motivated by the attitude observer dynamics subject to inertial sensor bias. Concluding remarks are discussed in Section 7.4.

### 7.1 Attitude observer

This section briefly describes the attitude observer, adopted to illustrate the analysis techniques proposed in this chapter. The observer closely resembles to that derived in

Chapter 6, where details on the observer derivation and properties can be found, and is briefly reviewed in this chapter for the sake of clarity.

The observer estimates the attitude of a rigid body with respect to a fixed inertial frame, by merging angular velocity measurements, with vectors observations obtained in body coordinates. The rigid body kinematics are described by

$$\dot{\mathcal{R}} = \mathcal{R}(\boldsymbol{\omega})_{\times},$$

where  $\mathcal{R}$  is the rotation matrix from body frame to the inertial frame coordinates, and  $\boldsymbol{\omega}$  is the body angular velocity expressed in body coordinates. The body angular velocity is measured by a rate gyro sensor triad, and the measurement model is

$$\boldsymbol{\omega}_r = \boldsymbol{\omega} + \mathbf{d}_{\boldsymbol{\omega}}, \quad (7.1)$$

where  $\mathbf{d}_{\boldsymbol{\omega}}$  is a measurement disturbance.

The vector observations are a function of the rigid body's attitude. The vectors coordinates are known and time-invariant in inertial frame, e.g. Earth's magnetic and gravitic fields, and measured in body coordinates by on-board sensors such as magnetometers and pendulums, among others. The vector measurement is expressed by

$$\mathbf{h}_{r_i} = {}^B\mathbf{h}_i,$$

where  ${}^B\mathbf{h}_i = \mathcal{R}^L\mathbf{h}_i$ , the leading superscripts  $B$  and  $I$  denote that the vector is expressed respectively in body and inertial coordinates,  $i = 1..n$  is the vector index, and  $n$  is the number of vector measuring sensors.

The vector measurements  $\mathbf{h}_{r_i}$  are introduced in the observer by means of a conveniently defined linear coordinate transformation, which is briefly described, for further details see Section 6.1. The transformed vectors expressed in inertial and body frames are respectively given by

$$\begin{aligned} {}^L\mathbf{u}_j &:= \sum_{i=1}^n a_{ij} {}^L\mathbf{h}_i \Leftrightarrow \mathbf{U}_H := \mathbf{H}\mathbf{A}_H, \\ {}^B\mathbf{u}_j &:= \sum_{i=1}^n a_{ij} \mathbf{h}_{r_i} \Leftrightarrow {}^B\mathbf{U}_H := \mathbf{H}_r\mathbf{A}_H \end{aligned} \quad (7.2)$$

where matrix  $\mathbf{A}_H := [a_{ij}] \in \mathbb{M}(n)$  is invertible by construction, and  $\mathbf{U}_H := [{}^L\mathbf{u}_1 \ \dots \ {}^L\mathbf{u}_n]$ ,  ${}^B\mathbf{U}_H := [{}^B\mathbf{u}_1 \ \dots \ {}^B\mathbf{u}_n]$ ,  $\mathbf{H} := [{}^L\mathbf{h}_1 \ \dots \ {}^L\mathbf{h}_n]$ ,  $\mathbf{H}_r := [\mathbf{h}_{r_1} \ \dots \ \mathbf{h}_{r_n}]$ ,  $\mathbf{U}_H, {}^B\mathbf{U}_H, \mathbf{H}, \mathbf{H}_r \in \mathbb{M}(3, n)$ . In this chapter, the transformation  $\mathbf{A}_H$  is defined such that  $\mathbf{U}_H \mathbf{U}_H^T = \mathbf{I}$ , to shape uniformly the directionality introduced by the vector readings. Also, it is assumed that there are at least two noncollinear vectors  ${}^L\mathbf{h}_i$ , so that all rotational degrees of freedom are observable. For more details on the adopted transformation and sensor configuration, see Section 6.1.2 for a discussion on the present observer characteristics.

The proposed observer estimates the attitude of the rigid body by computing the kinematics

$$\dot{\hat{\mathcal{R}}} = \hat{\mathcal{R}}(\hat{\boldsymbol{\omega}})_{\times}, \quad (7.3)$$

where  $\hat{\mathcal{R}}$  is the estimated attitude and  $\hat{\omega}$  is the feedback term constructed to compensate for the attitude estimation error.

The attitude observer estimates the rotation matrix by exploiting the non-ideal angular velocity measurements (7.1) and the vector observations (7.2) in the feedback term  $\hat{\omega}$ . The combination of Lyapunov and density functions is illustrated, by showing the stability of the attitude observer for the cases where  $\mathbf{d}_\omega$  is *i)* an unmodeled, bounded sensor disturbance, and *ii)* an unknown but constant sensor bias.

## 7.2 Stability in the presence of unmodeled inputs

This section discusses and formulates the combination of Lyapunov and density function techniques for the analysis of input-to-state stability, in the presence of unknown inputs. The proposed method is illustrated by analyzing the stability of the attitude observer, in the case where the inertial sensor reading is corrupted by a bounded disturbance.

### 7.2.1 Almost ISS using Lyapunov and density functions

The analysis of input-to-state stability, using the combination of Lyapunov and density function techniques, is considered for systems in the form

$$\dot{x} = f(x, u), \quad (7.4)$$

where  $x \in M$  is the state,  $M$  is a smooth manifold, and  $f : M \times U \rightarrow TM$ , is a locally Lipschitz manifold map which satisfies  $f(x, u) \in T_x M$ , for all  $x \in M$  and all  $u \in U \subset \mathbb{R}^m$ . The notion of ISS is classically defined using comparison functions [131]. However, the limitations to global stability on non-Euclidean spaces motivate the relaxation proposed in [5], formulated as follows.

**Definition 7.1** (Almost ISS, [5]). The system (7.4) is almost ISS with respect to the origin, denoted as  $0_M$ , if  $0_M$  is locally asymptotically stable and

$$\forall u \in U \quad \forall \text{a.a. } x(t_0) \in M \quad \limsup_{t \rightarrow \infty} |x(t)| \leq \gamma(\|u\|_\infty), \quad (7.5)$$

where  $\gamma$  is a class  $\mathcal{K}$  function,  $|\cdot|$  is the distance to the origin, and “ $\forall \text{a.a.}$ ” abbreviates the quantifier “for almost all”.

Expressed in words, almost ISS is verified when, for each valid input, all initial conditions outside a set of zero measure converge to a neighborhood of the origin, whose radius grows monotonically with the bound on the input. The density functions framework relaxes the concept of ISS, by considering that a zero measure set of trajectories can be effectively destabilized by the input, but that almost all trajectories converge to a neighborhood of the origin. Note that the quantifiers in (7.5) are not commutable in general, because the set of converging initial conditions is a function of the input  $u$ .

In this work, a method to derive almost ISS is obtained by combining the properties of Lyapunov and density functions. The adopted methodology has been sketched in [5], where it is motivated by means of examples, however it seems to have been unnoticed in subsequent literature. This section provides a contribution to the concept of combining Lyapunov and density functions, by formulating the technique in explicit mathematical statements, and characterizing the stability result as the combination of two ISS properties. These two ISS concepts are introduced in the following.

**Definition 7.2** (Local ISS). A system (7.4) is locally input-to-state stable with respect to  $0_M$ , if  $0_M$  is locally asymptotically stable and there exists  $r > 0$  such that

$$\forall u \in U \forall |x(t_0)| \leq r \limsup_{t \rightarrow \infty} |x(t)| \leq \gamma_1(\|u\|_\infty), \quad (7.6)$$

where  $\gamma_1$  is a class  $\mathcal{K}$  function.

**Definition 7.3** (Weakly almost ISS, [5]). A system (7.4) is weakly almost ISS with respect to  $0_M$ , if  $0_M$  is locally asymptotically stable and

$$\forall u \in U \forall \text{a.a. } x(t_0) \in M \liminf_{t \rightarrow \infty} |x(t)| \leq \gamma_2(\|u\|_\infty), \quad (7.7)$$

where  $\gamma_2$  is a class  $\mathcal{K}$  function.

Provided that these ISS properties are verified, the main result of this section shows that almost ISS is attained.

**Lemma 7.1** (Almost ISS). *Assume that the system (7.4) is locally ISS and weakly almost ISS, then, for all  $u \in \{u \in U : \gamma_2(\|u\|_\infty) < r\}$ , the system is almost ISS with  $\gamma = \gamma_1$ .*

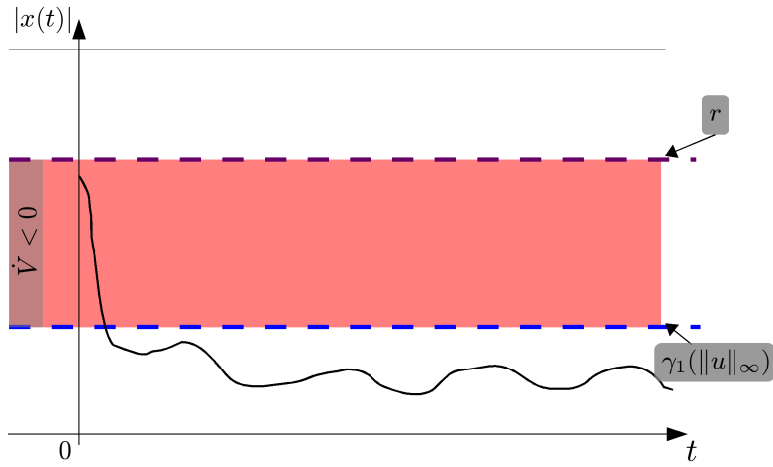
*Proof.* Weakly almost ISS, expressed in (7.7), implies that, by the continuity of the solutions of (7.4), almost every solution satisfies  $|x(t)| \leq \gamma_2(\|u\|_\infty) < r$  for some  $t$ , thus entering the region where the trajectories eventually satisfy the lim sup condition expressed in (7.6), yielding (7.5).  $\square$

The proposed ISS analysis technique is based on Lemma 7.1, which shows that almost ISS can be obtained by combining local ISS with weakly almost ISS, for sufficiently small inputs. Lyapunov methods can be used to derive local ISS [78], while weakly almost ISS is associated with density functions [5].

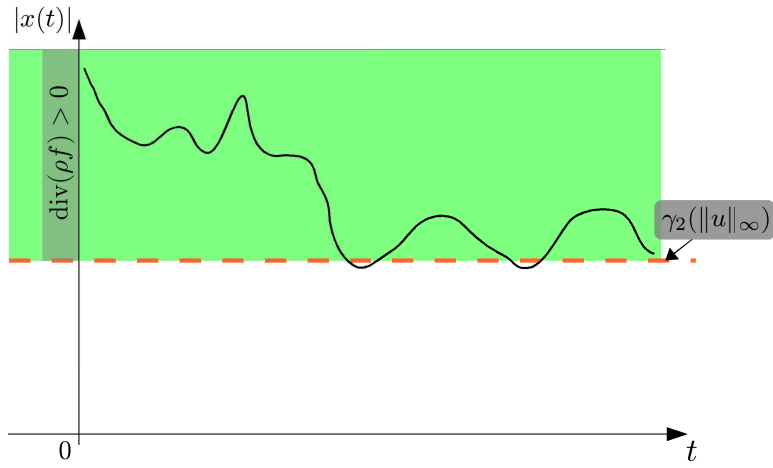
The stability analysis technique is illustrated in Fig. 7.1. Lyapunov techniques yield local ISS based on ultimate boundedness and/or ISS results [78, Theorems 4.18 and 4.19]. As shown in Fig. 7.1(a), Lyapunov methods find a region  $\{x : \gamma_1(\|u\|_\infty) < |x(t)| < r\}$  where the Lyapunov function  $V$  decreases along the system trajectories ( $\dot{V} < 0$ ), and drives the solutions to set  $\{x : |x(t)| < \gamma_1(\|u\|_\infty)\}$ , which is guaranteed to be positively invariant by appealing to the properties of the Lyapunov function.

However, the behavior of the solutions for  $|x(t)| \geq r$  is undetermined by the Lyapunov function analysis, and density functions techniques are adopted to guarantee that almost

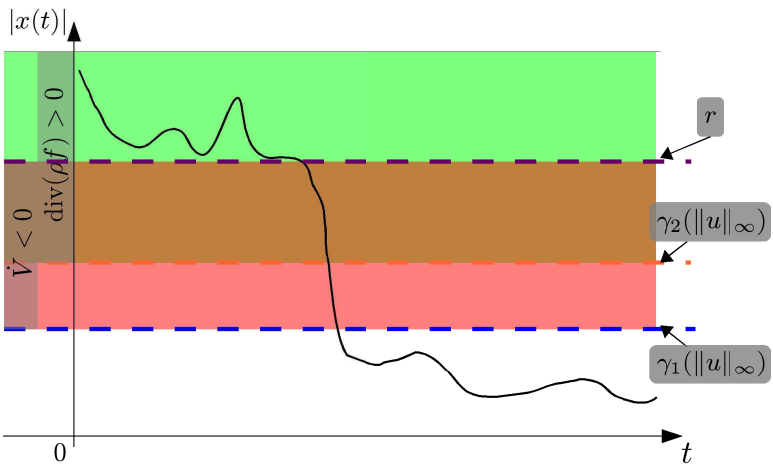




(a) Local ISS using Lyapunov function analysis: solutions emanating below the bound  $r$  converge to the region bounded by  $\gamma_1(\|u\|_\infty)$ .



(b) Weakly almost ISS using density function analysis: the  $\liminf$  property of almost all solutions satisfies the bound  $\gamma_2(\|u\|_\infty)$ .



(c) Almost ISS using Lyapunov and density functions analysis: by the  $\liminf$  property, almost all trajectories enter the region below the bound  $r$ , and converge to the region bounded by  $\gamma_1(\|u\|_\infty)$ .

Figure 7.1: Combination of Lyapunov and density functions for almost ISS of the origin.

all solutions enter  $\{x : |x(t)| < r\}$  for some time instant. This is obtained by finding a density function  $\rho$  such that  $\text{div}(\rho f) > 0$  in the region  $\{x : |x(t)| > \gamma_2(\|u\|_\infty)\}$ , which yields weakly almost ISS by [5, Theorem 4], reproduced in Appendix H.1. Hence, the trajectories of the system are endowed with the lim inf characteristic depicted in Fig. 7.1(b), and enter the region  $\{x : \gamma_1(\|u\|_\infty) < |x(t)| < r\}$  in finite time, as shown in Fig. 7.1(c). Consequently, almost ISS is obtained.

### 7.2.2 Stability of the nonlinear observer in the presence of inertial sensor noise

The combination of Lyapunov techniques is illustrated for the nonlinear observer described in Section 7.1, in the presence of bounded time-varying disturbances in the angular velocity measurements. The considered set of valid disturbances  $\mathbf{d}_\omega$  in (7.1) is given by  $U = \{\mathbf{d} \in \mathbb{R}^3 : \|\mathbf{d}\|_\infty \leq d_{\max}\}$ , and the feedback law  $\hat{\boldsymbol{\omega}}$  in (7.3) is defined as

$$\dot{\hat{\mathcal{R}}} = \hat{\mathcal{R}}(\hat{\boldsymbol{\omega}})_\times, \quad \hat{\boldsymbol{\omega}} = \hat{\mathcal{R}}' \mathbf{U}_H^B \mathbf{U}'_H \boldsymbol{\omega}_r - k_\omega \sum_{i=1}^n (\hat{\mathcal{R}}'^L \mathbf{u}_i) \times^B \mathbf{u}_i,$$

where  $k_\omega \in \mathbb{R}^+$  is the feedback gain, for more details and a motivation see Section 6.2. The resulting stability properties of the attitude observer are formulated by defining the attitude estimation error  $\tilde{\mathcal{R}} := \hat{\mathcal{R}}' \mathcal{R}$ . The closed loop kinematics of the attitude error are given by

$$\dot{\tilde{\mathcal{R}}} = -k_\omega \tilde{\mathcal{R}}(\tilde{\mathcal{R}} - \tilde{\mathcal{R}}') - \tilde{\mathcal{R}}(\mathbf{d}_\omega)_\times. \quad (7.8)$$

The trajectories of the system satisfy  $\tilde{\mathcal{R}}(t) \in \text{SO}(3)$  for all  $t$ , even in the presence of the angular velocity disturbance, and hence the kinematics (7.8) are well defined.

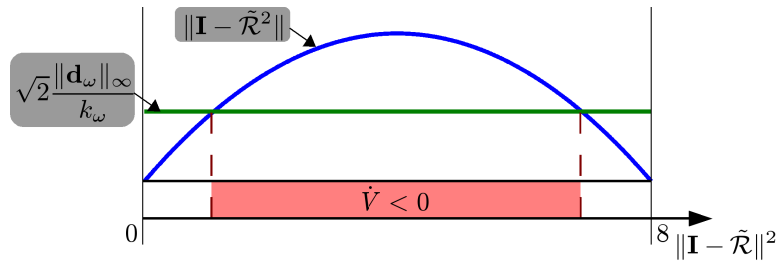
Although the origin of the unforced system is almost globally asymptotically stable (aGAS), as detailed in Theorem 6.3, generic exogenous disturbances may drive the trajectories of system (7.8) to the unstable equilibrium points of the unforced system. A simple example illustrates that the system (7.8) does not satisfy classical ISS, by choosing  $\mathbf{d}_\omega$  as the destabilizing feedback law for a given initial condition, as follows. Let  $\tilde{\mathcal{R}}(t, \tilde{\mathcal{R}}^*)$  denote the solution of the system

$$\dot{\tilde{\mathcal{R}}} = k_\omega \tilde{\mathcal{R}}(\tilde{\mathcal{R}} - \tilde{\mathcal{R}}'), \quad (7.9)$$

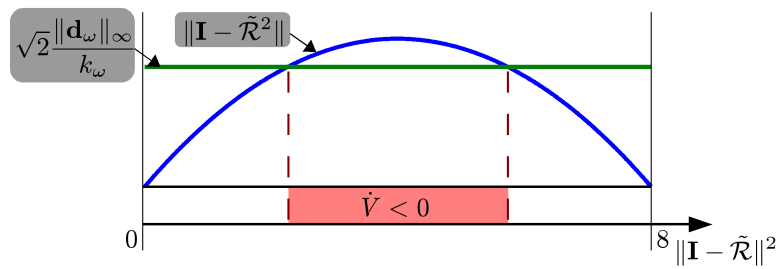
with an initial condition  $\tilde{\mathcal{R}}(t_0) = \tilde{\mathcal{R}}^*$ . Given that the origin of the unforced system (7.8) is almost GAS, with region of attraction  $\text{SO}(3) \setminus A$ , where

$$A = \{\tilde{\mathcal{R}} \in \text{SO}(3) : \|\mathbf{I} - \tilde{\mathcal{R}}\|^2 = 8\},$$

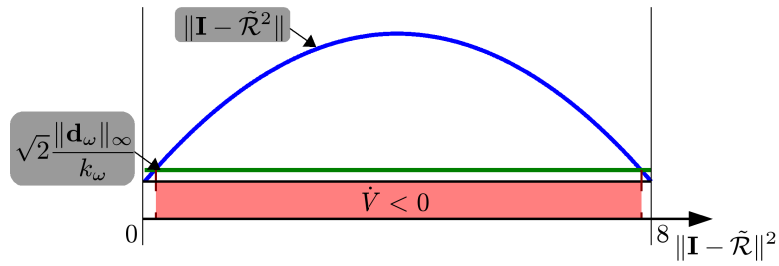
it is straightforward to show that almost all trajectories of (7.9) converge to the set  $A$ . Consequently, for the input  $\mathbf{d}_\omega(t) = -2k_\omega(\tilde{\mathcal{R}}(t, \tilde{\mathcal{R}}^*) - \tilde{\mathcal{R}}(t, \tilde{\mathcal{R}}^*)')$ , the trajectory  $\tilde{\mathcal{R}}(t, \tilde{\mathcal{R}}^*)$  converges to the set  $A$ , and the system is not ISS. However, the selected input is not



(a) Balanced noise bound and gain.



(b) Larger noise to gain ratio reduces the region where  $\dot{V} < 0$ .



(c) Smaller noise to gain ratio increases the region where  $\dot{V} < 0$ .

Figure 7.2: Region of convergence as a function of the noise to gain ratio  $\frac{\|\mathbf{d}_\omega\|_\infty}{k_\omega}$ .

necessarily destabilizing for  $\tilde{\mathcal{R}}(t_0) \neq \tilde{\mathcal{R}}^*$ , and hence the example does not preclude the almost ISS property.

As discussed in Section 7.2.1, the combination of Lyapunov techniques is demonstrated by using *i*) Lyapunov methods to attain local ISS, *ii*) density function techniques to yield weakly almost ISS, and *iii*) Lemma 7.1 to attain almost ISS. The next proposition bears local ISS by showing uniform ultimate boundedness [78], i.e. the trajectories emanating from initials conditions in a known neighborhood of the origin converge to a neighborhood of the origin in finite time, independently of  $t_0$ .

**Theorem 7.2.** *Let  $k_\omega > \frac{d_{\max}}{2}$ , then for any initial condition*

$$\tilde{\mathcal{R}}(t_0) \in \{\tilde{\mathcal{R}} \in \text{SO}(3) : \|\mathbf{I} - \tilde{\mathcal{R}}\|^2 < r(\|\mathbf{d}_\omega\|_\infty)\}, \quad (7.10a)$$

where  $r(d) = 4 \left(1 + \sqrt{1 - \frac{d^2}{4k_\omega^2}}\right)$ , there exists  $T$ , independent of  $t_0$ , such that the trajectory of the system (7.8) satisfies

$$\tilde{\mathcal{R}}(t) \in \{\tilde{\mathcal{R}} \in \text{SO}(3) : \|\mathbf{I} - \tilde{\mathcal{R}}\|^2 < \gamma_1(\|\mathbf{d}_\omega\|_\infty)\}, \quad (7.10b)$$

for all  $t \geq t_0 + T$ , where  $\gamma_1(d) = 4 \left(1 - \sqrt{1 - \frac{d^2}{4k_\omega^2}}\right)$ .

*Proof.* The proof is based on the derivation of boundedness for nonlinear systems presented in [78, Theorem 4.18], using Lyapunov methods. The time derivative of the Lyapunov function  $V = \frac{\|\mathbf{I} - \tilde{\mathcal{R}}\|^2}{2}$  along the system trajectories is given by

$$\dot{V} = -k_\omega \frac{\|\mathbf{I} - \tilde{\mathcal{R}}\|^2}{2} + \text{tr} \left( \frac{\tilde{\mathcal{R}} - \tilde{\mathcal{R}}'}{2} (\mathbf{d}_\omega)_\times \right).$$

Algebraic manipulation of  $\dot{V}$  produces

$$\begin{aligned} \dot{V} &\leq -k_\omega \frac{\|\mathbf{I} - \tilde{\mathcal{R}}\|^2}{2} + \frac{1}{2} \|\tilde{\mathcal{R}} - \tilde{\mathcal{R}}'\| \|(\mathbf{d}_\omega)_\times\| \\ &= -k_\omega \|\mathbf{I} - \tilde{\mathcal{R}}\| \left( \frac{1}{2} \|\mathbf{I} - \tilde{\mathcal{R}}\| - \frac{\|\mathbf{d}_\omega\|}{k_\omega \sqrt{2}} \right), \end{aligned}$$

where  $\text{tr}(\mathbf{A}'\mathbf{B}) < \sqrt{\text{tr}(\mathbf{A}'\mathbf{A}) \text{tr}(\mathbf{B}'\mathbf{B})}$  and  $2 \text{tr}(\mathbf{I} - \tilde{\mathcal{R}}^2) = \|\mathbf{I} - \tilde{\mathcal{R}}\|^2 = \|\tilde{\mathcal{R}} - \tilde{\mathcal{R}}'\|^2$  were used. It is immediate that

$$\frac{1}{2} \|\mathbf{I} - \tilde{\mathcal{R}}\| > \frac{\|\mathbf{d}_\omega\|_\infty}{k_\omega \sqrt{2}} \Rightarrow \dot{V} < 0.$$

Using  $\|\mathbf{I} - \tilde{\mathcal{R}}\|^2 = \frac{1}{2} (8 - \|\mathbf{I} - \tilde{\mathcal{R}}\|^2) \|\mathbf{I} - \tilde{\mathcal{R}}\|^2$  produces

$$\frac{\|\mathbf{I} - \tilde{\mathcal{R}}\|}{2} > \frac{\|\mathbf{d}_\omega\|_\infty}{k_\omega \sqrt{2}} \Leftrightarrow \frac{\gamma_1(\|\mathbf{d}_\omega\|_\infty)}{2} \leq V \leq \frac{r(\|\mathbf{d}_\omega\|_\infty)}{2}.$$

Consider the level sets defined by the Lyapunov function

$$\underline{\Omega}_t = \left\{ \tilde{\mathcal{R}} \in \text{SO}(3) : V(\tilde{\mathcal{R}}) \leq \frac{\gamma_1(\|\mathbf{d}_\omega\|_\infty)}{2} \right\}, \quad \bar{\Omega}_t = \left\{ \tilde{\mathcal{R}} \in \text{SO}(3) : V(\tilde{\mathcal{R}}) \leq \frac{r(\|\mathbf{d}_\omega\|_\infty)}{2} \right\},$$

then  $\tilde{\mathcal{R}} \in \{\bar{\Omega}_t - \underline{\Omega}_t\}$  implies that  $\dot{V} < 0$ . Hence  $\bar{\Omega}_t$  is a positively invariant set, the trajectories of the system starting in  $\bar{\Omega}_t$  enter  $\underline{\Omega}_t$  in finite time, see [78, Section 4.8] for a motivation of the level sets involved, and any solution starting in  $\underline{\Omega}_t$  will remain in the set since  $\dot{V} < 0$  in the corresponding boundary. The initial conditions given by (7.10a) satisfy  $\tilde{\mathcal{R}}(t_0) \in \bar{\Omega}_t$ ; any  $\tilde{\mathcal{R}} \in \underline{\Omega}_t$  satisfies (7.10b), which concludes the proof. The gain condition  $k_\omega > \frac{d_{\max}}{2}$  is required so that  $\{\bar{\Omega}_t - \underline{\Omega}_t\} \neq \emptyset$ .  $\square$

The results stated in Theorem 7.2 are obtained using Lyapunov stability theory, and guarantee that any trajectory emanating from (7.10a) converges to a bounded region, as shown in Fig. 7.1(a). Fig. 7.2 portrays the regions (7.10a) and (7.10b) as a function of the noise to gain ratio  $\frac{\|\mathbf{d}_\omega\|_\infty}{k_\omega}$ . The region (7.10a) is smaller for large noise/small gain configuration, as illustrated in Figs. 7.2(a) and 7.2(b), and, conversely, is larger for small noise/large gain configuration, as illustrated in Figs. 7.2(a) and 7.2(c).

Following the proposed technique, a density function is adopted to show that almost all trajectories of the system (7.8) satisfy a lim inf condition, whose bound guarantees that the solutions enter the set (7.10a) in finite time.

**Theorem 7.3.** *The system (7.8) is weakly almost ISS with respect to  $\mathbf{I}$ . Namely, the solutions verify*

$$\forall \mathbf{d}_\omega \in U \forall a.a. \tilde{\mathcal{R}}(t_0) \in \text{SO}(3) \quad \liminf_{t \rightarrow \infty} \|\mathbf{I} - \tilde{\mathcal{R}}(t)\|^2 < \gamma_2(\|\mathbf{d}_\omega\|_\infty), \quad (7.11)$$

$$\text{where } \gamma_2(d) = \frac{8\left(\frac{d}{k_\omega}\right)^2}{1 + \left(\frac{d}{k_\omega}\right)^2}.$$

*Proof.* The result is obtained by satisfying the conditions of Theorem H.2 found in Appendix H.1, with the density function

$$\rho(\tilde{\mathcal{R}}) = \frac{1}{\text{tr}^2(\mathbf{I} - \tilde{\mathcal{R}})}.$$

From the local ISS property obtained in Theorem 7.2, it is immediate that  $\tilde{\mathcal{R}} = \mathbf{I}$  is a locally stable equilibrium point for  $\mathbf{d}_\omega = 0$ .

The function  $f := \text{vec}\left(k\tilde{\mathcal{R}}(\tilde{\mathcal{R}}' - \tilde{\mathcal{R}}) - \tilde{\mathcal{R}}(\mathbf{d}_\omega)_\times\right)$  is locally Lipschitz over  $\text{SO}(3)$  and  $C^1$  over  $\text{SO}(3) \setminus \{\mathbf{I}\}$ . The density function  $\rho(\tilde{\mathcal{R}})$  is of class  $C^1$  over  $\text{SO}(3) \setminus \{\mathbf{I}\}$  and, given that  $\text{SO}(3)$  is compact, verifies

$$\int_{\text{SO}(3) \setminus U} \rho(\tilde{\mathcal{R}}) d\tilde{\mathcal{R}} < +\infty,$$

for all open neighborhoods  $U$  of  $0_M$ .

The divergence is given by

$$\text{div}(\rho f) = \frac{k_\omega}{\text{tr}^3(\mathbf{I} - \tilde{\mathcal{R}})} \left( \|\mathbf{I} - \tilde{\mathcal{R}}\|^2 + \frac{2}{k_\omega} \left( \tilde{\mathcal{R}} - \tilde{\mathcal{R}}' \right)'_{\otimes} \mathbf{d}_\omega \right),$$

where  $\text{div}(\rho f) = \rho \text{div}(f) + \nabla(\rho)' f$ ,  $\text{div}(f) = -2k_\omega \text{tr}(\tilde{\mathcal{R}})$  and  $\nabla(\rho) = 2 \text{tr}(\mathbf{I} - \tilde{\mathcal{R}})^{-3} \text{vec}(\mathbf{I})$ , more details on the computations of divergence and integrals in  $\text{SO}(3)$  can be found in

Appendix H.3 and in [30]. To attain the “density propagation inequality” (H.1) expressed in Appendix H.1, i.e.

$$\forall \mathbf{d}_\omega \in U \quad \forall \tilde{\mathcal{R}} \in \text{SO}(3) \quad \|\mathbf{I} - \tilde{\mathcal{R}}\|^2 \geq \gamma_2(\|\mathbf{d}_\omega\|) \Rightarrow \text{div}(\rho f) \geq Q(\tilde{\mathcal{R}}),$$

where  $\forall \text{a.a. } \tilde{\mathcal{R}} \in \text{SO}(3) \quad Q(\tilde{\mathcal{R}}) > 0$ , the sufficient condition

$$\|\mathbf{I} - \tilde{\mathcal{R}}\|^2 + \frac{2}{k_\omega} \left( \tilde{\mathcal{R}} - \tilde{\mathcal{R}}' \right)'_{\otimes} \mathbf{d}_\omega \geq \xi, \quad \xi > 0,$$

is analyzed, such that (H.1) is verified with  $Q(\tilde{\mathcal{R}}) = \frac{k_\omega}{\text{tr}^3(\mathbf{I} - \tilde{\mathcal{R}})} \xi > 0$  for almost all  $\tilde{\mathcal{R}} \in \text{SO}(3)$ . The inequality is satisfied if

$$\begin{aligned} \|\mathbf{I} - \tilde{\mathcal{R}}\|^2 > 4 \frac{\|\mathbf{d}_\omega\|}{k_\omega} \left\| \left( \frac{\tilde{\mathcal{R}} - \tilde{\mathcal{R}}'}{2} \right)'_{\otimes} \right\| &\Leftrightarrow \|\mathbf{I} - \tilde{\mathcal{R}}\|^2 > \sqrt{2} \frac{\|\mathbf{d}_\omega\|}{k_\omega} \|\mathbf{I} - \tilde{\mathcal{R}}\|^2 \\ &\Leftrightarrow \|\mathbf{I} - \tilde{\mathcal{R}}\|^2 > \frac{8 \left\| \frac{\mathbf{d}_\omega}{k_\omega} \right\|^2}{1 + \left\| \frac{\mathbf{d}_\omega}{k_\omega} \right\|^2} = \gamma_2(\|\mathbf{d}_\omega\|). \end{aligned}$$

Since  $\gamma_2(u)$  is a class  $\mathcal{K}$  function ( $\gamma_2(0) = 0$  and  $\frac{d\gamma_2(u)}{du} > 0$ ), the conditions of Theorem H.2 are verified with

$$\forall \mathbf{d}_\omega \in U \quad \forall \tilde{\mathcal{R}} \in \text{SO}(3) \quad \|\mathbf{I} - \tilde{\mathcal{R}}\|^2 > \gamma_2(\|\mathbf{d}_\omega\|) \Rightarrow \text{div}(\rho f) \geq \frac{k_\omega}{\text{tr}^3(\mathbf{I} - \tilde{\mathcal{R}})} \xi \text{ for some } \xi > 0,$$

producing the desired result (7.11).  $\square$

Using the result expressed in Lemma 7.1, almost ISS is obtained from the local ISS property derived in Theorem 7.2, and the weakly almost ISS analyzed in Theorem 7.3.

**Theorem 7.4.** *Let  $k_\omega > \frac{d_{\max}}{\sqrt{3}}$ . Then, the trajectories of the system (7.8) satisfy*

$$\forall \mathbf{d}_\omega \in U \quad \forall \text{a.a. } \tilde{\mathcal{R}}(t_0) \in \text{SO}(3) \quad \limsup_{t \rightarrow \infty} \|\mathbf{I} - \tilde{\mathcal{R}}(t)\|^2 < \gamma(\|\mathbf{d}_\omega\|_\infty), \quad (7.12)$$

where  $\gamma(d) = \gamma_1(d) = 4 \left( 1 - \sqrt{1 - \frac{d^2}{4k_\omega^2}} \right)$ , i.e. the attitude observer is almost ISS with respect to  $\mathbf{I}$ .

*Proof.* The proof is immediate from Lemma 7.1. However, it is re-derived to illustrate the combination of Lyapunov and density function techniques for the present attitude observer. Using the liminf condition (7.11), the trajectories of the system enter the positively invariant set (7.10a) for some  $t$ , if

$$\gamma_2(\|\mathbf{d}_\omega\|_\infty) < r(\|\mathbf{d}_\omega\|_\infty),$$

which is equivalent to  $\frac{2 \left( \frac{\|\mathbf{d}_\omega\|_\infty}{k_\omega} \right)^2}{1 + \left( \frac{\|\mathbf{d}_\omega\|_\infty}{k_\omega} \right)^2} < 1 + \sqrt{1 - \left( \frac{\|\mathbf{d}_\omega\|_\infty}{2k_\omega} \right)^2}$ , that is satisfied for  $\frac{\|\mathbf{d}_\omega\|_\infty}{k_\omega} < \sqrt{3}$ .

Consequently, almost all solutions enter the set defined in (7.10a) in finite time, and thus verify the limsup condition of Theorem 7.2, yielding almost ISS.  $\square$

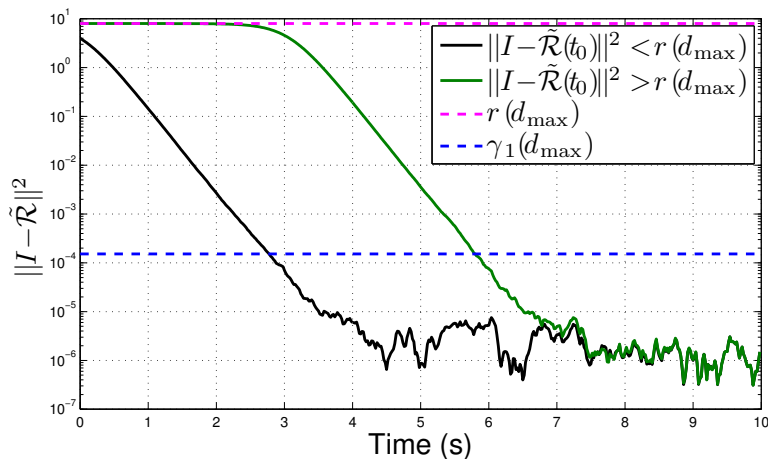


Figure 7.3: Simulation results of the attitude observer, illustrating almost ISS. Convergence for  $\|\mathbf{I} - \tilde{\mathcal{R}}(t_0)\|^2 \leq r(d_{\max})$  is guaranteed by Lyapunov methods; convergence for  $\|\mathbf{I} - \tilde{\mathcal{R}}(t_0)\|^2 > r(d_{\max})$  is guaranteed by combining Lyapunov and density functions.

Simulation results of the observer estimation error are depicted in Fig. 7.3. Note that the exponential convergence for  $\gamma_1(d_{\max}) < \|\mathbf{I} - \tilde{\mathcal{R}}(t)\|^2 < r(d_{\max})$  is justified by the fact that  $\dot{V} < -\alpha V$  in that region, for some  $\alpha \in \mathbb{R}^+$ . According to the proposed ISS derivation technique, based on Lemma 7.1, almost ISS of the attitude observer, formulated in (7.12), was obtained by combining the weakly almost ISS property (7.11), given by density function techniques, with the local ISS property (7.10), derived using Lyapunov techniques.

### 7.3 Local stability analysis using density functions

This section derives new results for local stability analysis of equilibrium points other than the origin, using density functions. By combining the proposed stability results with LaSalle's invariance principle, a new tool for global stability analysis of the origin is obtained. The proposed technique is illustrated for the case of a simple attitude observer with biased inertial measurements.

#### 7.3.1 Stability using density functions and LaSalle's invariance principle

The proposed stability analysis results are derived for autonomous nonlinear systems of the form

$$\dot{x} = f(x), \quad (7.13)$$

where  $f : \mathbb{R}^n \rightarrow \mathbb{R}^n$  is smooth, and the associated flow  $\phi_t : \mathbb{R}^n \rightarrow \mathbb{R}^n$  is defined by  $\phi_t(x_0) = x(t, x_0)$ , where  $x(t, x_0)$  denotes the solution of the system at time  $t$  with initial condition  $x_0$ . In the remainder of this work, it is assumed that  $\phi_t$  is well defined [125, Chapter 7].

**Assumption 7.1.** *The flow  $\phi_t$  is unique, continuous, and exists for all  $t$ .*

To formulate the stability results in the presence of multiple equilibrium points, some concepts and results are introduced, for more details the reader is referred to [125]. The values at time  $t$  and at the time interval  $t \in [\tau_0, \tau]$  of the trajectories starting in the set  $\mathcal{A}$ , are respectively denoted by

$$\phi_t(\mathcal{A}) = \{x : x = \phi_t(x_0), x_0 \in \mathcal{A}\}, \quad \phi_{[\tau_0, \tau]}(\mathcal{A}) = \{\phi_t(\mathcal{A}) : t \in [\tau_0, \tau]\}.$$

The local inset of  $x_w$  is the set of all initial conditions inside a neighborhood  $W$  of  $x_w$  that converge to  $x_w$  without leaving  $W$ , i.e.

$$\mathcal{Z}_W(x_w) = \{x \in W : \forall \epsilon \exists T \forall t > T |\phi_t(x) - x_w| < \epsilon \text{ and } \forall t > 0 \phi_t(x) \in W\}. \quad (7.14)$$

The global inset of  $x_w$ , denoted as  $\mathcal{W}(x_w)$ , is defined by taking (7.14) with  $W = \mathbb{R}^n$ .

The following theorem is a new result in density function methodologies, and provides sufficient conditions to show that an equilibrium point is not stable, given a suitable density function. This property is of interest to exclude the stability of equilibrium points other than the origin.

**Theorem 7.5.** *Let  $x_w \in \mathbb{R}^n$ , and suppose there exists a non-negative  $\rho \in C^1(\mathbb{R}^n \setminus \{0\}, \mathbb{R})$ , integrable in a neighborhood  $W$  of  $x_w$ , and with  $\text{div}(\rho f) > 0$  in  $W$ . Then, the global inset of  $x_w$  has zero measure.*

*Proof.* First, it is shown that the local inset, denoted as  $\mathcal{Z}_W$  with a slight abuse of notation, has zero measure. By Lemma H.9 presented in Appendix H.2, the local inset  $\mathcal{Z}_W$  is measurable. Using Lemma H.1 with  $D = W$  produces

$$0 \geq \int_{\phi_t(\mathcal{Z}_W)} \rho(x) dx - \int_{\mathcal{Z}_W} \rho(z) dz = \int_0^t \int_{\phi_\tau(\mathcal{Z}_W)} [\text{div}(\rho f)](x) dx d\tau.$$

Since  $\text{div}(\rho f) > 0$  in  $W$ , then  $\phi_t(\mathcal{Z}_W) \subset \mathcal{Z}_W \subset W$  has zero measure. The flow  $\phi_t$  is a diffeomorphism and hence  $\mathcal{Z}_W$  has zero measure, for results on set measure see Appendix H.2.

The forward propagation of  $\mathcal{Z}_W$  is  $\mathcal{Z}_W$  itself, i.e.  $\mathcal{Z}_W = \phi_{[0, \infty)}(\mathcal{Z}_W)$ . Therefore,  $\phi_{[0, \infty)}(\mathcal{Z}_W)$  has zero measure, and by the results expressed in Appendix H.2, the global inset, which can be expressed as  $\mathcal{W}(x_w) = \phi_{(-\infty, \infty)}(\mathcal{Z}_W)$ , has zero measure.  $\square$

The combination of the density function results presented in Theorem 7.5 with LaSalle's invariance principle can be used to provide almost global stability of the origin. The technique is based on using LaSalle's invariance principle to show that the trajectories approach a candidate set  $M$  in the sense discussed in [78]; and then using the  $\text{div}(\rho f) > 0$  property for  $M \setminus \{0\}$ , to show that the set of trajectories converging to  $M \setminus \{0\}$  is of zero measure, and hence that the origin is almost globally asymptotically stable.



**Lemma 7.6.** *Consider the system (7.13). Let  $V : \mathbb{R}^n \rightarrow \mathbb{R}$  be a continuously differentiable function such that the level sets  $\{x : V(x) \leq c\}$  are bounded and  $\dot{V}(x) \leq 0$ . Let  $M$  be the largest invariant set in  $\{x : \dot{V}(x) = 0\}$ . Suppose that  $M$  is a countable union of isolated points, and that there is a density function that satisfies the conditions of Theorem 7.5 for all  $x_w \in M \setminus \{0\}$ . Then the origin of (7.13) is almost GAS.*

*Proof.* The conditions on  $V(x)$  satisfy LaSalle's invariance principle [78, 125], and hence guarantee that the trajectories approach  $M$  as  $t \rightarrow \infty$ , i.e.

$$\forall x_0 \forall \varepsilon \exists T > 0 \forall t > T \inf_{y \in M} \|\phi_t(x_0) - y\| < \varepsilon.$$

By the continuity of  $\phi_t(x)$ , choosing  $\varepsilon < \min_{x,y \in M} \|x - y\|$  shows that each solution of (7.13) must converge to an isolated point  $x_w \in M$ . By Theorem 7.5, the condition  $\text{div}(\rho f) > 0$  for a neighborhood  $W$  of every  $x_w \in M \setminus \{0\}$  guarantees that the global inset of  $x_w$  has zero measure. The set of initial conditions that converge to  $M \setminus \{0\}$ , given by  $\cup_{x_w \in M \setminus \{0\}} \mathcal{W}(x_w)$ , is a countable union of zero measured sets and hence has zero measure. Consequently, almost all solutions converge to the origin, and hence the origin is almost globally asymptotically stable.  $\square$

### 7.3.2 Stability of the nonlinear observer in the presence of biased inertial readings

In this section, the proposed stability analysis is illustrated for the attitude observer, in a case where the disturbance in (7.1) is a constant bias, i.e.  $\dot{\mathbf{d}}_\omega = 0$ . Although the ISS results of Section 7.2 can be applied by considering the bias as an unmodeled disturbance, the bias dynamics are known. Therefore, the observer dynamics can be augmented to compensate for this non-ideality, yielding stronger stability properties.

The observer is augmented to estimate the bias, and the feedback laws are defined as follows

$$\begin{aligned} \dot{\hat{\mathcal{R}}} &= \hat{\mathcal{R}}(\hat{\omega})_\times, & \dot{\hat{\omega}} &= \hat{\mathcal{R}}' \mathbf{U}_H^B \mathbf{U}_H' (\omega_r - \hat{\mathbf{b}}_\omega) - k_\omega \mathbf{s}_\omega, \\ \dot{\hat{\mathbf{b}}}_\omega &= k_{b_\omega} \mathbf{s}_\omega, & \mathbf{s}_\omega &= \sum_{i=1}^n (\hat{\mathcal{R}}' L \mathbf{u}_i) \times^B \mathbf{u}_i, \end{aligned}$$

where  $k_\omega, k_{b_\omega} \in \mathbb{R}^+$  are feedback gains, and  $\hat{\mathbf{b}}_\omega$  is the rate gyro bias estimate, for more details on the adopted observer see Section 6.2. The closed loop error kinematics are given by

$$\dot{\tilde{\mathcal{R}}} = \tilde{\mathcal{R}} \left[ k_\omega (\tilde{\mathcal{R}}' - \tilde{\mathcal{R}}) + (\tilde{\mathbf{b}}_\omega)_\times \right], \quad \dot{\tilde{\mathbf{b}}}_\omega = k_{b_\omega} (\tilde{\mathcal{R}}' - \tilde{\mathcal{R}})_{\otimes}, \quad (7.15)$$

where  $\tilde{\mathbf{b}}_\omega = \hat{\mathbf{b}}_\omega - \mathbf{d}_\omega$  is the bias estimation error. The stability analysis technique is illustrated for the case where initial bias and attitude estimation errors exist along the z-axis, i.e.  $\mathbf{b}(t_0) = [0 \ 0 \ b_0]'$ ,  $b_0 \in \mathbb{R}$ , and  $\tilde{\mathcal{R}}(t_0) = \exp(\varphi_0 (\phi_0)_\times)$ ,  $\varphi_0 \in \mathbb{R}$ ,  $\phi_0 = [0 \ 0 \ 1]'$ .

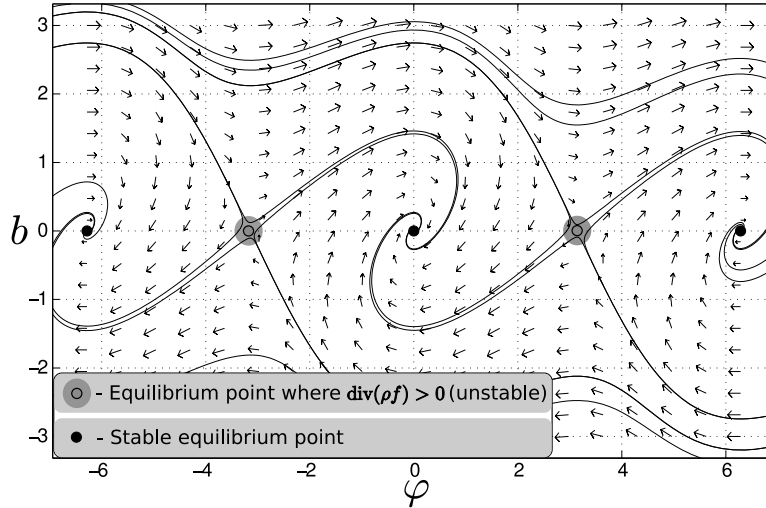


Figure 7.4: Phase portrait of the reduced order attitude observer. Using the density function property  $\text{div}(\rho f) > 0$  in a neighborhood of the equilibrium points  $(\varphi, b) = (\pi + 2\pi k, 0)$ ,  $k \in \mathbb{Z}$ , shows that these are unstable.

In this case, the trajectories of (7.15) are characterized by  $\tilde{\mathcal{R}}(t) = \exp(\varphi(t)(\phi_0)_\times)$ ,  $\mathbf{b}(t) = \begin{bmatrix} 0 & 0 & b(t) \end{bmatrix}'$ , and the dynamics can be reduced to

$$\dot{\varphi} = -\sin(\varphi) + b, \quad \dot{b} = -\sin(\varphi), \quad (7.16)$$

with initial conditions  $\varphi(t_0) = \varphi_0$ ,  $b(t_0) = b_0$ .

The stability of the second order system (7.16) is analyzed by following the proof of Lemma 7.6. Namely, using a Lyapunov function and LaSalle's invariance principle, an invariant set  $M$  is derived. Then, a density function and the results expressed in Theorem 7.5 are used to show that almost all solutions approach a subset of  $M$  as  $t \rightarrow \infty$ .

**Proposition 7.7.** *The trajectories of the system (7.16) approach  $M = \{(\varphi, b) : \varphi = \pi k, k \in \mathbb{Z}, b = 0\}$  as  $t \rightarrow \infty$ .*

*Proof.* The result is obtained by considering the Lyapunov function  $V = 2(1 - \cos(\varphi)) + b^2$ . The time derivative is given by  $\dot{V} = -2\sin^2(\varphi)$  and hence the result is immediate from LaSalle's invariance principle.  $\square$

The phase portrait of the system, depicted in Fig. 7.4, suggests that the equilibrium points in the set  $E = \{(\varphi, b) : \varphi = 2\pi k + \pi, k \in \mathbb{Z}, b = 0\} \subset M$  are unstable, and that almost all trajectories approach  $M \setminus E = \{(\varphi, b) : \varphi = 2\pi k, k \in \mathbb{Z}, b = 0\}$  as  $t \rightarrow \infty$ . This is demonstrated by combining Proposition 7.7 with the results based on density functions.

**Proposition 7.8.** *Almost all trajectories of the system (7.16) approach the set  $\{(\varphi, b) : \varphi = 2\pi k, k \in \mathbb{Z}, b = 0\}$  as  $t \rightarrow \infty$ .*

*Proof.* To exclude the points in the set  $E$ , we use the density function  $\rho = \frac{1}{2(1-\cos(\varphi))+b^2}$ . The divergence is

$$\operatorname{div}(\rho f) = \frac{2(1 - \cos(\varphi)) - \cos(\varphi)b^2}{(2(1 - \cos(\varphi)) + b^2)^2}.$$

There is a neighborhood of every point in  $E$  where  $\rho$  is integrable, and  $\operatorname{div}(\rho f) > 0$ . By Theorem 7.5, the set of initial conditions converging to each point in  $E$  has zero measure. The set  $E$  is a countable union of points, and hence the set of initial conditions that approach  $E$  has zero measure. Consequently, almost all the trajectories approach  $M \setminus E$ .  $\square$

## 7.4 Conclusions

This work addressed the combination of Lyapunov and density functions, for stability analysis of nonlinear systems. Almost ISS of the origin was formulated as the combination of local ISS and weakly almost ISS, that can be derived using the properties of Lyapunov and density functions, respectively. For the case of autonomous systems, it was shown that global stability of the origin can be obtained by combining LaSalle's invariance principle, with a density function that excludes the stability of undesirable equilibrium points. The proposed techniques were illustrated for the stability analysis of an attitude observer with non-ideal angular velocity readings.



## Chapter 8

# GPS/IMU based nonlinear navigation system

This chapter proposes a position and attitude nonlinear observer based on an inertial measurement unit (IMU) and GPS pseudorange readings. The GPS/IMU based nonlinear navigation system is characterized by a cascade composition of attitude and position observers, where the attitude subsystem is aided by vector measurements, or by multiple GPS units, which allows for a navigation solution based solely on GPS and IMU data. Exploiting the sensor measurements directly, the navigation system is formulated on  $SE(3)$  and yields exponential convergence of the position and attitude estimation errors to the origin. The proposed observer compensates for the bias in the angular velocity sensor and the clock offset in GPS pseudorange measurements. Nonmodeled disturbances in the inertial sensors are also considered, and the observer is shown to stabilize the position and attitude errors with explicit ultimate bounds, in the presence of bounded noise in the accelerometer and rate gyro measurements. The properties of the navigation system are illustrated in simulation for a rigid body equipped with low quality inertial sensors, and describing a challenging trajectory.

The chapter is organized as follows. In Section 8.1, the sensor suite adopted in the estimation problem is described and Section 8.2 proposes attitude and position observers based on the GPS, IMU, and vector readings. The stability and convergence properties of the estimation errors are derived and the observer equations are expressed as explicit functions of the sensor measurements. The stability and convergence of the observer estimates are illustrated in simulation in Section 8.3. Concluding remarks are presented in Section 8.4.

## 8.1 Sensor description

In this section, the sensor suite used in the attitude and position observer is introduced. The rigid body kinematics are described by

$$\dot{\mathcal{R}} = \mathcal{R}(\boldsymbol{\omega})_{\times}, \quad {}^E\dot{\mathbf{p}} = {}^E\mathbf{v}, \quad {}^E\dot{\mathbf{v}} = {}^E\mathbf{a},$$

where  $\mathcal{R}$  is the shorthand notation for the rotation matrix  $\frac{E}{B}\mathbf{R}$  from body frame  $\{B\}$  to Earth frame  $\{E\}$  coordinates,  $\boldsymbol{\omega}$  is the body angular velocity expressed in  $\{B\}$ ,  ${}^E\mathbf{p}$ ,  ${}^E\mathbf{v}$  and  ${}^E\mathbf{a}$  are the position, velocity and acceleration of the rigid body with respect to  $\{E\}$  expressed in  $\{E\}$ , respectively, and  $(\mathbf{s})_{\times}$  is the skew symmetric matrix defined by the vector  $\mathbf{s} \in \mathbb{R}^3$  such that  $(\mathbf{s})_{\times} \mathbf{b} = \mathbf{s} \times \mathbf{b}$ ,  $\mathbf{b} \in \mathbb{R}^3$ .

The inertial sensors measure the angular velocity and specific force of the body, which allows for the propagation of the attitude and position in time. The body angular velocity is measured by a rate gyro sensor triad, corrupted by a bias term

$$\boldsymbol{\omega}_r = \boldsymbol{\omega} + \mathbf{b}_{\omega}, \quad (8.1)$$

where the nominal bias is considered constant,  $\dot{\mathbf{b}}_{\omega} = \mathbf{0}$ . The triaxial accelerometer measures the specific force, which is the difference between the inertial and the gravitic accelerations of the rigid body [20],  ${}^B\mathbf{a}$  and  ${}^B\mathbf{g}$  respectively, expressed in body frame coordinates, bearing

$$\mathbf{a}_r = {}^B\mathbf{a} - {}^B\mathbf{g}.$$

As illustrated in Fig. 8.1, the GPS pseudorange measurements are given by the distance from the GPS satellites to the receiver and a distance offset due to the clock bias [62], yielding

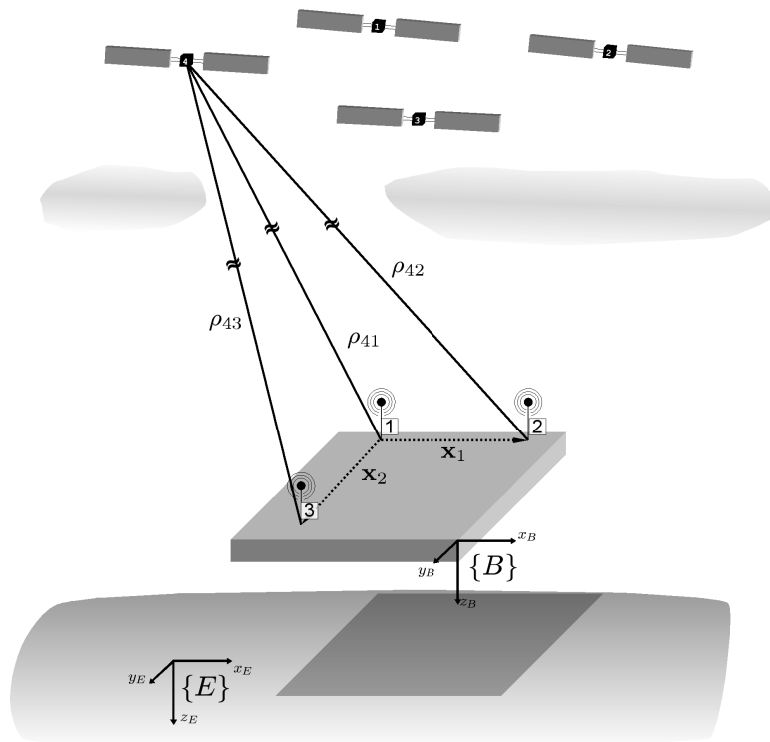
$$\rho_{ij} = \|{}^E\mathbf{p}_j - {}^E\mathbf{p}_{S_i}\| + b_{\rho}, \quad (8.2)$$

where  ${}^E\mathbf{p}_j$  and  ${}^E\mathbf{p}_{S_i}$  are the positions of the receiver  $j$  and satellite  $i$  expressed in  $\{E\}$ , the total number of GPS satellites and receivers are represented by  $s$  and  $r$ , respectively,  $j = 1..r$  and  $i = 1..s$ , and  $b_{\rho}$  is the range bias due to the offset between the receiver and satellite's clocks. In the communication process, the satellite coordinates  ${}^E\mathbf{p}_{S_i}$  are transmitted to the receiver. Without loss of generality, receiver 1 is considered to be at the origin of the body frame, i.e.  ${}^E\mathbf{p} = {}^E\mathbf{p}_1$ .

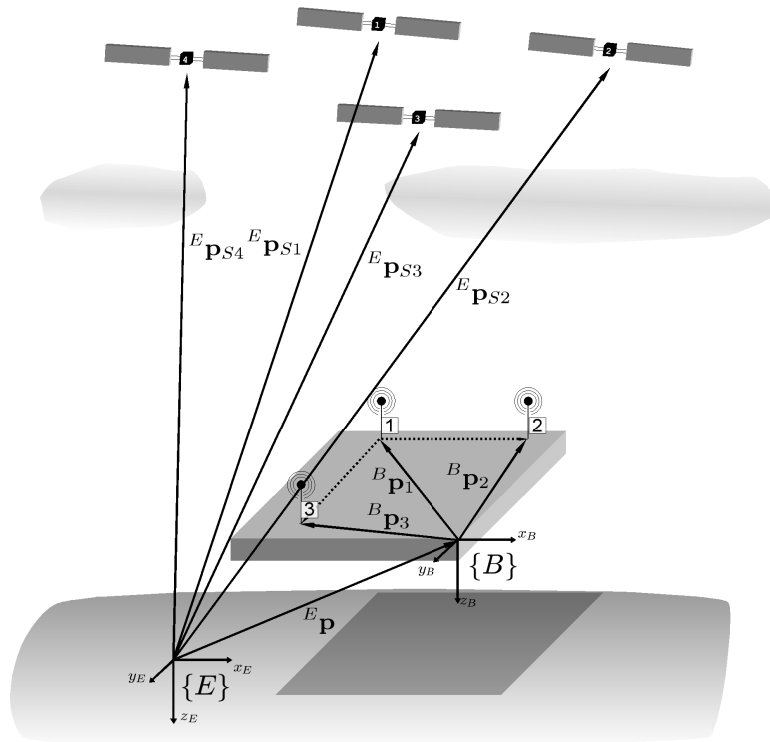
The objective of the present work is to exploit the information provided by the sensors, by deriving a position and attitude observer that combines the inertial measurements with the pseudorange readings and, if available, with the vector observations.

## 8.2 Observer architecture

As depicted in Fig. 8.2, the proposed observer is described by a cascaded composition, where the attitude observer estimates are fed into the position observer to rotate the



(a) Pseudorange measurements.



(b) Position of the GPS satellites ( ${}^E \mathbf{p}_{S_i}$ ), GPS receivers ( ${}^B \mathbf{p}_i$ ), and rigid body ( ${}^E \mathbf{p}$ ).

Figure 8.1: Navigation system configuration.

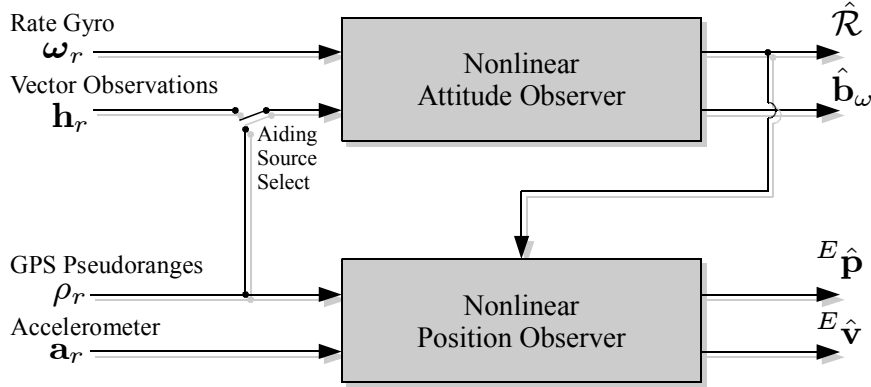


Figure 8.2: Cascaded position and attitude observer.

specific force readings to Earth frame. In this section the attitude and the position observers are detailed, and the associated properties are derived. Namely, the exponential convergence of the attitude and position estimation errors to the origin is evidenced, and it is shown that the attitude and position observer equations can be expressed as explicit functions of the IMU and GPS pseudorange measurements.

### 8.2.1 Attitude observer

The attitude observer considered in this section estimates the rotation matrix by exploiting the angular velocity measurements (8.1), and *i*) the pseudorange measurements (8.2) provided by multiple GPS receivers installed onboard the vehicle, or *ii*) vector observations. The latter is detailed in Chapter 6, where further insight on the observer derivation and stability properties can be found, and can be integrated directly in the architecture shown in Fig. 8.2.

The GPS based attitude observer is an alternative to vector based techniques for scenarios where these sensors measurements are corrupted, distorted or unavailable. For example, pendular readings are corrupted by external accelerations, including constant centripetal acceleration of helicoidal trimming trajectories, and magnetometers readings are distorted by electromagnetic interference, either created by other onboard devices or externally by nonmodeled sources. The attitude observer integrated in the cascade depicted in Fig. 8.2 allows for attitude and position estimation using only GPS and IMU measurements.

The architecture of the GPS based attitude observer is similar to that of the vector based attitude observer. The positions of two GPS receivers in body coordinates,  ${}^B\mathbf{p}_i$  and  ${}^B\mathbf{p}_1$ , are subtracted to define the vector

$${}^B\mathbf{x}_i := {}^B\mathbf{p}_{i+1} - {}^B\mathbf{p}_1, \quad (8.3)$$

which is known in body frame coordinates. Applying this operation to all the receivers produces  $\mathbf{X} := \begin{bmatrix} {}^B\mathbf{x}_1 & {}^B\mathbf{x}_2 & \dots & {}^B\mathbf{x}_{r-1} \end{bmatrix} \in \mathbf{M}(3, r-1)$ , that is illustrated in Fig. 8.3.



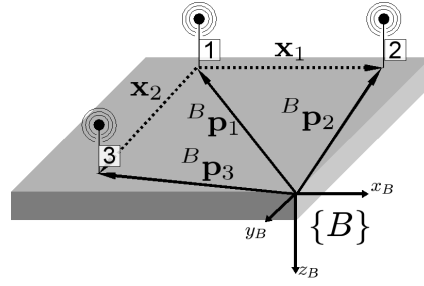


Figure 8.3: Body fixed vectors, defined by the position of the GPS receivers.

The attitude observer based on GPS units is dual to the attitude observer based on vector measurements in the sense that: in the latter, the vectors are measured in body frame and are known and constant in Earth frame; in the former observer, the vector quantities are known and constant in body frame, and can be measured in Earth frame using the position provided by the GPS units. Consequently, the attitude observer based on GPS units can be derived directly using the results presented in Chapter 6.

To derive the observer, define the linear combination of the body vectors as

$${}^B \mathbf{y}_j := \sum_{i=1}^{r-1} a_{ij} {}^B \mathbf{x}_i \quad \Leftrightarrow \quad \mathbf{Y}_X = \mathbf{X} \mathbf{A}_X, \quad (8.4)$$

where  $\mathbf{A}_X := [a_{ij}] \in M(r-1)$  is invertible by construction and  $\mathbf{Y}_X := [{}^B \mathbf{y}_1 \ \dots \ {}^B \mathbf{y}_{r-1}] \in M(3, r-1)$ . The nominal and the estimated coordinates of the transformed body vectors in Earth frame are respectively given by

$${}^E \mathbf{Y}_X := \mathcal{R} \mathbf{Y}_X, \quad {}^E \hat{\mathbf{Y}}_X := \hat{\mathcal{R}} \mathbf{Y}_X.$$

Some rotational degrees of freedom are unobservable if the vectors (8.3) are all collinear, as discussed in Section 6.1, and the following necessary condition is assumed.

**Assumption 8.1.** *There are at least two noncollinear vectors  ${}^B \mathbf{x}_i$ .*

Note that the condition of Assumption 8.1 is satisfied using at least three noncollinear GPS receivers, depicted in Fig. 8.3. The transformation  $\mathbf{A}_X$  is defined such that  $\mathbf{Y}_X \mathbf{Y}_X' = \mathbf{I}$ , to shape uniformly the directionality introduced by the vector readings. The desired  $\mathbf{A}_X$  exists if Assumption 8.1 is satisfied, as discussed in the derivation of the attitude observer based on vector observations, found in Section 6.1.

The attitude observer is derived using a synthesis Lyapunov based on the measurement error of the vectors  ${}^B \mathbf{x}$ , given by

$$V = \frac{1}{2} \sum_{i=1}^n \| {}^B \hat{\mathbf{x}}_i - {}^B \mathbf{x}_i \|^2,$$

that is similar to the Lyapunov function defined in (6.3), but given by a vector measurement error computed in body coordinates. Although the GPS based attitude observer can

be derived by finding a feedback law such that  $\dot{V} < 0$ , the observer can be directly obtained by considering the duality between the GPS based and the vector based observers. Taking the observer architecture formulated in Theorem 6.8, the GPS based observer is given by

$$\dot{\hat{\mathcal{R}}} = \hat{\mathcal{R}}(\hat{\omega})_{\times}, \quad \hat{\omega} = \hat{\mathcal{R}}'^E \mathbf{Y}_X \mathbf{Y}'_X (\omega_r - \hat{\mathbf{b}}_{\omega}) - k_{\omega} \mathbf{s}_{\omega}, \quad (8.5a)$$

$$\dot{\hat{\mathbf{b}}}_{\omega} = k_b \mathbf{s}_{\omega}, \quad \mathbf{s}_{\omega} = \sum_{i=1}^n (\hat{\mathcal{R}}'^E \mathbf{Y}_X \mathbf{e}_i) \times (\mathbf{Y}_X \mathbf{e}_i), \quad (8.5b)$$

where  $k_{\omega}, k_b > 0$  are feedback gains. Note that  $\mathbf{Y}_X$  can be seen as the dual of the matrix  $\mathbf{U}_H$  adopted in Chapter 6, that are defined, known, and constant in body and Earth coordinates, respectively.

The observer (8.5) is a function of the sensor measurements and states estimates. The terms  ${}^E \hat{\mathbf{Y}}_X$  and  ${}^E \mathbf{Y}_X$  are given by the observer estimates and the pseudorange measurements, respectively, as shown in the following proposition.

**Proposition 8.1.** *Assume that the position fix  $({}^E \mathbf{p}, b_{\rho})$  satisfying the pseudorange measurements (8.2) for all  $i = 1..s$  is unique. The attitude observer dynamics (8.5) are a function of the sensor measurements and observer estimates, where*

$${}^E \mathbf{Y}_X = - \begin{bmatrix} \mathbf{f}_p(\boldsymbol{\rho}_2) - \mathbf{f}_p(\boldsymbol{\rho}_1) & \dots & \mathbf{f}_p(\boldsymbol{\rho}_r) - \mathbf{f}_p(\boldsymbol{\rho}_1) \end{bmatrix} \mathbf{A}_X, \quad {}^E \hat{\mathbf{Y}}_X = \hat{\mathcal{R}} \mathbf{X} \mathbf{A}_X,$$

$\boldsymbol{\rho}_j := [\rho_{1j} \dots \rho_{mj}]$  is the vector of pseudoranges measured by receiver  $j$ ,  $\boldsymbol{\rho} := \boldsymbol{\rho}_1$ , and the function  $\mathbf{f}_p(\boldsymbol{\rho}_j)$  is given by

$$\mathbf{f}_p(\boldsymbol{\rho}_j) := \frac{1}{2} ({}^E \mathbf{U}' \mathbf{W}_{Sj} {}^E \mathbf{U})^{-1} {}^E \mathbf{U}' \mathbf{W}_{Sj} \mathbf{b}_{Sj},$$

which encompasses matrices described by the pseudoranges measurements and satellite's positions as follows

$$\begin{aligned} {}^E \mathbf{U} &:= \begin{bmatrix} {}^E \mathbf{p}'_{S2} - {}^E \mathbf{p}'_{S1} & \dots & {}^E \mathbf{p}'_{Ss} - {}^E \mathbf{p}'_{S1} \end{bmatrix}', \\ \mathbf{W}_{Sj} &:= 4 \Delta_{Sj} (4 \Delta_{Sj}' \Delta_{Sj} - 1)^{-1} \Delta_{Sj}' - \mathbf{I}_{(s-1) \times (s-1)}, \\ \Delta_{Sj} &:= \begin{bmatrix} \rho_{2j} - \rho_{1j} & \dots & \rho_{sj} - \rho_{1j} \end{bmatrix}', \\ \mathbf{b}_{Sj} &= \begin{bmatrix} \rho_{2j}^2 - \rho_{1j}^2 - (\|{}^E \mathbf{p}_{S2}\|^2 - \|{}^E \mathbf{p}_{S1}\|^2) \\ \vdots \\ \rho_{sj}^2 - \rho_{1j}^2 - (\|{}^E \mathbf{p}_{Ss}\|^2 - \|{}^E \mathbf{p}_{S1}\|^2) \end{bmatrix}. \end{aligned}$$

*Proof.* The formulation for  ${}^E \hat{\mathbf{Y}}_X$  is immediate from (8.4), and  ${}^E \mathbf{Y}_X$  is obtained by noting that  ${}^E \mathbf{Y}_X = \begin{bmatrix} {}^E \mathbf{p}_2 - {}^E \mathbf{p}_1 & \dots & {}^E \mathbf{p}_r - {}^E \mathbf{p}_1 \end{bmatrix} \mathbf{A}_X$  and using the derivation of  $\mathbf{f}_p(\boldsymbol{\rho}_j)$  presented in Appendix I.  $\square$

The stability properties of the observer are obtained directly from Theorem 6.3, for the case of ideal velocity readings, and Theorem 6.5, for the case of biased angular velocity measurements. The attitude estimation error adopted to described the stability properties is given by  $\tilde{\mathcal{R}} := \hat{\mathcal{R}}' \mathcal{R}$ .

**Theorem 8.2** (Unbiased Velocity Measurements). *Let  $\tilde{\mathbf{b}}_\omega = 0$ . Under Assumption 8.1, the closed-loop error kinematics of the attitude observer are given by*

$$\dot{\tilde{\mathcal{R}}} = -k_\omega \tilde{\mathcal{R}}(\tilde{\mathcal{R}} - \tilde{\mathcal{R}}'). \quad (8.6)$$

The equilibrium point  $\tilde{\mathcal{R}} = \mathbf{I}$  is exponentially stable, with region of attraction given by

$$R_A = \{\tilde{\mathcal{R}} \in \text{SO}(3) : \|\mathbf{I} - \tilde{\mathcal{R}}\|^2 < 8\}.$$

For any initial condition  $\tilde{\mathcal{R}}(t_0) \in R_A$ , the emanating trajectory satisfies

$$\|\tilde{\mathcal{R}}(t) - \mathbf{I}\| \leq \|\tilde{\mathcal{R}}(t_0) - \mathbf{I}\| e^{-\frac{1}{2}\gamma_{\mathcal{R}}(t-t_0)}, \quad (8.7)$$

where  $\gamma_{\mathcal{R}} = \frac{k_\omega}{2}(8 - \|\tilde{\mathcal{R}} - \mathbf{I}\|^2)$ .

**Theorem 8.3** (Biased Velocity Measurements). *Let  $\tilde{\mathbf{b}}_\omega \neq 0$ . Under Assumption 8.1, the closed loop dynamics are given by*

$$\dot{\tilde{\mathcal{R}}} = -k_\omega \tilde{\mathcal{R}}(\tilde{\mathcal{R}} - \tilde{\mathcal{R}}') + \tilde{\mathcal{R}} \left( \tilde{\mathbf{b}}_\omega \right)_\times, \quad \dot{\tilde{\mathbf{b}}}_\omega = -k_b \left( \tilde{\mathcal{R}} - \tilde{\mathcal{R}}' \right)_\otimes. \quad (8.8)$$

Let the feedback gain satisfy

$$k_b > \frac{\tilde{b}_0^2}{8 - c_0},$$

where  $c_0$  and  $\tilde{b}_0$  are the initial estimation errors bounds

$$\|\mathbf{I} - \tilde{\mathcal{R}}(t_0)\|^2 \leq c_0 < 8, \quad \|\tilde{\mathbf{b}}_\omega(t_0)\| \leq \tilde{b}_0. \quad (8.9)$$

Then the origin  $(\tilde{\mathcal{R}}, \tilde{\mathbf{b}}_\omega) = (\mathbf{I}, 0)$  is exponentially stable, uniformly in the set defined by (8.9). That is, let  $\mathbf{x}_{\mathcal{R}} := (\tilde{\mathcal{R}} - \mathbf{I}, \tilde{\mathbf{b}}_\omega)$ , there exists  $c_b, \gamma_b > 0$  independent of  $\mathbf{x}_{\mathcal{R}}(t_0)$  such that the trajectories of the system (8.8) satisfy

$$\|\mathbf{x}_{\mathcal{R}}(t)\| \leq c_b e^{-\frac{1}{2}\gamma_b(t-t_0)} \|\mathbf{x}_{\mathcal{R}}(t_0)\|. \quad (8.10)$$

**Remark 8.1.** An alternative GPS based attitude observer can be formulated, based on the difference of the satellites' positions in Earth frame, that is known and given by  ${}^E\mathbf{p}_{Si} - {}^E\mathbf{p}_{Sj}$ . This quantity can be measured in body coordinates by a set of receivers by exploiting the following duality: given that a constellation of satellites can be used to determine the position of a receiver in Earth coordinates, a set of receivers can be used to compute a satellite position in body coordinates. In this configuration, the vectors  ${}^E\mathbf{p}_{Si} - {}^E\mathbf{p}_{Sj}$  are known in Earth frame, and are measured in body frame, bearing the same estimation problem of the vector based attitude observer formulated in Chapter 6. However, the quantities  ${}^E\mathbf{p}_{Si} - {}^E\mathbf{p}_{Sj}$  are time varying due to the motion of the GPS satellites, and hence the directionality of the observer is time varying. This formulation requires for a time dependent transformation  $\mathbf{A}_H$ , and thus for accurate satellite position information, leading to a more complex observer implementation.

### 8.2.2 Position observer

This section derives the position observer based on the IMU and GPS readings, and on the attitude observer estimates. The position and velocity estimates are described by

$${}^E\dot{\hat{\mathbf{p}}} = {}^E\hat{\mathbf{v}} + \mathbf{s}_p, \quad {}^E\dot{\hat{\mathbf{v}}} = {}^E\hat{\mathbf{a}} + \mathbf{s}_v, \quad (8.11)$$

where  $\mathbf{s}_p$  and  $\mathbf{s}_v$  are feedback terms, the estimate of the acceleration in Earth coordinates is given by

$${}^E\hat{\mathbf{a}} = \tilde{\mathcal{R}}\mathbf{a}_r + {}^E\mathbf{g},$$

and the gravity representation in Earth coordinates  ${}^E\mathbf{g}$  is known. As shown in the block diagram of Fig. 8.2, the position observer uses the attitude estimate to rotate the accelerometer measurements  $\mathbf{a}_r$  to the Earth frame. Consequently, the attitude estimation error  $\tilde{\mathcal{R}}$  will influence the convergence and stability properties of the position observer.

The derivation of the feedback terms  $\mathbf{s}_p$  and  $\mathbf{s}_v$  in (8.11) is motivated by the Lyapunov function

$$V_p = \frac{1}{2}\|{}^E\tilde{\mathbf{p}}\|^2 + \frac{\alpha_v}{2}\|{}^E\tilde{\mathbf{v}}\|^2.$$

where  ${}^E\tilde{\mathbf{p}} = {}^E\hat{\mathbf{p}} - {}^E\mathbf{p}$  and  ${}^E\tilde{\mathbf{v}} = {}^E\hat{\mathbf{v}} - {}^E\mathbf{v}$  are the position and velocity estimation errors, respectively.

The Lyapunov function time derivative is described by

$$\dot{V}_p = {}^E\tilde{\mathbf{p}}'({}^E\tilde{\mathbf{v}} + \mathbf{s}_p) + \alpha_v {}^E\tilde{\mathbf{v}}'(\mathbf{u}_g + \mathbf{s}_v),$$

where  $\mathbf{u}_g = \mathcal{R}(\tilde{\mathcal{R}}' - \mathbf{I})\mathcal{R}'({}^E\mathbf{a} - {}^E\mathbf{g})$ . The feedback terms are defined as

$$\mathbf{s}_p = -k_p {}^E\tilde{\mathbf{p}}, \quad \mathbf{s}_v = -k_v {}^E\tilde{\mathbf{v}}, \quad (8.12)$$

where  $k_p, k_v > 0$ , and choosing  $\alpha_v = \frac{1}{k_v}$  produces

$$\dot{V}_p = -k_p \|{}^E\tilde{\mathbf{p}}\|^2 + \frac{1}{k_v} {}^E\tilde{\mathbf{v}}' \mathbf{u}_g.$$

which is sign indefinite due to the second term. The term  $\mathbf{u}_g$  is the compensation error generated by rotating the accelerometer readings to Earth frame using the estimated attitude. In particular, if  $\mathbf{u}_g = 0$ , then  $\dot{V}_p$  is negative definite and the stability properties of the position observer can be derived using Lyapunov stability theory. However, for  $\mathbf{u}_g \neq 0$ , the convergence properties of the position observer are influenced by the convergence properties of the attitude observer.

The position and velocity error dynamics are described by

$${}^E\dot{\tilde{\mathbf{p}}} = -k_p {}^E\tilde{\mathbf{p}} + {}^E\tilde{\mathbf{v}}, \quad (8.13a)$$

$${}^E\dot{\tilde{\mathbf{v}}} = -k_v {}^E\tilde{\mathbf{v}} + \mathbf{u}_g, \quad \mathbf{u}_g = \mathcal{R}(\tilde{\mathcal{R}}' - \mathbf{I})\mathcal{R}'({}^E\mathbf{a} - {}^E\mathbf{g}) \quad (8.13b)$$

which can be modeled as an autonomous system with an input. In this work, the stability of the position observer is obtained by using input-to-state stability theory [78, 131]. To that effect, it is assumed that the following condition for the rigid body acceleration is verified.

**Assumption 8.2.** *For any  $\gamma_g > 0$ , there exists  $c_g$  such that the acceleration of the rigid body satisfies*

$$\|{}^E\mathbf{a}(t) - {}^E\mathbf{g}\| \leq c_g e^{\gamma_g(t-t_0)}, \text{ for all } t > t_0.$$

The conditions of Assumption 8.2 guarantee that the convergence of the attitude estimation error  $(\mathbf{I} - \tilde{\mathcal{R}})$  dominates the acceleration term  $({}^E\mathbf{a} - {}^E\mathbf{g})$  in  $\mathbf{u}_g$  as  $t \rightarrow \infty$ . Interestingly enough, unbounded accelerations such as those that grow polynomially with time satisfy Assumption 8.2, which therefore poses a weak limitation for most practical applications.

We are now ready to present the stability and convergence properties of the cascaded attitude and position observers. As before, the properties are derived separately for unbiased and biased angular rate measurements.

**Theorem 8.4** (Unbiased Velocity Measurements). *Under Assumptions 8.1 and 8.2, the equilibrium point  $(\tilde{\mathcal{R}}, {}^E\tilde{\mathbf{p}}, {}^E\tilde{\mathbf{v}}) = (\mathbf{I}, \mathbf{0}, \mathbf{0})$  of the system (8.6, 8.13) is exponentially stable with region of attraction given by*

$$R_A = \{(\tilde{\mathcal{R}}, {}^E\tilde{\mathbf{p}}, {}^E\tilde{\mathbf{v}}) \in \text{SE}(3) \times \mathbb{R}^3 : \|\mathbf{I} - \tilde{\mathcal{R}}\|^2 < 8\}.$$

*Proof.* The stability and convergence of the position and attitude errors are shown by analyzing (8.6) and (8.13) as a cascaded system. The position and velocity error dynamics expressed in (8.13) are rewritten as

$$\dot{\mathbf{x}}_p = \mathbf{A}_p \mathbf{x}_p + \mathbf{B}_p \mathbf{u}_g, \quad (8.14)$$

where

$$\mathbf{x}_p = \begin{bmatrix} {}^E\tilde{\mathbf{p}}' & {}^E\tilde{\mathbf{v}}' \end{bmatrix}', \quad \mathbf{A}_p = \begin{bmatrix} -k_p \mathbf{I} & \mathbf{I} \\ -k_v \mathbf{I} & \mathbf{0} \end{bmatrix}, \quad \mathbf{B}_p = \begin{bmatrix} \mathbf{0} \\ \mathbf{I} \end{bmatrix}.$$

To derive the stability and convergence properties of the cascaded system, it is first shown that the system represented by (8.14) is input-to-state stable (ISS). It is a simple exercise to verify that  $\mathbf{A}_p$  is Hurwitz and, by the properties of linear systems [78], the system (8.14) is ISS.

The exponential convergence of the state  $(\tilde{\mathcal{R}}, {}^E\tilde{\mathbf{p}}, {}^E\tilde{\mathbf{v}})$  is obtained by the bounds on the solution of (8.14) and the exponential convergence of  $\mathbf{u}_g$ . The derivation is presented here for the sake of clarity and to provide for explicit convergence bounds. Using

$$\|\mathbf{u}_g\| \leq \|\mathcal{R}(\tilde{\mathcal{R}}' - \mathbf{I})\| \|\mathcal{R}'({}^E\mathbf{a} - {}^E\mathbf{g})\| = \|\tilde{\mathcal{R}} - \mathbf{I}\| \|{}^E\mathbf{a} - {}^E\mathbf{g}\|, \quad (8.15)$$

the exponential convergence of the attitude observer error (8.7), and Assumption 8.2, an exponential bound for the input is obtained

$$\|\mathbf{u}_g(t)\| \leq c_g e^{-\gamma_e(t-t_0)} \|\tilde{\mathcal{R}}(t_0) - \mathbf{I}\|, \quad (8.16)$$

where  $\gamma_e = \gamma_{\mathcal{R}} - \gamma_g$ . Choosing  $\gamma_g$  small enough, the exponential rate satisfies  $\gamma_e > 0$ . Therefore  $\|\mathbf{u}_g\| \rightarrow 0$  and, by the ISS property of (8.13),  $\|{}^E\tilde{\mathbf{p}}\| \rightarrow 0$  and  $\|{}^E\tilde{\mathbf{v}}\| \rightarrow 0$  as  $t \rightarrow \infty$ .

To see that the origin of the system (8.6, 8.13), is in fact exponentially stable, the results derived in Appendix J are adopted. Define the attitude, position and velocity estimation error state as  $\mathbf{x}_f := (\tilde{\mathcal{R}} - \mathbf{I}, \mathbf{x}_p) = (\tilde{\mathcal{R}} - \mathbf{I}, {}^E\tilde{\mathbf{p}}, {}^E\tilde{\mathbf{v}})$ . If the acceleration of the rigid body is limited, then exponential convergence of  $\|\mathbf{x}_f\|$  is obtained from Proposition J.4, by taking  $c_3 = \max_{t \in \mathbb{R}_0^+} \|{}^E\mathbf{a} - {}^E\mathbf{g}\|$ .

In the case where the acceleration satisfies Assumption 8.2, using (8.16) and Proposition J.4 produces

$$\|\mathbf{x}_p(t)\| \leq c_a e^{-\gamma_{\min}(t-t_0)} \left( \|\mathbf{x}_p(t_0)\| + \frac{c_g \|\mathbf{B}_p\|}{|\gamma_a - \gamma_e|} \|\tilde{\mathcal{R}}(t_0) - \mathbf{I}\| \right),$$

where  $\gamma_{\min} = \min(\gamma_e, \gamma_a)$ . Using (8.7),  $\gamma_e < \gamma_{\mathcal{R}}$ , and norm inequalities produces

$$\begin{aligned} \|\mathbf{x}_f(t)\| &\leq \|\mathbf{x}_p(t)\| + \|\tilde{\mathcal{R}}(t) - \mathbf{I}\| \\ &\leq c_a e^{-\gamma_{\min}(t-t_0)} \left( \|\mathbf{x}_p(t_0)\| + \frac{c_g \|\mathbf{B}_p\|}{|\gamma_a - \gamma_e|} \|\tilde{\mathcal{R}}(t_0) - \mathbf{I}\| \right) + e^{-\frac{1}{2}\gamma_{\mathcal{R}}(t-t_0)} \|\tilde{\mathcal{R}}(t_0) - \mathbf{I}\| \\ &\leq e^{-\gamma_{\min}(t-t_0)} \left( c_a \|\mathbf{x}_p(t_0)\| + \left( \frac{c_a c_g \|\mathbf{B}_p\|}{|\gamma_a - \gamma_e|} + 1 \right) \|\tilde{\mathcal{R}}(t_0) - \mathbf{I}\| \right) \\ &\leq e^{-\gamma_{\min}(t-t_0)} \left( c_a \|\mathbf{x}_f(t_0)\| + \left( \frac{c_a c_g \|\mathbf{B}_p\|}{|\gamma_a - \gamma_e|} + 1 \right) \|\mathbf{x}_f(t_0)\| \right) \\ &\leq c_{\max} e^{-\gamma_{\min}(t-t_0)} \|\mathbf{x}_f(t_0)\|, \end{aligned}$$

where  $c_{\max} = c_a + \frac{c_a c_g \|\mathbf{B}_p\|}{|\gamma_a - \gamma_e|} + 1$ . □

**Remark 8.2.** Following the proof of Theorem 8.4, it is possible to show that if the acceleration grows exponentially with time, then there is a sufficiently high gain  $k_\omega$  such that the origin is exponentially stable for all  $\|\mathbf{I} - \tilde{\mathcal{R}}(t_0)\|^2 \leq c_0 < 8$ .

The stability and convergence result for position and attitude estimation with biased angular velocity measurements is presented next.

**Theorem 8.5** (Biased Angular Velocity Measurements). *Let the bias feedback gain satisfy  $k_b > \frac{\tilde{b}_0^2}{8-c_0}$ . Under Assumptions 8.1 and 8.2, the equilibrium point  $(\tilde{\mathcal{R}}, \tilde{\mathbf{b}}_\omega, {}^E\tilde{\mathbf{p}}, {}^E\tilde{\mathbf{v}}) = (\mathbf{I}, \mathbf{0}, \mathbf{0}, \mathbf{0})$  of the system (8.8, 8.13) is exponentially stable, uniformly in the set defined by (8.9).*

*Proof.* By Theorem 8.3, the attitude observer error  $\mathbf{x}_{\mathcal{R}}$  is bounded by (8.10). Using  $\|\tilde{\mathcal{R}} - \mathbf{I}\| \leq \|\mathbf{x}_{\mathcal{R}}\|$ , the input of the ISS system (8.13) is bounded by

$$\|\mathbf{u}_g(t)\| \leq c_{be} e^{-\gamma_{be}(t-t_0)} \|\mathbf{x}_{\mathcal{R}}(t_0)\|,$$

where  $c_{be} := c_b c_g$  and  $\gamma_{be} := \frac{1}{2}\gamma_b - \gamma_g$ . Repeating the algebraic manipulations of the proof of Theorem 8.4 produces

$$\|\mathbf{x}_{bf}(t)\| \leq c_{\max} e^{-\gamma_{\min}(t-t_0)} \|\mathbf{x}_{bf}(t_0)\|,$$

where  $\mathbf{x}_{bf} = (\mathbf{x}_{\mathcal{R}}, \mathbf{x}_p) = (\tilde{\mathcal{R}} - \mathbf{I}, \tilde{\mathbf{b}}_\omega, {}^E\tilde{\mathbf{p}}, {}^E\tilde{\mathbf{v}})$  is the full attitude and position estimation error state,  $\gamma_{\min} = \min(\gamma_{be}, \gamma_a)$  and  $c_{\max} = c_a + \frac{c_a c_{be} \|\mathbf{B}_p\|}{|\gamma_a - \gamma_{be}|} + k_b$ .  $\square$

For the purpose of implementation, the dynamics of the position and velocity estimates, formulated in (8.11), should be expressed as a function of known quantities. The next proposition shows that the derived observer equations can be written as a function of the observer estimates and of the sensor measurements.

**Proposition 8.6.** *Assume that the position fix  $({}^E\mathbf{p}, b_\rho)$  satisfying the pseudorange measurements (8.2) for all  $i = 1..s$  is unique. The dynamics of the position and velocity estimates are a function of the sensor measurements and observer estimates*

$${}^E\dot{\hat{\mathbf{p}}} = -k_p ({}^E\hat{\mathbf{p}} + \mathbf{f}_p(\boldsymbol{\rho})) + {}^E\hat{\mathbf{v}}, \quad (8.17a)$$

$${}^E\dot{\hat{\mathbf{v}}} = -k_v ({}^E\hat{\mathbf{p}} + \mathbf{f}_p(\boldsymbol{\rho})) + \hat{\mathcal{R}}\mathbf{a}_r + {}^E\mathbf{g}. \quad (8.17b)$$

*Proof.* The formulation (8.17) is obtained by algebraic manipulation of (8.11) and (8.12), and by writing the nominal position term in  ${}^E\tilde{\mathbf{p}} = {}^E\hat{\mathbf{p}} - {}^E\mathbf{p}$  as a solution of the pseudorange measurements. The details of the derivation are presented in Appendix I.  $\square$

### 8.2.3 Stability in the presence of inertial sensor noise

The stability of the observer for inertial measurements with noise is addressed. The accelerometer and rate gyro measurements are modeled as

$$\mathbf{a}_r = {}^B\mathbf{a} - {}^B\mathbf{g} + \mathbf{n}_a, \quad \boldsymbol{\omega}_r = \boldsymbol{\omega} + \mathbf{n}_\omega,$$

where  $\mathbf{n}_a, \mathbf{n}_\omega \in \mathbb{R}^3$  are nonmodeled disturbances, bounded by  $\|\mathbf{n}_a\| \leq n_{a \max}$ ,  $\|\mathbf{n}_\omega\| \leq n_{\omega \max}$ , respectively.

The observer dynamics are given by (8.17) and by (8.5) with  $\tilde{\mathbf{b}}_\omega = \mathbf{0}$ , that is

$$\dot{\hat{\mathcal{R}}} = \hat{\mathcal{R}}(\hat{\boldsymbol{\omega}})_\times, \quad \dot{\hat{\boldsymbol{\omega}}} = \hat{\mathcal{R}}' {}^E\mathbf{Y}_X \mathbf{Y}'_X \boldsymbol{\omega}_r - k_\omega \sum_{i=1}^n (\hat{\mathcal{R}}' {}^E\mathbf{Y}_X \mathbf{e}_i) \times (\mathbf{Y}_X \mathbf{e}_i).$$

To attain boundedness of the input  $\mathbf{u}_g$  in the error kinematics (8.13), it is assumed that the acceleration of the body is bounded

$$\max_{t \in \mathbb{R}_0^+} \|{}^E\mathbf{a}(t) - {}^E\mathbf{g}\| \leq a_{\max}.$$

As shown in the next proposition, the attitude and position estimation errors are bounded in the presence of accelerometer disturbances, i.e. the observer is almost ISS with respect to  $(\tilde{\mathcal{R}}, {}^E\tilde{\mathbf{p}}, {}^E\tilde{\mathbf{v}}) = (\mathbf{I}, \mathbf{0}, \mathbf{0})$ .

**Theorem 8.7.** Let  $k_\omega > \frac{1}{\sqrt{3}}n_{\omega \max}$ . Then, almost all trajectories of the attitude and position observer satisfy

$$\limsup_{t \rightarrow \infty} \|\mathbf{I} - \tilde{\mathcal{R}}(t)\|^2 \leq \gamma(n_{\omega \max}), \quad (8.18a)$$

$$\limsup_{t \rightarrow \infty} \|({}^E \tilde{\mathbf{p}}, {}^E \tilde{\mathbf{v}})\| \leq \frac{c_a}{\gamma_a} (n_{a \max} + \gamma(n_{\omega \max})a_{\max}), \quad (8.18b)$$

where  $\gamma(n) = 4 \left(1 - \sqrt{1 - \frac{n^2}{4k_\omega^2}}\right)$ , and  $c_a, \gamma_a$  satisfy the bound  $\left\| e^{\begin{bmatrix} -k_p \mathbf{I} & \mathbf{I} \\ -k_v \mathbf{I} & \mathbf{0} \end{bmatrix} \tau} \right\| \leq c_a e^{-\gamma_a \tau}$ .

*Proof.* The result (8.18a) is obtained from the ISS properties of the attitude observer, formulated in Theorem 7.4.

The limit (8.18b) is obtained from the ISS properties of the position observer. The position estimation error dynamics are given by

$${}^E \dot{\tilde{\mathbf{p}}} = -k_p {}^E \tilde{\mathbf{p}} + {}^E \tilde{\mathbf{v}}, \quad {}^E \dot{\tilde{\mathbf{v}}} = -k_v {}^E \tilde{\mathbf{p}} + \mathbf{u}_g + \hat{\mathcal{R}} \mathbf{n}_a. \quad (8.19)$$

Using  $\left\| \begin{bmatrix} \mathbf{0}'_3 & (\mathbf{u}_g + \hat{\mathcal{R}} \mathbf{n}_a)' \end{bmatrix} \right\| = \|\mathbf{u}_g + \hat{\mathcal{R}} \mathbf{n}_a\|$ , the triangle inequality  $\|\mathbf{u}_g + \hat{\mathcal{R}} \mathbf{n}_a\| \leq \|\mathbf{u}_g\| + \|\hat{\mathcal{R}} \mathbf{n}_a\|$ , and  $\|\hat{\mathcal{R}} \mathbf{n}_a\| = \|\mathbf{n}_a\|$ , the solution of the LTI system (8.19) is bounded by

$$\|\mathbf{x}_p(t)\| \leq c_a e^{-\gamma_a(t-t_0)} \|\mathbf{x}_p(t_0)\| + \int_{t_0}^t c_a e^{-\gamma_a(t-\tau)} (\|\mathbf{u}_g(\tau)\| + \|\mathbf{n}_a(\tau)\|) d\tau.$$

where  $\mathbf{x}_p = \begin{bmatrix} {}^E \tilde{\mathbf{p}}' & {}^E \tilde{\mathbf{v}}' \end{bmatrix}'$ . Taking the bound  $\int_{t_0}^t e^{-\gamma_a(t-\tau)} \|\mathbf{n}_a(\tau)\| d\tau \leq \frac{n_{\max}}{\gamma_a}$  produces

$$\begin{aligned} \|\mathbf{x}_p(t)\| &\leq c_a e^{-\gamma_a(t-t_0)} \|\mathbf{x}_p(t_0)\| + \frac{c_a}{\gamma_a} n_{\max} + c_a \int_{t_0}^t e^{-\gamma_a(t-\tau)} \|\mathbf{u}_g(\tau)\| d\tau \\ &\leq c_a e^{-\gamma_a(t-t_0)} \|\mathbf{x}_p(t_0)\| + \frac{c_a}{\gamma_a} \left( n_{\max} + \sup_{t_0 \leq \tau \leq t} \|\mathbf{u}_g(\tau)\| \right). \end{aligned} \quad (8.20)$$

The result (8.20) satisfies the ISS condition. It is well known in ISS theory [131] that the inequality in the form (8.20) implies that

$$\limsup_{t \rightarrow \infty} \|\mathbf{x}_p(t)\| \leq \frac{c_a}{\gamma_a} (n_{\max} + \limsup_{t \rightarrow \infty} \|\mathbf{u}_g(t)\|).$$

Taking the inequality (8.15) and the ISS property (8.18a) shows that

$$\limsup_{t \rightarrow \infty} \|\mathbf{u}_g\| \leq a_{\max} \gamma(n_{\omega \max}),$$

which bears (8.18b).  $\square$

### 8.3 Simulations

In this section, simulation results for the proposed position and attitude observer are presented. The GPS based attitude observer was simulated using GPS receivers placed at

$${}^B \mathbf{p}_1 = \begin{bmatrix} 0 \\ 0 \\ 0 \end{bmatrix} \text{ m}, \quad {}^B \mathbf{p}_2 = \begin{bmatrix} 1.5 \\ 0 \\ 0 \end{bmatrix} \text{ m}, \quad {}^B \mathbf{p}_3 = \begin{bmatrix} 0 \\ 2 \\ 0 \end{bmatrix} \text{ m}.$$



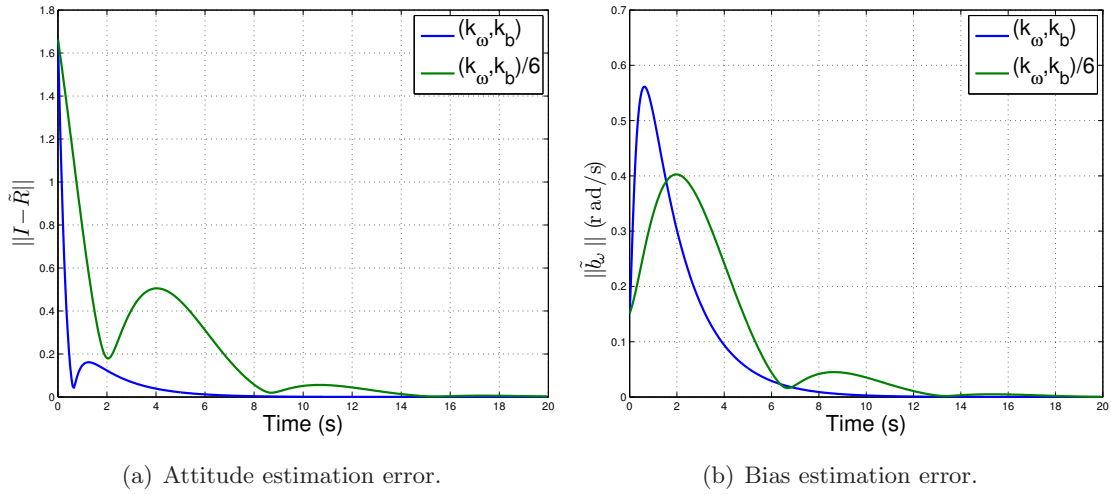


Figure 8.4: Attitude and bias estimation (biased angular velocity readings).

The satellites configuration is described by

$$\begin{aligned}
 {}^E \mathbf{p}_{S1} &= \begin{bmatrix} 0 \\ 0 \\ -20 \times 10^6 \end{bmatrix} \text{ m}, \quad {}^E \mathbf{p}_{S2} = \begin{bmatrix} 44 \times 10^6 \\ 0 \\ -20 \times 10^6 \end{bmatrix} \text{ m}, \quad {}^E \mathbf{p}_{S3} = \begin{bmatrix} 0 \\ 44 \times 10^6 \\ -20 \times 10^6 \end{bmatrix} \text{ m}, \\
 {}^E \mathbf{p}_{S4} &= \begin{bmatrix} 0 \\ 0 \\ 0 \end{bmatrix} \text{ m}, \quad {}^E \mathbf{p}_{S5} = \begin{bmatrix} 10^3 \\ 0 \\ 0 \end{bmatrix} \text{ m},
 \end{aligned}$$

where  $\mathbf{p}_{S4}$  and  $\mathbf{p}_{S5}$  are the coordinates of pseudo-satellites installed at ground level. The clock bias, expressed in distance, is  $b_\rho = 10^5$  m.

The feedback gains are given by  $k_\omega = 2, k_b = 1, k_p = 2, k_v = 2$  and the rigid body trajectory is computed using oscillatory angular rates and accelerations of 1 Hz. The initial estimation errors are

$$\begin{aligned}
 {}^E \tilde{\mathbf{p}}(t_0) &= \begin{bmatrix} -2 \\ 2 \\ 2 \end{bmatrix} \text{ m}, \quad {}^E \tilde{\mathbf{v}}(t_0) = \begin{bmatrix} 0.4 \\ 1 \\ 0.7 \end{bmatrix} \text{ m/s}, \quad \varphi(t_0) = \frac{4}{10} \pi \text{ rad}, \\
 \phi(t_0) &= \frac{1}{\sqrt{3}} \begin{bmatrix} 1 \\ 1 \\ 1 \end{bmatrix}, \quad \tilde{\mathbf{b}}_\omega = \frac{5\pi}{180} \begin{bmatrix} 1 \\ -1 \\ 1 \end{bmatrix} \text{ rad/s},
 \end{aligned}$$

The initial bias estimate is  $\hat{\mathbf{b}}_\omega(t_0) = \mathbf{0}$  rad/s. The bounds (8.9) are defined by

$$c_0 = 4 \left( 1 - \cos \left( \frac{3}{4} \pi \right) \right), \quad \tilde{b}_0 = \frac{5\sqrt{3}\pi}{180} \text{ rad/s},$$

that correspond to the maximum rotation error of  $\gamma(t_0) = \frac{3}{4}$  rad and to the minimum gain  $k_{b_\omega \text{ min}} = 1.95 \times 10^{-2}$ .

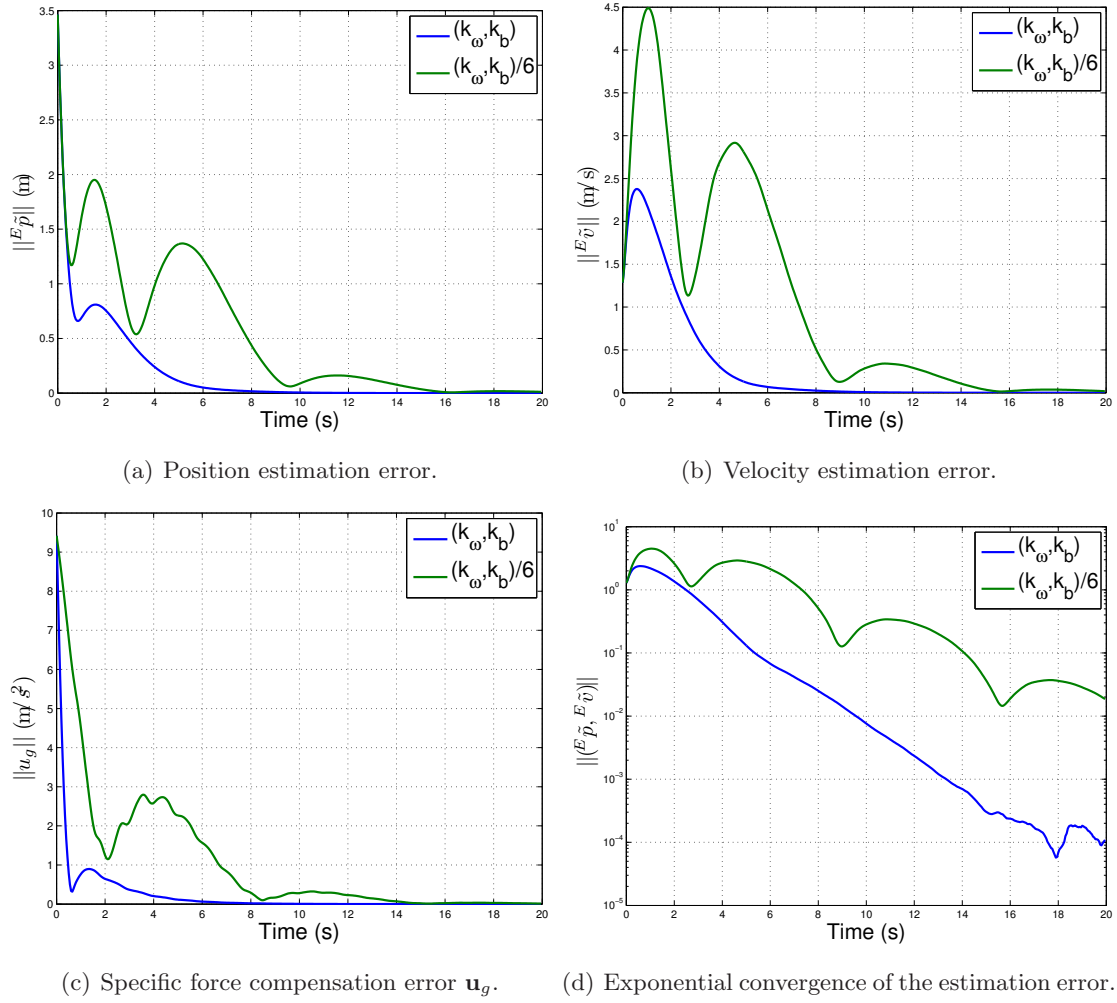


Figure 8.5: Position and velocity estimation (biased angular velocity readings).

The estimation results for the GPS based attitude observer are presented in Fig. 8.4, for the nominal values of the feedback gains  $k_\omega = 2$ ,  $k_b = 1$  and for  $k_\omega = \frac{2}{6}$ ,  $k_b = \frac{1}{6}$ . The attitude and bias estimation errors converge to the origin, as expected, and the characteristics of the observer are similar to the properties of the vector based observer proposed in Chapter 6. Namely, the trajectories converge exponentially fast, and larger feedback gains  $k_\omega$  and  $k_b$  bear faster convergence, as well as larger peaks in the estimation errors, that however do not degrade the convergence rate of the state  $(\tilde{\mathcal{R}} - \mathbf{I}, \tilde{\mathbf{b}}_\omega)$  due to the opposite phase of the transients in  $\|\tilde{\mathcal{R}} - \mathbf{I}\|$  and  $\|\tilde{\mathbf{b}}_\omega\|$ . The simulation results for an attitude observer based on vector observations yield similar results to those presented in Fig. 8.4, since the attitude and bias error dynamics are identical.

The position and velocity estimation errors converge to the origin, as shown in Fig. 8.5. The convergence rate of the position observer is influenced by the convergence of the attitude errors, and hence is faster for larger feedback gains  $k_\omega$  and  $k_b$ . The specific force compensation term  $\mathbf{u}_g$  is a function of the attitude error and of the rigid body acceleration, and hence the effect of oscillating acceleration is verified in the small ripples in  $\mathbf{u}_g$ , shown

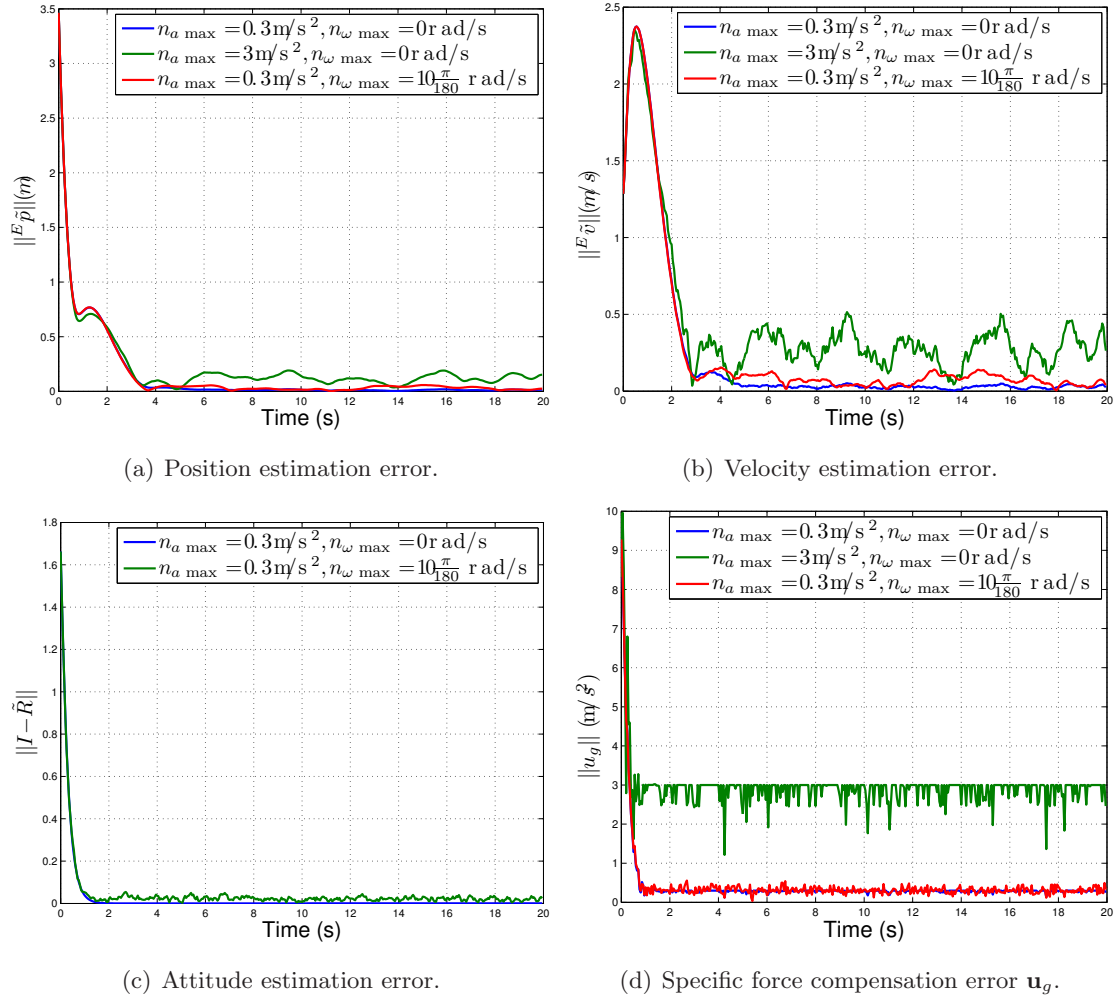


Figure 8.6: Attitude, position and velocity estimation (inertial sensor noise).

in Fig. 8.5(c). These oscillations are smoothed out in the velocity and position estimation, as shown Fig. 8.5(a) and 8.5(b), respectively. The exponential convergence of the state  $({}^E\tilde{\mathbf{p}}, {}^E\tilde{\mathbf{v}})$  is evidenced in Fig. 8.5(d), where a logarithmic scale is adopted.

To study the effect of noise in the inertial sensors, the accelerometer and angular velocity readings are distorted by Gaussian white noise  $\mathbf{n}_a \sim \mathcal{N}(\mathbf{0}, \sigma_a^2 \mathbf{I})$  and  $\mathbf{n}_\omega \sim \mathcal{N}(\mathbf{0}, \sigma_\omega^2 \mathbf{I})$ , bounded by  $\|\mathbf{n}_a\| \leq n_{a \max} = 3\sigma_a \text{ m/s}^2$ ,  $\|\mathbf{n}_\omega\| \leq n_{\omega \max} = 3\sigma_\omega \text{ rad/s}$ , respectively. The feedback bias  $k_\omega$  satisfies the condition for aISS of the attitude observer formulated in Theorem 8.7, given by  $k_\omega > \frac{1}{\sqrt{3}} n_{\omega \max}$ .

The estimation errors converge to a neighborhood of the origin, as evidenced in Fig. 8.6, where the attitude, position and velocity estimation errors are shown for *i)*  $\mathbf{n}_\omega = 0$  and  $\mathbf{n}_a \neq 0$  with  $\sigma_a = 0.1 \text{ m/s}^2$ , *ii)*  $\mathbf{n}_\omega = 0$  and  $\mathbf{n}_a \neq 0$  with  $\sigma_a = 1 \text{ m/s}^2$ , and *iii)*  $\mathbf{n}_\omega \neq 0$  and  $\mathbf{n}_a \neq 0$  with  $\sigma_\omega = 10 \frac{\pi}{180} \text{ rad/s}$  and  $\sigma_a = 0.1 \text{ m/s}^2$ .

The asymptotic bounds of the estimation errors are proportional to the noise variances, as expected. The degradation of the attitude estimate is small for the considered angular velocity noise, as shown in Fig. 8.6(c). Consequently, the degradation in  $\mathbf{u}_g$  is also small,

as evidenced Fig. 8.6(d), which is beneficial for the velocity and position estimates, since ill estimation of the attitude could induce large errors in the estimated velocity, due to the magnitude of  ${}^E\mathbf{g}$ . That is, due to the small ISS bounds of the attitude observer, the influence of the rate gyro noise in the velocity and position estimates is small, as shown in Fig. 8.6(a) and 8.6(b), respectively.

The norm of the specific force compensation term  $\mathbf{u}_g$  is proportional to  $\mathbf{n}_a$ , and hence scaling  $\mathbf{n}_a$  by a factor of 10 will also scale  $\mathbf{u}_g$  by the same factor, as shown in Fig. 8.6(d). Although the velocity estimate is corrupted by the increase of  $\mathbf{n}_a$ , the position estimate smooths out the accelerometer noise with the aiding position measurement, as shown in Fig. 8.6(a). The attitude estimates are unaffected by accelerometer noise, due to the cascade structure of the observer.

The considered noise variances correspond to very low quality, low cost sensors, and hence the asymptotic bounds of the estimation errors obtained in simulation are very encouraging, and justify further development of these algorithms for practical applications.

## 8.4 Conclusions

In this chapter, the framework of nonlinear observer design was adopted for the classical problem of GPS/IMU based navigation. While navigation solutions are often based on Kalman filtering techniques, this chapter showed that a nonlinear attitude and position observer can be derived using the techniques proposed in the second part of the thesis.

The navigation system structure was described by a cascade of an attitude and a position observers. The stability and convergence results obtained for the nonlinear observers derived in the previous chapters, were extended for the GPS/IMU nonlinear observer. Namely, exponential convergence of the position, attitude and bias estimation errors to the origin was derived, and the observer kinematics were expressed as an explicit function of the GPS and IMU measurements, exploiting the sensor readings directly. Stability in the presence of bounded accelerometer and rate gyro noise was obtained, using the almost ISS analysis based on the combination of Lyapunov and density functions, discussed in the previous chapter.

The simulation results illustrated the stability of the observer, and evidenced good convergence rate of the attitude, position and bias estimates. Stabilization of the position and attitude errors was obtained in the presence of large inertial sensor noise. These results motivate future work on the discrete-time implementation of the algorithm, for the purpose of practical implementation, and the study of the stability in the presence of noise in the aiding sensors.

## Chapter 9

# Concluding remarks

This thesis addressed the problem of nonlinear navigation system design for autonomous vehicles. Contributions were presented in the fields of Kalman filtering techniques, and of design of nonlinear observers, for position and attitude estimation.

Chapters 2 and 3 studied aiding techniques for inertial navigation systems (INS), using extended Kalman filtering (EKF). The proposed EKF/INS design methodologies were performance driven, and allowed for the integration of advanced aiding techniques, with a high accuracy multirate INS. In Chapter 2, a characterization of the vehicle dynamics in the frequency domain was exploited. The information about the vehicle motion was introduced in the EKF by modeling the pendular measurements as the result of a gravitic measurement, and of disturbances due to the vehicle motion characterized in the frequency domain. This simple approach was validated in simulation, and in experimental results using the DELFIMx catamaran, built at IST/ISR. It was demonstrated that the pendular measurements reduced the bias compensation errors, enhanced the accuracy of the position and attitude estimates, and increased the autonomy of the navigation system with respect to GPS aiding.

Chapter 3 studied the integration of a state model of the vehicle dynamics (VD) in the EKF/INS architecture. A new integration technique efficiently exploited the vehicle model, by using the VD to propagate the INS estimates. The proposed aiding technique significantly reduced the computational cost of VD aiding, and increased the flexibility in the integration of the vehicle model. High-accuracy estimation results were obtained. In particular, it was shown that the linear velocity information of the VD can be exploited in the form of a filter measurement residual, and hence that the associated computational cost boils down to computing the measurement matrix and the Kalman gain. The accuracy enhancements obtained by the linear velocity aiding suggest that the use of this component of the VD may be enough to satisfy the accuracy requirements of most applications. In such cases, the proposed technique brings about the integration of the vehicle model on low-cost, low-power hardware, yielding significant accuracy improvements for inexpensive navigation systems.

The implementation of a LASER range finder was also detailed, allowing for precise

distance-to-ground estimates, that are critical in VTOL maneuvers. Simulations results for a Vario X-Treme model-scale helicopter evidenced that the VD and LASER aiding bear a navigation system suitable for precise maneuvering of autonomous aerial vehicles.

In Chapter 4, a new navigation system, based on complementary Kalman filtering (CKF), was designed for stability, performance, and ease of implementation in autonomous surface crafts (ASC). Attitude was parameterized using Euler angles, that are an intuitive and simple representation, with the singularities located far away from the usual configurations of oceanic and terrestrial vehicles. Designed for simplicity, the navigation system was endowed with interesting theoretical properties. Namely, stability of the attitude and position complementary filters was demonstrated for almost all attitude configurations, and performance criteria was attained for operating conditions usually found in oceanic and terrestrial vehicles. The navigation system architecture was computationally efficient, and a multirate design methodology based on periodic systems was adopted, to address the problem of sampling sensors at different rates. Also, the steady-state feedback gains were designed in the frequency domain, exploiting the complementary sensor measurements, but a stochastic description of the sensors can be considered, yielding a flexible gain determination method.

Experimental results with the DELFIMx catamaran validated the navigation system properties, and evidenced that the proposed solution is highly suitable for ASCs. It was shown that the estimation results, and the autonomy of the system with respect to GPS outage, are equivalent to that of the EKF/INS architecture, with a quite smaller computational load. The simplicity of the CKF allowed for a straightforward implementation of the algorithm in low-cost, low-power hardware, and tuning of the filter parameters.

In review, the CKF is a simple, computationally efficient, and easy to tune algorithm, that produces accurate results, based on the classical combination of an inertial measurement unit (IMU) with a GPS unit and vector observations. The implementation of the EKF/INS can be fairly complex and computationally demanding when compared to the CKF, and stability of an EKF/INS is only guaranteed by extensive testing, whereas the stability and performance of the complementary filters was demonstrated analytically. However, the proposed CKF architecture is designed for a specific GPS/IMU configuration, and the EKF/INS architecture is a more flexible solution, that can be easily extended to exploit redundant aiding sources, and to account for other sensor non-idealities. The flexibility of EKF/INS systems was demonstrated in the integration of the vehicle model, that evidenced dramatic accuracy enhancements with a small computational cost. Also, the EKF model exploits coupling phenomena, e.g. the correlation between velocity and attitude errors produced by specific force measurements, and tightly-coupled GPS/INS architectures can be obtained using the EKF model [10, 22, 62, 74, 134]. Consequently, the choice between the proposed CKF and the EKF/INS architectures is subject to multiple criteria, namely *i*) position and attitude estimation accuracy requirements, *ii*) available computational resources, *iii*) available aiding sensors, and aiding information *iv*) ease of implementation, debugging, and tuning, *v*) system scalability, among others.

The design of nonlinear observers is a diverse approach from that adopted in Kalman filtering. Nonlinear observers are mostly obtained by an inventive process, where the feedback laws are tailored for the system at hand. The stability results are obtained by first assuming ideal sensors, and new sensor disturbances are progressively considered by extending the observer. The structure of nonlinear observers is often simple, and endowed with interesting stability properties. Following this framework, the second part of the thesis proposed nonlinear observers formulated on manifolds where attitude is naturally described, such as  $SO(3)$ , and emphasis was placed on stability properties in the presence of non-ideal sensors.

In Chapter 5, a nonlinear observer derivation technique was proposed, using a Lyapunov function defined by the measurement error of the aiding sensors. This technique was adopted to derive a nonlinear attitude and position observer, using landmark and velocity measurements. Almost global asymptotic stability (aGAS) and exponential convergence on  $SE(3)$  were obtained for the case of ideal sensors, and it was shown that the observer can be extended to compensate for bias in the velocity measurements. The proposed technique produced feedback laws that exploited the sensor readings directly in the observer, and that allowed for a characterization of the observer directionality given the landmark geometry. Also, topological obstacles to global stabilization on manifolds were illustrated, by characterizing explicitly the anti-stable manifolds and the regions of attraction on  $SE(3)$ . Interestingly enough, the observer design parameters allow for the shaping of the anti-stable manifold, and of the asymptotic behavior of the system trajectories.

In Chapter 6, the observer design methodology was reproduced for the case of an attitude observer, using vector observation and angular velocity measurements. Identical stability properties were obtained: aGAS and exponential convergence for ideal velocity sensors, and exponential stability for worst-case initial estimation errors for biased velocity readings. Directionality properties of the observer were derived in Appendix G, which are of interest to shape the feedback gains. Besides demonstrating the design technique, the observer derived in Chapter 6 motivated the new stability analysis techniques presented in this thesis.

Chapter 7 proposed new stability analysis techniques of nonlinear systems, by combining the dual characterizations provided by density and Lyapunov functions. It was shown that almost input-to-state stability (ISS) can be derived by studying weakly almost ISS and local ISS, that are stability properties associated with density and Lyapunov functions, respectively. Using this result, a method to analyze almost ISS of nonlinear systems was proposed, and was described by *i)* finding a Lyapunov function that yields local ISS, and *ii)* a density function such that, by means of weakly almost ISS, almost all trajectories enter the region where local ISS is verified. Almost global stabilization of nonlinear systems was also derived, resorting to a new, local analysis result based on density functions, that provides sufficient conditions for instability of an equilibrium point. Combined with LaSalle's invariance principle, the proposed result can be used to exclude undesirable equilibria, yielding almost global stability of the origin.



The results of Chapter 7 were illustrated for the attitude observer based on vector observations. The origin of the attitude error was stabilized for bounded disturbances in the velocity readings, and an explicit estimate of the ultimate bound for the attitude estimation error was obtained. The new analysis tools were also illustrated for a reduced order attitude observer with biased velocity measurements, producing a GAS of the origin.

Chapter 8 presented a GPS/IMU nonlinear observer formulated on  $SE(3)$ , using the design techniques proposed in Chapters 5 and 6, and the stability analysis tools derived in Chapter 7. Exponential stabilization of the position and attitude estimates was demonstrated, for a feedback law that exploited the inertial and GPS measurements directly. Stability in the presence of noise in the inertial sensors, i.e. rate gyro and accelerometers, was obtained using the almost ISS analysis technique proposed in this thesis. The convergence and stability properties of the observer were verified in simulation, and encouraging results were obtained, that motivate further research in the field of nonlinear observers.

In this thesis, the GPS/IMU sensor configuration was exploited using Kalman filtering techniques and nonlinear observers, providing a bridge between the first and second parts of the work. Extended Kalman filtering is driven by performance criteria, and a stochastic description of the state and measurements is used to compute the feedback gains. Due to the linearization of the system, the stability of the system is assessed only by extensive simulation and experimental validation of the navigation solution. On the opposite side, nonlinear observer design is driven by global stabilization criteria, formulated directly on the manifold of interest, however the formulation of well posed performance criteria is still under research [87]. The direct comparison of Kalman filtering techniques with the proposed nonlinear observers is a challenging issue, however an unbiased comparison is currently precluded by the distinct framework of the two design techniques.

Nonlinear observers are still at their infancy [37], and synthesis and analysis tools have been proposed in very recent literature [5, 16, 28, 84, 97, 131]. This suggests that new tools and mathematical insight will be brought into the light in the next years. The work presented in this thesis contributed to the development of nonlinear observers for sensor configurations found in autonomous vehicles applications. Given the obtained results, directions for future work are proposed in the ensuing.

## 9.1 Directions for future work

Attitude and position estimation is a nonlinear problem, that plays a leading role in the development of autonomous vehicles. Every advance in this research topic also springs new and interesting questions, that foster future research.

The proposed VD aiding solutions for EKF/INS architectures motivate further experimental validation, namely using the autonomous vehicles considered in the thesis, i.e. the DELFIMx catamaran and the Vario X-Treme model-scale helicopter. To effectively implement a VD aiding solution, accurate vehicle modeling techniques must be adopted. For example, the problem of determining the vehicle model parameters calls for system



identification techniques. A good first approach to the experimental validation would be to consider only the linear velocity aiding. Using the proposed VD aiding technique, this information can be introduced directly as a measurement residual, avoiding the caveats related to computational cost, and providing a first insight on the feasibility of vehicle model aiding. Encouraging results for a classical VD aiding technique, applied to underwater vehicles, can be found in [64].

The CKF solution provided for a simple navigation system architecture that can be subject to further developments. Stability and performance properties were derived separately for the proposed attitude and position filters, and should be generalized to the cascade navigation system. Although the offline accelerometer bias calibration was found suitable for the duration of the DELFIMx mission, online accelerometer bias compensation is of interest in most applications. Moreover, the online compensation of accelerometer bias is a challenging problem, because full observability of the filter states is not satisfied. The observability problem can be tackled by either adding extra aiding information, or by performing online calibration maneuvers [59, 60]. This suggests that persistency of excitation conditions must be considered for the stability analysis of a navigation system with online accelerometer bias compensation.

Nonlinear observer design is a very recent research field, and hence new directions for future work can be naturally proposed. A promising line of work is given by progressively considering sensor non-idealities that have long been accounted for in filtering estimation techniques. Noise in the aiding sensors is an exciting research topic, that may be addressed using some of the stability analysis tools adopted in the thesis. Interestingly enough, it poses new, fundamental design questions, namely how to integrate the sensor measurements in the observer (such that sensitivity to noise is small), what is the best feedback gain (in the sense that it is a trade-off between measurement and process noise), and how the scalar gains should be generalized to full matrices. An example of a contribution to this topic is the linear transformation of the landmark and vector readings, that can be adopted to counteract the directionality of the aiding sensor disturbances.

In this work, the stability results in the presence of bias and noise were presented separately. Each non-ideality was studied using state-of-the-art analysis techniques, that however use distinct approaches. New stability analysis tools are being presented in very recent literature, and can provide the answer to the problem of simultaneously accounting for bias and noise in the sensor readings. In particular, density functions step forward as a promising analysis tool, that provides for almost global stability results, as opposed to global stabilization using Lyapunov functions analysis, that cannot be obtained for systems defined on manifolds. Note that bias can be seen as a non-modeled disturbance, and hence ultimate bounds can be obtained for non-compensated bias, by using the stability results obtained in Chapter 8. This approach provides for a worst-case result, that guarantees convergence of the errors to a neighborhood of the origin. Extending the observer to dynamically compensate for the bias can only yield stronger stability results, assuming that the feedback law is properly designed. This suggests that interesting new results may

be derived in the near future.

The encouraging results obtained with nonlinear observers justify the practical, discrete-time implementation of the proposed algorithms. Experimental validation of nonlinear observers using naive discretization methods have presented good estimation results [80, 96]. More important, the last fifteen years have witnessed a remarkable progress in the development of rigorous numeric integration methods that preserve geometric properties. New algorithms have been proposed for integration of differential equations evolving on Lie groups [26, 38, 106, 110], that generalize Runge-Kutta methods, and perform computations directly using the Lie algebra. Applications of geometric numeric integration to dynamics evolving in  $SE(3)$  can be found in [19, 111]. Another approach is to re-derive the observers in the discrete-time domain. On one hand, this approach yields simple and computationally inexpensive estimation algorithms, similar to the continuous-time counterpart. On the other hand, it is based on the assumption that the nonlinear kinematics can be approximated by piecewise constant inputs, neglecting second order terms such as coning and sculling, and hence compromising accuracy results for highly maneuverable robotic platforms.

The density function techniques proposed in Chapter 7 pave the way to new advances in the stability analysis of nonlinear systems. The results for local analysis using density functions were derived for the case of isolated equilibrium points, which thus can be combined with LaSalle's invariance principle only if the invariant set is a countable union of isolated points. The derivation of the analysis technique resorted mostly to results that are valid for generic sets, and hence future work should address the rigorous extension of the stability results to sets.

Interestingly enough, the local stability analysis using density functions provided an alternative approach to the Hartman-Grobman theorem [125] for the classification of unstable equilibria. Given that the Hartman-Grobman theorem is conclusive only for the case of hyperbolic equilibrium points, it is of interest to evaluate the contribution of the proposed result for the stability analysis of equilibria in general. In particular, the nonlinear attitude observer derived in Chapter 6 bears a connected anti-stable manifold, where the Hartman-Grobman analysis will eventually be inconclusive. This strongly motivates the generalization of the proposed local density function analysis for systems defined on manifolds.

Finally, it should be noted that concepts well known in linear system theory are still being extended for nonlinear systems. A well-posed definition of performance in non-Euclidean spaces is an open question, although a recent contribution can be found in [87]. Therefore, the bridge between performance driven Kalman filtering techniques and the stability oriented nonlinear observers is under construction. The recent surge of stability results and new concepts in the nonlinear systems literature suggests that we are still on the onset of this exciting research area, and that the unification of the two methodologies addressed in this work may be only a matter of time and persistence.

# Appendix A

## Matrix results

This section contains elementary results from linear algebra that are adopted in this work.

### A.1 Linear algebra

Let  $\mathbf{A}, \mathbf{B} \in \mathbb{M}(n, m)$  and denote the matrix columns by  $\mathbf{a}_i, \mathbf{b}_i \in \mathbb{R}^n$ , respectively. Let  $\mathcal{R} \in \text{SO}(n)$ ,  $\mathbf{K} \in \mathbb{K}(n)$ ,  $\mathbf{K}_3 \in \mathbb{K}(3)$ ,  $\mathbf{S} \in \mathbb{L}(n)$  and  $\{\mathbf{u}, \mathbf{v}\} \in \mathbb{R}^3$

$$\begin{aligned}
 \sum_{i=1}^n \mathbf{a}'_i \mathbf{b}_i &= \text{tr}(\mathbf{A}\mathbf{B}'), & \sum_{i=1}^n \mathbf{a}_i \mathbf{b}'_i &= \mathbf{A}\mathbf{B}', \\
 \text{tr}(\mathbf{K}\mathbf{S}) &= 0, & \text{tr}(\mathbf{K}\mathbf{A}) &= \text{tr}\left(\frac{1}{2}\mathbf{K}(\mathbf{A} - \mathbf{A}')$$

### A.2 Special orthogonal group

Let  $\mathcal{R} \in \text{SO}(n)$ . The DCM formulation of  $\mathcal{R} = \text{rot}(\varphi, \boldsymbol{\phi})$  is given by

$$\begin{aligned}
 \mathcal{R} &= \cos(\varphi)\mathbf{I}_{3 \times 3} + \sin(\varphi)(\boldsymbol{\phi})_{\times} + (1 - \cos(\varphi))\boldsymbol{\phi}\boldsymbol{\phi}' \\
 &= \mathbf{I}_3 + \sin(\varphi)(\boldsymbol{\phi})_{\times} + (1 - \cos(\varphi))(\boldsymbol{\phi})_{\times}(\boldsymbol{\phi})_{\times},
 \end{aligned}$$

and the Euler angle-axis parameters are given by

$$\varphi = \arccos\left(\frac{\text{tr}(\mathcal{R}) - 1}{2}\right), \quad (\boldsymbol{\phi})_{\times} = \frac{\sqrt{2}(\mathcal{R} - \mathcal{R}')}{\|\mathcal{R} - \mathcal{R}'\|}.$$

The trace and the Frobenius norm of rotation matrices verify

$$\begin{aligned}\|\mathbf{I} - \mathcal{R}\|^2 &= 2 \operatorname{tr}(\mathbf{I} - \mathcal{R}) = 4(1 - \cos(\varphi)) = 8 - 4(1 + \cos(\varphi)), \\ \|\mathbf{I} - \mathcal{R}^2\|^2 &= 4(1 - \cos(2\varphi)) = \frac{1}{2}(8 - \|\mathbf{I} - \mathcal{R}\|^2)\|\mathbf{I} - \mathcal{R}\|^2, \\ \|\mathcal{R} - \mathcal{R}'\|^2 &= \|\mathbf{I} - \mathcal{R}^2\|^2, \quad -1 \leq \operatorname{tr}(\mathcal{R}) \leq 3.\end{aligned}$$

## Appendix B

# DELFINx characteristics

The autonomous catamaran DELFINx, an ASC built at IST-ISR and displayed in Fig. B.1, was designed for automatic marine data acquisition for risk assessment in semi-submerged structures [130]. This robotic platform allows for the access to remote and confined locations in a systematic way, as required for precise sonar and LIDAR data acquisition.

The DELFINx craft is a small Catamaran 4.5 m long and 2.45 m wide, with a mass of 300 Kg. Propulsion is ensured by two propellers driven by electrical motors, and the maximum rated speed of the vehicle with respect to the water is 6 knots. For integrated guidance and control, a path-following control strategy was adopted due to its enhanced performance, which translates into smoother convergence to the path and less demand on the control effort [58]. The vehicle has a wing shaped, central structure that is lowered during operations at sea. At the bottom of this structure, a low drag body is installed that can carry acoustic transducers. For bathymetric operations and sea floor characterization, the wing can be equipped with a Tritech Super SeaKing mechanically scanned pencil beam sonar or a RESON 8125 multibeam sonar. On top of this structure it is installed a SICK LD-LRS3100 laser range finder, to survey the emerged part of semi-submerged infra-structures like breakwaters.

The DELFINx hardware architecture developed by the ISR-IST is a self-contained system mounted on three cases which can be fit into and removed from the autonomous surface craft (ASC). The most sensitive parts are vibration isolated from the hull using a soft suspension mechanism, which acts as a low pass mechanical filter that provides further attenuation of the ASC vibration on the electronics. The hardware architecture is built around the low-cost low-power floating point Digital Signal Processor (DSP) TI TMS320C33, displayed in Fig. B.2(a), which is connected to the data acquisition hardware through a dual port RAM expansion board developed by IST-ISR. Special care was taken during the electronics development in order to implement measures that improve the Electromagnetic Compatibility (EMC). The data acquisition distributed architecture was built around the CAN (Controller Area Network) Industrial Real Time Network, for control and navigation purposes and on 100MBits/s Ethernet for payload data interface. A series of very low-power boards designed at ISR using the Phillips XAS3 16 bit microcontroller,

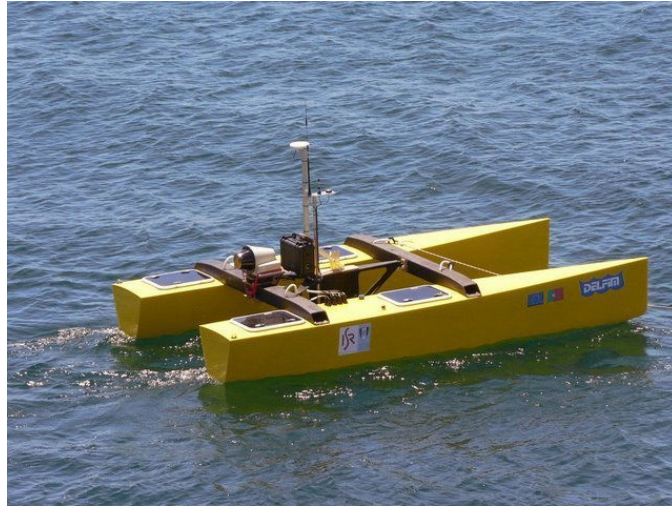
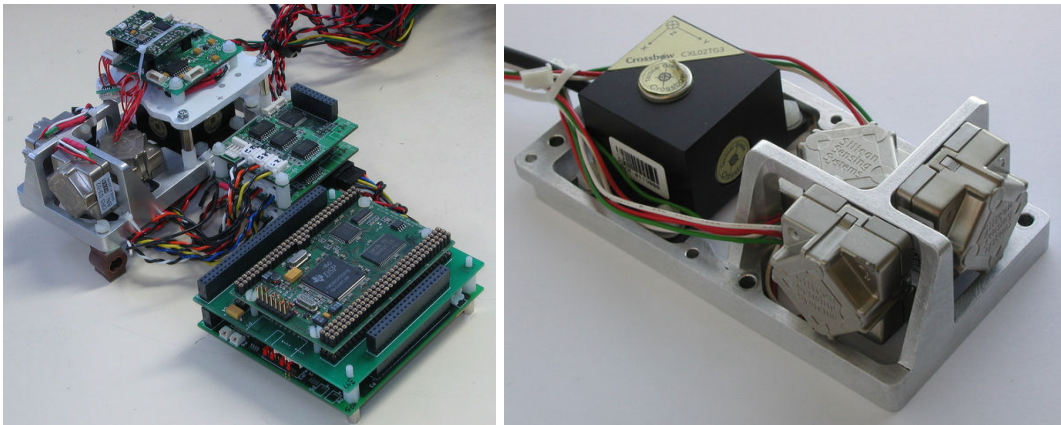


Figure B.1: The DELFIMx autonomous surface craft (length: 4.5 m; width: 2.45 m; mass: 300 Kg).



(a) Hardware architecture.

(b) Mounted inertial sensors.

Figure B.2: Hardware and sensors installed onboard the DELFIMx ASC.

and the ATMEL AT90CAN128 8-bit AVR® Flash microcontroller with extended CAN capabilities are used to interface all sensors and exchange data through the CAN Bus. In this architecture the TMS320C33 schedules all Guidance, Control, and Navigation tasks to meet their deadlines. Finally, a PC104 board connected to the CAN Bus and to Ethernet runs the mission control system and implements a blackbox where relevant data generated by the ASC are properly saved in a solid state disk for post-mission analysis.

The hardware architecture is also equipped with a Honeywell HMR3300 magnetometer, interfaced by a serial port connection with a sampling rate of 8 Hz. The GPS receiver installed on board the DELFIMx is a Thales Navigation DG14 receiver which presents an accuracy of 3.0 m Circular Error Probable (CEP) in autonomous mode and 0.40 m in differential mode. In the present work, the GPS works in autonomous mode and the measurements are provided at a 4 Hz sampling rate.

The Inertial Measurement Unit (IMU) on-board the DELFIMx craft is a strapdown

system comprising a triaxial XBOW CXL02LF3 accelerometer and three single axes Silicon Sensing CRS03 rate gyros mounted along three orthogonal axes. These sensors are attached orthogonally to a custom made stand that is presented in Fig. B.2(b) with the sensors assembled. The inertial sensors are sampled at 56 Hz using six Texas ADS1210 directly connected to a microcontroller board. The ADS1210 is a high precision, wide dynamic range, delta-sigma analog-to-digital converter with 24-bit resolution operating from a single +5V supply. The differential inputs are ideal for direct connection to transducers guaranteeing 20 bits of effective resolution which is a suitable accuracy for the set of inertial sensors used in the present application.

The hardware architecture is also equipped with a Honeywell HMR3300 magnetometer, interfaced by a serial port connection with a sampling rate of 8 Hz. The GPS receiver installed on board the DELFIMx is a Thales Navigation DG14 receiver which presents an accuracy of 3.0 m Circular Error Probable (CEP) in autonomous mode and 0.40 m in differential mode. In the present work, the GPS works in autonomous mode and the measurements are provided at a 4 Hz sampling rate.





## Appendix C

# Vario X-Treme helicopter model

This section briefly describes the nonlinear Vario X-Treme helicopter model presented in [40], deduced from first principles, and simplified under the assumptions described in [39]. As the complete model, the simplified model considers a six degrees of freedom rigid body dynamics driven by the external forces and moments generated by the several components of helicopter, however, the contributions of the fuselage, horizontal tailplane and vertical tail fin are considered to be negligible. This model also considers simplified versions of the first order dynamics for the main rotor blade pitch motion with Bell-Hiller mechanism, the steady state dynamics for the main rotor blade flap dynamics and the blade lag dynamics are neglected.

The motion of the helicopter is described using the rigid body equations of motion

$$\begin{aligned}\dot{\boldsymbol{\omega}} &= \mathbf{I}_B^{-1} (\mathbf{n}(\boldsymbol{\omega}, {}^B\mathbf{v}, \mathbf{u}_{hc}) - \boldsymbol{\omega} \times \mathbf{I}_B \boldsymbol{\omega}), \\ {}^B\dot{\mathbf{v}} &= -\boldsymbol{\omega} \times {}^B\mathbf{v} + \frac{1}{m} \mathbf{f}(\boldsymbol{\omega}, {}^B\mathbf{v}, \mathbf{u}_{hc}) + \mathcal{R}'^E \mathbf{g}, \\ \dot{\mathcal{R}} &= \mathcal{R}(\boldsymbol{\omega})_{\times},\end{aligned}$$

where  $m$  is the vehicle mass,  $\mathbf{I}_B$  is the tensor of inertia about the Center of Mass coordinate frame, denoted by  $\{G\}$ ,  $\mathbf{u}_{hc}$  is the helicopter command vector and  $\mathbf{f}$  and  $\mathbf{n}$  are the vectors of external forces and moments, respectively, along the same frame. The input vector  $\mathbf{u}_{hc} = [\varphi_{c_0} \ \varphi_{c_{1c}} \ \varphi_{c_{1s}} \ \varphi_{c_{0t}}]'$  comprises the blade pitch angle commands for the main rotor collective  $\varphi_{c_0}$ , main rotor longitudinal cyclic  $\varphi_{c_{1c}}$ , main rotor lateral cyclic  $\varphi_{c_{1s}}$  and the tail rotor collective  $\varphi_{c_{0t}}$ . To model the non symmetric shape of the rotor blades,  $\varphi_{c_0}$  and  $\varphi_{c_{0t}}$  swashplate inputs are corrected in the helicopter model using the variables  $\varphi_0 = \varphi_{c_0} + \alpha_0$  and  $\varphi_{0t} = \varphi_{c_{0t}} + \alpha_{0t}$ , where  $\alpha_0$  and  $\alpha_{0t}$  are the lift curve slope offsets for the main and tail rotor blades, respectively.

As noted before, for smooth low velocity maneuvers, the effects of the fuselage, horizontal tailplane and vertical fin on the overall dynamics are negligible. For this reason, the total force and moment vectors are modeled accounting only for the two most dominant components of a helicopter, the main rotor and the tail rotor, yielding

$$\mathbf{f} = \mathbf{f}_{mr} + \mathbf{f}_{tr}, \quad \mathbf{n} = \mathbf{n}_{mr} + \mathbf{n}_{tr},$$

where the subscripts  $mr$  and  $tr$  stand, respectively, for the main rotor and tail rotor components.

The main rotor is the primary source of lift, required to sustain the helicopter, and generates other forces and moments that allow for the control of position, orientation and velocity of the helicopter. The main rotor forces and moments are described by

$$\mathbf{f}_{mr} := \begin{bmatrix} X_{mr} \\ Y_{mr} \\ Z_{mr} \end{bmatrix} = -s_1 \begin{bmatrix} a_0 \left( \frac{1}{2} \varphi_{1s} \lambda_0 + \mu \lambda_0 \varphi_0 \right) + \delta_0 \mu \\ a_0 \left( \frac{1}{2} \varphi_{1c} \lambda_0 \right) \\ a_0 \left( \frac{2}{3} \varphi_0 - \lambda_0 \right) \end{bmatrix},$$

$$\mathbf{n}_{mr} = \begin{bmatrix} -k_\beta \beta_{1s} \\ -k_\beta \beta_{1c} \\ \frac{1}{2} s_2 \delta_0 + s_2 a_0 \left( \frac{2}{3} \varphi_0 \lambda_0 - \lambda_0^2 \right) \end{bmatrix} + \begin{bmatrix} Y_{mr} h_R \\ -X_{mr} h_R + Z_{mr} x_{cm} \\ -Y_{mr} x_{cm} \end{bmatrix},$$

where  $s_1$  and  $s_2$  are the main rotor's force and moment normalizing constants,  $a_0$  is the lift curve slope,  $\delta_0$  is the profile drag coefficient,  $k_\beta$  is the center-spring rotor stiffness, and  $x_{cm}$  and  $h_R$  determine the position of the main rotor hub aft and above the center of mass, respectively. The remaining undefined variables are defined hereafter.

In helicopters equipped with the Bell-Hiller mechanism [40], the cyclic blade pitch angles result from the combination of the commands introduced by the swashplate and the flybar flapping motion. The simplified first order blade pitch dynamics of the main rotor are described by

$$\dot{\varphi}_{1c} = C_{\varphi_1} \varphi_{1c} + C_{\varphi_3} \varphi_{c_{1c}}, \quad \dot{\varphi}_{1s} = C_{\varphi_1} \varphi_{1s} + C_{\varphi_3} \varphi_{c_{1s}} + C_{\varphi_8} \mu \lambda_0,$$

with the coefficients given by

$$C_{\varphi_1} = -\frac{\Omega \gamma_f}{4 \left[ \left( \frac{\gamma_f}{8} \right)^2 + 4 \right]}, \quad C_{\varphi_3} = \frac{\Omega (c_4 + c_1) \gamma_f}{4c_2 \left[ \left( \frac{\gamma_f}{8} \right)^2 + 4 \right]}, \quad C_{\varphi_8} = -\frac{\eta_2 \Omega \gamma_f}{2c_2 \left[ \left( \frac{\gamma_f}{8} \right)^2 + 4 \right]},$$

where  $\mu$  stands for the normalized forward velocity at the main rotor,  $\lambda_0$  is the normalized collective downwash induced by main rotor,  $\Omega$  is the main rotor angular speed,  $\gamma_f$  is the flybar lock number, and  $c_1$ ,  $c_2$  and  $c_4$  are flybar pitching parameters.

The main rotor blade flapping motion is described by the blade flap angle vector  $\boldsymbol{\beta} = [\beta_0 \ \beta_{1c} \ \beta_{1s}]$ , where  $\beta_0$  denotes the collective mode, and  $\beta_{1c}$  and  $\beta_{1s}$  represent the longitudinal and lateral cyclic modes, respectively. The blade flapping dynamics of the main rotor can be approximated by the simplified steady-state solution given by

$$\begin{aligned} \beta_0 &= C_{\beta_1} \varphi_0, \\ \beta_{1c} &= C_{\beta_3} \mu \varphi_0 + C_{\beta_4} \varphi_{1c} - C_{\beta_5} \varphi_{1s} + C_{\beta_6} \omega_x + C_{\beta_7} \omega_y + C_{\beta_8} \mu \lambda_0 - C_{\beta_4} \lambda_{1c}, \\ \beta_{1s} &= C_{\beta_9} \mu \varphi_0 + C_{\beta_5} \varphi_{1c} + C_{\beta_4} \varphi_{1s} + C_{\beta_7} \omega_x - C_{\beta_6} \omega_y + C_{\beta_{10}} \mu \lambda_0 - C_{\beta_5} \lambda_{1c}, \end{aligned}$$

with the state coefficients

$$\begin{aligned} C_{\beta_1} &= \frac{\frac{\gamma}{8}}{\frac{\gamma}{8}S_\beta + 1}, \quad C_{\beta_3} = -\frac{\frac{8}{3}}{S_\beta^2 + 1}, \quad C_{\beta_4} = \frac{S_\beta}{S_\beta^2 + 1}, \\ C_{\beta_5} &= \frac{1}{S_\beta^2 + 1}, \quad C_{\beta_6} = \frac{16}{\Omega\gamma} \frac{S_\beta}{S_\beta^2 + 1}, \quad C_{\beta_7} = \frac{16}{\Omega\gamma} \frac{1}{S_\beta^2 + 1}, \\ C_{\beta_8} &= \frac{2}{S_\beta^2 + 1}, \quad C_{\beta_9} = \frac{\frac{8}{3}S_\beta}{S_\beta^2 + 1}, \quad C_{\beta_{10}} = -\frac{2S_\beta}{S_\beta^2 + 1}, \end{aligned}$$

where  $S_\beta$  is the blade stiffness number,  $R_m$  is the main rotor radius and  $\gamma$  is the lock number.

The tail rotor, placed at the tail boom in order to counteract the moment generated by the rotation of the main rotor, provides yaw control of the helicopter. Following the same principles used for the main rotor and neglecting blade pitch, flap and lag dynamics, the simplified expressions for the tail rotor force and torque are given by

$$\begin{aligned} \mathbf{f}_{tr} &:= \begin{bmatrix} X_{tr} \\ Y_{tr} \\ Z_{tr} \end{bmatrix} = s_{1t} a_{0t} \begin{bmatrix} 0 \\ \frac{2}{3}\varphi_{0t} - \lambda_{0t} \\ 0 \end{bmatrix}, \\ \mathbf{n}_{tr} &= \begin{bmatrix} Y_{tr} h_{tr} \\ -\frac{1}{2}s_{2t}\delta_{0t} - s_{2t}a_{0t}\left(\frac{2}{3}\varphi_{0t}\lambda_{0t} - \lambda_{0t}^2\right) \\ -Y_{tr}(x_{cm} + l_{tr}) \end{bmatrix}, \end{aligned}$$

where  $\lambda_{0t}$  is the collective induced downwash of the tail rotor,  $s_{1t}$  and  $s_{2t}$  are the tail rotor's force and moment normalizing constants,  $a_{0t}$  is the tail rotor lift curve slope,  $\delta_{0t}$  is the tail rotor profile drag coefficient,  $l_{tr}$  is the distance from the tail rotor hub to the fuselage reference point and  $h_{tr}$  is the height of tail rotor hub above the fuselage reference point.

The induced downwash results from the thrust force generated at the surface of the rotating blades, that accelerates the air downwards creating a flowfield. By decomposing the downwash in Fourier series and neglecting the second and higher order terms, results in the collective, longitudinal and lateral cyclic components, respectively,  $\lambda_0$ ,  $\lambda_{1c}$  and  $\lambda_{1s}$ . The collective components of the induced downwash at the main and tail rotors are given by

$$\begin{aligned} \lambda_0 &= -\frac{a_0 s}{16} + \sqrt{\left(\frac{a_0 s}{16}\right)^2 + \frac{a_0 s}{12}\varphi_0}, \\ \lambda_{0t} &= -\frac{a_{0t} s_t}{16} + \sqrt{\left(\frac{a_{0t} s_t}{16}\right)^2 + \frac{a_{0t} s_t}{12}\varphi_{0t}}, \end{aligned}$$

where  $s$  and  $s_t$  are the solidity constants of the main and tail rotors, respectively. Finally, the main rotor longitudinal cyclic induced downwash and the forward normalized velocity

are described by

$$\lambda_{1c} = \begin{cases} 0, & \text{if } \mu = 0 \text{ (vertical flight)} \\ \lambda_0 \left( \sqrt{1 + \left(\frac{\lambda_0}{\mu}\right)^2} - \left|\frac{\lambda_0}{\mu}\right| \right), & \text{otherwise} \end{cases},$$

$$\mu = \frac{u_x - h_R \omega_y}{\Omega R_m},$$

whereas the main rotor lateral cyclic downwash is neglected  $\lambda_{1s} = 0$ , as well as both tail rotor cyclic downwash components.

## Appendix D

# Performance of the complementary attitude filter

The attitude filter estimation error kinematics, expressed in (4.7) as

$$\begin{bmatrix} \tilde{\boldsymbol{\lambda}}_{k+1} \\ \tilde{\mathbf{b}}_{k+1} \end{bmatrix} = \begin{bmatrix} \mathbf{Q}(\boldsymbol{\lambda}_k)(\mathbf{I} - K_{1\lambda})\mathbf{Q}^{-1}(\boldsymbol{\lambda}_{k-1}) & -T\mathbf{Q}(\boldsymbol{\lambda}_k) \\ -K_{2\lambda}\mathbf{Q}^{-1}(\boldsymbol{\lambda}_{k-1}) & \mathbf{I} \end{bmatrix} \begin{bmatrix} \tilde{\boldsymbol{\lambda}}_k \\ \tilde{\mathbf{b}}_k \end{bmatrix} \\ + \begin{bmatrix} -T\mathbf{Q}(\boldsymbol{\lambda}_k) & \mathbf{0} \\ \mathbf{0} & \mathbf{I} \end{bmatrix} \begin{bmatrix} \mathbf{w}_{\omega k} \\ \mathbf{w}_{b k} \end{bmatrix} + \begin{bmatrix} \mathbf{Q}(\boldsymbol{\lambda}_k)(\mathbf{I} - K_{1\lambda}) - \mathbf{Q}(\boldsymbol{\lambda}_{k-1}) \\ -K_{2\lambda} \end{bmatrix} \mathbf{v}_{\lambda k}.$$

can be written in the compact form as

$$\begin{bmatrix} \tilde{\boldsymbol{\lambda}}_{k+1} \\ \tilde{\mathbf{b}}_{k+1} \end{bmatrix} = (\mathbf{F}_k - \mathbf{K}_k\mathbf{H}_k) \begin{bmatrix} \tilde{\boldsymbol{\lambda}}_k \\ \tilde{\mathbf{b}}_k \end{bmatrix} + \mathbf{G}_k \begin{bmatrix} \mathbf{w}_{\omega k} \\ \mathbf{w}_{b k} \end{bmatrix} - \mathbf{K}_k\mathbf{Q}(\boldsymbol{\lambda}_{k-1})\mathbf{v}_{\lambda k}.$$

where

$$\mathbf{F}_k = \begin{bmatrix} \mathbf{I} & -T\mathbf{Q}(\boldsymbol{\lambda}_k) \\ \mathbf{0} & \mathbf{I} \end{bmatrix}, \quad \mathbf{G}_k = \begin{bmatrix} -T\mathbf{Q}(\boldsymbol{\lambda}_k) & \mathbf{0} \\ \mathbf{0} & \mathbf{I} \end{bmatrix}, \\ \mathbf{K}_k = \begin{bmatrix} \mathbf{Q}(\boldsymbol{\lambda}_k)(K_{1\lambda} - \mathbf{I})\mathbf{Q}^{-1}(\boldsymbol{\lambda}_{k-1}) + \mathbf{I} \\ K_{2\lambda}\mathbf{Q}^{-1}(\boldsymbol{\lambda}_{k-1}) \end{bmatrix}, \quad \mathbf{H}_k = \begin{bmatrix} \mathbf{I} & \mathbf{0} \end{bmatrix}.$$

It is well known [4] that the estimation error covariance, denoted by  $\boldsymbol{\Sigma}_{k+1|k} = E \left( \begin{bmatrix} \tilde{\boldsymbol{\lambda}}_{k+1} \\ \tilde{\mathbf{b}}_{k+1} \end{bmatrix} \begin{bmatrix} \tilde{\boldsymbol{\lambda}}'_{k+1} & \tilde{\mathbf{b}}'_{k+1} \end{bmatrix} \right)$ , satisfies the propagation equation

$$\begin{aligned} \boldsymbol{\Sigma}_{k+1|k} = & (\mathbf{F}_k - \mathbf{K}_k\mathbf{H}_k)\boldsymbol{\Sigma}_{k|k-1}(\mathbf{F}_k - \mathbf{K}_k\mathbf{H}_k)' + \mathbf{G}_k\Xi\mathbf{G}_k' \\ & + \mathbf{K}_k\mathbf{Q}(\boldsymbol{\lambda}_{k-1})\Theta\mathbf{Q}(\boldsymbol{\lambda}_{k-1})'\mathbf{K}_k'. \end{aligned} \quad (\text{D.1})$$

The estimation error covariance of the Kalman filter for the attitude kinematics (4.4), denoted by  $\mathbf{P}_{k+1|k}$ , satisfies

$$\mathbf{P}_{k+1|k} = \mathbf{F}_k\mathbf{P}_{k|k-1}\mathbf{F}_k' + \mathbf{G}_k\Xi\mathbf{G}_k' - \mathbf{F}_k\mathbf{P}_{k|k-1}\mathbf{H}_k'\mathbf{S}_{P k}^{-1}\mathbf{H}_k\mathbf{P}_{k|k-1}\mathbf{F}_k', \quad (\text{D.2})$$

where  $\mathbf{S}_{P k} = \mathbf{H}_k\mathbf{P}_{k|k-1}\mathbf{H}_k' + \Theta$ . The performance of the proposed attitude filter can be studied offline by comparing the estimation error covariance given by (D.1) with the optimal error covariance described by (D.2), as illustrated in the analysis presented in Section 4.3.



# Appendix E

## Extensions of the landmark based nonlinear observer

This section discusses some specific configurations of the landmark based nonlinear observer presented in Chapter 5. The problem of estimating directly the position of the rigid body with respect to Earth frame is discussed, and the formulation of the landmark transformation for three landmark measurements is described.

### E.1 Position estimation in Earth coordinate frame

The observer proposed in Section 5.2.3 was designed to estimate position with respect to the local frame. An estimate of the position with respect to Earth frame, denoted as  ${}^B\hat{\mathbf{p}}_E$ , can be constructed using  ${}^B\hat{\mathbf{p}}$  and  $\hat{\mathcal{R}}$  in (5.26). Proposition 5.7 showed that the estimation error  ${}^B\tilde{\mathbf{p}}_E$  converges exponentially fast to the origin, however  ${}^B\tilde{\mathbf{p}}_E = 0$  does not verify the exponential stability property as defined in the literature [78, 125]. This section discusses how the observer formulation can be modified to attain exponential stability of  ${}^B\tilde{\mathbf{p}}_E = 0$ .

As illustrated in Fig. 5.1, the position with respect to the Earth coordinate frame is described by

$${}^B\mathbf{p}_E = {}^B\mathbf{p} + \mathcal{R}'^E\mathbf{t}_L$$

where  ${}^E\mathbf{t}_L$  represents the coordinates of the origin of  $\{L\}$  with respect to  $\{E\}$ , expressed in  $\{E\}$ , and frames  $\{L\}$  and  $\{E\}$  have the same orientation by definition,  $\mathcal{R} = \frac{E}{B}\mathbf{R} = \frac{L}{B}\mathbf{R}$ . The nominal, estimated and error kinematics of  $\mathbf{p}_E$  are given by

$${}^B\dot{\mathbf{p}}_E = \mathbf{v} - (\boldsymbol{\omega})_{\times} {}^B\mathbf{p}_E, \quad {}^B\dot{\hat{\mathbf{p}}}_E = \hat{\mathbf{v}} - (\hat{\boldsymbol{\omega}})_{\times} {}^B\hat{\mathbf{p}}_E, \quad (\text{E.1a})$$

$${}^B\dot{\tilde{\mathbf{p}}}_E = (\hat{\mathbf{v}} - \mathbf{v}) - (\boldsymbol{\omega})_{\times} {}^B\tilde{\mathbf{p}}_E + ({}^B\hat{\mathbf{p}}_E)_{\times} (\hat{\boldsymbol{\omega}} - \boldsymbol{\omega}). \quad (\text{E.1b})$$

The landmark coordinates measured in body frame can be written as a function of  ${}^B\mathbf{p}_E$ , producing

$$\mathbf{q}_i = \mathcal{R}'^E \mathbf{x}_{Ei} - {}^B\mathbf{p}_E, \quad (\text{E.2})$$

where  ${}^E\mathbf{x}_{Ei} = {}^L\mathbf{x}_i + {}^E\mathbf{t}_L$  are the coordinates of landmark  $i$  in Earth frame.

The structure of the position kinematics (E.1) and of the landmark readings (E.2) for  ${}^B\mathbf{p}_E$ , is identical to the structure of the position kinematics (5.1), (5.5), (5.7b) and landmark readings (5.3) considered in the observer derivation. Consequently, an exponential stable position observer for  ${}^B\mathbf{p}_E$  can be obtained by rewriting the feedback term (5.24) as

$$\mathbf{s}_{vE} = {}^B\tilde{\mathbf{p}}_E. \quad (\text{E.3})$$

Given that  ${}^B\mathbf{p}$  and  ${}^B\mathbf{p}_E$  are described by similar kinematics, an exponentially stable observer can be designed using  $\mathbf{s}_{vE}$  in  $\hat{\mathbf{v}}$ , for example (5.23b) can be rewritten as

$$\hat{\mathbf{v}} = \mathbf{v} + ((\boldsymbol{\omega})_{\times} - k_v\mathbf{I})\mathbf{s}_{vE} + k_{\omega} ({}^B\hat{\mathbf{p}})_{\times} \mathbf{s}_{\omega},$$

producing position error kinematics that are identical to (5.25),

$${}^B\dot{\tilde{\mathbf{p}}}_E = -k_v {}^B\tilde{\mathbf{p}}_E, \quad (\text{E.4})$$

The trajectories of the system (E.4) converge exponentially to the origin for any initial condition, as desired. This observer formulation can also be adopted for the case of biased velocity readings described in Section 5.3.

The output feedback architecture of the observer, obtained in Section 5.2.4, can be formulated for the feedback term  $\mathbf{s}_{vE}$  by writing (E.3) as a function of the observer estimates and landmarks measurements. Based on the result (5.30),  $\mathbf{s}_{vE}$  is given by

$$\mathbf{s}_{vE} = {}^B\hat{\mathbf{p}}_E - \mathbf{Q}_r \mathbf{d}_{\alpha} = {}^B\hat{\mathbf{p}}_E - \sum_{i=1}^n \alpha_i \mathbf{q}_i, \quad (\text{E.5})$$

under the assumption that  $\mathbf{p}_E$  is given by a linear combination of the landmark readings

$${}^B\mathbf{p}_E = \sum_{i=1}^n \alpha_i \mathbf{q}_i = \mathbf{Q}_r \mathbf{d}_{\alpha}. \quad (\text{E.6})$$

where  $\mathbf{d}_{\alpha} = [\alpha_1 \ \dots \ \alpha_n]'$  can be seen as the generalization of  $\mathbf{d}_p = -\frac{1}{n}\mathbf{1}_n$ . The conditions under which  $\mathbf{s}_{vE}$  can be written as (E.5) are obtained by expanding (E.6), producing

$${}^B\mathbf{p}_E = \sum_{i=1}^n \alpha_i \mathcal{R}'^E \mathbf{x}_{Ei} - \sum_{i=1}^n \alpha_i {}^B\mathbf{p}_E \Leftrightarrow (\bar{\alpha} + 1) {}^B\mathbf{p}_E = \sum_{i=1}^n \alpha_i {}^E\mathbf{x}_{Ei},$$

where  $\bar{\alpha} = \sum_{i=1}^n \alpha_i$ . The right-hand side of the equation is constant, while the position is time-varying in general. Therefore,  $\mathbf{p}_E$  is a linear combination of the landmarks readings if  $\bar{\alpha} = -1$  and

$$\sum_{i=1}^n \alpha_i {}^E\mathbf{x}_{Ei} = 0, \quad (\text{E.7})$$

and the output feedback (E.5) is obtained under the following condition.



**Assumption E.1.** *The landmarks are placed such that the coordinates with respect to the Earth frame, denoted as  ${}^E\mathbf{x}_{Ei}$ , are linearly dependent.*

The landmark characterization described in Assumption E.1 is useful to analyze where the landmarks can be placed with respect to Earth frame, so that an output feedback observer is obtained. If the landmarks location is rigid and the origin of  $\{E\}$  is a design parameter, a characterization of valid  ${}^E\mathbf{t}_L$  can be produced by rewriting (E.7) as

$$\sum_{i=1}^n \alpha_i {}^L\mathbf{x}_i = {}^E\mathbf{t}_L. \quad (\text{E.8})$$

Although the coefficients  $\alpha_i$  are constrained by  $\bar{\alpha} = -1$ , the condition (E.8) is verified whenever  ${}^E\mathbf{t}_L$  is a linear combination of  ${}^L\mathbf{x}_i$ .

**Lemma E.1.** *The condition (E.8) is satisfied for some  $\alpha_i$  with  $\sum_{i=1}^n \alpha_i = -1$  if and only if  ${}^E\mathbf{t}_L$  is spanned by the landmark coordinates  ${}^L\mathbf{x}_i$ ,  $i = 1..n$ .*

*Proof.* ( $\Rightarrow$ ) Clearly, if (E.8) is verified, then  ${}^L\mathbf{t}_E$  is a linear combination of  ${}^L\mathbf{x}_i$ ,  $i = 1..n$ . ( $\Leftarrow$ ) If there are coefficients  $\beta_i$ ,  $i = 1..n$  such that

$$\sum_{i=1}^n \beta_i {}^L\mathbf{x}_i = {}^E\mathbf{t}_L,$$

define  $\bar{\beta} = \sum_{i=1}^n \beta_i$  and take  $\frac{1-\bar{\beta}}{n}\mathbf{1}_n$  which is contained in the null space of  $\mathbf{X}$

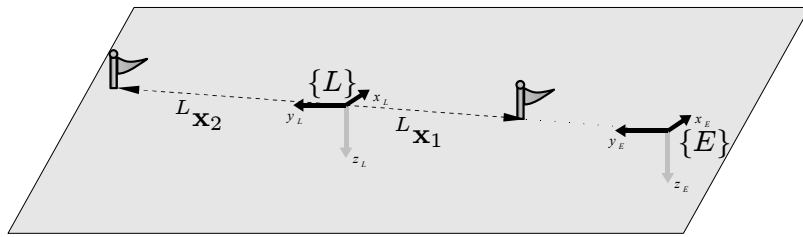
$$\sum_{i=1}^n {}^L\mathbf{x}_i = 0 \Leftrightarrow \frac{1-\bar{\beta}}{n} \sum_{i=1}^n {}^L\mathbf{x}_i = 0 \Leftrightarrow \sum_{i=1}^n \left( \beta_i + \frac{1-\bar{\beta}}{n} \right) {}^L\mathbf{x}_i = {}^L\mathbf{t}_E,$$

where  $\sum_{i=1}^n \left( \beta_i + \frac{1-\bar{\beta}}{n} \right) = 1$ . Making  $\alpha_i = \beta_i + \frac{1-\bar{\beta}}{n}$  concludes the proof.  $\square$

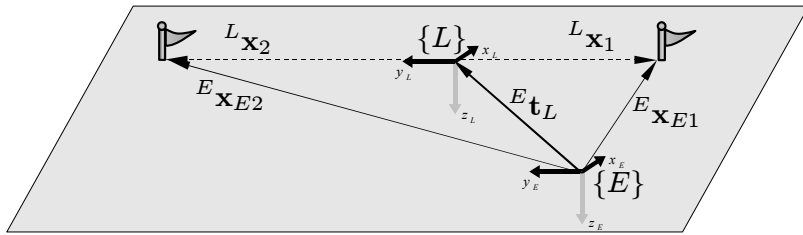
The following corollary characterizes where the origin of  $\{E\}$  should be defined, given the landmark coordinates  ${}^L\mathbf{x}_i$ , so that Assumption E.1 is verified and the output feedback law (E.5) can be obtained.

**Corollary E.2.** *Assumption E.1 is verified if and only if  ${}^E\mathbf{t}_L$  can be expressed as a linear combination of the landmark coordinates  ${}^L\mathbf{x}_i$ .*

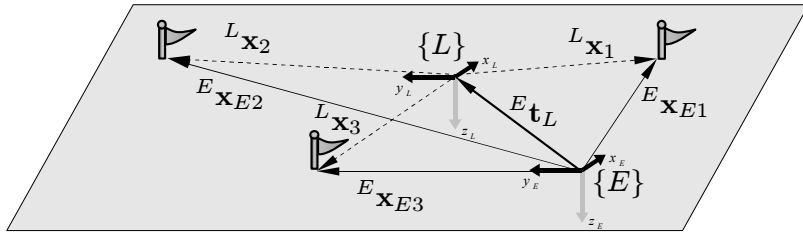
The conditions of Assumption E.1 are illustrated in Figure E.1. As depicted in Figure E.1(a), the assumption is satisfied if  ${}^E\mathbf{t}_L$  is collinear with the line defined by the two landmarks  ${}^L\mathbf{x}_1$  and  ${}^L\mathbf{x}_2$ , which is equivalent to the linear dependence of  ${}^E\mathbf{x}_{E1}$  and  ${}^E\mathbf{x}_{E2}$ . In the configuration illustrated in Figure E.1(b), the coordinates  ${}^E\mathbf{x}_{Ei}$  are linearly independent and the coordinates  ${}^L\mathbf{x}_i$  are not sufficient to describe  ${}^E\mathbf{t}_L$ . Adding a third landmark to the configuration allows for  ${}^E\mathbf{t}_L$  to be described as a linear combination of  ${}^L\mathbf{x}_i$ , as shown in Figure E.1(c). Interestingly enough, Assumption E.1 is automatically satisfied for any number of landmarks if the origin of frame  $\{E\}$  is a landmark itself, that is, if  ${}^L\mathbf{x}_i = {}^L\mathbf{t}_E$  for some  $i$ .



(a) Valid configuration: the landmarks  $L_{\mathbf{x}_i}$  and  $L_{\mathbf{t}E}$  are collinear.



(b) Invalid configuration: the landmarks  $L_{\mathbf{x}_i}$  do not span  $E_{\mathbf{t}L}$ .



(c) Valid configuration:  $E_{\mathbf{t}L}$  is spanned by the landmarks  $L_{\mathbf{x}_i}$ .

Figure E.1: Landmark configurations described by Assumption E.1 and Corollary E.2.

## E.2 Landmark coordinate transformation with minimal set of landmarks

Assumption 5.1 establishes that  $\text{rank}(\mathbf{X}) \geq 2$ , however  $\text{rank}(\mathbf{H}) = \text{rank}(\mathbf{X})$  and the coordinate transformation described in Proposition 5.13 requires  $\mathbf{H} = \mathbf{X}\mathbf{D}_X$  to be full rank. This section shows that, in case  $\text{rank}(\mathbf{X}) = 2$ , it is possible to augment matrix  $\mathbf{H}$  to produce  $\mathbf{H}_a$  such that  $\text{rank}(\mathbf{H}_a) = 3$ . Taking two linearly independent columns of  $\mathbf{H}$ ,  ${}^L\mathbf{h}_i$  and  ${}^L\mathbf{h}_j$ , the augmented matrix is given by

$$\mathbf{H}_a = \begin{bmatrix} \mathbf{H} & {}^L\mathbf{h}_i \times {}^L\mathbf{h}_j \end{bmatrix},$$

which is full rank. Defining  $\mathbf{U}_{Xa} := \mathbf{H}_a \mathbf{A}_{Xa}$ , by the steps of the proof of Proposition 5.13 there is  $\mathbf{A}_{Xa} \in M(n+1)$  nonsingular such that  $\mathbf{U}_{Xa} \mathbf{U}'_{Xa} = \mathbf{I}$ , as desired.

The cross product is commutable with rotation transformations,  $(\mathcal{R}'{}^L\mathbf{h}_i) \times (\mathcal{R}'{}^L\mathbf{h}_j) = \mathcal{R}'({}^L\mathbf{h}_i \times {}^L\mathbf{h}_j)$ , so the representation of the augmented matrices in body coordinates is simply given by

$${}^B\mathbf{U}_{Xa} = \mathcal{R}'\mathbf{U}_{Xa}, \quad {}^B\hat{\mathbf{U}}_{Xa} = \hat{\mathcal{R}}'\mathbf{U}_{Xa}, \quad \mathbf{U}_{Xa} = \mathbf{H}_a \mathbf{A}_{Xa}.$$

Therefore, the modified observer is obtained by replacing  $\mathbf{U}_X$  and  $\mathbf{H}$  by  $\mathbf{U}_{Xa}$  and  $\mathbf{H}_a$ , respectively, and the derived observer properties are obtained by simple change of variables. Namely, the output feedback term  $\mathbf{s}_\omega$  and  $\mathbf{s}_v$ , presented in Theorem 5.9, are given by

$$\mathbf{s}_\omega = \sum_{i=1}^n (\hat{\mathcal{R}}'\mathbf{H}_a \mathbf{A}_X \mathbf{e}_i) \times ({}^B\mathbf{U}_{Xa} \mathbf{e}_i), \quad \mathbf{s}_v = \hat{\mathbf{p}} + \frac{1}{n} \sum_{i=1}^n \mathbf{q}_i,$$

where  ${}^B\mathbf{U}_{Xa}$  is rewritten as  ${}^B\mathbf{U}_{Xa} = \begin{bmatrix} \mathbf{Q}\mathbf{D}_X & (\mathbf{Q}\mathbf{D}_X \mathbf{e}_i) \times (\mathbf{Q}\mathbf{D}_X \mathbf{e}_j) \end{bmatrix} \mathbf{A}_{Xa}$ . Clearly, the feedback law is a function of the landmark readings and state estimates, as desired.



## Appendix F

# Uniform exponential stability of parameterized time-varying systems

The following result from [93] establishes that if the parameterized nonlinear system is exponentially stable uniformly in  $\lambda$ , then uniform exponential stability (independent of the initial conditions) of the associated nonlinear system can be inferred. This result is presented here for the sake of clarity.

**Lemma F.1** ( $\lambda$ -UGES and UES [93]). *Consider*

- i) the nonautonomous system  $\dot{y} = f(t, y)$  where  $f : \mathbb{R}_{\geq 0} \times \mathcal{D}_y \rightarrow \mathbb{R}^n$  is piecewise continuous in  $t$  and locally Lipschitz in  $y$  uniformly in  $t$ , and  $\mathcal{D}_y \subset \mathbb{R}^n$  is a domain that contains the origin,*
- ii) the parameterized nonautonomous system  $\dot{x} = f_\lambda(t, \lambda, x)$ , where  $f_\lambda : \mathbb{R}_{\geq 0} \times \mathcal{D}_p \times \mathbb{R}^n \rightarrow \mathbb{R}^n$  is continuous, locally Lipschitz uniformly in  $t$  and  $\lambda$ ,  $\mathcal{D}_p = \mathbb{R}_{\geq 0} \times \mathcal{D}_\lambda$  and  $\mathcal{D}_\lambda \subset \mathbb{R}^n$  is a closed not necessarily compact set.*

*Let  $\mathcal{D}_y \subset \mathcal{D}_\lambda$  and assume that  $x(t) = 0$  is  $\lambda$ -UGES, i.e. there exist  $k_e$  and  $\gamma_e > 0$  such that, for all  $t \geq t_0$ ,  $\lambda \in \mathcal{D}_p$  and  $x_0 \in \mathbb{R}^n$ , the solution of the system verifies  $\|x(t, \lambda, t_0, x_0)\| \leq k_e \|x_0\| e^{-\gamma_e(t-t_0)}$ . If the solution of both systems coincide,  $y(t, y_0, t_0) = x(t, \lambda, x_0, t_0)$ , for  $\lambda = (t_0, y_0)$  and  $x_0 = y_0$ , then  $y(t) = 0$  is exponentially stable in  $\mathcal{D}_y$ .*

*Proof.* Let  $x_0 = y_0$  and  $\lambda = (t_0, y_0)$ , then  $x(t, \lambda, t_0, x_0) = y(t, t_0, y_0)$  and by change of variables, the solution satisfies  $\|y(t, t_0, y_0)\| \leq k_e \|y_0\| e^{-\gamma_e(t-t_0)}$ , and uniform exponential stability of  $y(t) = 0$  in  $\mathcal{D}_y$  is immediate.  $\square$



## Appendix G

# Directionality of the vector based nonlinear attitude observer

In Chapter 6, an attitude observer, based on vector observations, was derived using the techniques adopted for the design of the landmark based observer, presented in Chapter 5. The vector observations were used in the observer by means of a transformation  $\mathbf{A}_H$ , that shaped the directionality of the observer. In particular, the stability properties of the attitude observer presented in Chapter 6 were obtained for a  $\mathbf{A}_H$  that produced uniform directionality.

This section extends the stability properties of the attitude observer for a generic transformation  $\mathbf{A}_H$ . The attitude observer is obtained by using the feedback law of Proposition 6.8, that is

$$\begin{aligned}\hat{\boldsymbol{\omega}} &= \hat{\mathcal{R}}' \mathbf{H} \mathbf{A}_H \mathbf{A}'_H \mathbf{H}'_r (\boldsymbol{\omega}_r - \hat{\mathbf{b}}_\omega) - k_\omega \mathbf{s}_\omega, \\ \mathbf{s}_\omega &= \sum_{i=1}^n (\hat{\mathcal{R}}' \mathbf{H} \mathbf{A}_H \mathbf{e}_i) \times (\mathbf{H}_r \mathbf{A}_H \mathbf{e}_i),\end{aligned}$$

where  $\mathbf{A}_H$  is a generic, invertible matrix. The observer dynamics are

$$\dot{\hat{\mathcal{R}}} = \hat{\mathcal{R}} (\hat{\boldsymbol{\omega}})_\times, \quad \dot{\hat{\mathbf{b}}}_\omega = k_{b_\omega} \mathbf{s}_\omega,$$

and the angular velocity reading is given by

$$\boldsymbol{\omega}_r = \boldsymbol{\omega} + \mathbf{b}_\omega,$$

producing the attitude error dynamics

$$\dot{\tilde{\mathcal{R}}} = k_\omega \tilde{\mathcal{R}} (\tilde{\mathcal{R}}' \mathbf{U}_H \mathbf{U}'_H - \mathbf{U}_H \mathbf{U}'_H \tilde{\mathcal{R}}) + \tilde{\mathcal{R}} (\tilde{\mathbf{b}}_\omega)_\times, \quad (\text{G.1a})$$

$$\dot{\tilde{\mathbf{b}}}_\omega = k_{b_\omega} (\tilde{\mathcal{R}}' \mathbf{U}_H \mathbf{U}'_H - \mathbf{U}_H \mathbf{U}'_H \tilde{\mathcal{R}})_\otimes, \quad (\text{G.1b})$$

that are autonomous and, in the case where  $\mathbf{U}_H \mathbf{U}'_H = \mathbf{I}$ , produce the attitude observer dynamics (6.10).

For the case of ideal velocity measurements, i.e. known  $\mathbf{b}_\omega$ , the system (G.1) reduces to the error dynamics (5.19) of the landmark observer, and the directionality of the attitude observer is immediate from the properties derived in Section 5.2.

**Theorem G.1.** *Consider the system (G.1a) with  $\tilde{\mathbf{b}}_\omega = 0$ . The attitude error  $\tilde{\mathcal{R}} = \mathbf{I}$  is an exponentially stable and almost globally asymptotically stable with region of attraction given by*

$$R_A = \{\tilde{\mathcal{R}} \in \text{SO}(3) : \|\mathbf{I} - \tilde{\mathcal{R}}\|^2 < 8\}.$$

For any  $\tilde{\mathcal{R}}(t_0) \in R_A$ , the solution of the system satisfies

$$\|\tilde{\mathcal{R}}(t) - \mathbf{I}\| \leq \|\tilde{\mathcal{R}}(t_0) - \mathbf{I}\| e^{-\frac{1}{2}\gamma_{\mathcal{R}}(t-t_0)},$$

where  $\gamma_{\mathcal{R}} = \frac{k_\omega}{4}(8 - \|\tilde{\mathcal{R}}(t_0) - \mathbf{I}\|^2)\sigma_3(\mathbf{P}) = k_\omega(1 + \cos(\varphi(t_0)))\sigma_3(\mathbf{P})$ .

Denote the Euler angle-axis parameterization of the attitude error by  $\tilde{\mathcal{R}} = \text{rot}(\varphi, \boldsymbol{\phi})$ , and let the singular values of  $\mathbf{P} = \text{tr}(\mathbf{U}_X \mathbf{U}'_X)\mathbf{I} - \mathbf{U}_X \mathbf{U}'_X$  satisfy  $\sigma_1(\mathbf{P}) > \sigma_2(\mathbf{P}) > \sigma_3(\mathbf{P})$ . The asymptotic convergence of the Euler axis is described by

$$\begin{cases} \lim_{t \rightarrow \infty} \boldsymbol{\phi}(t) = \text{sign}(\mathbf{n}'_3 \boldsymbol{\phi}(t_0)) \mathbf{n}_3, & \text{if } \mathbf{n}'_3 \boldsymbol{\phi}(t_0) \neq 0 \\ \lim_{t \rightarrow \infty} \boldsymbol{\phi}(t) \in \{\mathbf{n}_1, \mathbf{n}_2\}, & \text{if } \mathbf{n}'_3 \boldsymbol{\phi}(t_0) = 0 \end{cases},$$

where  $\mathbf{n}_i$  is the unit eigenvector of  $\mathbf{P}$  associated with  $\sigma_i(\mathbf{P})$ .

*Proof.* The stability and convergence properties follow directly from Theorem 5.5 and Theorem 5.10.  $\square$

The stability properties for the more general system (G.1), with biased angular velocity measurements, are determined by showing first the exponential convergence of the trajectories emanating from a region around the origin, producing exponential stability of the origin given bounded initial estimation errors. Secondly, asymptotic stability of the origin for almost all initial conditions is demonstrated, which yields almost global stability with exponential convergence after some time instant  $t \geq t_0$ .

The Lyapunov function for stability analysis in the presence of bias is given by

$$\begin{aligned} V &= \frac{1}{2} \sum_{i=1}^n \|\hat{\mathbf{u}}^B - \mathbf{u}^B\|^2 + \frac{1}{2k_{b_\omega}} \|\tilde{\mathbf{b}}_\omega\|^2 = \frac{1}{4} \|\mathbf{I} - \tilde{\mathcal{R}}\|^2 \boldsymbol{\phi}' \mathbf{P} \boldsymbol{\phi} + \frac{1}{2k_{b_\omega}} \|\tilde{\mathbf{b}}_\omega\|^2, \\ \dot{V} &= -k_\omega \mathbf{s}'_\omega \mathbf{s}_\omega \leq 0. \end{aligned}$$

By Lemma 5.4, the set of points where  $\dot{V} = 0$  is given by

$$C_{\mathcal{R}} = \{(\tilde{\mathcal{R}}, \tilde{\mathbf{b}}_\omega) \in \text{SO}(3) \times \mathbb{R}^3 : \tilde{\mathcal{R}} = \mathbf{I} \vee \tilde{\mathcal{R}} = \text{rot}(\pi, \boldsymbol{\phi} \in \text{eigvec}(\mathbf{P}))\}. \quad (\text{G.2})$$

Sufficient conditions that guarantee that the trajectories do not converge to the set  $C_{\mathcal{R}} \setminus \{(\mathbf{I}, 0)\}$  are provided by the generalization of Lemma 6.4.



**Lemma G.2.** *The attitude and bias estimation errors,  $\tilde{\mathcal{R}}$  and  $\tilde{\mathbf{b}}_\omega$  respectively, are bounded. For any initial condition such that*

$$k_{b_\omega} > \frac{\|\tilde{\mathbf{b}}_\omega(t_0)\|^2}{4\sigma_3(\mathbf{P}) - \frac{1}{2}\|\mathbf{I} - \tilde{\mathcal{R}}(t_0)\|^2\sigma_1(\mathbf{P})}, \quad (\text{G.3a})$$

$$\|\mathbf{I} - \tilde{\mathcal{R}}(t_0)\|^2 < 8\frac{\sigma_3(\mathbf{P})}{\sigma_1(\mathbf{P})}, \quad (\text{G.3b})$$

the attitude error is bounded by  $\|\mathbf{I} - \tilde{\mathcal{R}}(t)\|^2 \leq c_{\max} < 8$  for all  $t \geq t_0$ .

*Proof.* The proof is obtained by reproducing the steps adopted in the demonstration of Lemma 5.14. Let  $\mathbf{x} := (\tilde{\mathcal{R}}, \tilde{\mathbf{b}}_\omega)$  and define the set  $\Omega_\rho = \{\mathbf{x} \in \mathbf{D} : V \leq \rho\}$  where  $\mathbf{D} = \text{SO}(3) \times \mathbb{R}^3$ . The Lyapunov function is lower bounded by the weighted distance of the state to the origin  $V \geq \frac{1}{4}\|\mathbf{I} - \tilde{\mathcal{R}}\|^2\sigma_3(\mathbf{P}) + \frac{1}{2k_{b_\omega}}\|\tilde{\mathbf{b}}_\omega\|^2$ , so the set  $\Omega_\rho$  is contained in the set defined by  $\frac{1}{4}\|\mathbf{I} - \tilde{\mathcal{R}}\|^2\sigma_3(\mathbf{P}) + \frac{1}{2k_{b_\omega}}\|\tilde{\mathbf{b}}_\omega\|^2 \leq \rho$  and thus is compact. The Lyapunov function decreases along the system trajectories,  $\dot{V} \leq 0$ , so any trajectory starting in  $\Omega_\rho$  will remain in  $\Omega_\rho$ . Consequently,  $\forall t \geq t_0$   $\frac{1}{2}(\frac{1}{2}\|\mathbf{I} - \tilde{\mathcal{R}}(t)\|^2\sigma_3(\mathbf{P}) + \frac{1}{k_{b_\omega}}\|\tilde{\mathbf{b}}_\omega(t)\|^2) \leq V(\mathbf{x}(t)) \leq V(\mathbf{x}(t_0))$  and the state is bounded for all  $t \geq t_0$ .

The conditions (G.3) imply that there exists  $\rho_{\max}$  such that  $V(\mathbf{x}(t_0)) \leq \rho_{\max} < 2\sigma_3(\mathbf{P})$ . The invariance of  $\Omega_\rho$ ,  $V(\mathbf{x}(t)) \leq V(\mathbf{x}(t_0))$ , and using  $\frac{\sigma_3(\mathbf{P})}{4}\|\mathbf{I} - \tilde{\mathcal{R}}\|^2 \leq V(\mathbf{x}(t))$ , produce  $\|\mathbf{I} - \tilde{\mathcal{R}}\|^2 \leq \frac{4}{\sigma_3(\mathbf{P})}\rho_{\max} < 8$  for all  $t \geq t_0$ .  $\square$

Using the parameterized LTV systems theory, the exponential convergence of the attitude estimation errors in the presence of biased inertial measurements is obtained, for the explicit region defined by (G.3).

**Theorem G.3.** *For any initial condition given by (G.3b), let the feedback gain satisfy (G.3a). Then the attitude and bias estimation errors converge exponentially fast to the stable equilibrium point  $(\tilde{\mathcal{R}}, \tilde{\mathbf{b}}_\omega) = (\mathbf{I}, \mathbf{0})$ .*

*Proof.* The proof is identical to that of Theorem 5.15 and generalizes the results of Theorem 6.5. The dynamics of the closed loop attitude and bias compensation errors are described in the quaternion form by

$$\dot{\tilde{\mathbf{q}}}_q = -k_\omega \mathbf{Q}(\tilde{\mathbf{q}})\mathbf{Q}'(\tilde{\mathbf{q}})\mathbf{P}\tilde{\mathbf{q}}_q + \frac{1}{2}\mathbf{Q}(\tilde{\mathbf{q}})\tilde{\mathbf{b}}_\omega, \quad \dot{\tilde{\mathbf{b}}}_\omega = -2k_{b_\omega}\mathbf{Q}'(\tilde{\mathbf{q}})\mathbf{P}\tilde{\mathbf{q}}_q, \quad (\text{G.4})$$

where  $\mathbf{Q}(\tilde{\mathbf{q}}) := \tilde{q}_s\mathbf{I} + (\tilde{\mathbf{q}}_q)_\times$ ,  $\dot{\tilde{q}}_s = k_\omega\tilde{q}_s\tilde{\mathbf{q}}_q'\mathbf{P}\tilde{\mathbf{q}}_q - \frac{1}{2}\tilde{\mathbf{q}}_q'\tilde{\mathbf{b}}_\omega$ , and  $\tilde{\mathbf{q}} = \begin{bmatrix} \tilde{\mathbf{q}}_q' & \tilde{q}_s \end{bmatrix}'$  is the Euler quaternion representation of matrix  $\tilde{\mathcal{R}}$ . Using  $\|\tilde{\mathbf{q}}_q\|^2 = \frac{1}{8}\|\tilde{\mathcal{R}} - \mathbf{I}\|^2$ , the Lyapunov function in quaternion coordinates is described by  $V = 2\tilde{\mathbf{q}}_q'\mathbf{P}\tilde{\mathbf{q}}_q + \frac{1}{2k_{b_\omega}}\|\tilde{\mathbf{b}}_\omega\|^2$ .

Define the system (G.4) in the domain  $\mathcal{D}_q = \{(\tilde{\mathbf{q}}_q, \tilde{\mathbf{b}}_\omega) \in \text{B}(3) \times \mathbb{R}^3 : V \leq 2\sigma_3(\mathbf{P})(1 - \varepsilon_q)\}$ ,  $0 < \varepsilon_q < 1$ . The set  $\mathcal{D}_q$  is given by the interior of the Lyapunov surface, so it is positively invariant and well defined. The feedback gain (G.3a) implies that any initial condition satisfying (G.3b) is in the set  $\mathcal{D}_q$  for  $\varepsilon_q$  small enough, and by Lemma G.2, the components of the attitude error quaternion are bounded by  $\|\tilde{\mathbf{q}}_q\|^2 \leq \frac{c_{\max}}{8}$  and  $\|\tilde{q}_s\|^2 \geq 1 - \frac{c_{\max}}{8}$ , with  $c_{\max} = 8(1 - \varepsilon_q)$ .

Define the parameterized linear time-varying system

$$\begin{bmatrix} \dot{\tilde{\mathbf{q}}_{q^*}} \\ \dot{\tilde{\mathbf{b}}_{\omega^*}} \end{bmatrix} = \begin{bmatrix} \mathcal{A}(t, \lambda) & \mathcal{B}'(t, \lambda) \\ -\mathcal{C}(t, \lambda) & \mathbf{0}_{3 \times 3} \end{bmatrix} \begin{bmatrix} \tilde{\mathbf{q}}_{q^*} \\ \tilde{\mathbf{b}}_{\omega^*} \end{bmatrix}, \quad (\text{G.5})$$

where  $(\tilde{\mathbf{q}}_{q^*}, \tilde{\mathbf{b}}_{\omega^*}) \in \mathbb{R}^3 \times \mathbb{R}^3$ ,  $\lambda \in \mathbb{R}_{\geq 0} \times \mathcal{D}_q$ , and the matrices

$$\begin{aligned} \mathcal{A}(t, \lambda) &= k_\omega \mathbf{Q}(\tilde{\mathbf{q}}(t, \lambda)) \mathbf{Q}'(\tilde{\mathbf{q}}(t, \lambda)) \mathbf{P}, & \mathcal{B}(t, \lambda) &= \frac{1}{2} \mathbf{Q}'(\tilde{\mathbf{q}}(t, \lambda)), \\ \mathcal{C}(t, \lambda) &= 2k_{b_\omega} \mathbf{Q}'(\tilde{\mathbf{q}}(t, \lambda)) \mathbf{P}, \end{aligned}$$

are bounded, so the system is well defined. The quaternion  $\tilde{\mathbf{q}}(t, \lambda)$  represents the solution of (G.4) with initial condition  $\lambda = (t_0, \tilde{\mathbf{q}}_q(t_0), \tilde{\mathbf{b}}_\omega(t_0))$ . If the parameterized LTV system (G.5) is  $\lambda$ -UGES, then the nonlinear system (G.4) is uniformly exponentially stable in the domain  $\mathcal{D}_q$ . The parameterized LTV system verifies the assumptions of [93, Theorem 1]:

- i) The elements of  $\mathcal{B}(t, \lambda)$  and  $\frac{\partial \mathcal{B}(t, \lambda)}{\partial t} = \frac{1}{2} \mathbf{Q}'(\dot{\tilde{\mathbf{q}}}(t, \lambda))$  are bounded for all  $\lambda \in \mathbb{R}_{\geq 0} \times \mathcal{D}_q$ ,  $t \geq 0$ .
- ii) The positive definite matrices

$$\mathbf{P}(t, \lambda) = 4k_{b_\omega} \mathbf{P}, \quad \mathbf{Q}(t, \lambda) = 8k_{b_\omega} k_\omega \mathbf{P} \mathbf{Q}(\tilde{\mathbf{q}}(t, \lambda)) \mathbf{Q}'(\tilde{\mathbf{q}}(t, \lambda)) \mathbf{P},$$

satisfy

$$\begin{aligned} \mathbf{P}(t, \lambda) \mathcal{B}'(t, \lambda) &= \mathcal{C}'(t, \lambda), & -\mathbf{Q}(t, \lambda) &= \mathcal{A}'(t, \lambda) \mathbf{P}(t, \lambda) + \mathbf{P}(t, \lambda) \mathcal{A}(t, \lambda) + \dot{\mathbf{P}}(t, \lambda), \\ 4k_{b_\omega} \sigma_3(\mathbf{P}) \mathbf{I} &\leq \mathbf{P}(t, \lambda) \leq 4k_{b_\omega} \sigma_1(\mathbf{P}) \mathbf{I}, & q_m \mathbf{I} &\leq \mathbf{Q}(t, \lambda) \leq q_M \mathbf{I}, \end{aligned}$$

with  $q_m = 8k_\omega k_{b_\omega} (1 - \frac{c_{\max}}{8}) \sigma_3^2(\mathbf{P})$  and  $q_M = 8k_\omega k_{b_\omega} \sigma_1^2(\mathbf{P})$ .

The system (G.5) is  $\lambda$ -UGES if and only if  $\mathcal{B}(t, \lambda)$  is  $\lambda$ -uniformly persistently exciting ( $\lambda$ -uPE) [93]. For any unit norm vector  $\mathbf{y}$  the persistency of excitation condition yields

$$\begin{aligned} \mathbf{y}' \int_t^{t+T} \mathcal{B}(\tau, \lambda) \mathcal{B}'(\tau, \lambda) d\tau \mathbf{y} &= \frac{1}{4} \mathbf{y}' \int_t^{t+T} \mathbf{I} - \tilde{\mathbf{q}}_q \tilde{\mathbf{q}}_q' d\tau \mathbf{y} \geq \frac{1}{4} \int_t^{t+T} 1 - \|\tilde{\mathbf{q}}_q\|^2 d\tau \\ &\geq \frac{1}{4} \int_t^{t+T} 1 - \frac{c_{\max}}{8} d\tau = \frac{T}{4} \left(1 - \frac{c_{\max}}{8}\right). \end{aligned}$$

Consequently, the parameterized LTV (G.5) is  $\lambda$ -UGES, and the nonlinear system (G.4) is exponentially stable in the domain  $\mathcal{D}_q$ . Using  $\|\tilde{\mathbf{q}}_q\|^2 = \frac{1}{8} \|\tilde{\mathcal{R}} - \mathbf{I}\|^2$  yields exponential stability of the nonlinear system (G.1).  $\square$

The trajectories of the attitude observer converge exponentially fast for any initial condition in a region characterized by (G.3). The convergence of the trajectories of the system emanating from anywhere in the domain is studied in the ensuing.

The equilibrium points of the system (G.1) are contained in  $C_{\mathcal{R}}$ , described in (G.2). By LaSalle's invariance principle, the trajectories of the system converge to the largest invariant set in  $C_{\mathcal{R}}$ , that is given by

$$\begin{aligned} I_{\mathcal{R}} &= C_{\mathcal{R}} \cap \{\tilde{\mathcal{R}}, \tilde{\mathbf{b}}_\omega \in \text{SO}(3) \times \mathbb{R}^3 : \tilde{\mathbf{b}}_\omega = \mathbf{0}\} \\ &= \{\tilde{\mathcal{R}}, \tilde{\mathbf{b}}_\omega \in \text{SO}(3) \times \mathbb{R}^3 : (\tilde{\mathcal{R}}, \tilde{\mathbf{b}}_\omega) = (\mathbf{I}, \mathbf{0}) \vee (\tilde{\mathcal{R}}, \tilde{\mathbf{b}}_\omega) = (\text{rot}(\pi, \text{eigvec}(\mathbf{P})), \mathbf{0})\}. \end{aligned}$$

If the eigenvectors of  $\mathbf{P}$  are distinct, then  $I_{\mathcal{R}}$  is a set of isolated equilibrium points, and local stability analysis allows for the identification of the stable and unstable equilibria. The next theorem summarizes the convergence properties of the attitude observer, which guarantee almost global asymptotic stability (aGAS) of the origin and exponential convergence within a region in the state space that is explicitly defined.

**Theorem G.4.** *Define  $\mathbf{A}_H$  such that the eigenvalues of  $\mathbf{P}$  are distinct. Under Assumption 6.1, the equilibrium point  $(\tilde{\mathcal{R}}, \tilde{\mathbf{b}}_\omega) = (\mathbf{I}, \mathbf{0})$  of the system (G.1) is almost globally asymptotically stable. Furthermore, every system solution emanating from the region of attraction of  $(\tilde{\mathcal{R}}, \tilde{\mathbf{b}}_\omega) = (\mathbf{I}, \mathbf{0})$  converges exponentially fast for  $t \geq t_e \geq t_0$ , where  $t_e$  is the time instant that verifies  $V(\tilde{\mathcal{R}}(t_e), \tilde{\mathbf{b}}(t_e)) \leq 2\sigma_3(\mathbf{P})$ .*

*Proof.* By LaSalle's invariance principle, the trajectories of the system converge to the set  $I_{\mathcal{R}}$ . The equilibrium points contained in  $I_{\mathcal{R}}$  are characterized using a local analysis, based on the local parameterization adopted in [29, Section 5], given by the first order terms of the DCM formulation

$$\tilde{\mathcal{R}} \approx \tilde{\mathcal{R}}^*(\mathbf{I} + (\eta)_\times), \quad \tilde{\mathbf{b}}_\omega \approx \tilde{\mathbf{b}}_\omega^* + \delta\mathbf{b}, \quad (\text{G.6})$$

where  $\eta, \delta\mathbf{b} \in \mathbb{R}^3$ ,  $\tilde{\mathcal{R}}^* = \text{rot}(\pi, \phi_i^*)$ ,  $\phi_i^* \in \text{eigvec}(\mathbf{P})$ ,  $\tilde{\mathbf{b}}_\omega^* = \mathbf{0}$  and  $i = 1, 2, 3$  is the index of the equilibrium point. Applying (G.6) in the system (G.1) and neglecting second order terms produces

$$\begin{bmatrix} \dot{\eta} \\ \delta\dot{\mathbf{b}} \end{bmatrix} = \begin{bmatrix} k_\omega(\tilde{\mathcal{R}}^*\mathbf{W}_H - \text{tr}(\tilde{\mathcal{R}}^*\mathbf{W}_H)\mathbf{I}) & \mathbf{I} \\ k_{b_\omega}(\tilde{\mathcal{R}}^*\mathbf{W}_H - \text{tr}(\tilde{\mathcal{R}}^*\mathbf{W}_H)\mathbf{I}) & \mathbf{0} \end{bmatrix} \begin{bmatrix} \eta \\ \delta\mathbf{b} \end{bmatrix}.$$

where  $\mathbf{W}_H = \mathbf{U}_H\mathbf{U}'_H$ . Let the eigenvalues of  $\mathbf{W}_H$  and  $\mathbf{P}$  be denoted by  $\alpha_l(\mathbf{W}_H)$  and  $\alpha_l(\mathbf{P})$ ,  $l = 1, 2, 3$ , respectively, with  $\alpha_1(\mathbf{W}_H) > \alpha_2(\mathbf{W}_H) > \alpha_3(\mathbf{W}_H)$  and  $\alpha_1(\mathbf{P}) > \alpha_2(\mathbf{P}) > \alpha_3(\mathbf{P})$ . From the definition of  $\mathbf{P}$ ,

$$\mathbf{P}\mathbf{v} = \alpha_l(\mathbf{P})\mathbf{v} \Leftrightarrow \mathbf{W}_H\mathbf{v} = (\text{tr}(\mathbf{W}_H) - \alpha_l(\mathbf{P}))\mathbf{v},$$

hence the eigenvectors of  $\mathbf{P}$  and  $\mathbf{W}_H$  are equal and the eigenvalue  $i$  satisfies

$$\alpha_i(\mathbf{P}) = \alpha_k(\mathbf{W}_H) + \alpha_j(\mathbf{W}_H),$$

where  $i, k$  and  $j$  are distinct. Using  $\tilde{\mathcal{R}}^* = 2\phi_i^*\phi_i^{*'} - \mathbf{I}$  and the spectral decomposition  $\mathbf{W}_H = \mathbf{U}\mathbf{D}\mathbf{U}' = \sum_{l=1}^3 \alpha_l(\mathbf{W}_H)\phi_l^*\phi_l^{*'}$ , where  $\mathbf{U} = [\phi_i^* \ \phi_j^* \ \phi_k^*] \in \text{O}(3)$  and  $\mathbf{D} = \text{diag}(\alpha_i(\mathbf{W}_H), \alpha_j(\mathbf{W}_H), \alpha_k(\mathbf{W}_H)) \in \text{D}^+(3)$  produces

$$\begin{aligned} & \tilde{\mathcal{R}}^*\mathbf{W}_H - \text{tr}(\tilde{\mathcal{R}}^*\mathbf{W}_H)\mathbf{I} \\ &= 2\phi_i^*\phi_i^{*'}\alpha_i(\mathbf{W}_H) - \mathbf{W}_H + (\alpha_j(\mathbf{W}_H) + \alpha_k(\mathbf{W}_H) - \alpha_i(\mathbf{W}_H))\mathbf{I} = \mathbf{U}\mathbf{\Lambda}\mathbf{U}', \end{aligned}$$

where  $\mathbf{\Lambda} = \text{diag}(\alpha_j(\mathbf{W}_H) + \alpha_k(\mathbf{W}_H), \alpha_k(\mathbf{W}_H) - \alpha_i(\mathbf{W}_H), \alpha_j(\mathbf{W}_H) - \alpha_i(\mathbf{W}_H))$ . The linearized system can be rewritten as

$$\begin{bmatrix} \dot{\eta} \\ \delta\dot{\mathbf{b}} \end{bmatrix} = \begin{bmatrix} k_\omega\mathbf{U}\mathbf{\Lambda}\mathbf{U}' & \mathbf{I} \\ k_{b_\omega}\mathbf{U}\mathbf{\Lambda}\mathbf{U}' & \mathbf{0} \end{bmatrix} \begin{bmatrix} \eta \\ \delta\mathbf{b} \end{bmatrix}.$$

The eigenvalues of  $\begin{bmatrix} k_\omega \mathbf{\Lambda} & \mathbf{I} \\ k_{b_\omega} \mathbf{\Lambda} & \mathbf{0} \end{bmatrix}$  and  $\begin{bmatrix} k_\omega \mathbf{U} \mathbf{\Lambda} \mathbf{U}' & \mathbf{I} \\ k_{b_\omega} \mathbf{U} \mathbf{\Lambda} \mathbf{U}' & \mathbf{0} \end{bmatrix} = \begin{bmatrix} \mathbf{U} & \mathbf{0} \\ \mathbf{0} & \mathbf{U} \end{bmatrix} \begin{bmatrix} k_\omega \mathbf{\Lambda} & \mathbf{I} \\ k_{b_\omega} \mathbf{\Lambda} & \mathbf{0} \end{bmatrix} \begin{bmatrix} \mathbf{U}' & \mathbf{0} \\ \mathbf{0} & \mathbf{U}' \end{bmatrix}$  are equal and given by

$$\alpha_l = \frac{k_\omega [\mathbf{\Lambda}]_{ll} + \sqrt{k_\omega^2 [\mathbf{\Lambda}]_{ll}^2 + 4k_{b_\omega} [\mathbf{\Lambda}]_{ll}}}{2}, \quad \alpha_{l+3} = \frac{k_\omega [\mathbf{\Lambda}]_{ll} - \sqrt{k_\omega^2 [\mathbf{\Lambda}]_{ll}^2 + 4k_{b_\omega} [\mathbf{\Lambda}]_{ll}}}{2},$$

where  $l = 1, 2, 3$ , and  $[\mathbf{\Lambda}]_{ll}$  denotes  $l^{\text{th}}$  diagonal element of  $\mathbf{\Lambda}$ . The real part of  $\alpha_1$  is always positive, and the real parts of  $\alpha_4$ ,  $\alpha_5$  and  $\alpha_6$  are always negative. The sign of the real parts of  $\alpha_2$  and  $\alpha_3$  depends on the equilibrium point but are always nonzero. Therefore, the equilibrium points are hyperbolic and unstable. By the Stable-Unstable Manifold theorem and the Hartman-Grobman theorem [29, 125], the stable manifold of  $(\tilde{\mathcal{R}}^*, \tilde{\mathbf{b}}_\omega^*) = (\text{rot}(\pi, \text{eigvec}(\mathbf{P})), \mathbf{0})$  has zero measure in  $\text{SO}(3) \times \mathbb{R}^3$  and the complement of the stable manifold is open and dense. Consequently, almost all initial conditions in  $\text{SO}(3) \times \mathbb{R}^3$  converge to the stable equilibrium point  $(\tilde{\mathcal{R}}, \tilde{\mathbf{b}}_\omega) = (\mathbf{I}, \mathbf{0})$ .

Almost global asymptotic stability of the origin implies that there exists a  $t_e \geq t_0$  such that the solution of the system enters the invariant set  $V \leq 2\sigma_3(\mathbf{P})$ . The exponential convergence for  $t \geq t_e$  is a direct consequence of the exponential stability results presented in Theorem G.3.  $\square$

The results of Theorem G.4 yield that almost all trajectories converge to the origin, exponentially fast for some  $t \geq t_e$ . In the case where initial estimation errors are bounded, exponential stability of the origin, for a sufficiently large feedback gain, follows directly from Theorem G.3.

**Corollary G.5.** *Assume that the initial estimation errors are bounded according to*

$$\|\mathbf{I} - \tilde{\mathcal{R}}(t_0)\| \leq c_0 < 8, \quad \|\tilde{\mathbf{b}}_\omega(t_0)\| \leq \tilde{b}_0, \quad (\text{G.7})$$

where  $c_0 < 8 \frac{\sigma_1(\mathbf{P})}{\sigma_3(\mathbf{P})}$ , and select  $k_{b_\omega}$  such that

$$k_{b_\omega} > \frac{\tilde{b}_0^2}{4\sigma_3(\mathbf{P}) - \frac{1}{2}c_0\sigma_1(\mathbf{P})}.$$

Then the origin  $(\tilde{\mathcal{R}}, \tilde{\mathbf{b}}_\omega) = (\mathbf{I}, \mathbf{0})$  is uniformly exponentially stable in the set defined by (G.7).

# Appendix H

## Supporting results for density function methods

This section presents some fundamental results adopted in the stability analysis based on density functions, presented in Chapter 7.

### H.1 Stability of nonlinear systems

A key proposition in density function methods is the following.

**Lemma H.1** ([115]). *Let  $f \in C^1(D, \mathbb{R}^n)$  where  $D \subset \mathbb{R}^n$  is open and let  $\rho \in C^1(D, \mathbb{R})$  be integrable. For  $x_0 \in \mathbb{R}^n$ , let  $\phi_t(x_0)$  be the solution  $x(t)$  of  $\dot{x} = f(x)$ ,  $x(0) = x_0$ . For a measurable set  $\mathcal{Z}$ , assume that  $\phi_\tau(\mathcal{Z}) = \{\phi_\tau(x) : x \in \mathcal{Z}\}$  is a subset of  $D$  for all  $\tau$  between 0 and  $t$ . Then*

$$\int_{\phi_t(\mathcal{Z})} \rho(x) dx - \int_{\mathcal{Z}} \rho(z) dz = \int_0^t \int_{\phi_\tau(\mathcal{Z})} [\operatorname{div}(\rho f)](x) dx d\tau.$$

Sufficient conditions for weakly almost ISS are formulated next, that are based on finding a density function that yields a positive definite divergence, almost everywhere outside a neighborhood of the origin.

**Theorem H.2** (Weakly almost ISS, [5]). *Consider that the system (7.4) is forward complete. Let  $0_M$  be a locally stable equilibrium point for  $u(\cdot) \equiv 0$ , and assume that a density function  $\rho : M \rightarrow \mathbb{R}_{\geq 0}$  be defined of class  $C^1$  over  $M \setminus \{0_M\}$  and such that*

$$\int_{M \setminus U} \rho(x) dx < +\infty,$$

*for all open neighborhoods  $U$  of  $0_M \in M$ . If there exist  $\gamma_2 \in \mathcal{K}$  and so that the following “density propagation inequality” is fulfilled*

$$\forall u \in U \forall x \in M |x| \geq \gamma_2(|u|) \Rightarrow \operatorname{div}[\rho(x)f(x, u)] \geq Q(x), \quad (\text{H.1})$$

*with  $Q(x) > 0$  for almost all  $x \in M$ , then the system is almost globally asymptotically stable and weakly almost ISS, with  $\gamma_2$  as the bounding class  $\mathcal{K}$  function.*

## H.2 Set measure results

This section presents some set measure results adopted in the derivation of the local analysis method, proposed in Section 7.3.

**Proposition H.3** ([125]). *If  $f$  is smooth then  $\phi_t$  is a diffeomorphism for each  $t$ .*

**Theorem H.4** ([121]). *Every Borel set is measurable. In particular, each open set and each closed set is measurable. The collection of measurable set is  $\sigma$ -algebra; that is the complement of a measurable set is measurable and the union (and intersection) of a countable collection of measurable sets is measurable.*

**Lemma H.5** ([85]). *Suppose  $\mathcal{A} \in \mathbb{R}^n$  has measure zero and  $F : \mathcal{A} \rightarrow \mathbb{R}^n$  is a smooth map. Then  $F(\mathcal{A})$  has measure zero.*

**Corollary H.6.** *If  $f$  is smooth, then the set  $\mathcal{A}$  has zero measure if and only if the set  $\phi_t(\mathcal{A})$  has zero measure.*

**Lemma H.7.** *Under Assumption 7.1, the set  $\phi_{[\tau_0, \tau]}(\mathcal{A})$  has zero measure if and only if  $\phi_{(-\infty, \infty)}(\mathcal{A})$  has zero measure.*

*Proof.* ( $\Leftarrow$ ) Immediate from  $\phi_{[\tau_0, \tau]}(\mathcal{A}) \subset \phi_{(-\infty, \infty)}(\mathcal{A})$ . ( $\Rightarrow$ ) If the set  $\phi_{[\tau_0, \tau]}(\mathcal{A})$  has zero measure, then  $\phi_t(\phi_{[\tau_0, \tau]}(\mathcal{A}))$  has zero measure by Corollary H.6. Using the properties of autonomous systems,  $\phi_t(\phi_{[\tau_0, \tau]}(\mathcal{A})) = \phi_{[\tau_0+t, \tau+t]}(\mathcal{A})$ . Let  $t_k = (\tau - \tau_0)k$ ,  $k \in \mathbb{Z}$ , then  $\phi_{(-\infty, \infty)}(\mathcal{A}) = \bigcup_{k \in \mathbb{Z}} \phi_{[\tau_0+t_k, \tau+t_k]}(\mathcal{A})$  is a countable union of zero measure sets, and hence has zero measure.  $\square$

**Corollary H.8.** *Under Assumption 7.1, the set  $\phi_{[0, \infty)}(\mathcal{A})$  has zero measure if and only if  $\phi_{(-\infty, \infty)}(\mathcal{A})$  has zero measure.*

**Lemma H.9.** *The local inset of an equilibrium point is measurable under Assumption 7.1.*

*Proof.* The local inset  $\mathcal{Z}_U$  is characterized by the intersection of a “stability” and a “convergence” sets, given by  $\mathcal{Z}_U = \mathcal{S} \cap \mathcal{C}$  where

$$\mathcal{S} = \{x \in U : \phi_t(x) \in U \text{ for all } t \geq 0\}, \quad \mathcal{C} = \{x \in U : \forall \epsilon \exists T \forall t > T \|\phi_t(x) - x_u\| < \epsilon\}.$$

The set  $\mathcal{S}$  can be described by  $\mathcal{S} = \bigcap_{k \in \mathbb{N}_0} \mathcal{S}_k$  where

$$\mathcal{S}_k = \{x \in U : \phi_t(x) \in U \text{ for } t \in [kT \ kT + T]\}.$$

By the continuous dependence of  $\phi_t(x)$  on the initial conditions [78, 125], and on  $t$ , for each  $x \in \mathcal{S}_k$  there exists  $\delta$  sufficiently small, such that  $\|x - y\| < \delta \Rightarrow \phi_t(y) \in U$  for the compact interval  $t \in [kT \ kT + T]$ . Consequently, the set  $\mathcal{S}_k$  is open, thus measurable, and the set  $\mathcal{S}$  is measurable.

The set  $\mathcal{C}$  can be described by  $\mathcal{C} = \bigcap_{n \in \mathbb{N}} \bigcup_{k \in \mathbb{N}_0} \mathcal{C}_{n,k}$ , where

$$\mathcal{C}_{n,k} = \{x \in U : \exists T \forall t \geq T \|\phi_t(x) - x_u\| < \frac{1}{n} \text{ for all } t \geq k\}.$$

The set  $\mathcal{C}_{n,k}$  is measurable, by the same arguments used for the measurability of  $\mathcal{S}$ . Consequently,  $\mathcal{C}$  is a countable union and intersection of measurable sets and is measurable, which concludes the proof.  $\square$

### H.3 Divergence of vector fields defined on SO(3)

This section details the computation of the divergence on SO(3), that is used in the stability analysis of the attitude observer. The rotation matrix  $\mathcal{R}$  is an element of SO(3)

$$\mathcal{R} = \begin{bmatrix} r_1 & r_4 & r_7 \\ r_2 & r_5 & r_8 \\ r_3 & r_6 & r_9 \end{bmatrix},$$

the tangent space of SO(3) is identified with  $T_{\mathcal{R}} \text{SO}(3) \sim \{\mathcal{R}\mathbf{K} \in \text{M}(3,3) : \mathbf{K} = -\mathbf{K}', \mathbf{K} \in \text{M}(3,3)\}$ , and let  $\mathbf{f} : \text{SO}(3) \rightarrow T_{\mathcal{R}} \text{SO}(3)$  be a vector field. In [30], explicit equations for the computation of the divergence in local coordinates are provided. Given that  $\mathcal{R}$  is an implicit parameterization of SO(3), the parameterization based on Euler angle-axis is considered instead

$$\mathcal{R}(\mathbf{v}_{\mathcal{R}}) = \mathbf{I} + \sin(\|\mathbf{v}_{\mathcal{R}}\|) \frac{(\mathbf{v}_{\mathcal{R}})_{\times}}{\|\mathbf{v}_{\mathcal{R}}\|} + (1 - \cos(\|\mathbf{v}_{\mathcal{R}}\|)) \frac{(\mathbf{v}_{\mathcal{R}})_{\times} (\mathbf{v}_{\mathcal{R}})_{\times}}{\|\mathbf{v}_{\mathcal{R}}\|^2},$$

$$\mathbf{v}_{\mathcal{R}} \in \{\mathbf{v}_{\mathcal{R}} \in \mathbb{R}^3 : \|\mathbf{v}_{\mathcal{R}}\| \leq \pi\},$$

where  $\mathbf{v}_{\mathcal{R}} = [v_1 \ v_2 \ v_3]'$  corresponds to the rotation axis and  $\|\mathbf{v}_{\mathcal{R}}\|$  is the rotation angle. The divergence is given by

$$\text{div}(f) = \sum_{i=1}^M \frac{1}{\sqrt{\det(\mathbf{G})}} \frac{\partial \sqrt{\det(\mathbf{G})} F_i}{\partial v_i}, \quad (\text{H.2})$$

where  $\mathbf{G} = \mathbf{J}'\mathbf{W}\mathbf{J}$  is the metric tensor,  $\mathbf{W}$  is a diagonal weight matrix,  $\mathbf{J}$  is the Jacobian matrix characterized by the basis vectors  $\frac{\partial \text{vec}(\mathcal{R})}{\partial v_i}$  for the tangent hyper-plane

$$\mathbf{J} = \begin{bmatrix} \frac{\partial \text{vec}(\mathcal{R})}{\partial v_1} & \frac{\partial \text{vec}(\mathcal{R})}{\partial v_2} & \frac{\partial \text{vec}(\mathcal{R})}{\partial v_3} \end{bmatrix} = \begin{bmatrix} \frac{\partial r_1}{\partial v_1} & \frac{\partial r_1}{\partial v_2} & \frac{\partial r_1}{\partial v_3} \\ \frac{\partial r_2}{\partial v_1} & \vdots & \vdots \\ \vdots & \vdots & \vdots \\ \frac{\partial r_9}{\partial v_1} & \frac{\partial r_9}{\partial v_2} & \frac{\partial r_9}{\partial v_3} \end{bmatrix},$$

and  $F_i$  are the coordinates of the vector field  $f$  in the tangent hyper-plane,

$$f = \sum_{i=1}^3 F_i \frac{\partial \text{vec}(\mathcal{R})}{\partial v_i} = \mathbf{J}\mathbf{F}, \quad (\text{H.3})$$

where  $\mathbf{F} = [F_1 \ F_2 \ F_3]'$  is  $(\mathbf{J}'\mathbf{J})^{-1}\mathbf{J}'f$ .

The divergence of a vector field  $f$  is computed using (H.2). The following lemma allows for the computation of a vector field  $\rho f$  given  $\text{div}(f)$ , where  $\rho$  is a scalar function defined on the manifold.

**Lemma H.10.** Let  $\rho(\mathcal{R}) : \text{SO}(3) \rightarrow \mathbb{R}$ , the divergence of the product  $\rho f$  satisfies

$$\text{div}(\rho f) = \rho \text{div}(f) + (\nabla_{\mathcal{R}}\rho)'f,$$

where  $\nabla_{\mathcal{R}}(\cdot)$  is the gradient with respect to the coordinates of  $\mathcal{R}$ , i.e.  $\nabla_{\mathcal{R}}\rho = \left[ \frac{\partial \rho}{\partial r_1} \quad \frac{\partial \rho}{\partial r_2} \quad \cdots \quad \frac{\partial \rho}{\partial r_9} \right]'$ .

*Proof.* The result is obtained by algebraic manipulation of (H.2) applied to  $\rho f$ ,

$$\begin{aligned} \text{div}(\rho f) &= \sum_{i=1}^M \frac{1}{\sqrt{\det(\mathbf{G})}} \frac{\partial \sqrt{\det(\mathbf{G})} \rho F_i}{\partial v_i} \\ &= \sum_{i=1}^M \frac{1}{\sqrt{\det(\mathbf{G})}} \left( \rho \frac{\partial \sqrt{\det(\mathbf{G})} F_i}{\partial v_i} + \sqrt{\det(\mathbf{G})} F_i \frac{\partial \rho}{\partial v_i} \right) \\ &= \rho \sum_{i=1}^M \frac{1}{\sqrt{\det(\mathbf{G})}} \frac{\partial \sqrt{\det(\mathbf{G})} F_i}{\partial v_i} + \sum_{i=1}^M F_i \frac{\partial \rho}{\partial v_i} \\ &= \rho \text{div}(f) + (\nabla_{\mathbf{v}}\rho)' \mathbf{F}, \end{aligned}$$

where  $\nabla_{\mathbf{v}}(\cdot)$  is the gradient with respect to the coordinates of  $\mathbf{v}_{\mathcal{R}}$ , i.e.  $\nabla_{\mathbf{v}}\rho = \left[ \frac{\partial \rho}{\partial v_1} \quad \frac{\partial \rho}{\partial v_2} \quad \frac{\partial \rho}{\partial v_3} \right]'$ .

Using the chain rule yields the well known result  $\frac{\partial \rho}{\partial v_i} = \sum_{j=1}^9 \frac{\partial \rho}{\partial r_j} \frac{\partial r_j}{\partial v_i} = (\mathbf{J}\mathbf{e}_i)' \nabla_{\mathcal{R}}\rho \Rightarrow \nabla_{\mathbf{v}}\rho = \mathbf{J}' \nabla_{\mathcal{R}}\rho$ , where  $\mathbf{e}_i$  is the unit norm vector with unit value at coordinate  $i$ . Consequently,

$$\text{div}(\rho f) = \rho \text{div}(f) + (\nabla_{\mathcal{R}}\rho)' \mathbf{J} \mathbf{F},$$

which, using (H.3), produces  $\text{div}(\rho f) = \rho \text{div}(f) + (\nabla_{\mathcal{R}}\rho)'f$ . □



## Appendix I

# Closed-form solution to the pseudorange equations

In this section, the solution to the GPS receiver position given the pseudorange measurements is derived. Algorithms to compute the position of the GPS receiver in Earth frame using the pseudorange measurements are presented in [6, 7, 14, 27, 91]. The present approach builds on the geometric method presented in [27] for  $s > 4$  satellites. Consider two pseudorange measurements obtained by receiver  $j$

$$\rho_{ij} = \|\mathbf{p}_j - \mathbf{p}_{S_i}\| + b_\rho, \quad \rho_{1j} = \|\mathbf{p}_j - \mathbf{p}_{S_1}\| + b_\rho,$$

with respect to satellites  $i$  and 1, respectively. Squaring and subtracting the pseudoranges yields

$$-2(\mathbf{p}_{S_i} - \mathbf{p}_{S_1})' \mathbf{p}_j + 2(\rho_{ij} - \rho_{1j})b_\rho = \rho_{ij}^2 - \rho_{1j}^2 - (\|\mathbf{p}_{S_i}\|^2 - \|\mathbf{p}_{S_1}\|^2),$$

which can be written in matrix formulation as

$$\mathbf{A}_{S_j} \begin{bmatrix} \mathbf{p}_j \\ b_\rho \end{bmatrix} = \mathbf{b}_{S_j}, \quad (\text{I.1})$$

where

$$\mathbf{A}_{S_j} := 2 \begin{bmatrix} -\mathbf{U} & \mathbf{\Delta}_{S_j} \end{bmatrix}, \quad \mathbf{b}_{S_j} = \begin{bmatrix} \rho_{2j}^2 - \rho_{1j}^2 - (\|\mathbf{p}_{S_2}\|^2 - \|\mathbf{p}_{S_1}\|^2) \\ \vdots \\ \rho_{sj}^2 - \rho_{1j}^2 - (\|\mathbf{p}_{S_s}\|^2 - \|\mathbf{p}_{S_1}\|^2) \end{bmatrix},$$

$$\mathbf{U} := \begin{bmatrix} \mathbf{p}'_{S_2} - \mathbf{p}'_{S_1} & \dots & \mathbf{p}'_{S_s} - \mathbf{p}'_{S_1} \end{bmatrix}', \quad \mathbf{\Delta}_{S_j} := \begin{bmatrix} \rho_{2j} - \rho_{1j} & \dots & \rho_{sj} - \rho_{1j} \end{bmatrix}'.$$

A solution of (I.1) is given by the Moore-Penrose inverse

$$\begin{bmatrix} \mathbf{p}_j \\ b_\rho \end{bmatrix} = (\mathbf{A}'_{S_j} \mathbf{A}_{S_j})^{-1} \mathbf{A}'_{S_j} \mathbf{b}_{S_j},$$

which, by algebraic manipulation and using the properties of the block matrix inverse, produces

$${}^E\mathbf{p}_j = -\frac{({}^E\mathbf{U}'\mathbf{W}_{Sj}{}^E\mathbf{U})^{-1}{}^E\mathbf{U}'\mathbf{W}_{Sj}\mathbf{b}_{Sj}}{2} = -\mathbf{f}_p(\boldsymbol{\rho}_j), \quad (\text{I.2})$$

where

$$\mathbf{W}_{Sj} := 4\boldsymbol{\Delta}_{Sj}(4\boldsymbol{\Delta}'_{Sj}\boldsymbol{\Delta}_{Sj} - 1)^{-1}\boldsymbol{\Delta}'_{Sj} - \mathbf{I}_{(s-1)\times(s-1)}.$$

The conditions for existence and uniqueness of a position fix  ${}^E\mathbf{p}_j$  given the pseudorange measurements  $\rho_{ij}$  depend on the user-satellite geometry for  $s = 4$  satellites [27, 91]. For  $s \geq 5$ , the solution is unique if the satellite geometry is nonplanar [1]. In case  $\text{rank}(\mathbf{A}_{Sj}) < 4$ , (I.1) yields multiple solutions, even if the position fix  ${}^E\mathbf{p}_j$  is unique.

The ambiguity in (I.1), if present, can be easily tackled for any nonplanar satellite configuration, under the proviso that the position fix  ${}^E\mathbf{p}_j$  is unique. The nonplanar satellite configuration bears  $\text{rank}({}^E\mathbf{U}) = 3$ , and the solution is determined by intersecting the one dimensional space defined by (I.2) with the cones defined by the pseudorange equations (8.2). Using the derivation [27, p.1024], the solution is given by

$$\begin{bmatrix} {}^E\mathbf{p}_j \\ b_\rho \end{bmatrix} = \mathbf{w}_{Sj} + \alpha\mathbf{a}_\perp, \quad \mathbf{w}_{Sj} = \mathbf{A}'_{Sj}(\mathbf{A}^*_{Sj}\mathbf{A}'_{Sj})^{-1}\mathbf{A}^*_{Sj}\mathbf{b}_{Sj},$$

where  $\mathbf{A}^*_{Sj} \in \mathbf{M}(3,4)$  is obtained by selecting the linearly independent lines of  $\mathbf{A}_{Sj}$ ,  $\mathbf{a}_\perp \in \mathbb{R}^4$  describes the null space of  $\mathbf{A}_{Sj}$ , i.e.  $\mathbf{A}_{Sj}\mathbf{a}_\perp = 0$ , and the coefficient  $\alpha$  is the solution of the quadratic equation

$$\begin{aligned} \alpha^2\mathbf{w}'_a\mathbf{Z}\mathbf{w}_a + 2\alpha\mathbf{w}'_a\mathbf{Z}\mathbf{a}_\perp + \mathbf{a}'_\perp\mathbf{Z}\mathbf{a}_\perp &= 0 \\ \mathbf{w}_a &= \mathbf{w}_{Sj} - \begin{bmatrix} {}^E\mathbf{p}'_{S1} & \rho_{1j} \end{bmatrix}', \quad \mathbf{Z} = \text{diag}(1, 1, 1, -1), \end{aligned}$$

which uniquely satisfies the pseudorange measurements  $\rho_{ij}$ . For further study and solutions for the planar configuration case, the reader is referred to [27, 91].

## Appendix J

# Exponential stability of a cascade system

This section studies the convergence properties for cascade systems in the form

$$\dot{\mathbf{x}}_1 = \mathbf{A}\mathbf{x}_1 + \mathbf{B}u(\mathbf{x}_2, t), \quad (\text{J.1a})$$

$$\dot{\mathbf{x}}_2 = f_2(\mathbf{x}_2), \quad (\text{J.1b})$$

where  $\mathbf{x}_1 \in \mathbb{R}^m$ ,  $\mathbf{x}_2 \in \mathbb{R}^n$ ,  $u : \mathbb{R}^n \times \mathbb{R}_0^+ \rightarrow \mathbb{R}^p$ ,  $\mathbf{A} \in \text{M}(m)$ ,  $\mathbf{B} \in \text{M}(m, p)$ , and  $f_2 : \mathbb{R}^n \rightarrow \mathbb{R}^n$  is locally Lipschitz.

The formulation (J.1) is motivated by the structure of the observer based on GPS measurements, depicted in Fig. 8.2 and given by (8.5, 8.17). The results presented in this section are adopted to derive the stability properties of the observer formulated in Chapter 8.

Sufficient conditions for the global stability of the origin of the cascade system (J.1) can be found in [78, 125], and the following stability results are well known in input-to-state stability theory [131].

**Theorem J.1** ([78]). *If the system (J.1a) is input-to-state stable, and if the origin of the system (J.1b) is globally asymptotically stable, then the origin of the cascade system (J.1) is globally asymptotically stable.*

**Theorem J.2** ([131]). *The system (J.1a) is input-to-state stable if and only if the matrix  $\mathbf{A}$  is Hurwitz.*

The results of Theorem J.1 yield global asymptotic stability of the origin of the cascade system. If the subsystem (J.1b) is exponentially stable, explicit convergence bounds of the solutions of (J.1) can be obtained due to the linear, time-invariant formulation of (J.1a), as shown in the ensuing. The following statement characterizes the solutions of (J.1a) for an exponentially decaying input.

**Proposition J.3.** *Consider the system*

$$\dot{\mathbf{x}}_1 = \mathbf{A}\mathbf{x}_1 + \mathbf{B}u. \quad (\text{J.2})$$

Assume that the origin of the system (J.2) is stable, and that there exist  $c_u, \gamma_u, u_0 > 0$  such that the input verifies

$$\|\mathbf{u}(t)\| \leq c_u e^{-\gamma_u(t-t_0)} u_0. \quad (\text{J.3})$$

Then the solution of the system (J.2) is bounded by

$$\|\mathbf{x}_1(t)\| \leq c_a e^{-\gamma_{\min}(t-t_0)} \left( \|\mathbf{x}_1(t_0)\| + \frac{c_u \|\mathbf{B}\|}{|\gamma_a - \gamma_u|} u_0 \right).$$

where  $\gamma_{\min} = \min\{\gamma_a, \gamma_u\}$ , and  $c_a, \gamma_a > 0$  satisfy  $\|e^{\mathbf{A}\tau}\| \leq c_a e^{-\gamma_a \tau}$ .

*Proof.* The solution of the LTI system (J.2) satisfies

$$\|\mathbf{x}_1(t)\| \leq c_a e^{-\gamma_a(t-t_0)} \|\mathbf{x}_1(t_0)\| + \int_{t_0}^t c_a e^{-\gamma_a(t-\tau)} \|\mathbf{B}\| \|\mathbf{u}(\tau)\| d\tau,$$

where the stability of the origin implies that there exists  $c_a$  and  $\gamma_a > 0$  such that  $\|e^{\mathbf{A}t}\| \leq c_a e^{-\gamma_a t}$  [78]. Applying (J.3), yields

$$\begin{aligned} \int_{t_0}^t c_a e^{-\gamma_a(t-\tau)} \|\mathbf{B}\| \|\mathbf{u}(\tau)\| d\tau &\leq c_a c_u \|\mathbf{B}\| u_0 \int_{t_0}^t e^{-\gamma_a(t-\tau) - \gamma_u(\tau-t_0)} d\tau \\ &= \frac{c_a c_u \|\mathbf{B}\| u_0}{\gamma_a - \gamma_u} \left( e^{-\gamma_u(t-t_0)} - e^{-\gamma_a(t-t_0)} \right). \end{aligned}$$

Using the inequalities

$$\frac{e^{-\gamma_u(t-t_0)} - e^{-\gamma_a(t-t_0)}}{\gamma_a - \gamma_u} \leq \frac{e^{-\gamma_{\min}(t-t_0)}}{|\gamma_a - \gamma_u|}, \quad e^{-\gamma_a(t-t_0)} \leq e^{-\gamma_{\min}(t-t_0)},$$

where  $\gamma_{\min} = \min(\gamma_u, \gamma_a)$ , produces the desired bound.  $\square$

The following result establishes convergence bounds for the trajectories of the cascade system (J.1).

**Proposition J.4.** *Assume that the origin of the system (J.1a) is stable, that the origin of the system (J.1b) is exponentially stable as follows*

$$\forall_{\|\mathbf{x}_2(t_0)\| < c} \exists_{c_2, \gamma_2 > 0} \|\mathbf{x}_2(t)\| \leq c_2 e^{-\gamma_2(t-t_0)} \|\mathbf{x}_2(t_0)\|, \quad (\text{J.4})$$

and that there exists  $c_3 > 0$  such that  $\|u(\mathbf{x}_2, t)\| \leq c_3 \|\mathbf{x}_2\|$ . Then the solution of the system (J.1) is exponentially stable, bounded by

$$\|\mathbf{x}(t)\| \leq c_{\max} e^{-\gamma_{\min}(t-t_0)} \|\mathbf{x}(t_0)\|,$$

for all  $\|\mathbf{x}_2(t_0)\| < c$ , where

$$\mathbf{x} = \begin{bmatrix} \mathbf{x}'_1 & \mathbf{x}'_2 \end{bmatrix}', \quad c_{\max} = c_a + c_2 + \frac{c_a c_3 c_2 \|\mathbf{B}\|}{|\gamma_a - \gamma_2|}, \quad \gamma_{\min} = \min\{\gamma_a, \gamma_2\},$$

and  $c_a, \gamma_a > 0$  satisfy  $\|e^{\mathbf{A}\tau}\| \leq c_a e^{-\gamma_a \tau}$ .

*Proof.* The input of system (J.1a) satisfies

$$\|u(\mathbf{x}_2, t)\| \leq c_3 c_2 e^{-\gamma_2(t-t_0)} \|\mathbf{x}_2(t_0)\|.$$

Using Proposition J.3 produces

$$\|\mathbf{x}_1(t)\| \leq c_a e^{-\gamma_{\min}(t-t_0)} \left( \|\mathbf{x}_1(t_0)\| + \frac{c_3 c_2 \|\mathbf{B}\|}{|\gamma_a - \gamma_2|} \|\mathbf{x}_2(t_0)\| \right).$$

Using (J.4), and the inequalities

$$\|\mathbf{x}\| \leq \|\mathbf{x}_1\| + \|\mathbf{x}_2\|, \quad \|\mathbf{x}_1\| \leq \|\mathbf{x}\|, \quad \|\mathbf{x}_2\| \leq \|\mathbf{x}\|,$$

produces the exponential bound

$$\begin{aligned} \|\mathbf{x}(t)\| &\leq \|\mathbf{x}_1(t)\| + \|\mathbf{x}_2(t)\| \\ &\leq c_a e^{-\gamma_{\min}(t-t_0)} \left( \|\mathbf{x}_1(t_0)\| + \frac{c_3 c_2 \|\mathbf{B}\|}{|\gamma_a - \gamma_2|} \|\mathbf{x}_2(t_0)\| \right) + c_2 e^{-\gamma_2(t-t_0)} \|\mathbf{x}_2(t_0)\| \\ &\leq e^{-\gamma_{\min}(t-t_0)} \left( c_a \|\mathbf{x}_1(t_0)\| + \left( \frac{c_a c_3 c_2 \|\mathbf{B}\|}{|\gamma_a - \gamma_2|} + c_2 \right) \|\mathbf{x}_2(t_0)\| \right) \\ &\leq e^{-\gamma_{\min}(t-t_0)} \left( c_a + \frac{c_a c_3 c_2 \|\mathbf{B}\|}{|\gamma_a - \gamma_2|} + c_2 \right) \|\mathbf{x}(t_0)\|. \end{aligned}$$

□



## Appendix K

# Magnetometer calibration in sensor frame

The EKF and CKF based navigation systems, derived in Chapters 2 and 4, resort to magnetometer measurements for attitude aiding. In the experimental validation of the algorithms using the DELFIMx catamaran, it was noted that the magnetometer measurements were corrupted by bias and scaling effects, and that distortions occurred when the sensor was mounted onboard the vehicle. Motivated by the magnetometer non-idealities found in the experimental setup, this appendix derives an algorithm for the onboard calibration of three-axis strapdown magnetometers. The proposed calibration method is written in the sensor frame, and compensates for the combined effect of all linear time-invariant distortions, namely soft iron, hard iron, sensor non-orthogonality, bias, among others. A Maximum Likelihood Estimator (MLE) is formulated to iteratively find the optimal calibration parameters that best fit to the onboard sensor readings, without requiring external attitude references. It is shown that the proposed calibration technique is equivalent to the estimation of a rotation, scaling and translation transformation, and that the sensor alignment matrix is given by the solution of the orthogonal Procrustes problem. Good initial conditions for the iterative algorithm are obtained by a suboptimal batch least squares computation. Simulation and experimental results with low-cost sensors data are presented and discussed, supporting the application of the algorithm to autonomous vehicles and other robotic platforms.

### K.1 Introduction to magnetometer calibration

Magnetometers are a key aiding sensor for attitude estimation in low-cost, high performance navigation systems [8, 31, 66, 100], with widespread application to autonomous air, ground and ocean vehicles. These inexpensive, low power sensors allow for accurate attitude estimates by comparing the magnetic field vector observation in body frame coordinates with the vector representation in Earth frame coordinates, available from geomagnetic charts and software [108]. In conjunction with vector observations provided by

other sensors such as star trackers or pendulums, the magnetometer triad yields complete 3-DOF attitude estimation [8, 98].

The magnetic field reading distortions occur in the presence of ferromagnetic elements found in the vicinity of the sensor and due to devices mounted in the vehicle's structure. Other sources of disturbances are associated with technological limitations in sensor manufacturing and installation. A comprehensive description of the magnetic compass theory can be found in [41].

Magnetometer calibration is an old problem in ship navigation and many calibration techniques have been presented in the literature. The classic compass swinging calibration technique proposed in [18] is a heading calibration algorithm that computes scalar parameters using a least squares algorithm. The major shortcoming of this approach is the necessity of an external heading information [55], which is a strong requirement in many applications. A tutorial work using a similar but more sound mathematical derivation is found in [41]. This book addresses the fundamentals of magnetic compass theory and presents a methodology to calibrate the soft and hard iron parameters in heading and pitch, resorting only to the magnetic compass data. However, the calibration algorithm is derived by means of successive approximations and is formulated in a deterministic fashion that does not exploit the data of multiple compass readings.

In recent literature, advanced magnetometer calibration algorithms have been proposed to tackle distortions such as bias, hard iron, soft iron and non-orthogonality directly in the sensor space, with no external attitude references and using optimality criteria. The batch least squares calibration algorithm derived in [44, 55] accounts for non-orthogonality, scaling and bias errors. A nonlinear, two-step estimator provides the initial conditions using a nonlinear change of variables to cast the calibration in a pseudo-linear least squares form. The obtained estimate of the calibration parameters is then iteratively processed by a linearized least squares batch algorithm.

The TWOSTEP batch method proposed in [3] is based on the observations of the differences between the actual and the measured unit vector, denoted as scalar-checking. In the first step of the algorithm, the centering approximation derived in [52] produces a good initial guess of the calibration parameters, by rewriting the calibration problem in a linear least squares form. In a second step, a batch Gauss-Newton method is adopted to iteratively estimate the bias, scaling and non-orthogonality parameters. In related work, [36] derives recursive algorithms for magnetometer calibration based on the centering approximation and on nonlinear Kalman filtering techniques.

Magnetic errors such as soft iron, hard iron, scaling, bias and non-orthogonality are modeled separately in [44]. Although additional magnetic transformations can be modeled, it is known that some sensor errors are compensated by an equivalent effect, e.g. the hard iron and sensor biases are grouped together in [55]. Therefore, the calibration procedure should address the estimation of the joint effect of the sensor errors, as opposed to estimating each effect separately.

In this work, the magnetometer reading error model is discussed and cast in a error



formulation which accounts for the combined effect of all linear time-invariant magnetic transformations. The calibration algorithm is derived rigorously using a comprehensive model of the sensor readings in  $\mathbb{R}^3$ , that clarifies and exploits the geometric locus of the magnetometer readings, given by an ellipsoid manifold. A rigorous geometric formulation simplifies the problem of compensating for the modeled and unmodeled magnetometer errors to that of the estimation of parameters lying on an ellipsoid manifold. A complete methodology to calibrate the magnetometer is detailed, and a Maximum Likelihood Estimator (MLE) allows for the formulation of the calibration problem as the optimization of the sensor readings likelihood. It is also shown that the calibration and alignment procedures are distinct.

The sensor calibration problem is naturally formulated in the sensor frame. The calibration parameters are estimated using the magnetometer readings, and without resorting to external information or models about the magnetic field. In addition, a closed form solution for the sensor alignment is also presented, based on the well known solution to the orthogonal Procrustes problem [61].

The proposed calibration methodology is assessed both in simulation and using experimental data. Because the calibration parameters are influenced by the magnetic characteristics of the payload, the geomagnetic profile of the terrain and diverse vehicle operating conditions, the online calibration of the magnetometers is analyzed. The calibration parameters are estimated for magnetometer data collected in ring shaped sets, corresponding to yaw and pitch maneuvers that are feasible for most land, air and ocean vehicles. Simulation and experimental results show that the algorithm performs a computationally fast calibration with accurate parameter estimation.

The appendix is organized as follows. In Section K.2, a unified magnetometer error parameterization is derived and formulated. It is shown that the calibration parameters describe an ellipsoid surface and that the calibration and alignment problems are distinct. A MLE formulation is proposed to calculate the optimal generic calibration parameters and an algorithm to provide good initial conditions is presented. Also, a closed form solution for the magnetometer alignment problem is obtained. Simulation and experimental results obtained with a low-cost magnetometer triad are presented and discussed in Section K.3.

## K.2 Magnetometer calibration and alignment

In this section, an equivalent parameterization of the magnetometer errors is derived. The main sources of magnetic distortion and bias are characterized, to yield a comprehensive structured model of the magnetometer readings. Using this detailed parameterization as a motivation, the magnetometer calibration problem is recast, without loss of generality, into a unified transformation parameterized by a rotation  $\mathcal{R}$ , a scaling  $\mathbf{S}$ , and an offset  $\mathbf{b}$ . Consequently, it is shown that for all linear transformations of the magnetic field, such as soft and hard iron, non-orthogonality, scaling factor and sensor bias, the magnetometer readings will always lie on an ellipsoid manifold.

A Maximum Likelihood Estimator formulation is proposed to find the optimal calibration parameters which maximize the likelihood of the sensor readings. The proposed calibration algorithm is derived in the sensor frame and does not require any specific information about the magnetic field's magnitude and body frame coordinates. This fact allows for magnetometer calibration without external aiding references. Also, a closed form optimal algorithm to align the magnetometer and body coordinate frames is obtained from the solution to the orthogonal Procrustes problem.

### K.2.1 Magnetometer errors characterization

The magnetometer readings are distorted by the presence of ferromagnetic elements in the vicinity of the sensor, the interference between the magnetic field and the vehicle structure, local permanently magnetized materials, and by sensor technological limitations.

#### Hard Iron / Soft Iron

The hard iron bias, denoted as  $\mathbf{b}_{HI}$ , is the combined result of the permanent magnets inherent to the vehicle's structure, as well as other elements installed in the vehicle, and it is constant in the vehicle's coordinate frame.

Soft iron effects are generated by the interaction of an external magnetic field with the ferromagnetic materials in the vicinity of the sensor. The resulting magnetic field depends on the magnitude and direction of the applied magnetic field with respect to the soft iron material, producing

$$\mathbf{h}_{SI} = \mathbf{C}_{SI} \mathbf{R}_E^B \mathbf{h}, \quad (\text{K.1})$$

where  $\mathbf{C}_{SI} \in \text{M}(3)$  is the soft iron transformation matrix,  $\mathbf{R}_E^B$  is the rotation matrix from body to Earth coordinate frames,  $\mathbf{R}_E^B := \mathbf{R}_E^B$ ,  $\mathbf{h}$  is the Earth magnetic field. As described in [41, chapter XI], the combined hard and soft iron effects are given by  $\mathbf{h}_{SI+HI} = \mathbf{h}_{SI} + \mathbf{b}_{HI}$ . The linearization of the ferromagnetic effects (K.1) yields the well known heading error  $\delta\psi$  model [41, 55] adopted in compass swinging calibration, which ignores the harmonics above  $2\psi$ . The formulation (K.1), adopted in this work, yields a rigorous approach to the simultaneous estimation of the hard and soft iron effects.

#### Non-orthogonality

The non-orthogonality of the sensors can be described as a transformation of vector space basis, parameterized by [45]

$$\mathbf{C}_{NO} = \begin{bmatrix} 1 & 0 & 0 \\ \sin(\psi) & \cos(\psi) & 0 \\ -\sin(\theta) & \cos(\theta) \sin(\phi) & \cos(\theta) \cos(\phi) \end{bmatrix},$$

where  $(\psi, \theta, \phi)$  are yaw, pitch and roll Euler angles, respectively.

### Scaling and Bias

The null-shift or offset of the sensor readings is modeled as a constant vector  $\mathbf{b}_M \in \mathbb{R}^3$ . The transduction from the electrical output of the sensor to the measured quantity is formulated as a scaling matrix  $\mathbf{S}_M \in D^+(3)$ , where  $D(n)$  denotes the set of  $n \times n$  diagonal matrices with real entries and  $D^+(n) = \{\mathbf{S} \in D(n) : \mathbf{S} > 0\}$ .

### Wideband noise

The disturbing noise is assumed wideband compared with the bandwidth of the system, yielding uncorrelated sensor sampled noise.

### Alignment with the body frame

The formulation of the proposed algorithm in the sensor frame allows for sensor calibration without determination of the alignment of the sensor with respect to a reference frame. An alignment procedure of the sensor triad is proposed in this work for the sake of completeness.

### Other effects

Generic and more complex effects related to sensor-specific characteristics and to the magnetic distortion are difficult to model accurately. The proposed calibration algorithm compensates for the combined influence of all linear time-invariant transformations that distort the magnetic field, which are estimated in the form of an equivalent linear transformation.

## K.2.2 Magnetometer error parameterization

In this section, an equivalent error model for the magnetometer readings is formulated. First, the estimation problem of the non-ideal magnetic effects described in Section K.2.1 is recast, without loss of generality, as the problem of estimating an affine linear transformation. Second, it is shown that the linear transformation is equivalent to a single rotation, scaling and translation transformation. In other words, to calibrate the magnetometer it is sufficient to estimate the center, orientation and radii of the ellipsoid that best fit to the acquired data.

Define a sphere and an ellipsoid as [133]

$$S(n) = \{\mathbf{x} \in \mathbb{R}^{n+1} : \|\mathbf{x}\|^2 = 1\}, \quad L(n) = \{\mathbf{x} \in \mathbb{R}^{n+1} : \|\mathbf{S}\mathcal{R}'\mathbf{x}\|^2 = 1\},$$

where  $\mathbf{S} \in D^+(n+1)$  and  $\mathcal{R} \in SO(n+1)$  describe the radii and orientation of the ellipsoid, respectively. The three-axis magnetometer reading is given by the Earth's magnetic field  ${}^E\mathbf{h}$  affected by the magnetic distortions and errors, yielding

$$\mathbf{h}_{ri} = \mathbf{S}_M \mathbf{C}_{NO} (\mathbf{C}_{SI}^B \mathbf{R}_i^E \mathbf{h} + \mathbf{b}_{HI}) + \mathbf{b}_M + \mathbf{n}_{mi}, \quad (\text{K.2})$$

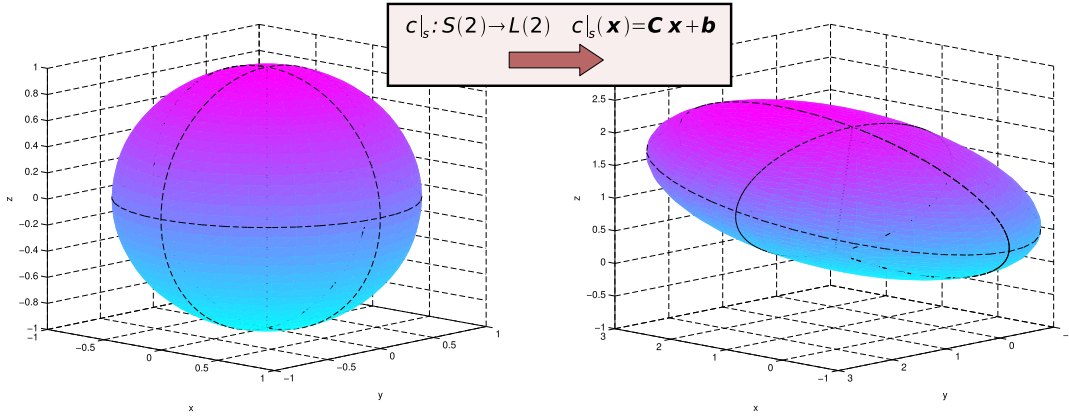


Figure K.1: Affine transformation of a two dimensional sphere.

where  $\mathbf{h}_r$  is the magnetometer reading in the (non-orthogonal) magnetometer coordinate frame,  $\mathbf{n}_m \in \mathbb{R}^3$  is the Gaussian wideband noise,  $\mathbf{S}_M$ ,  $\mathbf{C}_{NO}$ ,  $\mathbf{C}_{SI}$ ,  $\mathbf{b}_{HI}$  and  $\mathbf{b}_M$  are the magnetic distortions described in Section K.2.1, and  $i = 1, \dots, n$  denotes the index of the reading.

Without loss of generality, the magnetometer reading can be described by

$$\mathbf{h}_{r,i} = \mathbf{C}^B \mathbf{h}_i + \mathbf{b} + \mathbf{n}_{m,i}, \quad (\text{K.3})$$

where  $\mathbf{C} = \mathbf{S}_M \mathbf{C}_{NO} \mathbf{C}_{SI}$ ,  $\mathbf{b} = \mathbf{S}_M \mathbf{C}_{NO} \mathbf{b}_{HI} + \mathbf{b}_M$ ,  ${}^B \mathbf{h}_i = \frac{B}{E} \mathbf{R}_i^E \mathbf{h}$ ,  ${}^B \mathbf{h}_i \in S(2)$  is the magnetic field in body coordinate frame. In particular,  $\mathbf{C} \in M(3)$  and  $\mathbf{b} \in \mathbb{R}^3$  are unconstrained, so unmodeled linear time-invariant magnetic errors and distortions are also taken into account.

Given that the points  ${}^B \mathbf{h}_i$  are contained in the sphere, straightforward application of the Singular Value Decomposition (SVD) [133] shows that the magnetometer readings  $\mathbf{h}_{r,i}$  lie on an ellipsoid manifold, as illustrated in the example of Fig. K.1 and summarized in the following theorem. The proof is presented for the sake of clarity.

**Theorem K.1** ([133]). *Let  $c : \mathbb{R}^n \rightarrow \mathbb{R}^n, c(\mathbf{x}) = \mathbf{C}\mathbf{x}$  be a linear transformation where  $\mathbf{C} \in M(n)$  is full rank. Then  $c(\mathbf{x})$  is a bijective transformation between the sphere and an ellipsoid in  $\mathbb{R}^n$ , i.e. there is an ellipsoid  $L(n-1)$  such that the transformation  $c|_S : S(n-1) \rightarrow L(n-1)$ ,  $c|_S(\mathbf{x}) = \mathbf{C}\mathbf{x}$  is bijective.*

*Proof.* Let the s decomposition  $\mathbf{C} = \mathbf{U}\mathbf{\Sigma}\mathbf{V}'$ , where  $\mathbf{U}, \mathbf{V} \in O(n)$  and  $\mathbf{\Sigma} \in D^+(n)$ . Define the matrices  $\mathcal{R}_L := \mathbf{U}\mathbf{J}, \mathcal{S}_L := \mathbf{\Sigma}, \mathcal{V}_L := \mathbf{V}\mathbf{J}, \mathbf{J} := \begin{bmatrix} \det(\mathbf{U}) & \mathbf{0} \\ \mathbf{0} & \mathbf{I}_{n-1 \times n-1} \end{bmatrix}$ , which describe a modified singular value decomposition with at least one special orthogonal matrix  $\mathbf{C} = \mathcal{R}_L \mathcal{S}_L \mathcal{V}_L'$  where  $\mathcal{R}_L \in SO(n)$ ,  $\mathcal{S}_L \in D^+(n)$  and  $\mathcal{V}_L \in O(n)$ . The transformation  $c(\mathbf{x})$  applied to the sphere is given by

$$c|_S(\mathbf{x}) := \mathcal{R}_L \mathcal{S}_L \mathbf{y}, \quad (\text{K.4})$$

where  $\mathbf{y} := \mathcal{V}_L' \mathbf{x}$  verifies  $\|\mathbf{y}\|^2 = 1$ . Choosing the ellipsoid  $L(n-1) = \{\mathbf{x} \in \mathbb{R}^n : \|\mathcal{S}_L^{-1} \mathcal{R}_L' \mathbf{x}\|^2 = 1\}$  then  $c|_S(\mathbf{x}) \in L(n-1)$ . The function (K.4) is injective because

$\mathcal{R}_L \mathbf{S}_L$  is invertible. To see that it is surjective, given any  $\mathbf{z} \in \mathbb{L}(n-1)$ , the point  $\mathbf{y} = \mathbf{S}_L^{-1} \mathcal{R}_L' \mathbf{z} \in \mathbb{S}(n-1)$  satisfies  $c(\mathbf{y}) = \mathbf{z}$ .  $\square$

**Corollary K.2.** *Let  $\mathbf{C} \in \mathbb{M}(n)$  be a full rank matrix and let the singular value decomposition of  $\mathbf{C}$  be given by  $\mathbf{C} = \mathcal{R}_L \mathbf{S}_L \mathbf{V}_L'$  where  $\mathcal{R}_L \in \text{SO}(n)$ ,  $\mathbf{S}_L \in \mathbb{D}^+(n)$  and  $\mathbf{V}_L \in \text{O}(n)$ . The ellipsoid described by  $c|_S$  is spanned by the bijective transformation  $l: \mathbb{S}(n-1) \rightarrow \mathbb{L}(n-1)$ ,  $l(\mathbf{x}) = \mathcal{R}_L \mathbf{S}_L \mathbf{x}$ .*

Theorem K.1 implies that the magnetic field readings  $\mathbf{h}_{r_i}$  derived in (K.3) lie on the surface of an ellipsoid centered on  $\mathbf{b}$ , referred to as sensor ellipsoid. Corollary K.2 states that the sensor ellipsoid centered at  $\mathbf{b}$  is fully characterized the rotation  $\mathcal{R}_L$  and scaling  $\mathbf{S}_L$  matrices.

Define  ${}^C \mathbf{h}_i := \mathbf{V}_L' {}^B \mathbf{h}_i$ ,  ${}^C \mathbf{h}_i \in \mathbb{S}(2)$  where the coordinate frame  $\{C\}$  is obtained by the orthogonal transformation  $\mathbf{V}_L'$  of  $\{B\}$ , i.e. by the alignment matrix  $\mathbf{V}_L$ . The equivalent model for the magnetometer readings (K.3) is described by

$$\mathbf{h}_{r_i} = \mathcal{R}_L \mathbf{S}_L {}^C \mathbf{h}_i + \mathbf{b} + \mathbf{n}_{m_i}. \quad (\text{K.5})$$

Clearly, the calibration process is equivalent to the estimation of the ellipsoid's parameters  $\mathbf{b}$ ,  $\mathcal{R}_L$  and  $\mathbf{S}_L$ . As expected, the alignment matrix  $\mathbf{V}_L$  is not observable in the calibration process given that  ${}^C \mathbf{h}_i$  and  ${}^B \mathbf{h}_i$  are not measured.

The sensor description (K.5) is a function of the calibration parameters  $(\mathcal{R}_L, \mathbf{S}_L, \mathbf{b})$  lying on the manifold  $\text{SO}(3) \times \mathbb{D}^+(3) \times \mathbb{R}^3$ . Optimization tools on Riemannian manifolds are required to solve for the calibration parameters directly on  $\text{SO}(3) \times \mathbb{D}^+(3) \times \mathbb{R}^3$ , see [43, 51] for a comprehensive introduction to the subject. Fortunately, an equivalent calibration can be performed in the Euclidean space  $\mathbb{M}(3)$  by estimating  $\mathbf{C}$  directly, but where the fact that the alignment matrix  $\mathbf{V}_L$  cannot be determined must be considered.

The sensor calibration and alignment algorithm is structured as follows. In the *calibration* step, the parameters  $\mathcal{R}_L$ ,  $\mathbf{S}_L$  and  $\mathbf{b}$  are estimated, using a Maximum Likelihood Estimator formulated on  $\mathbb{M}(3)$ . In the *alignment* step, the determination of the orthogonal transformation  $\mathbf{V}_L$  is obtained from a closed form optimal algorithm using vector readings in  $\{C\}$  and  $\{B\}$  frames.

### K.2.3 Magnetometer calibration

The calibration parameters are computed using a Maximum Likelihood Estimator. An intermediate estimator is formulated on the manifold  $\Theta := \text{SO}(3) \times \mathbb{D}^+(3) \times \mathbb{R}^3$  to evidence that the sensor alignment cannot be determined by a calibration algorithm written in the sensor frame. However, the use of classical optimization tools in Euclidean spaces is allowed for by writing an equivalent estimator formulation on  $\mathbb{M}(3)$ .

Assuming that the noise on the magnetometer readings is a zero mean Gaussian process with variance  $\sigma_{m_i}^2$ , the probability density function (p.d.f.) of each  $\mathbf{h}_{r_i}$  is also Gaussian

$$\mathbf{n}_{m_i} \sim \mathcal{N}(0, \sigma_{m_i}^2 \mathbf{I}) \Rightarrow \mathbf{h}_{r_i} \sim \mathcal{N}(\mathcal{R}_L \mathbf{S}_L {}^C \mathbf{h}_i + \mathbf{b}, \sigma_{m_i}^2 \mathbf{I}).$$

The MLE finds the parameters that maximize the conditional p.d.f. of each sensor reading given the optimization parameters [75]. The resulting minimization problem of the weighted log-likelihood function is described by

$$\min_{\substack{(\mathcal{R}_L, \mathbf{S}_L, \mathbf{b}) \in \Theta \\ {}^C \mathbf{h}_i \in \mathbb{S}(2), i=1, \dots, n}} \sum_{i=1}^n \left( \frac{\|(\mathbf{h}_{r_i} - \mathbf{b}) - \mathcal{R}_L \mathbf{S}_L {}^C \mathbf{h}_i\|}{\sigma_{m_i}} \right)^2. \quad (\text{K.6})$$

The minimum of (K.6) is computed iteratively by gradient or Newton-like methods on manifolds [43, 51]. Note that solving the minimization problem (K.6) implies estimating  $n$  auxiliary magnetic field vectors  ${}^C \mathbf{h}_i$ , and the dimension of the search space is  $(2n + \dim \Theta)$  whereas the dimension of the calibration parameters space is  $\dim \Theta = \dim \text{SO}(3) + \dim \text{D}^+(3) + \dim \mathbb{R}^3 = 9$ .

The minimization problem (K.6) finds the ellipsoid points  $(\mathcal{R}_L \mathbf{S}_L {}^C \mathbf{h}_i)$  that best fit the sensor readings  $(\mathbf{h}_{r_i} - \mathbf{b})$ . Intuitively, the minimization problem can be rewritten to find the sphere points  ${}^C \mathbf{h}_i$  that best fit to the pullback of the ellipsoid to the sphere  $(\mathbf{S}_L^{-1} \mathcal{R}_L'(\mathbf{h}_{r_i} - \mathbf{b}))$ , yielding

$$\min_{\substack{(\mathcal{R}_L, \mathbf{S}_L, \mathbf{b}) \in \Theta \\ {}^C \mathbf{h}_i \in \mathbb{S}(2), i=1, \dots, n}} \sum_{i=1}^n \left( \frac{\|\mathbf{S}_L^{-1} \mathcal{R}_L'(\mathbf{h}_{r_i} - \mathbf{b}) - {}^C \mathbf{h}_i\|}{\sigma_{m_i}} \right)^2. \quad (\text{K.7})$$

The minimization problem (K.7) is suboptimal with respect to the unified error model (K.5), but can be rigorously derived using a MLE formulation by assuming that the noise is external to the sensor, as detailed in the Section K.4.1. More important, the log-likelihood function (K.7) can be optimized by searching only in the parameter space  $\Theta$ .

**Proposition K.3.** *The solution  $(\mathcal{R}_L^*, \mathbf{S}_L^*, \mathbf{b}^*)$  of (K.7) also minimizes*

$$\min_{(\mathcal{R}_L, \mathbf{S}_L, \mathbf{b}) \in \Theta} \sum_{i=1}^n \left( \frac{\|\mathbf{S}_L^{-1} \mathcal{R}_L'(\mathbf{h}_{r_i} - \mathbf{b})\| - 1}{\sigma_{m_i}} \right)^2. \quad (\text{K.8})$$

*Proof.* Given  $(\mathcal{R}_L^*, \mathbf{S}_L^*, \mathbf{b}^*)$ , the optimal  ${}^C \mathbf{h}_i^*$  satisfies

$${}^C \mathbf{h}_i^* = \operatorname{argmin}_{{}^C \mathbf{h}_i \in \mathbb{S}(2)} \|\mathbf{v}_i^* - {}^C \mathbf{h}_i\|^2, \quad (\text{K.9})$$

where  $\mathbf{v}_i^* := \mathbf{S}_L^{*-1} \mathcal{R}_L^{*'}(\mathbf{h}_{r_i} - \mathbf{b}^*)$ . The minimization problem (K.9) corresponds to the projection of  $\mathbf{v}_i^*$  on the unit sphere, which has the closed form solution  ${}^C \mathbf{h}_i^* = \frac{\mathbf{v}_i^*}{\|\mathbf{v}_i^*\|}$ . Therefore, the minimization problem (K.7) can be written as

$$\min_{(\mathcal{R}_L, \mathbf{S}_L, \mathbf{b}) \in \Theta} \sum_{i=1}^n \left( \frac{\|\mathbf{S}_L^{-1} \mathcal{R}_L'(\mathbf{h}_{r_i} - \mathbf{b}) - \frac{\mathbf{v}_i}{\|\mathbf{v}_i\|}\|}{\sigma_{m_i}} \right)^2,$$

where  $\mathbf{v}_i := \mathbf{S}_L^{-1} \mathcal{R}_L'(\mathbf{h}_{r_i} - \mathbf{b})$ . Using simple algebraic manipulation produces the likelihood function (K.8).  $\square$

The minimization problem (K.8) can be formulated on the Euclidean space, which allows for the use of optimization tools for unconstrained problems [12].

**Proposition K.4.** *Let  $(\mathbf{T}^*, \mathbf{b}_T^*)$  denote the solution of the unconstrained minimization problem*

$$\min_{\mathbf{T} \in \mathbf{M}(3)} \sum_{i=1}^n \left( \frac{\|\mathbf{T}(\mathbf{h}_{ri} - \mathbf{b}_T)\| - 1}{\sigma_{mi}} \right)^2, \quad (\text{K.10})$$

and take the singular value decomposition of  $\mathbf{T}^* = \mathbf{U}_T^* \mathbf{S}_T^* \mathbf{V}_T^{*'}$ ,  $\mathbf{U}_T \in \mathbf{O}(3)$ ,  $\mathbf{S}_T \in \mathbf{D}^+(3)$ ,  $\mathbf{V}_T \in \mathbf{SO}(3)$ . The solution of (K.8) is given by  $\mathbf{R}_L^* = \mathbf{V}_T^*$ ,  $\mathbf{S}_L^* = \mathbf{S}_T^{*-1}$ ,  $\mathbf{b}^* = \mathbf{b}_T^*$ .

*Proof.* Using the equality  $\|\mathbf{V}_L \mathbf{S}_L^{-1} \mathcal{R}'_L(\mathbf{h}_{ri} - \mathbf{b})\| = \|\mathbf{S}_L^{-1} \mathcal{R}'_L(\mathbf{h}_{ri} - \mathbf{b})\|$  for any  $\mathbf{V}_L \in \mathbf{O}(3)$ , and the fact that, by the singular value decomposition,  $\mathbf{T} := \mathbf{V}_L \mathbf{S}_L^{-1} \mathcal{R}'_L$  is a generic element of  $\mathbf{M}(3)$ , produces the desired results.  $\square$

By Proposition K.4, the calibration parameters of equation (K.5) are obtained by solving (K.10) and decomposing the resulting  $\mathbf{T}^*$ . Although (K.10) could be derived using (K.3), the intermediate derivations (K.7) and (K.8) were presented to show that (i) the sensor readings lie on an ellipsoid manifold parameterized by  $\mathcal{R}_L$ ,  $\mathbf{S}_L$  and  $\mathbf{b}$  (ii) the alignment matrix, represented by  $\mathbf{V}_L$  (or  $\mathbf{U}_T^*$ ) cannot be determined in the calibration process, given that there are no body referenced measurements.

In this work, the minimization problem (K.10) is solved by using the gradient and Newton-descent method for Euclidean spaces [12], and the Armijo rule for the step size determination. The gradient and Hessian of the log-likelihood function are computed analytically and presented in the Section K.4.1.

Given the calibration parameters  $(\mathcal{R}_L, \mathbf{S}_L, \mathbf{b})$ , an unbiased and unit norm representation of the Earth magnetic field in the calibration frame  $\{C\}$  is obtained by algebraic manipulation of (K.5), resulting in

$${}^C \mathbf{h}_i = \mathbf{S}_L^{-1} \mathcal{R}'_L(\mathbf{h}_{ri} - \mathbf{b}). \quad (\text{K.11})$$

A good initial guess of the scaling and bias calibration parameters is produced by the two-step estimator proposed in [55]. The locus of measurements described by

$$\|{}^E \mathbf{h}\|^2 = \|\mathbf{S}^{-1}(\mathbf{h}_r - \mathbf{b})\|^2,$$

is expanded and, by defining a nonlinear change of variables, it is rewritten as a pseudo-linear least squares estimation problem

$$H(\mathbf{h}_r) f(\mathbf{b}, \mathbf{s}) = b(\mathbf{h}_r), \quad (\text{K.12})$$

where the matrix  $H(\mathbf{h}_r) \in \mathbf{M}(n, 6)$  and the vector  $b(\mathbf{h}_r) \in \mathbb{R}^n$  are nonlinear functions of the vector readings and the vector of unknowns  $f(\mathbf{b}, \mathbf{s}) \in \mathbb{R}^6$  is a nonlinear function of the calibration parameters. The closed form solution to the least squares problem (K.12) is found to yield a good first guess of the calibration parameters [45].



In alternative, the algorithm proposed in [24] can produce an initial ellipsoid guess based on the difference-of-squares error criterion using a semidefinite programming (SDP) formulation. However, the SDP algorithm is computationally feasible only for no more than a few hundred samples, whereas the pseudo-linear least squares formulation (K.12) allows for efficient processing of the several thousands of points contained in the calibration data, which are required in practice.

### K.2.4 Magnetometer alignment

The representation of  ${}^B\mathbf{h}_i$  in the body frame is necessary in attitude determination algorithms [98]. Although the alignment and calibration procedures are independent, the magnetometer alignment algorithm is detailed for the sake of completeness.

The magnetometer alignment with respect to a reference frame is represented by the orthogonal matrix  $\mathbf{V}_L \in \text{O}(3)$  contained in the unified transformation  $\mathbf{C}$ , see Corollary K.2. Given that  ${}^C\mathbf{h}_i := \mathbf{V}'_L {}^B\mathbf{h}_i$ ,  ${}^C\mathbf{h}_i \in \text{S}(2)$ , the matrix  $\mathbf{V}_L$  is computed using the  ${}^C\mathbf{h}_i$  observations given by the calibrated sensor reading (K.11), and the  ${}^B\mathbf{h}_i$  measurements obtained from external information sources, such as heading reference units or external localization systems.

As illustrated in Fig. K.2, two vector readings are sufficient to characterize a rigid rotation  $\mathbf{V}_L \in \text{SO}(3)$ , or a rotation with reflection  $\mathbf{V}_L \in (\text{O}(3) \setminus \text{SO}(3))$ , but the determination of an orthogonal transformation  $\mathbf{V}_L \in \text{O}(3)$  requires at least three linearly independent vectors readings. The well known results for the orthogonal Procrustes problem [61] are adopted to determine  $\mathbf{V}_L \in \text{O}(3)$ .

**Theorem K.5** (Orthogonal Procrustes Problem). *Take two sets of vector readings in  $\{C\}$  and  $\{B\}$  coordinate frames, concatenated in the form  ${}^C\mathbf{X} = [{}^C\mathbf{h}_1 \ \dots \ {}^C\mathbf{h}_n]$  and  ${}^B\mathbf{X} = [{}^B\mathbf{h}_1 \ \dots \ {}^B\mathbf{h}_n]$  where  $n \geq 3$ . Assume that  ${}^B\mathbf{X}{}^C\mathbf{X}'$  is nonsingular, and denote the corresponding SVD as  ${}^B\mathbf{X}{}^C\mathbf{X}' = \mathbf{U}\mathbf{\Sigma}\mathbf{V}'$ , where  $\mathbf{U}, \mathbf{V} \in \text{O}(3)$ ,  $\mathbf{\Sigma} \in \text{D}^+(3)$ . The optimal orthogonal matrix  $\mathbf{V}'_L \in \text{O}(3)$  that minimizes the transformation from  $\{B\}$  to  $\{C\}$  coordinates frames in least squares sense*

$$\min_{\mathbf{V}_L \in \text{O}(3)} \sum_{i=1}^n \|{}^C\mathbf{h}_i - \mathbf{V}'_L {}^B\mathbf{h}_i\|^2,$$

is unique and given by  $\mathbf{V}'_L{}^* = \mathbf{V}\mathbf{U}'$ .

Using (K.11), the calibrated and aligned magnetic field vector reading is given by

$${}^B\mathbf{h}_i = \mathbf{V}_L \mathbf{S}_L^{-1} \mathcal{R}'_L (\mathbf{h}_{r_i} - \mathbf{b}).$$

Given that the vector magnitude is not relevant for the attitude determination algorithms [98], it is assumed without loss of generality that  ${}^E\mathbf{h}$  lies on the unit sphere, and the norm scaling factor is thus incorporated in the scaling matrix  $\mathbf{S}_L$ . Clearly, if  $\|{}^E\mathbf{h}\| = \alpha$ ,  $\alpha \neq 1$ , the calibrated sensor reading  ${}^B\mathbf{h}_{i\alpha}$  is given by  ${}^B\mathbf{h}_{i\alpha} = \alpha {}^B\mathbf{h}_i$ .



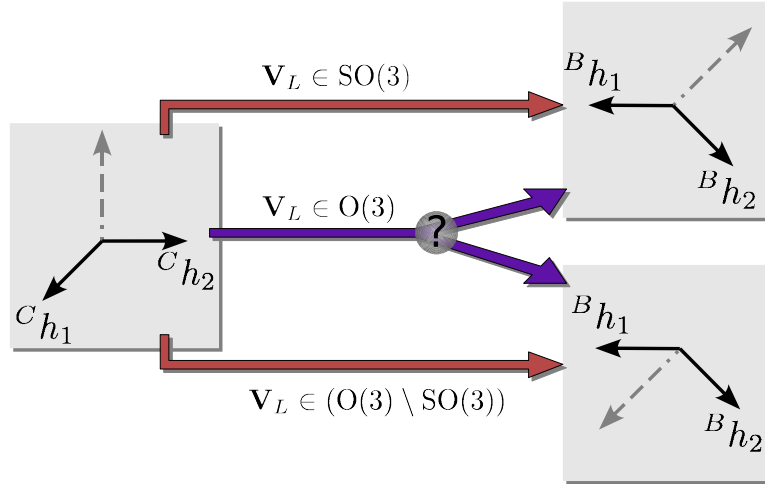


Figure K.2: Alignment estimation ambiguity with two vector readings.

### K.3 Algorithm implementation and results

In this section, the proposed calibration algorithm is validated using simulated and experimental data from a triad of low-cost magnetometers.

#### K.3.1 Simulation results

The calibration algorithm was first analyzed using simulated data. The reference calibration parameters from (K.2) are

$$\mathbf{S}_M = \text{diag}(1.2, 0.8, 1.3), \quad \begin{bmatrix} \psi \\ \theta \\ \phi \end{bmatrix} = \begin{bmatrix} 2.0^\circ \\ 1.0^\circ \\ 1.5^\circ \end{bmatrix}, \quad \mathbf{b}_{HI} = \begin{bmatrix} -1.2 \\ 0.2 \\ -0.8 \end{bmatrix} \text{ G},$$

$$\mathbf{b}_M = \begin{bmatrix} 1.5 \\ 0.4 \\ 2.7 \end{bmatrix} \text{ G}, \quad \mathbf{C}_{SI} = \begin{bmatrix} 0.58 & -0.73 & 0.36 \\ 1.32 & 0.46 & -0.12 \\ -0.26 & 0.44 & 0.53 \end{bmatrix},$$

and the magnetometer noise, described in the sensor space, is a zero mean Gaussian noise with standard deviation  $\sigma_m = 5 \text{ mG}$ . The likelihood function  $f$  is normalized by the number of samples  $n$  and the stop condition of the minimization algorithm is  $\|\nabla f|_{\mathbf{x}_k}\| < \varepsilon = 10^{-3}$ .

In a strapdown sensor architecture, the swinging of the magnetometer triad is constrained by the vehicle's maneuverability and, consequently, only some sections of the ellipsoid can be traced. The magnetic field readings are obtained for two specific cases, illustrated in Fig. K.3. In the first case, a ring shaped uniform set of points is obtained for unconstrained yaw and a pitch sweep interval of  $\theta \in [-20, 20]^\circ$ . Note that the constraint in the pitch angle can be found in most terrestrial vehicles. In the second case, the ellipsoid's curvature information is reduced by constraining the yaw to  $\psi \in [-90, 90]^\circ$ .

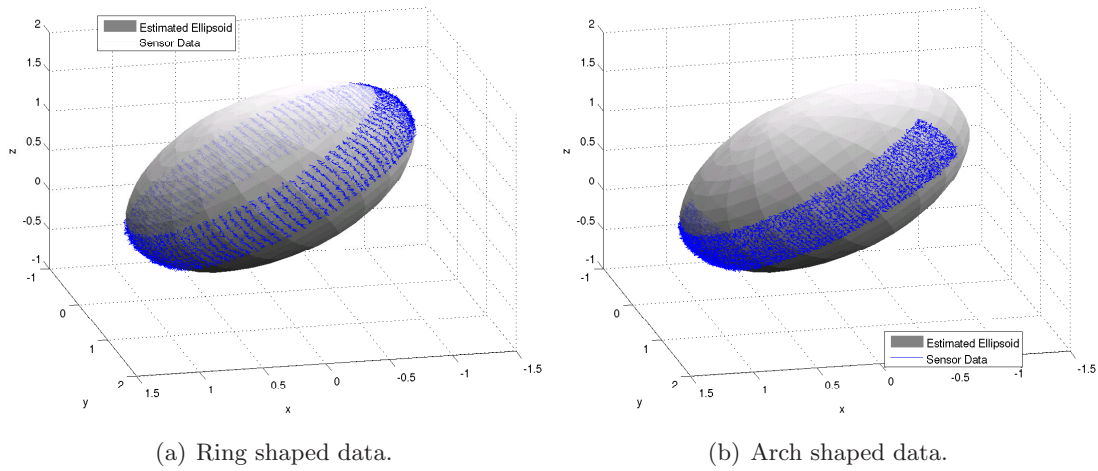


Figure K.3: Ellipsoid fitting (simulation data).

The results of 20 Monte Carlo simulations using  $10^4$  magnetometer readings are presented in Tables K.1 and K.2 and depicted in Fig. K.3. Given the large likelihood cost of the noncalibrated data, denoted by  $f(\mathbf{x}_{-1})$ , the initial condition draws the cost function into the vicinity of the optimum, and the iterations yield a 20% improvement over the initial guess.

Table K.1: Calibration results (gradient method).

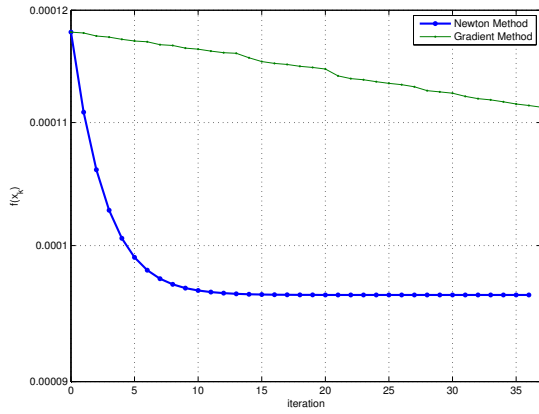
	$f(\mathbf{x}_{-1})$	$f(\mathbf{x}_0)$	$f(\mathbf{x}^*)$	iterations	$\theta_e$	$\mathbf{s}_e$	$\mathbf{b}_e$
Ring Shaped Data	$3.28 \times 10^{-1}$	$1.17 \times 10^{-4}$	$9.64 \times 10^{-5}$	2246	$1.74 \times 10^{-3}$	$7.61 \times 10^{-3}$	$3.54 \times 10^{-4}$
Arch Shaped Data	$4.36 \times 10^{-1}$	$1.18 \times 10^{-4}$	$9.62 \times 10^{-5}$	1932	$1.46 \times 10^{-2}$	$1.65 \times 10^{-2}$	$1.74 \times 10^{-2}$

Table K.2: Calibration results (Newton method).

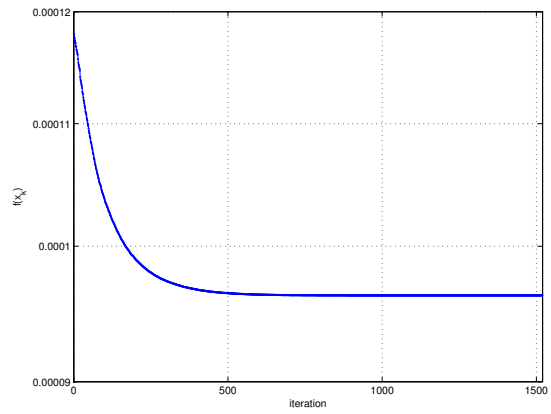
	$f(\mathbf{x}_{-1})$	$f(\mathbf{x}_0)$	$f(\mathbf{x}^*)$	iterations	$\theta_e$	$\mathbf{s}_e$	$\mathbf{b}_e$
Ring Shaped Data	$3.28 \times 10^{-1}$	$1.18 \times 10^{-4}$	$9.64 \times 10^{-5}$	37.0	$1.74 \times 10^{-3}$	$7.61 \times 10^{-3}$	$3.54 \times 10^{-4}$
Arch Shaped Data	$4.37 \times 10^{-1}$	$1.18 \times 10^{-4}$	$9.62 \times 10^{-5}$	37.2	$1.46 \times 10^{-2}$	$1.65 \times 10^{-2}$	$1.75 \times 10^{-2}$

The Newton algorithm converges faster than the gradient algorithm, exploiting the second order information of the Hessian, as illustrated in Fig. K.4 and Fig. K.5. Although the Hessian computations are more complex, the Newton method takes only 5 s to converge to in a Matlab 7.3 implementation running on a standard computer with a Pentium Celeron 1.6 Ghz processor.

Defining the distance between the estimated and the actual parameter as  $\mathbf{s}_e := \|\mathbf{S}^* - \mathbf{S}\|$ ,  $\mathbf{b}_e := \|\mathbf{b}^* - \mathbf{b}\|$ , and  $\theta_e := \arccos\left(\frac{\text{tr}(\mathcal{R}^* \mathcal{R}') - 1}{2}\right)$ , Tables K.1 and K.2 show that the arch shaped data set contains sufficient eccentricity information to estimate the equivalent mag-

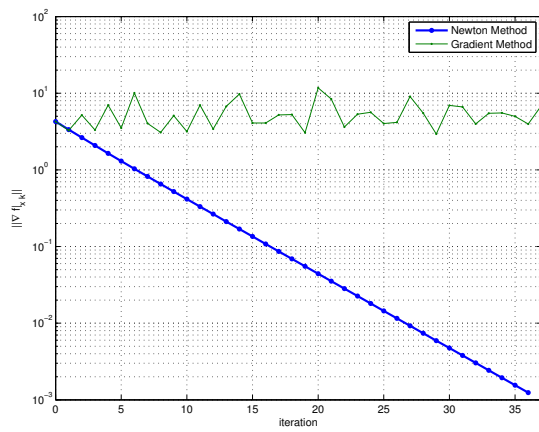


(a) Newton (vs gradient) method.

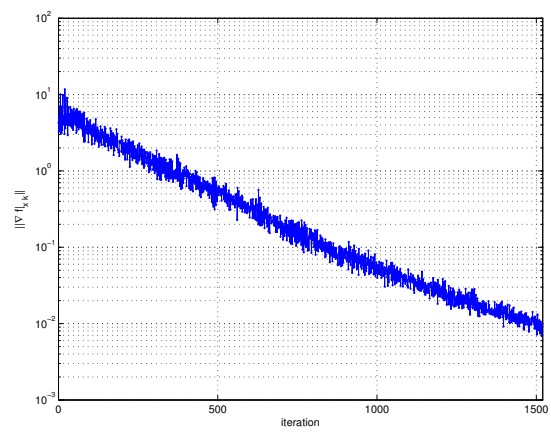


(b) Gradient method iterations.

Figure K.4: Convergence of the log-likelihood function (arch shaped data).



(a) Newton (vs gradient) method.



(b) Gradient method iterations.

Figure K.5: Convergence of the log-likelihood gradient (arch shaped data).

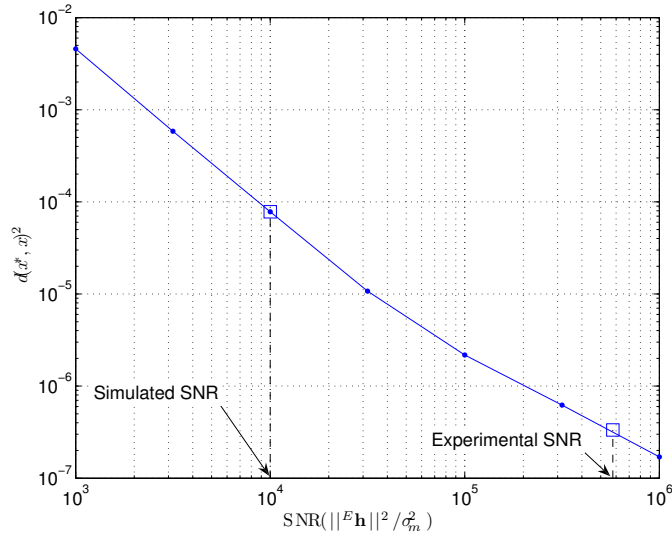


Figure K.6: Estimation error vs. signal-to-noise ratio (100 MC, ring shaped data).

netometer errors quantities  $\mathcal{R}$ ,  $\mathbf{s}$  and  $\mathbf{b}$ . For platforms with limited maneuverability, the proposed optimization algorithm identifies the calibration parameters with good accuracy. As expected, reducing the information about the ellipsoid curvature slightly degrades the sensor calibration errors.

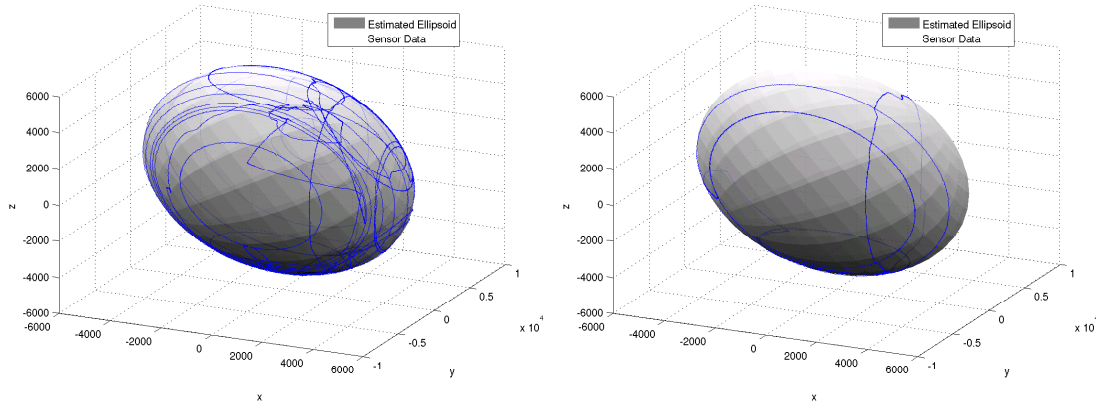
As depicted in Fig. K.3, although the noise is formulated in the sensor frame, the suboptimal formulation (K.8) yields accurate results with unit likelihood weights  $\sigma_{mi}^2$ . Let the distance in the parameter space be given by  $d(\mathbf{x}^*, \mathbf{x})^2 := \theta_e^2 + \mathbf{s}_e^2 + \mathbf{b}_e^2$ , the influence of the noise power in the estimation error is illustrated in Fig. K.6, where the magnetic field magnitude in the San Francisco Bay area is adopted,  $\|{}^E \mathbf{h}\| = 0.5$  G.

### K.3.2 Experimental results

The algorithm proposed in this work was used to estimate the calibration parameters for a set of  $6 \times 10^4$  points obtained from an actual magnetometer triad. The magnetometer was a Honeywell HMC1042L 2-axis magnetometer and a Honeywell HMC1041Z for the third (Z) axis, sampled with a TI MSC12xx microcontroller with a 24bit Delta Sigma converter, at 100Hz, see [44] for details.

A gimbal system was maneuvered to collect (i) a set of sensor readings spanning the ellipsoid surface, Fig. K.7(a), (ii) only four ellipsoid sections, Fig. K.7(b). The calibration algorithm converged to a minimum within 60 Newton method iterations, taking less than 40s and yielding  $f(\mathbf{x}^*) = 2.51 \times 10^{-6}$  for the ellipsoid surface data set and  $f(\mathbf{x}^*) = 2.67 \times 10^{-6}$  for the ellipsoid sections data set. Although the second data set included less data points, the results were similar because the collected data were sufficient to characterize the ellipsoid's eccentricity and rotation, as depicted in Fig. K.7(b).

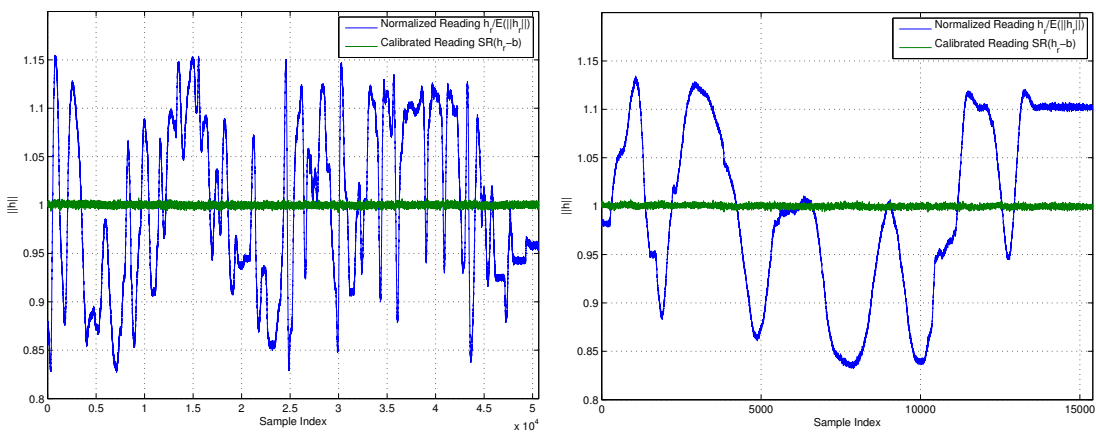
Given the calibration parameters, the sensor noise is characterized by rewriting (K.5) as  $\mathbf{n}_{mi} = \mathbf{h}_r - (\mathcal{R}_L^* \mathbf{S}_L^* \mathcal{C}_L^* \mathbf{h}_i^* + \mathbf{b}^*)$  where  $\mathcal{C}_L^*$  is given in the proof of Proposition K.3. The



(a) Ellipsoid surface data.

(b) Ellipsoid sections data.

Figure K.7: Ellipsoid fitting (real data).



(a) Ellipsoid surface data.

(b) Ellipsoid sections data.

Figure K.8: Magnetometer data fitting.

obtained experimental standard deviation of the sensor noise is  $\sigma_m = 0.65$  mG, which evidences that the signal-to-noise ratio of a typical low-cost magnetometer is better than that assumed in the simulations of Section K.3.1, as depicted in Fig. K.6.

The calibrated magnetometer data are compared to the raw data in Fig. K.8. The calibrated readings are near to the unit circle locus, which validates the proposed unified error formulation of Theorem K.1 and shows that the combined effect of the magnetic distortions is successfully compensated for.

## K.4 Auxiliary results

This section presents auxiliary results adopted in the derivation of the magnetometer calibration algorithm.

### K.4.1 External magnetic noise

In the proposed error model (K.2), electronic interference and sensor specific technology are the main sources of noise. In the case where the main sources of electromagnetic interference are external, the magnetic noise influence in the magnetometer reading can be modeled as

$$\begin{aligned} \mathbf{h}_{r_i} &= \mathbf{S}_M \mathbf{C}_{NO} (\mathbf{C}_{SI} (\mathbf{R}_i^B \mathbf{h} + \mathbf{R}_i^B \mathbf{n}_{m_i}) + \mathbf{b}_{HI}) + \mathbf{b}_M = \mathbf{C}^B \mathbf{h}_i + \mathbf{C}_N^B \mathbf{R} \mathbf{n}_{m_i} + \mathbf{b} \\ &= \mathcal{R}_L \mathbf{S}_L^C \mathbf{h}_i + \mathcal{R}_L \mathbf{S}_L \mathbf{V}'_L \mathbf{R}_i^B \mathbf{n}_{m_i} + \mathbf{b}, \end{aligned}$$

where  $\mathbf{R}_i^B$  rotates from the coordinate frame  $\{N\}$  where the magnetic noise is defined, to the body coordinate frame. Assuming that  $\mathbf{n}_{m_i}$  is a zero mean Gaussian process with variance  $\sigma_{m_i}^2$ , the p.d.f. of each  $\mathbf{h}_{r_i}$  is also Gaussian

$$\mathbf{n}_{m_i} \sim \mathcal{N}(0, \sigma_{m_i}^2 \mathbf{I}) \Rightarrow \mathbf{h}_{r_i} \sim \mathcal{N}(\mathcal{R}_L \mathbf{S}_L^C \mathbf{h}_i + \mathbf{b}, \sigma_{m_i}^2 \mathcal{R}_L \mathbf{S}_L^2 \mathcal{R}'_L).$$

Using the p.d.f. of the  $\mathbf{h}_{r_i}$ , straightforward analytical derivations show that MLE formulation is given by (K.7). As convincingly argued in [53], if the noise exists in the sensor frame (K.5), the ellipsoid obtained by (K.7) tends to fit best the points with lower eccentricity. This effect can be balanced by defining appropriate curvature weights [53]  $\sigma_{m_i}^2$ , producing results close to the optimal solution of (K.6).

### K.4.2 Likelihood function derivatives

Let  $\mathbf{u}_i := \mathbf{h}_{r_i} - \mathbf{b}$ , the gradient of the likelihood function

$$f := \sum_{i=1}^n \left( \frac{\|\mathbf{T}(\mathbf{h}_{r_i} - \mathbf{b})\| - 1}{\sigma_{m_i}} \right)^2,$$

denoted by  $\nabla f|_{\mathbf{x}} = \begin{bmatrix} \nabla f|_{\mathbf{T}} & \nabla f|_{\mathbf{b}} \end{bmatrix}$ , is described by the submatrices

$$\nabla f|_{\mathbf{T}} = \sum_{i=1}^n \frac{2c_T}{\sigma_{m_i}^2} \mathbf{u}_i \otimes \mathbf{T} \mathbf{u}_i, \quad \nabla f|_{\mathbf{b}} = \sum_{i=1}^n \frac{-2c_T}{\sigma_{m_i}^2} \mathbf{T}' \mathbf{T} \mathbf{u}_i,$$

where  $c_T := 1 - \|\mathbf{T}\mathbf{u}_i\|^{-1}$  and  $\otimes$  denotes the Kronecker product [94]. The Hessian  $\nabla^2 f|_{\mathbf{x}} = \begin{bmatrix} \mathbf{H}_{\mathbf{T},\mathbf{T}} & \mathbf{H}_{\mathbf{T},\mathbf{b}} \\ \mathbf{H}'_{\mathbf{T},\mathbf{b}} & \mathbf{H}_{\mathbf{b},\mathbf{b}} \end{bmatrix}$  is given by the following submatrices

$$\begin{aligned} \mathbf{H}_{\mathbf{T},\mathbf{T}} &= \sum_{i=1}^n \frac{2}{\sigma_{m_i}^2} \left[ \frac{(\mathbf{u}_i \mathbf{u}'_i) \otimes (\mathbf{T}\mathbf{u}_i \mathbf{u}'_i \mathbf{T}')}{\|\mathbf{T}\mathbf{u}_i\|^3} + c_T [(\mathbf{u}_i \mathbf{u}'_i) \otimes \mathbf{I}] \right], \\ \mathbf{H}_{\mathbf{T},\mathbf{b}} &= \sum_{i=1}^n \frac{-2}{\sigma_{m_i}^2} \left[ \frac{(\mathbf{u}_i \otimes \mathbf{T}\mathbf{u}_i) \mathbf{u}'_i \mathbf{T}' \mathbf{T}}{\|\mathbf{T}\mathbf{u}_i\|^3} + c_T (\mathbf{u}_i \otimes \mathbf{T} + \mathbf{I} \otimes \mathbf{T}\mathbf{u}_i) \right], \\ \mathbf{H}_{\mathbf{b},\mathbf{b}} &= \sum_{i=1}^n \frac{2}{\sigma_{m_i}^2} \left[ \frac{\mathbf{T}' \mathbf{T}\mathbf{u}_i \mathbf{u}'_i \mathbf{T}' \mathbf{T}}{\|\mathbf{T}\mathbf{u}_i\|^3} + c_T \mathbf{T}' \mathbf{T} \right]. \end{aligned}$$





# Bibliography

- [1] J. Abel and J. Chaffee. Existence and uniqueness of GPS solutions. *IEEE Transactions on Aerospace and Electronic Systems*, 27(6):952–956, November 1991.
- [2] A. Alcocer, P. Oliveira, and A. Pascoal. Study and implementation of an EKF GIB-based underwater positioning system. *IFAC Journal of Control Engineering Practice*, 15(6):689–701, June 2007.
- [3] R. Alonso and M. D. Shuster. Complete linear attitude-independent magnetometer calibration. *The Journal of the Astronautical Sciences*, 50(4):477–490, October-December 2002.
- [4] Brian D. O. Anderson and John B. Moore. *Optimal Filtering*. Dover Publications Inc., 1979.
- [5] D. Angeli. An almost global notion of input-to-state stability. *IEEE Transactions on Automatic Control*, 49(6):866–874, 2004.
- [6] J. L. Awange and E. W. Grafarend. Algebraic solution of GPS pseudo-ranging equations. *GPS Solutions*, 5(4):20–32, April 2002.
- [7] S. Bancroft. An algebraic solution of the GPS equations. *IEEE Transactions on Aerospace and Electronic Systems*, AES-21(1):56–59, January 1985.
- [8] I. Y. Bar-Itzhack and R. R. Harman. Optimized TRIAD algorithm for attitude determination. *AIAA Journal of Guidance, Control, and Dynamics*, 20(1):208–211, January 1997.
- [9] I. Y. Bar-Itzhack and J. Meyer. On the convergence of iterative orthogonalization processes. *IEEE Transactions on Aerospace and Electronic Systems*, AES-12(2):146–151, March 1976.
- [10] Yaakov Bar-Shalom, X. Rong Li, and Thiagalingam Kirubarajan. *Estimation with Applications to Tracking and Navigation*. Wiley-Interscience, 2001.
- [11] P. Batista, C. Silvestre, and P. Oliveira. Position and velocity navigation filters for marine vehicles. In *17th IFAC World Congress*, Seoul, South Korea, July 2008.
- [12] D. P. Bertsekas. *Nonlinear Programming*. Athena Scientific, 2nd edition, 1999.

- [13] S. P. Bhat and D. S. Bernstein. A topological obstruction to continuous global stabilization of rotational motion and the unwinding phenomenon. *Systems and Control Letters*, 39(1):63–70, January 2000.
- [14] I. Biton, M. Koifman, and I. Y. Bar-Itzhack. Improved direct solution of the global positioning system equation. *Journal of Guidance, Control, and Dynamics*, 21(1):45–49, January-February 1998.
- [15] S. Bittanti, P. Colaneri, and G. Nicolao. An algebraic riccati equation for the discrete-time periodic prediction problem. *Systems and Control Letters*, pages 71–78, 1990.
- [16] S. Bonnabel, P. Martin, and P. Rouchon. Symmetry-preserving observers. *IEEE Transactions on Automatic Control*, 53(11):2514–2526, Dec. 2008.
- [17] J. E. Bortz. A new mathematical formulation for strapdown inertial navigation. *IEEE Transactions on Aerospace and Electronic Systems*, 7(1):61–66, January 1971.
- [18] N. Bowditch. *The American Practical Navigator*. Hydrographic/Topographic Center, Defense Mapping Agency, 1984.
- [19] S. Brás, J. F. Vasconcelos, C. Silvestre, and P. Oliveira. Pose observers for unmanned air vehicles. In *Proceedings of the 2009 European Control Conference*, Budapest, Hungary, August 2009.
- [20] K. R. Britting. *Inertial Navigation Systems Analysis*. John Wiley & Sons, Inc., 1971.
- [21] R. G. Brown. Integrated navigation systems and Kalman filtering: A perspective. *Journal of the Institute of Navigation*, 19(4):355–362, 1972.
- [22] R. G. Brown and P. Y. C. Hwang. *Introduction to Random Signals and Applied Kalman Filtering*. John Wiley & Sons, Inc., third edition, 1997.
- [23] M. Bryson and S. Sukkarieh. Vehicle model aided inertial navigation for a UAV using low-cost sensors. In *Australasian Conference on Robotics and Automation*, Canberra, Australia, December 2004.
- [24] G. Calafiore. Approximation of n-dimensional data using spherical and ellipsoidal primitives. *IEEE Transactions on Systems, Man and Cybernetics - Part A: Systems and Humans*, 32(2):269–278, March 2002.
- [25] M. J. Caruso. Applications of magnetoresistive sensors in navigation systems. Technical report, Honeywell Inc., 1998.
- [26] E. Celledoni, A. Marthinsen, and B. Owren. Commutator-free Lie group methods. *Future Generation Computer Systems*, 19(3):341–352, 2003.
- [27] J. Chaffee and J. Abel. On the exact solutions of pseudorange equations. *IEEE Transactions on Aerospace and Electronic Systems*, 30(4):1021–1030, October 1994.

- [28] N. A. Chaturvedi, A. M. Bloch, and N. H. McClamroch. Global stabilization of a fully actuated mechanical system on a Riemannian manifold including control saturation effects. In *Decision and Control, 2006 45th IEEE Conference on*, pages 6116–6121, Dec. 2006.
- [29] N. A. Chaturvedi and N. H. McClamroch. Asymptotic stabilization of the hanging equilibrium manifold of the 3D pendulum. *International Journal of Robust and Nonlinear Control*, 17(16), 2007.
- [30] G. S. Chirikjian and A. B. Kyatkin. *Engineering Applications of Noncommutative Harmonic Analysis: With Emphasis on Rotation and Motion Groups*. CRC, 2000.
- [31] D. Choukroun, I. Y. Bar-Itzhack, and Y. Oshman. Optimal-request algorithm for attitude determination. *Journal of Guidance, Control, and Dynamics*, 27(3):418–425, May-June 2004.
- [32] D. Choukroun, I.Y. Bar-Itzhack, and Y. Oshman. Novel quaternion kalman filter. *Aerospace and Electronic Systems, IEEE Transactions on*, 42(1):174–190, Jan. 2006.
- [33] D. Choukroun, H. Weiss, I.Y. Bar-Itzhack, and Y. Oshman. Kalman filtering for matrix estimation. *Aerospace and Electronic Systems, IEEE Transactions on*, 42(1):147–159, Jan. 2006.
- [34] J. J. Craig. *Introduction to Robotics: Mechanics and Control*. Prentice-Hall, 3 edition, 2003.
- [35] J. L. Crassidis. Sigma-point Kalman filtering for integrated GPS and inertial navigation. *IEEE Transactions on Aerospace and Electronic Systems*, 42(2):750–756, 2006.
- [36] J. L. Crassidis, K. Lai, and R. R. Harman. Real-time attitude-independent three-axis magnetometer calibration. *Journal of Guidance, Control, and Dynamics*, 28(1):115–120, January-February 2005.
- [37] J. L. Crassidis, F. L. Markley, and Y. Cheng. Survey of nonlinear attitude estimation methods. *Journal of Guidance, Control, and Dynamics*, 30(1):12–28, January-February 2007.
- [38] P.E. Crouch and R. Grossman. Numerical integration of ordinary differential equations on manifolds. *Journal of Nonlinear Science*, 3(1):1–33, 1993.
- [39] R. Cunha, B. Guerreiro, and C. Silvestre. Vario X-treme helicopter nonlinear model: Complete and simplified expressions. Technical report, Institute for Systems and Robotics, 2005.
- [40] R. Cunha and C. Silvestre. Dynamic modeling and stability analysis of model-scale helicopters with bell-hiller stabilizing bar. *AIAA Guidance, Navigation and Control Conference*, 2003.

- [41] W. Denne. *Magnetic Compass Deviation and Correction*. Sheridan House Inc, 3rd edition, 1979.
- [42] G. Dissanayake and S. Sukkarieh. The aiding of a low-cost strapdown inertial measurement unit using vehicle model constraints for land vehicle applications. *IEEE Transactions on Robotics and Automation*, 17(5):731–747, October 2001.
- [43] A. Edelman, T. A. Arias, and S. T. Smith. The geometry of algorithms with orthogonality constraints. *SIAM Journal on Matrix Analysis and Applications*, 20(2):303–353, 1998.
- [44] G. H. Elkaim and C. Foster. Development of the metasensor: A low-cost attitude heading reference system for use in autonomous vehicles. In *Proceedings of the ION Global Navigation Satellite Systems Conference (ION-GNSS 2006)*, Fort Worth, TX, USA, September 2006.
- [45] G. H. Elkaim and C. Foster. Extension of a non-linear, two-step calibration methodology to include non-orthogonal sensor axes. *IEEE Journal of Aerospace Electronic Systems*, Technical Note, submitted August 2006, accepted for publication, 2006.
- [46] J. Farrell and M. Barth. *Global Positioning System and Inertial Navigation*. McGraw-Hill, 1999.
- [47] T. I. Fossen. *Guidance and Control of Ocean Vehicles*. Wiley, 1994.
- [48] T. I. Fossen, S. I. Sagatun, and A. J. Srensen. Identification of dynamically positioned ships. *Journal of Control Engineering Practice*, 4(3):369–376, March 1996.
- [49] D. Fragopoulos and M. Innocenti. Stability considerations in quaternion attitude control using discontinuous Lyapunov functions. *IEE Proceedings on Control Theory and Applications*, 151(3):253–258, May 2004.
- [50] G. F. Franklin, J. D. Powell, and M. Workman. *Digital Control of Dynamic Systems*. Addison Wesley, 3rd edition, 1998.
- [51] D. Gabay. Minimizing a differentiable function over a differential manifold. *Journal of Optimization Theory and Applications*, 37(2):177–219, June 1982. Communicated by D. G. Luenberger.
- [52] B. Gambhir. Determination of magnetometer biases using module RESIDG. Technical Report 3000-32700-01TN, Computer Sciences Corporation, March 1975.
- [53] W. Gander, G. H. Golub, and R. Strebel. Least-squares fitting of circles and ellipses. *BIT*, 43:558–578, 1994.
- [54] Yuan Gao, Wen-Jing Jia, Xiao-Jun Sun, and Zi-Li Deng. Self-tuning multisensor weighted measurement fusion kalman filter. *Aerospace and Electronic Systems, IEEE Transactions on*, 45(1):179–191, January 2009.

- [55] D. Gebre-Egziabher, G. H. Elkaim, J. D. Powell, and B. W. Parkinson. Calibration of strapdown magnetometers in magnetic field domain. *ASCE Journal of Aerospace Engineering*, 19(2):1–16, April 2006.
- [56] A. Gelb. *Applied Optimal Estimation*. MIT Press, 1974.
- [57] P. Gomes, C. Silvestre, A. Pascoal, and R. Cunha. A path-following controller for the delfimx autonomous surface craft. In *7th IFAC Conference of Manoeuvring and Control of Marine Craft*, Lisbon, Portugal, September 2006.
- [58] P. Gomes, C. Silvestre, A. Pascoal, and R. Cunha. A coastline following preview controller for the DELFIMx vehicle. In *17th International Offshore and Polar Engineering Conference & Exhibition*, Lisbon, Portugal, July 2007.
- [59] D. Goshen-Meskin and I. Y. Bar-Itzhack. Observability analysis of piece-wise constant systems - Part I: Theory. *IEEE Transactions on Aerospace and Electronic Systems*, 28(4):1056–1067, October 1992.
- [60] D. Goshen-Meskin and I. Y. Bar-Itzhack. Observability analysis of piece-wise constant systems - Part II: Application to inertial navigation in-flight alignment. *IEEE Transactions on Aerospace and Electronic Systems*, 28(4):1068–1075, October 1992.
- [61] J. C. Gower and G. B. Dijkstra. *Procrustes Problems*. Number 30 in Oxford Statistical Science Series. Oxford University Press, USA, 2004.
- [62] M. S. Grewal, L. R. Weill, and A. P. Andrews. *Global Positioning Systems, Inertial Navigation, and Integration*. Wiley-Interscience, 2nd edition, 2007.
- [63] B. Guerreiro, C. Silvestre, P. Oliveira, and J. F. Vasconcelos. Nonlinear and geometric optimization methods for ladar calibration. In *IEEE International Conference on Robotics and Automation*, pages 1406–1411, May 2008.
- [64] O. Hegrenaes, E. Berglund, and O. Hallingstad. Model-aided inertial navigation for underwater vehicles. In *IEEE International Conference on Robotics and Automation*, pages 1069–1076, May 2008.
- [65] W. T. Higgins. A comparison of complementary and Kalman filtering. *IEEE Transactions on Aerospace and Electronic Systems*, AES-11(3):321–325, 1975.
- [66] T. E. Humphreys, M. L. Psiaki, E. M. Klatt, S. P. Powell, and Jr. P. M. Kintner. Magnetometer-based attitude and rate estimation for spacecraft with wire booms. *Journal of Guidance, Control, and Dynamics*, 28(4):584–593, July-August 2005.
- [67] M. B. Ignagni. Efficient class of optimized coning compensation algorithms. *AIAA Journal of Guidance, Control, and Dynamics*, 19(2):424–429, March-April 1996.
- [68] M. B. Ignagni. Duality of optimal strapdown sculling and coning compensation algorithms. *Journal of the Institute of Navigation*, 45(2):85–95, 1998.

- [69] Andrew H. Jazwinski. *Stochastic Processes and Filtering Theory*. Academic Press, 1970.
- [70] S. J. Julier and H. F. Durrant-Whyte. On the role of process models in autonomous land vehicle navigation systems. *IEEE Transactions on Robotics and Automation*, 19(1):1–13, February 2003.
- [71] S. J. Julier and J. K. Uhlmann. Unscented filtering and nonlinear estimation. *Proceedings of the IEEE*, 92(3):401–422, Mar 2004.
- [72] D. Jung and P. Tsiotras. Inertial attitude and position reference system development for a small UAV. In *AIAA Infotech at Aerospace, Rohnert Park, CA*, May 2007.
- [73] B. Kågström. Bounds and perturbation bounds for the matrix exponential. *BIT Numerical Mathematics*, 17(1):39–57, 1977.
- [74] E.D. Kaplan and C.J. Hegarty. *Understanding GPS: principles and applications*. Artech House Publishers, 2006.
- [75] S. M. Kay. *Fundamentals of Statistical Signal Processing: Estimation*. Prentice-Hall, Upper Saddle River, New Jersey, USA, 1993.
- [76] Myron Kayton and Walter R. Fried. *Avionics Navigation Systems*. Wiley-Interscience, 2 edition, 1997.
- [77] H. K. Khalil. *Nonlinear Systems*. Prentice Hall, 2nd edition, 1996.
- [78] H. K. Khalil. *Nonlinear Systems*. Prentice Hall, 3rd edition, 2001.
- [79] J. C. Kinsey, R. M. Eustice, and L. L. Whitcomb. A survey of underwater vehicle navigation: Recent advances and new challenges. In *7th IFAC Conference of Manoeuvring and Control of Marine Craft*, Lisbon, Portugal, September 2006. Invited paper.
- [80] J. C. Kinsey and L. L. Whitcomb. Adaptive identification on the group of rigid-body rotations and its application to underwater vehicle navigation. *IEEE Transactions on Robotics*, 23(1):124–136, February 2007.
- [81] D. E. Koditschek. The application of total energy as a Lyapunov function for mechanical control systems. *Control Theory and Multibody Systems*, 97:131–151, 1989.
- [82] M. Koifman and I. Y. Bar-Itzhack. Inertial navigation system aided by aircraft dynamics. *IEEE Transactions on Control Systems Technology*, 7(4):487–493, July 1999.
- [83] C. Lageman, R. Mahony, and J. Trumpf. State observers for invariant dynamics on a Lie group. In *18th International Symposium on Mathematical Theory of Networks and Systems*, page 8, 2008.

- [84] C. Lageman, J. Trumppf, and R. Mahony. Gradient-like observers for invariant dynamics on a Lie group. *IEEE Transactions on Automatic Control*, 2008. Conditionally accepted for publication August 2008.
- [85] J.M. Lee. *Introduction to Smooth Manifolds*. Springer, 2002.
- [86] P. M. Lee, B. H. Jeon, S. M. Kim, H. T. Choi, C. M. Lee, T. Aoki, and T. Hyakudome. An integrated navigation system for autonomous underwater vehicles with two range sonars, inertial sensors and doppler velocity log. In *OCEANS 2004. Proceedings of MTS/IEEE*, volume 3, pages 1586–1593, November 2004.
- [87] T. Lee, M. Leok, and N. H. McClamroch. Global symplectic uncertainty propagation on  $so(3)$ . In *Decision and Control, 2008 47th IEEE Conference on*, pages 61–66, Dec. 2008.
- [88] T. Lee, M. Leok, N. H. McClamroch, and A. Sanyal. Global attitude estimation using single direction measurements. In *Proceedings of the 2007 American Control Conference*, pages 3659–3664, New York, USA, July 2007.
- [89] Taeyoung Lee, N. A. Chaturvedi, A. Sanyal, M. Leok, and N. H. McClamroch. Propagation of uncertainty in rigid body attitude flows. In *Decision and Control, 2007 46th IEEE Conference on*, pages 2689–2694, Dec. 2007.
- [90] E. J. Lefferts, F. L. Markley, and M. D. Shuster. Kalman filtering for spacecraft attitude estimation. *Journal of Guidance, Control, and Dynamics*, 5(5):417–429, 1982.
- [91] J. L. Leva. An alternative closed-form solution to the GPS pseudo-range equations. *IEEE Transactions on Aerospace and Electronic Systems*, 32(4):1430–1439, October 1996.
- [92] A. Loría. Explicit convergence rates for MRAC-type systems. *Automatica*, 40(8):1465–1468, August 2004.
- [93] A. Loría and E. Panteley. Uniform exponential stability of linear time-varying systems: Revisited. *Systems and Control Letters*, 47(1):13–24, September 2002.
- [94] H. Lütkepohl. *Handbook of Matrices*. John Wiley & Sons, 1997.
- [95] X. Ma, S. Sukkarieh, and J. Kim. Vehicle model aided inertial navigation. In *IEEE Intelligent Transportation Systems*, volume 2, pages 1004–1009, Shanghai, China, October 2003.
- [96] R. Mahony, T. Hamel, and J.-M. Pfimlin. Nonlinear complementary filters on the special orthogonal group. *IEEE Transactions on Automatic Control*, 53(5):1203–1218, June 2008.
- [97] M. Malisoff, M. Krichman, and E. D. Sontag. Global stabilization for systems evolving on manifolds. *Journal of Dynamical and Control Systems*, 12(2):161–184, April 2006.



- [98] F. L. Markley. Attitude determination and parameter estimation using vector observations: Theory. *The Journal of the Astronautical Sciences*, 37(1):41–58, January-March 1989.
- [99] F. L. Markley. Attitude error representations for Kalman filtering. *AIAA Journal of Guidance, Control, and Dynamics*, 26(2):311–317, March-April 2003.
- [100] F. L. Markley and D. Mortari. Quaternion attitude estimation using vector observations. *Journal of the Astronautical Sciences*, 40(2/3):359–380, 2000.
- [101] G. Meinsma. On Rantzer’s density function. In *25th Benelux Meeting*, Heeze, The Netherlands, March 2006.
- [102] Shmuel Merhav. *Aerospace Sensor Systems and Applications*. Springer-Verlag New York Inc., 1998.
- [103] P. Monzon. On necessary conditions for almost global stability. *IEEE Transactions on Automatic Control*, 48(4):631–634, April 2003.
- [104] A. Morawiec. *Orientations and Rotations: Computations in Crystallographic Textures (Engineering Materials and Processes)*. Springer, 2003.
- [105] M. Morgado, C. Silvestre, P. Oliveira, and J. F. Vasconcelos. Improving aiding techniques for USBL tightly-coupled inertial navigation system. In *17th IFAC World Congress*, Seoul, Korea, July 2008.
- [106] H. Munthe-Kaas. High order Runge-Kutta methods on manifolds. *Applied Numerical Mathematics*, 29(1):115–127, 1999.
- [107] R. M. Murray, Z. Li, and S. S. Sastry. *A Mathematical Introduction to Robotic Manipulation*. CRC, 1994.
- [108] National Oceanic and Atmospheric Administration, U. S. Department of Commerce. *NOAA Technical Report: The US/UK World Magnetic Model for 2005-2010*, 2004.
- [109] A. V. Oppenheim, R. W. Schaffer, and J. R. Buck. *Discrete-Time Signal Processing*. Signal Processing. Prentice-Hall, 2 edition, 1999.
- [110] B. Owren. Order conditions for commutator-free Lie group methods. *Journal of Physics A-Mathematical and General*, 39(19):5585–5600, 2006.
- [111] J. Park and W.K. Chung. Geometric integration on euclidean group with application to articulated multibody systems. *IEEE Transactions on Robotics*, 21(5):850–863, 2005.
- [112] Sanghyuk Park. *Avionics and Control System Development for Mid-Air Rendezvous of Two Unmanned Aerial Vehicles*. PhD thesis, MIT, February 2004.



- [113] A. Pascoal, I. Kaminer, and P. Oliveira. Navigation system design using time varying complementary filters. *IEEE Aerospace and Electronic Systems*, 36(4):1099–1114, October 2000.
- [114] M. E. Pittelkau. Rotation vector in attitude estimation. *AIAA Journal of Guidance, Control, and Dynamics*, 26(6):855–860, November-December 2003.
- [115] A. Rantzer. A dual to Lyapunov’s stability theorem. *Systems and Control Letters*, 42(3):161–168, March 2000.
- [116] A. Rantzer. An converse theorem for density functions. In *41st IEEE Conference on Decision and Control*, volume 2, pages 1890–1891, Dec. 2002.
- [117] H. Rehbinder and B. K. Ghosh. Pose estimation using line-based dynamic vision and inertial sensors. *IEEE Transactions on Automatic Control*, 48(2):186–199, February 2003.
- [118] J. Roberts, P. Corke, and G. Buskey. Low-cost flight control system for a small autonomous helicopter. In *IEEE International Conference on Robotics and Automation*, pages 546–551, Taipei, September 2003.
- [119] Robert M. Rogers. *Applied Mathematics in Integrated Navigation Systems*. AIAA, 2003.
- [120] K. M. Roscoe. Equivalency between strapdown inertial navigation coning and sculling integrals/algorithms. *AIAA Journal of Guidance, Control, and Dynamics*, 24(2):201–205, March-April 2001.
- [121] Halsey Royden. *Real Analysis*. Prentice Hall, 1988.
- [122] W. J. Rugh. *Linear System Theory*. Prentice-Hall, 2 edition, 1995.
- [123] S. Salcudean. A globally convergent angular velocity observer for rigid body motion. *IEEE Transactions on Automatic Control*, 36(12):1493–1497, December 1991.
- [124] Amit K. Sanyal, Taeyoung Lee, Melvin Leok, and N. Harris McClamroch. Global optimal attitude estimation using uncertainty ellipsoids. *Systems & Control Letters*, 57(3):236–245, 2008.
- [125] S. S. Sastry. *Nonlinear systems: analysis, stability, and control*. Interdisciplinary Applied Mathematics. Springer, 1999.
- [126] P. G. Savage. Strapdown inertial navigation integration algorithm design part 1: Attitude algorithms. *AIAA Journal of Guidance, Control, and Dynamics*, 21(1):19–28, January-February 1998.

- [127] P. G. Savage. Strapdown inertial navigation integration algorithm design part 2: Velocity and position algorithms. *AIAA Journal of Guidance, Control, and Dynamics*, 21(2):208–221, March-April 1998.
- [128] P. G. Savage. *Strapdown Analytics*, volume 1. Strapdown Associates, Inc., Maple Plain, MN, 2000.
- [129] M. D. Shuster and S. D. Oh. Three-axis attitude determination from vector observations. *AIAA Journal of Guidance, Control, and Dynamics*, 4(1):70–77, January-February 1981.
- [130] C. Silvestre, P. Oliveira, A. Pascoal, L. Silva, J. Santos, and M. Neves. Inspection and diagnosis of the Sines West breakwater. In *ICCE2004 29th, International Conference on Coastal Engineering*, Lisbon, September 2004.
- [131] E. D. Sontag. Input to state stability: Basic concepts and results. In P. Nistri and G. Stefani, editors, *Nonlinear and Optimal Control Theory*, pages 163–220. Springer-Verlag, Berlin, 2007.
- [132] D. M. Steinke and B. J. Buckham. A Kalman filter for the navigation of remotely operated vehicles. In *OCEANS 2005. Proceedings of MTS/IEEE*, volume 1, pages 581–588, September 2005.
- [133] Gilbert Strang. *Linear Algebra and Its Applications*. Brooks Cole, 3rd edition, 1988.
- [134] S. Sukkarieh, E. M. Nebot, and H. F. Durrant-Whyte. A high integrity IMU/GPS navigation loop for autonomous land vehicle applications. *Robotics and Automation, IEEE Transactions on*, 15(3):572–578, June 1999.
- [135] J. Thienel and R. M. Sanner. A coupled nonlinear spacecraft attitude controller and observer with an unknown constant gyro bias and gyro noise. *IEEE Transactions on Automatic Control*, 48(11):2011–2015, November 2003.
- [136] J. F. Vasconcelos, C. Silvestre, and P. Oliveira. Embedded vehicle dynamics and laser aiding techniques for inertial navigation systems. In *AIAA Guidance, Navigation, and Control Conference*, Keystone, CO, USA, August 2006.
- [137] J. F. Vasconcelos, C. Silvestre, and P. Oliveira. A landmark based nonlinear observer for attitude and position estimation with bias compensation. In *17th IFAC World Congress*, Seoul, Korea, July 2008.
- [138] J. F. Vasconcelos, C. Silvestre, and P. Oliveira. A nonlinear GPS/IMU based observer for rigid body attitude and position estimation. In *47th IEEE Conference on Decision and Control*, Cancun, Mexico, December 2008.
- [139] G. Wahba. A least-squares estimate of satellite attitude. *SIAM Review*, 7(3):409 problem 65–1, 1965.

- [140] J. Wertz, editor. *Spacecraft Attitude Determination and Control*. Kluwer Academic, 1978.
- [141] L. L. Whitcomb, D. R. Yoerger, and H. Singh. Combined Doppler/LBL based navigation of underwater vehicles. In *11th International Symposium on Unmanned Untethered Submersible Technology*, New Hampshire, USA, August 1999.
- [142] N. Wiener. *Extrapolation, Interpolation and Smoothing of Stationary Time Series*. John Wiley and Sons, New York, 1949.
- [143] X. Yun, E. R. Bachmann, R. B. McGhee, R. H. Whalen, R. L. Roberts, R. G. Knapp, A. J. Healey, and M. J. Zyda. Testing and evaluation of an integrated GPS/INS system for small AUV navigation. *IEEE Journal of Oceanic Engineering*, 24(3):396–404, Jul 1999.



# Publications

J. F. Vasconcelos, J. Calvário, P. Oliveira, and C. Silvestre. GPS aided IMU for unmanned air vehicles. In *5th IFAC/EURON Symposium on Intelligent Autonomous Vehicles*, Lisbon, Portugal, July 2004.

J. F. Vasconcelos, P. Oliveira, and C. Silvestre. Inertial navigation system aided by GPS and selective frequency contents of vector measurements. In *AIAA Guidance, Navigation, and Control Conference*, San Francisco, USA, August 2005.

M. Morgado, P. Oliveira, C. Silvestre, and J. F. Vasconcelos. USBL/INS integration technique for underwater vehicles. In *7th IFAC Conference on Manoeuvring and Control of Marine Vehicles*, Lisbon, Portugal, September 2006.

M. Morgado, P. Oliveira, C. Silvestre, and J. F. Vasconcelos. USBL/INS tightly-coupled integration technique for underwater vehicles. In *9th International Conference on Information Fusion*, Florence, Italy, July 2006.

J. F. Vasconcelos, M. Athans, S. Fekri, C. Silvestre, and P. Oliveira. Uncertainty vs performance tradeoffs in robust feedback control: A MIMO case study. In *45th IEEE Conference on Decision and Control*, San Diego, CA, USA, December 2006. IEEE.

J. F. Vasconcelos, C. Silvestre, and P. Oliveira. Embedded vehicle dynamics and laser aiding techniques for inertial navigation systems. In *AIAA Guidance, Navigation, and Control Conference*, Keystone, CO, USA, August 2006.

M. Morgado, P. Oliveira, C. Silvestre, and J. F. Vasconcelos. Vehicle dynamics aiding technique for USBL/INS underwater navigation system. In *IFAC Conference on Control Applications in Marine Systems*, Bol, Croatia, 2007.

J. F. Vasconcelos, R. Cunha, C. Silvestre, and P. Oliveira. Landmark based nonlinear observer for rigid body attitude and position estimation. In *46th IEEE Conference on Decision and Control*, December 2007.

B. Guerreiro, C. Silvestre, P. Oliveira, and J. F. Vasconcelos. Nonlinear and geometric optimization methods for ladar calibration. In *IEEE International Conference on Robotics and Automation*, pages 1406–1411, May 2008.

M. Morgado, C. Silvestre, P. Oliveira, and J. F. Vasconcelos. Improving aiding techniques for USBL tightly-coupled inertial navigation system. In *17th IFAC World Congress*, Seoul, Korea, July 2008.

J. F. Vasconcelos, G. Elkaim, C. Silvestre, P. Oliveira, and B. Cardeira. A geometric approach to strapdown magnetometer calibration in sensor frame. In *IFAC Workshop on Navigation, Guidance, and Control of Underwater Vehicles*, Killaloe, Ireland, April 2008.

J. F. Vasconcelos, C. Silvestre, and P. Oliveira. A landmark based nonlinear observer for attitude and position estimation with bias compensation. In *17th IFAC World Congress*, Seoul, Korea, July 2008.

J. F. Vasconcelos, C. Silvestre, and P. Oliveira. A nonlinear GPS/IMU based observer for rigid body attitude and position estimation. In *47th IEEE Conference on Decision and Control*, Cancun, Mexico, December 2008.

J. F. Vasconcelos, C. Silvestre, and P. Oliveira. Nonlinear observer for rigid body attitude estimation using vector observations. In *17th IFAC World Congress*, Seoul, Korea, July 2008.

S. Brás, R. Cunha, J. F. Vasconcelos, C. Silvestre, and P. Oliveira. Nonlinear attitude estimation using active vision and inertial measurements. In *48th IEEE Conference on Decision and Control*, Shanghai, China, December 2009.

S. Brás, J. F. Vasconcelos, C. Silvestre, and P. Oliveira. Pose observers for unmanned air vehicles. In *Proceedings of the 2009 European Control Conference*, Budapest, Hungary, August 2009.

J. F. Vasconcelos, M. Athans, S. Fekri, C. Silvestre, and P. Oliveira. Stability- and performance-robustness tradeoffs: MIMO mixed- $\mu$  vs complex- $\mu$  design. *International Journal of Robust and Nonlinear Control*, 19(3):259–294, 2009.

J. F. Vasconcelos, R. Cunha, C. Silvestre, and P. Oliveira. Stability of a nonlinear attitude observer on  $SO(3)$  with nonideal angular velocity measurements. In *Proceedings of the 2009 European Control Conference*, Budapest, Hungary, August 2009.

J. F. Vasconcelos, A. Rantzer, C. Silvestre, and P. Oliveira. Combination of Lyapunov functions and density functions for stability of rotational motion. In *48th IEEE Conference on Decision and Control*, Shanghai, China, December 2009.

J. F. Vasconcelos, C. Silvestre, P. Oliveira, P. Batista, and B. Cardeira. Discrete time-varying attitude complementary filter. In *Proceedings of the 2009 American Control Conference*, St. Louis, Missouri, USA, June 2009.

J. F. Vasconcelos, B. Carneira, C. Silvestre, P. Oliveira, and P. Batista. Discrete-time complementary filters for attitude and position estimation: Design, analysis and experimental validation. *IEEE Transactions on Control Systems Technology*, accepted for publication, 2010.

J. F. Vasconcelos, R. Cunha, C. Silvestre, and P. Oliveira. A nonlinear position and attitude observer on  $SE(3)$  using landmark measurements. *Systems & Control Letters*, accepted for publication, 2010.

J. F. Vasconcelos, G. Elkaim, C. Silvestre, P. Oliveira, and B. Carneira. A geometric approach to strapdown magnetometer calibration in sensor frame. *IEEE Transactions on Aerospace and Electronic Systems*, accepted for publication, 2010.

J. F. Vasconcelos, C. Silvestre, P. Oliveira, and B. Guerreiro. Embedded UAV model and LASER aiding techniques for inertial navigation systems. *Control Engineering Practice*, accepted for publication, 2010.